

Advances in Civil Engineering

Transfer Process, Retardation Measures of Industrial Pollutants and Heat in Soils

Lead Guest Editor: Bing Bai

Guest Editors: Reza Taherdangkoo, Xianze Cui, and Xingxin Chen





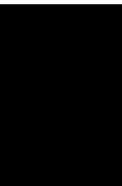
**Transfer Process, Retardation Measures of
Industrial Pollutants and Heat in Soils**

Advances in Civil Engineering

**Transfer Process, Retardation Measures
of Industrial Pollutants and Heat in
Soils**

Lead Guest Editor: Bing Bai

Guest Editors: Reza Taherdangkoo, Xianze Cui, and
Xingxin Chen



Copyright © 2022 Hindawi Limited. All rights reserved.

This is a special issue published in "Advances in Civil Engineering." All articles are open access articles distributed under the Creative Commons Attribution License, which permits unrestricted use, distribution, and reproduction in any medium, provided the original work is properly cited.






Chief Editor

Cumaraswamy Vipulanandan, USA














Associate Editors

Chiara Bedon , Italy
Constantin Chalioris , Greece
Ghassan Chehab , Lebanon
Ottavia Corbi, Italy
Mohamed ElGawady , USA
Husnain Haider , Saudi Arabia
Jian Ji , China
Jiang Jin , China
Shazim A. Memon , Kazakhstan
Hossein Moayedi , Vietnam
Sanjay Nimbalkar, Australia
Giuseppe Oliveto , Italy
Alessandro Palmeri , United Kingdom
Arnaud Perrot , France
Hugo Rodrigues , Portugal
Victor Yepes , Spain
Xianbo Zhao , Australia

Academic Editors

José A.F.O. Correia, Portugal
Glenda Abate, Italy
Khalid Abdel-Rahman , Germany
Ali Mardani Aghabaglou, Turkey
José Aguiar , Portugal
Afaq Ahmad , Pakistan
Muhammad Riaz Ahmad , Hong Kong
Hashim M.N. Al-Madani , Bahrain
Luigi Aldieri , Italy
Angelo Aloisio , Italy
Maria Cruz Alonso, Spain
Filipe Amarante dos Santos , Portugal
Serji N. Amirkhania, USA
Eleftherios K. Anastasiou , Greece
Panagiotis Ch. Anastasopoulos , USA
Mohamed Moafak Arbili , Iraq
Farhad Aslani , Australia
Siva Avudaiappan , Chile
Ozgur BASKAN , Turkey
Adewumi Babafemi, Nigeria
Morteza Bagherpour, Turkey
Qingsheng Bai , Germany
Nicola Baldo , Italy
Daniele Baraldi , Italy

Eva Barreira , Portugal
Emilio Bastidas-Arteaga , France
Rita Bento, Portugal
Rafael Bergillos , Spain
Han-bing Bian , China
Xia Bian , China
Huseyin Bilgin , Albania
Giovanni Biondi , Italy
Hugo C. Biscaia , Portugal
Rahul Biswas , India
Edén Bojórquez , Mexico
Giosuè Boscato , Italy
Melina Bosco , Italy
Jorge Branco , Portugal
Bruno Briseghella , China
Brian M. Broderick, Ireland
Emanuele Brunesi , Italy
Quoc-Bao Bui , Vietnam
Tan-Trung Bui , France
Nicola Buratti, Italy
Gaochuang Cai, France
Gladis Camarini , Brazil
Alberto Campisano , Italy
Qi Cao, China
Qixin Cao, China
Iacopo Carnacina , Italy
Alessio Cascardi, Italy
Paolo Castaldo , Italy
Nicola Cavalagli , Italy
Liborio Cavaleri , Italy
Anush Chandrappa , United Kingdom
Wen-Shao Chang , United Kingdom
Muhammad Tariq Amin Chaudhary, Kuwait
Po-Han Chen , Taiwan
Qian Chen , China
Wei Tong Chen , Taiwan
Qixiu Cheng, Hong Kong
Zhanbo Cheng, United Kingdom
Nicholas Chileshe, Australia
Prinya Chindaprasirt , Thailand
Corrado Chisari , United Kingdom
Se Jin Choi , Republic of Korea
Heap-Yih Chong , Australia
S.H. Chu , USA
Ting-Xiang Chu , China


Zhaofei Chu , China
Wonseok Chung , Republic of Korea
Donato Ciampa , Italy
Gian Paolo Cimellaro, Italy
Francesco Colangelo, Italy
Romulus Costache , Romania
Liviu-Adrian Cotfas , Romania
Antonio Maria D'Altri, Italy
Bruno Dal Lago , Italy
Amos Darko , Hong Kong
Arka Jyoti Das , India
Dario De Domenico , Italy
Gianmarco De Felice , Italy
Stefano De Miranda , Italy
Maria T. De Risi , Italy
Tayfun Dede, Turkey
Sadik O. Degertekin , Turkey
Camelia Delcea , Romania
Cristoforo Demartino, China
Giuseppe Di Filippo , Italy
Luigi Di Sarno, Italy
Fabio Di Trapani , Italy
Aboelkasim Diab , Egypt
Thi My Dung Do, Vietnam
Giulio Dondi , Italy
Jiangfeng Dong , China
Chao Dou , China
Mario D'Aniello , Italy
Jingtao Du , China
Ahmed Elghazouli, United Kingdom
Francesco Fabbrocino , Italy
Flora Faleschini , Italy
Dingqiang Fan, Hong Kong
Xueping Fan, China
Qian Fang , China
Salar Farahmand-Tabar , Iran
Ilenia Farina, Italy
Roberto Fedele, Italy
Guang-Liang Feng , China
Luigi Fenu , Italy
Tiago Ferreira , Portugal
Marco Filippo Ferrotto, Italy
Antonio Formisano , Italy
Guoyang Fu, Australia
Stefano Galassi , Italy

Junfeng Gao , China
Meng Gao , China
Giovanni Garcea , Italy
Enrique García-Macías, Spain
Emilio García-Taengua , United Kingdom
DongDong Ge , USA
Khaled Ghaedi, Malaysia
Khaled Ghaedi , Malaysia
Gian Felice Giaccu, Italy
Agathoklis Giaralis , United Kingdom
Ravindran Gobinath, India
Rodrigo Gonçalves, Portugal
Peilin Gong , China
Belén González-Fonteboa , Spain
Salvatore Grasso , Italy
Fan Gu, USA
Erhan Güneyisi , Turkey
Esra Mete Güneyisi, Turkey
Pingye Guo , China
Ankit Gupta , India
Federico Gusella , Italy
Kemal Hacıfendioglu, Turkey
Jianyong Han , China
Song Han , China
Asad Hanif , Macau
Hadi Hasanzadehshooiili , Canada
Mostafa Fahmi Hassanein, Egypt
Amir Ahmad Hedayat , Iran
Khandaker Hossain , Canada
Zahid Hossain , USA
Chao Hou, China
Biao Hu, China
Jiang Hu , China
Xiaodong Hu, China
Lei Huang , China
Cun Hui , China
Bon-Gang Hwang, Singapore
Jijo James , India
Abbas Fadhil Jasim , Iraq
Ahad Javanmardi , China
Krishnan Prabhakan Jaya, India
Dong-Sheng Jeng , Australia
Han-Yong Jeon, Republic of Korea
Pengjiao Jia, China
Shaohua Jiang , China

MOUSTAFA KASSEM , Malaysia
Mosbeh Kaloop , Egypt
Shankar Karuppannan , Ethiopia
John Kechagias , Greece
Mohammad Khajehzadeh , Iran
Afzal Husain Khan , Saudi Arabia
Mehran Khan , Hong Kong
Manoj Khandelwal, Australia
Jin Kook Kim , Republic of Korea
Woosuk Kim , Republic of Korea
Vaclav Koci , Czech Republic
Loke Kok Foong, Vietnam
Hailing Kong , China
Leonidas Alexandros Kouris , Greece
Kyriakos Kourousis , Ireland
Moacir Kripka , Brazil
Anupam Kumar, The Netherlands
Emma La Malfa Ribolla, Czech Republic
Ali Lakirouhani , Iran
Angus C. C. Lam, China
Thanh Quang Khai Lam , Vietnam
Luciano Lamberti, Italy
Andreas Lampropoulos , United Kingdom
Raffaele Landolfo, Italy
Massimo Latour , Italy
Bang Yeon Lee , Republic of Korea
Eul-Bum Lee , Republic of Korea
Zhen Lei , Canada
Leonardo Leonetti , Italy
Chun-Qing Li , Australia
Dongsheng Li , China
Gen Li, China
Jiale Li , China
Minghui Li, China
Qingchao Li , China
Shuang Yang Li , China
Sunwei Li , Hong Kong
Yajun Li , China
Shun Liang , China
Francesco Liguori , Italy
Jae-Han Lim , Republic of Korea
Jia-Rui Lin , China
Kun Lin , China
Shibin Lin, China

Tzu-Kang Lin , Taiwan
Yu-Cheng Lin , Taiwan
Hexu Liu, USA
Jian Lin Liu , China
Xiaoli Liu , China
Xuemei Liu , Australia
Zaobao Liu , China
Zhuang-Zhuang Liu, China
Diego Lopez-Garcia , Chile
Cristiano Loss , Canada
Lyan-Ywan Lu , Taiwan
Jin Luo , USA
Yanbin Luo , China
Jianjun Ma , China
Junwei Ma , China
Tian-Shou Ma, China
Zhongguo John Ma , USA
Maria Macchiaroli, Italy
Domenico Magisano, Italy
Reza Mahinroosta, Australia
Yann Malecot , France
Prabhat Kumar Mandal , India
John Mander, USA
Iman Mansouri, Iran
André Dias Martins, Portugal
Domagoj Matesan , Croatia
Jose Matos, Portugal
Vasant Matsagar , India
Claudio Mazzotti , Italy
Ahmed Mebarki , France
Gang Mei , China
Kasim Mermerdas, Turkey
Giovanni Minafò , Italy
Masoomah Mirrashid , Iran
Abbas Mohajerani , Australia
Fadzli Mohamed Nazri , Malaysia
Fabrizio Mollaioli , Italy
Rosario Montuori , Italy
H. Naderpour , Iran
Hassan Nasir , Pakistan
Hossein Nassiraei , Iran
Satheeskumar Navaratnam , Australia
Ignacio J. Navarro , Spain
Ashish Kumar Nayak , India
Behzad Nematollahi , Australia

Chayut Ngamkhanong , Thailand
Trung Ngo, Australia
Tengfei Nian, China
Mehdi Nikoo , Canada
Youjun Ning , China
Olugbenga Timo Oladinrin , United Kingdom
Oladimeji Benedict Olalusi, South Africa
Timothy O. Olawumi , Hong Kong
Alejandro Orfila , Spain
Maurizio Orlando , Italy
Siti Aminah Osman, Malaysia
Walid Oueslati , Tunisia
SUVASH PAUL , Bangladesh
John-Paris Pantouvakis , Greece
Fabrizio Paolacci , Italy
Giuseppina Pappalardo , Italy
Fulvio Parisi , Italy
Dimitrios G. Pavlou , Norway
Daniele Pellegrini , Italy
Gatheeshgar Perampalam , United Kingdom
Daniele Perrone , Italy
Giuseppe Piccardo , Italy
Vagelis Plevris , Qatar
Andrea Pranno , Italy
Adolfo Preciado , Mexico
Chongchong Qi , China
Yu Qian, USA
Ying Qin , China
Giuseppe Quaranta , Italy
Krishanu ROY , New Zealand
Vlastimir Radonjanin, Serbia
Carlo Rainieri , Italy
Rahul V. Ralegaonkar, India
Raizal Saifulnaz Muhammad Rashid, Malaysia
Alessandro Rasulo , Italy
Chonghong Ren , China
Qing-Xin Ren, China
Dimitris Rizos , USA
Geoffrey W. Rodgers , New Zealand
Pier Paolo Rossi, Italy
Nicola Ruggieri , Italy
JUNLONG SHANG, Singapore





Nikhil Saboo, India
Anna Saetta, Italy
Juan Sagaseta , United Kingdom
Timo Saksala, Finland
Mostafa Salari, Canada
Ginevra Salerno , Italy
Evangelos J. Sapountzakis , Greece
Vassilis Sarhosis , United Kingdom
Navaratnarajah Sathiparan , Sri Lanka
Fabrizio Scozzese , Italy
Halil Sezen , USA
Payam Shafigh , Malaysia
M. Shahria Alam, Canada
Yi Shan, China
Hussein Sharaf, Iraq
Mostafa Sharifzadeh, Australia
Sanjay Kumar Shukla, Australia
Amir Si Larbi , France
Okan Sirin , Qatar
Piotr Smarzewski , Poland
Francesca Sollecito , Italy
Rui Song , China
Tian-Yi Song, Australia
Flavio Stochino , Italy
Mayank Sukhija , USA
Piti Sukontasukkul , Thailand
Jianping Sun, Singapore
Xiao Sun , China
T. Tafsirojjaman , Australia
Fujiao Tang , China
Patrick W.C. Tang , Australia
Zhi Cheng Tang , China
Weerachart Tangchirapat , Thailand
Xiixin Tao, China
Piergiorgio Tataranni , Italy
Elisabete Teixeira , Portugal
Jorge Iván Tobón , Colombia
Jing-Zhong Tong, China
Francesco Trentadue , Italy
Antonello Troncone, Italy
Majbah Uddin , USA
Tariq Umar , United Kingdom
Muahmmad Usman, United Kingdom
Muhammad Usman , Pakistan
Mucteba Uysal , Turkey

Ilaria Venanzi , Italy
Castorina S. Vieira , Portugal
Valeria Vignali , Italy
Claudia Vitone , Italy
Liwei WEN , China
Chunfeng Wan , China
Hua-Ping Wan, China
Roman Wan-Wendner , Austria
Chaohui Wang , China
Hao Wang , USA
Shiming Wang , China
Wayne Yu Wang , United Kingdom
Wen-Da Wang, China
Xing Wang , China
Xiuling Wang , China
Zhenjun Wang , China
Xin-Jiang Wei , China
Tao Wen , China
Weiping Wen , China
Lei Weng , China
Chao Wu , United Kingdom
Jiangyu Wu, China
Wangjie Wu , China
Wenbing Wu , China
Zhixing Xiao, China
Gang Xu, China
Jian Xu , China
Panpan , China
Rongchao Xu , China
HE YONGLIANG, China
Michael Yam, Hong Kong
Hailu Yang , China
Xu-Xu Yang , China
Hui Yao , China
Xinyu Ye , China
Zhoujing Ye, China
Gürol Yildirim , Turkey
Dawei Yin , China
Doo-Yeol Yoo , Republic of Korea
Zhanping You , USA
Afshar A. Yousefi , Iran
Xinbao Yu , USA
Dongdong Yuan , China
Geun Y. Yun , Republic of Korea

Hyun-Do Yun , Republic of Korea
Cemal YİĞİT , Turkey
Paolo Zampieri, Italy
Giulio Zani , Italy
Mariano Angelo Zanini , Italy
Zhixiong Zeng , Hong Kong
Mustafa Zeybek, Turkey
Henglong Zhang , China
Jiupeng Zhang, China
Tingting Zhang , China
Zengping Zhang, China
Zetian Zhang , China
Zhigang Zhang , China
Zhipeng Zhao , Japan
Jun Zhao , China
Annan Zhou , Australia
Jia-wen Zhou , China
Hai-Tao Zhu , China
Peng Zhu , China
QuanJie Zhu , China
Wenjun Zhu , China
Marco Zucca, Italy
Haoran Zuo, Australia
Junqing Zuo , China
Robert Černý , Czech Republic
Süleyman İpek , Turkey

Contents


In Situ Research on the Spatiotemporal Variations in the Temperature and Deformation of Aeolian Sand-Modified Soil Roadbed Constructed in Cold Regions

Gao Li , Fubiao Zhou , Zhandong Su , Jingshan Bo, Xiang Chen, and Chi Li 
Research Article (18 pages), Article ID 7323463, Volume 2022 (2022)

Experimental Study on the Effect of Large Temperature Difference on Compressive Strength and Pore Structure of Semirigid Base

Ming Dai, Jia Pan , Yanjun Shen , Jianbo Deng, and Yeermulati Muhadeer
Research Article (17 pages), Article ID 4603007, Volume 2022 (2022)

Stability Evaluation of Proppant in Fractures of Gas Storage in Yulin Gas Field

Ping Wang, TianLi Gu , Zhanwu Gao, Jiayong Fan, Hai Huang, Zhan Qu, Qiang Han, and Zongxiao Ren
Research Article (12 pages), Article ID 2044561, Volume 2022 (2022)

Numerical Simulation of Coupling Support for High-Stress Fractured Soft Rock Roadway in Deep Mine

Wenhua Yuan , Ke Hong, Run Liu, Lianjie Ji, and Long Meng
Research Article (10 pages), Article ID 7221168, Volume 2022 (2022)




Influencing Factors of Snow Melting and Deicing on Carbon Fiber Embedded in Bridge Decks

Yan Tan , Shuang Zheng , Henglin Xiao , and JiaMing Xing 
Research Article (10 pages), Article ID 8773149, Volume 2022 (2022)


Geotechnical Characteristic Assessments of Floodplain Soils Using SCPTU Data in Nanjing, China

Mingfei Zhang, Liyuan Tong , and Qiang Wang 
Research Article (19 pages), Article ID 1669511, Volume 2022 (2022)

Study on the Nonlinear Damage Creep Model of the Weak Interlayer

Erjian Wei , Bin Hu , Kunyun Tian , Peishan Cen, Zhen Zhang, Zeqi Wang, and Shuxiang Chang
Research Article (8 pages), Article ID 3566521, Volume 2022 (2022)

Optimization Analysis of Mechanical Properties of Fly Ash-Based Multicontent Gasification Slag Paste Filling Material

Denghong Chen , Tianwei Cao, Ran Chen, and Chao Li
Research Article (11 pages), Article ID 5908317, Volume 2022 (2022)

Influence of Multistage Target Temperature and Cyclic Loading/Unloading on the Permeability of Polypropylene Fiber Concrete

Peishan Cen, Erjian Wei , and Kunyun Tian 
Research Article (11 pages), Article ID 6756069, Volume 2022 (2022)

Swelling Characteristics of Fractal-Textured Bentonite Eroded by Alkaline Solution

Guosheng Xiang , Weimin Ye, Zhijie Hu, Lei Ge, and Yinkang Zhou
Research Article (9 pages), Article ID 9100822, Volume 2022 (2022)

A Statistic Damage Model of Rocks considering the Effect of Loading Rate

Kai Cui, Bin Hu , and Jing Li 



Research Article (9 pages), Article ID 9124208, Volume 2022 (2022)

Breakage Characteristics of Quartz Sand Based on Ring Shear Tests: Implications for the Fragmentation Processes of Rock Avalanches

Xinxin Zheng , Ruichen Chen , Jian Chen , Song Chen , and Lulu Shi 


Research Article (12 pages), Article ID 7879067, Volume 2022 (2022)

Nonlinear Viscoelastic-Plastic Creep Model of Rock Based on Fractional Calculus

Erjian Wei, Bin Hu , Jing Li , Kai Cui, Zhen Zhang, Aneng Cui, and Liyao Ma



Research Article (7 pages), Article ID 3063972, Volume 2022 (2022)

Study on Strengthening Mechanism of Epoxy Resin/Rubber Concrete Interface by Molecular Dynamics Simulation

Lijuan Li, Dajing Qin , Zhijun Xu , and Yong Feng

Research Article (9 pages), Article ID 5100758, Volume 2022 (2022)

Research and Analysis on the Influence of Small Clear Distance Drilling and Blasting Method on the Existing Tunnel Structure

Haibin Huang, Peng Li, Chuang Wang, Bingxiang Yuan , Minjie Chen , and Weimin Feng

Research Article (8 pages), Article ID 4730936, Volume 2021 (2021)

Research Article

In Situ Research on the Spatiotemporal Variations in the Temperature and Deformation of Aeolian Sand-Modified Soil Roadbed Constructed in Cold Regions

Gao Li ^{1,2,3}, Fubiao Zhou ⁴, Zhandong Su ^{5,6}, Jingshan Bo,^{1,2,5} Xiang Chen,⁷ and Chi Li ⁸

¹Key Laboratory of Earthquake Engineering and Engineering Vibration, Institute of Engineering Mechanics, China Earthquake Administration, Harbin 150000, China

²Key Laboratory of Earthquake Disaster Mitigation, Ministry of Emergency Management, Harbin 150000, China

³China Non-ferrous Metals Resource Geological Survey, Beijing 100012, China

⁴Institute of Karst Geology, Chinese Academy of Geological Sciences, Guilin 541004, China

⁵Geological Engineering Department, Institute of Disaster Prevention, Sanhe 065201, China

⁶Hebei Key Laboratory of Earthquake Disaster Prevention and Risk Assessment, Sanhe 065201, China

⁷School of Civil Engineering, Beijing Jiaotong University, Beijing 100044, China

⁸College of Civil Engineering, Inner Mongolia University of Technology, Hohhot 010051, China

Correspondence should be addressed to Gao Li; 496527941@qq.com and Zhandong Su; szdchris@163.com

Received 7 January 2022; Revised 17 May 2022; Accepted 21 June 2022; Published 12 August 2022

Academic Editor: Ahad Javanmardi

Copyright © 2022 Gao Li et al. This is an open access article distributed under the Creative Commons Attribution License, which permits unrestricted use, distribution, and reproduction in any medium, provided the original work is properly cited.

Aiming at the cracking phenomenon of an aeolian sand-modified soil roadbed in an actual project near Tongliao city in eastern Inner Mongolia, Northeast China, an in situ test was conducted. Temperature-compensated fiber Bragg grating (FBG) strain sensors and moisture sensors were embedded into the test roadbed to monitor and observe the relationships between the temperature, moisture, and deformation of the roadbed with respect to variations in climate conditions in such a cold region. For the core issues of roadbed soil deformation and impact on the project, two climate conditions, namely, temperature and rainfall, were taken as external factors, while the temperature and moisture of the roadbed soil were taken as internal factors controlling the deformation and failure of the roadbed soil. A correlation analysis of the test roadbed monitoring data showed that the roadbed soil moisture was weakly affected by environmental conditions. The roadbed soil temperature was independent of the rainfall but was significantly related to air temperature variation (the correlation coefficient ranged from 0.6301 to 0.8926). Limited by the boundary conditions of the roadbed, the response of the variation in the roadbed soil temperature to the air temperature variation gradually weakened from the shallow surface to the deeper parts and the lag in the roadbed soil temperature variation relative to the air temperature variation became more evident. A correlation analysis of the monitoring data of the roadbed soil deformation, soil temperature, and soil moisture showed that the roadbed soil moisture had a weak correlation with the roadbed soil temperature. The roadbed soil deformation was independent of the soil moisture but was strongly related to the roadbed soil temperature. Therefore, the strain of the test roadbed could reflect the roadbed deformation as temperature deformation. The temperature deformation of the roadbed superficial soil was significantly greater than that of the deep soil.

1. Introduction

Aeolian sand, also known as desert sand, wind-blown sand, and dune sand, is sand that is formed, carried, and deposited by wind. The total area of desert, Gobi desert, and desertified land in China is 1.533 million km², including the arid regions of Xinjiang, Gansu, Qinghai, Ningxia, and western Inner

Mongolia, as well as the semiarid regions of eastern Inner Mongolia, northern Shaanxi, Liaoning, Jilin, and western Heilongjiang. Summers are scorching, winters are cold, and there is minimal rainfall in these locations. The yearly and daily temperature differences are both significant, with the average annual temperature difference ranging from 30 to 40°C [1]. With the gradual implementation of China's Belt

and Road Initiative and improvement in China's domestic transportation infrastructure, more roads and railroads are expected to eventually pass through desertification zones with large temperature differences.

In cold and arid desert areas, gravel supplies for highway and railway construction are limited. The use of aeolian sand, which is abundant, cheap, and easy to collect, is being explored as a road construction material. However, natural aeolian sand has low bearing capacity, low shear strength, poor uniform particle gradation, lack of cohesion, high porosity, high permeability coefficient, noncollapsibility, low plasticity, and low water content, among other properties. Natural aeolian sand must be modified to generate aeolian sand-modified soil before being used in actual high-grade line engineering. Aeolian sand-modified soil, which is also called aeolian sand-ameliorated/sand-treated/sand-improved soil or aeolian sand-stabilized soil, is a type of mixed material with stable properties realized by adding a modifier into natural aeolian sand. Cement was the very first modification used to improve the compressive and shear strengths of aeolian sand soil [2]. Currently, extensive studies have been conducted on the preparation of materials for cement-modified (stabilization) aeolian sand (including filled sand grading) [3] in terms of the cement content (8%–25%) [4], water-to-cement ratio, and curing time [2, 4, 5]; and comprehensive modification schemes [6], mechanical properties (including the compressive strength [2–5, 7–10], California bearing ratio (CBR) characteristics [7], shear strength [8, 11–13]; tensile strength [3, 10], maximum dry density, and optimal moisture content [5, 7, 8]); performance testing methods (such as a comparison between compaction methods [14]); and road construction technology [15]. These studies have shown that after full curing, the compressive and shear strengths of aeolian sand-modified soil mixed with an appropriate proportion of cement may be considerably enhanced, meeting roadbed engineering criteria. The findings provide scientific support for the engineering applications of aeolian sand-modified soils.

The surface of a high railway roadbed with aeolian sand-modified soil under construction in Ke'erqin District, Inner Mongolia, was found to exhibit transverse cracks at significantly low temperatures. This case has demonstrated the severity of temperature deformation disease in projects where aeolian sand-modified soil roadbed were constructed [16]. A series of physical and mechanical parameters should be considered in the modification of aeolian sand soil roadbeds in cold and arid regions: thermally induced soil deformation, heat convection between air and soil, internal heat conduction in soil, soil internal temperature field and stress field coupling interaction, degree of soil saturation, soil medium, and soil microstructure. Extensive research has been conducted on thermally induced soil deformation. According to the theoretical framework of thermodynamics and based on soil structure, the interaction of medium in soil caused by temperature variation has been considered [17], and a thermo-hydro-mechanical coupling model of soil has been established [18]. Studies on the cooling and shrinkage deformation law of cement-stabilized aeolian sand-modified soil have found significant soil shrinkage in a

negative-temperature environment [19, 20]. Laboratory investigations revealed that the lower the temperature, the lower the specific heat capacity, and the higher the thermal conductivity of cement-modified (stabilized) soil samples. Under appropriate conditions, a mixture of aeolian sand, cement, and clay can help minimize the temperature sensitivity of modified soils [16, 21, 22].

Existing research on the temperature deformation of aeolian sand-modified soil has mostly focused on theoretical analyses and laboratory soil sample testing; however, there has been no in situ testing of aeolian sand-modified roadbed deformation in a natural environment. The physical and mechanical parameters of aeolian sand-modified soil differ from those of real soil due to sample size limitations; a small-sample test cannot reflect the difference in the internal temperature deformation due to the spatial difference in the soil temperature during the internal heat conduction process. To address these issues, a large-scale in situ test roadbed filled with aeolian sand-modification soil was built beside the Tongliao–Xinmin northern railway project in the cold zone for this study. The monitoring sensor arrangement inside the roadbed was innovatively developed, with several types of sensors paired in nearby areas. This study, for the first time, has achieved multiparameter remote and autonomous monitoring of the soil moisture, temperature, and deformation of a large aeolian sand-modified soil roadbed constructed in a cold climate setting. This article discusses the temporal and spatial variations in the temperature and deformation of the aeolian sand-modified soil roadbed in cold regions based on the measured data. Moreover, it provides a scientific basis for temperature disease control of aeolian sand-modified soil roadbeds in such regions based on field tests.

2. Materials and Methods

2.1. Geographical Location of the Test Site. The test site was located in Ke'erqin, Inner Mongolia, China (Figure 1). The deformation characteristics of the aeolian sand-modified soil roadbed in a cold region with significant temperature variation were studied relying on the Tongliao–Xinmin high-speed railway project under construction.

The test site is located in the Ke'erqin Sandy Land, which is near the Tongliao city in the middle and lower reaches of the Xiliao River in eastern Inner Mongolia. Bounded by the Daxing'an Mountains in the northwest and the northern Hebei–Liaoxi mountains and hills in the south, high in the west, north, and south, low in the east and in the middle, the Ke'erqin Sandy Land forms a topography with a triangular zone that opens to the east, with an elevation range of 120–1500 m [23]. The Ke'erqin Sandy Land used to be the Ke'erqin Prairie with luxuriant aquatic plants given that the Xiliao River and the Xila Mulun River run through the area from west to east. Due to the open reclamation of wasteland in the late Qing Dynasty and a period of land reclamation in the early days of the founding of the People's Republic of China, the sandy soil layer under the Ke'erqin grassland gradually became desertified. Particularly in recent years, an increase in overloaded grazing and human activities,



FIGURE 1: Geographical location of the test site.

coupled with the dry climate, have made parts of this once beautiful grassland to evolve into the largest sandy land in China [24]. The aeolian sand-modified soil made of local natural aeolian sand as the filling material for the Tongliao–Xinmin high-speed railway roadbed is the most economical and reasonable choice for the construction of the Ke'erqin Sandy Railway.

The Tongliao–Xinmin high-speed railway has a total length of 197 km and a design speed of 250 km/h. The railway departs from Tongliao Station and passes through Kezuohou Banner and Zhangwu County, Liaoning Province, and connects to Xinmin North Station of Beijing–Shenyang high-speed railway (Figure 1). Crossing the two provinces of Inner Mongolia and Liaoning, it is the first high-speed railway in Inner Mongolia that is connected to the nationally planned “eight horizontal and eight vertical” high-speed rail network. This is of great significance for Tongliao city to further integrate into the Bohai Sea Rim, Central South Liaoning, and the Northeast Economic Circle, as well as for the integration of Beijing–Tianjin–Hebei and fostering economic development [25].

2.2. Climatic Conditions of the Test Site. The Ke'erqin Sandy Land, where the test site is located, has a temperate semiarid continental monsoon climate, and temperature variation has resulted in a natural temperature load on the Tongliao–Xinmin high-speed railway roadbed. Ke'erqin Sandy Land is cold and long in winter, windy and dry in spring, hot

and rainy in summer, and cool and short in autumn [24]. The annual precipitation in this area is in the range of 200–650 mm, of which 70% of the precipitation is concentrated during June to August. The annual evaporation is in the range of 1600–2400 mm, mainly concentrated during April to September, which is higher than 78% of the annual evaporation; the multiyear average relative moisture is 55% [26, 27]. Under the influence of the warm low pressure in the Pacific and the cold high pressure in Mongolia, the northwest wind and northerly wind prevail in winter and spring, and the southeast wind prevails in summer. The average annual wind speed is 3.5 m/s, the maximum wind speed is 21.7 m/s, and the number of windy days often reaches approximately 30 days [26, 28]. The annual sunshine hours are above 2800 h, and the annual average frost-free period is 140–150 days [27, 28]. The annual average air temperature is 6.6°C, the extreme maximum air temperature is 36.48°C, and the extreme minimum air temperature is –27.64°C. The temperature difference of the soil at a depth of 1 cm below the ground can reach 30°C or more between day and night. The maximum freezing depth of the sand is 205 cm [29, 30].

2.3. Materials and Parameters. The aeolian sand utilized in the test roadbed was obtained from the same area of the Tongliao–Xinmin northern railway project. It primarily contained quartz with small quantities of plagioclase and potash feldspar. The maximum dry density was 1.863 g/cm³,



FIGURE 2: Spatial relationship diagram of the test roadbed and the railway under construction.

the specific gravity of the soil particles was 2.685, the nonuniformity coefficient C_u was $2.1 < 5$, and the curvature coefficient C_c was $0.92 < 1$, suggesting that the particles were reasonably uniform and had a poor gradation [21]. The aeolian sand modifier was prepared with regular Portland cement and clay. Portland cement has a strength grade of P.O. 42.5 and an initial setting time of 117 min. Clay has an average moisture content of 8.8%, a plastic index of 10.19, and a liquid index of -0.59 . The maximum dry density of the aeolian sand-modified soil mixed with 5% cement and 10% clay was 1.87 g/cm^3 , and the best water content was 11.5%, based on laboratory experiments. The unconfined compressive strength and splitting tensile strength of the standard specimen were 0.7479 and 0.0398 MPa, respectively, after seven days of curing [16]. The linear expansion coefficient was $12.15 \cdot 10^{-6} / ^\circ\text{C}$ [22].

2.4. Scheme of the Test Roadbed. The test roadbed was built between and parallel to the Tongliao–Xinmin high-speed railway and the existing railway (Figure 2), with a total length of 150 m. It was divided into five equal roadbed sections constructed with five different modified materials. The bottom width of the roadbed is 15 m, the top width is 7 m, and the height is 4 m. This article discusses the influence of climate on the temperature and deformation of the roadbed of aeolian sand-modified soil based on only the test data of test roadbed Section 1. The mass ratio of the aeolian sand-modified soil material used in the roadbed of test roadbed Section 1 is as follows: cement mixing ratio—5%, clay soil mixing ratio—10%, and aeolian sand mixing ratio—85%.

The test roadbed was located approximately 10 km from the packing mixing station, and the material transit time was

less than 20 min. Pumping wells provided water for material mixing and roadbed maintenance near the mixing station and the test section. The mixing station could adjust the moisture content based on the temperature throughout the material mixing operation. The mixing moisture contents were 11.5%, 12.5%, and 13.5% in the temperature ranges of 20–25, 25–30, and 30–35°C, respectively. Eight dump-type transport vehicles ($26.5 \text{ m}^3/\text{vehicle}$) were employed to fill the roadbed. To maximize the management of water, the top of the transport vehicle was covered with light-colored geotextiles while transporting the supplies. After the packing was brought to the dumping location, the paving and rolling of the packing were completed promptly, and a bulldozer and a roller were used for continuous paving and rolling. Light-colored geotextiles were covered after rolling to avoid moisture (Figure 2). The duration between the start of material transportation and the completion of roadbed compaction should not exceed 117 min; that is, compaction must be finished prior to the initial setting of cement. Because the transverse cracks were presented before the surface roadbed material and auxiliary facilities setting, the roadbed surface materials of the experimental section and the actual operation roadbed are therefore not the same.

Roadbed filling: the filling and compaction tests were conducted in accordance with the Construction Code for Railway Roadbed (TB 10202–2002) [31]. The paving method combining layered filling, vibration compaction, and static compression is based on the assumption that the compaction degree is not less than 92% and that the seven-day unconfined compressive strength is not less than 0.25 MPa. By layering each layer with a thickness of 35 cm (compaction thickness of 30 cm and a loosening coefficient of 1.16), the optimal moisture content was 11.5%, and there were six



(a)



(b)



(c)



(d)



(e)



(f)

FIGURE 3: Continued.



FIGURE 3: Temperature, humidity, and deformation sensors embedded in the test roadbed soil and data collection terminal. (a) Buried groove excavation, (b) fiber optic cable layout, (c) humidity sensor, (d) burying of humidity sensor, (e) humidity sensor data collection terminal, (f) fiber grating (temperature) strain sensor, (g) embedded fiber grating (temperature) strain sensor, and (h) strain sensor data acquisition terminal.

compaction cycles (static pressure 1 time \rightarrow weak vibration 1 time \rightarrow strong vibration 2 times \rightarrow weak vibration 1 time \rightarrow static pressure 1 time). A combination of 22 t and 18 t rollers was used; the first static compaction and vibration compaction were performed by the 22 t roller, and the last static compaction and vibration compaction was performed by the 18 t roller. The longitudinal roller track overlap between the rows was greater than 40 cm, the longitudinal lap length was greater than 2 m, and the staggered joints of the upper and lower layers were greater than 3 m. Huge rollers cannot be employed within a 1 m range of the roadbed slope; therefore, small vibration rammer compaction was used instead. When a layer of filling qualified in the initial setting before the next filling layer is built, no additional care is required. If the next layer of paving is not completed before the initial setting due to sensor embedment or other reasons, the geotextile sprinkler maintenance must be completed within seven days.

2.5. Sensors and Layout. An appropriate number of temperature-compensated FBG strain sensors (mark graphic \blacktriangle , code TS, used for both temperature and deformation monitoring), FBG ordinary strain sensors (mark graphic \triangle , code S, used for soil deformation monitoring) [32], and plug-in probe soil moisture sensors (mark graphic \circ , code W, used for soil moisture monitoring) were embedded into the test roadbed. This was done to monitor the spatial distributions of the temperature, deformation, and moisture of the test roadbed soil in the cold climate environment, considering the sensor spatial distribution and cost (Figure 3). The sensors were embedded at the same time as roadbed filling. The sensors and wire were embedded in the positioning layer by digging a 0.2m deep trench after the

filler was filled 0.2 m above each positioning layer (F1–F5). Before the paving of next layer, the trench was backfilled with aeolian sand-modified soil before initial setting and compacted.

All the sensors were embedded at the space monitoring node of the test roadbed formed by the intersection of three vertical planes perpendicular to the long axis of the roadbed (abbreviated as cross sections H1, H2, and H3 from NW to SE), five horizontal planes (abbreviated as horizontal planes F1–F5 from bottom to top), and seven vertical longitudinal planes parallel to the long axis of the roadbed (abbreviated as longitudinal sections L1–L7 from NE to SW) (Figure 4). The long axis of all the deformation sensors embedded into the roadbed soil was consistent with the long axis of the test roadbed, and the deformation of the roadbed soil measured by the sensors was the deformation along the long axis of the roadbed.

Using a combination of letters and Arabic numerals to mark the sensors in the monitoring node in the roadbed, the first letter H corresponds to the cross section, and the numbers 1 to 3 represent cross sections H1–H3, respectively. The second letter F corresponds to the horizontal plane, and the numbers 1–5 represent the horizontal planes F1–F5, respectively. The third letter L corresponds to the longitudinal section, and the numbers 1 to 7 correspond to the longitudinal sections L1 to L7, respectively. For example, node numbers H2-F3-L4 represent nodes where cross section H2, the horizontal plane F3, and the longitudinal section L4 intersect. Furthermore, each sensor in the roadbed is assigned a unique number: node number + sensor type code, for example, the number H1-F2-L3-TS represents the temperature-compensated FBG strain sensor embedded at the monitoring node “H1-F2-L3” (the intersection between cross section H1, horizontal plane F2, and longitudinal section L3).

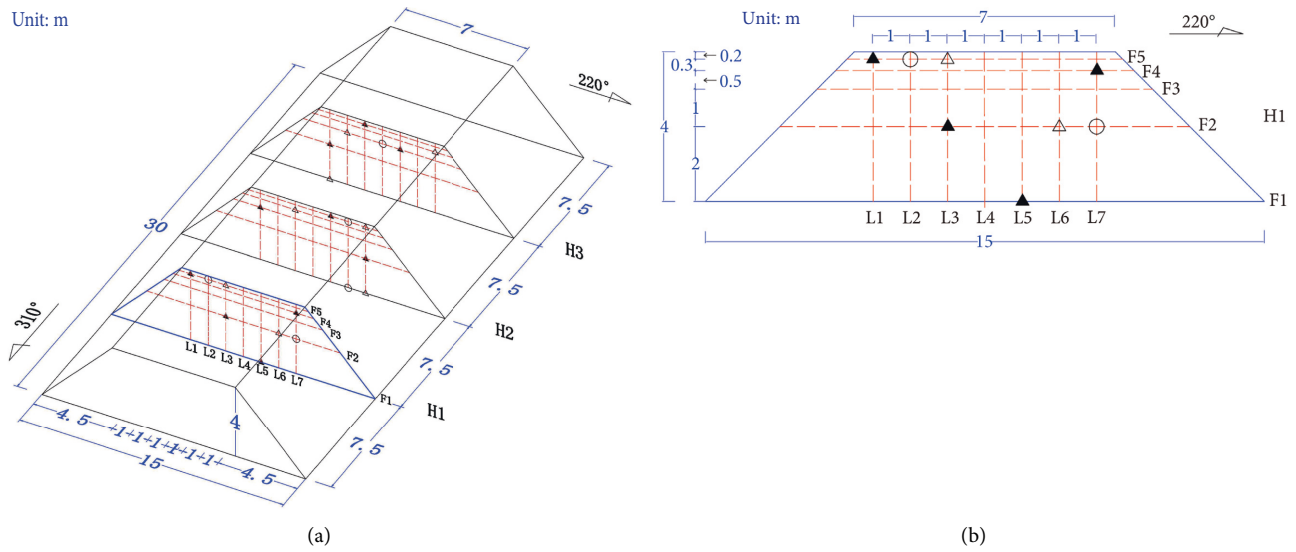


FIGURE 4: Schematic of the size of a single section of the aeolian sand-modified soil test roadbed and the location of the sensors. (a) Three-dimensional spatially diagram of the embedded sensor nodes and (b) position of the five horizontal planes and seven longitudinal planes.

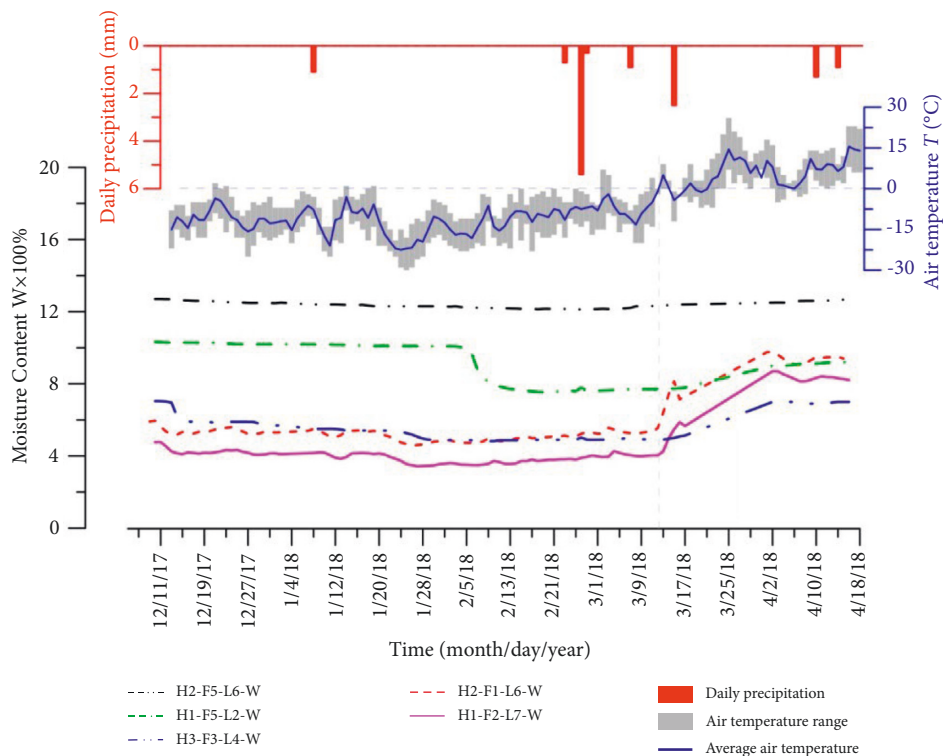


FIGURE 5: Curves of soil moisture of each layer in the roadbed under climatic conditions.

The sensors in the test roadbed were connected to the modem and data acquisition equipment via signal cables, and the moisture, temperature, and strain data were automatically collected and uploaded to the cloud platform through a wireless network. Thus, the monitoring data were collected remotely and uninterruptedly.

3. Monitoring Results

The sensors embedded into the roadbed produced monitoring data for a winter spanning from December 2017 to April 2018. The air temperature and rainfall data of the study area during the same monitoring period were obtained from the website of China National Meteorological Administration.

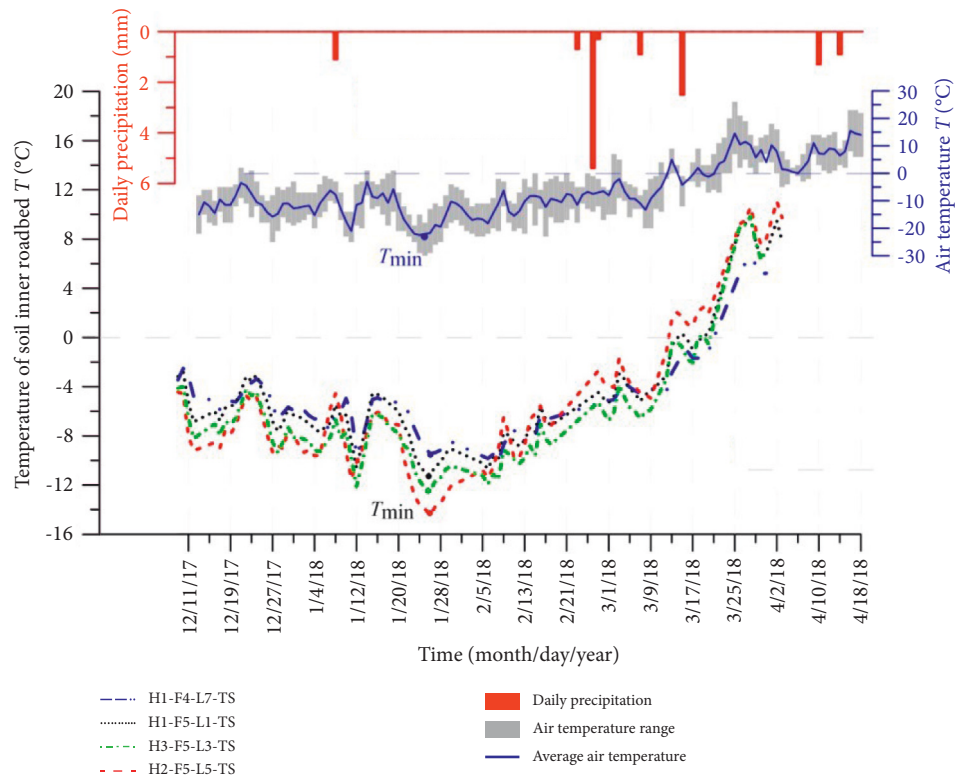


FIGURE 6: Curves of soil temperature in the F5 and F4 layers of the roadbed under climatic conditions.

3.1. Temporal and Spatial Variations in the Soil Moisture under Climatic Conditions. Figure 5 shows that during the monitoring period, the soil moisture in the F5 layer of the roadbed is relatively high, the soil moisture variation at H2-F5-L6-W is in the range of 12.1%–12.7% under the influence of the air temperature and rainfall, and the soil moisture variation curve is relatively straight. However, the curve of the soil moisture at H1-F5-L2-W drops significantly around February 5, 2018. It is speculated that the cause of this phenomenon is the cracking and expansion of the soil, which makes the low-temperature air to enter and the water to freeze, thus resulting the decline in soil moisture. The moisture in the soil layers F1, F2, and F3 is mainly in the range of 4%–6% during the period of negative average air temperature. When the average air temperature rises to positive (-2°C on March 12, 2018, 3°C on March 13, 2018), the soil moisture in the F1, F2, and F3 layers increased, of which F1 and F2 increased significantly, with an increase of approximately 5%, while the increase in the soil moisture of layer F3 is relatively small, with an increase of approximately 2%. The daily precipitation on February 26, 2018 was 5.4 mm; however, the moisture in each layer of the roadbed did not vary significantly due to the rainfall, indicating that the moisture of the roadbed soil is slightly affected by the small rainfall in cold and arid areas.

3.2. Temporal and Spatial Variations in the Soil Temperature under Climatic Conditions. The distances from the top surface of the test roadbed to the F5 and F4 layers are 20 and

50 cm, respectively. Figure 6 shows that the soil temperature curves of the three sensors in the F5 layer are more consistent and have better synchronization with the air temperature variation, while the soil temperature curve of the F4 layer slightly lags behind the air temperature variation, particularly when the air temperature changes from negative to positive. The temperature of the soil near the top of the roadbed responds more instantly and sensitively to variations in the air temperature in general.

The distance from the top surface of the test roadbed to the F2 layer is 200 cm. Figure 7 shows that the soil temperature of the F2 layer in the roadbed remains at negative temperature when the air temperature rises to positive. There is an evident lag effect between the time of the lowest temperature of the roadbed soil and the time of the lowest air temperature.

Figure 8 shows that the closer to the surface of the roadbed, the greater the effect of the air temperature on the soil temperature and the greater the range of soil temperature variation. When the air temperature varies in the range of -22.5 – 18°C , the sensors H1-F5-L1-TS, H1-F4-L7-TS, and H1-F2-L3-TS record the soil temperature varying in the ranges of -11.2 – 9.7°C , -10 – 9.8°C , and -9.3 to -1.3°C , respectively, and the time of the lowest soil temperature lags behind the lowest air temperature by 2, 15, and 38 days, respectively. This shows that the shallower the monitoring node, the more sensitive the soil temperature to the air temperature variation. The specific performance is as follows: in the cooling process, the soil temperature at the shallow node cools faster, and the lowest temperature is

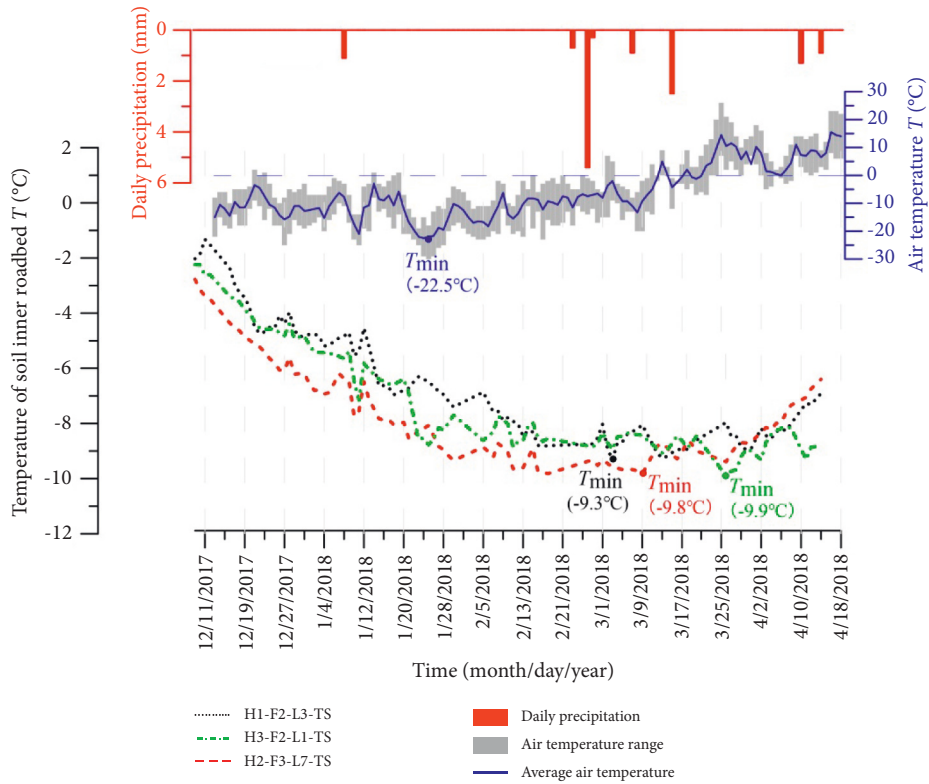


FIGURE 7: Curves of the soil temperature of the F2 layer in the roadbed under climatic conditions.

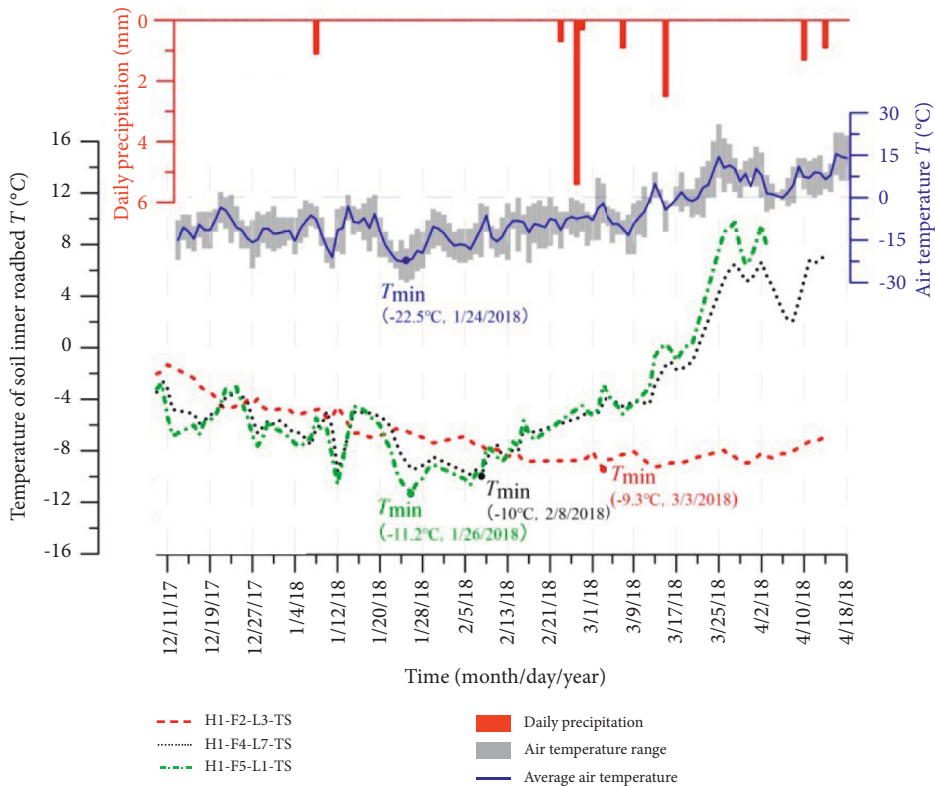


FIGURE 8: Curves of soil temperature in the F5, F4, and F2 layers of the roadbed under climatic conditions.

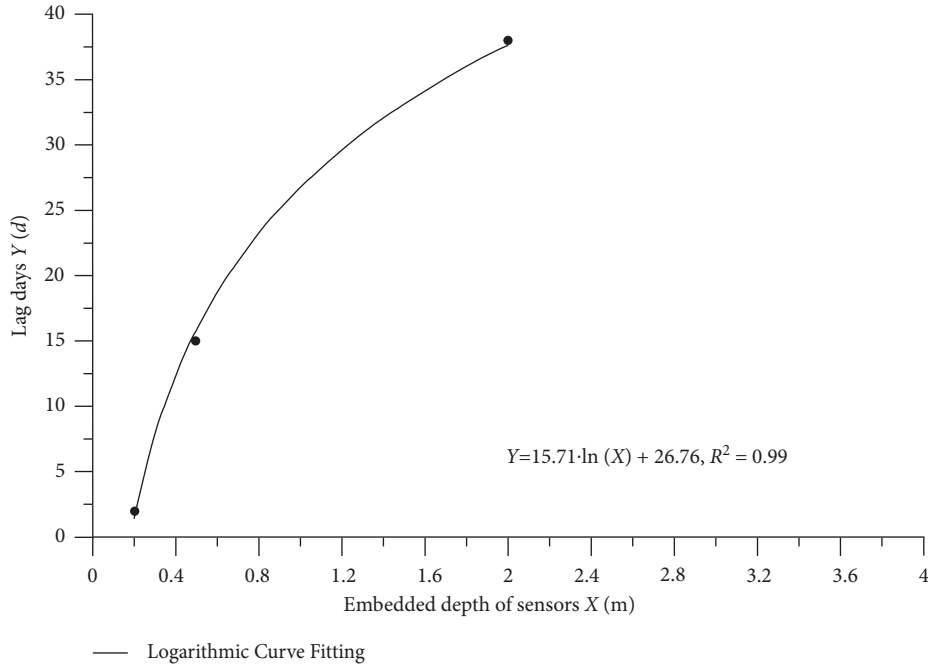


FIGURE 9: Relationship between the lag days of the minimum soil temperature relative to the minimum air temperature and the embedded depth of the monitoring sensor.

TABLE 1: Lag days of the minimum soil temperature relative to the minimum air temperature, the embedded depth of the monitoring sensor, and the variation range of the soil temperature.

Sensor number	Lag days (d)	Depth (m)	Minimum soil temperature (°C)	Variation range of the soil temperature (°C)
H1-F5-L1-TS	2	0.2	-11.2	-11.2 to 9.7
H1-F4-L7-TS	15	0.5	-10	-10 to 9.8
H1-F2-L3-TS	38	2.0	-9.3	-9.3 to -1.3

lower than that at the deep node. In the heating process, the soil temperature at the shallow node rises faster, and the highest temperature at that node is relatively higher. Based on Figures 6–8, it can be seen that from the surface to the inside, from shallow to deep, the internal soil temperature of the test roadbed is unevenly distributed and varies with time differently under the cold climatic condition.

A relationship is established (Figure 9) on the basis of the lag days of the minimum soil temperature relative to the minimum air temperature and the embedded depth (the distance between the monitoring node and the top surface of the roadbed) of the monitoring sensors (Table 1).

Figure 9 shows that the farther away from the top surface of the roadbed, the more evident the hysteresis effect of the lowest soil temperature relative to the lowest air temperature. The relationship between the lag days (Y) and the embedded depth of the sensor (X) is logarithmic curve fitted, and the equation of the logarithmic curve is $Y = 15.71 \cdot \ln(X) + 26.76$, $R^2 = 0.99$.

3.3. Temporal and Spatial Variations in the Soil Deformation under Climatic Conditions. The unit of the small deformation of the modified soil recorded by the strain sensors is microstrain ($\mu\epsilon$). A positive strain reading indicates that the

strain sensor is under tension, that is, the soil where the sensor is embedded has expanded or stretched. Conversely, a negative strain reading indicates that the strain sensor is compressed, that is, the soil where the sensor is located has shrunk.

The soil strain variation curves in Figure 10 show that the strain of the soil in the F5 layer is much greater than that in the F2 layer. The soil strain variation in the F2 layer is -73.8 to $214.8 \mu\epsilon$ during the monitoring period; however, the soil strain variation in the F5 layer is -889.5 to $694.9 \mu\epsilon$. The trend in the soil strain variation at the same layer is the same, and the difference in the soil strain at different positions in the same layer is small, but significant in different layers.

Figure 11 shows that the variation trend and magnitude of the soil strain at each layer in the roadbed are different under the same climatic condition. The positive and negative soil strains in the F3, F4, and F5 layers of the roadbed are greater than those in the F1 and F2 layers in general. The absolute value of the soil maximum strain in the F1 and F2 layers does not exceed $300 \mu\epsilon$, but those in the F3, F4, and F5 layers are greater than $600 \mu\epsilon$. During the period of negative air temperature, the soil strains in the F3, F4, and F5 layers are all negative, and the soil strain amount relationship is $F5 > F4 > F3$. During the period of positive air temperature, the soil strains in the F3, F4, and F5 layers are positive, and the soil strain amount relationship is the same, $F5 > F4 > F3$.

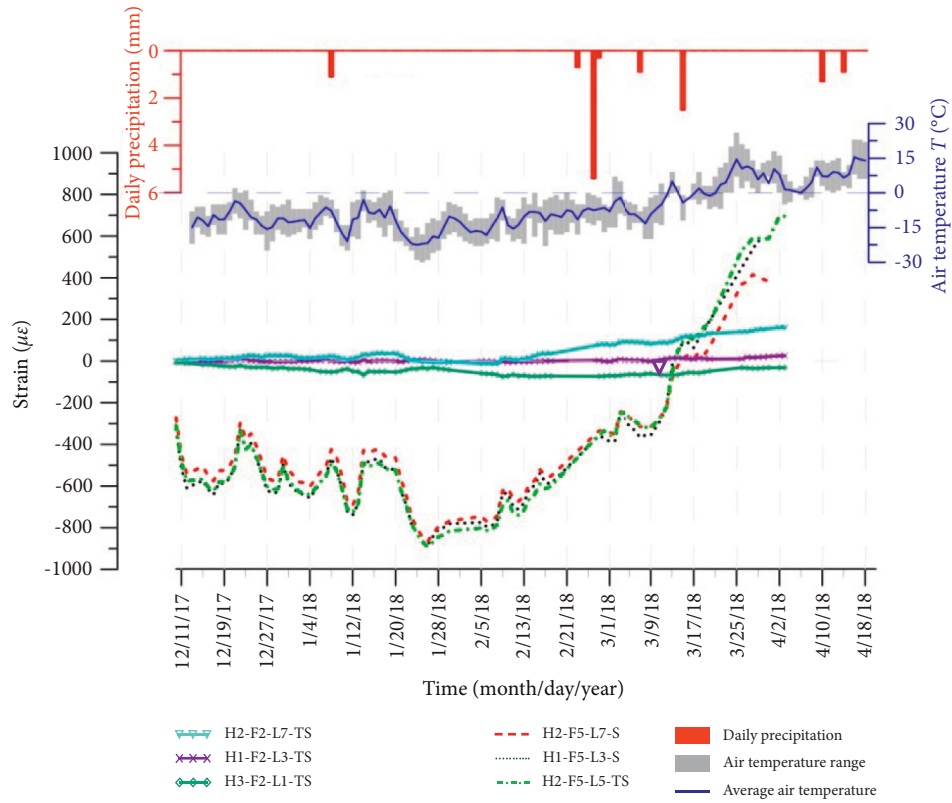


FIGURE 10: Curves of soil deformation in the F5 and F2 layers of the roadbed under climatic conditions.

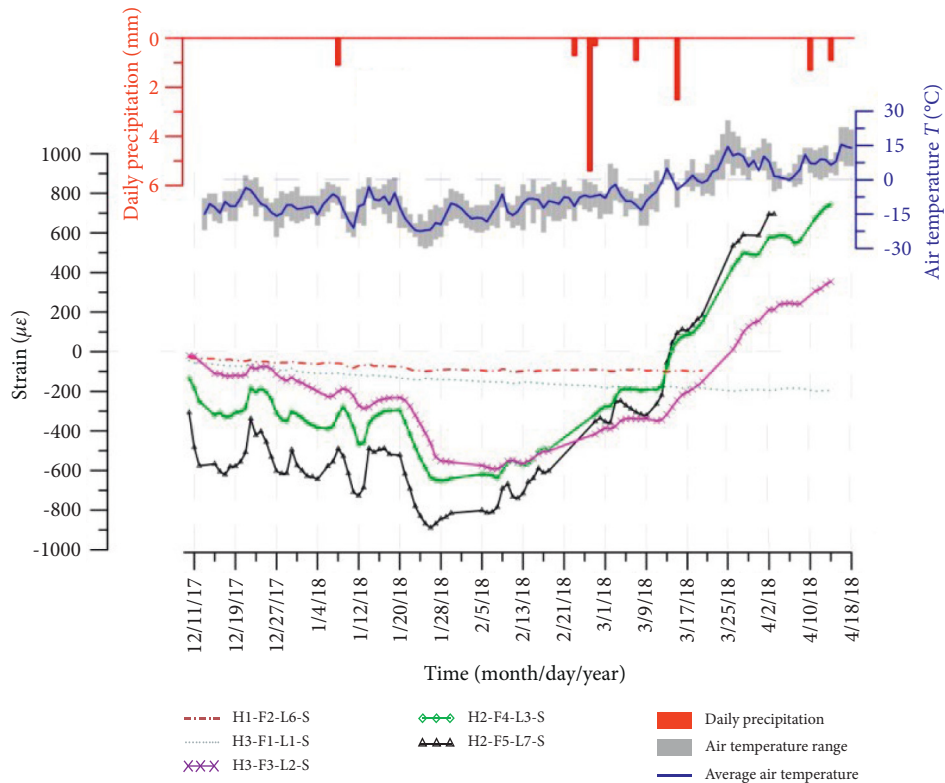


FIGURE 11: Curves of soil deformation of five layers in the roadbed under climatic conditions.

TABLE 2: Relationship between correlation coefficient $|r_{xy}|$ and strength of correlation.

$ r_{xy} $	0–0.2	0.2–0.4	0.4–0.6	0.6–0.8	0.8–1.0
Strength of correlation	Irrelevant	Weak correlation	Moderate correlation	Strong correlation	Very strong correlation

TABLE 3: Correlation between the variations in the soil temperature and air temperature and rainfall.

Sensor number of soil temperature	Correlation between the variations in soil temperature and air temperature $ r_{xy} $	Correlation between the variations in soil temperature and rainfall $ r_{xy} $
H1-F5-L1-TS	0.8059	0.0855
H2-F5-L5-TS	0.8926	0.1232
H3-F5-L3-TS	0.8171	0.1190
H1-F4-L7-TS	0.6301	0.0778

The soil deformation monitoring results show that during negative air temperature, the soil in the F3, F4, and F5 layers exhibited shrunk deformation, and all have tensile deformation during positive air temperature. However, the strain amounts of these three layers are different even when they are under the same air temperature. The closer to the top surface of the roadbed, the greater the negative strain of the soil at the low temperature and the positive strain at high temperature, the greater the amplitude of the strain variation, and the more evident and sensitive the response of the soil strain to the air temperature.

The response of the soil strain at different locations of the test roadbed to the same air temperature has significant temporal and spatial differences, resulting in an uneven distribution of the soil deformation in the roadbed, which is the fundamental reason for cracking in the roadbed soil. According to a previous study, the critical tensile strain for cracking and deformation of the top surface of the roadbed is $600 \mu\epsilon$ [33]. Therefore, based on the results of the roadbed strain monitoring data, the following part of the article will focus on the analysis of the factors affecting soil deformation and cracking in roadbed layers F3, F4, and F5.

4. Correlation Analysis of Factors Influencing Roadbed Soil Deformation

The change process of the soil moisture, temperature, and deformation over time in the static roadbed can be attributed to the variation in the external environment conditions, which are the air temperature and rainfall. The variations in the air temperature and rainfall directly cause changes in the temperature and humidity of the roadbed soil. The changes in the temperature of the roadbed soil further lead to changes in the soil deformation and soil moisture, and the impact of the soil moisture change on the soil deformation should be evaluated.

The variations in the soil moisture, temperature, deformation, and air temperature constitute four types of data series. The correlation analysis method is used to explore the effects of the air temperature on the soil temperature, humidity, and strain to determine the main external influencing factors leading to soil deformation and crack formation. The value of the correlation coefficient between the variation in the air temperature and the change in the soil

temperature, and soil humidity is determined, as well as the correlation coefficient between the change in the soil temperature, soil humidity, and soil strain, to judge the strength of the correlation. If the correlation is strong, the impact will be significant, and vice versa, the impact will be small. The correlation analysis method is as follows:

Suppose there are two data series: $X = \{x_i\}$ and $Y = \{y_i\}$, $i = 1, 2, 3, \dots, n$, and their average values can be expressed as

$$\bar{x} = \frac{1}{n} \sum_{i=1}^n x_i \quad (1)$$

$$\bar{y} = \frac{1}{n} \sum_{i=1}^n y_i.$$

The correlation coefficient r_{xy} of the two data series is calculated using the following formula:

$$r_{xy} = \frac{\sum_{i=1}^n (x_i - \bar{x}) \cdot (y_i - \bar{y})}{\sqrt{(\sum_{i=1}^n (x_i - \bar{x})^2) \cdot (\sum_{i=1}^n (y_i - \bar{y})^2)}} \quad (2)$$

The value range of the correlation coefficient is $-1 \leq r_{xy} \leq +1$, where $r_{xy} < 0$ indicates that X is negatively correlated with Y ; $r_{xy} > 0$ indicates that X and Y are related; and $r_{xy} = 0$ implies that X and Y are irrelevant [34, 35]. The greater the $|r_{xy}|$ value, the stronger the relationship between X and Y . The correlation coefficient $|r_{xy}|$ and the related degree of the recommended classification comparison relationship was referred from Xiao Yong and Shao Fan [36, 37], as listed in Table 2. The following qualitative description of the correlation strength follows the recommended interpretation of r_{xy} : 0.0–0.2: irrelevant; 0.2–0.4: weak correlation; 0.4–0.6: moderate correlation; 0.6–0.8: strong correlation; and 0.8–1.0: very strong correlation, although other interpretations have been made [38–40].

4.1. Correlation Analysis between Internal Factors of Roadbed Soil Deformation and External Factors. In the crack formation and deformation processes of the soil, the internal factors are direct influencing factors, whereas the external factors indirectly affect the soil deformation by affecting the internal factors. A correlation analysis between the external factors (air temperature and rainfall) and the internal factors

TABLE 4: Correlation between the variation in the soil moisture and the rainfall.

Sensor number of soil moisture	Correlation between the variation in the soil moisture and the rainfall $ r_{xy} $
H1-F5-L2-W	0.1595
H2-F5-L6-W	0.0117
H3-F3-L4-W	0.0886

TABLE 5: Correlation coefficient of roadbed soil temperature and soil moisture.

Correlation coefficient of soil temperature and soil moisture $ r_{xy} $	H1-F5-L1-TS	H2-F5-L5-TS	H3-F5-L3-TS	H1-F4-L7-TS
H1-F5-L2-W	0.3230	0.5724	0.3367	0.1754
H2-F5-L6-W	0.2219	0.0390	0.2126	0.3263
H3-F3-L4-W	0.1127	0.1550	0.0829	0.2758

TABLE 6: Correlation coefficient of roadbed soil deformation and soil moisture.

Sensor number of soil moisture	Sensor number of soil deformation	Correlation coefficient between soil deformation and soil moisture $ r_{xy} $
H1-F5-L2-W	H1-F5-L3-S	0.5064
	H1-F5-L1-TS	0.1458
H2-F5-L6-W	H2-F5-L7-S	0.0875
	H2-F5-L5-TS	0.0650

TABLE 7: Correlation coefficient of roadbed soil deformation and soil temperature.

Sensor number of soil temperature	Sensor number of soil deformation	Correlation coefficient between soil deformation and soil temperature $ r_{xy} $
H3-F5-L3-TS	H3-F5-L3-TS	0.9332
	H2-F5-L7-S	0.9652
	H2-F5-L5-TS	0.9508
	H1-F5-L3-S	0.9593
H2-F5-L5-TS	H2-F5-L5-TS	0.9744
	H2-F5-L7-S	0.9651
	H2-F5-L5-TS	0.9533
	H1-F5-L3-S	0.9665
H1-F5-L1-TS	H1-F5-L1-TS	0.8227
	H2-F5-L7-S	0.9708
	H2-F5-L5-TS	0.9515
	H1-F5-L3-S	0.9571
H1-F4-L7-TS	H1-F4-L7-TS	0.9598
	H2-F4-L3-S	0.9845
	H3-F4-L7-S	0.9758

(soil temperature and soil moisture) that produce deformation and cracks in the roadbed soil should be conducted.

Table 3 shows that the correlation coefficient between the soil temperature in the F5 layer and the air temperature is greater than 0.8, which represents a very strong correlation; the value of the correlation coefficient between the soil temperature in the F4 layer and the air temperature is between 0.6 and 0.8, representing a strong correlation, while the correlation coefficients between the soil temperature in the F5 and F4 layers and rainfall are less than 0.2, representing an irrelevant result. The correlation analysis results show that the change in the roadbed soil temperature is significantly affected by the variation in the air temperature, irrespective of the rainfall. The variation in the air temperature is the main reason for the change in the soil temperature of the roadbed.

Table 4 shows the correlation analysis results of the change in the soil moisture monitored by the moisture sensors in the F3 and F5 layers and the rainfall recorded in Figure 5. The results show that the correlation coefficients between the roadbed soil moisture and rainfall are less than 0.2, representing an irrelevant result. This shows that the very little rainfall in the cold and arid areas cannot significantly affect the change in the soil moisture in the roadbed, particularly when the moisture content of the roadbed soil is very low.

4.2. Correlation Analysis between Deformation of Roadbed Soil and the Internal Directly Influencing Factors. The above correlation analysis shows that the air temperature variation significantly affects the change in the roadbed soil temperature and that the influence of rainfall on the roadbed soil

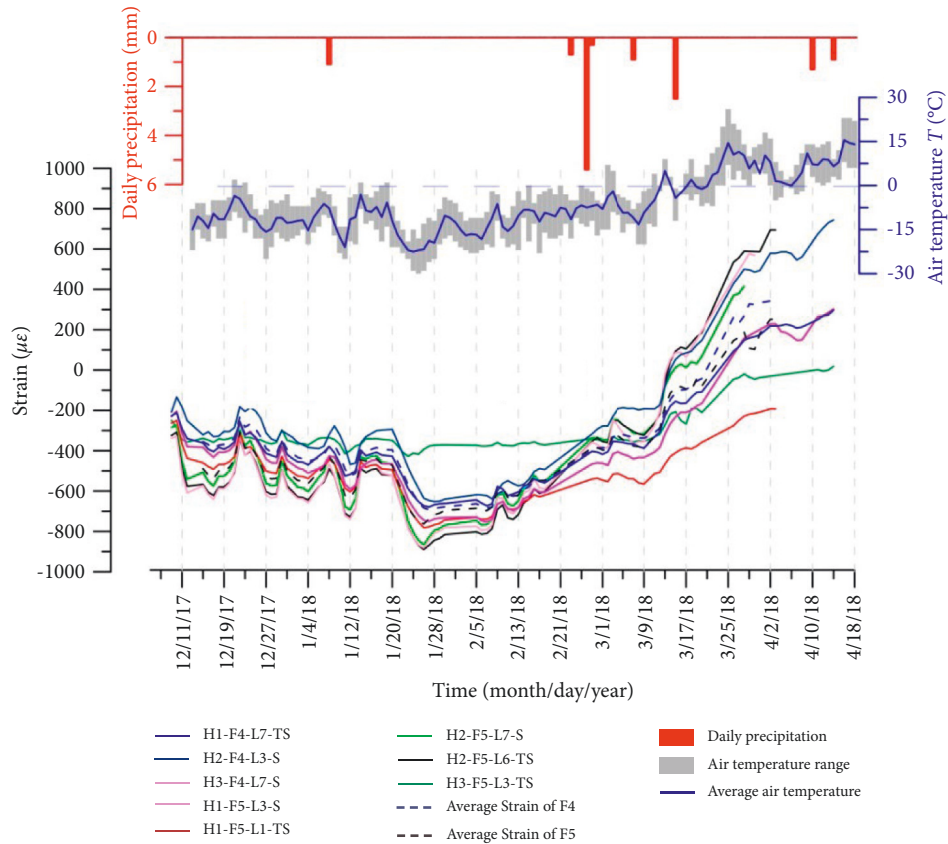


FIGURE 12: Curves of monitoring strain variation and calculated average strain in the F4 and F5 layers of the roadbed under climatic conditions.

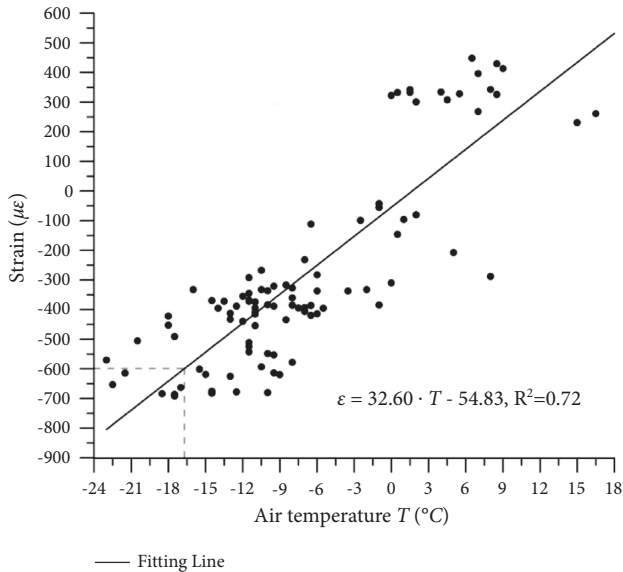


FIGURE 13: Relationship between the average strain of the F4 layer soil of the roadbed and the air temperature.

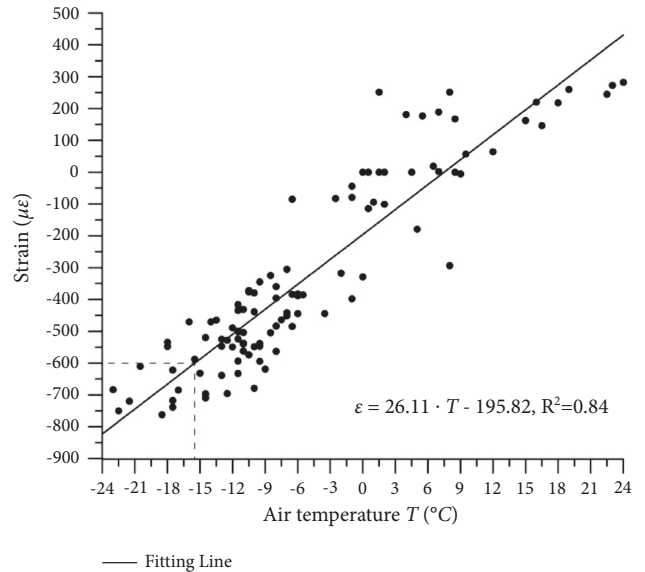


FIGURE 14: Relationship between the average strain of the F5 layer soil of the roadbed and the air temperature.

moisture is negligible. The correlation analysis between the roadbed soil deformation and the internal directly influencing factors (soil temperature and soil moisture) is presented below.

(1) *Correlation Analysis between Soil Temperature and Soil Moisture of Roadbed.* Table 5 shows the correlation analysis results of the soil moisture in the F5 and F3 layers of the roadbed in Figure 5 and the soil temperature in the F5 and

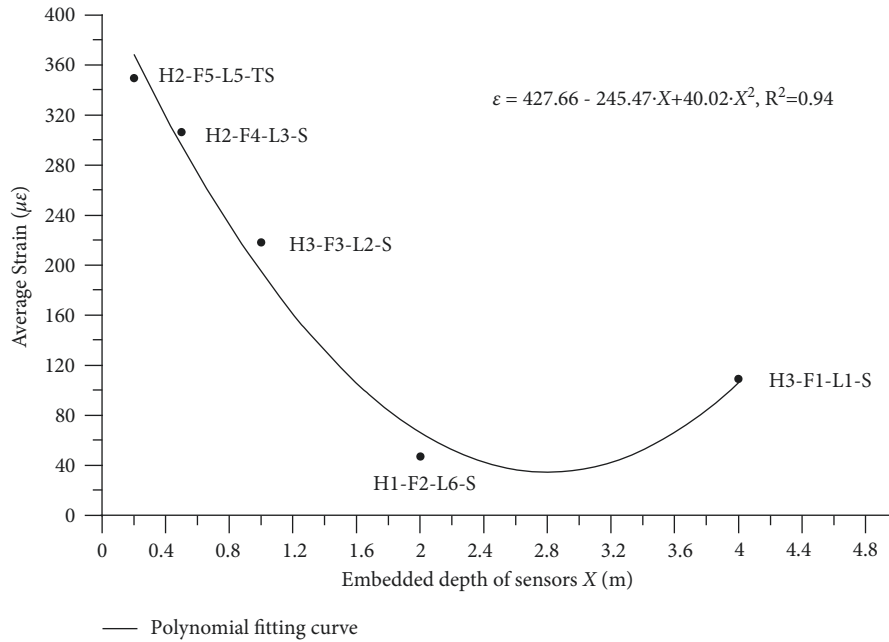


FIGURE 15: Relationship between the embedded depth of the sensors and the average strain of the soil.

F4 layers of the roadbed in Figure 6. From the F3 to F5 layers of the roadbed, the correlation coefficient between the change in the soil moisture and the change in the soil temperature is mostly less than 0.4, indicating that the change in the soil moisture is weakly correlated to the change in the soil temperature. When the soil moisture content in the upper part of the roadbed in the cold and arid areas is low, the change in the soil temperature of the roadbed has a weak effect on the moisture content.

(2) *Correlation Analysis between Soil Deformation and Soil Moisture of Roadbed.* Table 6 shows the correlation analysis results of the soil moisture recorded by the two moisture sensors placed in the F5 layer of roadbed cross sections 1 and 2 and the soil strain variation recorded by the two strain sensors placed beside the moisture sensor. From Table 6, it can be found that the correlation coefficients between the strain variation at different positions of the soil in the F5 layer and the moisture variation of the soil at the close position are mostly lower than 0.2, which is irrelevant. Therefore, it can be considered that the strain variation of the roadbed soil is independent of the change in the soil moisture.

(3) *Correlation Analysis between Soil Deformation and Soil Temperature of Roadbed.* Table 7 shows the correlation analysis results between the soil temperature variation in the roadbed recorded by the temperature sensors in the F5 and F4 layers and the soil strain variation recorded by the strain sensors at different locations in the same layer. Table 7 shows that the correlation coefficients between the soil temperature variation in the F5 and F4 layers of the roadbed and the soil strain variation at different positions in the same layer are greater than 0.8, representing a very strong correlation. Therefore, it is determined that the temperature change in

the roadbed soil is the key factor leading to deformation and cracking of the roadbed soil.

Combining the results listed in Tables 4 and 5, the soil strain change of the roadbed is found to be independent of the change in the soil moisture and is strongly correlated with the soil temperature variation, proving that the roadbed soil temperature and the soil moisture are weakly correlated indirectly. The results listed in Table 5 show that the two factors, soil temperature variation and soil moisture variation, that affect the deformation of the roadbed soil are independent of each other and that the soil strain is mainly affected by the soil temperature. The air temperature variation (external factor) is converted into soil temperature changes via soil heat conduction, and soil temperature changes (inner factor) are the direct factors leading to soil strain changes.

The above research reflects that the soil deformation of the test roadbed during the monitoring period is the temperature deformation.

4.3. Temporal and Spatial Variation Laws of Temperature Deformation of Roadbed Soil. The average strains in the F5 and F4 layers of the roadbed can be calculated from the strain monitoring data of the five sensors located in the F5 layer and the three sensors located in the F4 layer (Figure 12).

From the relationship between the average strain of the F5 and F4 layers and the air temperature in Figure 12, two statistical graphs of the average strain in the F4 and F5 layers as a function of the air temperature are drawn, and the data trend is linearly fitted, as shown in Figures 13 and 14.

Figures 13 and 14 show that the strain of the soil at different positions at the same level (same depth) inside the roadbed is different under the same air temperature, but the

average strain of the soil is linearly correlated with the air temperature overall. When the air temperature drops from 0°C to -24°C , the strain of the soil shows a negative value and a linear downward trend, indicating that the roadbed soil continues to shrink and deform as the air temperature drops. When the air temperature rises from 0°C to 18 or 24°C , the negative strain of the soil decreases, and the positive strain gradually increases, indicating that the shrinkage and deformation of the roadbed soil continue to decrease and turn into expansion and deformation during the rise in the air temperature. The fitting equations for the relationship between the average strain in the F4 and F5 layers of the roadbed and the air temperature variation are $\varepsilon_4 = 32.60 \cdot T - 54.83$ ($R^2 = 0.72$) and $\varepsilon_5 = 26.11 \cdot T - 195.82$ ($R^2 = 0.84$), respectively. The air temperatures corresponding to the critical tensile strain of $600 \mu\epsilon$ of the soil in the F4 and F5 layers of the roadbed are -16.72°C and -15.47°C , respectively. The slope of the fitted straight-line equation is the rate of change in the soil strain with the soil temperature, that is, the thermal expansion coefficient of the modified soil obtained from the field test. The thermal expansion coefficients of the F4 and F5 roadbed layers are 32.6×10^{-6} and $26.11 \times 10^{-6}/^{\circ}\text{C}$, respectively, which differ from the linear expansion coefficients of the aeolian sand-modified soil measured in the laboratory [22], perhaps due to different sizes and boundaries. The tested expansion coefficient is the linear expansion coefficient of the sample strip along the long axis, and the size of the sample strip used for measuring the indoor thermal expansion coefficient was only $10 \text{ mm} \times 10 \text{ mm} \times 50 \text{ mm}$. However, the boundary of the surrounding soil affects the deformation of the modified soil in a large-scale field roadbed test, which can better reflect the actual scenario.

The embedded depth of the sensor is the distance below the datum level of the roadbed's upper surface. For example, the buried depth of the sensor in the F5 layer is 0.2 m from the roadbed's upper surface; hence, its hidden depth is 0.2 m , as are the buried depths of the four other layer sensors (Figure 4(b)). The relationship between the embedded depth of the sensors and the average strain of the soil can be obtained by calculating the absolute value of the average strain of the soil at different layers, as shown in Figure 15.

Figure 15 shows that the soil deformation of the roadbed does not decrease monotonously with the increase in the embedded depth of the sensor, but first decreases and then increases sensor. The polynomial fitting equation for the relationship between the average strain of the roadbed soil (ε) and the embedded depth of the sensor (X) is $\varepsilon = 427.66 - 245.47 \cdot X + 40.02 \cdot X^2$ ($R^2 = 0.94$), which indicates that the strain of the roadbed soil at different depths is different. The closer it is to the top surface of the roadbed, the greater the temperature deformation of the roadbed soil. Based on field monitoring data, aeolian sand-modified soil roadbed was found to shrink at low temperatures, and the shrinkage strain of the soil at different depths varied significantly at low temperatures. The strain on the surface of the roadbed exceeded the critical value of roadbed cracking strain; however, the strain near the bottom of the roadbed was lower than the critical value. The surface of the aeolian

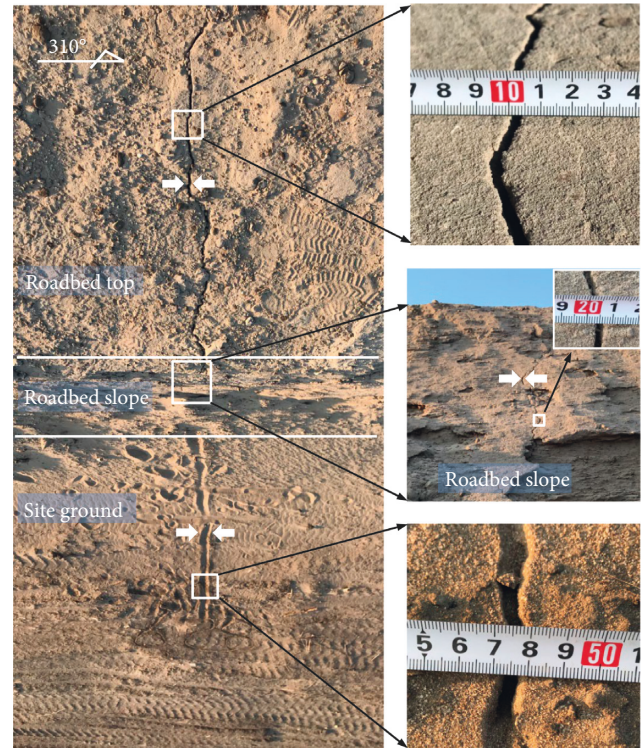


FIGURE 16: Top view and crack detail of the roadbed and site.

sand-modified soil road roadbed fractured in cold areas due to the process of low-temperature shrinkage and uneven surface and inner shrinking. Notably, the average strain at the bottom of the roadbed is greater than that of the soil above it, which may be attributed to the thermal expansion and contraction of the site at the bottom of the roadbed. Because the test section of the roadbed was built on a nonrigid site, although it was cleaned and rolled before paving the test section, the nonrigid site would still deform in cold climates, affecting the deformation of the test section's bottom. Field investigations in winter (December 27, 2017) revealed that the ground around the site where the test roadbed was located had ground cracks that were nearly perpendicular to the roadbed direction, and the ground cracks penetrated the roadbed Figure 16; the freeze-shrinkage deformation of the site where the test roadbed was located had a nonnegligible effect on the soil strain at the bottom of the roadbed.

5. Conclusions

Based on cracks induced in an aeolian sand-modified soil roadbed, this study considered a high-speed railway roadbed project under construction in a cold area to establish a large-scale in situ aeolian sand-modified soil roadbed to study the temporal and spatial variations in the temperature and deformation inside the roadbed of the aeolian sand-modified soil. The variations in the soil temperature, moisture, and strain of the roadbed under the influence of the climatic condition in this cold region were monitored using fiber Bragg grating (FBG) strain sensors embedded into the

roadbed. The correlation analysis method was used to analyze the correlation between the monitoring data (soil temperature, moisture, and strain) and the climatic conditions (air temperature and rainfall), to explore the correlation between the internal and external factors that cause the roadbed soil to deform, and to determine the main influencing factors that cause the roadbed soil to deform and crack. The following conclusions can be drawn from the study:

- (1) The change in the soil moisture in the aeolian sand-modified soil roadbed had little effect on the deformation of the modified soil roadbed, and the strain variation in the roadbed soil was independent of the change in the soil moisture. The soil moisture content in the aeolian sand-modified soil roadbed was relatively low, and the very little rainfall in the cold and arid areas had a weak effect on the change in the soil moisture content in the roadbed.
- (2) The direct cause of roadbed soil deformation in a low-air-temperature environment was found to be the variation in the roadbed soil temperature, and the variation in the roadbed soil temperature was due to the change in the air temperature. The roadbed boundary controlled the uneven spatial distribution of the soil temperature inside the roadbed, leading to significant differences in the thermally induced soil temperature. The surface of the aeolian sand-modified soil roadbed fractured in cold areas due to the process of low-temperature shrinkage and uneven surface and inner shrinking. The variation in the internal deformation of the modified soil roadbed had a strong correlation with the temperature change of the roadbed soil. The response of the roadbed soil temperature to the air temperature exhibited a hysteresis effect. The farther away from the roadbed surface, the more evident the hysteresis effect.
- (3) The deformation of the aeolian sand-modified soil roadbed was linearly related to the air temperature change. A negative air temperature caused the roadbed soil to shrink and deform. The amount of soil shrinkage and deformation increased with the decrease in the negative air temperature. The air temperature changed from negative to positive, and the negative strain of the soil gradually decreased and turned positive. The deformation amount of the roadbed soil first decreased and then increased with increasing embedded depth of the sensor. The temperature deformation of the site foundation had a significant effect on the soil at the bottom of the roadbed.

In a field test with the aeolian sand-modified soil roadbed, the soil temperature field and soil strain field of the roadbed under the influence of the air temperature were intuitively monitored using a temperature-compensated optical fiber sensor. Some valuable data were obtained, and some laws based on the field test data were determined.

However, there remain shortcomings in the test; for example, the number of sensors was insufficient, and the soil deformation was measured only in one direction. In the future, increasing the number of monitoring points and performing the deformation monitoring of the roadbed soil in three orthogonal directions can help obtain a more in-depth and comprehensive understanding of the temperature deformation of the roadbed soil.

Data Availability

The field test data used to support the findings of this study are available from the corresponding author upon request.

Conflicts of Interest

The authors declare that they have no conflicts of interest regarding the publication of this article.

Acknowledgments

This work was supported by the Special Innovation Team Project for Fundamental Scientific Research Business Expenses of Central Universities (Grant no. ZY20180106). The authors are grateful to MJEditor (<http://www.mjeditor.com>) for its linguistic assistance during the preparation of this manuscript.

References

- [1] G. J. Zhang, *Eremology*, China Forestry Press, Beijing, China, 1996.
- [2] I. H. Kahn, "Soil studies for highway construction in arid zones," *Engineering Geology*, vol. 19, no. 1, pp. 47–62, 1982.
- [3] A. Ghrieb, R. Mitiche-Kettab, and A. Bali, "Stabilization and utilization of dune sand in road engineering," *Arabian Journal for Science and Engineering*, vol. 39, no. 3, pp. 1517–1529, 2014.
- [4] K. Moosavi and B. Kalantari, "Improving load bearing capacity of wind-blown sand using ordinary Portland cement," *Journal of Engineering and Computer Sciences(Oassim University)*, vol. 16, pp. 1267–1274, 2011.
- [5] J. Wei, *Characteristic Research on Strength of Cement Improved Aeolian Sand and Deformation of Aeolian Sand Used to Fill Roadbed for Heavy Haul Railway*, Lanzhou Jiaotong University, China, 2017.
- [6] M. López-Querol and S. Lopez-Querol, "Aeolian sands: characterization, options of improvement and possible employment in construction - the State-of-the-art," *Construction and Building Materials*, vol. 73, no. 30, pp. 728–739, 2014.
- [7] Z. A. Rahman and M. A. Rahman, "The potential of cement kiln dust for the stabilization of dune sand in highway construction," *Building and Environment*, vol. 25, no. 4, pp. 285–289, 1990.
- [8] M. Y. Al-Aghbari, Y. E.-A. Mohamedzein, and R. Taha, "Stabilisation of desert sands using cement and cement dust," *Proceedings of the Institution of Civil Engineers - Ground Improvement*, vol. 162, no. 3, pp. 145–151, 2009.
- [9] S. Lopez-Querol, J. Arias-Trujillo, M. GM-Elipse, A. Matias-Sanchez, and B. Cantero, "Improvement of the bearing capacity of confined and unconfined cement-stabilized aeolian

- sand," *Construction and Building Materials*, vol. 153, pp. 374–384. in press, 2017.
- [10] G. F. Li, X. D. Shen, J. C. Wu, W. Dong, H. J. Xue, and X. Liu, "Experimental study on shrinkage deformation of aeolian sand concrete," *Bulletin of the Chinese Ceramic Society*, vol. 35, no. 4, pp. 1213–1218, 2016.
 - [11] S. A. Aiban, "A study of sand stabilization in Eastern Saudi Arabia," *Engineering Geology*, vol. 38, no. 1-2, pp. 65–79, 1994.
 - [12] H. I. Wahhab and I. M. Asi, "Improvement of marl and dune sand for highway construction in arid areas," *Building and Environment*, vol. 32, no. 3, pp. 271–279, 1997.
 - [13] G. S. Guo, Y. Zhang, and S. M. Du, "Grassroots-level shear strength experimental study of aeolian sand with cement," *Science Technology and Engineering*, vol. 15, pp. 327–331, 2017.
 - [14] B. X. Fu, *Research on Road Performance of Aeolian Sand with Different Mud Content*, Chang'an University, China, 2006.
 - [15] Y. K. Luo, Y. Q. Yuan, J. Wang, Y. D. Fan, and M. S. Feng, "Cure for wind-blown soil of rich water by cement stabilization," *Road Machinery & Construction Mechanization*, vol. 28, no. 01, pp. 29–32, 2011.
 - [16] F. B. Zhou, *Mechanism of and Solution for Frost Damage of Aeolian Sand Roadbed in Cold Region*, China University of Geosciences, Beijing, China, 2018.
 - [17] B. Bai, Q. K. Nie, Y. K. Zhang, X. L. Wang, and W. Hu, "Cotransport of heavy metals and SiO₂ particles at different temperatures by seepage," *Journal of Hydrology*, vol. 597, Article ID 125771, 2021.
 - [18] B. Bai, R. Zhou, G. Q. Cai, W. Hu, and G. C. Yang, "Coupled thermo-hydro-mechanical mechanism in view of the soil particle rearrangement of granular thermodynamics," *Computers and Geotechnics*, vol. 137, no. 8, 2021.
 - [19] D. C. Li, "Study on road performance of cement stabilized aeolian sand," *Technology of Highway and Transport*, vol. 1, pp. 24–27, 2005.
 - [20] C. H. Wang, X. C. Wang, and X. Q. Tan, "Preparation of road aeolian sand curing agent and its mixture performance," *J Cent South Univ*, vol. 42, no. 1, pp. 192–198, 2011.
 - [21] Z. D. Su, J. Z. Sun, F. B. Zhou, and Y. Zheng, "Test and analysis of thermophysical properties of aeolian sand modified soil," *Water Resources and Hydropower Engineering*, vol. 50, no. 7, pp. 153–159, 2019.
 - [22] F. B. Zhou, Z. D. Su, M. N. Tian, G. Li, X. Chen, and J. Z. Sun, "Effect of clayey soil and fiber on thermal expansion of aeolian sand modified soil," *Bulletin of the Chinese Ceramic Society*, vol. 39, no. 01, pp. 199–205, 2020.
 - [23] G. Han, L. You, and Y. Q. Cheng, "Characteristics of ground wind regimes in the horqin sandy land when A cold front passed in spring," *Journal of Desert Research*, vol. 36, no. 4, pp. 1087–1096, 2016.
 - [24] L. W. Jing, Z. K. Wang, Z. Q. Meng, and B. Y. Li, "Discussion on the causes and recovery of desertification in horqin grassland," *Journal of Inner Mongolia University for Nationalities*, vol. 11, no. 3, pp. 105–106, 2015.
 - [25] *Inner Mongolia Communications Investment Co. LTD. [OL]*, <http://www.nmgjtz.com/c/nmgjtzjt/2336>.
 - [26] Q. L. Bao, X. L. Li, H. Y. Dai et al., "Climatic characteristics of cold and warm sharp turnaround in khorchin sandy land under global warming," *Journal of Northwest Forestry University*, vol. 35, no. 3, pp. 17–22, 2020.
 - [27] X. M. Liu, H. L. Zhao, and A. F. Zhao, *Wind-Sandy environment and Vegetation in the Horoin Sandy Land*, Science Press, China. Beijing, 1996.
 - [28] D. F. Li, T. X. Liu, X. Y. Liu, and L. M. Duan, "Analysis of soil temperature and freeze-thaw process in the horqin sandy land with sand-meadow land features," *Yellow River*, vol. 34, no. 5, pp. 82–85, 2012.
 - [29] P. Zhang, H. S. Zhang, and J. L. Du, "Analysis of the surface temperature over keerqin sand area in inner Mongolia," *Acta Scientiarum Naturalium Universitatis Pekinensis*, vol. 47, no. 4, pp. 655–663, 2011.
 - [30] C. T. Yue, X. Y. Liu, T. X. Liu, Y. Q. Fu, W. M. Cao, and Q. L. Liu, "Change rules of soil temperature and maximum freezing depth during freezing-thawing period in horqin sand and meadow," *Bulletin of Soil and Water Conservation*, vol. 36, no. 6, pp. 84–91, 2016.
 - [31] *TB 10202-2002, "Code for Construction on Roadbed of Railway*, China Railway Press, Beijing, 2002.
 - [32] R. You, L. Ren, and G. Song, "A novel fiber Bragg grating (FBG) soil strain sensor," *Measurement*, vol. 139, no. 6, pp. 85–91, 2019.
 - [33] J. B. Cai, *Study on Deformation Mechanism and Measures against Embankment's Longitudinal Cracking*, 2018.
 - [34] S. Q. Zhang, J. N. Lu, Z. Jiang, and L. Zhang, "Study of the correlation coefficients in mathematical statistics," *Mathematics in Practice and Theory*, vol. 39, no. 19, pp. 102–107, 2009.
 - [35] Y. X. Chen, "Understanding of the meaning of correlation coefficient," *Chinese Examination*, vol. 7, pp. 15–19, 2011.
 - [36] Y. Xiao, Y. Zhao, Z. D. Tu, B. Qian, and R. M. Chang, "Topology checking method for low voltage distribution network based on improved Pearson correlation coefficient," *Power System Protection and Control*, vol. 47, no. 11, pp. 37–43, 2019.
 - [37] F. Shao, C. Chen, M. J. Ge, Y. L. Hang, and W. H. Chen, "Analysis of technology innovation and application based on the power line loss Pearson algorithm," *Scientific and Technological Innovation*, vol. 14, pp. 54–55, 2017.
 - [38] R. A. Fisher, *Statistical Methods for Research Workers*, Hafner, New York, 13th edition, 1958.
 - [39] C. B. Zhu, G. Weatherill, F. Cotton, M. Pilz, D.Y. Kwak, and H. Kawase, "An open-source site database of strong-motion stations in Japan: K-NET and KiK-net (v1.0.0)," *Earthquake Spectra*, vol. 37, no. 3, pp. 2126–2149, 2021.
 - [40] K. W. Bozorgnia and Y. Bozorgnia, "Ground motion models for the horizontal components of arias intensity (AI) and cumulative absolute velocity (CAV) using the NGA-West2 database," *Earthquake Spectra*, vol. 35, no. 3, pp. 1289–1310, 2019.

Research Article

Experimental Study on the Effect of Large Temperature Difference on Compressive Strength and Pore Structure of Semirigid Base

Ming Dai,¹ Jia Pan ,² Yanjun Shen ,³ Jianbo Deng,¹ and Yeermulati Muhadeer¹

¹China Railway Construction Xinjiang Jingxin Expressway Co., Urumchi 830000, China

²College of Architecture and Civil Engineering, Xi'an University of Science and Technology, Xi'an 710054, China

³College of Geology and Environment, Xi'an University of Science and Technology, Xi'an 710054, China

Correspondence should be addressed to Yanjun Shen; shenyj@xust.edu.cn

Received 22 January 2022; Revised 17 March 2022; Accepted 24 March 2022; Published 7 June 2022

Academic Editor: Xingxin Chen

Copyright © 2022 Ming Dai et al. This is an open access article distributed under the Creative Commons Attribution License, which permits unrestricted use, distribution, and reproduction in any medium, provided the original work is properly cited.

Understanding the evolution of mechanical properties and pore structure of semirigid base under large temperature difference is of great significance for evaluating the durability and safety of semirigid base structure and studying the damage cracking mechanism and prevention technology of semirigid base induced by large temperature difference climate. This paper studies the variation law of peak stress and dynamic modulus, the evolution characteristics of pore structure, and the pore size distribution of semirigid base after different cycles at different temperature intervals. Based on the analysis of peak stress and dynamic modulus test results, the degradation effect of freeze-thaw environment ($-20^{\circ}\text{C}\sim 20^{\circ}\text{C}$) on semirigid base is far greater than that of high-temperature environment ($20^{\circ}\text{C}\sim 60^{\circ}\text{C}$) and low-temperature environment ($-5^{\circ}\text{C}\sim -30^{\circ}\text{C}$). There are significant decreases in peak stress and dynamic modulus of semirigid base in the late cycle (12 to 15 cycles). Under low-temperature and freeze-thaw environments, the axial load resistance of semirigid base is significantly correlated with the deformation resistance, and the correlation between the two is not significant under high-temperature environment. The variability of the thermal expansion and contraction characteristics of the internal microscopic phases of the semirigid base and the force characteristics of the pore interface phases are the root causes of the damage and cracking of the pavement base in a large temperature difference climate.

1. Introduction

Northwest China, influenced by topography, latitude, and altitude factors, formed a more unique and typical temperate continental cold and arid climate; in many areas, the maximum temperature difference between day and night is up to $25\sim 30^{\circ}\text{C}$, the maximum annual temperature difference is up to $70\sim 80^{\circ}\text{C}$, and the characteristics of the large temperature difference are obvious, so the durability of high-grade highway infrastructure by the large temperature difference appeared to be a significant impact. Semirigid materials, especially cement-stabilized materials, have a strong sensitivity to temperature and humidity due to their structural properties. Under the effect of continuous and periodic high temperature in the summer in the northwest,

semirigid base materials inevitably produce drying shrinkage cracking due to changes in humidity and moisture [1,2]. Continuous and cyclic low temperature in winter can easily lead to brittle cracking of semirigid base material [3]. In early spring, the alternating cycle effect of positive and negative temperature is obvious, and the semirigid base material is subject to temperature change and humidity change and produces obvious temperature shrinkage cracking and drying shrinkage cracking [4, 5]. It can be seen that the violent fluctuation of temperature in the area of large temperature difference has a very serious effect on the internal pore cracks of the semirigid base material.

Currently, in the field of road material and pavement design, the main means of monitoring microscopic pore cracks in inorganic solid material are CT techniques [6],

electron microscopy scanning (SEM) techniques [7], digital image correlation (DIC) techniques [8], acoustic emission (AE) techniques [9], and so on. Hu et al. [10] used an X-ray CT device to observe the internal pore space morphology of porous asphalt concrete during their study of the clogging resistance of porous asphalt concrete, thus establishing a link between the pore characteristics and the clogging resistance. Zhao et al. [11] further quantitatively described the proportional pore size and spatial distribution of effective and ineffective pores within porous asphalt concrete. Liang et al. [12] studied the indoor preparation method and field compaction process of cement-stabilized gravel (CSM) material, and the three-dimensional internal structure, pore number, and pore gradation of CSM were studied by industrial CT analysis. SEM techniques have been widely used in recent years for the microstructure characterization of road material and are often combined with X-ray diffraction (XRD) and energy spectrometry (EDS) techniques to characterize the mineral phase changes and elemental distribution of road concrete material [13, 14]. Liu et al. [15] used a combination of SEM and EDS to characterize the pore structure and elemental content of pavement base material mixed with different contents of steel slag (30%, 50%, and 70%), and the results showed that the addition of steel slag significantly improved the frost resistance and dry shrinkage of the pavement base. DIC technology and AE technology have a wide range of applications for the dynamic tracking and quantitative monitoring of the cracking expansion of microcracks throughout the road material [16–18]. However, the application of this technology often requires the use of relevant mechanical tests (three-point bending test and semicircular bending test) to study the mechanism of cracking and expansion of microcracks in the fracture affected area of asphalt concrete [19–21]. However, all of these methods have many limitations, CT technique is costly, SEM is cumbersome and can only be observed locally, DIC technique is based on a macroscopic view of fractures, and AE technique is an indirect study of microporosity through acoustic parameters. Nuclear magnetic resonance (NMR) techniques are fast, accurate, nondestructive, and inexpensive, and most importantly, NMR can quantitatively characterize pore size changes and the number of pores [22]. The cracking of road pavements has been a long-standing problem and has become one of the most serious types of pavement engineering diseases. In recent years, the application of NMR technology in rock, concrete, and even asphalt mixtures has certain significance [22–24]. Menapace et al. [25, 26] used the NMR technique to develop a model between RHI and T_2 values and viscosity as quantitative characterization of asphalt mixture aging. Zhang et al. [27, 28] used ^{29}Si and ^{27}Al MAS-NMR techniques to characterize the amorphous phase Si and the low crystalline phase Al in road-based material, thereby obtaining the degree of polymerization and coordination of silicoaluminate chains. Nicula et al. [29] investigated the freeze-thaw damage condition and porosity magnitude of three blast furnace slag road concrete under a freeze-thaw environment using the NMR technique.

However, in fact, the deterioration mechanism of microcrack pores inside the semirigid base material is often promoted by the mechanical behavior, so the macroscopic mechanical behavior performance must have some inevitable connection with the microfine pore development characteristics; an in-depth study of their relationship can help to reveal the intrinsic cracking mechanism of the material [22–24]. Most focus mainly on the study of thermodynamic parameters and properties of semirigid base material [5,30–35]. Lv et al. [36] found that the strength and frost resistance of cement-stabilized gravel material increase with increasing curing time and cement content through unconfined compressive test, flexural test, and freeze-thaw test studies. Bai et al. [32] investigated the suitability of open-graded cement-stabilized aggregates (OGCSM) produced from recycled aggregates at different replacement rates based on unconfined compressive strength test, indirect tensile strength test, compressive rebound modulus test, dry shrinkage test, frost resistance test, and infiltration test, and the results showed that, with the addition of a certain percentage of recycled aggregates, OGCSM has some potential applications as a base material. However, few studies have dealt with the effects of large temperature differences on the mechanical properties and pore structure deterioration of semirigid base.

This paper combined the local climatic conditions to conduct high-temperature cycle, low-temperature cycle, and freeze-thaw cycle tests on the original samples, respectively. Then, the damage deterioration of the strength and modulus of the semirigid base under the above environmental test conditions was investigated and analyzed by means of the unconfined lateral compressive strength test and dynamic modulus test. Finally, the NMR technique and SEM technique were used to deeply analyze the pore size distribution, pore content, pore structure evolution law with temperature change, and temperature cycle number of semirigid base and finally establish the relationship between strength damage and pore change. The research results of this paper can provide relevant data support and reference to reveal the cracking mechanism of pavement cracks in large temperature difference areas.

2. Materials and Methods

2.1. Materials and Sample Preparation. The samples required for this experiment were obtained by drilling and core sampling of the pavement along the Wumu section of the Jing-Xin Expressway from the Qianshan Interchange (K2 + 690) to the Kusu Interchange (K22 + 027). The specimens were cement-stabilized gravel base material, consisting of 0–5 mm particle size fine aggregate, 5–10 mm particle size coarse aggregate, 10–20 mm particle size coarse aggregate, 20–30 mm particle size coarse aggregate, and P.O42.5 (five) of Portland cement prepared in accordance with 27:18:34:12 (four). The cement comes from Hami Tianshan Cement Co., Ltd. Details of the mineral grade are shown in Table 1, and the physical parameters of raw material are shown in Table 2.

TABLE 1: Semirigid base mineral grading table.

Sieve hole size	31.5 mm	26.5	19	9.5	4.75	2.36	0.6	0.075
Quality pass percentage (%)	100	—	76.8	46.4	29.3	19.9	9.4	2.7
Target grading range	Upper limit	100	86	85	32	28	15	3
	Lower limit	100	—	68	35	22	8	0

TABLE 2: Table of physical parameters of semirigid base.

Binding material dosage (%)	5.0
Maximum dry density (g/cm ³)	2.283
Optimal water content (%)	5.0
Required compaction (%)	98

The original sample in the field needs to be processed for this test as follows: (A) According to the “Highway Engineering Inorganic Binder Stabilized Material Test Specification” (JTGE51-2009), the original sample is cut and polished to the cylindrical sample. (B) Cut part of the cylindrical sample in step 1 into cylindrical sample. (C) Polish and level the cut cylindrical sample to make the upper and lower surfaces smooth and flat. The process is shown in Figure 1.

2.2. Test Methods. The main test steps taken were as follows: (a) The samples were dried and processed by an electric blast dryer, and then the dried samples were soaked in a water tank in combination with the on-site humidity monitoring data until the samples reached the optimum moisture content [32,37,38]. (b) Based on the local climatic and hydrological conditions, this experiment set the temperature intervals as 60~20°C, 20~-20°C, and -5~-30°C, which simulated summer, early spring, and winter environments, respectively, which often constituted a large temperature difference. The temperature environment simulation in summer is 16 hours at a constant temperature of 60°C, and then 8 hours at a constant temperature of 20°C, a total of 24 hours as a cycle. The temperature environment simulation in early spring was -20°C constant temperature for 16 hours and then 20°C constant temperature for 8 hours, a total of 24 hours as a cycle. The temperature environment simulation in winter is -30°C constant temperature for 16 hours, and then -5°C constant temperature for 8 hours, a total of 24 hours as a cycle [4]. Put the soaked sample into the constant temperature and humidity test chamber after wrapping it with cling film. (c) T2 spectral scanning and pore structure analysis of specimens using NMR microstructure analysis system. (d) Measure the longitudinal wave velocity of the specimen using a nonmetallic ultrasonic monitoring analyzer. (e) The uniaxial compression test adopts MTS2000kN universal testing machine, and the loading rate is 1 mm/min. (f) Use a field emission scanning electron microscope to observe the microstructure and pore distribution of the sample after uniaxial compression failure. The detailed test procedure is shown in Figure 1.

3. Results and Discussion

3.1. The Peak Strength and Modulus of Semirigid Base Material. The uniaxial compression test was conducted by an MTS2000 kN universal testing machine produced by

Shanghai Jiezhun Instruments Equipment Co., Ltd. The test was carried out in different temperature ranges (20°C~60°C, -20°C~20°C, and -5°C~-30°C) and different cycles on UTM according to “Test Regulations for Stabilizing Material of Inorganic Binders for Highway Engineering” (JTGE51-2009) uniaxial compression test with multiple times (0 times, 3 times, 6 times, 9 times, 12 times, and 15 times), the test loading rate was 1 mm/min, and 3 sets of parallel tests were carried out at each cycle number. The test results are shown in Tables 3–5. The values in the table can be obtained from equation (1):

$$\sigma_c = \frac{4P}{\pi D^2}, \quad (1)$$

where σ_c is the peak stress in the semirigid base material, MPa; P is the maximum pressure when the semirigid base material fails, N; D is the diameter of semirigid base material, mm.

3.2. The Effect of Temperature Interval. The variation pattern of peak stress and difference (the difference of peak stress before and after cycling) of semirigid base material under different temperature intervals is shown in Figure 2(a). As can be seen from the figure, when the number of cycles is small, the peak stress of the semirigid base material is significantly higher in the high-temperature environment (20°C~60°C) than it is in the freeze-thaw environment (-20°C~20°C) and the low-temperature environment (-5°C~-30°C). And when the number of cycles is higher, the peak stress of the semirigid base material is significantly higher in the low-temperature environment than it is in the freeze-thaw environment and the high-temperature environment. It can be seen that the low-temperature environment is more significant for the peak stress deterioration of the semirigid base material in the low cycle region, and the high-temperature environment has a certain improvement effect on the mechanical properties of the semirigid base material. The damage effect of the freeze-thaw environment on the peak stress of semirigid base materials is gradually highlighted in the high-cycle region, and the low-temperature environment has a certain improvement effect on the mechanical properties of semirigid base materials. The magnitude of the peak stress variation in Figure 2(b) is given by equation (2); from Figure 2(b), it can be seen that the mechanical strength of the semirigid base material under freeze-thaw environment shows an overall trend of accelerated deterioration with a deterioration rate of 3.89%/time. The mechanical strength of the semirigid base material under high-temperature environment showed an overall trend of improvement followed by deterioration, the

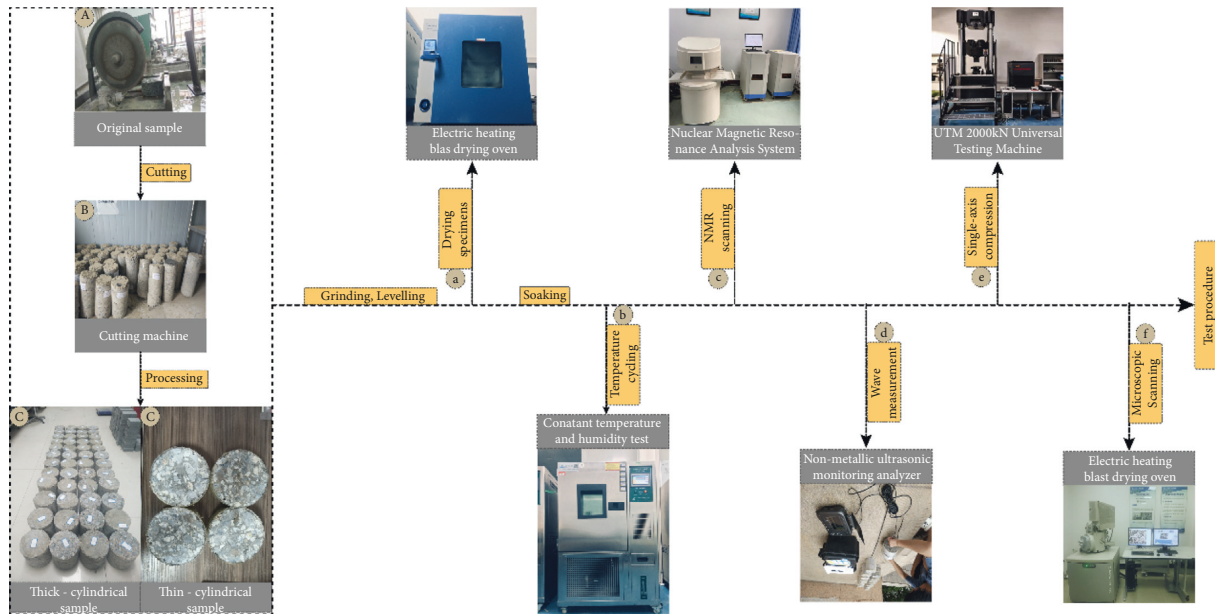


FIGURE 1: Specimen preparation and test procedure flow.

TABLE 3: Uniaxial compression experimental results of semirigid base material under the temperature range of 20°C~60°C.

Number of cycles	Parallel strength test value (MPa)			Intensity representative value (MPa)	Standard deviation	Coefficient of variation (%)
0	10.61	12.82	14.06	12.50	1.75	13.95
3	17.43	16.06	15.42	16.3	1.03	6.3
6	12.84	13.15	15.31	13.77	1.35	9.77
9	11.72	13.21	15.63	13.52	1.97	14.6
12	10.88	11.67	13.91	12.15	1.57	12.93
15	11.94	9.55	10.22	10.57	1.23	11.66

TABLE 4: Uniaxial compression experimental results of semirigid base material under the temperature range of -20°C~20°C.

Number of cycles	Parallel strength test value (Mpa)			Intensity representative value (MPa)	Standard deviation	Coefficient of variation (%)
0	10.61	12.82	14.06	12.50	1.75	13.95
3	11.00	11.50	13.49	12.00	1.32	10.98
6	9.61	12.61	9.79	10.67	1.68	15.77
9	8.61	8.72	8.89	8.74	0.14	1.61
12	7.47	8.21	6.78	7.49	0.72	9.55
15	6.59	5.38	6.53	6.16	0.67	10.93

TABLE 5: Uniaxial compression experimental results of semirigid base material under the temperature range of -5°C~-30°C.

Number of cycles	Parallel strength test value (MPa)			Intensity representative value (MPa)	Standard deviation	Coefficient of variation (%)
0	10.61	12.82	14.06	12.50	1.75	13.95
3	11.21	9.72	10.13	10.35	1.32	10.98
6	12.37	9.41	12.71	11.50	1.68	15.77
9	12.73	16.00	15.12	14.62	0.14	1.61
12	11.70	14.26	15.61	13.86	0.72	9.55
15	11.69	14.56	14.12	13.46	0.67	10.93

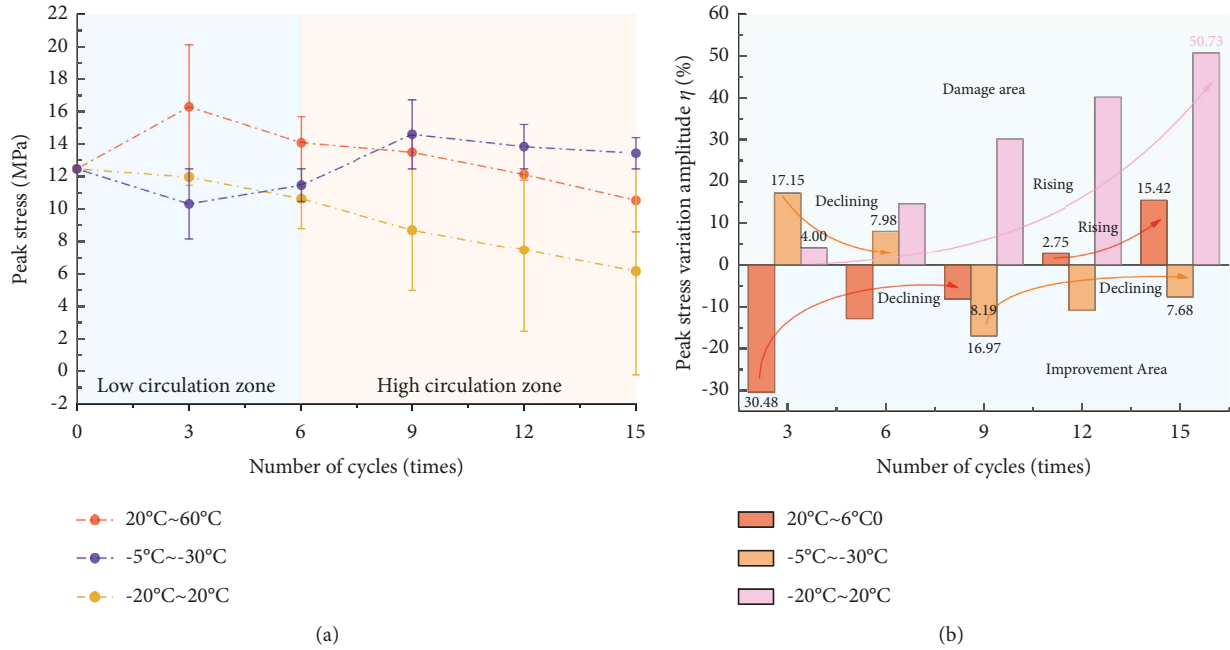


FIGURE 2: Peak strength of semirigid base at different temperature intervals. (a) Variation of peak stress at different temperature intervals. (b) Variation of peak stress at different temperature intervals.

improvement effect gradually weakened, the deterioration effect gradually increased, and the deterioration rate was 4.22%/time. The mechanical strength of semirigid base material under low-temperature environment showed the characteristics of first damage and then improvement, the deterioration effect and improvement effect both gradually weakened, and the deterioration rate was -3.06%/time. It can be seen that the damage effect of freeze-thaw environment on the mechanical properties of semirigid base materials is continuous.

$$\eta = \left[\frac{\sigma_{c,c} - \sigma_{c,t}}{\sigma_{c,c} \times 100} \right], \quad (2)$$

where η is the change in peak stress of semirigid base material before and after cycling, %; $\sigma_{c,c}$ is the peak stress in semirigid base material before cycling, MPa; $\sigma_{c,t}$ is the peak stress of semirigid base material after cycling, MPa.

The longitudinal wave velocity detection of semirigid base materials using MM-A4 nonmetallic ultrasonic monitoring analyzer produced by Beijing Kekangrui Co., Ltd. The link between the dynamic modulus E_D of the semirigid base material and the longitudinal wave velocity V_p is established by (3) [39]. The test results are shown in Tables 6-8.

$$E_D = \left[\frac{\rho V_p^2 (1 + \mu)(1 - 2\mu)}{(1 - \mu)} \right], \quad (3)$$

where E_D is the dynamic modulus, MPa; ρ is the density of semirigid base material, g/cm^3 , and this paper takes $\rho = 2.283$; V_p is the longitudinal wave speed of semirigid base material, m/s; μ is Poisson's ratio of semirigid base material, and this paper takes $\mu = 0.3$.

The variation of dynamic modulus with the number of cycles measured at different temperature intervals is shown in Figure 3. As can be seen from the figure, the overall dynamic modulus value of the semirigid base material in low-temperature environment is low, and the average value can reach 5500 MPa, which is much higher than the modulus value in high-temperature environment (4800 MPa) and freeze-thaw environment (4800 MPa). It can be seen that the semirigid base material has better resistance to deformation in low-temperature environment than in freeze-thaw environment and high-temperature environment. Based on the expectation and standard deviation equation to evaluate the damage factor of dynamic modulus of semirigid base material under different environments (Figure 4(b)), it can be seen that the damage degree of dynamic modulus of semirigid base material under freeze-thaw environment is generally more serious, and the damage impact area is concentrated in 0.67~0.77. The high-temperature environment and low-temperature environment on the dynamic modulus of semirigid base material have a wider range of influence, and the damage impact area is 0.33~0.65 and 0.48~0.66, respectively; thus, it can be seen that the semirigid base material deformation resistance under the action of the periodic freeze-thaw environment is significantly reduced.

3.3. The Influence of the Number of Cycles. The influence of the number of cycles on the peak stress of the semirigid base is shown in Figure 4(a). Under the high-temperature environment, the peak stress of the semirigid base material increased and then decreased with the increase of the number of cycles; the peak stress reached the maximum value of 16.30 MPa after 3 cycles and decreased to the minimum value of 10.57 MPa after 15 cycles, which reduced the stress intensity by 1.5 times.

TABLE 6: Experimental results of dynamic modulus of semirigid base material under the temperature range of 20°C~60°C.

Number of cycles	Parallel modulus test value (MPa)			Modulus representative value (MPa)	Standard deviation	Coefficient of variation (%)
0	8601	9361	10375	9445	889.91	9.42
3	8693	6440	7520	7551	1126.77	14.92
6	3585	4405	3468	3820	510.55	13.37
9	3165	2841	3468	3158	313.46	9.93
12	4774	4785	6300	5286	877.93	16.61
15	3548	4911	4758	4406	746.86	16.65

TABLE 7: Experimental results of dynamic modulus of semirigid base material under the temperature range of -5°C~-30°C.

Number of cycles	Parallel modulus test value (MPa)			Modulus representative value (MPa)	Standard deviation	Coefficient of variation (%)
0	11940	13290	12726	12652	678.12	5.36
3	5394	4928	4547	4956	424.18	8.56
6	4312	4367	5167	4616	478.48	10.37
9	8341	7009	8166	7839	723.48	9.23
12	5180	4722	6175	5359	742.88	13.86
15	4819	4132	5267	4739	571.98	12.07

TABLE 8: Experimental results of dynamic modulus of semirigid base material under the temperature range of -20°C~20°C.

Number of cycles	Parallel modulus test value (MPa)			Modulus representative value (MPa)	Standard deviation	Coefficient of variation (%)
0	17129	16249	18480	17286	1123.68	6.50
3	5483	6142	7250	6292	892.98	14.19
6	4453	4622	5678	4918	663.91	13.50
9	4034	4790	5029	4618	519.85	11.26
12	4834	3928	4333	4365	453.82	10.40
15	3783	3566	4717	4022	611.69	15.21

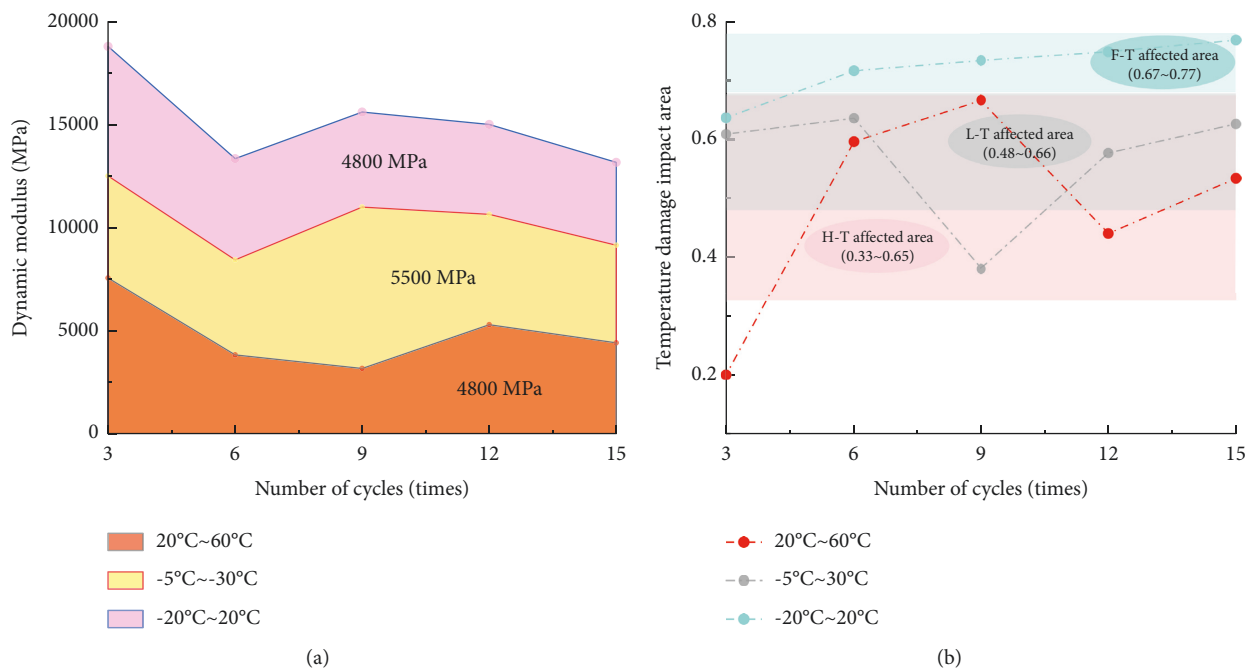


FIGURE 3: Variation of dynamic modulus of semirigid base material under different temperature intervals. (a) Dynamic modulus stacking diagram at different temperature intervals. (b) Temperature damage impact area.

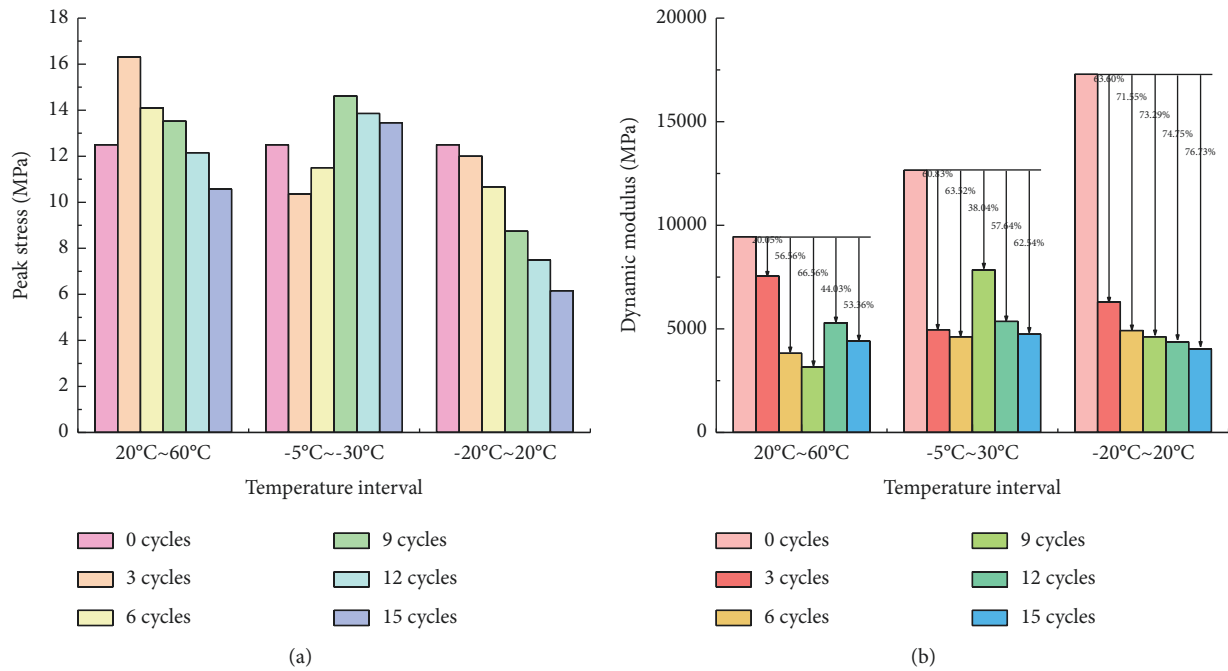


FIGURE 4: Variation of peak stress and dynamic modulus of semirigid base material with the number of cycles. (a) Variation of peak stress with the number of cycles. (b) Variation of dynamic modulus with the number of cycles.

Under the low-temperature environment, the peak stress of semirigid base material decreases and then increases with the increase of the number of cycles, and the peak stress reaches the minimum value of 10.35 MPa after 3 cycles and the maximum value of 14.62 MPa after 9 cycles, which expands the stress intensity by 1.4 times. Under the freeze-thaw environment, the peak stress of the semirigid base material gradually decreased with the increase of the number of cycles, from 12.50 MPa after 0 cycles to 6.16 MPa after 15 cycles, and the stress intensity was reduced by a factor of 2. Accordingly, it can be seen that the number of freeze-thaw cycles has the most significant deterioration effect on the mechanical properties of the semirigid base material.

The influence of the number of cycles on the dynamic modulus of the semirigid base is shown in Figure 4(b). Under the action of high-temperature cycling, the deformation resistance of semirigid base material is very unstable, and the deformation resistance first weakens, then strengthens, and finally weakens with the increase of cycling times. Compared with the dynamic modulus after 0 cycles, the decreases in dynamic modulus after 3 to 15 cycles were 20.05%, 56.56%, 66.56%, 44.03%, and 53.36%, respectively. Under the action of low-temperature cycling, the dynamic modulus of the semirigid base material is basically maintained at about 5500~6000 MPa. Compared with the dynamic modulus after 0 cycles, the decrease of dynamic modulus after 3 to 15 cycles was 60.83%, 63.52%, 38.04%, 57.64%, and 62.54%, respectively. Under the action of freeze-thaw cycling, the damage of the dynamic modulus of the semirigid substrate is very serious; compared with the dynamic modulus after 0 cycles, the decrease of dynamic modulus after 3~15 cycles is 63.60%, 71.55%, 73.29%, 74.75%, and 76.73% respectively.

3.4. Correlation Analysis of Peak Stress and Dynamic Modulus. Based on the above analysis, this paper tries to establish the relationship between peak stress σ_c and dynamic modulus E_D of the semirigid base material by the number of cycles under the effect of large temperature difference so as to analyze the complex characteristics of semirigid base material under large temperature difference [30,35]; its purpose is as follows. First, the later study can predict the elastic-plastic properties or mechanical behavior of the semirigid base material under a large temperature difference environment only by measuring the relevant test parameters [40]. Secondly, it is convenient to analyze and reveal the pore evolution characteristics and damage cracking mechanism of semirigid base material later on [41]. Figures 5(a) to 5(c) show the fitted curves of the peak stress and dynamic modulus of the semirigid base material with the number of cycles at different temperature intervals. The specific fitting equations are shown in Table 9.

Analysis of Figures 5(a) to 5(c) shows that, under high-temperature environment, the resistance to deformation of semirigid base material first decreases and then increases as the mechanical strength decreases. Under freeze-thaw conditions, the resistance to deformation of semirigid base material continues to weaken as the mechanical strength decreases. Under low-temperature environment, the resistance to deformation of the semirigid base material increases with increasing mechanical strength and decreases thereafter with decreasing mechanical strength, but the peaks of both are not at the same number of cycles. Further analysis shows that the peak stress of the semirigid base material shows a certain positive correlation with the dynamic modulus, but this correlation gradually becomes less obvious with the

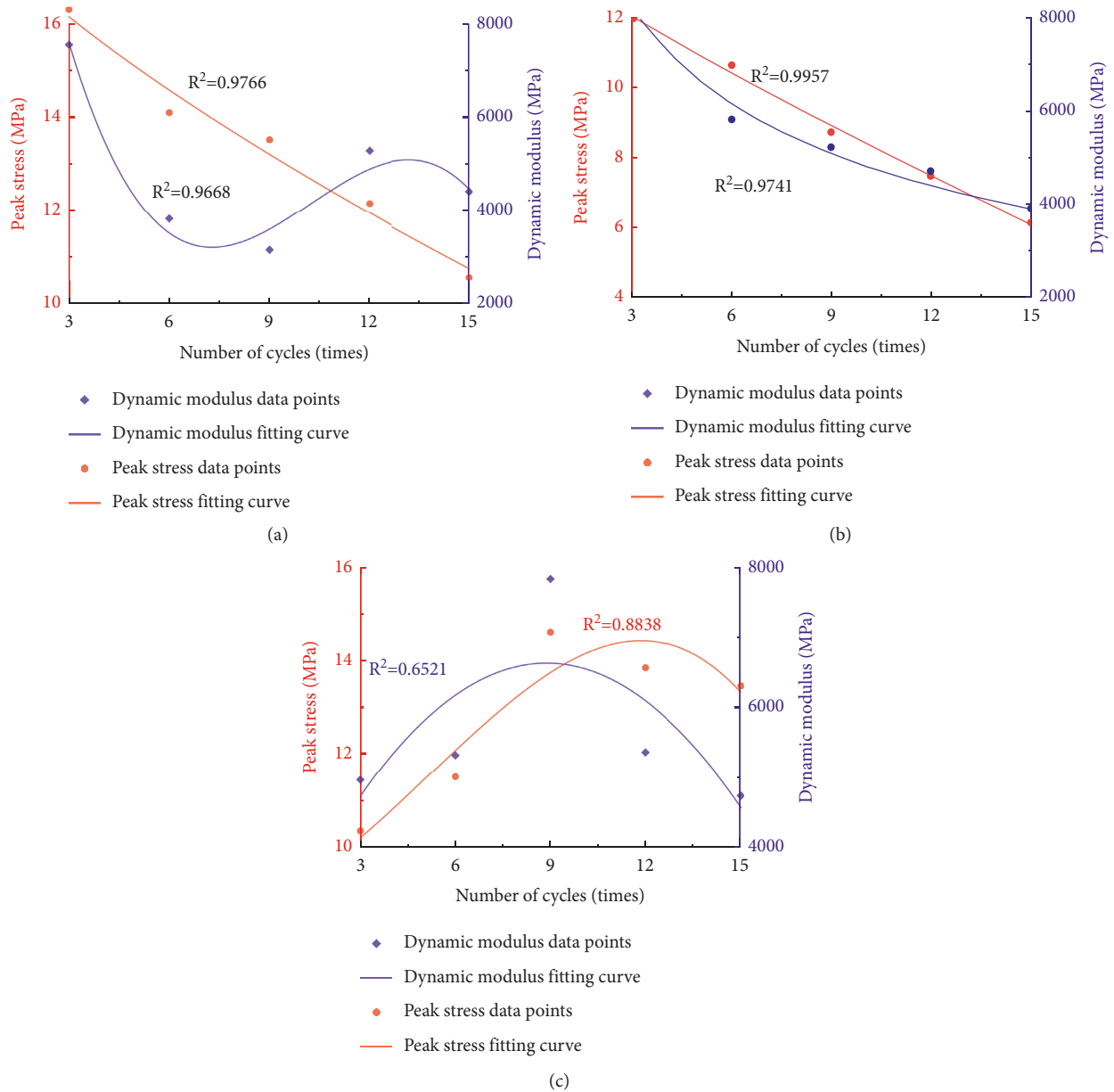


FIGURE 5: Fitting curves of peak stress and dynamic modulus of semirigid base material versus the number of cycles. (a) Fitting curve at 20°C~60°C. (b) Fitting curve at -20°C~20°C. (c) Fitting curve at -5°C~-30°C.

TABLE 9: Fitting equations for semirigid base material under different temperature intervals.

Temperature interval	Relationship	Fitting equations
20°C ~60°C	σ_c-N E_D-N	$\sigma_c = 18.445 - 1.007 N^{-0.750}$ $E_D = 18788.943 - 5243.348 N + 558.736 N^2 - 18.192 N^3$
-20°C ~20°C	σ_c-N E_D-N	$\sigma_c = 14.053 - 0.771 N^{0.861}$ $E_D = 8313.630 N^{-0.274}$
-5°C ~-30°C	σ_c-N E_D-N	$\sigma_c = 8.956 + 0.226 N + 0.097 N^2 - 0.005 N^3$ $E_D = 2277.745 + 981.578 N - 55.255 N^2$

increase of the number of cycles, indicating that the semirigid base material is not significantly correlated with the axial deformation resistance and load resistance under high-temperature environment, which may be caused by the

inhomogeneity of the semirigid base material. Under the freeze-thaw environment, the peak stresses of the semirigid base material showed a linear positive correlation with the dynamic modulus, indicating a significant correlation

between the axial deformation resistance and load resistance of the semirigid base material under the freeze-thaw environment. Under the low-temperature environment, the peak stress of the semirigid base material and the dynamic modulus show a linear positive correlation, which shows that the semirigid base material has a certain significant correlation in the axial antideformation ability and the antiloading ability under the low-temperature environment.

3.5. Analysis of Breakage Patterns and Microscopic Damage Characteristics. Figure 6 shows the compression damage patterns of the semirigid base specimens after different numbers of cycles at different temperature intervals. According to this figure, it can be seen that, under the high-temperature environment, the semirigid base material is damaged with cracks all around, and the cracks produced are mainly vertical cracks, indicating that the semirigid base material is damaged by tension along the interface phase between the aggregate particles and the cement matrix. There is a peeling phenomenon on the surface, and it becomes more and more obvious as the number of cycles increases. Under low-temperature environment, the damage of the semirigid base material is covered with vertical strip cracks around the circumference, which indicates that the semirigid base material produces tension failure along the interfacial phase around the aggregate particles. There is a peeling phenomenon on the surface, and the peeling phenomenon is most serious when it is cycled 6 times to 9 times. Under the freeze-thaw environment, the semirigid base material is covered with cracks around the circumference of the damage, the cracks produced are mainly vertical cracks, and other secondary crack angles are between 0° and 15° , indicating that the semirigid base material produces mixed tensile-shear failure. The scale of surface material shedding increases with the number of cycles. It is easy to see that the damage characteristics of semirigid subgrade materials under different environmental conditions are significantly different, but the damage mode is mainly the tensile damage of the weak interface phase.

The spatial variation and damage evolution of the internal pore structure of the material seriously restrict the macroscopic mechanical properties of the material. In order to better recognize the internal spatial damage condition of the semirigid base material after uniaxial compression under the condition of large temperature difference, SEM tests were conducted on the semirigid material damaged by compression after 12 cycles under different environments, as shown in Figure 7. When the SEM is magnified 5000 times, it can be seen that the drying shrinkage caused by the evaporation of water at high temperature leads to a few through cracks on the surface of the cement matrix, and the through cracks lead to the reduction of the material strength, as can be well demonstrated in Figure 4(a). And a large amount of flocculated C-S-H (calcium silicate hydrate) is produced on the material surface under low-temperature environment, which effectively fills the material microporous cracks and increases the material denseness to some extent, which is consistent with the analysis in Figure 4(a). Under the freeze-

thaw environment, the material is affected by the freezing and swelling force generated by the action of the water-ice phase and the contraction force induced by the temperature change together to produce a large number of cracked pores, and the increase of the pore content will inevitably lead to the loss of its bearing capacity, which well explains the deterioration of the peak stress under the freeze-thaw environment in Figure 4(a).

Based on the above analysis, it can be seen that, under the condition of large temperature difference, the semirigid base material is subject to different degrees of rupture damage caused by the drying shrinkage stress induced by water evaporation, the low-temperature shrinkage force induced by temperature reduction, and the freeze-swelling force caused by repeated freezing and thawing, and the degree of damage is affected by the number of cycles and shows significant variability. This damage variability is visualized in the ups and downs of macroscopic mechanical properties (strength and modulus) and fluctuations. Quantitative analysis of the correlation between peak stress and microscopic pore structure and pore size is of great importance to reveal the damage evolution mechanism of semirigid base material under large temperature difference environment. The NMR technique was used to measure the NMR signal intensity of semirigid base material under different environments and after different numbers of cycles; according to (4) [24,42], the relationship between material pore radius and T_2 transverse relaxation time is established, as shown in Figures 8 and 9. According to the research results of Zhang et al. [23,43], the internal pores of the semirigid base material can be classified into the following four classes, as shown in Table 10.

$$\gamma = \rho_2 F_s T_2, \quad (4)$$

where γ is the pore radius of semirigid base material, nm; ρ_2 is the transverse relaxation strength of semirigid base material, $\mu\text{m/ms}$, and this paper takes $\rho_2 = 0.003$; F_s is the shape geometry factor, and this paper takes $F_s = 3$; T_2 is the transverse relaxation time of semirigid base material, ms.

According to the analysis of Figures 8 and 9, it can be seen that the lateral relaxation time T_2 distribution curve contains 3~4 peaks, which correspond to less harmful pores, harmful pores, and more harmful pores from left to right. The specific analysis is as follows.

Under the high-temperature environment, the area enclosed by the left peak is the largest, indicating that the number of harmful pores accounted for a large proportion of the material. At the beginning of the cycle (0 to 3 times), the right peak and the middle peak area appeared to decrease, and then the right peak area and the middle peak area gradually increased with the increase of the cycle times, indicating that the number of harmful pores and multiple harmful pores of the semirigid base material first decreased and then gradually increased. The reason is that, under the action of high-temperature cycle in the early stage, semirigid base material aggregate particles by thermal expansion make the material primary cracks gradually closed, and at this time, the material internal water evaporation effect is not significant, so as to enhance the bond between the aggregate

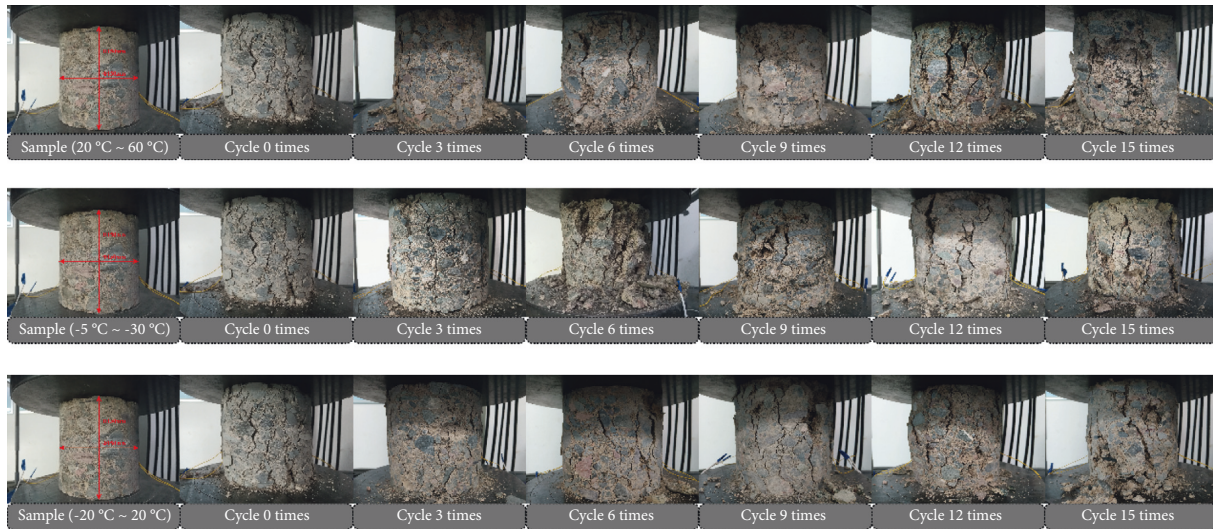


FIGURE 6: Failure modes at different temperature intervals and number of cycles.

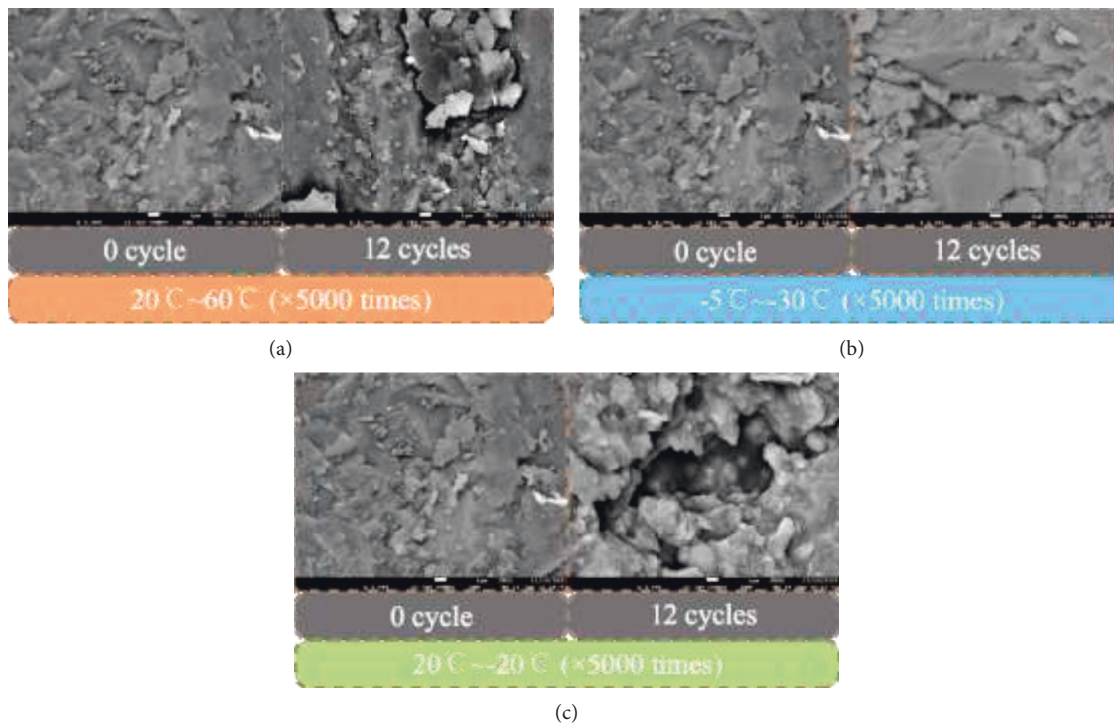


FIGURE 7: SEM images of specimens damaged by compression after 12 cycles at different temperature intervals. (a) $20^{\circ}\text{C}\sim 60^{\circ}\text{C}$ ($\times 5000$ times). (b) $-5^{\circ}\text{C}\sim -30^{\circ}\text{C}$ ($\times 5000$ times). (c) $20^{\circ}\text{C}\sim -20^{\circ}\text{C}$ ($\times 5000$ times).

and cement matrix and improve the mechanical strength of the material semirigid base material; with the increase of the number of cycles and cycle time, the excessive expansion thermal stress and the temperature stress generated by the evaporation of a large amount of water make the concrete aggregate particles between the extrusion breakage and cement matrix shrinkage cracking, thus producing a large number of harmful pores and multiharmful pores, which eventually lead to the reduction of mechanical strength of semirigid base materials [44].

Under the low-temperature environment, the sum of the area occupied by each peak gradually decreases with the increase of the number of cycles, indicating that the number of pores of the material as a whole becomes a decreasing trend. At the beginning of the cycle (3~6 times), the area occupied by the right and middle peaks was the largest and then decreased with the increase of the cycle number, indicating that the mechanical strength of the semirigid base material was seriously damaged at the beginning of the cycle and then slowly rebounded with the cycle number. The precooling shrinkage of the aggregate

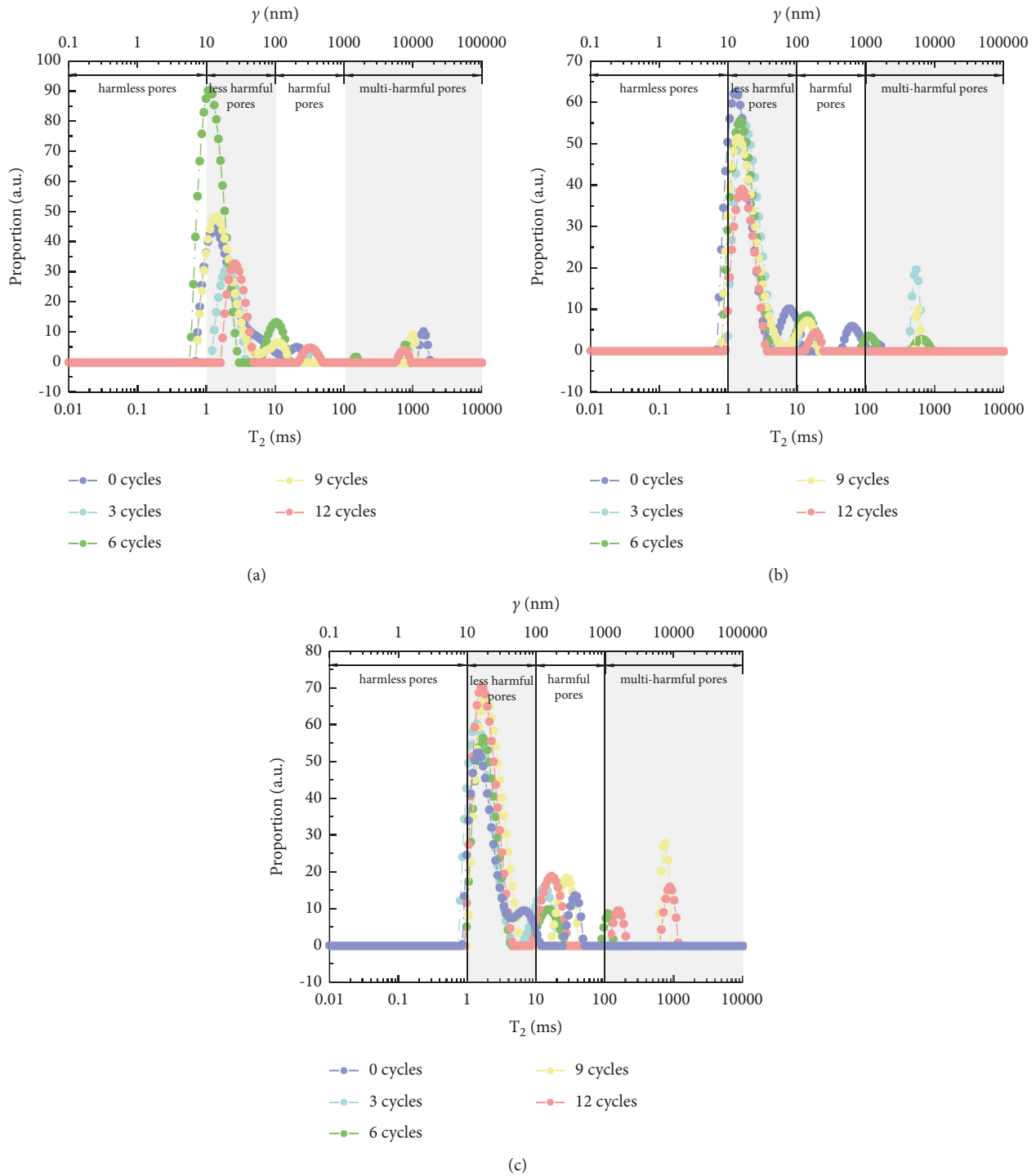


FIGURE 8: Pore distribution characteristics of semirigid base material after different cycles at different temperature intervals. (a) 20°C~60°C. (b) -5°C~-30°C. (c) 20°C~-20°C.

inside the semirigid base material at the early stage of the low-temperature cycle makes the cracks near the interface phase gradually expand; while the pore water is affected by the low temperature to produce water-ice phase change, volume expansion leads to the pore wall extrusion breakage, resulting in a significant reduction in strength compared to room temperature; as the low-temperature cycle continues, the pore water-

ice phase change completely fills the internal pores of the material, so that it forms an “organic whole” with the semirigid base; in addition, the continuous low-temperature cycle leads to a reduction in the difference between the contraction characteristics of each microphase inside the semirigid base, which eventually leads to an increase in the strength of the semirigid base material [45].

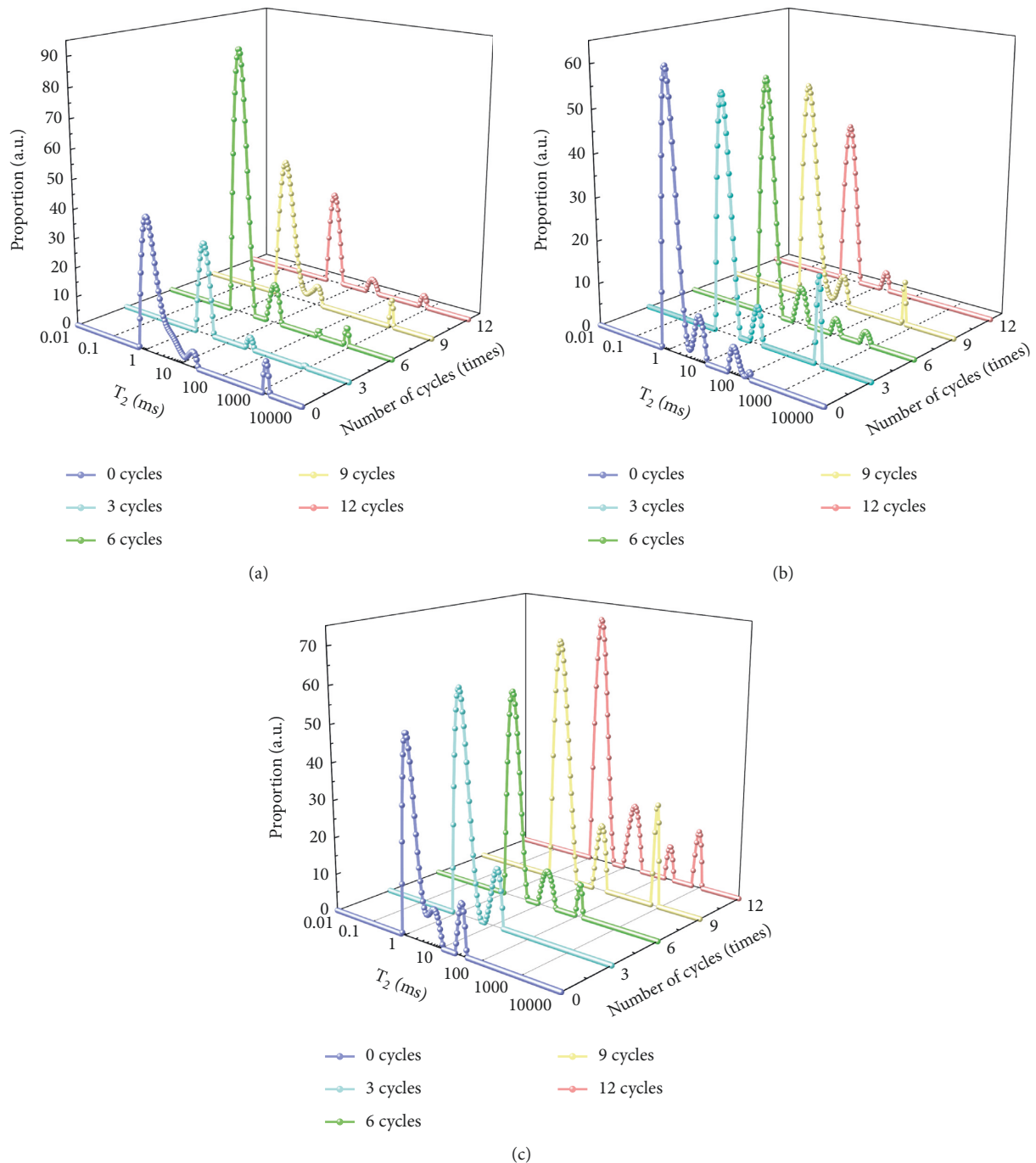


FIGURE 9: Pore distribution characteristics of semirigid base material after different cycles at different temperature intervals (3D). (a) 20°C~60°C. (b) -5°C~-30°C. (c) 20°C~-20°C.

Under the freeze-thaw environment, the area occupied by each peak shows an increasing trend with the increase of the number of cycles, among which the number of harmful pores and the number of multiharmful pores increase more obviously, which shows that the freeze-thaw cycle has a more significant effect on the change of pore results of the semirigid base material. As a temperature-sensitive material, the semirigid base is particularly sensitive to the freeze-thaw environment, which can be seen from the above analysis. The pore water in the material produces frost heaving stress

superposition on the pores under the repeated action of “freeze-thaw,” the thermal expansion and cold contraction characteristics of each microscopic phase are significantly different under the repeated action of “freezing-thawing,” which easily produces shrinkage stress superposition on the interface phase, and the large increase of harmful pores leads to significant deterioration of mechanical strength of the base material [46].

The area distribution of T_2 spectrum is proportional to the decay of free water inside the pores of different pore

TABLE 10: Pore grade classification (Liu et al. and Zhang et al.) [23, 43].

Pore category	Harmless pores	Less harmful pores	Harmful pores	Multiple harmful pores
Aperture size	<10 nm	10 nm~100 nm	100 nm~1000 nm	>1000 nm

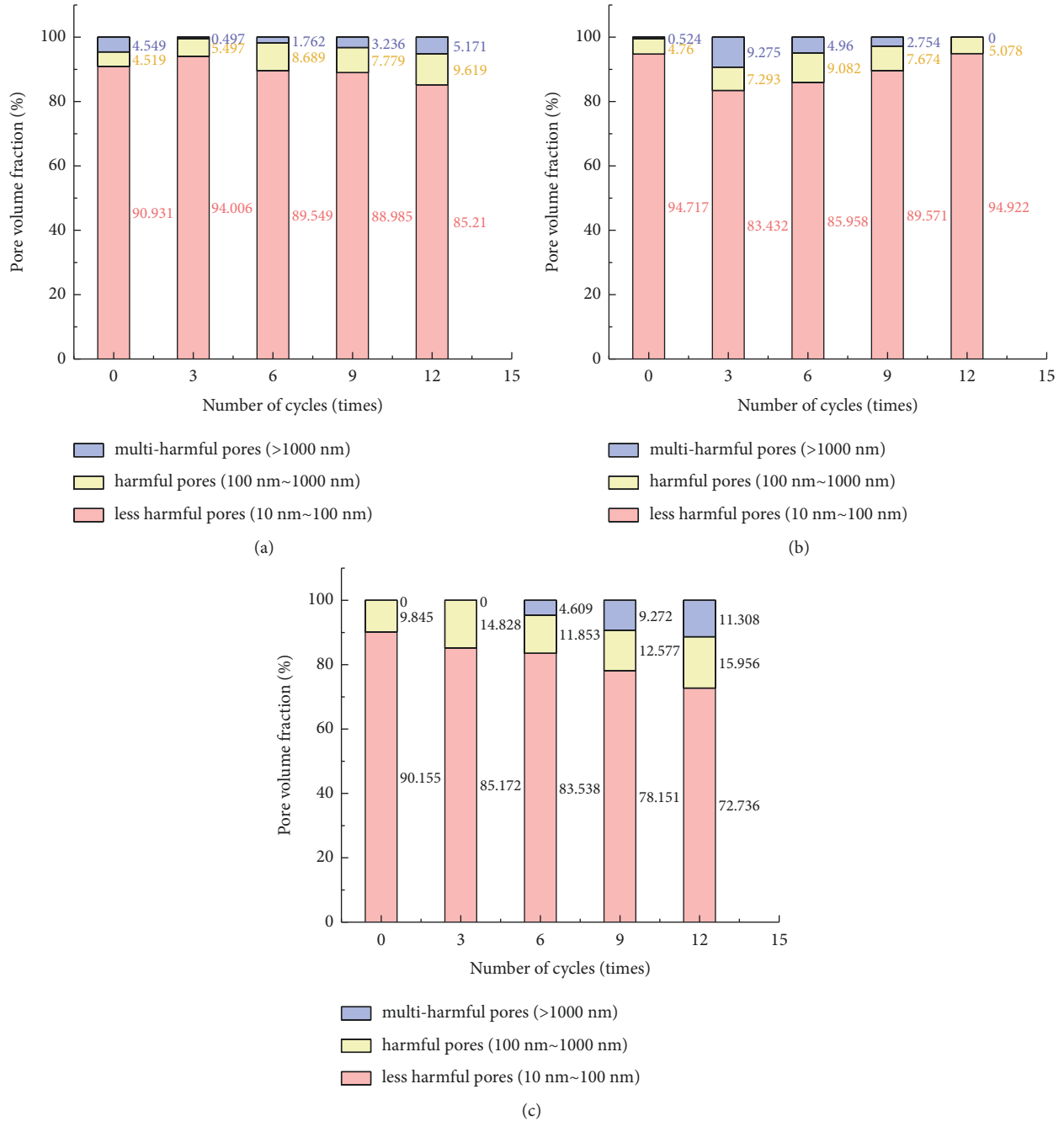


FIGURE 10: Pore volume fraction distribution of semirigid base material under different cycle times. (a) 20°C~60°C. (b) -5°C~-30°C. (c) -20°C~20°C.

TABLE 11: NMR spectral area of semirigid base after different number of cycles at different temperature intervals.

Temperature intervals (°C)	Number of cycles (times)	Total area of T2 spectrum (cm ²)	Less harmful hole area (cm ²)	Harmful hole area (cm ²)	More harmful hole area (cm ²)
20~60	0	905.89	823.738	40.939	41.213
	3	360.64	339.023	19.824	1.793
	6	1403.905	1257.177	121.987	24.742
	9	858.835	764.234	66.805	27.796
	12	390.767	332.972	37.589	20.207
-5~-30	0	1029.081	974.708	48.98	5.393
	3	895.551	747.175	65.314	83.062
	6	890.148	765.157	80.847	44.144
	9	872.389	781.408	66.951	24.03
	12	501.842	476.357	25.485	0
-20~20	0	894.658	806.581	88.077	0
	3	1027.467	875.112	152.354	0
	6	869.981	726.762	103.12	40.099
	9	1292.425	1010.037	162.551	119.837
	12	1305.531	949.593	208.309	11.308

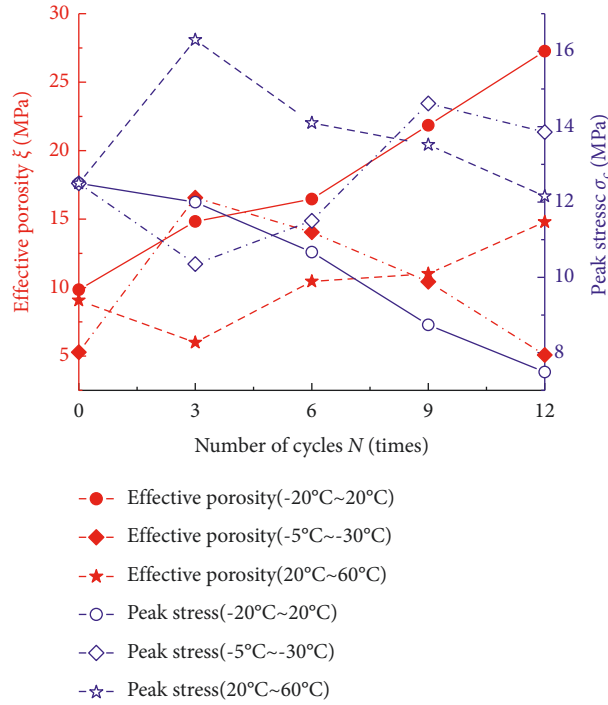


FIGURE 11: Peak stress and effective porosity after different number of cycles.

sizes; thus, it can visually reflect the changes of the internal structure of the pores [47], and the NMR spectral areas of the semirigid base after different number of cycles at different temperature intervals are detailed in Table 11. The percentage of T_2 spectral area of different pore classes (less harmful pores, harmful pores, and more harmful pores) to the total T_2 spectral area is approximated as the pore volume fraction, as shown in Figure 10. Combined with the analysis in Table 11 and Figure 10, it can be seen that, regardless of the environment, the percentage of the number of less harmful pores far exceeds the percentage of the number of harmful pores and the percentage of the number of more

harmful pores. The freeze-thaw environment damages the material more deeply, resulting in a significantly higher percentage of harmful pore counts and more harmful pore counts than those in high- and low-temperature environments. Specifically, the percentage of harmful pores and multiple harmful pores under freeze-thaw environment varied with the number of cycles as 9.85%, 14.83%, 11.85%, 12.58%, 15.96%, 0.00%, 0.00%, 4.61%, 9.27%, and 11.31%, respectively. The percentage of harmful pores and multi-harmful pores under high-temperature environment varied with the number of cycles as 4.52%, 5.50%, 8.69%, 7.78%, 9.62%, 4.55%, 0.50%, 1.76%, 3.24%, and 5.17%, respectively.

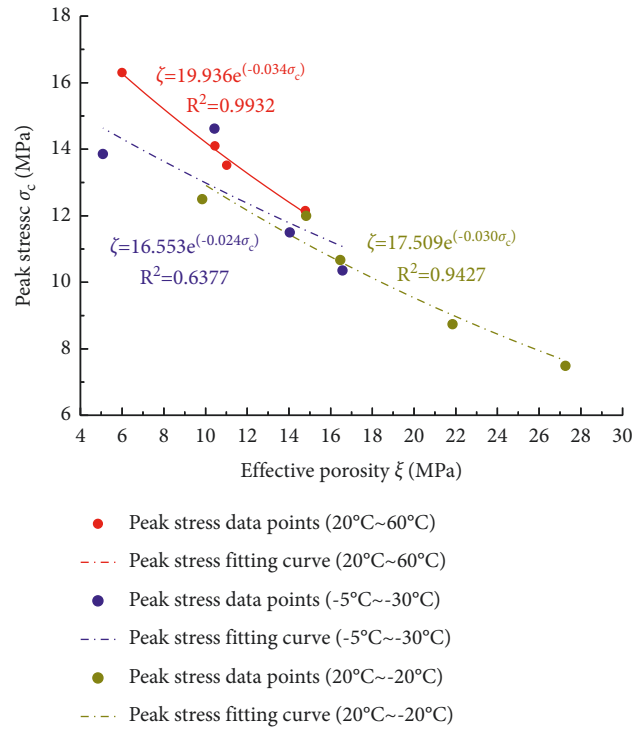


FIGURE 12: Relationship between pore efficiency and peak stress at different temperature intervals.

The percentage of harmful pores and multiharmful pores varied with the number of cycles in low-temperature environment as 4.76%, 7.29%, 9.08%, 7.67%, 5.08%, 0.52%, 9.36%, 4.96%, 2.75%, and 0.00%, respectively.

Based on the above analysis, this paper defines the sum of the percentage of harmful pores and the percentage of multiple harmful pores as the effective porosity of the semirigid base material ξ . This paper describes the evolution of mechanical properties of semirigid base material after different cycles under different environments based on the change of pore content (Figure 11) so as to analyze the macrofine scale linkage of damage characteristics of semirigid base material under large temperature difference conditions and provide relevant data support and reference value for the subsequent study of this kind of pavement engineering problems. According to the test results, the relationship curve between the effective porosity of NMR and peak stress was established, as shown in Figure 12. Combining Figures 11 and 12, it can be seen that the peak stress is negatively correlated with the change of effective porosity as the number of cycles increases, and the effective porosity shows a decreasing trend with the number of cycles at low temperatures, and vice versa at high-temperature and freeze-thaw environments. It is shown that the mechanical properties of semirigid base material under freeze-thaw and high-temperature environments decrease exponentially as a function of the increase in effective porosity, while the mechanical properties of semirigid base material under low-temperature environments increase exponentially as a function of the decrease in effective porosity. This is more consistent with the results of Zhang et al. [23,48].

4. Conclusions

The variation patterns of peak stress and dynamic modulus of semirigid base materials under different temperature intervals show significant variability. The freeze-thaw environment shows an overall deterioration of the peak stress of the material, and the dynamic modulus damage temperature damage influence factor is as high as 0.67~0.77. The effect of freeze-thaw environment is the most significant.

In a high-temperature environment, peak stress and dynamic modulus show a power function and polynomial functions, respectively, with respect to the number of cycles. In a low-temperature environment, the peak stress, dynamic modulus, and the number of cycles show polynomial functions. In the freeze-thaw environment, both peak stress and dynamic modulus show a power function with respect to the number of cycles. There is a significant correlation between the axial load resistance and deformation resistance of semirigid base material under freeze-thaw and low-temperature environments.

The differences in damage characteristics of the semirigid base under different environments are mainly reflected in the dynamic evolution of pore structure and pore size, which are rooted in the differences in the expansion and contraction characteristics of each microscopic phase of the material and the differences in the mechanical interface effects on the internal pores, but the macroscopic damage mode is mainly based on tensile damage. The peak stress and effective porosity of the semirigid base under different environments are exponentially related.

Data Availability

The data used to support the findings of this study are available from the corresponding author upon request.

Conflicts of Interest

The funders had no role in the design of the study; in the collection, analyses, or interpretation of data; in the writing of the manuscript; or in the decision to publish the results. Moreover, The authors declare that there are no conflicts of interest regarding the publication of this paper.

Authors' Contributions

Jia Pan and Yanjun Shen carried out the figure preparation, analysis, manuscript preparation, and editing. Ming Dai planned and designed the research. Jianbo Deng conducted the study. Yeermulati Muhadeer performed the data collection.

Acknowledgments

This research was supported by the National Natural Science Foundation of China (Grant no. 41772333), the Foundation of Shaanxi Key Laboratory of Safety and Durability of Concrete Structures, Xijing University (Grant no. XJKFJJ201802), and Yulin 2020 Science and Technology Plan (Industry University Research) Project (CXY-2020-034).

References

- [1] A. Toktorbai uulu, H. Katsuchi, H. Kim, H. Yamada, and Y. Ijima, "Study on thermal parameters of asphalt concrete for countermeasures against high surface temperature of pavement in tunnel," *Road Materials and Pavement Design*, vol. 22, no. 4, pp. 954–968, 2021.
- [2] Y. Zhao, J. Jiang, Y. Dai, L. Zhou, and F. Ni, "Thermal property evaluation of porous asphalt concrete based on heterogeneous meso-structure finite element simulation," *Applied Science-Basel*, vol. 10, no. 5, p. 1671, 2020.
- [3] X. Wang, K. Li, Y. Zhong, Q. Xu, and C. Li, "XFEM simulation of reflective crack in asphalt pavement structure under cyclic temperature," *Construction and Building Materials*, vol. 189, pp. 1035–1044, 2018.
- [4] M. He, S. Ma, C. Liu, J. Zhang, and S. Yuan, "Effect of microcracking on the shrinkage cracking and durability performance of cement-treated macadam material," *International Journal of Pavement Engineering*, vol. 2021, pp. 1–14, 2021.
- [5] Y. Wang, Y. Tan, M. Guo, Z. Liu, and X. Wang, "Study on the dynamic compressive resilient modulus and frost resistance of semi-rigid base materials," *Road Materials and Pavement Design*, vol. 18, no. 3, pp. 259–269, 2017.
- [6] J. Li, F. Wang, F. Yi, J. Ma, and Z. Lin, "Fractal analysis of the fracture evolution of freeze-thaw damage to asphalt concrete," *Materials*, vol. 12, no. 14, p. 2288, 2019.
- [7] F. Xu, M. Zhou, J. Chen, and S. Ruan, "Mechanical performance evaluation of polyester fiber and SBR latex compound-modified cement concrete road overlay material," *Construction and Building Materials*, vol. 63, pp. 142–149, 2014.
- [8] B. Doll, H. Ozer, J. Rivera-Perez, I. L. Al-Qadi, and J. Lambros, "Damage zone development in heterogeneous asphalt concrete," *Engineering Fracture Mechanics*, vol. 182, pp. 356–371, 2017.
- [9] S. Li, G. Wu, and H. Shi, "Acoustic emission characteristics of semi-rigid bases with three moisture conditions during bending tests," *Road Materials and Pavement Design*, vol. 20, no. 1, pp. 187–198, 2019.
- [10] J. Hu, Z. Qian, P. Liu, D. Wang, and M. Oeser, "Investigation on the permeability of porous asphalt concrete based on microstructure analysis," *International Journal of Pavement Engineering*, vol. 21, no. 13, pp. 1683–1693, 2020.
- [11] Y. Zhao, X. Wang, J. Jiang, and L. Zhou, "Characterization of interconnectivity, size distribution and uniformity of air voids in porous asphalt concrete using X-ray CT scanning images," *Construction and Building Materials*, vol. 213, pp. 182–193, 2019.
- [12] C. Liang, Y. Wang, G. Tan, L. Zhang, Y. Zhang, and Z. Yu, "Analysis of internal structure of cement-stabilized macadam based on industrial CT scanning," *Advances in Materials Science and Engineering*, vol. 2020, Article ID 5265243, 2020.
- [13] W.-x. Zheng, X.-y. Xiao, C.-g. Chang et al., "Characterizing properties of magnesium oxychloride cement concrete pavement," *Journal of Central South University*, vol. 26, no. 12, pp. 3410–3419, 2019.
- [14] A. Pandey and B. Kumar, "Effects of rice straw ash and micro silica on mechanical properties of pavement quality concrete," *Journal of Building Engineering*, vol. 26, Article ID 100889, 2019.
- [15] J. Liu, B. Yu, and Q. Wang, "Application of steel slag in cement treated aggregate base course," *Journal of Cleaner Production*, vol. 269, Article ID 121733, 2020.
- [16] N. Hasheminejad, C. Vuye, A. Margaritis et al., "Investigation of crack propagation and healing of asphalt concrete using digital image correlation," *Applied Science-Basel*, vol. 9, no. 12, p. 2459, 2019.
- [17] B. Behnia, W. Buttlar, and H. Reis, "Evaluation of low-temperature cracking performance of asphalt pavements using acoustic emission: a review," *Applied Sciences*, vol. 8, no. 2, p. 306, 2018.
- [18] Y. Tan, Z. Sun, X. Gong, H. Xu, L. Zhang, and Y. Bi, "Design parameter of low-temperature performance for asphalt mixtures in cold regions," *Construction and Building Materials*, vol. 155, pp. 1179–1187, 2017.
- [19] H. Liu, W. Li, G. Luo, S. Liu, and X. Lyu, "Mechanical properties and fracture behavior of crumb rubber basalt fiber concrete based on acoustic emission technology," *Sensors*, vol. 20, no. 12, 2020.
- [20] H. Wei, B. Hu, F. Wang, J. Zheng, J. Jin, and C. Liu, "Temporal-spatial evolution characteristics of acoustic emission in asphalt concrete cracking process under low temperature," *Construction and Building Materials*, p. 248, 2020.
- [21] L. Gao, F. Ni, C. Ling, and J. Yan, "Evaluation of fatigue behavior in cold recycled mixture using digital image correlation method," *Construction and Building Materials*, vol. 102, no. 1, pp. 393–402, 2016.
- [22] B. Bai, R. Zhou, G. Cai, W. Hu, and G. Yang, "Coupled thermo-hydro-mechanical mechanism in view of the soil particle rearrangement of granular thermodynamics," *Computers and Geotechnics*, vol. 137, no. 8, Article ID 104272, 2021.
- [23] K. Zhang, J. Zhou, and Z. Yin, "Experimental study on mechanical properties and pore structure deterioration of

- concrete under freeze-thaw cycles,” *Materials*, vol. 14, no. 21, 2021.
- [24] J. Li, R. B. Kaunda, and K. Zhou, “Experimental investigations on the effects of ambient freeze-thaw cycling on dynamic properties and rock pore structure deterioration of sandstone,” *Cold Regions Science and Technology*, vol. 154, pp. 133–141, 2018.
- [25] I. Menapace, L. Garcia Cucalon, F. Kaseer, E. Masad, and A. Epps Martin, “Application of low field nuclear magnetic resonance to evaluate asphalt binder viscosity in recycled mixes,” *Construction and Building Materials*, vol. 170, pp. 725–736, 2018.
- [26] I. Menapace, E. Masad, G. Papavassiliou, and E. Kassem, “Evaluation of ageing in asphalt cores using low-field nuclear magnetic resonance,” *International Journal of Pavement Engineering*, vol. 17, no. 10, pp. 847–860, 2016.
- [27] Y. Zhang, X. Liu, Y. Xu, B. Tang, Y. Wang, and E. Mukiza, “Preparation and characterization of cement treated road base material utilizing electrolytic manganese residue,” *Journal of Cleaner Production*, vol. 232, pp. 980–992, 2019.
- [28] Y. Zhang, X. Liu, Y. Xu, B. Tang, Y. Wang, and E. Mukiza, “Synergic effects of electrolytic manganese residue-red mud-carbide slag on the road base strength and durability properties,” *Construction and Building Materials*, vol. 220, pp. 364–374, 2019.
- [29] L. M. Nicula, O. Corbu, I. Ardelean, A. V Sandu, M. Iliescu, and D. Simedru, “Freeze-thaw effect on road concrete containing blast furnace slag: NMR relaxometry investigations,” *Materials*, vol. 14, no. 12, 2021.
- [30] D. R. Biswal, U. C. Sahoo, and S. R. Dash, “Non-destructive strength and stiffness evaluation of cement-stabilised granular lateritic soils,” *Road Materials and Pavement Design*, vol. 21, no. 3, pp. 835–849, 2020.
- [31] X. Sun, S. Wu, J. Yang, and R. Yang, “Mechanical properties and crack resistance of crumb rubber modified cement-stabilized macadam,” *Construction and Building Materials*, vol. 259, Article ID 119708, 2020.
- [32] B. Bai, Q. Nie, Y. Zhang, X. Wang, and W. Hu, “Cotransport of heavy metals and SiO₂ particles at different temperatures by seepage,” *Journal of Hydrology*, vol. 597, Article ID 125771, 2021.
- [33] Y. Zhao, X. Yang, Q. Zhang, N. Liang, Y. Xiang, and M. Qin, “Crack resistance and mechanical properties of polyvinyl alcohol fiber-reinforced cement-stabilized macadam base,” *Advances in Civil Engineering*, vol. 2020, Article ID 6564076, 15 pages, 2020.
- [34] X. Yan, L. Chen, Q. You, and Q. Fu, “Experimental analysis of thermal conductivity of semi-rigid base asphalt pavement,” *Road Materials and Pavement Design*, vol. 20, no. 5, pp. 1215–1227, 2019.
- [35] D. R. Biswal, U. C. Sahoo, and S. R. Dash, “Characterization of granular lateritic soils as pavement material,” *Transportation Geotechnics*, vol. 6, pp. 108–122, 2016.
- [36] S. Lv, C. Xia, H. Liu et al., “Strength and fatigue performance for cement-treated aggregate base materials,” *International Journal of Pavement Engineering*, vol. 22, no. 6, pp. 690–699, 2021.
- [37] T.-h. Wang, L.-j. Su, and J.-y. Zhai, “A case study on diurnal and seasonal variation in pavement temperature,” *International Journal of Pavement Engineering*, vol. 15, no. 5, pp. 402–408, 2014.
- [38] B. Zhang, X. Zhang, Y. Zhong, X. Li, M. Hao, and J. Liu, “Dynamic inversion analysis of structural layer modulus of semirigid base pavement considering the influence of temperature and humidity,” *Advances in Civil Engineering*, vol. 2020, pp. 1–12, 2020.
- [39] A. Moghadam, N. B. Harris, K. Ayranci, J. S. Gomez, N. A. Angulo, and R. Chalaturnyk, “Brittleness in the devonian horn river shale, british columbia, Canada,” *Journal of Natural Gas Science and Engineering*, vol. 62, pp. 247–258, 2019.
- [40] I. Barisic, S. Dimter, and T. Rukavina, “Elastic properties of cement-stabilised mixes with steel slag,” *International Journal of Pavement Engineering*, vol. 17, no. 9, pp. 753–762, 2016.
- [41] Z. Rong-rong and M. Dong-dong, “Effects of curing time on the mechanical property and microstructure characteristics of metakaolin-based geopolymer cement-stabilized silty clay,” *Advances in Materials Science and Engineering*, vol. 2020, Article ID 9605941, 9 pages, 2020.
- [42] T. M. AlGhamdi, C. H. H. Arns, and R. Y. Y. Eyvazzadeh, “Correlations between NMR-relaxation response and relative permeability from tomographic reservoir-rock images,” *SPE Reservoir Evaluation and Engineering*, vol. 16, no. 4, pp. 369–377, 2013.
- [43] L. Liu, Z. He, X. Cai, and S. Fu, “Application of low-field NMR to the pore structure of concrete,” *Applied Magnetic Resonance*, vol. 52, no. 1, pp. 15–31, 2021.
- [44] G. Turuallo and M. N. Soutsos, “Supplementary cementitious materials: strength development of self-compacting concrete under different curing temperature,” *Procedia Engineering*, vol. 125, pp. 699–704, 2015.
- [45] T. J. MacLean and A. Lloyd, “Compressive stress-strain response of concrete exposed to low temperatures,” *Journal of Cold Regions Engineering*, vol. 33, no. 4, 2019.
- [46] B. Zhang, B. Wang, Y. Zhong, X. Li, Y. Zhang, and S. Li, “Damage characteristics and microstructures of low-exothermic polymer grouting materials under F-T cycles,” *Construction and Building Materials*, vol. 294, Article ID 123390, 2021.
- [47] X. Wang, X. Shen, H. Wang, C. Gao, and T. Zhang, “Nuclear magnetic resonance analysis of freeze-thaw damage in natural pumice concrete,” *Materials DE Construction*, vol. 66, no. 322, 2016.
- [48] R. Kumar and B. Bhattacharjee, “Porosity, pore size distribution and in situ strength of concrete,” *Cement and Concrete Research*, vol. 33, no. 1, pp. 155–164, 2003.

Research Article

Stability Evaluation of Proppant in Fractures of Gas Storage in Yulin Gas Field

Ping Wang,¹ TianLi Gu ,¹ Zhanwu Gao,² Jiayong Fan,¹ Hai Huang,¹ Zhan Qu,¹ Qiang Han,¹ and Zongxiao Ren¹

¹*Xi'an Shiyou University, Xi'an, China*

²*PetroChina Changqing Oilfield Company, Xi'an, China*

Correspondence should be addressed to TianLi Gu; 20212010062@stumail.xsyu.edu.cn

Received 9 March 2022; Revised 15 April 2022; Accepted 19 April 2022; Published 28 May 2022

Academic Editor: Xianze Cui

Copyright © 2022 Ping Wang et al. This is an open access article distributed under the Creative Commons Attribution License, which permits unrestricted use, distribution, and reproduction in any medium, provided the original work is properly cited.

In nearly a hundred years of construction, underground gas storage has become the main natural gas storage and peak regulation means in the world. For the gas storage, the large production and high flow rate of the gas well in the actual production process will cause the backflow of proppant filled in the supporting fracture, which will bring great harm to the gas field production. In this article, when the proppant fracture reaches a stable state in the process of gas injection and production, the stress of proppant particles is analyzed, the critical velocity of proppant reflux is calculated, and then the critical production model is established; calculate the permeability change during proppant migration, then calculate the fluid velocity and production, and determine the fluid velocity range of injection and production wells in gas storage. The parameter sensitivity of velocity and flow model is analyzed. The results show that with the increase of closure stress, the critical gas flow and critical gas velocity of proppant backflow gradually increase, and the proppant filling layer is more stable. The smaller the thickness and width of the filling layer, the greater the critical gas flow and critical gas velocity of proppant backflow, the more stable the proppant filling layer, and the lesser the chance of backflow. The higher the saturation, the lower the critical gas velocity, and the more prone the proppant to reflux. It has important guiding significance for realizing the optimization of gas well production and maintaining efficient production efficiency.

1. Introduction

During the gas injection and production process of the gas storage, the reservoir pressure changes rapidly and sharply, and the proppant in a stable state rolls and is brought into the wellbore, which causes the migration of particles in the reservoir and leads to sand production. The production experience of injection-production wells in gas storage shows that sand production will not only cause permanent damage to the reservoir but also cause erosion damage to the tubing. Due to the lack of data on proppant migration and backflow in gas storage, quite a number of scholars at home and abroad have studied sand production in gas well production and proppant backflow during fracturing, which can provide some ideas and inspiration for our research.

As early as 1970, Hall proposed the concept of “sand arch” for the problem of loose sand production [1]. Based on

this theory, Bratli, Milton Taylor, Gidley, Bybee, Karen, Romero, and Feraud [2–6] believed that proppant particles would also form a hemispherical “support arch,” and proppant settlement would form in the packing zone. The early stages of stabilizing the structure lead to the formation of small irregular channels on the top and interior of the crack. As the fluid velocity in the fracture increases, the free grains outside the pack continue to erode the sand body until backflow occurs. The instability of sand arch and the erosion of proppant particles were observed through experimental study, and the critical flow rate was determined. Javier, Tooseh [7, 8] established a theoretical model. When the flow rate is steadily increased until a certain point is reached, the proppant particles no longer remain stationary, but “fluidize” under the action of the fluid flow or moisture stream. Taking gas storages in low permeability aquifers as objects, experiments on gas-water-rock interaction and factors

affecting gas storage capacity were carried out. When the original conditions of the reservoir (pH value, temperature, pressure, etc.) remain unchanged, the reservoir is in a stable state. However, when the pH value of the reservoir fluid changes or the flow rate is too fast, its stable state is destroyed, and it is easy to cause acid sensitivity and particle migration in the reservoir [9–13].

Domestic Aspects. Li et al. [14–17] conducted a mechanical analysis of the proppant in gas well production and derived the latest wellbore critical sand-carrying formula that conforms to the actual situation of gas wells. A new formula for the critical production rate of fracture sand production is deduced by proppant stress analysis. Assuming that the proppant accumulates in the fracturing fracture, the relationship between the critical sand production and the bottom hole flow pressure when the gas well fracture is damaged is obtained. Based on the stability similarity and force balance principle between proppant arch and sand arch, Fu and Liu [18, 19] systematically studied the mechanism of proppant backflow during the production process of fracturing gas wells, established a mathematical model of proppant backflow mechanics, and wrote a software for predicting proppant backflow during gas well production. Jin et al. [20, 21] used proppant combinations of different particle sizes to fill fractures to maintain high fracture conductivity. A mathematical model of the movement characteristics of proppant in fractures during fracturing fluid flowback after fracturing is established to simulate the flowback process of fracturing fluid and proppant in fractures when proppant sizes of different particle sizes are combined. Kang [22] conducted an experimental simulation of particle migration caused by rapid changes in gas injection pressure in gas storage wells and revealed the mechanism of particle migration caused by dynamic changes in gas injection pressure in gas storage wells.

As the flow rate increases, the resistance increases. When the flow rate reaches a certain value, the proppant no longer maintains a mechanical equilibrium state and is carried and moved by the fluid, resulting in the backflow of the proppant in the gas well. In this article, the force analysis of proppant in artificial fractures under injection and production conditions is carried out, the prediction model of proppant backflow under high-strength injection and production conditions is established, the critical flow rate is determined, the critical production model is established, and the stability of proppant in fractures is optimized and improved.

2. Critical Condition for No Rolling of Proppant under Injection

Most scholars at home and abroad focus on the research and analysis on proppant backflow during fracturing but there are few studies on proppant backflow caused by gas flowing down at high speed in gas storage. On the one hand, when the gas is injected and produced in the gas storage, the high-speed flow of the gas in the gas storage causes the proppant, which was in a stable state, to be rolled and carried to the wellbore. Alternate changes in pore pressure lead to changes

in effective stress, resulting in particle migration in the reservoir, resulting in sand production. This article analyzes the migration of proppant particles caused by gas flow during gas storage injection and production, which can provide reference value for gas storage to improve gas production efficiency.

Model assumptions are as follows:

- (1) The supporting seam is a vertical seam, and the height and width of the seam are constant.
- (2) Fracture flow is gas-liquid two-phase linear flow.
- (3) The size of proppant particles is uniform, and the particles are in point contact, regardless of the deformation of the proppant.
- (4) Compared with other parameters, proppant gravity has little effect on backflow, and gravity parameters are not considered in this article.

The proppant primarily supports the pressure-opened fracture, preventing it from closing and providing access for gas injection and recovery. In the construction of gas storage using depleted gas wells, when proppant fractures reach a stable state before gas injection, the force analysis of proppant is shown in Figure 1.

On the one hand, as the gas flows down the fracture from the formation, a pressure gradient is formed in the fracture, and this pressure gradient creates a drag force on the proppant propping up the fracture in the direction of the gas flow. On the other hand, in the process of fracturing, the residual fracturing fluid, the formation water, and the formation itself are attached to the surface of the proppant particles by liquid film droplets to produce capillary resistance to the flow of natural gas in the fracture, and the capillary force reacts on the solid particles and becomes the proppant reflux power.

Therefore, the critical condition for proppant backflow is

$$P_{\text{drag}} + \sigma'_c < f_n, \quad (1)$$

where P_{drag} is the drag force of gas, σ'_c is the equivalent capillary force strength, and f_n is the strength of static friction force.

2.1. Force Analysis of Proppant Particles

- (1) Drag force of gas is

$$P_{\text{drag}} = -\frac{d_p}{3} \cdot \frac{dP}{dx}, \quad (2)$$

where d_p is the proppant diameter, m .

- (2) Strength of static friction force f_n is

$$f_n = \mu P_c, \quad (3)$$

where f_n is the static friction force, μ is the static friction coefficient, and P_c is the closing stress.

- (3) Equivalent capillary force σ'_c strength is

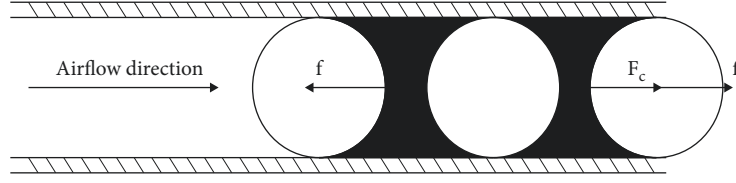


FIGURE 1: Schematic diagram of proppant stress.

$$\sigma'_c = \frac{2(1-\varphi)}{\varphi} \frac{\pi \sigma \sin \alpha_c^2}{d_p} \left(\frac{1}{f_1(\alpha_c)} - \frac{1}{f(\alpha_c)} \right). \quad (4)$$

During the production process of fracturing gas wells, the change of stress state and the deduced effective stress principle [23, 24] provide a reference for this article. When the fluid breaks through the capillary force, proppant particles are initiated by forces and drag forces that are consistent with the direction of flow, as seen from the action and reaction forces. This force is called the equivalent capillary force.

2.2. Critical Velocity at Which Proppant Cannot Be Transported. From the previous analysis, the mechanical conditions expressed in (1) must be satisfied for the proppant to backflow. The critical condition for proppant backflow is

$$P_{dr\ ag} + \sigma'_c = f_n. \quad (5)$$

Substitute Equations (2), (3), and (4) in (5) to obtain

$$\frac{R\mu_{gi}ZT_i\rho_a d_p}{87P_{wf}k_g(1-S_{wi})}v + \frac{RZT_i\beta\gamma_g\rho_a^2 d_p}{87P_{wf}}v^2 + \frac{2(1-\varphi)}{\varphi} \frac{\pi \sigma \sin \alpha_c^2}{d_p} \left(\frac{1}{f_1(\alpha_c)} - \frac{1}{f(\alpha_c)} \right) - \mu P_c = 0. \quad (8)$$

Make $A = RZT_i\beta\gamma_g\rho_a^2 d_p/87P_{wf}$,

$$B = \frac{R\mu_{gi}ZT_i\rho_a d_p}{87P_{wf}k_g(1-S_{wi})}, \quad (9)$$

$$C = \frac{2(1-\varphi)}{\varphi} \frac{\pi \sigma \sin \alpha_c^2}{d_p} \left(\frac{1}{f_1(\alpha_c)} - \frac{1}{f(\alpha_c)} \right) - \mu P_c.$$

Formula (8) can be simplified into

$$Av^2 + Bv + C = 0. \quad (10)$$

The critical flow rate of proppant that does not start is

$$v = \frac{-B + \sqrt{B^2 + 4AC}}{2A}. \quad (11)$$

If the flow velocity is less than the proppant critical flow rate, the proppant in the pressure fracture will remain static. The width of the fracture is assumed to be ω_f and the height of the fracture h . According to the flow characteristics in the fracture, as long as the sand particles along the wall are not

$$\frac{d_p}{3} \cdot \frac{dP}{dx} + \frac{2(1-\varphi)}{\varphi} \frac{\pi \sigma \sin \alpha_c^2}{d_p} \left(\frac{1}{f_1(\alpha_c)} - \frac{1}{f(\alpha_c)} \right) = \mu P_c. \quad (6)$$

According to the non-Darcy flow model of gas,

$$\frac{dP}{dx} = \frac{R\mu_{gi}ZT_i\rho_a}{29P_{wf}k_g(1-S_{wi})}v + \frac{RZT_i\beta\gamma_g\rho_a^2}{29P_{wf}}v^2. \quad (7)$$

Among them, $\beta = 5.5 \times 10^9/k^{1.25}\varphi^{0.75}$ where K is the permeability, φ is the porosity, Z is the natural gas deviation factor, dimensionless, R is the dimensionless Pratt constant of gas, T_i is the formation temperature, K ; μ_{gi} is the viscosity of natural gas in the formation, $\text{MPa} \cdot \text{s}$; ρ_a is the air density, kg/m^3 , γ_g is the relative density of natural gas, dimensionless, P_{wf} is the bottomhole flow pressure, MPa , k_g is the absolute fracture permeability, μm^2 , β is the inertial resistance coefficient, $1/\text{m}$, and v is the gas velocity, m/s . The negative sign indicates that the direction of the fluid velocity is opposite to the direction of the pressure gradient.

Substituting (7) in Equation (6), a quadratic equation with one variable about gas velocity v is obtained:

pushed, the sand particles throughout the fracture will not be pushed. For this reason, when considering the flow rate, take the velocity of the fracture in the wellbore wall as the standard and assume that all gas flows into the wellbore through the fracture. So, the production of the gas well is

$$Q = \frac{2\omega_f h v 866400}{B_g}, \quad (12)$$

where ω_f is the width of the fracture; h is the height of the propped fracture, m ; B_g is the volume coefficient of natural gas, m^3 ; and Q is the natural gas production, m^3/d .

Substitute the critical velocity in (11) to obtain the critical flow.

3. Critical Conditions under Which Proppant Is Not Discharged under Recovery Conditions

The critical condition of proppant rolling start was obtained by force analysis of proppant particles in the gas production channel, and then the law of proppant migration was analyzed.

3.1. Force Analysis of a Single Stationary Proppant Particle.

It is assumed that the proppant particles in the gas production channel are spherical, and the packing mode is shown in Figure 2. The proppant particle radius is set as r , and the static proppant particles in the fluid are mainly subjected to pressure gradient force, gas impact force, and the gravity of the proppant particles themselves.

(1) Pressure gradient force F_P is

$$F_P = \frac{4}{3}\pi r^3 \left(\frac{R\mu_{gi}ZT_i\rho_a}{29P_{wf}k_g(1-S_{wi})}v + \frac{RZT_i\beta\gamma_g\rho_a^2}{29P_{wf}}v^2 \right). \quad (13)$$

(2) Gravity F_G is

$$F_G = \frac{4}{3}\pi r^3 \left(\rho_s - \frac{28.97\gamma_g P}{RTZ} \right) g. \quad (14)$$

3.2. Rolling Starting Conditions of Proppant Particles. In the case of contact point A, the pressure gradient force and the impact force of the gas cause the proppant to roll around A, while the gravity hinders the proppant particle rolling. The moment generated by the interaction force between proppant particles 2 (see the right picture) through point A is zero, and the force generated by proppant particles 1 plays a main role in its rolling. When the proppant particles and proppant particles 1 just get out of contact, the force is zero, and the proppant particles start rolling. According to the principle of torque balance, when the active torque is greater than the retarded torque, the proppant particles will roll. That is,

$$F_P L_y \geq F_G L_x, \quad (15)$$

where L_x and L_y are the hindrance moment arm and the main force moment arm, respectively. Its moment arm can be obtained from geometric relations.

When the gas flow rate meets (15), proppant particles will roll. Substitute the above force expressions (13) and (14) in Equation (15) to obtain the following:

$$\begin{aligned} & \left[\frac{4}{3}\pi r^3 \left(\frac{R\mu_{gi}ZT_i\rho_a}{29P_{wf}k_g(1-S_{wi})}v + \frac{RZT_i\beta\gamma_g\rho_a^2}{29P_{wf}}v^2 \right) \frac{\sqrt{3}}{2}r \right. \\ & \left. \geq \left[\frac{4}{3}\pi r^3 \left(\rho_s - \frac{28.97K_g P}{RTZ} \right) g \right] \frac{r}{2} \right. \end{aligned} \quad (16)$$

Similarly, a quadratic equation with one variable about gas velocity v is obtained:

$$\begin{aligned} & \frac{R\mu_{gi}ZT_i\rho_a}{29P_{wf}k_g(1-S_{wi})}v + \frac{RZT_i\beta\gamma_g\rho_a^2}{29P_{wf}}v^2 \\ & + \frac{\sqrt{3}}{3} \left(\frac{28.97\gamma_g P}{RTZ} - \rho_s \right) \geq 0. \end{aligned} \quad (17)$$

Make $A_1 = RZT_i\beta\gamma_g\rho_a^2/29P_{wf}$,

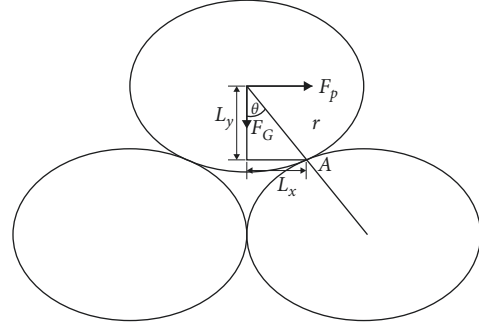


FIGURE 2: Analysis of proppant stress during gas recovery.

$$B_1 = \frac{R\mu_{gi}ZT_i\rho_a}{29P_{wf}k_g(1-S_{wi})}, \quad (18)$$

$$C_1 = \frac{\sqrt{3}}{3} \left(\frac{28.97\gamma_g P}{RTZ} - \rho_s \right).$$

Formula (18) can be simplified into

$$A_1 v^2 + B_1 v + C_1 \geq 0. \quad (19)$$

Therefore, the proppant velocity of the produced gas should meet the following requirements:

$$v \geq \frac{-B_1 + \sqrt{B_1^2 + 4A_1C_1}}{2A_1}. \quad (20)$$

Therefore, the critical velocity of proppant particle rolling is

$$v_g = \frac{-B_1 + \sqrt{B_1^2 + 4A_1C_1}}{2A_1}. \quad (21)$$

3.3. Rolling Start-Up Conditions under Different Proppant Arrangements. In the actual gas production channel, proppant particles are not necessarily arranged in the gas production channel as shown in Figure 2, some proppant grains may be submerged, and some may be embedded in other grains. The grain arrangement after the gas production channel has the following three forms as shown in Figure 4, and the distance from the contact point of proppant grains to the lower boundary of proppant grains is defined as the coverage depth h_r .

The proppant particles are spherical particles with equal particle size, and the coverage depth can be calculated based on the geometric relationship. In the proppant arrangement, the particle size of the proppant particles is assumed to be ds , and the distance between the center of the next two particles is $ds + \delta$, where $0 \leq \delta \leq ds$:

$$h_r = \frac{ds - \sqrt{ds^2 - (ds + \delta/2)^2}}{2}. \quad (22)$$

When $\delta = 0$, the proppant is arranged in the form shown in Figure 4(a), and the minimum coverage depth of proppant particles is $h_r = 0.067 ds$. When $\delta = ds$, the proppant is

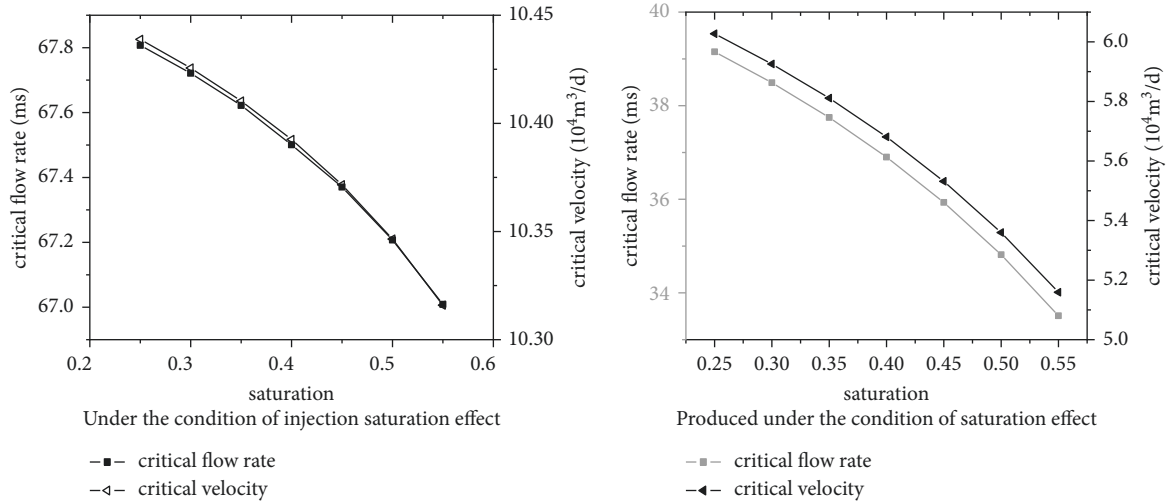


FIGURE 3: Influence diagram of saturation under injection-production conditions.

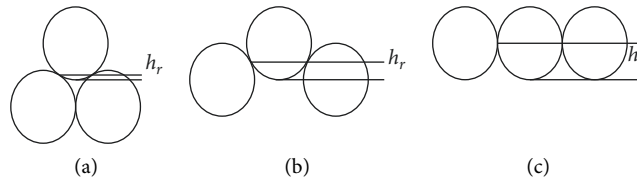


FIGURE 4: Schematic diagram of proppant arrangement during gas recovery.

arranged in the form shown in Figure 4(c), and the maximum coverage depth of proppant particles is $h_r = 0.5 ds$.

Different proppant particle coverage will affect the moment arms of each force when the particle rolling starts. After considering the proppant particle coverage, the moment arms of each force are

$$l_x = \frac{d_s + \delta}{4} = \frac{\sqrt{d_s^2 h_r - h_r^2}}{2}, l_y = \frac{\sqrt{d_s^2 - ((d_s + \delta)/2)^2}}{2} \quad (23)$$

$$= \frac{d_s}{2} - h_r.$$

By substituting the force arm formula (23) into formula (21), the critical rolling velocity of proppant particles considering the arrangement of proppant can be obtained. In addition, the critical rolling velocity considering the arrangement of proppant particles and the shape of proppant particles can be obtained by combining the equivalent particle size formula of different proppant shapes.

Substitute the critical velocity in (12) to obtain the critical flow formula as follows:

$$Q_{qc} = \frac{2w_f h v_g 86400}{B_g} \quad (24)$$

Thus, as long as the production rate of the gas well is less than Q_{qc} , the gas well will not destroy the supporting sand in the fracture, so that the fracture can maintain long-term effectiveness.

4. Calculation Model of Proppant Migration Fluid Velocity

When the proppant is sheared or stretched by the fluid, the proppant particles fall off from the surface of the rock skeleton. After the particles fall off, the force of the proppant in the pore fluid is different under different fluid conditions, which determines whether the proppant particles can be taken away by the fluid or remain in place after falling off from the surface of the rock skeleton. The research of scholars in other fields can provide us with some references. [26–28] When proppant particles migrate, deposit, and plug in pores, they will cause changes in reservoir physical parameters, especially porosity and permeability, and then affect reservoir productivity.

Before the reservoir rock is deformed, its original porosity is

$$\varphi_0 = \frac{V_p}{V_f} = \frac{V_f - V_r}{V_f} \quad (25)$$

where V_f is the total volume of rock, m^3 , V_p is the pore volume, m^3 , and V_r is the volume of rock skeleton, m^3 .

In the stable production stage of the gas storage, the bottom hole pressure remains unchanged and the resulting pressure drop remains constant. The pressure at any point of the gas storage can be regarded as unchanged, and the influence of pressure on it can be ignored. When most mobile proppant particles stop migration, the permeability will gradually stabilize.

Then, the porosity of proppant after being carried out of gas storage by liquid is

$$\varphi = \varphi_0 + (1 - \varphi_0) \frac{R_c}{\rho_s} \quad (26)$$

Seepage velocity is

$$v_s = \frac{14.4W}{A\varphi} \quad (27)$$

Substitute equation (26) in

$$v_s = \frac{14.4W}{A[\varphi_0 + (1 - \varphi_0)R_c/\rho_s]} \quad (28)$$

where W is the liquid volume flow. The above formula is the velocity of proppant migration.

The determination of proppant carrying fluid velocity aims at improving the single well production of gas storage wells, and the single well production formula is

$$Q = \frac{kh\Delta p}{141^2 \mu \beta (p_j + s)} \quad (29)$$

where Q is the gas production, k is the reservoir permeability, h is the reservoir thickness, β is the fluid volume coefficient, s is the skin coefficient of wellbore, and p_j is the desorption pressure at point j .

When the liquid flows slowly in the gas production channel, proppant particles may deposit and block in the channel. When the fluid velocity is too high, it may scour the gas production channel wall, which may cause a large number of proppant particles to discharge and close the crack. In order to prevent deposition, wall scouring, and proppant discharge in the gas production channel, the fluid velocity should not be too large or too small. Under the condition of ensuring the maximum permeability, selecting an appropriate flow rate can improve the production of gas storage and gas production efficiency. Accordingly, the flow rate should be the following:

Under injection conditions: $v_i \ll v_{D1} \ll v_s$

Under recovery conditions: $v_g \ll v_{D2} \ll v_s$

By comparing with the production data of 20 wells in the gas storage in the Yulin gas field, critical velocity, critical flow, and fluid flow range all verify the rationality of the calculation results in this article.

5. Sensitivity Analysis of Influencing Factors

5.1. Basic Parameters. The southwest reservoir of Yulin gas field gas storage has a buried depth of 2850 ~ 3100 m, a formation temperature of 90°C, and a storage capacity of $177.62 \times 108 \text{ m}^3$, an average thickness of 10.1 m, and a porosity of 4.1 ~ 8.3%, and the average porosity is 6.4%. The permeability is 0.1 ~ 20.3 mD, belonging to low porosity and low permeability gas reservoir. The basic parameters calculated by the model are as follows: formation pressure of 27.7 MPa, reservoir temperature of 364°C, air density of 1.3 kg/m^3 , natural gas volume coefficient of 0.0041, natural

gas relative density of 0.625 kg/m^3 , natural gas viscosity of 0.02 MPa·s, proppant of 20/40 mesh, deviation factor of 0.78, gas proctor constant of 8.314, relative density of 3.34 kg/m^3 , and proppant apparent density of 2.2 g·m^{-3} . The bulk density of proppant is 1.59 g·m^{-3} , the strength of proppant is 20.7–34.5 MPa, the internal friction angle is 30°, and the uniaxial compressive strength is 12 MPa.

5.2. Crack Width. It can be seen from Figure 5 that with the increase in the width of the supporting crack, the critical air velocity gradually decreases, the filling layer is more unstable, and the proppant is prone to backflow. On the contrary, the smaller the fracture width, the higher the critical air velocity, the more stable the filling layer, and the more difficult it is to reflow.

The wider the supporting fracture is, the easier the backflow is, but the higher the critical production of the gas well is. On the contrary, the narrower the supporting fracture is, the less likely the backflow is, but the lower the critical production of the gas well is. In other words, there is a certain contradiction between proppant backflow prevention and gas well production. We must find an optimal fracture width to reconcile the contradiction between the two and achieve optimization.

5.3. Closure Stress. As shown in Figure 6, the greater the closure stress, the more stable the proppant filling layer, and the greater the critical flow rate of reflux. The closure stress is equal to the formation pressure minus the pore pressure. With the continuous production of natural gas, the pore pressure decreases and the closure stress increases gradually.

As the closure stress increases, the critical flow rate and critical velocity of proppant reflux gradually increase, and the proppant filling layer becomes more stable. There is an obvious linear relationship between the critical flow rate and the closure stress.

5.4. Saturation. As shown in Figure 3, the influence of water irreducible saturation on the stability of the filling layer is very obvious. The smaller the S_w is, the greater the critical air velocity is, and the more stable the filling layer is. On the contrary, the larger the S_w is, the lower the critical gas velocity is, and the more likely the proppant is to reflux.

At the initial stage of gas storage well production, S_w is large, the fracture flow is gas-liquid two-phase flow, and the pressure gradient is large. At this time, the supporting fracture is the most unstable, so the gas well production should not be too high. With the flow of natural gas, the working fluid flows out together, and the stability of supporting fractures is enhanced, which can appropriately increase the production of gas wells.

5.5. Production Differential Pressure. The greater the production pressure difference, the lower the critical velocity of proppant backflow, the more unstable the support crack, and the proppant backflow is easy to occur.

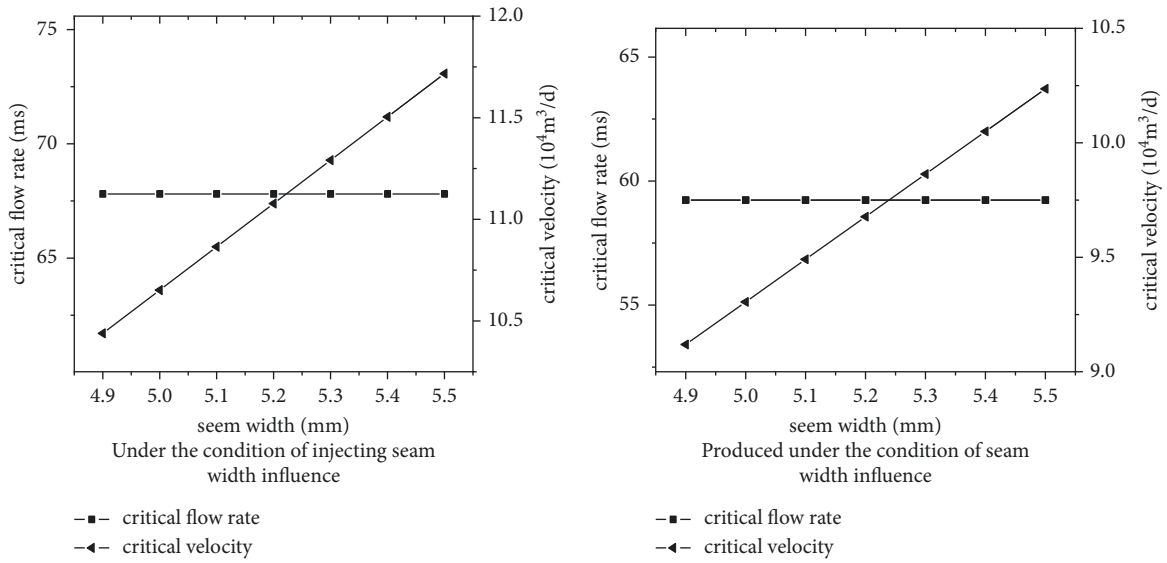


FIGURE 5: Influence diagram of fracture width under injection-production conditions.

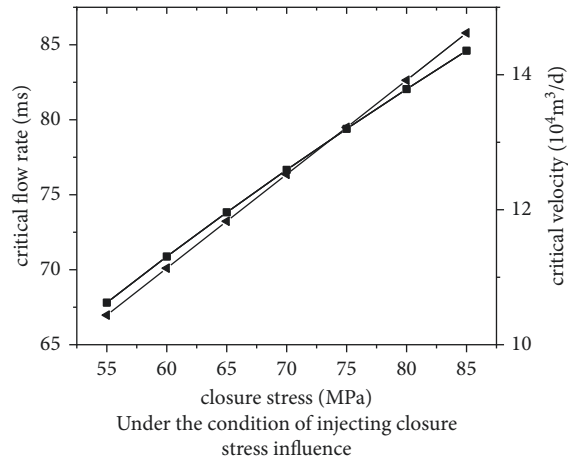


FIGURE 6: Influence diagram of closure stress under injection condition.

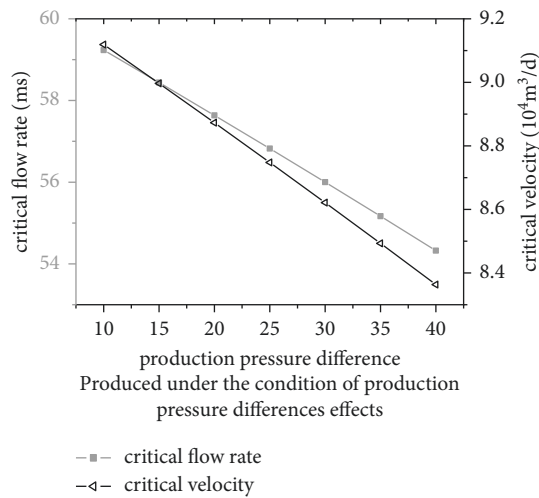


FIGURE 7: Influence diagram of production pressure difference under production conditions.

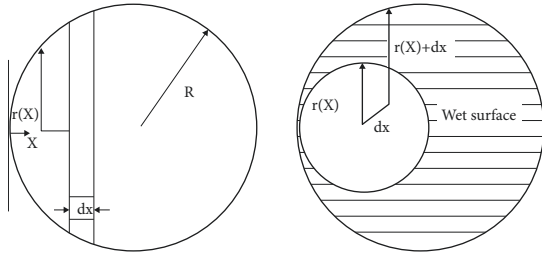


FIGURE 8: Schematic diagram of the calculation model of drag force.

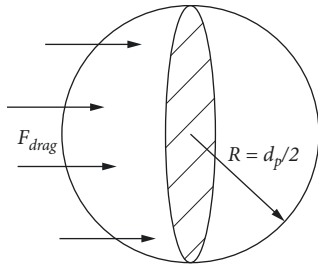


FIGURE 9: Schematic diagram of proppant stress.

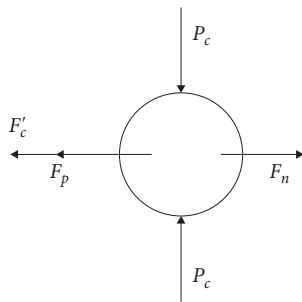


FIGURE 10: Analysis of proppant stress during gas injection.

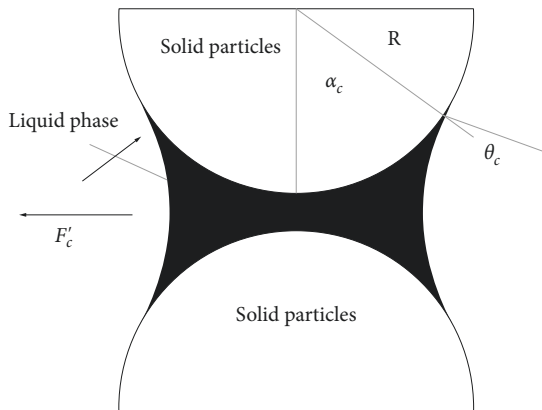


FIGURE 11: Schematic diagram of capillary force action.

As shown in Figure 7, with the increase in production differential pressure, the production of gas wells increases. However, the greater the differential pressure, the lower the critical flow rate and production of proppant backflow in gas

wells. In other words, if the production pressure difference is too large, it is easy to cause proppant backflow, resulting in the reduction of fracture conductivity.

6. Conclusion

- (1) When the supporting fracture reaches a stable state in the process of gas injection and production, the range between the critical velocity of backflow and the velocity of proppant migration is determined through the force analysis of proppant, and the maximum permeability of the reservoir is determined, which can improve the gas production efficiency to the greatest extent.
- (2) When the proppant is no longer in a stable state, the proppant migrates, which will have a certain impact on the porosity and permeability of the gas production channel. Moderately discharging a certain amount of separated proppant particles can increase the gas production efficiency and improve the gas production.
- (3) With the increase of closure stress, the critical gas flow and critical gas velocity of proppant backflow gradually increase, and the proppant filling layer is more stable. The critical flow rate and critical flow measured at the closure stress point have an obvious linear relationship with the closure stress, which has a strong regularity.
- (4) The smaller the thickness of the filling layer is, the greater the critical gas flow and critical gas velocity of proppant backflow, the more stable the proppant filling layer is, and the chance of backflow is reduced. There is a consistent relationship between the critical velocity and critical flow and the fracture width.
- (5) The influence of irreducible water saturation on the stability of the filling layer is very obvious; the greater the production differential pressure, the lower the critical velocity of proppant backflow, and the more unstable the support fracture, which is prone to proppant backflow. The production differential pressure should be controlled within a reasonable range during gas well production.

Appendix

A. Critical Condition for No Rolling of Proppant under Injection Part Formula Derivation

Force analysis of proppant particles

(1) *Drag Force of Gas.* In the actual production process of a gas well, the high-speed flow of gas in the proppant fracture is linear non-Darcy two-phase flow, and the pressure changes along the fracture length with a parabola. For uniform pressure gradient, the flow pressure changes linearly with distance, and then

$$P(x) = P_0 + \frac{dP}{dx}x, \quad (\text{A.1})$$

where the $P(x)$ is the fluid pressure, P_0 is the uniform pressure gradient, and x is the strength.

When calculating the drag force acting on a single proppant, the gas-liquid two-phase flow in the propped fracture is considered. For both gas-phase flow and liquid-phase flow, the total pressure drop of the entire joint length is assumed to be dP/dx , and the fluid pressure drop produces drag force. The wet phase surface is projected on the plane normal of the flow direction, as shown in Figure 8.

A segment of microelement distance dx on a single proppant particle is taken, and the drag force acting on this segment is

$$dF_{\text{drag}(x)} = P(x)dA_{wp}, \quad (\text{A.2})$$

where $F_{\text{drag}(x)}$ is the drag force at the distance between the proppant particles; A_{wp} is the $P(x)$ applied to the area at the distance between proppant particles, m^2 ; and $P(x)$ is the pressure, MPa

The unit stressed area on the proppant particle at x is

$$dA_{wp} = 2\pi r(x)dr. \quad (\text{A.3})$$

Substituting Equations (A.1) and (A.3) in Equation (A.2), we can get

$$dF_{\text{drag}(x)} = \left(P_0 + \frac{dP}{dx}x \right) 2\pi r(x)dr. \quad (\text{A.4})$$

Equation (A.4) describes the drag force acting on a segment of the proppant particle. The total drag force acting on the entire proppant particle can be viewed as a proppant particle composed of an infinite number of such segments:

$$F_{\text{drag}} = 2\pi P_0 \int_0^{2R} (R-x)dx + 2\pi \frac{dP}{dx} \int_0^{2R} x(R-x)dx. \quad (\text{A.5})$$

Integrate Equation (A.5) to obtain

$$F_{\text{drag}} = -\frac{4}{3}\pi \frac{dP}{dx}R^3. \quad (\text{A.6})$$

As the fluid flows through the propped fracture, the flow pressure drop generates a drag force, the action of which is shown in Figure 9.

The drag force F_{drag} is applied to the shaded area shown in the figure. It can be seen from the figure that the stressed area A_p is half of the spherical area of proppant particles, $A_p = 2\pi R^2$. The intensity of drag force acting on A_p is

$$P_{\text{drag}} = \frac{F_{\text{drag}}}{2\pi R^2}, \quad (\text{A.7})$$

where P_{drag} is the strength of drag force, MPa.

Substituting Equation (A.6) in Equation (A.7), we can get [18]

$$P_{\text{drag}} = -\frac{2R}{3} \cdot \frac{dP}{dx}. \quad (\text{A.8})$$

If the diameter of proppant particle is d_p , then $R = d_p/2$ is substituted into Equation (A.8) to obtain

$$P_{\text{drag}} = -\frac{d_p}{3} \cdot \frac{dP}{dx}, \quad (\text{A.9})$$

where d_p is the proppant diameter, m .

(2) *Strength of Static Friction Force f_n* . The value of static friction force is proportional to the product of closing pressure, particle contact area, and static friction coefficient. The larger the closing pressure, the larger the particle contact area, the rougher the particle surface, and the greater the static friction force. The less likely the proppant is to start (Figure 10).

The maximum static friction force can be expressed as

$$f_n = \mu P_c, \quad (\text{A.10})$$

where f_n is the static friction force, μ is the static friction coefficient, and P_c is the closing stress.

(3) *Equivalent Capillary Force σ_c Strength*. During the production process of fractured gas wells, there are multi-phase fluids in fractures, including working fluid residual in fractures and formation fluid. The flow in fractures is gas-liquid two-phase. With the flow of natural gas, capillary resistance occurs, and the direction is opposite to the flow direction of the fluid, hindering the flow of the fluid. When the fluid breaks through the capillary force, it can be seen from the acting and reaction forces that the proppant particles are started by a force consistent with the flow direction and a drag force. This force is called the equivalent capillary force, which is equal to the capillary force and opposite to the capillary force, as shown in Figure 11.

Assuming that the proppant particle size is uniform, tangential contact capillary force of particles with uniform size can be expressed as

$$F'_c = \frac{1}{2} \pi \sigma d_p \sin^2 \alpha_c \left(\frac{1}{f_1(\alpha_c)} - \frac{1}{f(\alpha_c)} \right). \quad (\text{A.11})$$

Among them,

$$f_1(\alpha_c) = \left\{ \frac{1}{\cos \alpha_c} [\sin \alpha_c \cos \alpha_c + (1 - \cos \alpha_c)(\sin(\theta_c + \alpha_c) - 1)] \right\},$$

$$f(\alpha_c) = \frac{1 - \cos \alpha_c}{\cos \alpha_c},$$

(A.12)

where θ_c is the contact angle, α_c is the angle between the radius of the solid-liquid boundary on the proppant particle and the vertical axis, σ is the interfacial tension between fluids, N/m, and d_p is the diameter of the proppant. Since there is no difference in particle size, the capillary force strength in tangential contact of particles can be expressed as

$$\sigma'_c = \frac{1 - \phi}{\phi} \frac{\pi \sigma \sin^2 \alpha_c}{R} \left(\frac{1}{f_1(\alpha_c)} - \frac{1}{f(\alpha_c)} \right), \quad (\text{A.13})$$

where d_p is the diameter of proppant, so $R = d_p/2$. Put in the above equation to obtain the following:

$$\sigma'_c = \frac{2(1-\varphi)}{\varphi} \frac{\pi\sigma \sin \alpha'_c}{d_p} \left(\frac{1}{f_1(\alpha'_c)} - \frac{1}{f(\alpha'_c)} \right). \quad (\text{A.14})$$

B. Critical Conditions under Which Proppant Is Not Discharged under Recovery Conditions Part Formula Derivation

(1) *Pressure Gradient Force F_p* . The fluid flows under the action of pressure gradient, within which the force on the surface of proppant particles is different, and the resultant force on the surface is the pressure gradient force of proppant particles, which can be expressed as

$$F_p = 2\pi r^2 \int_0^\pi \left(P_0 + r(1 + \cos \theta) \frac{\partial P}{\partial x} \right) \cos \theta \sin \theta d\theta = \frac{4}{3} \pi r^3 \frac{\partial P}{\partial x} \quad (\text{B.1})$$

where r is the radius of the proppant particle, $\partial P/\partial x$ is the pressure gradient, and its direction is consistent with the movement direction of the proppant particle.

Under a certain pressure gradient, the liquid will flow. According to the non-Darcy seepage formula, it can be seen that

$$-\frac{dP}{dx} = \frac{R\mu_{gi}ZT_i\rho_a}{29P_{wf}k_g(1-S_{wi})} v + \frac{RZT_i\beta\gamma_g\rho_a^2}{29P_{wf}} v^2. \quad (\text{B.2})$$

Substitute the above equation in Equation (B.2), and the force generated by the pressure gradient can be expressed by fluid velocity as follows:

$$F_p = \frac{4}{3} \pi r^3 \left(\frac{R\mu_{gi}ZT_i\rho_a}{29P_{wf}k_g(1-S_{wi})} v + \frac{RZT_i\beta\gamma_g\rho_a^2}{29P_{wf}} v^2 \right). \quad (\text{B.3})$$

(2) *Gravity F_G* . The gravity of proppant particles in the gas is the gravity after considering the buoyancy force, and its relationship is

$$F_G = \frac{4}{3} \pi r^3 (\rho_s - \rho_q) g, \quad (\text{B.4})$$

where ρ_s is the density of proppant and ρ_q is the density of gas. The gas density $\rho_q = 28.97\gamma_g P/RTZ$ is substituted in equation (B.4):

$$F_G = \frac{4}{3} \pi r^3 \left(\rho_s - \frac{28.97\gamma_g P}{RTZ} \right) g. \quad (\text{B.5})$$

C. Calculation Model of Proppant Migration Fluid Velocity Part Formula Derivation

Before the reservoir rock is deformed, its original porosity is

$$\begin{aligned} \varphi_0 &= \frac{V_p}{V_f} \\ &= \frac{V_f - V_r}{V_f}, \end{aligned} \quad (\text{C.1})$$

where V_f is the total volume of rock, m^3 , and V_p is the pore volume, m^3 , and V_r is the volume of rock skeleton, m^3 .

(1) *Effect of Pressure Change*. In the process of gas storage injection and production, when the formation conditions change from initial state (P_0, t_0) to state (P, t_0), the volumetric strain coefficient of rock in this process is ε_v . Then, the total volume change of rock is

$$\Delta V_f = V_f \varepsilon_v. \quad (\text{C.2})$$

(2) *Influence of Proppant Separation, Deposition, and Blockage*. The separation of proppant, deposition on pore surface, and blockage in throat are attributed to the change of rock skeleton volume, which makes the skeleton volume decrease to negative and increase to positive. Therefore, the change of rock skeleton volume can be expressed as

$$\Delta V_s = V_r \left(\frac{R_r}{\rho_s} + \frac{R_d}{\rho_s} + \frac{R_p}{\rho_s} \right), \quad (\text{C.3})$$

where R_r is the mass separation amount of skeleton proppant on unit volume rock, kg/m^3 ; R_d is the mass deposition of proppant on the pore surface per unit volume of rock, kg/m^3 ; R_p is the mass retention of proppant in pore throat blockage on unit volume rock, kg/m^3 .

R_r is determined by the skeleton stripping constitutive equation as follows:

$$R_r = \rho_s \lambda (1 - \varphi_0) C_s q^{0.5}, \quad (\text{C.4})$$

where λ is the liquefaction coefficient of rock, which is determined by experimental test; q is the volume of fluid and proppant mixture flowing through unit area in unit time; and C_s is the volume concentration of proppant.

R_d is determined by the pore surface deposition equation as follows:

$$R_d = \begin{cases} K_{d1} v C_s \rho_s, \\ K_{d1} v C_s \rho_s - K_{d2} R_d (v - v_{g1j}), \end{cases} \quad (\text{C.5})$$

where K_{d1} and K_{d2} are surface deposition rate constants.

$$R_p = K_p V C_s \rho_s, \quad (\text{C.6})$$

where K_p is the pore throat plugging rate constant. When $t = 0$, $R_p = 0$, so the porosity of rock under pressure and after proppant separation, deposition, and plugging at pore throat is

$$\varphi = \frac{(V_f + \Delta V_f) - (V_r + \Delta V_s)}{V_f + \Delta V_f}. \quad (\text{C.7})$$

Substitute equation (C.1) and equation (C.2) into equation (C.7):

$$\varphi = 1 - \frac{1 - \varphi_0}{1 + \varepsilon_v} \left(1 - \frac{R_r - R_d - R_p}{\rho_s} \right). \quad (\text{C.8})$$

$R_c = R_r - R_d - R_p$ where R_c is the discharge amount of particles per unit volume of rock with liquid, kg/m^3 . Then, the porosity after proppant is carried out of the reservoir by liquid is

$$\varphi = 1 - \frac{1 - \varphi_0}{1 + \varepsilon_v} \left(1 - \frac{R_c}{\rho_s} \right). \quad (\text{C.9})$$

In the stable production stage of the gas storage, the bottom hole pressure remains unchanged and the resulting pressure drop remains constant. The pressure at any point of the gas storage can be regarded as unchanged, and the influence of pressure on it can be ignored. When most mobile proppant particles stop migration, the permeability will gradually stabilize. Then, the porosity of proppant after being carried out of gas storage by liquid is

$$\varphi = \varphi_0 + (1 - \varphi_0) \frac{R_c}{\rho_s}. \quad (\text{C.10})$$

Data Availability

The data (data type) used to support the findings of this study are included within the article.

Conflicts of Interest

The authors declare that they have no conflicts of interest.

Acknowledgments

The experiments in this research program were supported by the key laboratory of well stability and fluid and rock mechanics in oil and gas reservoir of Shaanxi province. This research was funded by the National Natural Science Foundation of China (Grant nos. 51974255 and 51874240), the Natural Science Basic Research Program of Shaanxi (Program number: 2020JM-544), the Shaanxi Province Key Research and Development Plan (Program number: 2020KW-027), the Shaanxi Provincial Science Fund for Distinguished Young Scholars (Program number: 2022JC-37), and the Xi'an Shiyou University Graduate Innovation and Practice Ability Training Program (Project number: YCS20213149).

References

- [1] C. D. Hall Jr and W. H. Harrisberger, "Stability of sand arches: a key to sand control," *Journal of Petroleum Technology*, vol. 22, no. 7, pp. 821–829, 1970.
- [2] R. K. Bratli and R. Risnes, "Stability and failure of sand arches," *Society of Petroleum Engineers Journal*, vol. 21, no. 2, pp. 236–248, 1981.
- [3] M. Tayler, C. Stephenson, and M. I. Asgian, "Factors affecting the stability of proppant in propped fractures: results of a laboratory study," in *Proceedings of the SPE Annual Technical Conference and Exhibition*, WashingtonDC, October 1992.
- [4] J. L. Gidley, G. S. Penny, and R. R. McDaniel, "Effect of proppant failure and fines migration on conductivity of propped fractures," *SPE Production and Facilities*, vol. 10, no. 1, pp. 20–25, 1995.
- [5] N. Goel and N. S. Subhash, "Experimental investigation of proppant flow back phenomena using a large scale fracturing simulation," vol. 10, 1999.
- [6] J. Romero and J. P. Feraud, "Stability of proppant pack reinforced with fiber for proppant flow back control," *Society of Petroleum Engineers Journal*, no. 2, pp. 231–237, 1996.
- [7] M. Javier, "Avoiding proppant flow back in tight-gas completions with improved fracture design," vol. 10, 2003.
- [8] T. Esmaeel Kazemi, J. Arezou, and T. Ali, "Gas-water-rock interactions and factors affecting gas storage capacity during natural gas storage in a low permeability aquifer," *Petroleum Exploration and Development*, vol. 45, no. 6, pp. 1123–1128, 2018.
- [9] Z. Qu, Q. Lin, T. Guo, and Y. Wang, "Experimental study on conductivity of carbonate acid etched fractures in Shunbei Oilfield," *Fault-Block Oil & Gas Field*, vol. 26, no. 4, pp. 533–536, 2019.
- [10] M. Cesar, "Cerde. Mobilization of quartz fines in porous media," *Clays and Clay Minerals*, vol. 36, no. 6, 1988.
- [11] H. Reza, P. Peyman, V. Ali, and S. Abdolhamid, "Application of silica nanofluid to control initiation of fines migration," *Petroleum Exploration and Development Online*, vol. 44, no. 5, 2017.
- [12] Q. Chen, "Quantitative calculation method of particle transport critical velocity and damage radius," *Petroleum Geology and Engineering*, vol. 30, no. 4, pp. 113–114+118, 2016.
- [13] D. Chen, Z. Pan, Z. Ye, B. Hou, D. Wang, and L. Yuan, "A unified permeability and effective stress relationship for porous and fractured reservoir rocks," *Journal of Natural Gas Science and Engineering*, vol. 29, pp. 401–412, 2016.
- [14] Li Yao, Y. Xie, H. Xue, and Y. Zhang, "Analysis of sand production mechanism and determination of reasonable production allocation of gas wells in Yulin gas field," *Petrochemical applications*, vol. 35, no. 11, 2016.
- [15] Y. Zou, J. Guo, and C. Fu, "Study on determination method of critical sand production in fractured gas wells," *Natural gas exploration and development*, vol. 32, no. 03, 2009.
- [16] T. Li, *Study on ancient fracturing theory and application technology in Yulin gas field*, Southwest Petroleum University, Chengdu City, 2009.
- [17] L. Li, "Study and application of critical production model for fracture sand production in gas wells," *Petrochemical applications*, no. 04, pp. 15–17, 2005.
- [18] Y. Fu, *Study on proppant backflow mechanism in fracturing gas well production*, Southwest Petroleum University, Chengdu City, 2006.
- [19] G. Liu, *Study on proppant backflow and control in fracturing gas well production*, Southwest Petroleum University, Chengdu City, 2018.
- [20] Z. Jin, J. Guo, J. Zhao, J. Wang, and Z. Zhao, "Dan Kuang Experimental study on the effect of proppant combination with different particle size on fracture conductivity," *Petroleum Geology and Engineering*, no. 06, pp. 88–90, 2007.
- [21] L. Wang and S. Zhang, "Experimental study on the effect of backflow prevention fiber on the conductivity of proppant," *Drilling and Production Technology*, vol. 33, no. 04, 2010.
- [22] Y. Kang, J. Shao, L. You et al., "Experimental simulation of particle migration induced by sharp change of gas injection

- pressure in gas storage wells,” *Oil drilling and production technology*, vol. 42, no. 6, pp. 797–803+810, 2020.
- [23] B. Bai, Q. Nie, Y. Zhang, X. Wang, and W. Hu, “Cotransport of heavy metals and SiO₂ particles at different temperatures by seepage,” *Journal of Hydrology*, vol. 597, Article ID 125771, 2021.
- [24] B. Bai, R. Zhou, G. Cai, W. Hu, and G. Yang, “Coupled thermo-hydro-mechanical mechanism in view of the soil particle rearrangement of granular thermodynamics,” *Computers and Geotechnics*, vol. 137, no. 8, Article ID 104272, 2021.
- [25] F. Zhang, *Study on damage mechanism and repair technology of gas production channel in coalbed methane well*, China University of Petroleum, China, 2013.
- [26] X. Y. Wang, Z. Ma, and Y. T. Zhang, “Research on safety early warning standard of large-scale underground utility tunnel in ground fissure active period,” *Frontiers of Earth Science*, vol. 10, 2022.
- [27] X. Wang, Q. Song, and H. Gong, “Research on deformation law of deep foundation pit of station in core region of saturated soft loess based on monitoring,” *Advances in Civil Engineering*, vol. 2022, pp. 1–16, Article ID 7848152, 2022.
- [28] N. Liu, L. Cui, Y. Wang, and E. Yilmaz, “Analytical assessment of internal stress in cemented paste backfill,” *Advances in Materials Science and Engineering*, vol. 2020, pp. 1–13, Article ID 6666548, 2020.

Research Article

Numerical Simulation of Coupling Support for High-Stress Fractured Soft Rock Roadway in Deep Mine

Wenhua Yuan , Ke Hong, Run Liu, Lianjie Ji, and Long Meng

School of Civil Engineering and Architecture, Anhui University of Science and Technology, Huainan, Anhui 232001, China

Correspondence should be addressed to Wenhua Yuan; whyuan@aust.edu.cn

Received 24 January 2022; Revised 26 April 2022; Accepted 27 April 2022; Published 17 May 2022

Academic Editor: Xingxin Chen

Copyright © 2022 Wenhua Yuan et al. This is an open access article distributed under the Creative Commons Attribution License, which permits unrestricted use, distribution, and reproduction in any medium, provided the original work is properly cited.

Aiming at the difficulties during the support of high-stress fractured soft rock roadway in deep mine, a comprehensive surrounding rock management method of bolt-net-cable-grout coupling support is proposed and the mechanism of interaction between coupling support and surrounding rock is analyzed by numerical simulation. The effectiveness of the coupling support is proved by an application in the east wing return-air roadway in the Qingdong Coal Mine of Huaibei Mining Group. The results show that the surrounding rock plastic zone near the sidewall and floor of high-stress fractured soft rock roadway is larger than that near the roadway roof, and its distribution range can be reduced by using the coupling support. And, the coupling support can improve the reliability of roadway support and the stability of surrounding rock by reducing the axial stress of anchor bolts, the stress concentration of surrounding rock caused by anchor bolt, the roadway surface displacement, and deep displacement of surrounding rock.

1. Introduction

There are about 73.2% of China's coal reserves are buried below 600 m. With the increase of energy demand and the decrease of shallow coal resources, the mining industry has gradually entered into the stage of deep energy exploitation [1]. However, the increasing depth of coal mining brings frequent engineering disasters, such as rock burst, gas explosion, large deformation, high ground temperature, and others, which seriously threaten the safe and efficient exploitation of deep coal resources. Therefore, the rock mechanics and support in deep resource mining have always been one of the research hotspots in the industry [2–4]. Under the influence of high in situ stress, the deep rock mass is in a state of high compressive deformation or failure limit and its mechanical properties are obviously different from shallow rock mass. In deep strata, the disturbance and failure of surrounding rock caused by excavation lead to large deformation and support difficulties of roadway and seriously threaten the safe production of coal mines [5–10].

Fault fracture zone is a common adverse geological phenomenon during roadway excavation, and its

distribution area is one of the unstable sections of surrounding rock. The problems ubiquitous in the fault fracture zone, including high stress concentration, poor self-stability of fissured surrounding rock, and easy collapse of surrounding rock, often lead to geological disasters such as roof collapse and water inrush during excavation of roadway.

The high-stress fractured soft rock roadway is threatened by both the high in situ stress and the fault fracture zone mentioned above, and its support technology needs to be proposed and improved. In fact, in order to effectively control the large deformation of high-stress fractured soft rock roadway in a deep mine, researchers and technicians have carried out some studies and put forward some control techniques. By analyzing the deformation reasons of deep high-stress soft rock roadway, Yang et al. [11] proposed a combined supporting technology to coordinate nonuniform deformation of surrounding rock, control squeeze flow of floor heave, and strengthen the bearing structure of the surrounding rock. Chen et al. [12] put forward an innovative “relief-retaining” control technology of floor heave, which is a comprehensive measure that is composed of cutting groove in the floor, drilling for pressure relief at the roadway

side, and setting retaining piles at the junction of roadway side and floor. Based on numerical simulation, Zheng et al. [13] improved the bearing structure of support and proposed a high-strength combined support system with higher integrity and bearing capacity, which is consisted of cable bolt, fiber-reinforced shotcrete, steel mesh, split sets, resin bolt, and cement grouting. Wang et al. [14] proposed a double-shell grouting technology with low-pressure grouting and high-pressure split grouting to improve the overall mechanical properties of the surrounding coal and rock mass and prevent the large deformation and failure of the roadway. Meng et al. [15] adopted the finite difference program FLAC3D to analyze the distribution characteristics of supporting stress induced by bolt and anchor cable under different conditions of pretightening force and inter-row distance. Jiang et al. [16] analyzed the characteristics of rock large deformation and bolting component failure under different methods of support and put forward a support technology of the bolting, U-shaped yielding steel arches and back filling in synergy, which provided an effective measure for the soft rock roadway control in 1000 m or more deep coal mines. He et al. [17] proposed the bolt-mesh-anchor coupling support technology for the floor heave of deep coal roadway, which effectively controlled the large deformation and floor heave of deep coal roadway. By analyzing the stress environment and failure mechanism of the surrounding rock, Xu and Wei [18] put forward the combined control technology of “prestressed grouting anchor cable + grouting anchor bolt + grouting behind the wall + floor reconstruction” to control the occurrence of roadway floor heave.

By combining numerical simulation with the field test, this paper studies the deformation mechanism of high-stress fractured soft rock roadway then puts forward the joint reinforcement plan of bolt-net-cable-grout coupling support.

2. Project Overview

East wing return-air roadway is located in the seventh mining area near the BF2 fault in the Qingdong Coal Mine of Huaibei Mining Group, to its east is the east wing transport roadway and to its west is the 854 working face. The roadway has an altitude between -630 m to -629 m, and it passes through No.8 coal seam, No.7 coal seam, and No.5 coal seam, siltstone, aluminous mudstone, and mudstone. The inclination direction of coal and rock seam ranges from 30° to 48° , and the dip angle is about 12° . The east wing return-air roadway is in the influence area of the BF2 fault. The BF2 fault is a normal boundary fault between the 5th mining area and 7th mining area, with an NE strike, a dip angle of 55° to 70° , and a height from 70 m to 170 m. The BF2 fault has a long extension and suffers obvious tectonic stress. According to the in situ stress test results, the in situ stress field of the roadway is mainly tectonic stress and the principal stress is distributed horizontally. The horizontal stress component in the north-south direction is large, which is 15.9 MPa. The above-given information indicates that the roadway is a typical high-stress fractured soft rock roadway.

3. Parameters of Bolt-Net-Cable-Grout Coupling Support

The traditional roadway support generally composed of bolt-mesh, and steel belts cannot meet the support needs of the high-stress fractured soft rock roadway. The excavation of the east wing return-air roadway proved the above-mentioned viewpoint because the BF2 fault and high in situ stress caused a series of problems in the roadway with traditional support, such as the roof fracture and separation, the sinking of mesh bag and top roof, the large deformation of roadway, and the floor heave. Obviously, a new type of support is needed to be proposed to solve the problem of high-stress fractured soft rock roadway.

In order to effectively control the deformation and damage of high-stress fractured soft rock roadway, a new two-step coupling support technology is proposed, which is composed with “bolt + net + steel belt + shotcrete + cable + grout.” The two-step can be described as the primary support and secondary support. The new coupling support is first used in the east wing return-air roadway, as shown in Figure 1, to try to solve the problems existing.

3.1. Primary Support. The primary support adopts a coupling support of “bolt + net + shotcrete + cable + roof and side grout” with the following parameters.

3.1.1. Anchor Bolt. High-strength screw-thread steel bolt ($\Phi 22 \times 2600$ mm) is adopted with a spacing of 800×800 mm and 13 bolts in each row. An anchor bolt is used along with the JSMZ20-22 new bolting device. The new bolting device has a spacing of 1600×1600 mm with 5 devices in each row. Each bolt is anchored with 2 rolls of Z2550 resin anchor agent. The size of the bolt tray is $200 \times 200 \times 10$ mm.

3.1.2. Anchor Cable. A hollow grouting anchor cable ($\Phi 21.6 \times 7000$ mm) is used with a spacing of 1600×3200 mm and 3 cables in each row. All of the cables are used along with the JSMZ20-22 new bolting device. The anchor cable tray is a special tray with a size of $300 \times 300 \times 16$ mm. Each anchor cable is anchored with 3 rolls of Z2550 type resin anchor agent.

3.1.3. Net. Reinforcing steel mesh ($\Phi 6 \times 2500 \times 900$ mm) is used with a grid of 100×100 mm and lap length of 100 mm. Reinforcing steel mesh is laid in full section and hooked or tied with double strands of no less than 14# iron wire in a spacing of 200 mm.

3.1.4. Shotcrete. P.O 42.5 cement, sand with a particle size greater than 0.35 mm, stone with a particle size between 5 mm and 10 mm, and J85 accelerating agent are chosen as mixing materials. The mass ratio of cement, sand, stone, and the accelerating agent is 1 : 2 : 2 : 0.04. The prepared shotcrete has a strength of C20 and a thickness of 50 mm.

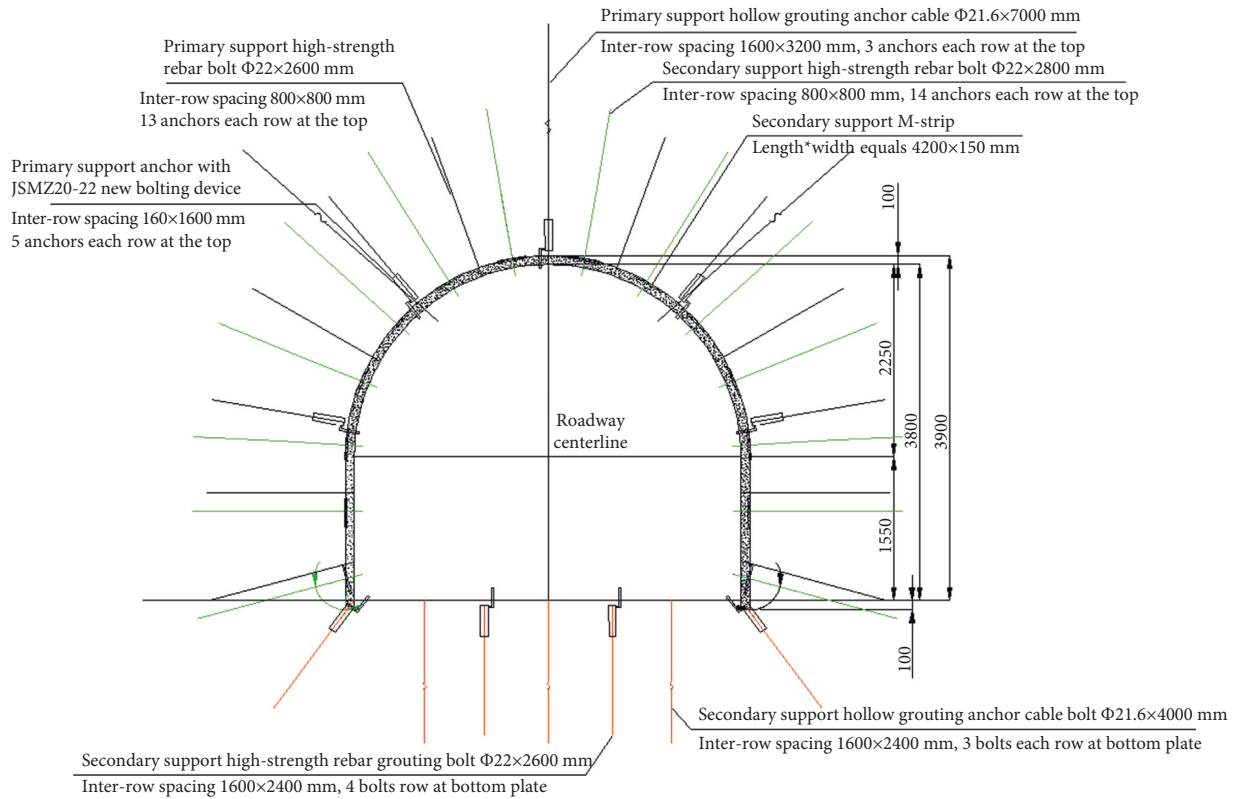


FIGURE 1: Full-section of bolt-net-cable-grout coupling support.

3.2. Secondary Support. Secondary support adopts a coupling support of “bolt + net + shotcrete + steel belt + floor grout.”

3.2.1. Anchor Bolt. High-strength screw-thread steel bolt ($\Phi 22 \times 2800$ mm) is adopted, with a spacing of 800×800 mm and 14 bolts in each row. Each bolt is anchored with 2 rolls of Z2550 resin anchor agent. A special tray for the M-mode steel belt is used.

3.2.2. Steel Belt. M-mode steel belt with a length of 4200 mm and width of 150 mm is arranged along the roadway direction.

3.2.3. Net. Reinforcing steel mesh for the secondary support is the same as that for the primary support.

3.2.4. Shotcrete. The secondary support has the same mix proportion of shotcrete as the primary shotcrete. But the thickness of shotcrete is 70 mm for the secondary support.

3.2.5. Floor Anchor Bolt. High-strength screw-thread steel bolt ($\Phi 22 \times 2600$ mm) is adopted with a spacing of 1600×2400 mm and 4 bolts in each row. An anchor bolt is used along with the JSMZ20-22 new bolting device. Each bolt is anchored with 2 rolls of Z2550 resin anchor agent. The size of the bolt tray is $200 \times 200 \times 10$ mm.

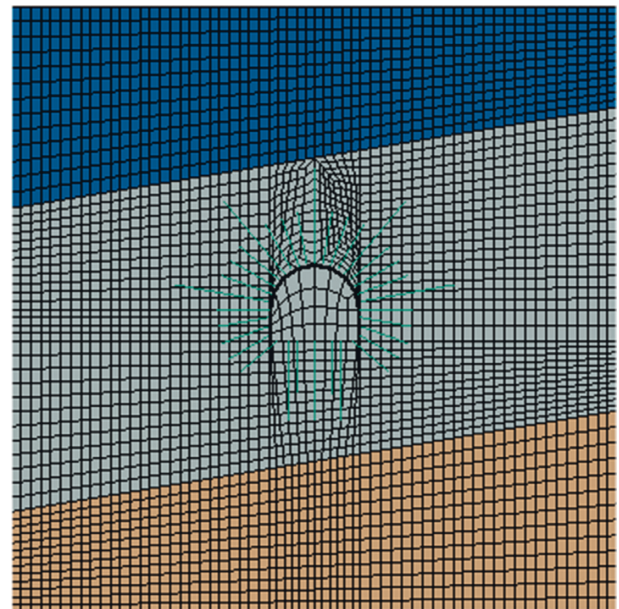


FIGURE 2: Grid diagram of a numerical model.

3.2.6. Floor Anchor Cable. A hollow grouting anchor cable ($\Phi 21.6 \times 4000$ mm) is used with a spacing of 1600×2400 mm and 3 cables in each row. Each anchor cable is anchored with 3 rolls of Z2550 type resin anchor agent. The anchor cable tray is a special tray with a size of $300 \times 300 \times 16$ mm.

TABLE 1: Mechanical parameters of rock strata.

Rock stratum	Elastic modulus E (GPa)	Internal friction angle φ ($^\circ$)	Cohesive force c (MPa)	Poisson's ratio μ	Density ρ (kg/m^3)
Mudstone	14	32	2	0.245	2668
Siltstone	22.7	38	4	0.203	2658
Fine sandstone	43.2	35	5	0.148	2666

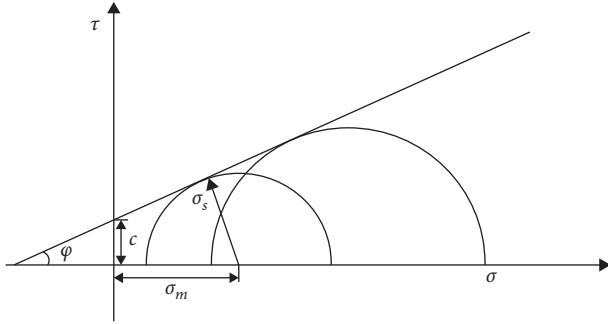


FIGURE 3: Illustration of Mohr-Coulomb yield criterion.

4. Numerical Simulation of the Coupling Support

4.1. Numerical Modeling. According to the rock stratum and support parameters of the return-air roadway, a fine 2D numerical model with a size of 30×30 m has been established by the finite element software ABAQUS. From top to bottom, the rock strata with a dip angle of 10° in the model are composed by siltstone (7.5 m), mudstone (15 m), and fine sandstone (7.5 m). Both the horizontal displacement and the vertical displacement constraints are applied on the side boundaries and bottom boundaries of the numerical model. A vertical stress of 16.33 MPa calculated according to the buried depth of the model is set at the top boundary of the model. The horizontal lateral pressure coefficient is 0.8. The grid diagram of the numerical model under the initial stress state is shown in Figure 2. The mechanical parameters of rock strata are shown in Table 1.

The classic Mohr-Coulomb constitutive model [19] as shown in Figure 3 is adopted as the failure criteria of mudstone, siltstone, and fine sandstone.

The Mohr-Coulomb constitutive model can be expressed as follows:

$$\sigma_s + \sigma_m \sin \varphi - c \cos \varphi = 0, \quad (1)$$

where σ_s and σ_m are the deviating stress and the average principal stress, and they can be expressed as follows:

$$\begin{cases} \sigma_s = \frac{1}{2}(\sigma_1 - \sigma_3), \\ \sigma_m = \frac{1}{2}(\sigma_1 + \sigma_3), \end{cases} \quad (2)$$

where σ_1 and σ_3 are the maximum principal stress and the minimum principal stress, respectively.

4.2. Numerical Implementation of Anchor Bolt. Shotcrete anchor support is often involved in underground projects

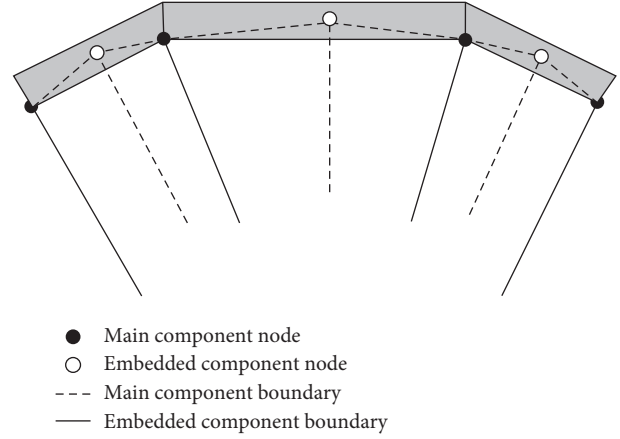


FIGURE 4: Distribution diagram of embedded elements.

such as tunnels, including anchoring support and lining support [20, 21]. The anchor bolt in the support system is constrained by surrounding rock and is in a tension state, so it can be simulated by rod element or beam element in finite element analysis. The “EMBEDDED” command provided by the finite element software ABAQUS can be used to simulate the interaction between the nonprestressed anchor bolt and surrounding rock, whether the anchor bolt element node coincides with the surrounding rock node or not. By using this command, the anchor bolt element can be embedded into rock elements to participate in finite element iterative calculation. The embedded instruction is to embed a specified component or a group of components into the main component, which can be used to simulate reinforcement.

The distribution of embedded elements in the main components is shown in the shaded part of Figure 4.

Generally, there are several types of embedded elements: 2D model, axisymmetric model, and 3D model. In this paper, the beam element model in the 2D model is used to realize the embedding of the anchor element, in which the interaction between bolt and surrounding rock stratum can be simulated without considering whether the embedded position structure is empty or not.

The embedded constraint has been used to define the interactions among anchor bolt and surrounding rock masses. The embedded element technique has been adopted to simulate the anchor bolt, which includes the embedded constraint. The embedded element technique can be used to model rebar reinforcement. Abaqus searches for the geometric relationships between nodes of the embedded elements (rock bolts) and the host elements (surrounding rock masses). If a node of an embedded element lies within a host element, the translational degrees of freedom at the node are eliminated and the node becomes an “embedded node.” The translational degrees of freedom of the embedded node are

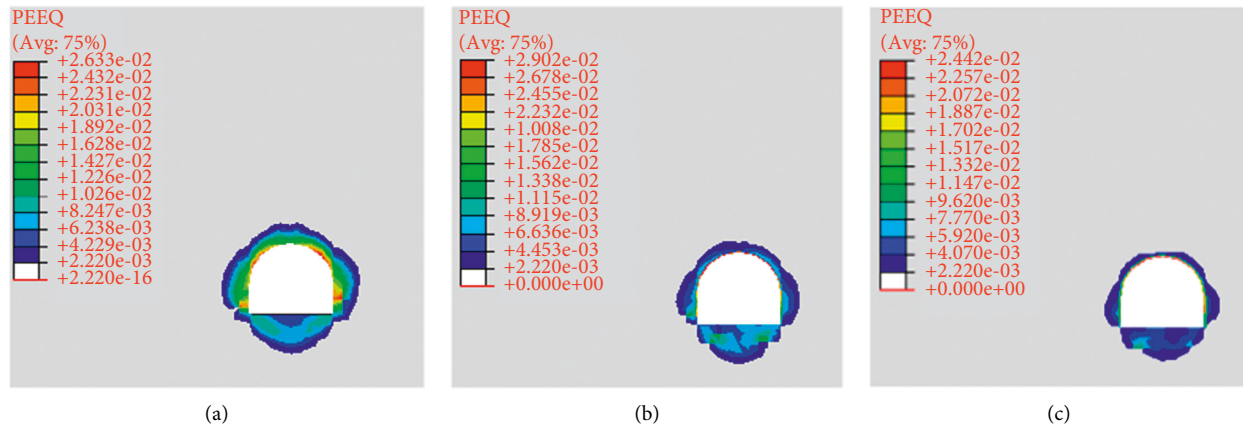


FIGURE 5: Plastic zone distribution of surrounding rock under different conditions: (a) case 1, (b) case 2, and (c) case3.

constrained to the interpolated values of the corresponding degrees of freedom of the host element. Embedded elements are allowed to have rotational degrees of freedom, but these rotations are not constrained by the embedding. Therefore, the deformation and stress of surrounding rock masses can transfer to rock bolts by the embedded element technique, which is similar to the interactions among anchor bolts and surrounding rock masses.

4.3. Analysis of Numerical Simulation Results. According to the composition of the coupling support, three cases are set as follows to analyze support response and surrounding rock response under different working conditions:

Case 1: full-section excavation without support

Case 2: full-section excavation with primary support

Case 3: full-section excavation with primary support and secondary support

The main excavation response factors, including the surface displacement of roadway, anchorage force, deep displacement of surrounding rock, and plastic zone of surrounding rock, have been analyzed under the three different cases.

4.3.1. Plastic Zone Distribution of Surrounding Rock. The plastic zone of surrounding rock can reflect the stability and safety of the roadway. Figure 5 shows the equivalent plastic strain cloud diagram of surrounding rock under three different cases, in which, PEEQ represents the value of equivalent plastic strain to reflect the cumulative result of plastic strain in the whole deformation process.

Figure 5 shows that the surrounding rock plastic zone is mainly distributed near the roadway surface, and the surrounding rock of case 1 has a larger plastic zone range compared to that of case 2 and case 3. That is to say, the application of support can effectively reduce the distribution range of the surrounding rock plastic zone. In any case, the surrounding rock plastic zone near the roadway sidewall and floor are larger than that near the roadway roof.

As shown in Figure 5(a), when the roadway is not supported, the size of the surrounding rock plastic zone near the roadway sidewall is about 30% of the roadway span, and those near the roadway floor and roof are about 56% and 27% of the roadway height. Figure 5(b), the figure of the surrounding rock plastic zone near the roadway with primary support, shows that the sizes of the surrounding rock plastic zone near the roadway sidewall and roof are significantly reduced compared with case 1, which are about 25% of the roadway span and 17% of the roadway height, respectively. However, the size of the surrounding rock plastic zone near the roadway floor is the same as in case 1. As shown in Figure 5(c), the range of the surrounding rock plastic zone further decreases after secondary support is applied, the sizes of the surrounding rock plastic zone near the roadway sidewall, floor, and roof are reduced by about 19% of the roadway span, 44%, and 10% of the roadway height. Obviously, the secondary support plays a key role in reducing the surrounding rock plastic zone.

To sum up, the application of support is helpful to reduce the surrounding rock plastic zone range and improve the stability of the surrounding rock, and the coupling support is better than the primary support alone.

Of course, Figure 5 also reflects that the maximum value of PEEQ of surrounding rock increases from 0.02633 in case 1 to 0.02902 in case 2, due to the stress concentration of surrounding rock caused by the action of the anchor bolt. Obviously, the stress concentration of surrounding rock is improved when the coupling support with a relatively dense bolt is adopted, and the maximum value of PEEQ of surrounding rock is reduced to 0.02442 in case 3.

4.3.2. Stress of Anchor Bolt and Cable. The axial stress of anchor bolts and cables under different conditions is shown in Figure 6.

Figure 6 shows that in all working conditions, the axial stress of anchor bolts and cables always decreases with the increase of the buried depth and the axial stress reaches the maximum value near the roadway surface. Obviously, this phenomenon accords with the mechanical characteristics of bonded bolts. Under the influence of the rock strata dip

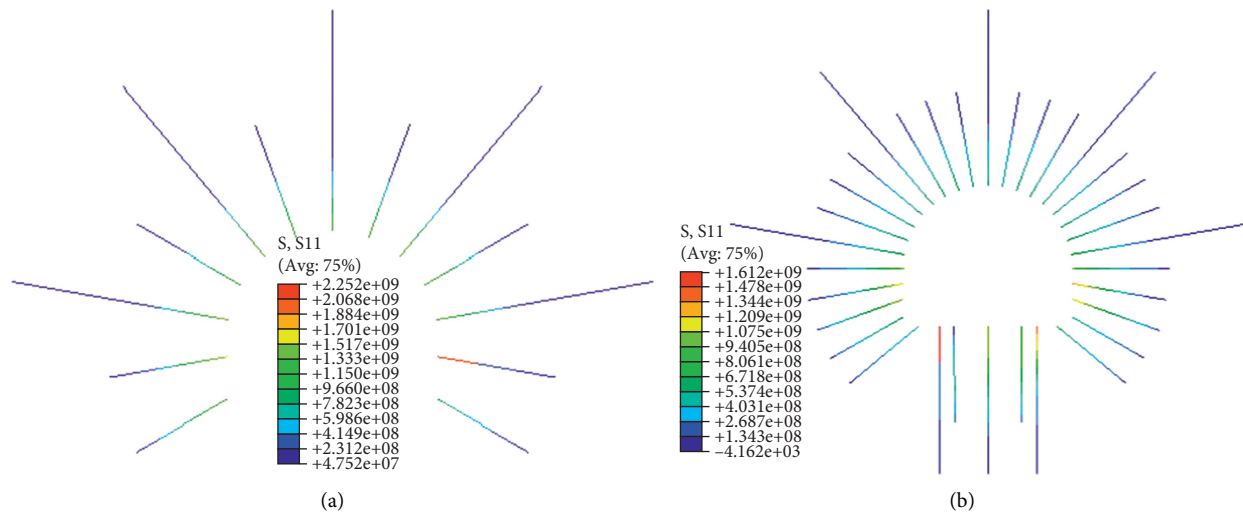


FIGURE 6: Axial stress clouds of anchor bolts and cables under different conditions (unit: Pa): (a) case 2 and (b) case 3.

angle, the axial stress of anchor bolts and cables arranged in different directions is different in the same buried depth.

In case 2, the maximum axial stress of anchor bolts and cables is about 2.252 GPa, which appears near the roadway sidewall. However, in case 3, the maximum axial stress of anchor bolts and cables decreases to 1.612 GPa, which appears near the roadway floor, while the maximum axial stress of bolt near the roadway sidewall is only 1.28 GPa. Obviously, the application of secondary support significantly reduces the maximum axial stress of the bolt system and changes the action mode of the bolt system. The large axial stress of the anchor bolts and cables near the roadway floor indicates that the anchor bolts and cables effectively limit the trend of floor heave and the occurrence of floor failure.

Therefore, the secondary support can change the mechanical state of surrounding rock and reduce the axial stress of anchor bolts and cables by increasing the distribution density of bolt and further improve the reliability of roadway support and the stability of surrounding rock. The coupling support can solve the problem of insufficient strength of supporting members of high-stress fractured soft rock roadway.

4.3.3. Roadway Surface Displacement. Roadway surface displacement can reflect the stability of surrounding rock and support. Therefore, as shown in Figure 7, four typical measurement points are set on roadway sidewalls, floor, and roof to carry out the comparison of roadway surface displacement under different support forms.

The roadway surface displacement under the three cases is shown in Table 2.

Table 2 shows that when the roadway is not supported, the displacement values of the four measurement points are relatively close and the maximum value appears at the roadway floor. After the application of primary support, the displacement of measurement points A, C, and D at the roadway roof and sidewall decreases rapidly by 47.3%, 28.9%, and 45.6%, respectively, while the displacement of

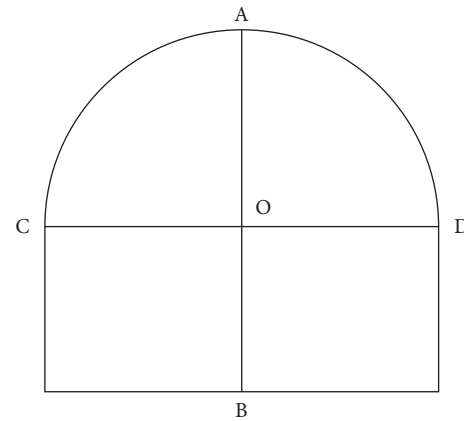


FIGURE 7: Surface measurement points arrangement of the roadway.

TABLE 2: Surface displacement of monitoring points of the roadway under different conditions.

Calculation conditions	Surface displacement of measurement points of roadway (mm)			
	A	B	C	D
Case 1	18.99	19.67	17.17	18.74
Case 2	10.00	18.79	12.21	10.20
Case 3	6.63	17.24	7.82	7.83

measurement point B at the roadway floor decreases by only 4.5%. The application of secondary support further reduces the roadway surface displacement, but the measurement points with significant displacement reduction are still located at the roadway roof and sidewall. The displacement of measurement points A, C, and D decreased by 65.1%, 54.5%, and 58.2%, respectively, compared with case 1, but the measurement point D still has a small displacement change.

Therefore, the application of support can reduce the roadway surface displacement, especially the displacement

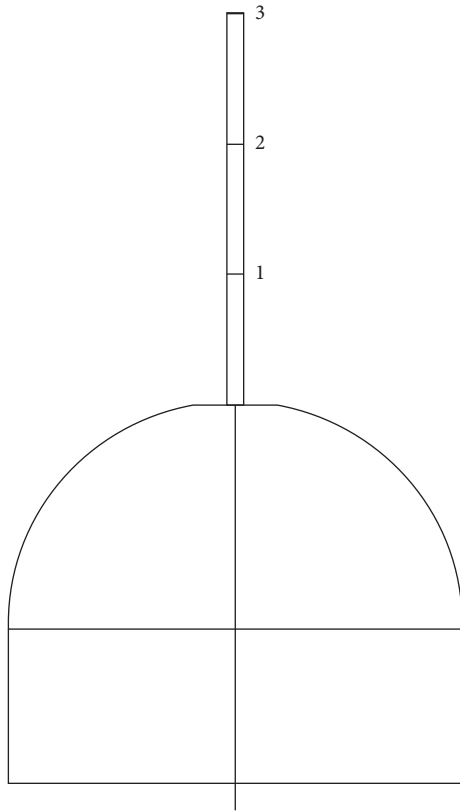


FIGURE 8: Measurement point for the deep displacement of surrounding rock.

at the roadway roof and sidewall. However, the effect of roadway support on inhibiting the displacement at the roadway floor is not obvious, which is basically consistent with the analysis result of inhibiting effect of roadway support on the surrounding rock plastic zone. On the whole, the coupling support has a stronger inhibition displacement ability and better supporting effect than single primary support for a high-stress fractured soft rock roadway.

4.3.4. Deep Displacement of Surrounding Rock. The deep displacement of surrounding rock is an important parameter to reflect the relaxation response and deformation law of surrounding rock induced by excavation. For the deep displacement of surrounding rock, three measurement points above the roadway roof are selected on the vertical axis of the model, numbered as 1, 2, and 3 in sequence and the distances between the measurement points and the roadway roof are 2.0 m, 5.0 m, and 8.0 m, as shown in Figure 8.

Table 3 shows the displacements of three measurement points in the surrounding rock above the roadway roof under different cases.

It can be seen from Table 3 that no matter what support method is adopted, the deep displacement of surrounding rock decreases in accordance with nonlinear law as the distance between measurement points and roadway surface increases. In case 3, the displacement of all measurement points is smaller than that in case 2, and the displacements of

three measurement points are reduced by 33.2%, 17.2%, and 15.1%, respectively. That is to say, the increase of support strength caused by the application of secondary support effectively controls the deep displacement of surrounding rock and reduces the loosening range of surrounding rock.

Combined with the displacement of the roadway roof described in Table 2, the maximum relative displacement of measurement points appears between measurement point 1 and measurement point 2, so it can be considered that the main range of surrounding rock loosening does not exceed measuring point 2.

Therefore, the application of support can reduce not only the roadway surface displacement but also the deep displacement of surrounding rock. For high-stress fractured soft rock roadway, coupling support has a stronger ability to suppress deep displacement of surrounding rock than single primary support. Under the roadway support, the loosening of surrounding rock mainly occurs within 5 m from the roadway surface.

5. Support Effect Monitoring Analysis

Based on the analysis of support bearing characteristics by numerical simulation, the coupling support technology proposed in this paper is applied in the east wing return-air roadway in the Qingdong Coal Mine of Huaibei Mining Group. The applicability and reliability of the coupling support in high-stress fractured soft rock roadway are verified by field monitoring.

The measurement points of roadway surface displacement are arranged by using the cross-point method, and the location is shown in Figure 7. The spacing of measuring points along the axis of the roadway is about 30 m~40 m. 12 measurement points on 3 sections are set up during the monitoring process. The surface displacements of the roadway on the two observed sections are shown in Figure 9.

According to Figure 9, when the coupling support is done, all the displacements of measurement points are greater than the numerical simulation results. This phenomenon is mainly due to the well-known time effect [22, 23] of surrounding rock deformation, and the large time difference between support application and roadway excavation causes large initial deformation. Obviously, the influence of the time effect is difficult to predict in numerical simulation. In addition, the measured displacement of roadway floor is less than that of roadway sidewall and roof, which is opposite to the numerical simulation results. It shows that the deformation of surrounding rock near the roadway floor is less affected by time effect than that of the surrounding rock near the roadway sidewall and roof. It is beneficial and necessary to control the large deformation of surrounding rock by timely supporting following the roadway excavation.

It can be seen from Figure 9 that the deformation of all the measurement points gradually increases with time and eventually tends to a stable state, and the displacement of the roadway floor is always smaller than that of the roadway sidewall and roof. After 5 months of measurement, the maximum value of roof sinking, floor heave, and sidewall

TABLE 3: Deep displacement of surrounding rock under different conditions.

Calculation conditions	Displacement of roof measurement point (mm)		
	Measurement point 1	Measurement point 2	Measurement point 3
Case 2	9.52	5.46	4.82
Case 3	6.36	4.52	4.09

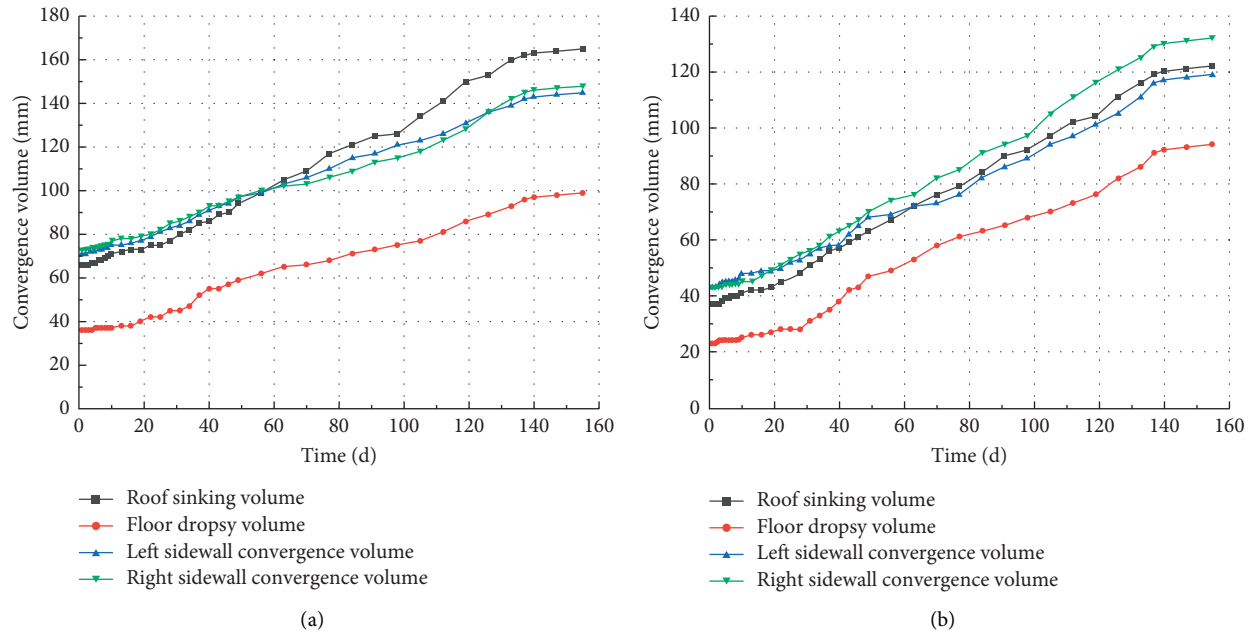


FIGURE 9: Convergence curve of measurement points at the return-air roadway: (a) measurement point 1 and (b) measurement point 2.



FIGURE 10: Support effect of the return-air roadway: (a) support effect of the roof and (b) support effect of the sidewall.

convergence of the roadway finally reached about 160 mm, 100 mm, and 150 mm, respectively. These deformation values seem to be large, but in fact, they are all within the controllable range. At the end of monitoring, the displacement of roadway support no longer increases significantly, which indicates that the deformation of surrounding rock has reached a stable state, and the deformation of surrounding rock caused by roadway excavation has been effectively controlled by the coupling support. The roadway with coupling support is shown in Figure 10.

6. Conclusions

A bolt-net-cable-grout coupling support is proposed to solve the problem in the supporting of high-stress fractured soft rock roadway. The mechanism of interaction between coupling support and surrounding rock is analyzed by numerical simulation, and the excavation responses of coupling support and surrounding rock, such as stress and displacement, are studied. Under the guidance of numerical simulation results, the coupling support is applied to an

actual roadway, and the measurement results show that the coupling support is effective. The key conclusions of the study are as follows:

- (1) The surrounding rock plastic zone near the roadway sidewall and floor is larger than that near the roadway roof, and the coupling support is more effective to reduce the distribution range of the surrounding rock plastic zone than the primary support alone. In addition, the coupling support can reduce the stress concentration of surrounding rock caused by the anchor bolt.
- (2) The coupling support can change the mechanical state of surrounding rock and reduce the axial stress of anchor bolts and cables by increasing the distribution density of bolt and further improve the reliability of roadway support and the stability of surrounding rock.
- (3) The coupling support has a stronger inhibition displacement ability than single primary support for a high-stress fractured soft rock roadway, especially for the displacement at the roadway roof and sidewall.
- (4) Coupling support can reduce not only roadway surface displacement but also deep displacement and plastic zone size of surrounding rock. For high-stress fractured soft rock roadway, the coupling support has a stronger ability to suppress the deep displacement of surrounding rock than the single support.
- (5) Field monitoring data indicate that bolt-net-cable-grout coupling support changes the structure of high-stress fractured soft rock roadway and restrains the occurrence of floor heave, which proves that the comprehensive treatment of surrounding rock is effective.

Data Availability

The datasets generated and analyzed during the current study are available from the corresponding author on reasonable request.

Conflicts of Interest

The authors declare that there are no conflicts of interest.

Acknowledgments

This work was financially supported by the National Natural Science Foundation of China (No. 52074005).

References

- [1] Q. H. Qian, "The current development of nonlinear rock mechanics: The mechanics problems of deep rock mass," in *Proceedings of the 8th Rock Mechanics and Engineering Conference*, pp. 10–17, Science Press, Beijing, China, 2004.
- [2] M. C. He, H. P. Xie, S. P. Peng, and Y. D. Jiang, "Study of rock mechanics in deep mining," *Chinese Journal of Rock Mechanics and Engineering*, vol. 24, no. 16, pp. 2803–2813, 2005.
- [3] D. F. Malan and S. M. Spottiswoode, "Time-dependent fracture zone behavior and seismicity surrounding deep level stopping operations," in *Proceedings of the Rockburst and Seismicity in Mines*, pp. 173–177, A. A. Balkema, Rotterdam, 1997.
- [4] E. J. Sellers and P. Klerck, "Modelling of the effect of discontinuities on the extent of the fracture zone surrounding deep tunnels," *Tunnelling and Underground Space Technology*, vol. 15, no. 4, pp. 463–469, 2000.
- [5] X. C. Kang, D. Guo, and Z. Y. Lu, "Mechanism of roadway floor heave controlled by floor corner pile in deep roadway under high horizontal stress," *Advances in Civil Engineering*, vol. 2021, pp. 1–10, Article ID 6669233, 2021.
- [6] W. Zheng, Y. Zhao, Q. Bu, and S. I. Kundalwal, "The coupled control of floor heave based on a composite structure consisting of bolts and concrete antiarches," *Mathematical Problems in Engineering*, vol. 2018, Article ID 3545423, 14 pages, 2018.
- [7] J. Shi and D. S. Kong, "Floor heave mechanism and anti-slide piles control technology in deep and large-span chamber," *Applied Sciences*, vol. 11, no. 10, p. 4576, 2021.
- [8] Q. Wang, R. Pan, B. Jiang, S. C. Li, M. C. He, and H. B. Sun, "Study on failure mechanism of roadway with soft rock in deep coal mine and confined concrete support system," *Engineering Failure Analysis*, vol. 81, pp. 155–177, 2017.
- [9] H. S. Jia, L. Y. Wang, K. Fan, B. Peng, and K. Pan, "Control technology of soft rock floor in mining roadway with coal pillar protection: A case study," *Energies*, vol. 12, no. 15, p. 3009, 2019.
- [10] C. Wang, Y. P. Wu, S. J. Chen et al., "Analysis and application on inverted arch support of cross-cut floor heave," *Journal of Physics: Conference Series*, vol. 2002, no. 1, pp. 713–720, Article ID 012069, 2021.
- [11] R. S. Yang, Y. L. Li, D. M. Guo et al., "Causes of deformation damage and support technology for deep high stress soft rock roadways," *Journal of Mining & Safety Engineering*, vol. 34, no. 6, pp. 1035–1041, 2017.
- [12] A. Chen, X. B. Li, X. S. Liu, Y. L. Tan, K. Xu, and H. L. Wang, "Relief-retaining control technology of floor heave in mining roadway with soft rock: A case study," *Advances in Civil Engineering*, vol. 2021, Article ID 1455052, 13 pages, 2021.
- [13] L. J. Zheng, Y. J. Zuo, Y. F. Hu, and W. Wu, "Deformation mechanism and support technology of deep and high-stress soft rock roadway," *Advances in Civil Engineering*, vol. 2021, Article ID 6634299, 14 pages, 2021.
- [14] F. N. Wang, S. Z. Chen, P. Gao, Z. B. Guo, and Z. G. Tao, "Research on deformation mechanisms of a high geostress soft rock roadway and double-shell grouting technology," *Geofluids*, vol. 2021, Article ID 6215959, 13 pages, 2021.
- [15] Q. B. Meng, L. J. Han, F. Zhang, J. Zhang, J. W. Nie, and S. Y. Wen, "Coupling support effect on high-stress deep soft rock roadway and its application," *Rock and Soil Mechanics*, vol. 38, no. 5, pp. 1234–1235+1444, 2017.
- [16] P. F. Jiang, H. P. Kang, Z. G. Wang et al., "Principle, technology and application of soft rock roadway strata control by means of rock bolting, U-shaped yielding steel arches and back filling in synergy in 1 000 m deep coal mines," *Journal of China Coal Society*, vol. 45, no. 3, pp. 1020–1035, 2020.
- [17] M. C. He, G. F. Zhang, G. L. Wang, Y. L. Xu, C. Z. Wu, and Q. D. Tang, "Research on mechanism and application to floor

- heave control of deep gateway,” *Chinese Journal of Rock Mechanics and Engineering*, vol. 28, pp. 2593–2598, 2009.
- [18] L. Z. Xu and S. J. Wei, “Control technology and simulation study of floor heave in high stress soft rock roadway,” *Geotechnical & Geological Engineering*, vol. 38, no. 4, pp. 4045–4058, 2020.
- [19] H. W. Ma, L. Liu, P. Wang, S. Yuan, Q. R. He, and X. L. Yang, “Calculation method and mechanism of ultimate side resistance of screw pile,” *Marine Georesources & Geotechnology*, vol. 2021, Article ID 2014003, 15 pages, 2021.
- [20] B. Bai, R. Zhou, G. Q. Cai, W. Hu, and G. C. Yang, “Coupled thermo-hydro-mechanical mechanism in view of the soil particle rearrangement of granular thermodynamics,” *Computers and Geotechnics*, vol. 137, no. 8, Article ID 104272, 2021.
- [21] B. Bai, G. C. Yang, T. Li, and G. S. Yang, “A thermodynamic constitutive model with temperature effect based on particle rearrangement for geomaterials,” *Mechanics of Materials*, vol. 139, Article ID 103180, 2019.
- [22] L. Liu, H. W. Ma, X. L. Yang, Q. R. He, and S. Yuan, “A calculation method of bearing capacity of single squeezed branch pile based on load transfer method,” *Advances in Materials Science and Engineering*, vol. 2022, pp. 1–9, Article ID 9597047, 2022.
- [23] H. W. Ma, Y. Y. Wu, Y. Tong, and X. Q. Jiang, “Research on bearing theory of squeezed branch pile,” *Advances in Civil Engineering*, vol. 2020, Article ID 6637261, 12 pages, 2020.

Research Article

Influencing Factors of Snow Melting and Deicing on Carbon Fiber Embedded in Bridge Decks

Yan Tan ^{1,2} Shuang Zheng ^{1,2} Henglin Xiao ^{1,2} and JiaMing Xing ³

¹College of Civil Engineering, Architecture and Environment, Hubei University of Technology, Wuhan 430068, China

²Pilot Test Base for Melting Snow and Ice, Hubei University of Technology, Wuhan 430068, China

³Hubei Communications Investment Northwest Expressway Operation Management Co., Ltd., Hubei, China

Correspondence should be addressed to Henglin Xiao; xiaohenglin@hbut.edu.cn

Received 16 March 2022; Accepted 18 April 2022; Published 29 April 2022

Academic Editor: Xianze Cui

Copyright © 2022 Yan Tan et al. This is an open access article distributed under the Creative Commons Attribution License, which permits unrestricted use, distribution, and reproduction in any medium, provided the original work is properly cited.

To study the general law of the influence of embedded carbon fiber heating wires on the melting of snow and ice on bridge decks and to solve the problem of icing on large bridges in winter, relevant model tests were carried out. In this experiment, a carbon fiber heating wire was used as the heat source to make a large-scale asphalt concrete bridge deck model with a built-in carbon fiber heating wire. The effect of different heating powers, ambient temperatures, snow and ice thicknesses, and wind levels on the melting of snow and ice on bridge decks was studied. The snow-melting and ice-melting tests performed at different heating powers show that as the heating power increases within a certain range, the time required for the snow and ice layers to melt and the power consumption decrease. Under certain conditions, to ensure the rapid melting of snow and ice layers on the surface of road bridges, a heating power of 400 W/m^2 is selected. At this time, the heating effect is the best, and this method is economical and practical. The snow-melting and ice-melting tests performed at different ambient temperatures and with different thicknesses of the snow and ice layers show that as the ambient temperature decreases or the thickness of the ice layer increases within a certain range while keeping the other factors constant, the time required for the snow to melt and the power consumption increase, and the power consumption is relatively large. The snow-melting test performed at different wind levels shows that with the increase in the wind level within a certain range while keeping the other factors constant, the uniformity of the overall temperature distribution on the surface of the specimen worsens, the snow-melting time increases, and the temperature rises. The rate of temperature increase decreases. Therefore, in actual engineering applications, when the wind speed is too high, the methods of manually or mechanically removing snow can increase the snow removal rate on bridge decks. Under different conditions, choosing the right heating power can effectively improve the efficiency of melting snow and ice on bridge decks. The research results of this paper provide a theoretical reference for the actual construction of bridge decks in the future.

1. Introduction

As the elevated part of a bridge is suspended in the air, cold wind blows on the bridge from all directions, which causes the heat of the bridge body to be lost in all directions [1], making bridge decks prone to icing in winter and causing accidents. According to statistics, approximately 40,000 people die in traffic accidents caused by bridge icing every year in China [2]. It is particularly important to solve the problem of icing on bridge pavement.

At present, the methods of melting snow and ice on bridge decks are mainly divided into two categories: passive deicing methods and active deicing methods. Passive deicing

methods mainly include artificial methods, mechanical methods, and deicing agent methods. The manual method [3] cannot be applied in a large area due to the high labor cost and low removal efficiency. The mechanical method will cause a certain degree of damage to the bridge deck due to its high gravity, and due to the subsequent maintenance cost being high, it cannot be widely used [4]. In addition, the use of snow-melting agents causes irreversible damage to the environment, buildings, and vegetation, so it is not vigorously promoted for use [5]. On the other hand, the active deicing method mainly includes the thermal melting method, and the electric heating method in the thermal melting method uses a heating cable as a heating element.

The method involves heat exchange between the surface and ice and snow [6–8]. Compared with the passive deicing method, the heating cable heating system has the advantages of no pollution, convenient construction, and remote control, so it has been widely studied. Yanfeng Li [9] et al. studied the selection of carbon fiber heating wires, the depth of burial, and the spacing of heating wires. They studied road surface changes through carbon fiber melting of snow and ice combined with finite element analysis. The results showed that the external climatic conditions (especially temperature) are the main factors of the snow-melting effect of heating cables. Hongming Zhao [10] et al. studied the influence of different spacings of heating wires on the surface temperature characteristics of concrete slabs through finite element modeling and studied the relationship between the input power and temperature rise of concrete slabs through indoor temperature rise experiments on concrete slabs. The results showed that under certain conditions that used a carbon fiber heating plate surface, the average temperature was above 0°C, and the temperature distribution met the requirements of uniform snow and ice melting. Bu Yin [11] et al. analyzed the heat dissipation of a carbon fiber heating bridge deck and studied the utilization and loss mechanism of the heat generated by carbon fiber heating wire. The results showed that convective heat transfer and latent heat affect the heat dissipation of carbon fiber heating bridge decks. In this method, temperature has the greatest effect on melting snow and ice on carbon fiber-heated bridge decks, followed by wind speed, and ice thickness has the least effect. Bai Bing [12] et al. developed a theoretical model describing their cotransport. The results showed that temperature and Darcy velocity have a negligible effect on the transport of individual HMs and that the recovery ratio of Cd²⁺ is higher than that of Pb²⁺. And it established a coupled thermo-hydro-mechanical mechanism in view of the soil particle rearrangement for saturated/unsaturated soils under the framework of granular thermodynamics. The deduced generalized phase stresses differ from the classical effective principle based on linear elastic porous media and can automatically consider the impact of the stress path, temperature path, and soil structure [13].

Iftekar Gull [14] et al. investigated the effect of mechanical depolymerization of carbon fibers in a mixture of methylcellulose and sodium dodecylbenzene sulfonate water on the dispersion of carbon fibers in self-compacting concrete (SCC) as a way to improve the properties of concrete. Sherif A. Yehia [15] et al. performed a thermoelectric-coupled finite element analysis to study the Joule heating of a conductive concrete overlay [16–18]. Quantao Liu [19] et al. concluded that induction heating can improve the self-healing rate of asphalt mastic and porous asphalt concrete. This method has the advantages of a wide range of material sources and simple preparation [20,21]. The current disadvantage is that the mechanical and electrical properties of the researched conductive concrete cannot be well balanced, and its high price makes its use difficult in a wide range of applications. Abubakar Gambo Mohammed [22] et al. investigated a novel resistance heating method for deicing and snow melting. Three different forms of carbon fiber were

embedded in concrete samples, and their heating properties were tested. To simulate the condition of concrete exposed to low temperature, an environmental chamber was used to study the effect of various parameters such as thermal power density, ambient temperature, heating plate installation depth, concrete humidity, and carbon fiber form on temperature variation. The test results show that the carbon fiber electric heating method can effectively remove the icing and snow problems of the road. Yong Lai [23,24] et al. proposed a method for snow melting with carbon fiber grilles buried in airport sidewalks. At –3°C to –1°C, power is supplied to the airport sidewalk by using carbon fiber grille. The results show that when the input power is 350 W/m², the maximum road surface temperature can reach 4.63 °C, and the 2.7 cm-thick snow can be melted within 2 h.

Li et al. [25] takes the airport pavement as the background to explore the law of temperature rise. Li et al. [26] conducted an experimental study on the effect of melting snow and ice on the bridge deck with carbon fiber heating wires. Analysis shows that carbon fiber is a new high-performance fiber-reinforced material, and its performance is excellent, with high strength, high modulus, high-temperature resistance, friction resistance, fatigue and creep resistance, and many other excellent properties, so it can provide a viable solution for melting snow and ice on bridge decks. Therefore, in this paper, we choose a 24 K carbon fiber heating line as the heat source and make a large asphalt concrete bridge deck model with a built-in carbon fiber heating line to study the effects of different heating powers, ambient temperatures, snow and ice thicknesses, and wind levels on the melting of snow and ice on the bridge deck to provide a reference for future applications in melting snow and ice on actual bridges.

2. Materials and Methods

2.1. Model. This test mainly explores the rate of temperature increase of a bridge deck and the melting of snow and ice, so the stress and load-bearing capacity of the specimens are not considered. The asphalt concrete specimens are shown in Tables 1–3 for each surface layer type.

The test specimens are 50 cm long, 50 cm wide, and 30 cm high. From top to bottom, they are a 4 cm thick AC-13 upper layer, 6 cm thick AC-20 lower layer, and 20 cm thick cement concrete pavement. The carbon fiber heating wire is pre-embedded inside the specimen and is distributed in a “U” shape 11 cm from the surface of the model. And the Keysight temperature recorder is used to read the surface temperature of the sample. To reduce heat loss, a 3 cm thick XPS board is pasted on the bottom and four sides of the mold for thermal insulation. The three-dimensional model of the asphalt concrete specimen is shown in Figure 1, and the cross-sectional view is shown in Figure 2. The Keysight temperature recorder is shown in Figure 3.

2.2. Experiment Material. As a new type of high-performance fiber material for reinforcement, carbon fiber has excellent performance and properties, such as high strength,

TABLE 1: C30 concrete mix ratio (kg).

Material	Water	Cement	Gravel	Pebble	Admixture
Quality	8.75	23.05	25.6	62.6	0

TABLE 2: AC-20 asphalt concrete mix ratio (kg).

Particle size (mm)	15~20	10~15	5~10	3~5	0~3
Quality	24	22	21	4	26

TABLE 3: AC-13 asphalt concrete mix ratio (kg).

Particle size (mm)	10~15	5~10	0~3
Quality	60	8	13

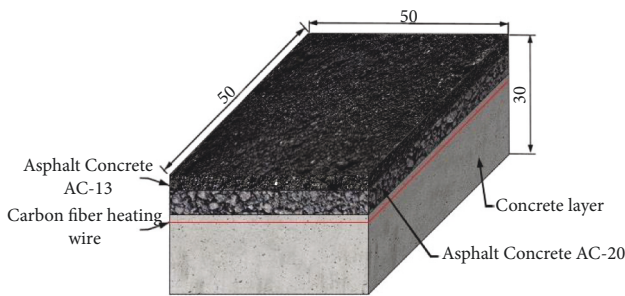


FIGURE 1: Three-dimensional model of an asphalt concrete specimen (cm).

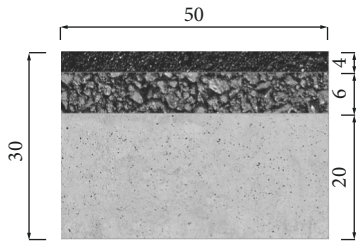


FIGURE 2: Cross-sectional view of an asphalt concrete specimen (cm).

high modulus, high-temperature resistance, friction resistance, fatigue and creep resistance, and many other excellent properties. The experiment uses 24K carbon fiber heating wire products, each of which has a total length of 12 m and is evenly arranged in the model in a “U” shape, and the adjacent spacing is 10 cm. The total length embedded in the specimen is 5 m, and the length exposed to the air is 7 m. The resistance of the heating wire is $17 \Omega/m$, the maximum voltage in the laboratory is 220 V, and the maximum heating power applied to the model is 400 W/m^2 . Similarly, when the voltages are 180 V and 200 V, the corresponding heating powers are 260 W/m^2 and 320 W/m^2 . The layout of the carbon fiber heating wire is shown in Figure 4.

2.3. Test Conditions. The test is mainly divided into two parts: the snow-melting test and the ice-melting test. In the snow-melting test and deicing test, snow and ice are spread



FIGURE 3: Keysight temperature recorder.

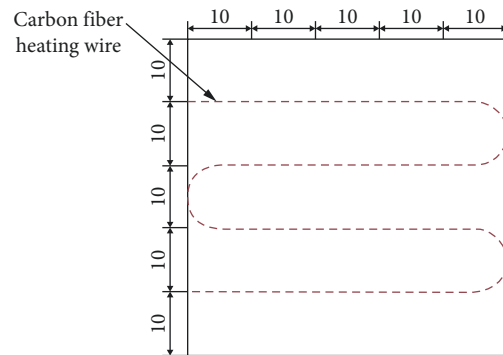


FIGURE 4: Layout of the heating wire (unit: cm).

on the surface of the test specimen in advance, and then, the power is turned on to heat the model when the thickness of the ice and snow required by the working condition is reached to carry out the test. The general rules of the influence of different heating powers, ambient temperatures, snow and ice thicknesses, and wind powers on the melting of snow and ice on bridge decks are studied. The four working conditions of the snow-melting test are shown in Table 4, and the two working conditions of the deicing test are shown in Table 5.

3. Results and Discussion

3.1. Research on the Influencing Factors of the Snow-Melting Test

3.1.1. Heating Power. The set working conditions are an initial ambient temperature of -3°C , Class 0 wind, and a snow thickness of 2 cm, and the effects of three different heating powers of 260 W/m^2 , 320 W/m^2 , and 400 W/m^2 on the time required for snow melting and power consumption influence are explored. The surface temperature change curve of the specimen at different powers is shown in Figure 5.

Figure 5 shows that when the heating power is 400 W/m^2 and the heating time is 0.49 h, the surface temperature of the test specimen can reach 0°C ; at this time, the snow starts to melt. When it is heated for 1.83 h, the surface snow melts completely. At this time, the temperature is 4.43°C , and the total power consumption is 0.73 kW h/m^2 . When the heating powers are 320 W/m^2 and 260 W/m^2 , the surface temperature can reach 0°C after the heating time exceeds 1.01 h and

TABLE 4: Snow-melting test conditions.

Group class	Heating power (W/m ²)	Environmental temperature (°C)	Wind rating	Snow thickness (cm)
A	260	-3	0	2
	320			
	400			
B	400	-3	0	4
		-6		
		-9		
C	400	-3	0	2
				4
				6
D	400	-3	0	4
			1	
			2	

TABLE 5: Deicing test conditions.

Group class	Heating power (W/m ²)	Environmental temperature (°C)	Wind rating	Ice thickness (mm)
A	260	-3	0	5
	320			
	400			
B	400	-3	0	5
				10
				15

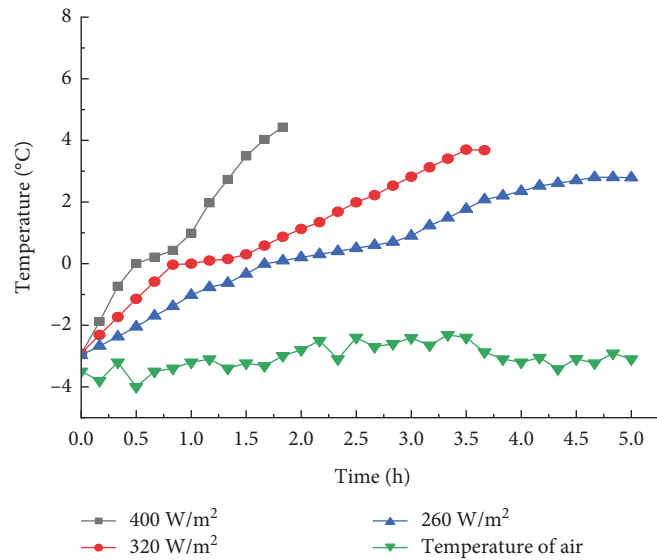


FIGURE 5: Curve of the surface temperature change of the test specimen under different powers.

2.03 h, respectively. The snow began to melt at this time. When heating for 3.67 h and 5.0 h, the surface snow can be melted. At this time, the temperatures are 3.68 °C and 2.79 °C, and the total power consumptions are 1.17 kW h/m² and 1.3 kW h/m², respectively.

In the snow-melting tests at the three powers, when the heating power is changed from 260 W/m² to 320 W/m², the time for complete snow melting is shortened by 1.33 h, and the power consumption is approximately 10% less than that in the case of 260 W/m². When the heating power is changed from 260 W/m² to 400 W/m², the time to completely melt the snow

is reduced by 3.17 h, and the power consumption is reduced by 43.8% compared with that of the case of 260 W/m².

The rates of the surface temperature increase of the specimen at different powers are shown in Table 6. Comparing the rates of temperature increase under the three working conditions within 0~1.83 h shows that at 260 W/m², when the surface temperature of the test specimen increases from -2.972°C to -0.100°C, the rate of temperature increase is 1.760 °C/h. At 320 W/m², when the surface temperature of the specimen increases from -2.913°C to 0.872°C, the rate of temperature increase is 2.143 °C/h. At 400 W/m², the surface

TABLE 6: Rates of the surface temperature increase of the test specimen at different powers.

Heating power (W/m ²)	Initial ambient temperature (°C)	Average temperature when heating for 1.83 h (°C)	Rate of temperature increase (°C/h)
260	-2.972	0.100	1.679
320	-2.913	0.872	2.068
400	-2.931	4.432	4.023

temperature of the specimen increases from -2.931°C to 4.432°C , and the rate of temperature increase is 4.023°C/h .

In summary, at heating powers of 260 W/m^2 and 320 W/m^2 , the rate of temperature increase is close and far less than the rate of temperature increase at 400 W/m^2 . Combining the snow-melting time and power consumption analyses at different powers shows that under the conditions of an initial ambient temperature of -3°C , a wind level of 0, and a snow thickness of 2 cm, to ensure that the snow on the road bridge surface melts quickly without inconveniencing travel, a heating power of 400 W/m^2 is selected to heat the road surface. At this time, the heating effect is the best, and it is economical and practical.

3.1.2. Environmental Temperature. The set working conditions are a heating power of 400 W/m^2 , Class 0 wind, and a snow thickness of 4 cm, and the influence of three different ambient temperatures of -3°C , -6°C , and -9°C on the time required for snow melting and power consumption are explored. The surface temperature change curve of the test specimens is shown in Figure 6.

Figure 6 shows that when the ambient temperature is -3°C and the heating time is 1.27 h, the surface temperature of the test specimen can reach 0°C ; at this time, the snow starts to melt. When heated for 2.93 h, the surface snow melts completely. At this time, the temperature is 4.89°C , and the total power consumption is 1.17 kW h/m^2 . When the ambient temperatures are -6°C and -9°C and the heating times exceed 2.13 h and 3.15 h, respectively, the surface temperature reaches above 0°C , and the snow begins to melt at this time. When heating for 4.27 h and 5.33 h, the surface snow melts completely. At this time, the temperatures are 4.68°C and 4.93°C , respectively, and the total power consumptions are 1.71 kW h/m^2 and 2.13 kW h/m^2 , respectively.

In the snow-melting tests at three different initial ambient temperatures, when the initial ambient temperature changes from -3°C to -6°C , the time to completely melt the snow will increase by 1.34 h, and the power consumption will increase by approximately 46.1% compared with that of the case of -3°C . When the initial ambient temperature changes from -3°C to -9°C , the time to completely melt the snow will increase by 2.40 h, and the power consumption will increase by 82.1% compared with that of the case of -3°C .

The rate of temperature increase of the specimen surface at different initial ambient temperatures is shown in Table 7. Comparing the rates of temperature increase under the three working conditions within 0~2.93 h shows that at an initial ambient temperature of -3°C , when the surface temperature of the test specimen increases from -3.130°C to 4.891°C , the rate of temperature increase is 2.738°C/h . At an initial

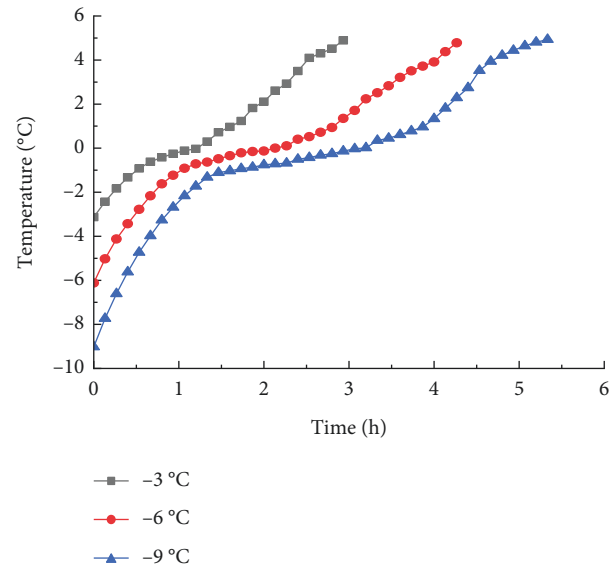


FIGURE 6: Temperature change curve of the surface of the test specimen at different ambient temperatures.

ambient temperature of -6°C , when the surface temperature of the specimen increases from -6.121°C to 1.352°C , the rate of temperature increase is 2.551°C/h . At an initial ambient temperature of -9°C , the surface temperature of the specimen increases from -9.023°C to -0.136°C , and the rate of temperature increase is 3.126°C/h .

In summary, at initial ambient temperatures of -3°C and -6°C , the rates of temperature increase are close to and less than the rate of temperature increase under the -9°C operating condition. Combining the snow-melting time and power consumption analyses at different initial ambient temperatures shows that as the initial ambient temperature decreases within a certain range while keeping the other factors constant, the time required for snow melting and the power consumption increase and the loss increases.

3.1.3. Snow Thickness. The working conditions are a heating power of 400 W/m^2 , Class 0 wind, and an ambient temperature of -3°C , and the effects of three different snow thicknesses of 2 cm, 4 cm, and 6 cm on the time required for snow melting and power consumption are explored. The curve of the surface temperature of the test specimens with different snow thicknesses is shown in Figure 7.

Figure 7 shows that when the thickness of the snow cover is 2 cm, the surface temperature of the test specimen reaches 0°C when heated for 0.49 h, and the snow starts to melt. When heated for 1.87 h, the surface snow melts completely. The hourly temperature is 4.432°C , and the total power

TABLE 7: Rates of the temperature increase of the specimen surface at different initial ambient temperatures.

Heating power (W/ m ²)	Initial ambient temperature (°C)	Average temperature when heating for 2.93 h (°C)	Rate of temperature increase (°C/h)
400	-3.130	4.891	2.738
	-6.121	1.352	2.551
	-9.023	-0.136	3.126

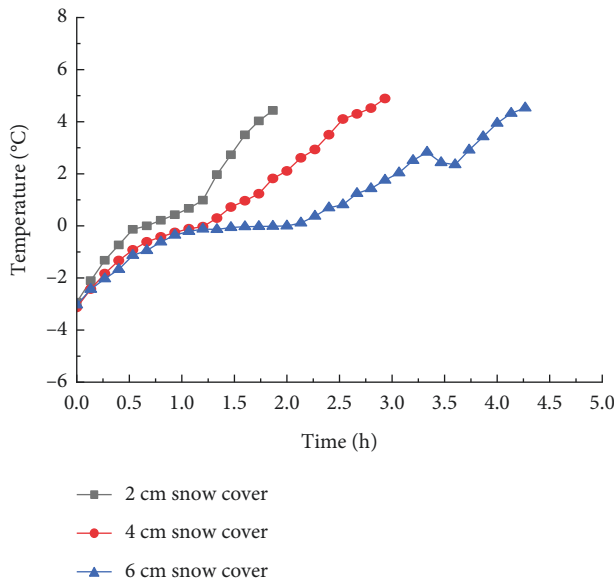


FIGURE 7: Curves of surface temperature changes of specimens with different snow thicknesses.

consumption is 0.73 kW h/m². When the snow thicknesses are 4 cm and 6 cm, the heating time exceeds 1.27 h. After 2.01 h, the surface temperature reaches above 0°C. Now, the snow begins to melt. When heating for 2.93 h and 4.27 h, the surface snow melts. At this time, the temperatures are 4.891 °C and 4.531 °C, and the total power consumptions are 0.17 kW h/m² and 1.71 kW h/m², respectively.

In the snow-melting tests with three different snow thicknesses, when the snow thickness is increased from 2 cm to 4 cm, the time for complete snow-melting increases by 1.06 h, and the power consumption increases by approximately 60.3% compared with that of the case where the snow thickness is 2 cm. When the snow thickness is increased from 2 cm to 6 cm, the time to completely melt the snow increases by 2.40 h, and the power consumption increases by 134.2% compared with that of the case where the snow thickness is 2 cm.

The rates of surface temperature increase of the test specimen with different snow thicknesses are shown in Table 8. Comparing the rates of temperature increase under the three working conditions within 0~1.87 h shows that when the snow thickness is 2 cm, the surface temperature of the test specimen changes from -2.931°C to 4.432°C, and the rate of temperature increase is 3.937 °C/h. When the snow thickness is 4 cm and the surface temperature of the specimen increases from -3.131°C to 1.821°C, the rate of temperature increase is 2.648 °C/h. When the snow thickness is 6 cm, the surface temperature of the specimen increases

from -3.031°C to -0.015°C, and the rate of temperature increase is 1.629 °C/h.

In summary, under certain conditions, as the thickness of the snow increases, the rate of temperature increase decreases. The analyses of snow-melting time and power consumption with different snow thicknesses show that other factors remain unchanged in specific actual projects. With the increase in snow thickness within a certain range, the time required to melt snow and the power consumption increase, and the power consumption is relatively large.

3.1.4. Wind Rating. The set working conditions are a heating power of 400 W/m², an ambient temperature of -3°C, and a snow thickness of 4 cm to explore three wind levels: class 0 (0 m/s), class 1 (1.35 m/s), and class 2 (2.74 m/s). The impact of different wind levels on the time required for snow melting and power consumption is investigated. The surface temperature change curve of the specimen is shown in Figure 8.

Figure 8 shows that when the wind power level is class 0 and the surface temperature of the specimen reaches 0°C when heated for 1.27 h, the snow begins to melt. When heated for 2.93 h, the surface snow is completely melted. The hourly temperature is 4.891°C, and the total power consumption is 1.17 kW h/m². When the wind power levels are level 1 and level 2, the surface temperature reaches above 0°C after the heating times exceed 1.49 h and 1.93 h, respectively, and the snow begins to melt. When heating for 3.47 h and 5.20 h, the surface snow melts. At this time, the temperatures are 4.502 °C and 4.835 °C and the total power consumptions are 1.39 kW h/m² and 2.08 kW h/m², respectively.

In the snow-melting test with three different wind levels, when the wind level changes from level 0 to level 1, the time to completely melt the snow increases by 0.54 h, and the power consumption increases by approximately 18.8% compared with that of the case where the wind level is level 0. When the level is changed from level 0 to level 2, the time to completely melt the snow will increase by 0.91 h, and the power consumption will increase by 77.8% compared with that of the case where the wind level is level 0.

The rate of temperature increase of the specimen surface at different wind levels is shown in Table 9. Comparing the rate of temperature increase under the three working conditions within 0~2.93 h shows that in the working condition with a wind power rating of 0, when the surface temperature of the specimen increases from -3.131°C to 4.891°C, the rate of temperature increase is 2.738 °C/h. In the working condition with a wind power level of 1, when the surface temperature of the test specimen increases from -3.021°C to 3.684°C, the rate of temperature increase is 2.288 °C/h. In the working condition with a wind power level of 2,

TABLE 8: Rates of the temperature increase of the specimen surface with different snow thicknesses.

Snow thickness (cm)	Initial ambient temperature (°C)	Average temperature when heating for 1.87 h (°C)	Rates of temperature increase (°C/h)
2	-2.931	4.432	3.937
4	-3.131	1.821	2.648
6	-3.031	-0.015	1.629

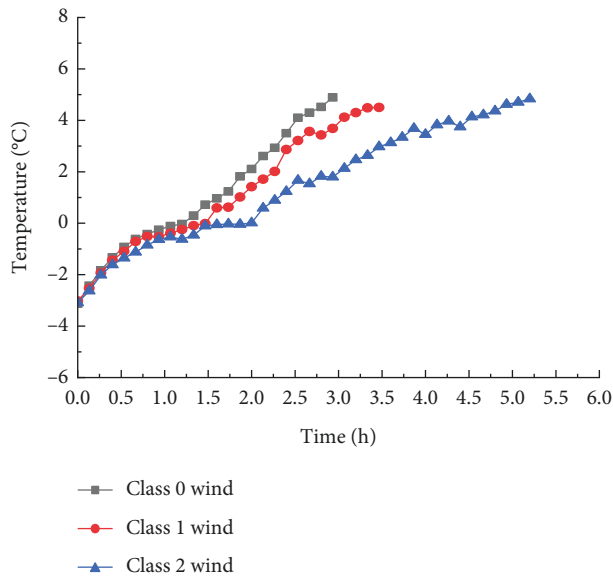


FIGURE 8: Curve of the surface temperature of the specimen with different wind levels.

when the surface temperature of the specimen increases from -3.094°C to 1.798°C , the rate of temperature increase is 1.670°C/h .

In summary, when keeping the other factors constant, as the wind level increases within a certain range, the uniformity of the overall temperature distribution on the surface of the specimen worsens, and the snow-melting time increases. In addition, the rate of temperature increase decreases. Therefore, when the wind speed is too high in actual engineering applications, the methods of manually or mechanically removing snow increase the rate of snow removal from bridge decks.

3.2. Research on Influencing Factors of the Deicing Test

3.2.1. Heating Power. The research method in this section is the same as the snow-melting process. Working conditions are set as an initial ambient temperature of -3°C , a wind power level of 0, and an ice thickness of 5 cm to explore the melting time and power consumption with three different heating powers of 260 W/m^2 , 320 W/m^2 , and 400 W/m^2 and deicing impact. The surface temperature change curve of the specimen at different powers is shown in Figure 9.

Figure 9 shows that when the heating power is 400 W/m^2 and the heating time is 0.67 h, the surface temperature of the test specimen can reach 0°C ; at this time, the ice layer begins to melt. When it is heated for 2.33 h, the surface ice layer is melted. At this time, the temperature is 3.32°C and the total

power consumption is 0.93 kW h/m^2 . When the heating powers are 320 W/m^2 and 260 W/m^2 , the surface temperature can reach 0°C after the heating times exceed 1.17 h and 2.01 h, respectively, and the ice begins to melt at this time. When heating for 3.83 h and 5.5 h, the surface ice layer melts. At this time, the temperatures are 3.14°C and 2.58°C and the total power consumptions are 1.23 kW h/m^2 and 1.43 kW h/m^2 , respectively.

In the ice-melting tests at the three powers, when the heating power is increased from 260 W/m^2 to 320 W/m^2 , the time for the complete melting of the ice layer is shortened by 1.67 h, and the power consumption is approximately 14.0% less than that in the case of 260 W/m^2 . When the heating power is increased from 260 W/m^2 to 400 W/m^2 , the time to completely melt the ice layer is shortened by 3.17 h, and the power consumption is reduced by 35.0% compared with that of the case of 260 W/m^2 .

The rate of temperature increase of the specimen surface at different powers is shown in Table 10. Comparing the rates of temperature increase under the three working conditions within 0~2.33 h shows that at 260 W/m^2 , when the surface temperature of the specimen increases from -2.931°C to 0.199°C , the rate of temperature increase is 1.357°C/h . At 320 W/m^2 , when the surface temperature of the specimen increases from -2.973°C to 1.134°C , the rate of temperature increase is 1.763°C/h . At 400 W/m^2 , the surface temperature of the specimen increases from -2.962°C to 3.321°C , and the rate of temperature increase is 2.683°C/h .

In summary, at heating powers of 260 W/m^2 and 320 W/m^2 , the rates of temperature increase are close to and less than the rate of temperature increase at 400 W/m^2 . Combining the ice-melting time and power consumption analyses at different powers shows that as the heating power increases within a certain range while keeping the other factors constant, the time required for ice melting and the power consumption are reduced. In addition, the heating effect is best at a heating power of 400 W/m^2 ; this condition is economical and practical, and deicing is more efficient.

3.2.2. Ice Thickness. The set working conditions are a heating power of 400 W/m^2 , Class 0 wind, and an ambient temperature of -3°C , and the effects of three different ice thicknesses of 5 mm, 10 mm, and 15 mm on the time required for ice melting and power consumption are explored. The surface temperature curve of the specimen with different ice layer thicknesses is shown in Figure 10.

Figure 10 shows that when the thickness of the ice layer is 5 mm and heating for 0.533 h, the surface temperature of the test specimen can reach 0°C ; at this time, the ice layer begins to melt. When it is heated for 2.27 h, the surface ice layer is

TABLE 9: Rate of the temperature increase of the specimen surface at different wind levels.

Wind rating	Initial ambient temperature (°C)	Average temperature after heating for 2.93 h (°C)	Rate of temperature increase (°C/h)
0	-3.131	4.891	2.738
1	-3.021	3.684	2.288
2	-3.094	1.798	1.670

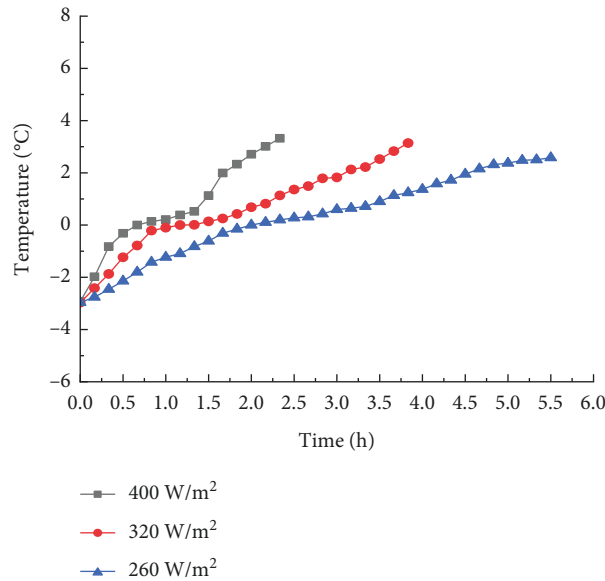


FIGURE 9: Curve of the surface temperature change of the test specimen at different powers.

TABLE 10: Rate of the surface temperature increase of the test specimen at different powers.

Heating power (W/m ²)	Initial ambient temperature (°C)	Average temperature when heating for 2.33 h (°C)	Rate of temperature increase (°C/h)
260	-2.931	0.199	1.357
320	-2.973	1.134	1.763
400	-2.962	3.321	2.683

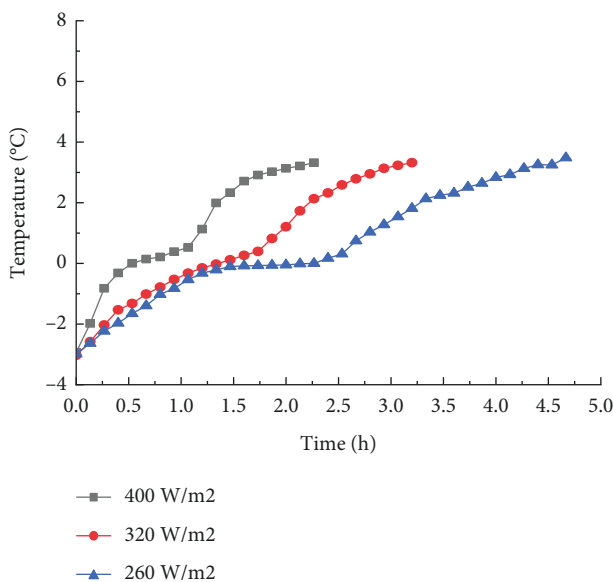


FIGURE 10: Temperature change curve of the specimen surface with different ice thicknesses.

completely melted. When the temperature is 3.32 °C, the total power consumption is 0.93 kW h/m². When the thicknesses of the ice layer are 10 mm and 15 mm and the heating times exceed 1.467 h and 2.267 h, respectively, the surface temperature can exceed 0 °C. Now, the ice begins to melt. When heating is continued for 3.21 h and 4.67 h, the surface ice layer melts. At this time, the temperatures are 3.322 °C and 3.482 °C, and the total power consumptions are 1.28 kW h/m² and 1.87 kW h/m², respectively.

In the three ice-melting tests with different ice thicknesses, when the thickness of the ice layer is increased from 5 mm to 10 mm, the complete melting time of the ice layer increases by 0.94 h, and the power consumption increases by approximately 37.6% compared with that of the case where the thickness of the ice layer is 5 mm. When the thickness of the ice layer is increased from 5 mm to 15 mm, the time for the ice layer to completely melt increases by 2.4 h, and the power consumption increases by 101.1% compared with that of the case where the ice layer thickness is 5 mm.

The rates of temperature increase of the specimen surface with different ice layer thicknesses are shown in Table 11. Comparing the rates of temperature increase under

TABLE 11: Rate of temperature increase of the specimen surface with different ice thicknesses.

Ice thickness (mm)	Initial ambient temperature (°C)	Average temperature when heating for 2.27 h (°C)	Rate of temperature increase (°C/h)
5	-2.931	3.321	2.754
10	-3.031	2.133	2.275
15	-2.983	0.001	1.315

the three working conditions within 0~2.27 h shows that when the ice layer thickness is 5 mm and the surface temperature of the specimen increases from -2.931°C to 3.321°C , the rate of temperature increase is 2.754°C/h . When the ice layer thickness is 10 mm and the surface temperature of the specimen increases from -3.031°C to 2.133°C , the rate of temperature increase is 2.275°C/h . When the ice layer thickness is 15 mm and the surface temperature of the specimen increases from -2.983°C to 0.001°C , the rate of temperature increase is 1.315°C/h .

In summary, under certain conditions, as the thickness of the ice layer increases, the rate of temperature increase decreases. The analyses of the snow-melting time and power consumption at different snow thicknesses show that as the thickness of the ice layer increases within a certain range while keeping the other factors constant, the time required for the ice layer to melt and the power consumption increase. The power loss is large.

4. Conclusion

In this paper, an experimental study on snow melting and ice melting has been carried out, and the main conclusions are as follows:

- (1) As the heating power increases within a certain range, the time required for the snow and ice layers to melt and the power consumption decrease. Under certain conditions, to ensure the rapid melting of snow and ice layers on the surface of road bridges, a heating power of 400 W/m^2 is selected. At this time, the heating effect is the best, and this method is economical and practical.
- (2) As the ambient temperature decreases or the thickness of the ice layer increases within a certain range while keeping the other factors constant, the time required for the snow to melt and the power consumption increase, and the power consumption is relatively large.
- (3) With the increase in the wind level within a certain range while keeping the other factors constant, the uniformity of the overall temperature distribution on the surface of the specimen worsens, the snow-melting time increases, and the temperature rises. The rate of temperature increase decreases. Therefore, in actual engineering applications, when the wind speed is too high, the methods of manually or mechanically removing snow can increase the snow removal rate on bridge decks. And it provides a theoretical reference for the actual construction of bridge decks in the future.

Data Availability

The data used to support the findings of this study are included in the article. Some or all data, models, or codes that support the findings of this study are available from the corresponding authors on request.

Conflicts of Interest

The authors declare no conflicts of interest.

Authors' Contributions

T.Y., H.X., and J.X. performed investigation and validation. Z.S. performed conceptualization, investigation, and formal analysis and wrote the original draft. All authors have read and agreed to the published version of the manuscript.

Acknowledgments

The authors acknowledge the support of the Hubei Province Technical Innovation Special Project (2018AAA028).

References

- [1] B. Guo, *Research on the Technology of Melting Snow and Ice on Asphalt concrete Bridge Deck with Embedded Carbon Fiber Heating Wire*, Henan University, Henan, China, 2018.
- [2] W. Zhu, F. Jun, G. Gao, and S. Jia, "The status quo and development trend of snow removal equipment," *Agricultural Equipment and Technology*, vol. 37, no. 4, pp. 22-25, 2011.
- [3] R. Wang, "Analysis of key points of expressway rapid snow removal and skid prevention construction," *Inner Mongolia Highway and Transportation*, vol. 38, no. 6, pp. 59-60, 2013.
- [4] Y. Tan, Y. Zhu, H. Xiao, and Q. Tang, "Model experimental study of carbon fiber heating wire for deicing and snow melting on a bridge deck," *Advances in Civil Engineering*, vol. 2020, pp. 1-15, 2020.
- [5] C. Cui, G. Jing, and T. Kang, "The application status and development trend of organic salt snow melting agent," *Chemical Industry Management*, vol. 33, no. 4, pp. 103-104, 2020.
- [6] Y. Shi and Y. Zhou, *Detailed Explanation of ABAQUS Finite Element Analysis Examples*, Machinery Industry Publishing, Beijing, China, 2006.
- [7] D. Chen, C. Qian, H. Wang, and J.-H. Liu, "Research on determination and calculation method of specific heat capacity of cement-based materials," *Journal of Building Materials*, vol. 10, no. 2, 2007.
- [8] F. Yang, *Technical Research on Carbon Fiber Heating Wire Used in Road Deicing and Snow Removal*, Chang'an University, Xi'an, China, 2014.
- [9] Y. Li, H. Wu, G. Wang, B. Zhu, and B. Shi, "Experimental research on heating cables used for melting snow and ice on

- road surface,” *Journal of Beijing University of Technology*, vol. 33, no. 3, pp. 217–222, 2006.
- [10] H. Zhao, Z. Wu, and G. Che, “Study on the spacing between carbon fiber heating wires arranged on the road surface to melt snow and ice,” *Concrete*, vol. 32, no. 3, pp. 142–144, 2010.
- [11] Y. Bu, C. Zhou, S. Wang, and J. Zhu, “Analysis of heat dissipation of carbon fiber heating bridge deck,” *China & Foreign Highway*, vol. 40, no. 5, pp. 311–315, 2020.
- [12] B. Bai, R. Zhou, G. Cai, W. Hu, and G. Yang, “Coupled thermo-hydro-mechanical mechanism in view of the soil particle rearrangement of granular thermodynamics,” *Computers and Geotechnics*, vol. 137, no. 8, 2021.
- [13] B. Bai, Q. Nie, Y. Zhang, X. Wang, and W. Hu, “Cotransport of heavy metals and SiO₂ particles at different temperatures by seepage,” *Journal of Hydrology*, vol. 597, Article ID 125771, 2021.
- [14] I. Gull and M. A. Tantray, “Dispersion of electrically conductive carbon fibres in self-compacting concrete using chemical and mechanical dispersing techniques,” *International Journal of Microstructure and Materials Properties*, vol. 15, no. 3, 2020.
- [15] Y. Christopher, “Tuan. Conductive concrete overlay for bridge deck deicing,” *Materials Journal*, vol. 96, no. 3, 1999.
- [16] C. Y. Tuan, D. Ferdon, and B. Chen, “Conductive concrete overlay for bridge deck deicing: mixture proportioning, optimization, and properties,” *Materials Journal*, vol. 97, no. 2, 2000.
- [17] A. Yehia and C. Y. Tuan, “Thin conductive concrete overlay for bridge deck deicing and anti-icing,” *Transportation Research Record*, vol. 1698, no. 1, 2000.
- [18] Y. Tuan, “Electrical resistance heating of conductive concrete containing steel fibers and shavings,” *Materials Journal*, vol. 101, no. 1, 2004.
- [19] E. Schlangen, M. van de Ven, G. van Bochove, and J. van Montfort, “Evaluation of the induction heating effect of porous asphalt concrete through four point bending fatigue test,” *Construction and Building Materials*, vol. 29, 2012.
- [20] E. Schlangen, Á García, and M. van de Ven, “Induction heating of electrically conductive porous asphalt concrete,” *Construction and Building Materials*, vol. 24, no. 7, 2009.
- [21] Á García, E. Schlangen, and M. van de Ven, “Induction heating of asphalt mastic and porous asphalt concrete,” *Construction and Building Materials*, vol. 25, no. 9, 2011.
- [22] A. G. Mohammed, G. Ozgur, and E. Sevkat, “Electrical resistance heating for deicing and snow melting applications: experimental study,” *Cold Regions Science and Technology*, vol. 160, pp. 128–138, 2019.
- [23] Y. Lai, Y. Liu, and D. Ma, “Automatically melting snow on airport cement concrete pavement with carbon fiber grille,” *Cold Regions Science and Technology*, vol. 103, pp. 57–62, 2014.
- [24] X. Su, Y. Lai, Y. Liu, D. Ma, P. Wang, and M. Guo, “Research of deicing and melting snow on airport asphalt pavement by carbon fiber heating wire,” *Advances in Materials Science and Engineering*, vol. 2020, pp. 1–6, 2020.
- [25] C. Li, W. Xu, Q. Li et al., “Experimental study on the temperature rise of continuous carbon fiber self-heating airport pavement,” *Fiberglass Composites*, vol. 42, no. 11, pp. 64–70, 2015.
- [26] R. Li, W. Chao, Y. Zhu, and Y. Yang, “Experimental research on melting snow and ice on bridge deck paving of carbon fiber heating wire,” *China & Foreign Highway*, vol. 39, no. 6, pp. 241–244, 2019.

Research Article

Geotechnical Characteristic Assessments of Floodplain Soils Using SCPTU Data in Nanjing, China

Mingfei Zhang,¹ Liyuan Tong^{2,3} and Qiang Wang⁴

¹Civil Engineering and Architecture Institute, Zhengzhou University of Aeronautics, Zhengzhou 450046, Henan, China

²Institute of Geotechnical Engineering, Southeast University, Nanjing 210096, China

³Jiangsu Key Laboratory of Urban Underground Engineering and Environmental Safety, Nanjing 211189, China

⁴School of Civil Engineering and Architecture, Anhui University of Science and Technology, Huainan 232001, Anhui, China

Correspondence should be addressed to Liyuan Tong; 101010519@seu.edu.cn

Received 19 February 2022; Accepted 14 March 2022; Published 22 April 2022

Academic Editor: Xianze Cui

Copyright © 2022 Mingfei Zhang et al. This is an open access article distributed under the Creative Commons Attribution License, which permits unrestricted use, distribution, and reproduction in any medium, provided the original work is properly cited.

In order to improve the understanding of such floodplain sediments and determining the validity of the tests, an extensive series of multifunctional seismic piezocone tests with pore pressure dissipation phase have been performed and supplemented with conventional borings, standard penetration, laboratory testing, and so forth. Sounding results from SCPTU were used to determine the stratigraphic profiles and the soil characteristics of two anchorage sites. A comparison of the boring and laboratory results with the CPTU profiles showed that the CPTU provided excellent information on soil stratigraphy and good guidance for determination of behavior and engineering implications of recent Yangtze River floodplain. At an area where local correlations based on modern SCPTU do not exist, methods for estimating coefficient of earth pressure at rest (K_0), hydraulic permeability (k_h), and equivalent stiffness (G_0) associated with bridge foundation design are presented, compared, and verified. Results also illustrate the complexity and variability of the floodplain stratigraphy and soil properties, which means that the suggestions in this study should be updated when more local experience is obtained. This case study suggests that such enhanced seismic piezocone test should be considered as a potential tool and the instrument of first choice in site characterization programs for design of bridges founded on complicated soils in China.

1. Introduction

As representative of the most dynamic region economically in China, Nanjing city is located on the alluvial and diluvial floodplain of the Yangtze River Delta. In the past and at the expected time of the following five to ten years, 16 cross-river passageways including bridges and tunnels were (or are being) constructed in the top shallow recent floodplain sediments, as illustrated in Figure 1. Undoubtedly, site characterization of recent floodplain soils is the first and the most significant. However, the variation of the palaeoclimate influenced the evolution of the lower reaches of the Yangtze River Delta and resulted in a very complicated sedimentary environment. The Quaternary deposit is composed of an alternated multi-sandy-clayey soil; in particular, intermediate soil (silt mixtures and sand mixtures) is widespread. In

such situations, it is often difficult to accurately define a complete soil profile and determine soil characteristics including strength, deformation, stress history, flow, and consolidation by using conventional boring methods supplemented by a few laboratory tests.

Construction experience in this area in the last two decades, such as the deep excavation of previously built bridges foundations, subway lines and tunnels under rivers, and retaining walls, shows that the following geohazards occurred or possibly occur during the construction and maintenance of infrastructures: (i) accidents associated with deep excavation, including slope sliding and collapse, quicksand and piping hazards, as well as water seepage through bracing of foundation pit; (ii) pumping induced hazards to surrounding environment, including land subsidence, settlement and cracking of pipeline, and differential

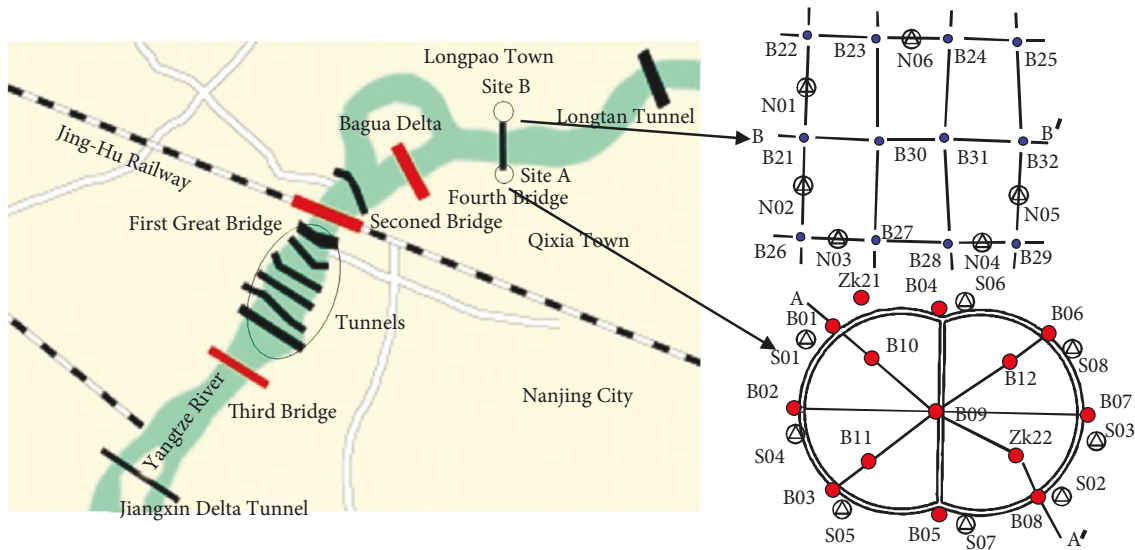


FIGURE 1: Layout of existing bridges and new alignments crossing the Yangtze River and location of the study area.

consolidation settlement of soft soil; (iii) long-term settlement due to the seasonal fluctuation of groundwater level; and (iv) liquefaction potential of sandy clay and silts during earthquake. The planned Nanjing Fourth Bridge will also face the abovementioned threats during construction, and a limited subsurface exploration was performed in 2007 and 2008 to study bridge alignment for the preliminary design. The exploration programs have included a mix of soil test boring, “undisturbed” sampling, standard penetration test (SPT), predrilled pressuremeter tests (PMT), downhole shear wave testing, and laboratory testing. In reality, it is quite unrealistic and inappropriate to rely solely on soil test boring, a single N -value, and a few laboratory tests due to a number of difficulties recognized with routine drilling practices in obtaining field test values, drive samples, and undisturbed samples [1].

As a complement or alternative measure to soil boring with SPT N -values and laboratory tests, seismic piezocone penetration tests with dissipation phases are particularly useful for geotechnical site investigation as they can provide approximately continuous simultaneous measurements of tip resistance (q_t), sleeve friction (f_s), and pore pressure, as well as shear wave velocity [2]. The piezocone method is gaining popularity in the Euro-American countries. It has not been, however, much used in China during the past few decades due to the lack of equipment and corresponding application study [3–6].

First, this paper reviews the state of the art of piezocone tests in China and their further development briefly. Then, we study the behavior and engineering implications of the floodplain soil in the Nanjing Fourth Bridge site, concerned by the geoengineers and designers in the case of deep excavation, by using seismic piezocone tests. The primary objective of the research was to compare the results of soil parameters from laboratory tests and in situ tests, with emphasis on SCPTU. Specific comparisons presented here are for results from permeability tests, CPTU profiles, and other in situ or laboratory tests. Geotechnical design

parameters obtained from CPTU and dissipation tests are also evaluated in this area through the existing methods. At last, the paper presents an assessment of the applicability of SCPTU tests to interpret the engineering properties of the Yangtze River floodplain sediments and concludes with recommendations for use of the SCPTU for foundation design of bridge in this floodplain.

2. The State of the Art of Piezocone Tests in China and Their Common Problems

As described by literature [3, 4], the cone penetration test without pore pressure measurement is widely used for site investigations in China, which can provide two measurements, q_c and f_s , or just one measurement, p_s . Comparatively, the piezocone tests with dissipation phases can provide four independent readings with depth from a single sounding, as well as time-rate information [7]. Of particular note is the seismic piezocone penetrometer test (SCPTU), which is a hybrid field method, combining the virtues of the CPT with downhole geophysics [8]. With the measurements of q_b , f_s , u_2 , shear wave (V_s), and dissipation processes taken together, an entire stress-strain-strength-flow representation can be derived for all depths in the soil profile [9]. The main advantages of the piezocone tests over the conventional Chinese CPT include the following: (i) calibrating measured data to describe soil characteristics accurately; (ii) evaluating soil flow and consolidation characteristics; (iii) distinguishing between drained, undrained, and partially drained strength; and (iv) improving the reliability of soil profiling and classification.

Due to these advantages, the Holland CPTU was introduced into China in the early 1980s. Several research projects on CPTU were performed at Shanghai-Nanjing highway and Zhujiang Delta area [10, 11]. Similar probe cones were produced by Nanjing Hydraulic Research Institute and other research institutes. However, compared with western countries, the reliability and repeatability of the

Chinese piezocone have always been questionable. In particular, the methodologies, digital and multifunctional sensor technology, and application range in China are considerably lagging. For instance, SeisCPT, ResisCPT, and other derivatives were quickly becoming popular in western countries, while their application is very limited in China. During the recent five years, several research institutes in China, including Southeast University, Hohai University, and Tongji University, have introduced the latest equipment from Europe and the United States, for example, the Vertek-Hogentogler CPTU system, which is also used in this study, and the Geotech AB cordless CPT system. The relevant research is now conducted step by step in China, which will be very useful for optimizing the engineering design and enhancing international communication. Furthermore, the CPTU data require a good estimate of correlation coefficients to determine soil parameters, which depend on the geologic formation and can be site-specific. The database of piezocone tests in China is very important for the validation of existing CPTU-based methods.

3. Database

3.1. Project Details and Description of Site. The Nanjing Fourth Bridge will be constructed in the following three to five years, which will be a three-span suspension bridge. The project site is approximately 20.5 km north to the Nanjing Great Bridge between the towns of Longpao and Qixia, where the north and south cable anchorages will be constructed, respectively, as shown in Figure 1. Several underwater tunnels are also considered for connecting the two sides of the Yangtze River. The south anchorage (referred to as Site A) lies in the south bank of the Yangtze River, 150 m to the Yangtze River embankment. The diaphragm wall has been designed as the bracing structure in the case of deep excavation, with the shape of ∞ (82×59 m), the height range from 40 to 50 meters, and the thickness of 1.5 m. Oppositely, the north anchorage (referred to as Site B) is located on the north bank of the river, 90 m to the north embankment, with the shape of rectangle (60×59 m). The open caisson foundation is selected, with the height of approximately 55 m.

3.2. Regional Geology Outline and General Surface Conditions. The project area belongs to the floodplain of lower reaches of the Yangtze River. The ground surface is flat, with a mean elevation of 3 to 5 m and a general inclination from west to east. The ground water level is found at 0.85 to 1.35 m, fluctuated with tidal motion and seasonal variation. The geological sketch is marked by alluvial, diluvial, silted, and lacustrine deposits of the Yangtze River Delta. The Quaternary deposits, which range from Late Pleistocene to Holocene, primarily consist of alternating clay to silty clay, slits and sands, and gravel. Due to the varying depositional mechanisms and environments, the stratigraphy is always complex with silt mixtures and sand mixtures widespread. The thickness of Quaternary deposits varies greatly from less than 10 meters to more than tens of meters. The underlying

bedrock is primarily formed by Cretaceous sandstone and conglomerate. Occasionally, the soft mudstone and muddy siltstone are interbedded. The deepest depth to bedrock surface underlies the Quaternary deposits at a depth of 34 to 65 m below ground surface.

In a typical vertical profile of the Quaternary sediments in this project region, a dual structure can be identified, the top of which is hydrostatic deposition and the lower part is alluvial, deluvial, and lacustrine deposition, except the top soil formed by arable land or backfilling of only 0.5~1.5 m in thickness. From the top layer down, the grain size in sedimentation becomes coarser, and the deposit changes in sequence of silty clay, mucky silty clay, silt mixtures, sand mixtures, and gravel. Due to the fact that the recent floodplain deposits are characterized by high water content, high void ratio, high compressibility, and low shear strength, as well as low hydraulic permeability clayey soil or complicated intermediate soil (silty mixtures and sandy mixtures), construction experiences from the existing projects show that the shallow recent floodplain soft soil will influence the construction of subgrade and piles, especially in the deep excavation.

3.3. In Situ Testing and Subsurface Investigation Program. As part of the major projects in Nanjing, a detailed site characterization study was carried out at the two anchorage sites in the Yangtze River Delta. One of the sites is near Longpao town and the other is near Qixia town. The total geotechnical investigation program completed in 2007 and 2008 consisted of a combination of laboratory and in situ tests, including 21 borings, various conventional laboratory testings, 8 downhole shear wave testings, 4 predrilled pressuremeter tests, and 14 seismic CPTU. Of particular interests are the piezocone tests designed to deliver more detailed information about the stratigraphy and properties of the soils found on site, taking advantage of the investigations conducted previously and adjacently. It is hoped that a by-product of this tentative research will be development of greater confidence in the CPTU as a site investigation tool in China. The CPTU can be used economically in partnership with other in situ testing methods or laboratory tests, as well as in the establishment of a database of in situ soil parameters for the optimization of bridge foundation design. Furthermore, a comparison is made between the interpreted soil parameters from CPTU and those obtained from laboratory tests and other in situ tests, primarily focusing on the K_0 and the coefficient of the permeability. The data obtained will be also used further for calibration and comparison.

Laboratory testing mainly included moisture content, particle size distribution, Atterberg limits, unit weight, one-dimensional consolidation, direct simple shear, consolidation quick direct shear, undrained triaxial tests, and falling head permeability test. All the laboratory tests were performed in general accordance with the Chinese Code for Investigation of Geotechnical Engineering [12] and the Chinese Standard for Soil Test Method [13], which are compatible with ASTM standards.

As mentioned above, a classical type-2 CPTU device (15 t cone), with a penetration speed of 2 cm/s and readings every 5 cm, was employed in this study, which is produced by Vertek-Hogentogler Co. of USA. The equipment is a versatile piezocone system equipped with advanced digital cone penetrometers fitted with 60° tapered and 10 cm² tip area cones, which can provide measurements of five independent readings: tip resistance (q_t), sleeve friction (f_s), penetration pore-water pressures (shoulder u_2), vertical inclination with depth, and downhole shear wave velocity (V_s), which is recorded at 1 m deep intervals during the pause of connecting the rod. Particularly important in piezocone tests, pore pressure dissipation tests can be performed in steady-state in situ conditions at specific depths during a pause following one sounding, yield information about the coefficient of consolidation and permeability of a soil deposit. Note that, to have a good pore pressure response during piezocone penetration, a rigid procedure to assemble and saturate the piezocone system presented by Lunne et al. [14] is employed.

A series of six seismic CPTU were carried out around Site B adjacent to the borings. The investigated depth was generally ranging from 35 to 40 m. Eight other seismic CPTU tests were performed at Site A with depths up to 40 m below ground surface. The test locations were also planned around the designed diaphragm walls.

4. Interpretation and Evaluation of Piezocone Results

4.1. Soil Delineating and Profiling. Based on the boring logs and indoor experiment, summary plots of index parameters are shown in Figure 2, including natural water content, plastic limit, liquid limit, percent fines, as well as the N_{60} value. The profiles of Overconsolidation Ratio (OCR) results obtained from laboratory odometer tests indicate that such floodplain sediments are under normally consolidated to slightly overconsolidated condition throughout the profiles. The overconsolidated state at shallow depths in Site A, where the OCR ranges from 3 to 7, was believed to be caused by man-made construction activities. At great depths, it is likely that the slightly overconsolidated state is caused by a combination effect of aging and removal of overburden.

At Site A, four obvious geotechnical-stratigraphic units are identified based on changes in N_{60} and other laboratory indexes, named ①, ②, ④, and ⑦ from top to bottom, and subdivided using Arabic numbers. The uppermost Holocene sediments of unit ① mainly consist of 5.3 to 11.7 m of silty clay and mucky silty clay, followed by interbedded silty sand and silty clay with depth of 19.9~56.6 m; note that lenses of fine sand can be detected somewhere. The sediments of following unit ②, which is also of Holocene age, are silty sand and silty clay with varying thickness (9.9~30.4 m), which occur interbedded or with a diffuse horizontal lamination of silt or coarse sand and gravel. The next unit ④ of Late Pleistocene age mainly consists of silty sand, gravel, and silty clay with thickness from 6 to 14.8 m; lenses of fine sand may also occur somewhere. Of particular concern is the fact

that unit ④ is discontinuous; in particular, the gravel and silty clay are always missing. The underlying stratum is bedrock unit ⑦ of Cretaceous age formed by sandstone, glutenite, and conglomerate which is partially penetrating.

At Site B, the general architecture of the floodplain consists of four lithological units, which from top to bottom are as follows: (i) an uppermost unit of silty clay and muddy silty clay underlain by silty sand with thickness of 14.8~29.5 m, with a silt interlayer also detected in the mucky silty clay layer; (ii) fine sand with lenses of medium sand forming a lower aquifer, usually massive with thickness of 23.9~34 m, with little obvious stratification; (iii) late Pleistocene alluvial deposits made of fine sand angle gravel; and (iv) a lower unit made of Cretaceous siltite.

From the boring logs, the most prominent feature of the profiles is the significant stratigraphic variations due to depositional environment fluctuation, whereas the deposit of Site B is seemingly more simple and consistent than that of Site A. The general architecture frame has been characterized as inhomogeneous bodies with highly interbedded layers of clays, sands, silt mixtures, and sand mixtures. Proper characterization of layered soils, such as layer clay, is important for assessment of anisotropic soil behavior as well as for studying paleoclimatic history.

However, the above-mentioned deposit sequences were mainly identified by visual description of boring logs simply supplemented by limited laboratory tests. For sands/silts or transitional soils (sand mixtures and silt mixtures), limited boring numbers, low sampling rate, unclear soil interface, and thin layering may result in erroneous judgment or loss of important information about the stratigraphy, for example, location of critical layers or soft zones and subtle changes within a deposit. Of particular note is the fact that highly stratified deposits may include small seams, laminations, lenses, and intrusions, each having significant implications on engineering behavior and design, which also result in the complexity. At the same time, subject to the limited budgets of the exploration program, the increase of boring number and continuous core sampling are always unrealistic. So, as a quick, expedient, and economical way, the versatile seismic piezocone tests with dissipation phases offer an optimal complement or alternate for improved site stratigraphy and layer characterization, which are continuous or at least near-continuous soil profiling techniques to delineate subsurface stratigraphy and soil properties.

Representative sets of readings from seismic piezocone tests taken at the two sites are presented in Figure 3. The superpositions of q_t , f_s , and u_2 diagrams for Site A show very poor repeatability in the record data. The results for q_t , f_s , and u_2 display significant variation at most depths. Definitely, highly variations of q_t and f_s are attributed to the highly interbedded deposits, which agree well with the testing boring logs. The frequent spikes in the tip resistance and drops in the pore water pressure show that silty sand or silt seams occur within the silty clay layers. Meanwhile, the highly excess pore water pressure response, strongly influenced by the thin layers, indicates that thin clay layers or silty layers are encountered within silty sand or silt clays. These permeable or impermeable intralayers or small interface

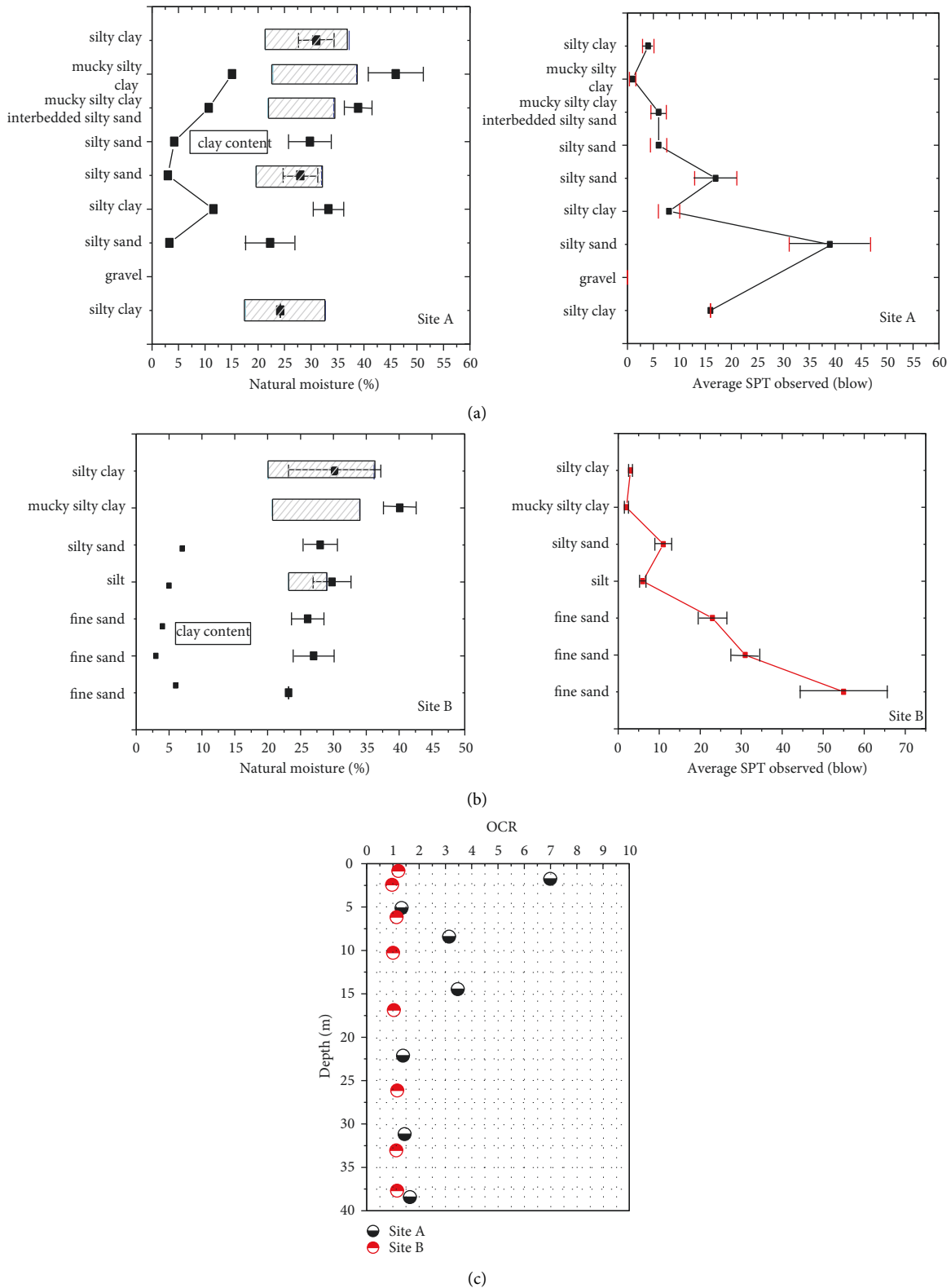
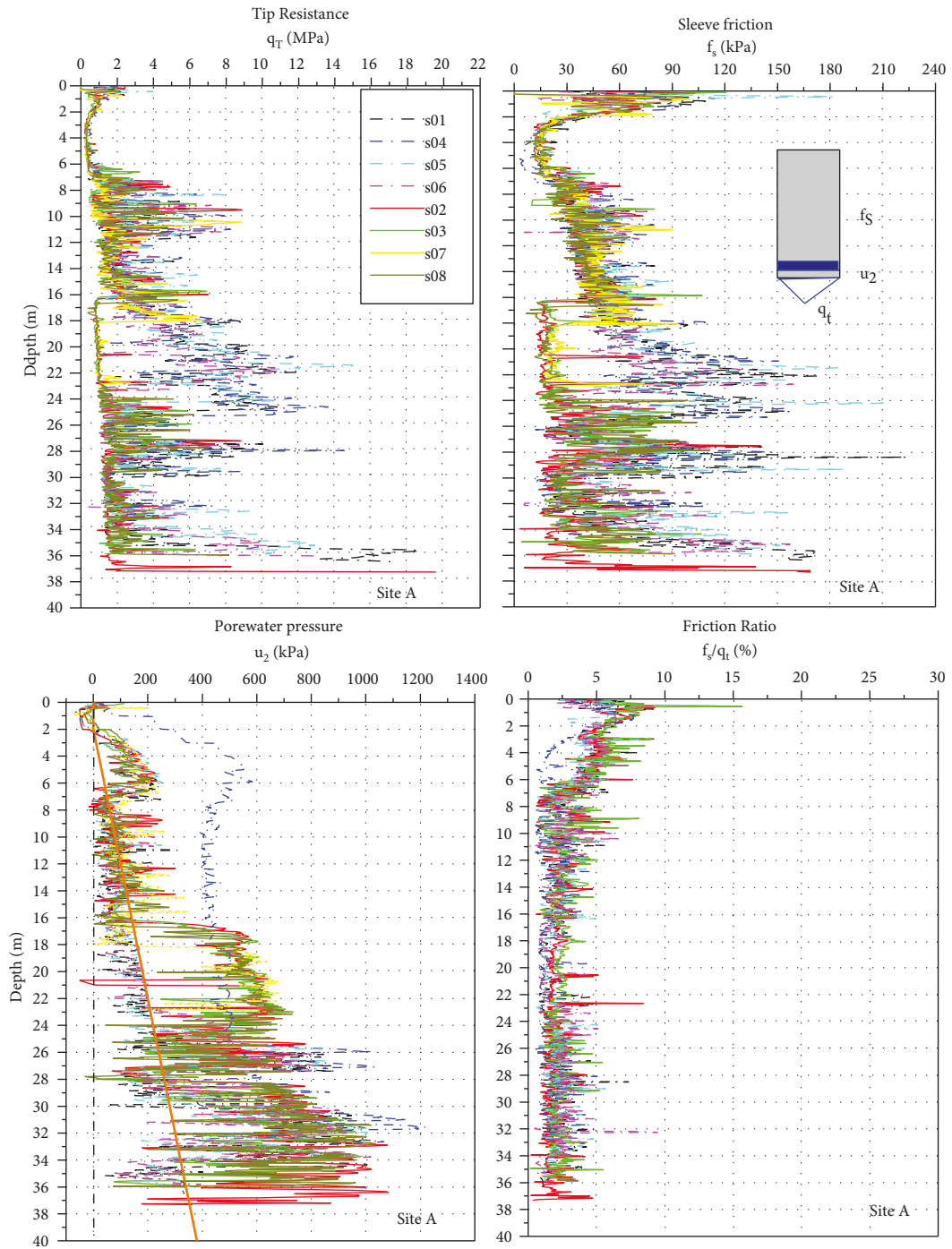


FIGURE 2: Summary of soil indexes. (a) Average index properties: natural water content, void ratio, Atterberg limits, and percent fines content; (b) average SPT observed; (c) overconsolidation ratio.

changes are always not represented by the discrete SPT test N_{60} values as illustrated in Figure 2 or overlooked on the portion of boring logs. However, detection of stratigraphic

interfaces and thin layers can be critical to the construction for these interfaces or weak layers, if sufficiently numerous, continuous, and permeable (or impermeable), may promote



(a)

FIGURE 3: Continued.

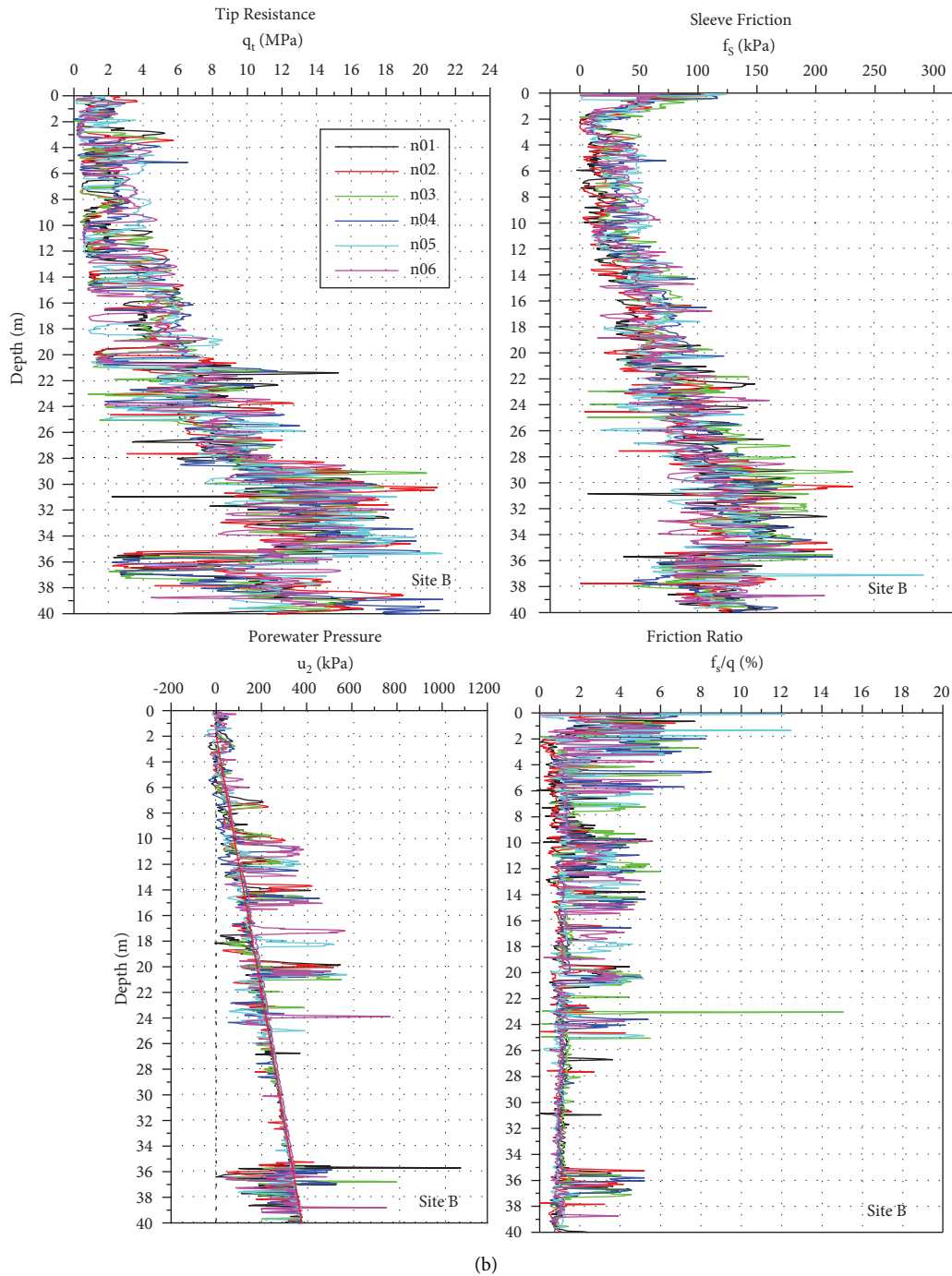


FIGURE 3: Series of piezocone penetration tests at the two sites.

anisotropic soil properties or alter groundwater flow regimes, then resulting in accidents, for example, increasing the likelihood of slope failure in the case of deep excavation, hinder or accelerate rates of consolidation, and so forth.

We also notice that the responses of q_b , f_s , and u_2 appear to be consistent except at the depth from 16 to 22 m. Close examination of the distribution of CPTU holes highlights that the recordings of four CPT holes, s02, s03, s07, and s08 (referred to as Series-1), are similar, which is different from another series of CPT holes, s01, s04, s05, and s06 (referred to as Series-2). The

explanation is evident when compared with the cross section obtained from boring logs. The encounter of silty clay at the corresponding depth of Series-1 results in the decrease of tip resistance and large pore water pressure response, while Series-2 reflects the existence of silty sand at the same depth. Of particular note is the abnormal pore water pressure response of s04 caused by malfunction of pore water element when conducting a special resistivity piezocone testing, not discussed in this paper. As representative of Series-1, s03 is selected to conduct soil classification illustratively using the soil classification chart

proposed by Robertson et al. [15]. The soil types in Figure 4 predict that, below the depth of about 6 m, many thinly intralayers are identified, supporting the sediment logical variations.

It can be seen that the deposit at Site B is a relatively simple deposit. The repeatability and consistency of recording data are acceptably good, which is also in accordance with boring logs. The prominent feature of Site B is silty sand and fine sand constituted the main soil layer below the depth of about 12 m, overlain (mucky) silty clay interbedded with silt. However, within the silty sand layer or fine sand layer, the low permeability silty clay layers are often encountered as shown in Figure 5, especially at elevations between 12 and 25 m approximately. Even at the top of the site (0~12 m), the thickness of clayey soil (mainly silty clay) at Site B is far less than that at Site A. By contrast, the silty clay layers become weak, thin layers which may be more compressible than nearby materials, often resulting in more differential settlement or uncertain slope failure, of particular interest to geoengineering agencies and companies. The overall pore water pressure response of Site B is very different from that of Site A, the overall trend of which is nearly close to hydrostatic pore water pressure except encountering thin clayey layers. Comparatively, the potential problems associated with the sediments at Site B mainly consist of quick sand, piping, collapse, and water intruding.

It is shown that using the piezocone with multiple soundings as a supplement to borings significantly improved the precision and accuracy of the anchorage sites delineation for the Nanjing Fourth Bridge project, especially detection of small interface changes and thin permeable or impermeable layers. Moreover, for the Yangtze River floodplain, with seasonally depositional environment, the pore water pressure measurements show particular advantages compared to the conventional boring and the Chinese CPT (generally without pore pressure measurement) in detecting local variations at the small scale of a few centimeters, for example, thin sandy seams within silty clays or thin clayey layers within sandy layers, which is also demonstrated by other literatures [16–18]. The obvious benefit of more reliable knowledge on soil stratigraphy and layer characterization, including the existence, thickness, and composition of floodplain deposits, obtained from boring tests supplemented by piezocone tests, is that such detailedly improved investigations will enable more cost-efficient management of construction processes.

4.2. Coefficient of Earth Pressure at Rest (K_0). In situ horizontal stress, σ'_{ho} , and the coefficient of lateral stress at rest, K_0 , are important parameters, both for use in design and as an intermediate parameter in interpretation of CPT results [14]. However, there are presently no reliable methods of determining K_0 from either lab or field tests in fine-grained soils or sandy soils [14].

Many methods have been proposed for estimation of K_0 from CPTU data [14, 19, 20]. Most methods are based either on the OCR or directly on the piezocone measurements. According to different soil types, silty clay, or silty sands, the following methods were selected in this study to predict K_0 from CPTU data. These methods are summarized as below.

Schmertmann [21] suggested estimating K_0 based on the OCR as follows: firstly, from CPTU data either estimate S_u and then S_u/σ'_{v0} or estimate OCR; then use the plasticity index and S_u/σ'_{v0} or OCR estimate K_0 from a correlation chart [22] in fine-grained soils or using the following equation:

$$K_0 = (1 - \sin \phi') OCR^{\sin \phi'} \quad (1)$$

Kulhawy and Mayne [23] related K_0 with the normalized net cone resistance $(q_t - \sigma_{v0})'/\sigma'_{v0}$ and suggested the following equation:

$$K_0 = k \left(\frac{q_T - \sigma_{v0}}{\sigma'_{v0}} \right) \quad (2)$$

With $k = 0.1$, which is used for uncemented, unaged, and mechanically overconsolidated fine grained soils, the value of k may be soil type and site dependent.

If it is possible to assess OCR from geological evidence or from neighboring clay layers, then K_0 may be derived from the following empirical correlation [24]:

$$\frac{K_{0(oc)}}{K_{0(nc)}} = OCR^m, \quad (3)$$

where $K_0(nc)$ corresponds to the NC horizontal stress coefficient. For clays, $K_{0(nc)} = 1 - \sin \phi'$; for sands, $K_{0(nc)} = 0.95 - \sin \phi'$; ϕ' is the effective stress friction angle. Lunne and Christophersen [24] recommended $m = 0.45$. However, Mayne and Kulhawy [25] recommended $m = 0.65$. Moreover, Mayne [26] tentatively suggested the following formula for practical use in coarse-grained soils:

$$K_0 = 0.35 OCR^{0.65} \quad (4)$$

Using a large database ($n = 590$) compiled from 26 separate series of calibration chamber tests, Mayne [9] suggested the following simplified regression equation for NC and OC sands ($r^2 = 0.871$):

$$K_0 = 1.33 (q_T)^{0.22} (\sigma'_{v0})^{-0.31} OCR^{0.27}, \quad (5)$$

where q_t is in MPa and σ_{v0} is in kPa. It should be noted that the formulation applies only to unaged and uncemented quartzitic sands and has been verified by a limited number of field test sites [27].

For mixed soils (sands, silts, and clays), when $0.1 < B_q < 1.0$ and with a range of $20^\circ < \phi' < 45^\circ$, an approximate form for effective stress friction angle from NTNU method is given [28] by

$$\phi' (\text{deg}) = 29.5^0 B_q^{0.121} [0.256 + 0.336 B_q + \log Q], \quad (6)$$

where B_q is pore pressure parameter $(= (u_2 - u_0)/(q_t - \sigma_{v0}))$ and Q is normalized cone resistance $= (q_t - \sigma_{v0})'/\sigma'_{v0}$.

Additionally, for $B_q < 0.1$ corresponding to granular soils, the following expression for clean sands would apply [23]:

$$\phi' (\text{deg}) = 17.6 + 11.0 \cdot \log \left[\frac{q_T}{\sqrt{\sigma_{v0}/\sigma_{\text{atm}}}} \right] \quad (7)$$

Then equation (1) is used to estimate K_0 .

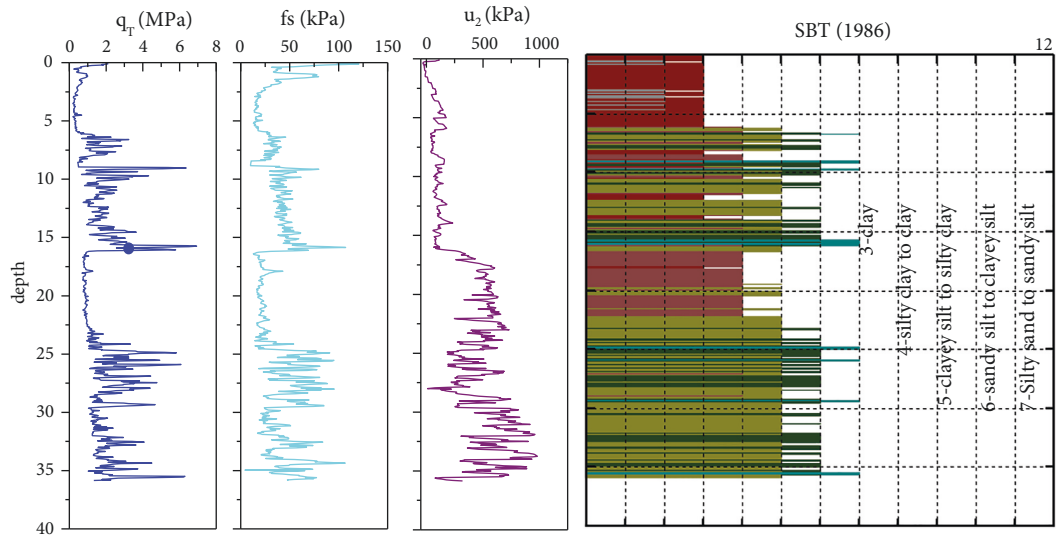


FIGURE 4: Illustrative profile of soil classification of s05 using Robertson et al.'s method [15].

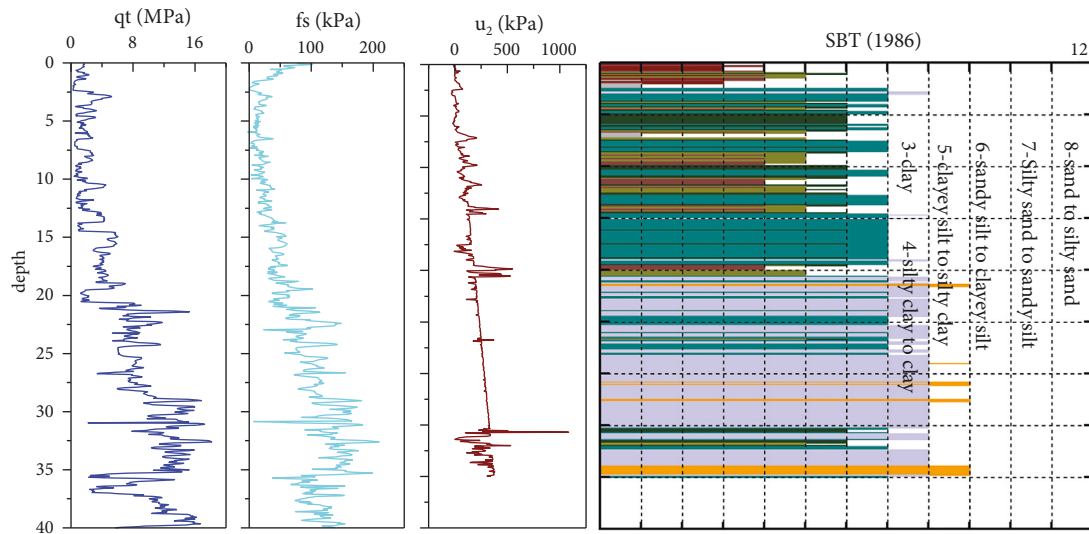


FIGURE 5: Typical results showing soil types of N01 at Site B.

In this study, the aforementioned methods were evaluated for their capability to reasonably predict K_0 utilizing the piezocone data. These methods are referred to as the Andersen and Kolstad [22] method, the Kulhawy and Mayne [23] method, the Mayne and Kulhawy [25] method, the Mayne [9] method, and the NTNU method [28] method. It should be noted that these methods are applied to different soil types, the first two are both used for fine-grained soils, the next two are used for coarse-grained soils, and the last one is used for mixed soil types. The predicted K_0 s were then compared with the measured K_0 s obtained from the predrilled pressuremeter tests at the same sites. Figures 5(a)–(c) present this comparison for different methods. The soil profiling was accepted as given in the case records.

Based on the results of this analysis, the overall performance of these CPTU-based methods was then examined. Taking the PMT measured K_0 as the actual reference

values, it is indicated clearly that the overall reasonable trends are observed although considerable scatter exists between all the selected prediction methods. Again, Figure 6 shows that at Site A all the prediction methods tend to overestimate the measured K_0 , while at site B all the prediction methods tend to slightly underestimate the measured K_0 . In general, at Site A, the selected methods exhibit a higher dispersion than that at Site B due to the more highly stratified and layered nature of the deposit. Moreover, for intermediate soils (silty clay, silty sands, and silts), the variable estimated K_0 values show more uncertainty than those for relatively homogeneous sands, except for some of data points in Figure 6(c). For fine-grained soils (silty clay or mucky silty clay), the estimated K_0 values from the Andersen and Kolstad [22] method and the NTNU method [28] method are more close to the reference values from PMT tests compared to those from the Kulhawy and Mayne [23]

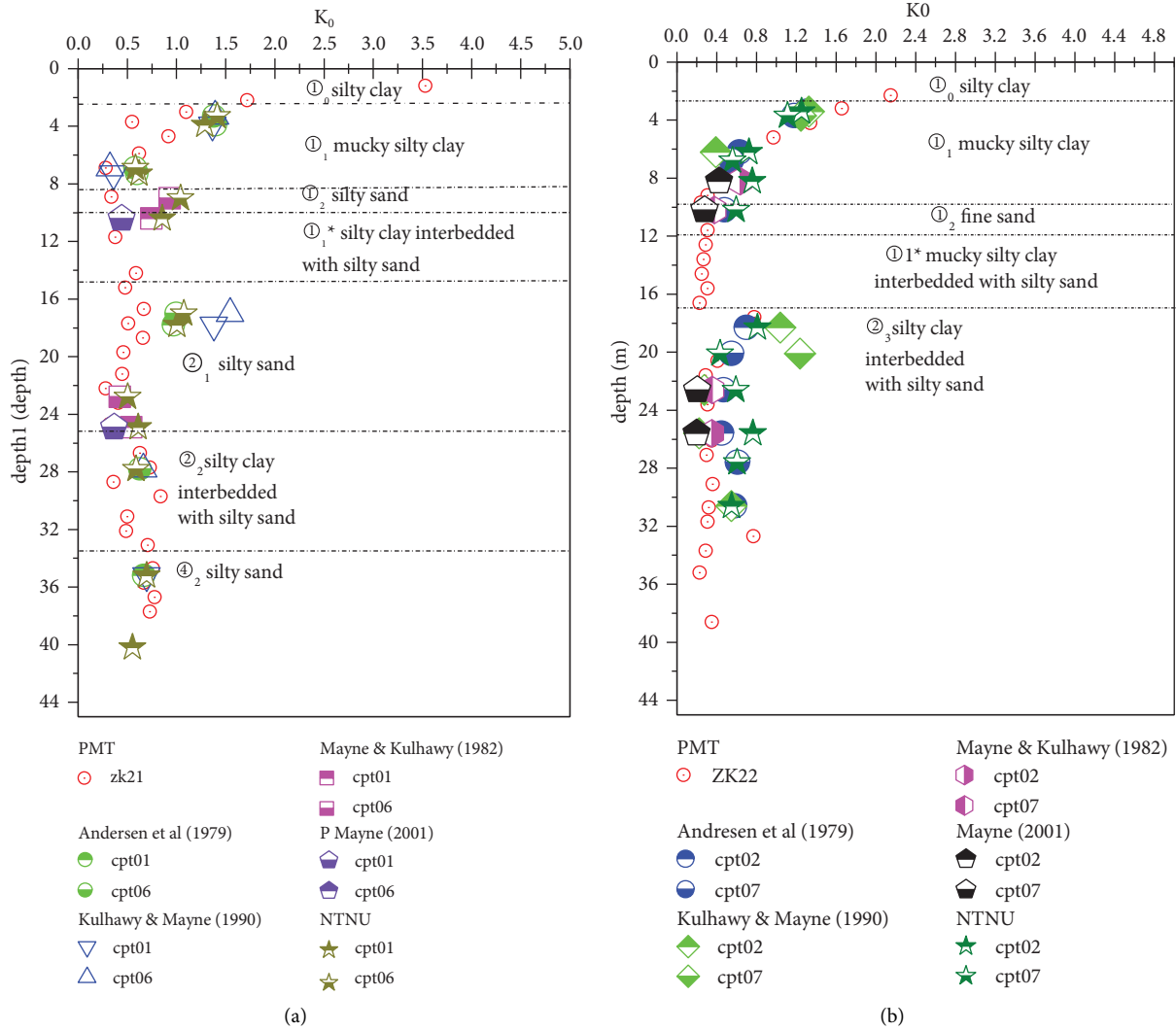


FIGURE 6: Continued.

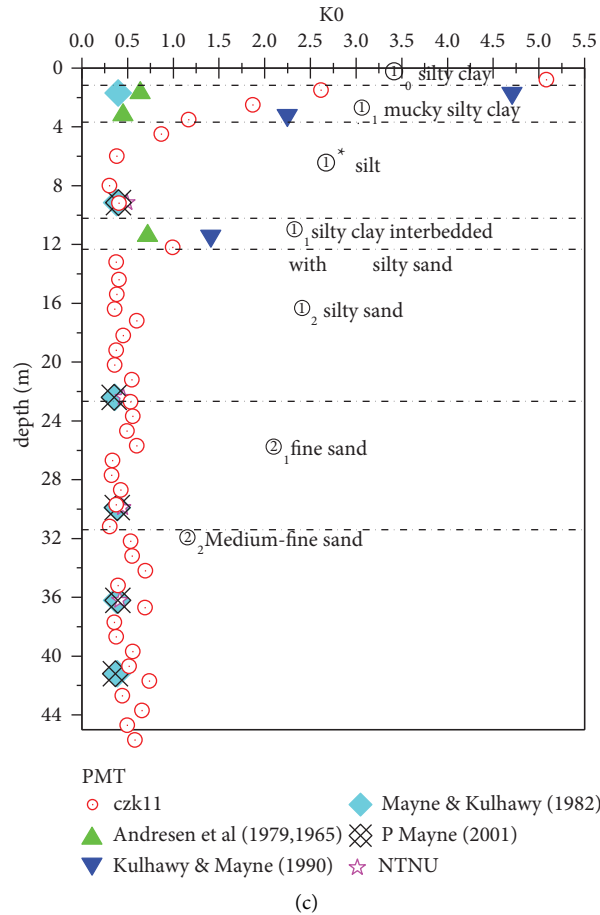


FIGURE 6: Estimated versus measured K_0 using different methods.

method. For coarse-grained soils (silty sand or sands), the estimated K_0 values from the Mayne and Kulhawy [25] method, the Mayne [9] method, and the NTNU method [28] are similar, especially the Mayne [9] method, which shows relatively good agreement to the reference values. Meanwhile, due to the disturbance when conducting predrilled pressuremeter tests, the reference K_0 values may be uncertain more or less, and the floodplain sediments have highly stratified characteristics; it is difficult to conclude that one method is definitely superior to another method.

Based on the above discussion, it is recommended to evaluate K_0 in such floodplain sediments from CPTU as follows: For projects where little experience is available, the Andersen and Kolstad [22] method and the NTNU method [28] method are recommended to estimate K_0 for fine-grained soils, while the Mayne [9] method and the NTNU method [28] are applied to coarse-grained soils. It is specially noted that the above values must be considered as a guide. If previous experience is available in the same deposit, the estimated values should be adjusted to reflect this experience.

4.3. Permeability Evaluations. Knowledge of hydraulic properties of soil deposits is one of the most critical aspects of geotechnical engineering, because it determines the rate of

flow of groundwater through the subsurface, which controls seepage in rock and soil. Additionally, it is of great importance for geoenvironmental risk assessment involving groundwater inflow into excavations and basements, as well as for water resources management, consolidation, and dewatering [29–33], which are also the concerned geotechnical aspects for the deep excavation engineering in the Fourth Yangtze River Bridge sites.

The coefficient of permeability in the horizontal or radial direction (k_h) can be obtained with field tests, such as the pumping tests or the Matsuo Akai permeability test, and laboratory tests, such as constant head permeability test or falling-head permeability test. These conventional methods, however, may be time-consuming and expensive and even of low reliability. So, some researchers give another way to augment hydraulic conductivity data using seismic piezocone penetration tests with dissipation phases. Several methods for CPTU dissipation tests interpretation have been proposed [34–38].

Typical pressure dissipation tests performed at Site A indicate that u_2 pore pressure decreases almost monotonically. Due to the approximately monotonic pore pressure response exhibited in the dissipation tests, the following empirical methods are used to infer the horizontal soil permeability (k_h). Common methods mainly include (i) the

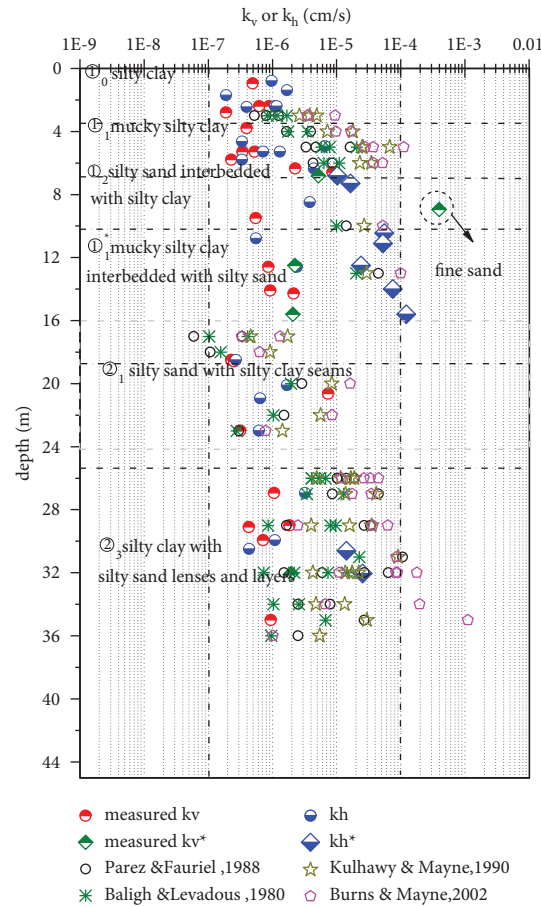


FIGURE 7: Comparison of vertical or horizontal k values obtained from laboratory tests to k_h values obtained using SCPTU-based methods (note: *samples with silty sand seam).

Baligh and Levadoux method [39], (ii) the Parez and Faureil method [40], (iii) the Burns and Mayne method [36], and the Kulhawy and Mayne method [23].

In order to assess the aforementioned methods, comparisons were made with laboratory-determined permeability values from falling-head permeability tests. The results of the comparison for the soft clays at Site A are presented in Figure 7, demonstrating significant scatter between different methods. With the exception of some measurements in the homogeneous clays, most of the lab k_h values are significantly lower than the CPTU-determined k_h values. This is especially the case for the great depth at the ranges of 10–14 and 28–36 m. The reasons are mainly related to the layer clay containing embedded and more or less continuous permeable layers or discontinuous lenses and the unavoidable disturbance of laboratory tests. The grain content curve also reflects the nonhomogeneity of the floodplain sediments (see Figure 8), which raises the uncertainty of the prediction.

Overall, it is observed that the lab measured k_h values are generally lower than those estimated from SCPTU within 1-2 orders of magnitude or even 3 orders. The CPTU-determined k_h and the laboratory-determined k_h values from samples with thin silty sand layers, however, are approximately within the same range (see Table 1). An important aspect is the relationship that

exists between the lab-measured horizontal permeability and vertical permeability at Site A with an average of $k_h/k_v = 2$, indicating anisotropic characteristic of the floodplain sediments. At some depths, this value reaches 10 or more, even 60, which is also in line with the description by Robertson [37].

If taking the predicted k_h values from the Parez and Faureil method as a check, the horizontal coefficient of permeability k_h obtained from the Baligh and Levadoux method shows similar trend but generally smaller. Meanwhile, k_h values determined using the other two methods were significantly larger than the reference values. Of additional note is the fact that the reported field pump tests gave more large values of k_v (averaged $4.97E-3$ cm/s), mainly because of the existence of highly permeable silty sand interbedded with silty clay. According to the approximate estimate of soil hydraulic conductivity using the nonnormalized (or normalized) CPT/SBT chart by Robertson et al. [8, 41], the results from Kulhawy and Mayne method and Burns and Mayne method seem more reasonable. Additionally, while the two latter methods are based on very different approaches to evaluating the permeability, strikingly similar results are produced. For the most part, the velocity-based method tends to significantly overpredict the laboratory-measured values of hydraulic permeability. The reason may be involved in speed effect. It must be pointed out that the estimation of soil

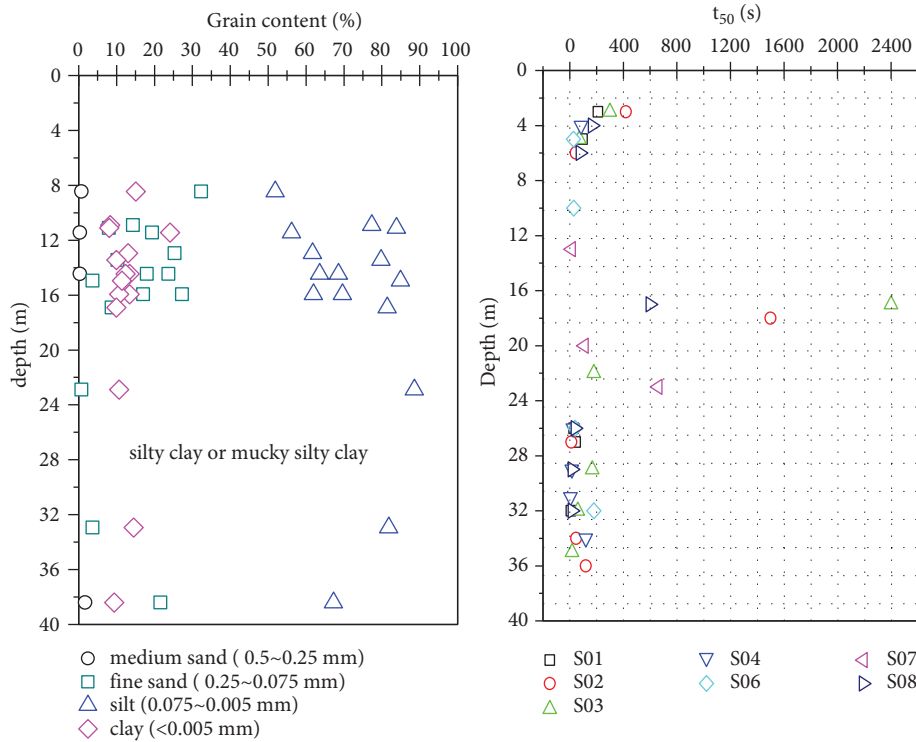


FIGURE 8: Grain content curve and t50 from pressure dissipation tests.

TABLE 1: Summary of results from laboratory and CPTU evaluations of hydraulic conductivity (k_h and k_v).

Soil type	SCPTU predicted k_h (10^{-7} cm/s)				lab k (10^{-7} cm/s)	
	Parez and Faureil	Baligh & Levadoux	Kulhawy and Mayne	Burns and Mayne	k_v	k_h
① ₀ silty clay	5.3~39.4 (16.3)	8.4~35.3 (18)	26.4~180.3 (73)	35.1~168 (86.3)	1.91~1.93 (1.92)	3.98~17 (10.5)
① ₁ mucky silty clay	33.3~162.6 (74.5)	58.2~207 (103.3)	230.7~671.1 (351.5)	279~1110 (532.4)	2.29~5.28 (3.67)	3.38~165* (53)
① ₁ * mucky silty clay interbedded silty sand	142.6~448.2 (295.4)	99.4~202.5 (151)	270.1~295 (282.5)	526~994 (760)	5.53~24.1 (16.3)	239~1209* (656)
② ₃ silty clay interbedded with silty sand	15.2 ~1065.9 (192.2)	7.3~226.2 (53.8)	9.2~908.8 (147.2)	6.3~889 (288.5)	2.3~19.7 (8.64)	2.7~253* (58.6)

Notes: min-max (average); * values from samples with thin silty sand layers.

permeability from CPTU dissipation data is relatively uncertain and should be used as reference only.

The results of this study show the remarkable variability in k_h value when using different test methods and different predicted methods. Some of this variability is due to factors such as variable soil properties, stratified and layered nature of the deposit, specimen size and orientation, sample homogeneity, different boundary constraints, and the particle size produced by the method of placement. Another important source of variability is the different measuring locations of q_b , u_2 , and shear wave velocity along the shaft which may result in serious influence on the predicted values at such highly stratified deposits. It may also be argued that no one method was found to be superior to the others based on this limited set of tests performed on such silt mixtures and sand mixtures. Of future interest, the grain composition and depositional environment may be

subtly investigated and considered when using the aforementioned predicted methods. Although these estimates are approximate at best, they can provide a guide to variations of possible permeability [39].

4.4. Prediction of Equivalent Stiffness. The deformation characteristics of soils include the consolidation indices (C_c , C_s , and C_r) and elastic moduli (E and G), as well as rate and creep parameters. The stiffness of soils is needed in evaluating deflections of shallow and deep foundations, retaining walls, excavations, and embankments, in addition to site-specific seismicity and amplification analyses [9, 42]. In fact, most of the activity of interest in earthwork deformations takes place close to the in situ K_0 state and corresponding small-strain region characterized by G_{max} or expressed by the initial soil stiffness G_0 , given as the following formula:

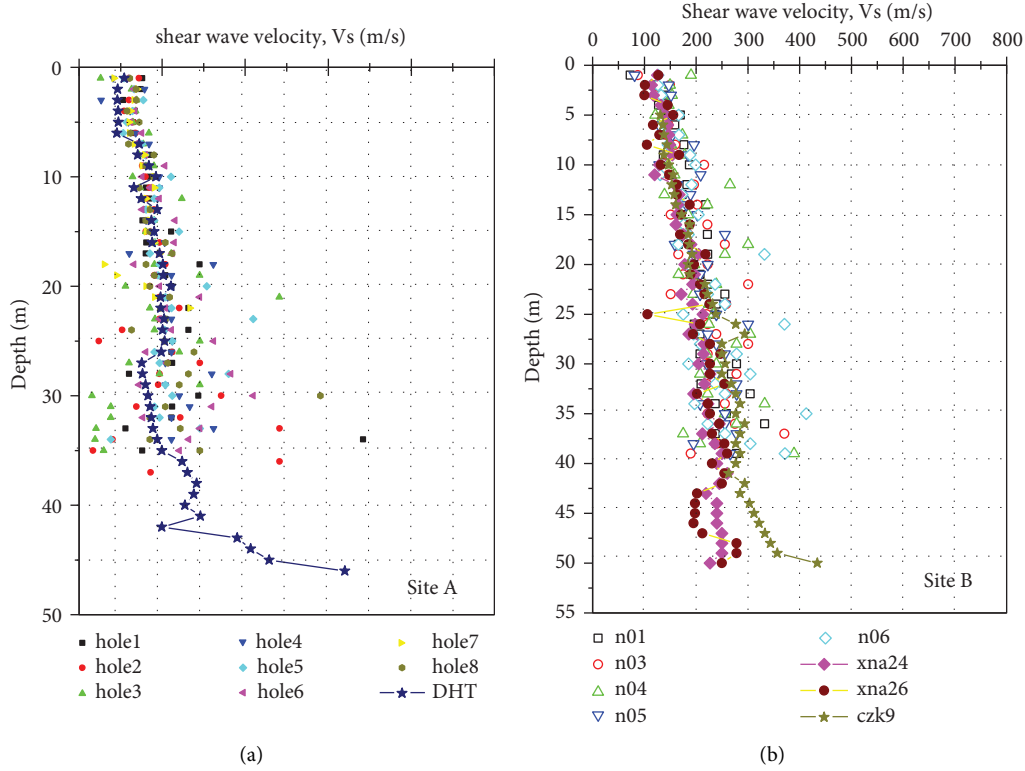


FIGURE 9: Comparison of SCPTU and DHT data from Site A (a) and Site B (b).

$$G_0 \text{ or } G_{\max} = \rho_T V_s^2, \quad (8)$$

where ρ_T is total mass density $= \gamma_T/g$, γ_T is soil unit weight, and gravitational constant $g = 9.8 \text{ m/s}^2$. V_s is shear wave velocity determined by various field and laboratory methods [43]. Seismic piezocone tests (SCPTU) provide an economical and expedient means of assessing small-strain properties (G_0) and large-strain behavior (τ_{\max}) of soil deposits from a single sounding and measurements are taken at complete opposite ends of the stress-strain response for soils. In this paper, a series of SCPTU soundings are performed for site-specific mapping of V_s in conjunction with a conventional downhole series (DHT) for the Nanjing Fourth Bridge project. Figure 9 presents the results derived from downhole testing using the SCPTU and DHT. The two methods appear in general agreement and confirm that the SCPTU is advisable. The general trends of V_s profiles are evident and show the increase with depth, followed by a suddenly big change at greater depths of 40 m. The fairly low shear wave velocity also can be seen at the depths where there are mucky silty clay deposits at Site A. As expected, it is obvious from these figures that SCPTU-measured V_s show more scatter than those obtained from DHT tests. Moreover, the variability of Site B is also relatively less than that of Site A. This is corresponding to the complexity of such floodplain sediments.

It is also interesting to observe that the DHT-measured V_s values seem to be equal to the average of SCPTU-measured V_s values. This is especially obvious from Figure 9(a).

In other words, considering the high cost of DHT tests and their time consumption, SCPTU can be taken as a main means for V_s measurement, while the DHT test can be used as a check.

In order to derive the profile of initial stiffness which is particularly valuable for both static and dynamic geotechnical analyses, the following equation proposed by Mayne [9] is used:

$$\rho_T = 0.85 \log V_s - 0.16 \log z, \quad (9)$$

where z is depth below the soil surface in meters and V_s is in m/s. The obtained profiles of saturated mass density at Site A and Site B are illustrated in Figure 10. It can be seen that the predicted values using equation (9) are generally lower than the laboratory measured values. In this case, by using data from silty clay, silts, and silty sand, the following correlation between V_s , ρ_T , and depth was developed ($n = 263$, $r^2 = 0.99$, shown in Figure 11):

$$\rho_T = 0.89 \log V_s - 0.13 \log z. \quad (10)$$

At some cases without V_s measurements, $V_s - q_t$ relations also can be possibly established because the cone tip resistance and shear wave velocity depend on the effective geostatic state of stress [42]. Burns and Mayne [44] related V_s with q_t and void ratio (e_0) and suggested the following equation to estimate V_s from the piezocone data:

$$V_s = 9.44 (q_t)^{0.435} (e_0)^{-0.532}. \quad (11)$$

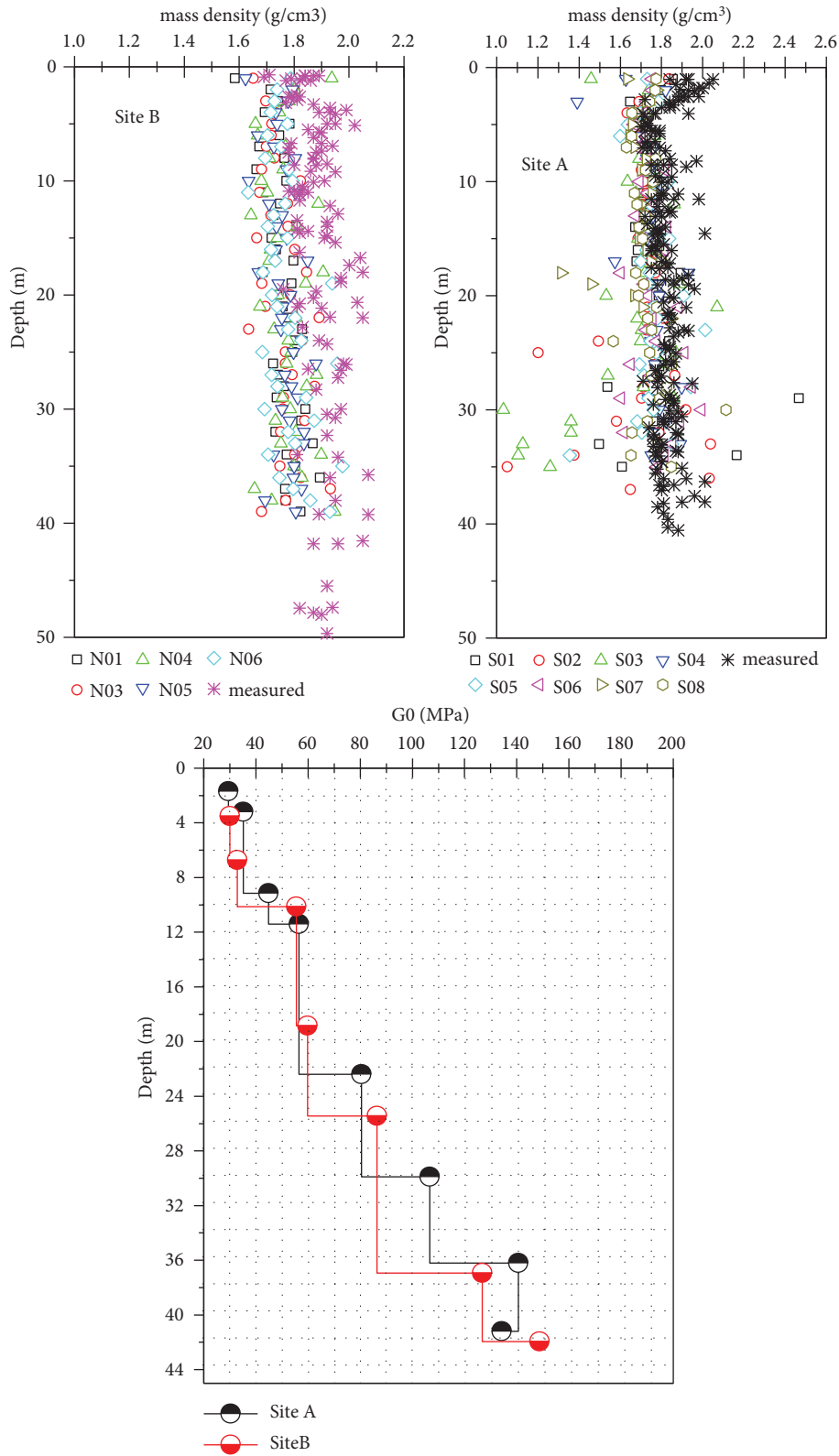


FIGURE 10: Mass density and initial shear modulus profiles at Sites A and B.

Figure 12 shows the comparison between measured V_s and predicted V_s using equation (11) at Sites A and B. Somewhat scatter can be seen, especially for sandy soils,

maybe due to the database in which the aforementioned equation used mainly consists of only clay sites. So, the more reasonable correlations for Sites A and B can be obtained by

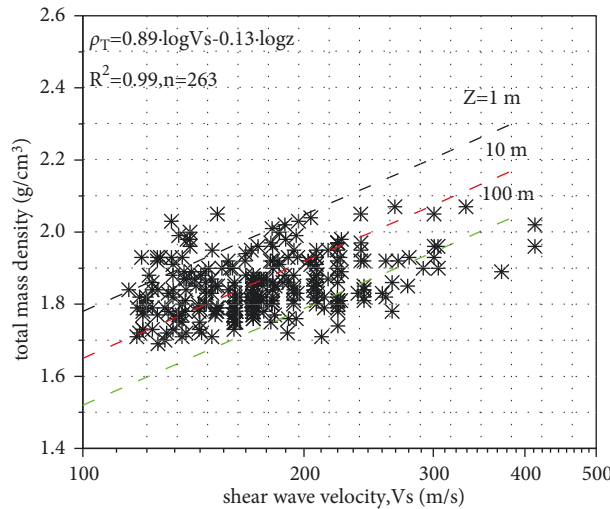


FIGURE 11: Correlation for specific density from depth and V_s .

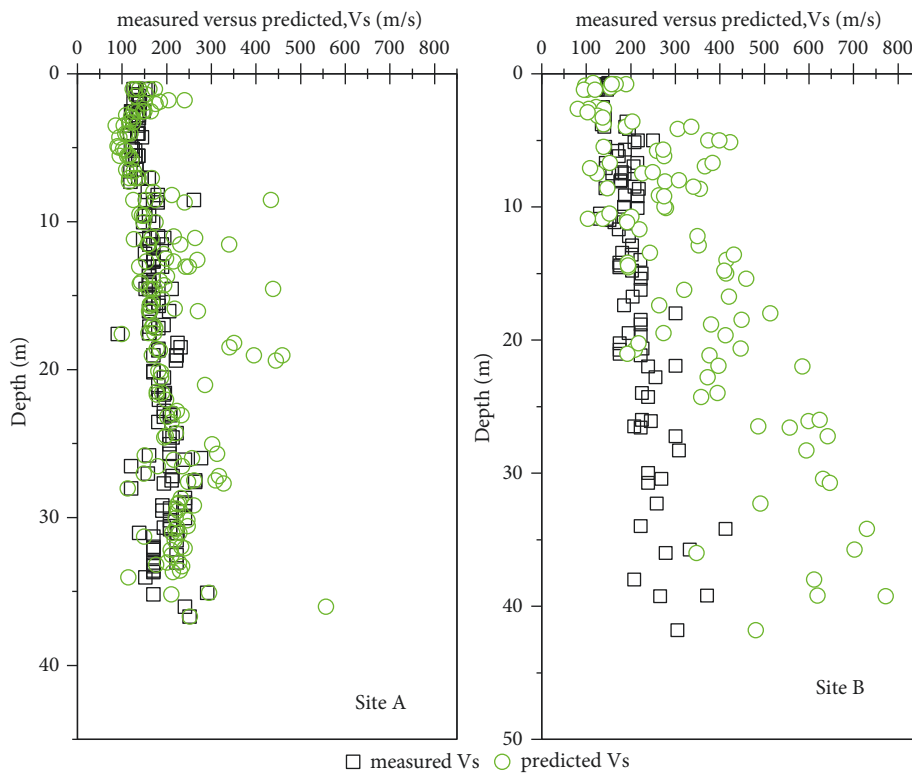


FIGURE 12: Measured versus predicted shear wave velocities at Sites A and B.

multiple regression. By using data from intact clays and sands, the following correlations between V_s , q_t and σ'_v or e_0 were developed:

$$\begin{aligned}
 V_s &= 229 (q_t)^{0.11} (\sigma'_v)^{0.15}, n = 263, r^2 = 0.62, & \text{where } V_s \text{ (m/s), } q_t \text{ (MPa) and } \sigma'_v \text{ (MPa),} \\
 V_s &= 38.8 (q_t)^{0.21} (e_0)^{-0.03}, n = 263, r^2 = 0.75, & \text{where } V_s \text{ (m/s) and } q_t \text{ (KPa).}
 \end{aligned}
 \tag{12}$$

Figure 13 indicates the trend and resulting statistics from multiple regression with data superimposed for comparison.

A strong correlation was observed between the cone resistance and the measured shear wave velocity. Rough

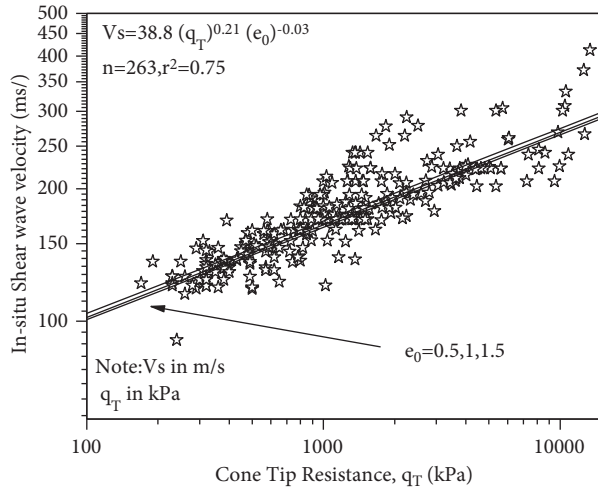


FIGURE 13: Shear wave velocity-cone tip resistance- e_0 correlations at Sites A and B.

estimates of V_s solely as a function of q_t and σ'_v can be made; however, the correlation will be definitely improved when the void ratio is also included as a correlative parameter. This is also verified by Burns and Mayne [44]. Because e_0 is recognized to change slightly within the range of 0.6~1.45 (averaged value = 0.97), the influence of e_0 is not noticeable in this study. Of particular importance is the fact that, through inversion of the equations, e_0 and ρ_{sat} can be evaluated approximately and immediately.

5. Conclusions

The piezocone (CPTU) is a widely accepted tool in western countries. However, CPTU has limited use in China due to some complicated reasons. In this study, several series of SCPTU data were collected at two bridge anchorage sites in Nanjing, China. Although the number of sites involved in the study was limited, some valuable findings resulted from this study, including the detailed subsurface stratigraphic profiling and evaluation of soil properties in the Yangtze River floodplain. Such information is useful in the planning phase of any civil engineering works. It also allows better design of field surveys, including the selection of the most appropriate techniques to use. Comparisons made between the original soil boring logs, conventional field and laboratory tests, and piezocone tests showed that the evaluation of soil behavior based on SCPTU was reasonably accurate at these sites. The following conclusions can be drawn:

- (1) A comprehensive program has been directed at the improved understanding of Yangtze River floodplain soils which are comprised of intermediate soils (silty clay, silts to silty sands, etc.). It is evident that the use of multifunctional SCPTU system in conjunction with drilling, sampling, and lab testing has improved the ability to resolve small changes in soil stratigraphy and associated soil properties, such as stratigraphic interfaces, thin soil layers, lenses and inclusions, and intralayer properties. The feasibility

of using piezocones with pore pressure measurements to improve site stratigraphy and layer characterization for the Yangtze River Bridge project was demonstrated. The Yangtze River floodplain sediments are unusual in that they exhibit behavioral features of both clays and sands, thus creating a complicated situation in practice.

- (2) Five existing CPTU-based methods to predict K_0 for the Yangtze River floodplain soils are evaluated and compared to the PMT-based method. The outcome of the study showed clearly that the Andersen and Kolstad [22] method and NTNU method [28] can be utilized to estimate K_0 for fine-grained soils, while the Mayne [9] method and the NTNU method [28] can be applied for coarse-grained soils.
- (3) The applicabilities of four piezocone-based methods to predict the hydraulic permeability are compared and evaluated for intermediate soils (silty clay to silts). Although no one method seems to be superior to the others for determining k_h in this study, the variability of results reflects both the stratified and layered nature of the floodplain deposit and the variability in particle composition. Compared to the laboratory falling head tests, the CPTU-determined k_h values are generally larger than the lab-measured values within 1-2 orders of magnitude. If taking both the laboratory and field pumping testing and experiences into consideration, the results from Kulhawy and Mayne method and Burns and Mayne method based on CE-CSSM model seem more reasonable.
- (4) The seismic piezocone provides information about soil behavior at very small and high strain within the same sounding. Empirical $V_s \sim q_t$ and $V_s \sim \rho_T$ relations in layer soils at the Fourth Bridge site are developed for estimating the low-strain shear modulus ($G_{max} = \rho_T V_s^2$), which is important in the design of statically and cyclically loaded foundations. Moreover, the proposed relationships can be used to obtain preliminary G_{max} profiles of similar floodplain sediments in the absence of direct measurements of shear wave velocity.

Data Availability

The data used to support the findings of this study are included within the Supplementary Materials.

Conflicts of Interest

The authors declare that they have no conflicts of interest to report regarding the present study.

Acknowledgments

Dr. Cai and Dr. Liu are greatly appreciated for their insightful comments and suggestions that have led to a substantial improvement of this paper. Much of the work presented in this paper was supported by the National

Natural Science Foundation of China (Grants nos. 41902266 and 51878157), Key R&D and Promotion Projects in Henan Province (tackling key problems in science and technology) (Grants nos. 212102310275, 202102310240, 202102310572, 212102310967, 222102320358, and 212102310968), training plan for young backbone teachers in Colleges and Universities of Henan Province (2021GGJS116), 2022 Science and Technology R&D Plan of China Railway Construction Group Co., Ltd. (22-76D), and Youth Elite Scientists Sponsorship Program by Henan Association for Science and Technology (2022HYTP011), and these financial supports are gratefully acknowledged. The assistance of Gao Y., Li J. N., and Zeng Q. H. is also highly appreciated.

Supplementary Materials

Detailed information on 14 seismic CPTU tests: (1) 8 seismic CPTU tests at Site A. (2) 6 seismic CPTU tests at Site B. (*Supplementary Materials*)

References

- [1] P. W. Mayne and C. Dumas, "Enhanced in situ geotechnical testing for bridge foundation analysis," *Transportation Research Record: Journal of the Transportation Research Board*, vol. 1569, no. 1, pp. 26–35, 1997.
- [2] H. Ma, M. Zhou, Y. Hu, and M. Shazzad Hossain, "Interpretation of layer boundaries and shear strengths for soft-stiff-soft clays using CPT data: LDFE analyses," *Journal of Geotechnical and Geoenvironmental Engineering*, vol. 142, no. 1, Article ID 04015055, 2016.
- [3] G. T. Meng, D. B. Zhang, S. L. Liu, and Y. C. Zhang, "The significance of piezocone penetration test," *Chinese Journal of Geotechnical Engineering*, vol. 22, no. 3, pp. 314–318, 2000, in Chinese.
- [4] S. Y. Liu and Y. K. Wu, "On the state-of-art and development of CPT in China," *Chinese Journal of Geotechnical Engineering*, vol. 26, no. 4, pp. 553–556, 2004, in Chinese.
- [5] L. Y. Tong, Q. Wang, G. Y. Du, and S. Liu, "Determination of undrained shear strength using piezocone penetration test in clayey soil for bridge foundation," *Journal of Southeast University*, vol. 27, no. 2, pp. 201–205, 2011.
- [6] L. Tong, H. Che, and M. Zhang, "Review of shear-wave velocity prediction equations based on piezocone penetration test data: example from Yangtze river floodplain deposits at Nanjing, jiangsu province, China," *The Quarterly Journal of Engineering Geology and Hydrogeology*, vol. 51, no. 2, pp. 229–246, 2018.
- [7] P. W. Mayne, "Enhanced geotechnical site characterization by seismic piezocone penetration tests," in *Proceedings of the Fourth International Geotechnical Conference*, San Francisco, CA, USA, September 2000.
- [8] P. K. Robertson, "In-situ testing and its application to foundation engineering," *Canadian Geotechnical Journal*, vol. 23, pp. 573–594, 1986.
- [9] P. W. Mayne, "Invited keynote: stress-strain-strength-flow parameters from enhanced in-situ tests," in *Proceedings of the International Conference on In-Situ Measurement of Soil Properties & Case Histories (In-Situ 2001)*, Bali, Indonesia, May 2001.
- [10] M. Zhang and L. Tong, "Statistical assessment of simplified cptu-based hydraulic conductivity curves," *Geofluids*, vol. 2021, Article ID 6656867, 8 pages, 2021.
- [11] G. T. Meng, S. H. Wang, D. B. Zhang, and S. L. Liu, "Determination of consolidation coefficient by piezo-cone penetration test," *Earth Science - Journal of China University of Geosciences*, vol. 26, no. 1, pp. 93–98, 2001.
- [12] Ministry of Construction of the People's Republic of China, *Code for Investigation of Geotechnical Engineering: GB50021-2001*, China Construction Industry Press, Beijing, China, 2002.
- [13] Ministry of housing and Urban-Rural Construction of the people's Republic of China, *Standard for Geotechnical Testing Method: GB/T 50123-2019*, China Planning Press, Beijing, China, 2019.
- [14] T. Lunne, P. K. Robertson, and J. J. M. Powell, *Cone Penetration Testing in Geotechnical Practice*, Blackie Academic & Professional, UK, 1997.
- [15] P. K. Robertson, R. G. Campanella, D. Gillespie, and A. Rice, "Seismic CPT to measure in-situ shear wave velocity," *Journal of Geotechnical Engineering*, vol. 112, no. 8, pp. 71–803, 1986.
- [16] P. W. Mayne, "Piezocone profiling of clays for maritime site investigations," in *Proceedings of the 11th Baltic Sea Geotechnical Conference, Geotechnics in Maritime Engineering*, Poland, Europe, September 2008.
- [17] C. C. Hird and S. M. Springman, "Comparative performance of 5 cm² and 10 cm² piezocones in a lacustrine clay," *Géotechnique*, vol. 56, no. 6, pp. 427–438, 2006.
- [18] D. Dasenbrock, "Improved site stratigraphy and layer characterization using cone penetration testing methods on Minnesota DOT projects," *Geo-Frontiers Congress*, vol. 2005, pp. 130–142, 2005.
- [19] P. K. Robertson and K. L. Cabal, *Guide to Cone Penetration Testing*, Gregg Drilling & Testing, Inc, Signal Hill, CA, USA, 3rd edition, 2009.
- [20] P. W. Mayne, *Cone Penetration Testing: A Synthesis of Highway Practice*, Transportation Research Board, Washington, DC, USA, 2007.
- [21] J. H. Schmertmann, "Measurement of in-situ shear strength," in *Proceedings of the ASCE Specialty Conference on In-Situ Measurement of Soil Properties*, pp. 57–138, North Carolina, USA, June 1975.
- [22] A. Andersen and P. Kolstad, "The NGI 54-mm samplers for undisturbed sampling of clays and representative sampling of coarser materials," in *Proceedings of the International Symposium Soil Sampling*, Singapore, 1979.
- [23] F. H. Kulhawy and P. W. Mayne, *Manual on Estimating Soil Properties for Foundation Design*, Electric Power Research Institute, Palo Alto, CA, USA, 1990.
- [24] T. Luune and H. P. Christophersen, "Interpretation of cone penetrometer data for offshore sands," in *Proceedings of the Offshore Technology Conference, USA*, pp. 1–12, Texas, TX, USA, May 02 1983.
- [25] P. W. Mayne and F. H. Kulhawy, "K₀-OCR relationships in soil," *ASCE Journal of Geotechnical engineering Division*, vol. 108, no. GT6, pp. 851–872, 1982.
- [26] P. W. Mayne, "Tentative method for estimating h₀ from qc data in sands," in *Proceedings of the International Symposium on Calibration Chamber Testing*, Potsdam, NY, USA, 1992.
- [27] P. W. Mayne, "CPT determination of OCR and lateral stresses in clean quartz sands," in *Proceedings of the International Symposium on Cone Penetration Testing*, Sweden, October 1995.
- [28] P. W. Mayne and R. G. Campanella, "Versatile site characterization by seismic piezocone tests," in *Proceedings of the 16th International Conference on Soil Mechanics & Geotechnical Engineering*, Japan, September 2005.

- [29] S. E. Burns and P. W. Mayne, "Monotonic and dilatatory pore-pressure decay during piezocone tests in clay," *Canadian Geotechnical Journal*, vol. 35, no. 6, pp. 1063–1073, 1998.
- [30] B. Bai, R. Zhou, G. Q. Cai, W. Hu, and G. C. Yang, "Coupled thermo-hydro-mechanical mechanism in view of the soil particle rearrangement of granular thermodynamics," *Computers and Geotechnics*, vol. 137, no. 8, Article ID 104272, 2021.
- [31] B. Bai, G. C. Yang, T. Li, and G. S. Yang, "A thermodynamic constitutive model with temperature effect based on particle rearrangement for geomaterials," *Mechanics of Materials*, vol. 139, Article ID 103180, 2019.
- [32] M. F. Zhang, L. Y. Tong, Y. J. Yang, H. B. Che, and H. S. Pan, "In situ determination of hydraulic conductivity in Yangtze Delta deposits using a modified piezocone model," *Bulletin of Engineering Geology and the Environment*, vol. 77, no. 1, pp. 153–164, 2018.
- [33] M. F. Zhang and L. Y. Tong, "Determination of hydraulic conductivity using a modified cylindrical -half-spherical piezocone model," *International Journal of Civil Engineering*, vol. 17, pp. 161–170, 2019.
- [34] C. I. Teh and G. T. Houlsby, "An analytical study of the cone penetration test in clay," *Géotechnique*, vol. 41, no. 1, pp. 17–34, 1991.
- [35] J. P. Sully, P. K. Robertson, R. G. Campanella, and D. J. Woeller, "An approach to evaluation of field cptu dissipation data in overconsolidated fine-grained soils," *Canadian Geotechnical Journal*, vol. 36, no. 2, pp. 369–381, 1999.
- [36] S. E. Burns and P. W. Mayne, "Interpretation of seismic piezocone results for the estimation of hydraulic conductivity in clays," *Geotechnical Testing Journal*, vol. 25, no. 3, pp. 334–341, 2002.
- [37] P. K. Robertson, "Interpretation of cone penetration tests a unified approach," *Canadian Geotechnical Journal*, vol. 46, no. 11, pp. 1337–1355, 2009.
- [38] H. Mahmoodzadeh, M. F. Randolph, and D. Wang, "Numerical simulation of piezocone dissipation test in clays," *Géotechnique*, vol. 64, no. 8, pp. 657–666, 2014.
- [39] M. M. Baligh and J. N. Leivadoux, *Pore Pressure Dissipation after Cone Penetration*, Massachusetts Institute of Technology Research Report, Cambridge, MA, UK, 1980.
- [40] L. Parez and R. Faureil, "Le piezocone. Améliorations apportées à la reconnaissance de sols," *Revue Française de Géotechnique*, vol. 44, pp. 13–27, 1988.
- [41] P. K. Robertson, "Soil classification using the cone penetration test," *Canadian Geotechnical Journal*, vol. 27, no. 1, pp. 151–158, 1990.
- [42] P. W. Mayne and G. J. Rix, "Closure: correlations between shear wave velocity and cone tip resistance in natural clays," *Soils and Foundations*, vol. 36, no. 3, pp. 144–145, 1996.
- [43] P. W. Mayne and J. A. Schneider, "Evaluating axial drilled shaft response by seismic cone," *Foundations and Ground Improvement*, ASCE, vol. 113, pp. 655–669, 2001.
- [44] S. E. Burns and P. W. Mayne, *Small and High-Strain Measurements of in Situ Soil Properties Using the Seismic Cone Penetrometer*. *Transportation Research Record*, National Academy Press, Washington, DC, USA, 1996.

Research Article

Study on the Nonlinear Damage Creep Model of the Weak Interlayer

Erjian Wei ^{1,2}, Bin Hu ^{1,2}, Kunyun Tian ³, Peishan Cen,⁴ Zhen Zhang,^{1,2} Zeqi Wang,^{1,2} and Shuxiang Chang^{1,2}

¹School of Resources and Environmental Engineering, Wuhan University of Science and Technology, Wuhan, Hubei, China

²Hubei Key Laboratory for Efficient Utilization and Agglomeration of Metallurgic Mineral Resources, Wuhan, Hubei, China

³School of Resource and Security Engineering, Henan University of Engineering, Zhengzhou, Henan, China

⁴School of Construction Engineering, Zhengzhou Shengda University, Zhengzhou, Henan, China

Correspondence should be addressed to Erjian Wei; weierjian@wust.edu.cn

Received 17 March 2022; Accepted 28 March 2022; Published 8 April 2022

Academic Editor: Xianze Cui

Copyright © 2022 Erjian Wei et al. This is an open access article distributed under the Creative Commons Attribution License, which permits unrestricted use, distribution, and reproduction in any medium, provided the original work is properly cited.

The weak interlayer has become a weak link in slope engineering due to its rheological effect. It is of great significance to study the nonlinear creep model of weak interlayer for long-term stability of the slope. In this paper, based on the creep curve characteristics of weak interlayer and considering the influence of aging damage, the nonlinear improvement of a classical viscoplastic body under stress and time-double threshold conditions is carried out, so that it can more accurately reflect the accelerated creep characteristics of the weak interlayer. By analyzing the relationship between failure load and time, the accelerated creep time threshold of the weak interlayer is obtained. On this basis, a nonlinear damage creep constitutive model of the weak interlayer is constructed and its creep equation is derived. By using the self-defined function fitting tool of Origin software and the Levenberg-Marquardt optimization algorithm, the creep test data of weak interlayer are fitted and compared. The fitting curve is in good agreement with the test data, which shows the rationality and applicability of the nonlinear creep model. The results show that the nonlinear damage creep model constructed in this paper can well describe the creep characteristics of the weak interlayer and the model has important theoretical reference significance for the study of long-term stability of slope with the weak interlayer.

1. Introduction

Rock rheological effect is a common phenomenon in geotechnical engineering. A large amount of slope engineering and tunnel engineering damage is caused by rock rheological effect [1–5]. As a special structural plane, the weak interlayer has low mechanical strength and obvious rheological effect, which often constitutes the weak link in the slope, so it poses a serious threat to the slope stability [6–10]. Therefore, it is necessary to study the rheological mechanical properties of the weak interlayer, and the study of the creep constitutive model of the weak interlayer is the core content [11–15]. Therefore, the study of the creep constitutive model of the weak interlayer has important theoretical significance and practical value for ensuring the long-term stability of slope engineering [16–18].

Generally speaking, there are two methods to establish the rheological constitutive model: the first one is directly fitting the rock rheological test curve with the empirical equation through the rheological test of rock. This method has a good fitting effect, but the physical meaning of the model is not clear. The second is based on the rheological test results, which is composed of series and parallel combinations of traditional model components, and then, the unknown rheological model component parameters are determined by identifying the component model and parameter inversion method [6]. Xia et al. [19] established a unified rheological mechanical model including 15 rheological mechanical properties. Nevertheless, since the traditional rheological model is composed of linear components, no matter how many components are in the

model, the model is more complex. The final model can only reflect the characteristics of linear viscoelastoplasticity and cannot describe the accelerated rheological stage [20]. Therefore, more and more nonlinear rheological models are proposed. Yang et al. [21] proposed a new nonlinear rheological element NRC model by assuming that the nonlinear shear rheological model of rock is a Weibull distribution function of time and combined it with the time function to describe the accelerated rheological stage. Zhao et al. [22] established a new viscoelastic-plastic creep damage model by combining the Burgers model and nonlinear Mohr-Coulomb plastic element in series. Xu et al. [23] defined the piecewise function of the greenschist creep damage variable changing with time by analyzing the whole creep curve of greenschist, proposed the conjecture that creep damage only appeared in the accelerated rheological stage, and established the generalized Bingham model considering the damage variable. Zhang et al. [24] improved the NRC model proposed by Xu et al. combined with the traditional Kelvin model to form a four-element nonlinear viscoelastic-plastic rheological model. Zhu et al. [25] and Huang et al. [26] assumed the creep damage variable of rock as a negative exponential function and used the damage Burgers model to describe the creep characteristics of the rock.

A large number of research results have been achieved in the nonlinear creep model of the rock. However, the research on the creep model of the weak interlayer is relatively rare, and there are few reports on the construction of a nonlinear creep model based on the double thresholds of stress and time. In view of this, based on the series-parallel connection of classical components, this paper introduces the damage variable in the accelerated rheological stage and considers the influence of the time threshold to establish the damage constitutive model that describes the nonlinear rheological properties of the weak interlayer. On this basis, the creep test results of the weak interlayer are nonlinearly fitted to verify the rationality and applicability of the constructed model.

2. Establishment of the Nonlinear Creep Model of the Weak Interlayer

2.1. Creep Curve Characteristics of the Weak Interlayer. The creep of the weak interlayer is a complex process in which multiple deformations such as elasticity, viscosity, plasticity, viscoelasticity, and viscoplasticity coexist. When the stress of the weak interlayer is less than its long-term strength, the creep curve of the weak interlayer is as shown in Figure 1. The weak interlayer generates elastic strain ε_0 at the moment of loading and then enters the attenuation creep stage. The creep deformation increases continuously, while the creep rate decreases continuously. At time t_a , the creep rate attenuates to zero, and the strain is stable at ε_a . In this case, the classical element combination model can be used to describe the creep characteristics of the rock. When the stress of the weak interlayer exceeds its long-term strength, the creep curve of the weak interlayer is as shown in Figure 2. At the initial stage of loading, the creep characteristics of the

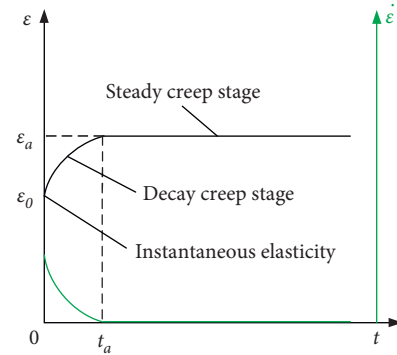


FIGURE 1: Steady-state creep curve.

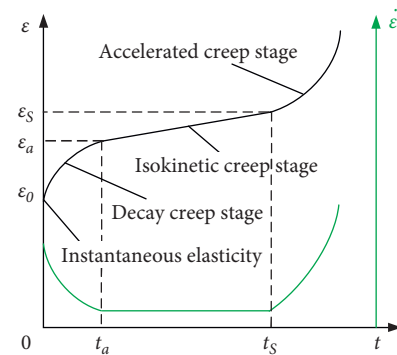


FIGURE 2: Creep failure curve.

weak interlayer are the same as those mentioned above. They all go through the instantaneous elasticity first and then enter the attenuation creep stage. However, starting from the t_a moment, the weak interlayer enters the constant creep stage, the strain of the weak interlayer is still increasing at this stage and the creep rate is a constant value. When the time reaches t_s , the weak interlayer enters the accelerated creep stage and ε_s is the critical strain value of accelerated creep initiation. Since the traditional creep components are linear components, the classical component combination model cannot describe the nonlinear characteristics of accelerated creep. In this paper, the classical components are improved to construct a creep model that can reflect the nonlinear characteristics of the weak interlayer.

2.2. Nonlinear Viscoplastic Body Based on Double Threshold Conditions. The viscoplastic body composed of classical elements is shown in Figure 3, which is composed of a plastic switch element and a viscous element in parallel. In the figure, τ is the shear stress, η is the viscosity coefficient of the viscous element, and τ_s is the long-term shear strength of the rock. When the stress of the plastic element is not more than τ_s , the plastic element is not opened and the viscoplastic body does not produce strain. When the stress of the plastic element is more than τ_s , the plastic element is opened and the viscoplastic body produces strain. Since the viscous element of the viscoplastic body is a linear element, it cannot describe the nonlinear accelerated creep stage of rock, so it

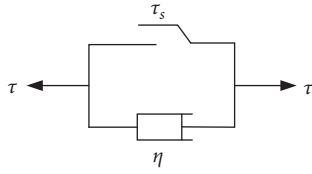


FIGURE 3: Classical viscoplastic body.

needs to be improved. The idea of improvement is to conduct nonlinear treatment of viscous components. A large number of tests show that when the stress of rock is less than its long-term strength, the rock is in the first two stages of creep and no accelerated creep failure occurs. When the stress of the rock exceeds its long-term strength, it is not immediately leading to accelerated creep failure, but at a certain time t_s , the rock enters the accelerated creep stage. According to the current relevant research [6], the aging damage of rock will occur when it enters accelerated creep. Therefore, based on the double threshold conditions of stress and time and considering the influence of aging damage, this paper improves the classical viscoplastic body, and the improved nonlinear viscoplastic body is shown in Figure 4. In the figure, D is the damage variable, t_s is the start time of accelerated creep, and the meaning of other parameters is the same as that of the corresponding parameters in Figure 3.

The damage variable D can be expressed as follows:

$$D = \begin{cases} 0 & t \leq t_s \\ 1 - \frac{1}{a} \exp[-a(t - t_s)] & t > t_s. \end{cases} \quad (1)$$

Here, a is the material parameter, which can be determined by fitting test data; t is the creep time, and t_s is the start time of accelerated creep. The damage variable D value is 0~1. If $t \leq t_s$, then $D=0$; that is, the weak interlayer is not damaged, When t approaches infinity, $D=1$, indicating that the weak interlayer has been destroyed.

Based on the above analysis, we can construct the creep equation of a nonlinear viscoplastic body.

When $\tau \leq \tau_s$, the plastic switch of the nonlinear viscoplastic body is closed and there is no strain in the viscoplastic body; that is, $\varepsilon=0$. When $\tau > \tau_s$ and $t \leq t_s$, the plastic switch of the nonlinear viscoplastic body will be opened, but it has not entered the acceleration stage and the aging damage has not occurred. We regard it as a classical viscoplastic body, so its creep equation can be expressed as follows:

$$\varepsilon = \frac{\tau - \tau_s}{\eta} t. \quad (2)$$

When $\tau > \tau_s$ and $t > t_s$, the plastic switch has been opened and the aging damage has also occurred. The nonlinear viscoplastic body enters the accelerated creep stage. The constitutive equation of the nonlinear viscoplastic body can be expressed as follows:

$$\tau = \tau_s + \eta(1 - D)\dot{\varepsilon} = \tau_s + \eta \frac{1}{a} \exp[-a(t - t_s)]\dot{\varepsilon}. \quad (3)$$

From formula (3),

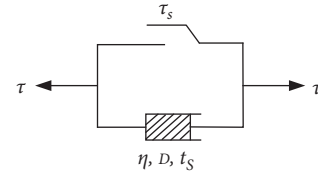


FIGURE 4: Nonlinear viscoplastic body.

$$\dot{\varepsilon} = \frac{\tau - \tau_s}{\eta} a \exp[a(t - t_s)]. \quad (4)$$

The creep equation of the nonlinear viscoplastic body is obtained by integrating both sides of (4):

$$\varepsilon = \frac{\tau - \tau_s}{\eta} \exp[a(t - t_s)]. \quad (5)$$

2.3. Determination of Accelerated Creep Time Threshold. From the previous section, we can see that the accelerated creep time threshold t_s reflects the opening time of the accelerated creep of the weak interlayer. It is an important parameter of the creep characteristics of the weak interlayer, which can be determined by the following method.

According to the research of some scholars [27], the failure load of the weak interlayer decreases with the increase in failure time, as shown in Figure 5. τ_0 is the instantaneous strength of the weak interlayer, τ_∞ is the long-term strength of the weak interlayer, and the stress corresponding to the accelerated creep start time t_s is τ . When the stress of the weak interlayer is higher than its long-term strength, the relationship between accelerated creep time threshold and stress can be established from Figure 5, as shown in the following equation:

$$\tau = \exp(-\alpha t_s + \beta). \quad (6)$$

From formula (6),

$$t_s = \frac{\beta - \ln \tau}{\alpha}. \quad (7)$$

Here, α and β are undetermined parameters, which can be determined by fitting test data. The accelerated creep time threshold of the weak interlayer can be determined by formula (7).

2.4. Establishment of the Nonlinear Creep Model. According to the creep characteristics of the weak interlayer, when the stress is less than the stress threshold of accelerated creep, the weak interlayer generates instantaneous elastic strain, decay creep, and steady creep. At this time, the Bergs model can be used to describe the creep characteristics of the weak interlayer. When the stress exceeds the stress threshold of accelerated creep, the rock will eventually enter the nonlinear accelerated creep stage at a certain time point after experiencing the creep deformation of the first two stages. A nonlinear viscoelastic-plastic damage creep model which can describe the whole creep process of the weak interlayer

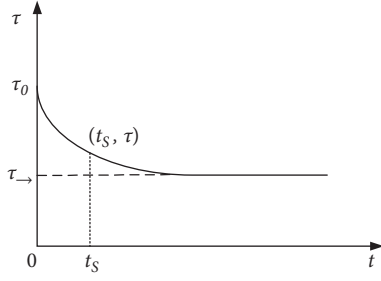


FIGURE 5: Relationship between failure load and time.

can be constructed by using the improved nonlinear viscoplastic body and Bergs body in series. The model is shown in Figure 6. In the figure, I describes the instantaneous elastic strain of the weak interlayer, II reflects the viscoelasticity of the weak interlayer, III reflects the viscosity of the weak interlayer, II and III describe the attenuation creep stage and steady creep stage of the weak interlayer, and IV reflects the nonlinear viscoplasticity of the weak interlayer, which describes the nonlinear accelerated creep stage of the weak interlayer.

It can be seen from Figure 6 that when $\tau \leq \tau_s$, I, II, and III are all involved in creep deformation. The state equations of the creep model are as follows:

$$\begin{cases} \tau = \tau_1 = \tau_2 = \tau_3 \\ \varepsilon = \varepsilon_1 + \varepsilon_2 + \varepsilon_3 \\ \tau_1 = G_1 \varepsilon_1 \\ \tau_2 = \tau_{21} + \tau_{22} = G_2 \varepsilon_2 + \eta_1 \dot{\varepsilon}_2 \\ \tau_3 = \eta_2 \dot{\varepsilon}_3. \end{cases} \quad (8)$$

From formula (8),

$$\varepsilon = \frac{\tau}{G_1} + \frac{\tau}{G_2} \left[1 - \exp\left(-\frac{G_2 t}{\eta_1}\right) \right] + \frac{\tau}{\eta_2} t. \quad (9)$$

When $\tau > \tau_s$, and $t \leq t_s$, I, II, III, and IV all participate in creep deformation; however, the viscoplastic body has not entered the accelerated creep stage, and it has not been damaged. At this time, the state equation of the creep model is as follows:

$$\begin{cases} \tau = \tau_1 = \tau_2 = \tau_3 = \tau_4 \\ \varepsilon = \varepsilon_1 + \varepsilon_2 + \varepsilon_3 + \varepsilon_4 \\ \tau_1 = G_1 \varepsilon_1 \\ \tau_2 = \tau_{21} + \tau_{22} = G_2 \varepsilon_2 + \eta_1 \dot{\varepsilon}_2 \\ \tau_3 = \eta_2 \dot{\varepsilon}_3 \\ \tau_4 = \tau_s + \eta_3 \dot{\varepsilon}_4. \end{cases} \quad (10)$$

From formula (10),

$$\varepsilon = \frac{\tau}{G_1} + \frac{\tau}{G_2} \left[1 - \exp\left(-\frac{G_2 t}{\eta_1}\right) \right] + \frac{\tau}{\eta_2} t + \frac{\tau - \tau_s}{\eta_3} t. \quad (11)$$

When $\tau > \tau_s$, and $t > t_s$, I, II, III, and IV all participate in creep deformation, the viscoplastic body has been damaged, and it has entered the accelerated creep stage. At this time, the state equation of the creep model is as follows:

$$\begin{cases} \tau = \tau_1 = \tau_2 = \tau_3 = \tau_4 \\ \varepsilon = \varepsilon_1 + \varepsilon_2 + \varepsilon_3 + \varepsilon_4 \\ \tau_1 = G_1 \varepsilon_1 \\ \tau_2 = \tau_{21} + \tau_{22} = G_2 \varepsilon_2 + \eta_1 \dot{\varepsilon}_2 \\ \tau_3 = \eta_2 \dot{\varepsilon}_3 \\ \tau_4 = \tau_s + \eta_3 (1 - D) \dot{\varepsilon}_4 = \tau_s + \eta_3 \frac{1}{a} \exp[-a(t - t_s)] \dot{\varepsilon}_4. \end{cases} \quad (12)$$

From formula (12),

$$\varepsilon = \frac{\tau}{G_1} + \frac{\tau}{G_2} \left[1 - \exp\left(-\frac{G_2 t}{\eta_1}\right) \right] + \frac{\tau}{\eta_2} t + \frac{\tau - \tau_s}{\eta_3} \exp[a(t - t_s)]. \quad (13)$$

Therefore, the nonlinear damage creep equation of the weak interlayer is as follows:

$$\begin{cases} \varepsilon = \frac{\tau}{G_1} + \frac{\tau}{G_2} \left[1 - \exp\left(-\frac{G_2 t}{\eta_1}\right) \right] + \frac{\tau}{\eta_2} t & (\tau \leq \tau_s), \\ \varepsilon = \frac{\tau}{G_1} + \frac{\tau}{G_2} \left[1 - \exp\left(-\frac{G_2 t}{\eta_1}\right) \right] + \frac{\tau}{\eta_2} t + \frac{\tau - \tau_s}{\eta_3} t & (\tau < \tau_s, t \leq t_s), \\ \varepsilon = \frac{\tau}{G_1} + \frac{\tau}{G_2} \left[1 - \exp\left(-\frac{G_2 t}{\eta_1}\right) \right] + \frac{\tau}{\eta_2} t + \frac{\tau - \tau_s}{\eta_3} \exp[a(t - t_s)] & (\tau < \tau_s, t > t_s). \end{cases} \quad (14)$$

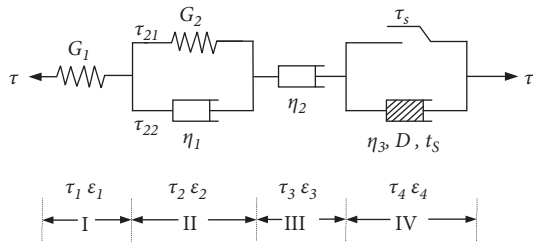


FIGURE 6: Nonlinear damage creep model.

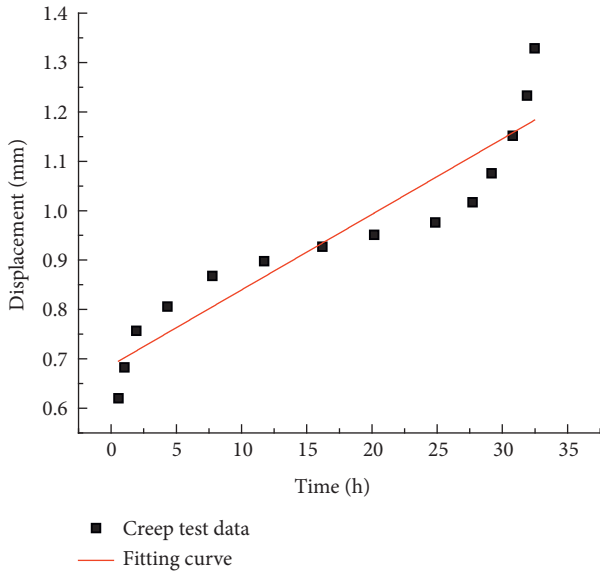


FIGURE 7: Fitting of the integral method.

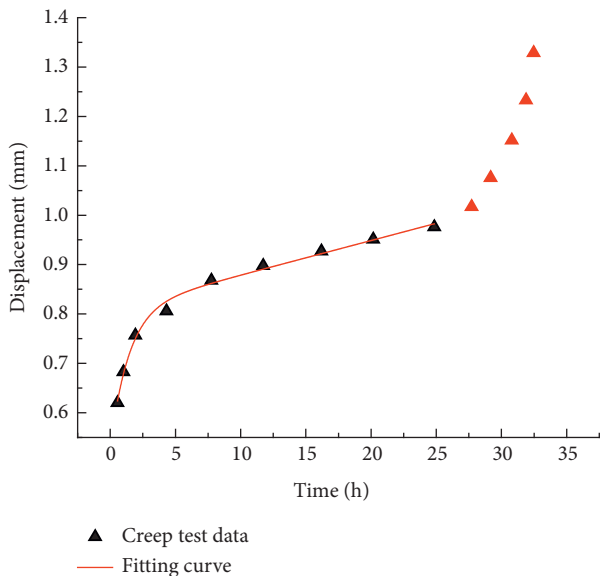


FIGURE 8: Fitting of the first two creep stages.

3. Verification of the Creep Model

By fitting the creep equation derived in the above section to the creep test data of the weak interlayer, the rationality and applicability of the model constructed in this paper can be

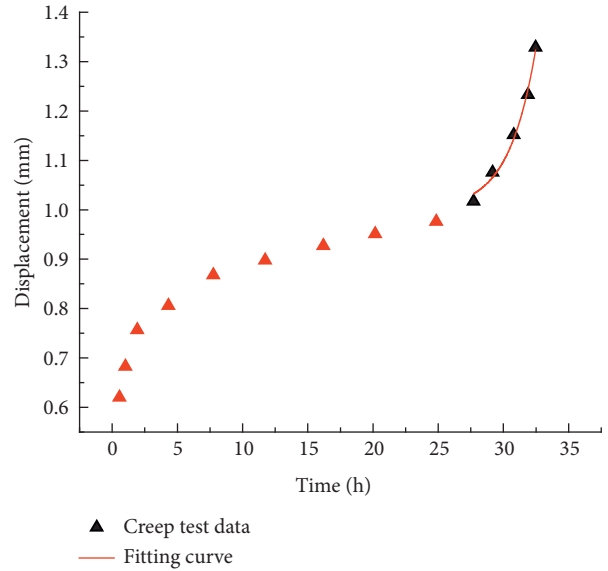


FIGURE 9: Fitting of the accelerated creep stage.

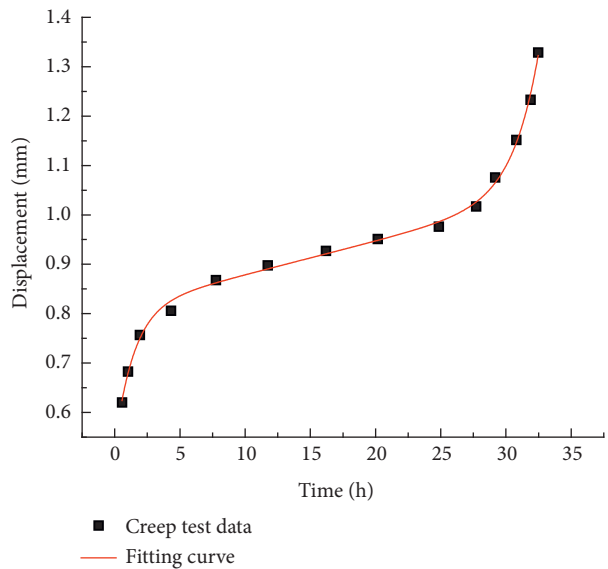


FIGURE 10: Fitting of the improved integral method.

verified. In this paper, data of Zhu et al. [28] were used to conduct shear creep test of the weak interlayer. In the first group of tests, creep tests were carried out on the rock samples with weak interlayers under the normal stress of 0.5 MPa by applying the shear stress step by step. The shear stresses applied at all levels were 0.10 MPa, 0.19 MPa, 0.29 MPa, 0.39 MPa, and 0.59 MPa, respectively. According to the test results, the long-term shear strength of the weak interlayer under this state was 0.423 MPa. In the second group, the creep test was carried out on the rock samples of weak interlayers under a normal stress of 0.7 MPa by applying shear stress in different grades. The applied shear stresses at different levels were 0.216 MPa, 0.432 MPa, 0.648 MPa, 0.864 MPa, 1.080 MPa, and 1.296 MPa, respectively. According to the test results, the long-term shear

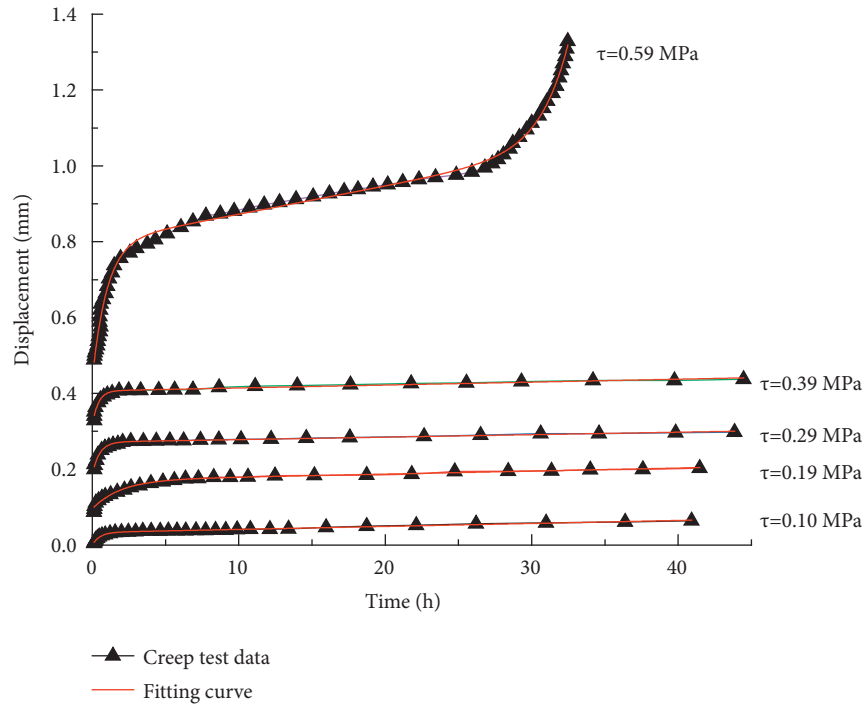


FIGURE 11: Experimental data and the fitting curves ($\sigma = 0.5$ MPa; $\tau = 0.10\sim 0.59$ MPa).

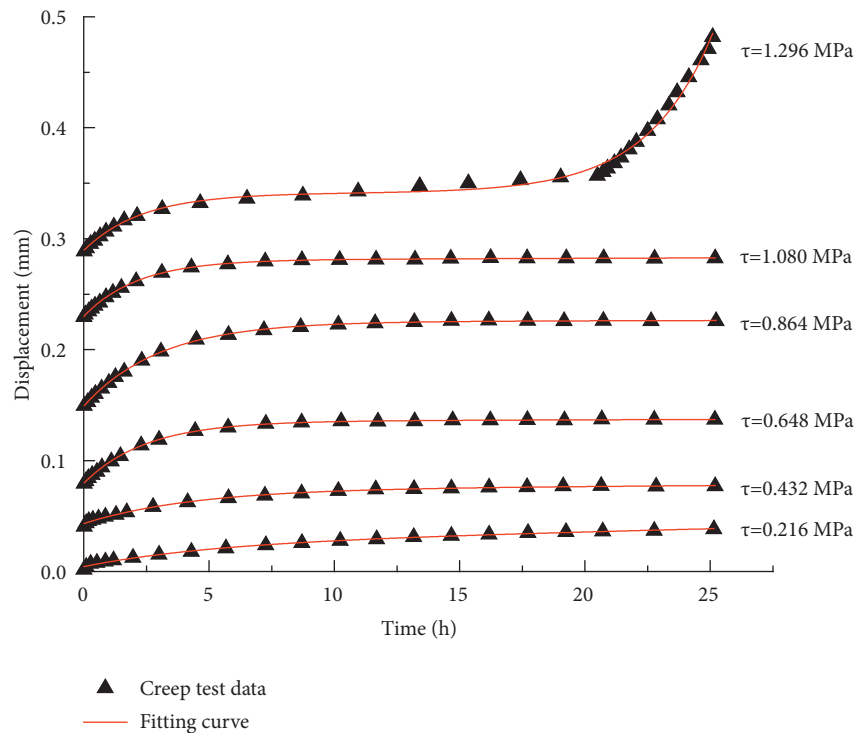


FIGURE 12: Experimental data and the fitting curves ($\sigma = 0.7$ MPa; $\tau = 0.216\sim 1.296$ MPa).

strength of the weak interlayer under this condition was 1.080 MPa. Based on the test results, using the custom function fitting tool of Origin software and Levenberg–Marquardt optimization algorithm, the creep test data of weak interlayers under different shear stresses are fitted and analyzed.

It should be pointed out that for the three stages of complete creep, because the creep equation is more complex, the creep parameters are more and the initial value of the parameters to be optimized is difficult to determine; if the whole method is used for fitting, the results will be as shown in Figure 7, indicating that the fitting has failed. Therefore,

TABLE 1: Creep parameter identification results ($\sigma = 0.5$ MPa; $\tau = 0.10\sim 0.59$ MPa).

τ /MPa	G1/MPa	G2/MPa	η_1 /MPa-mm-1 h	η_2 /MPa-mm-1 h	η_3 /MPa-mm-1 h	a	R2
0.1	3.01	2.98	1.53	127.34			0.9937
0.19	1.99	2.49	4.77	239.54			0.9851
0.29	1.55	3.38	1.64	446.51			0.9893
0.39	1.24	4.21	1.66	505.75			0.9758
0.59	1.34	1.64	1.65	79.41	5.61	0.51	0.9963

TABLE 2: Creep parameter identification results ($\sigma = 0.7$ MPa; $\tau = 0.216\sim 1.296$ MPa).

τ /MPa	G1/MPa	G2/MPa	η_1 /MPa-mm-1 h	η_2 /MPa-mm-1 h	η_3 /MPa-mm-1 h	a	R2
0.216	49.11	10.34	53.49	402.27			0.9942
0.432	10.01	13.91	61.04	3256.51			0.9954
0.648	8.15	11.61	28.67	9076.81			0.9968
0.864	5.79	11.34	34.44	21063.37			0.9989
1.080	4.69	21.21	45.61	14321.18			0.9983
1.296	4.47	25.05	58.41	3.93	8.78	0.38	0.9931

the fitting method needs to be improved. Firstly, the complete creep curve is divided into two parts, which are the first two stages of the creep curve and the accelerated creep curve. They are fitted, respectively, and the initial values of each creep parameter are obtained, as shown in Figure 8 and Figure 9. Secondly, by using these initial creep parameters and using the integral method to fit the complete creep curve, the ideal fitting effect can be obtained, as shown in Figure 10.

This method is used to fit the creep test data of these two groups of weak interlayers. The fitting curves are shown in Figures 11 and 12. The creep model parameters are obtained by fitting, as shown in Tables 1 and 2.

From Figures 11 and 12, it can be seen that the creep test data of weak interlayers under various loads are in good agreement with their fitting curves and the correlation coefficients in Tables 1 and 2 are basically above 0.95, which indicates that the nonlinear damage creep model constructed in this paper can well describe the instantaneous deformation, attenuation creep stage, steady creep stage, and accelerated creep stage of the weak interlayer, which further illustrates the rationality and applicability of the model.

4. Conclusions

- (1) Based on the double threshold conditions of stress and time and considering the influence of aging damage, the classical viscoplastic body is improved in this paper. The improved nonlinear viscoplastic body can more accurately reflect the characteristics of the accelerated creep stage.
- (2) In the fitting analysis of creep curves containing complete three stages, the effect of the complete method is usually poor. In this paper, a piecewise fitting method with a good fitting effect is innovatively proposed.
- (3) The creep test data of weak interlayers are fitted and analyzed by the creep model constructed in this paper. The results show that the fitting curve is in good agreement with the experimental data,

indicating that the nonlinear damage creep model constructed in this paper can well describe the creep characteristics of the weak interlayer. This model can provide important theoretical support for the study of long-term stability of slopes with weak interlayers.

Data Availability

The data used to support the findings of this study are included within the article.

Conflicts of Interest

The authors declare that they have no conflicts of interest.

Acknowledgments

This work was financially supported by the National Natural Science Foundation of China under Grants U1802243 and 41672317, in part by the Hubei Province Technical Innovation Special (major projects) Project under Grant 2017ACA184, in part by the Major Science and Technology Projects of WUST Cultivate Innovation Teams under Grant 2018TDX01, in part by the Program for Innovative Research Team (in Science and Technology) in University of Henan Province under Grant 22IRTSTHN009, and in part by the Science and Technology Project of Henan Province for Tackling Key Problems under Grant 222102320466.

References

- [1] B. Bai, Q. Nie, Y. Zhang, X. Wang, and W. Hu, "Cotransport of heavy metals and SiO₂ particles at different temperatures by seepage," *Journal of Hydrology*, vol. 597, Article ID 125771, 2021.
- [2] H. Tang, D. P. Wang, and Z. Duan, "New maxwell creep model based on fractional and elastic-plastic elements," *Advances in Civil Engineering*, vol. 2020, Article ID 9170706, 11 pages, 2020.
- [3] G. Peng, Z. Q. Chen, and J. R. Chen, "Research on rock creep characteristics based on the fractional calculus meshless

- method," *Advances in Civil Engineering*, vol. 2018, Article ID 1472840, 6 pages, 2018.
- [4] B. Hu, P.-Z. Pan, W.-W. Ji, S. Miao, D. Zhao, and T. Yao, "Study on probabilistic damage constitutive relation of rocks based on maximum-entropy theory," *International Journal of Green Nanotechnology*, vol. 20, no. 2, pp. 1–10, Article ID 06019018, 2020.
- [5] S.-Q. Yang, P. Xu, Y.-B. Li, and Y.-H. Huang, "Experimental investigation on triaxial mechanical and permeability behavior of sandstone after exposure to different high temperature treatments," *Geothermics*, vol. 69, pp. 93–109, 2017.
- [6] J. Sun, "Rock rheological mechanics and its advance in engineering applications," *Chinese Journal of Rock Mechanics and Engineering*, vol. 26, pp. 1081–1106, 2007.
- [7] H. Lin, X. Zhang, Y. X. Wang et al., "Improved nonlinear nishihara shear creep model with variable parameters for rock-like materials," *Advances in Civil Engineering*, vol. 2020, Article ID 7302141, 15 pages, 2020.
- [8] Q. Zhang, Z. P. Song, J. B. Wang, Y. W. Zhang, and T. Wang, "Creep properties and constitutive model of salt rock," *Advances in Civil Engineering*, vol. 2021, Article ID 8867673, 29 pages, 2021.
- [9] R.-l. Shan, Y. Bai, Y. Ju, T.-y. Han, H.-y. Dou, and Z.-l. Li, "Study on the triaxial unloading creep mechanical properties and damage constitutive model of red sandstone containing a single ice-filled flaw," *Rock Mechanics and Rock Engineering*, vol. 54, no. 2, pp. 833–855, 2021.
- [10] B. Bai, R. Zhou, G. Cai, W. Hu, and G. Yang, "Coupled thermo-hydro-mechanical mechanism in view of the soil particle rearrangement of granular thermodynamics," *Computers and Geotechnics*, vol. 137, Article ID 104272, 2021.
- [11] H. Li, N. T. William, J. Daemen, J. Zhou, and C.-k. Ma, "A power function model for simulating creep mechanical properties of salt rock," *Journal of Central South University*, vol. 27, no. 2, pp. 578–591, 2020.
- [12] L. Yang and Z.-d. Li, "Nonlinear variation parameters creep model of rock and parametric inversion," *Geotechnical & Geological Engineering*, vol. 36, no. 5, pp. 2985–2993, 2018.
- [13] Z.-y. Wang, J. Xu, Y.-p. Li, and Y. Wang, "Rheological damage FEA of hydro-mechanical coupling for rock mass," *Journal of Central South University of Technology*, vol. 14, no. S1, pp. 324–328, 2007.
- [14] B. Hu, E. J. Wei, J. Li, X. Zhu, K. Y. Tian, and K. Cui, "Nonlinear creep model based on shear creep test of granite," *Geomechanics and Engineering*, vol. 27, no. 5, pp. 527–535, 2021.
- [15] Y. Zhao, Y. Wang, W. Wang, W. Wan, and J. Tang, "Modeling of non-linear rheological behavior of hard rock using triaxial rheological experiment," *International Journal of Rock Mechanics and Mining Sciences*, vol. 93, pp. 66–75, 2017.
- [16] R. Hou, K. Zhang, J. Tao, X. Xue, and Y. Chen, "A nonlinear creep damage coupled model for rock considering the effect of initial damage," *Rock Mechanics and Rock Engineering*, vol. 52, no. 5, pp. 1275–1285, 2019.
- [17] P. Cao, Y. D. Wen, Y. X. Wang, H. P. Yuan, and B. X. Yuan, "Study on nonlinear damage creep constitutive model for high-stress soft rock," *Environmental Earth Sciences*, vol. 75, pp. 1–8, 2016.
- [18] E. J. Wei, B. Hu, J. Li et al., "Nonlinear viscoelastic-plastic creep model of rock based on fractional calculus," *Advances in Civil Engineering*, vol. 2022, Article ID 3063972, 7 pages, 2022.
- [19] C. C. Xia, X. D. Wang, C. B. Xu, and C. S. Zhang, "Method to identify rheological model by unified rheological model theory and case study," *Chinese Journal of Rock Mechanics and Engineering*, vol. 27, pp. 1594–1600, 2008.
- [20] B.-R. Chen, X.-J. Zhao, X.-T. Feng, H.-B. Zhao, and S.-Y. Wang, "Time-dependent damage constitutive model for the marble in the Jinping II hydropower station in China," *Bulletin of Engineering Geology and the Environment*, vol. 73, no. 2, pp. 499–515, 2014.
- [21] S. Q. Yang, W. Y. Xu, and S. L. Yang, "Investigation on shear rheological mechanical properties of shale in Longtan Hydropower Project," *Rock and Soil Mechanics*, vol. 28, no. 5, pp. 895–902, 2007.
- [22] Y. L. Zhao, J. Z. Tang, and C. C. Fu, "Rheological test of separation between viscoelastic-plastic strains and creep damage model," *Chinese Journal of Rock Mechanics and Engineering*, vol. 35, no. 7, pp. 1297–1308, 2016.
- [23] W. Y. Xu, S. Q. Yang, and W. J. Chu, "Nonlinear viscoelastoplastic rheological model (hohai model) of rock and its engineering application," *Chinese Journal of Rock Mechanics and Engineering*, vol. 25, no. 3, pp. 433–447, 2006.
- [24] Z. L. Zhang, W. Y. Xu, and W. Wang, "Study of triaxial creep tests and its nonlinear visco-elastoplastic creep model of rock from compressive zone of dam foundation in Xiangjiaba hydropower station," *Chinese Journal of Rock Mechanics and Engineering*, vol. 30, no. 1, pp. 132–140, 2011.
- [25] J. B. Zhu, B. Wang, and A. Q. Wu, "Study of unloading triaxial rheological tests and its nonlinear damage constitutive model of Jinping hydropower station green sandstone," *Chinese Journal of Rock Mechanics and Engineering*, vol. 29, no. 3, pp. 528–534, 2010.
- [26] Y. Y. Huang and H. Zheng, "Preliminary study of equivalent damage rheological model for jointed rock," *Rock and Soil Mechanics*, vol. 32, pp. 3566–3570, 2011.
- [27] L. Q. Li, W. Y. Xu, and W. Wang, "A nonlinear viscoelastoplastic rheological model based on Nishihara's model," *Chinese Journal of Theoretical and Applied Mechanics*, vol. 41, no. 5, pp. 671–680, 2009.
- [28] S. N. Zhu, Y. P. Yin, and B. Li, "Shear creep behavior of soft interlayer in Permian carbonaceous shale," *Rock and Soil Mechanics*, vol. 40, no. 4, pp. 1377–1386, 2019.

Research Article

Optimization Analysis of Mechanical Properties of Fly Ash-Based Multicontent Gasification Slag Paste Filling Material

Denghong Chen ^{1,2}, Tianwei Cao,^{1,2} Ran Chen,^{1,2} and Chao Li^{1,2}

¹School of Mining Engineering, Anhui University of Science and Technology, Huainan 232001, China

²Institute of Energy, Hefei Comprehensive National Science Center, Anhui, Hefei 230031, China

Correspondence should be addressed to Denghong Chen; dhchen@aust.edu.cn

Received 9 January 2022; Accepted 20 January 2022; Published 30 March 2022

Academic Editor: Bing Bai

Copyright © 2022 Denghong Chen et al. This is an open access article distributed under the Creative Commons Attribution License, which permits unrestricted use, distribution, and reproduction in any medium, provided the original work is properly cited.

In view of the difficult utilization of a large amount of coal-based solid waste produced by coal electrification in the Ningdong mining area, especially the large storage and low utilization rate of gasified slag, combined with the advantages of high paste filling concentration, fast efficiency, and low construction cost, it is of great significance to study the appropriate proportion of fly ash-based multicontent gasified slag paste filling material for green mining and large-amount utilization of gasified slag. Based on the microstructure, composition, and particle size distribution of gasification slag, fly ash, broken coal gangue, furnace bottom slag, and desulfurization gypsum tested by XRD, SEM, and particle size sorting screen, the mass fraction (X_1), gasification slag content (X_2), m (c): m (FA) (X_3). 29 groups of schemes are designed by four factors: mass fraction X_1 refers to the proportion of solid in the filling paste, the amount of gasification slag in the solid X_2 refers to the proportion of gasification slag in the solid, and m (c): m (FA) X_3 refers to the proportion of fly ash and cement in the solid excluding gasification slag, coal gangue, desulfurization gypsum, and furnace bottom slag. The amount of desulfurization gypsum in the solid X_4 refers to the proportion of desulfurization gypsum in the solid. The flow and strength characteristics of each group are analyzed. It is found that before proportioning, coal gangue of 2.5~5 mm accounts for 80.8%, furnace bottom slag of less than 2.5 mm accounts for 56.5%, fly ash of 20~80 μm accounts for 80%, and fly ash of 10~20 μm accounts for 90%. XRD patterns reveal that the main components of four solid wastes and cement are SiO_2 and Ca_3SiO_5 , and the chemical composition of desulfurization gypsum is $\text{Ca}(\text{SO}_4)(\text{H}_2\text{O})_2$. The regularity of size change tends to be consistent, and the uniaxial compressive strength of 3 days later in group thirteenth exceeds 0.991 MPa. Combined with the flow characteristics, it is determined that there are 6 optimization groups in the inclined ladder area with the expansion of 200~250 mm and the uniaxial compressive strength of 0.6~1.4 MPa. The compressive strength increases with the increase of the mass fraction of single-factor analysis. The response surface method of C shows that the significance of X_1 , X_2 , X_3 , and X_4 decreases in turn. The central combination design is used to predict that the mix proportion of X_1 is 84%, X_2 is 15%, X_3 is 1:5, and X_4 is 7%, the content of coal gangue is 10%, and the content of furnace bottom slag is 5% which is the best. The supplementary experimental results show that σ_{3d} is 1.35 MPa and the expansion is 200 mm. Combined with SEM, it is found that the microstructure before and after optimization is rich in hydration products and the internal structure is well cemented, which further explains σ_C . The above research provides important basic parameters for large-scale disposal and green filling mining which is difficult to deal with a large amount of stockpiled gasification slag.

1. Introduction

At present, the main body of energy utilization in China is coal. Coal gangue, fly ash, desulfurization gypsum, and coal gasification slag produced in the process of coal mining and utilization are common coal-based solid wastes. According to incomplete statistics, the annual output of coal-based solid

waste is about 1.5 billion tons, accounting for more than half of the output of industrial solid waste. At present, the comprehensive utilization of coal-based solid waste is still limited. In this way, the utilization status in the form of temporary storage will not only cause serious environmental pollution problems, such as the occupation and waste of land resources caused by open-air storage and the impact of floating dust on the quality of

the atmospheric environment, but also cause the harmful substances in coal-based solid waste enter the surface water body and penetrate into the ground with rainwater, polluting the water environment. It causes certain potential safety hazards to a human living environment. [1] Taking Ningdong mining area as an example, the output of solid waste increased from 4.4 million T to 24 million T from 2010 to 2020, of which the output of coal gasification slag has exceeded 7 million T, mostly buried and stacked in the open air (Figure 1, coal electrification base). Due to the high cost of treatment and utilization of solid wastes such as gasification slag and great technical difficulty, the comprehensive utilization rate of solid wastes in Ningdong base was only 28.9% in 2018 and the utilization rate of gasification slag was low [2]. The total amount of ash and slag in the Ningdong area is very large, with an annual emission of nearly 20 million tons, mainly including fly ash, coal chemical gasification ash, desulfurization gypsum, coal gangue, of which coal chemical gasification ash and fly ash account for the largest proportion [3]. The research on the utilization of gasification slag mainly focuses on the preparation of building materials, soil improvement, and water restoration, separation and utilization of residual carbon, preparation of catalyst carriers and ceramic materials, preparation of silicon-based materials, etc. [4]. At present, the application is relatively single and the degree of effective treatment is not high. Its treatment will not only increase the transportation cost but also cause environmental problems such as land occupation and dust pollution [5]. Many scholars have made many research achievements on the utilization of gasified slag. Shen Wang, Cheng Zhenyun, and Chen Haixia tested the fresh mixing performance of alkali-activated gasified slag fly ash cement mortar with the substitution rate of gasified slag of 0%, 10%, 20%, and 30%, respectively, and the physical and mechanical properties of alkali-activated gasified slag fly ash mortar under two different curing conditions of 20°C and 60°C, respectively. However, the improvement of mechanical properties is strongly dependent on conditions, which has an impact on the disposal of a large amount of gasification slag; Ma Chao et al. studied the ammonia nitrogen adsorption performance of the bulk coal gasification slag produced in the coal gasification process after separation by a water-based cyclone, but the process is complex and the utilization rate is limited. Zhao Aijing et al. use coal-based solid wastes such as gasification slag as a silicon source and aluminum source to prepare nanoporous materials with high added value. There are few studies on the influence of many factors such as high cost and performance stability. In order to prepare nanoporous materials with high added value, there are few studies on the influence of many factors such as high cost and performance stability. At the same time, the mining of coal resources by the full caving method also has a serious impact on surface subsidence and water and soil loss. In conclusion, it is urgent to study the green filling materials with high content of gasified slag, high strength, and good fluidity, so as to meet the low construction cost and large-scale disposal of a large amount of gasified slag stored in the Ningdong mining area. This paper intends to use a variety of research methods to analyze the microstructure and physicochemical properties of filling raw materials, obtain the particle size of fly ash and cement with a laser particle size analyzer, analyze the composition of

multisource coal-based solid waste by X-ray diffraction technology, and design by the response surface method. The filling matching scheme is designed by response surface method, which is mainly composed of multi-content gasified slag and supplemented by fly ash content, $m(c)$: m (FA) and desulfurization gypsum content. The regularity of single factor on the early strength of filling materials is analyzed by considering the influence of four factors: solid mass fraction, multi content gasified slag, $m(c)$: m (FA), and desulfurization gypsum content on the early strength of filling materials; the regularity of single factor on the early strength of the filling material is analyzed and the suitable filling mix proportion scheme is limited in combination with the flow characteristics. The influence ranking of X_1 , X_2 , X_3 , and X_4 is obtained by the response surface method of σ_C , and the optimal ratio is predicted by using the central combination design, which provides a new path for the multicontent gasification slag solid waste filling material with low utilization rate and difficult disposal.

2. Main Components and Particle Size Distribution of Coal-Based Solid Waste in the Ningdong Area

In this paper, fly ash-based gasification slag with high content is taken as the main research object, supplemented by coal gangue, desulfurization gypsum, and furnace bottom slag, and then mixed with ordinary 42.5 Portland cement to prepare green filling material [6]. The microcomponents of the five solid wastes were analyzed using a SmartLab X-ray diffractometer (XRD) to analyze the mineral phase of the raw materials (equipment parameters: angle of 5°~65°, scanning speed of 10°/min). Under these conditions, the XRD main components of the five coal-based solid wastes shown in Figure 2 were obtained. The micromorphology of coal-based solid waste was observed by daily FLEXSEM 1000 SEM. Under the condition of accelerating voltage of 10.0 kV, the microstructure of coal-based solid waste raw material and filling material cement was obtained. The experimental instruments used are shown in Figure 3.

The main mineral phase of gasification slag is quartz SiO_2 , which contains trace heavy metal element arsenic. The main mineral phase of fly ash is SiO_2 . The main mineral phase of desulfurized gypsum is $\text{Ca}(\text{SO}_4)(\text{H}_2\text{O})_2$. The main mineral phase of furnace bottom slag is SiO_2 [7]. The main mineral phases of cement are calcium silicate and tricalcium silicate Ca_3SiO_5 , which determine its early strength [8].

2.1. Gasification Slag. The gasification slag is taken from the coal to oil branch of Ningxia coal industry group, Ningdong coal power base. The gasification slag is the waste slag generated in the production process of the gasifier.

2.2. Fly Ash. The fly ash used in this experiment comes from the coal to oil branch affiliated to the Ningxia coal industry group. The fly ash used belongs to fine external ash with a small particle size. The particle size measured with the laser particle size analyzer is mainly less than 200 μm (Figure 4(c)), of which 20~80 μm particles of M account for

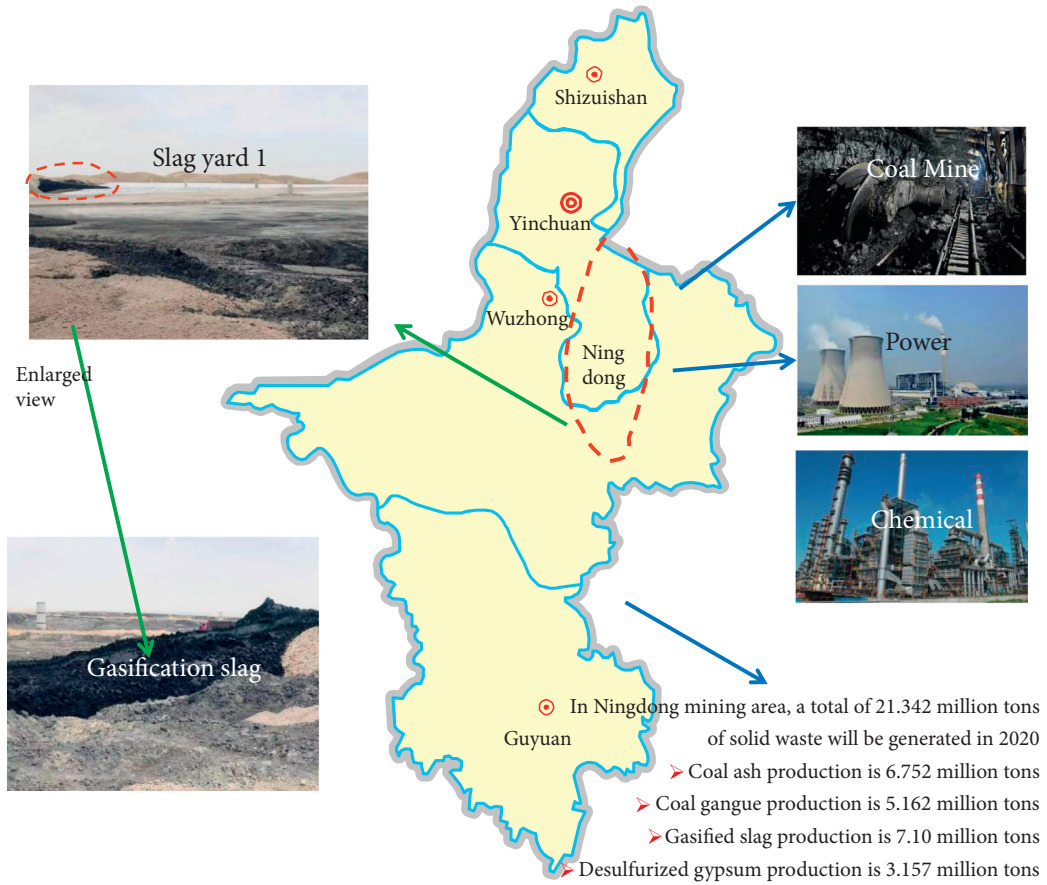


FIGURE 1: Analysis of coal-based solid waste output in the Ningdong mining area.

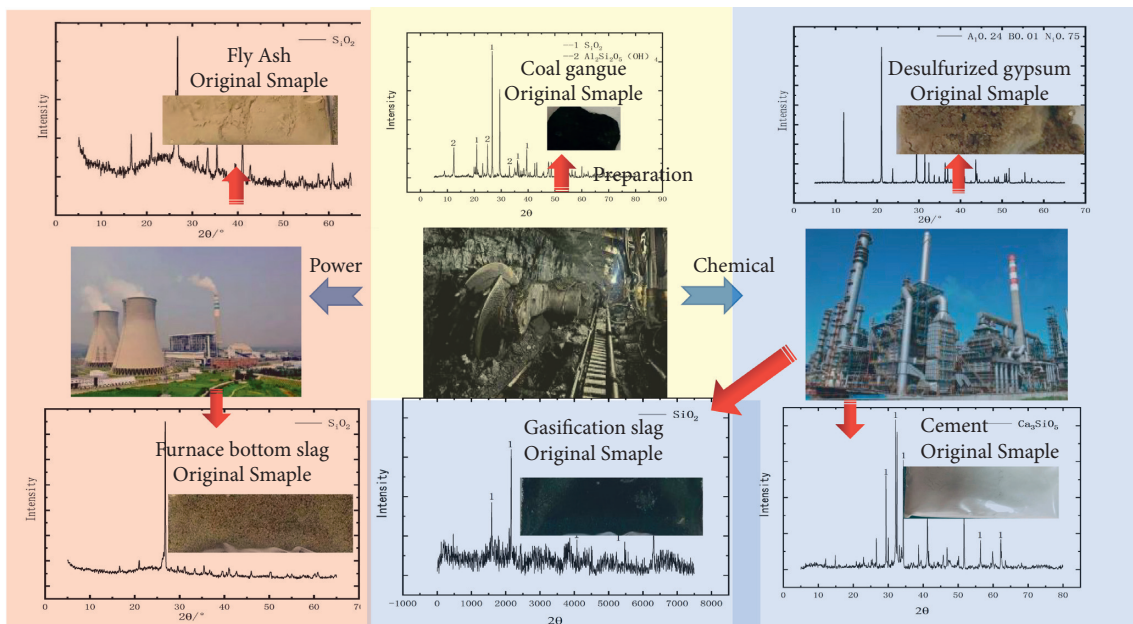


FIGURE 2: XRD spectra of five solid wastes in the Ningdong mining area.

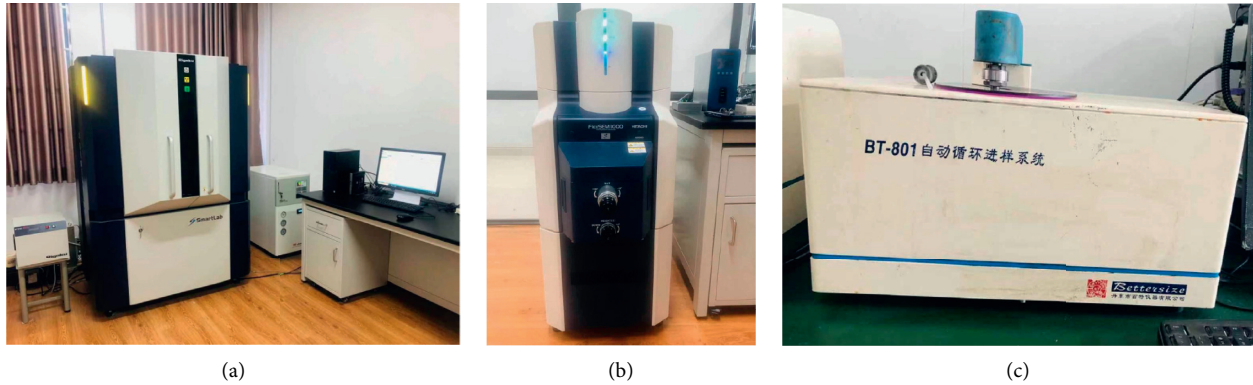


FIGURE 3: Microstructure and composition analysis instrument. (a) X-ray diffractometer. (b) SEM. (c) Laser particle size analyzer.

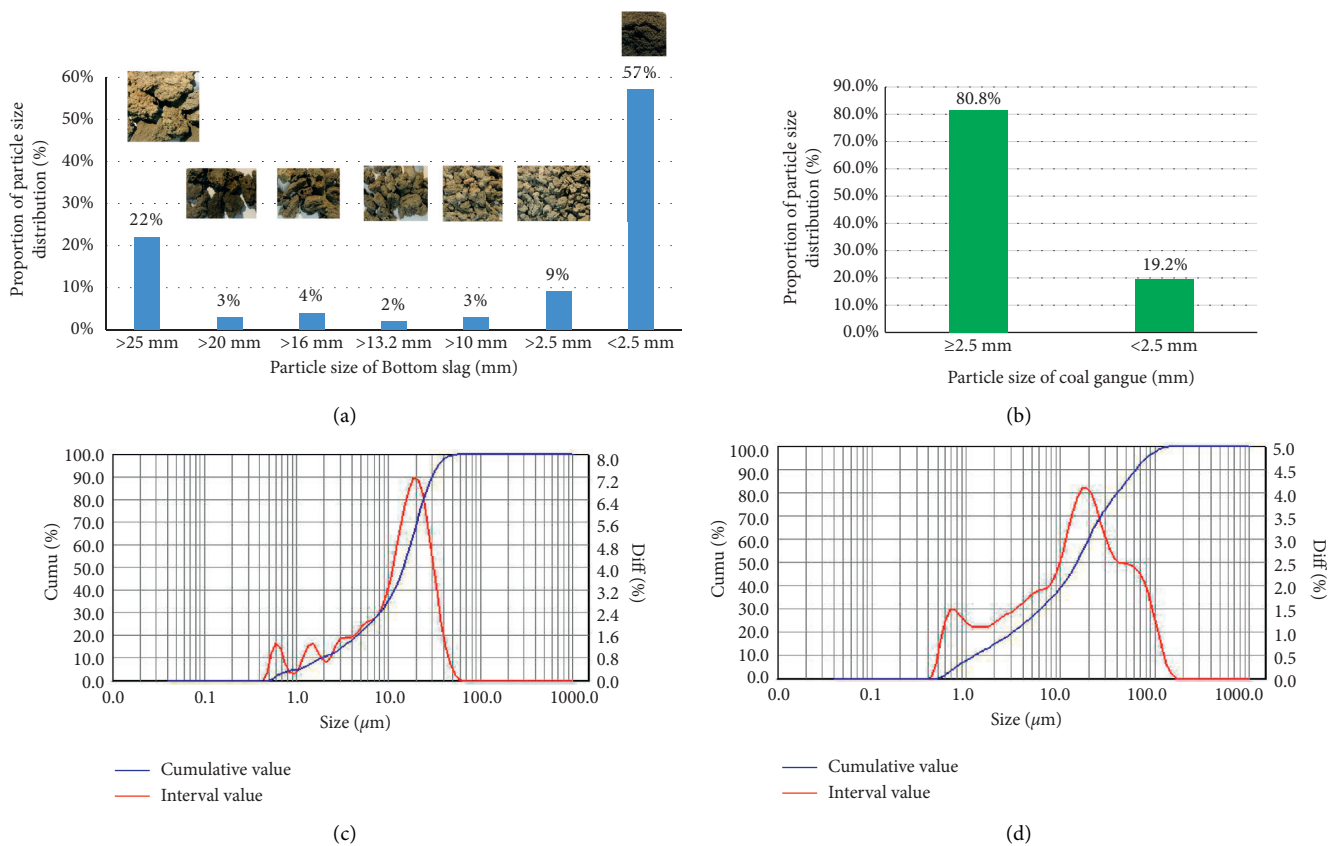


FIGURE 4: Statistical analysis of particle size distribution of furnace bottom slag, broken coal gangue, and fine particle raw materials before proportioning experiment. (a) Furnace bottom slag. (b) Coal gangue. (c) Fly ash. (d) Cement.

the majority and they are fine particles. When combined with the aggregate, it is conducive to improving the early strength of the consolidated body.

2.3. Desulfurized Gypsum. The desulfurized gypsum is taken from the coal to oil branch of Ningxia coal industry group, Ningdong coal power base, and is an earthy yellow viscous block.

2.4. Coal Gangue. The coal gangue is taken from Renjiazhuang coal mine affiliated to Ningxia coal industry group, Ningdong

coal power base, and is a gray-black block. At the same time, according to the method [9] specified in the standard for geotechnical test methods 1, the two-stage jaw crusher is used to crush the coal gangue to about 2.5 mm. After grading and screening 6 kg of crushed coal gangue by the sieve analysis method, its particle size distribution is as shown in Figure 4(b).

2.5. Furnace Bottom Slag. The furnace bottom slag is taken from the coal to oil branch affiliated to Ningxia coal industry group in the Ningdong coal power base. The furnace bottom slag is the waste slag generated in the production process of

2 kg of gasifier. Original furnace bottom slag is graded and screened by the screening method. The particle size distribution is shown in Figure 4(a). It is used randomly in the experiment.

3. Analysis of Proportioning Results of Coal-Based Solid Waste Filling Materials

3.1. Experimental Scheme. Based on the understanding of the main components and particle size distribution of five kinds of solid wastes, the research on the mix proportion optimization of fly ash-based filling materials with multi-content gasification slag is carried out. We prepare multi-source solid waste paste filling materials with a large amount of gasified slag, with good fluidity and high strength, so as to realize the combination of a large amount of coal-based solid waste [10], especially the solid waste consumption of a large amount of stacked gasified slag (7.1 million tons of gasified slag in the Ningdong area in 2020) [11] and green filling mining [12]. The experiment used $70.7 \times 70.7 \times 70.7$ mm triple standard mold. Due to the low utilization value and difficult treatment of gasification slag in the Ningdong base mining area, it is mainly mixed with more gasification slag. In addition, considering the compressive strength of the filling body, different levels of cement and a small amount of desulfurization gypsum are used to study their influence on the compressive strength. In this experiment, coal gangue with a particle size of 2.5–5 mm after secondary jaw crushing is used. Considering that the crushing cost of bulk coal gangue is too high, there is no too much research on coal gangue, furnace bottom slag, and other relatively easy-to-dispose solid wastes, supplemented by desulfurization gypsum, coal gangue, furnace bottom slag, and fly ash. The experimental factors and levels are shown in Table 1 [13]. The content of fixed bottom slag is 5%, and the content of coal gangue is 10%. Here, C:FA = cement:fly ash.

According to the requirements of strength test standards, the gasification slag is used as a multicontent raw material through the flow chart (Figure 5), mixed with fly ash, desulfurization gypsum, furnace bottom slag, and coal gangue and evenly stirred for 180 s to make a $70.7 \times 70.7 \times 70.7$ mm specimen which shall be taken out after reaching the testing age of 3 d, 7 d, and 14 d, and the uniaxial compressive strength test of the specimen shall be completed on the RMT testing machine [14].

3.2. Experimental Results and Single-Factor and Two-Factor Analysis. The response surface experimental design scheme and results are shown in Table 2. Using Box–Behnken design expert software, 29 groups of filling material proportioning experimental schemes with four factors and three levels are designed, and the response surface function relationship of early compressive strength of paste at 3 d age is established.

$$R_{3d} = 0.99 - 0.089X_1 + 0.24X_2 - 0.076X_3 + 0.057X_4. \quad (1)$$

Through the compressive strength test of multiple groups of proportioned test blocks at different ages on the

TABLE 1: Factors and levels in the design scheme of the central composite experiment.

Factor	Level		
	-1	0	1
X1 (mass fraction/%)	75	80	85
X2 (content of gasification slag in solid/%)	15	20	25
X3 (m(c):m(FA))	1: 5	1: 6	1: 7
X4 (content of desulfurized gypsum in solid/%)	6	9	12

RMT testing machine, the change trend of compressive strength of the same group of proportioned test blocks at different ages can be obtained. At the age of 3 d, 7 d, and 14 d, the change law of uniaxial compressive strength of the same proportion number tends to be consistent, and the compressive strength of filling materials increases with the increase in age, as shown in Figure 6(a). The mean value of uniaxial compressive strength of 29 groups of proportioned test blocks at the age of 3 d, 7 d, and 14 d is calculated, and the calculation result is $\bar{R}_{3d} = 0.991$ MPa, $\bar{R}_{7d} = 1.411$ MPa, and $\bar{R}_{14d} = 2.107$ MPa. The stress-strain curves of high- and low-strength test blocks are obtained, as shown in Figure 6(b). It can be concluded that there are 13 groups of high-strength proportion at 3d age, and the specific proportion number is as follows: 3, 4, 5, 7, 9, 11, 14, 16, 17, 18, 22, 23, and 24. The results show that the mass fraction has the highest influence on the early compressive strength of paste filling materials, and it has a positive correlation with the early compressive strength. The higher the mass fraction concentration, the higher the 3 d uniaxial compressive strength and the higher the influence on the later compressive strength. When the mass fraction is 80%, the strength is distributed as follows: X_4 has the least effect on compressive strength. X_1 has a negative correlation with the compressive strength, X_2 and X_3 have a positive correlation with the compressive strength, and X_4 has the characteristic of slow increase in the early compressive strength of the filling material. The increase in the gasification slag content can inhibit the increase in compressive strength. With the increase in mass concentration and cement content, the compressive strength increases gradually.

Combined with the high concentration paste filling technology [15], in order to better adapt to the current situation of bulk coal-based solid waste disposal in the Ningdong mining area, considering that the filling material has relatively good fluidity and provides large flow transportation for underground filling, in this paper, the suitable expansion of paste filling material is 200–250 mm [16] and the compressive strength of filling material is 0.6–1.4 MPa. The inclined step area obtained is circled according to the relevant parameters of uniaxial compressive strength and fluidity, so as to obtain the best ratio in this range, as shown in Figure 7. It can be seen from the figure that the six groups of filling materials with ratios 4, 11, 16, 18, 20, and 22 are the best under the interaction of uniaxial compressive strength and fluidity, as shown in Table 3.

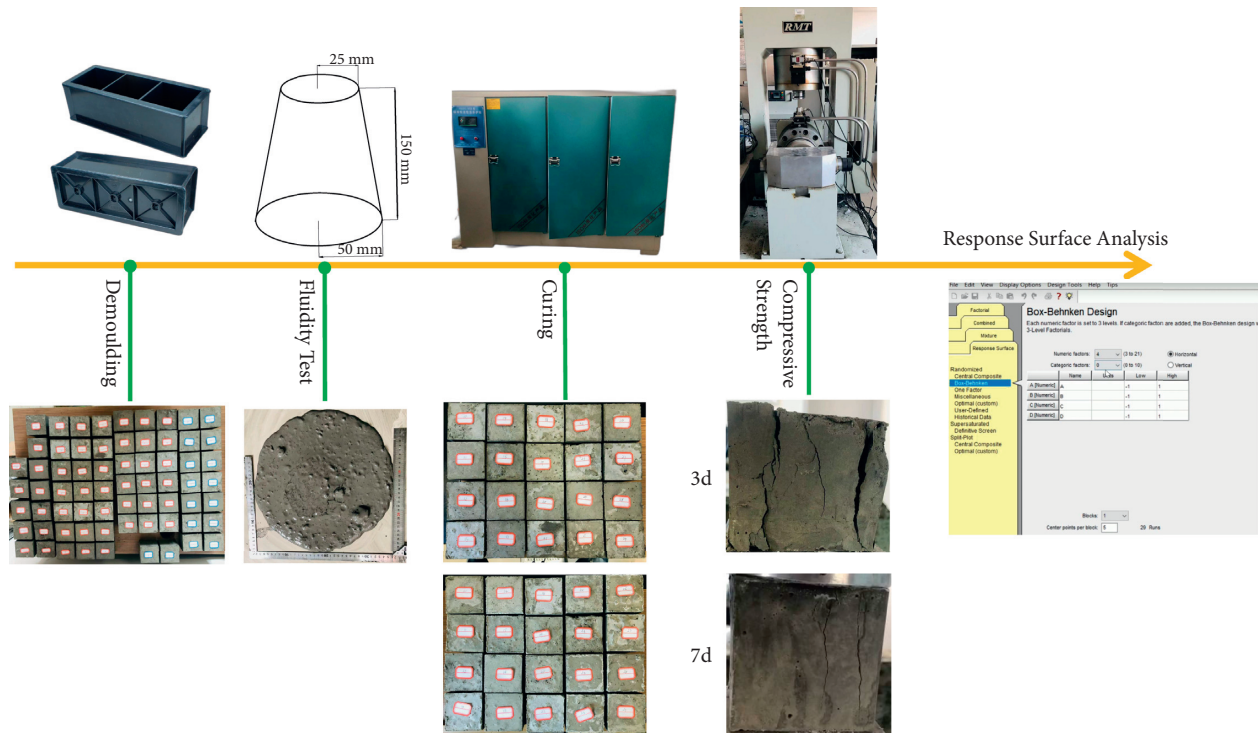


FIGURE 5: Test flow chart of coal-based solid waste filling material.

TABLE 2: Response surface design and results.

No.	Level				Early compressive strength (MPa)			No.	Level				Early compressive strength (MPa)		
	X ₁	X ₂	X ₃	X ₄	3 d	7 d	14 d		X ₁	X ₂	X ₃	X ₄	3 d	7 d	14 d
1	-1	-1	0	0	0.544	0.868	2.4	16	0	1	1	0	1.404	2.173	3.3
2	1	-1	0	0	0.588	0.704	1.2	17	-1	0	-1	0	1.380	1.673	2.6
3	-1	1	0	0	1.252	1.877	2.3	18	1	0	-1	0	1.016	1.200	1.8
4	1	1	0	0	1.468	2.153	3.5	19	-1	0	1	0	0.936	1.032	1.2
5	0	0	-1	-1	1.080	2.141	3.1	20	1	0	1	0	0.740	0.844	0.9
6	0	0	1	-1	0.908	1.548	3.5	21	0	-1	0	-1	0.736	0.848	0.9
7	0	0	-1	1	1.032	1.929	3.1	22	0	1	0	-1	0.992	1.092	2.1
8	0	0	1	1	0.748	1.232	2.6	23	0	-1	0	1	1.588	2.561	2.6
9	-1	0	0	-1	1.256	2.197	4.1	24	0	1	0	1	1.460	2.157	2.2
10	1	0	0	-1	0.920	1.204	1.8	25	0	0	0	0	0.876	1.236	1.9
11	-1	0	0	1	1.088	1.348	1.5	26	0	0	0	0	0.932	1.312	1.5
12	1	0	0	1	0.656	0.812	1.1	27	0	0	0	0	0.764	1.180	1.7
13	0	-1	-1	0	0.712	0.760	1.2	28	0	0	0	0	0.984	1.164	1.6
14	0	1	-1	0	1.072	1.753	3.0	29	0	0	0	0	0.976	1.304	1.6
15	0	-1	1	0	0.640	0.608	0.8	Response surface design method-central combination design method							

4. Analysis and Discussion of the Response Surface Method Model

4.1. Model Analysis and Significance Evaluation under Response Surface Methodology. Based on the significance of the influence between the factors of the response surface regression model and the response value, the error source of the model equation is analyzed [17]. The importance of the model is determined by *F* and *P* values. The larger the *F* value is, the smaller the *P* value is and the more significant the influence is [18]. The *F* value of the

established regression model is 3.86, which shows that the regression effect of the model is remarkable, and the model fits the experimental values well. The significance of single factor is $X_1 > X_2 > X_3 > X_4$. The model is used to determine the correlation coefficient to evaluate the accuracy and reliability of the regression model. The larger the *F* value of each factor, the more significant it is, as shown in Table 4. The model judgment correlation coefficient interprets the difference between the response surface and the real value [19] and analyzes the fitting degree of each model of the response surface method. The

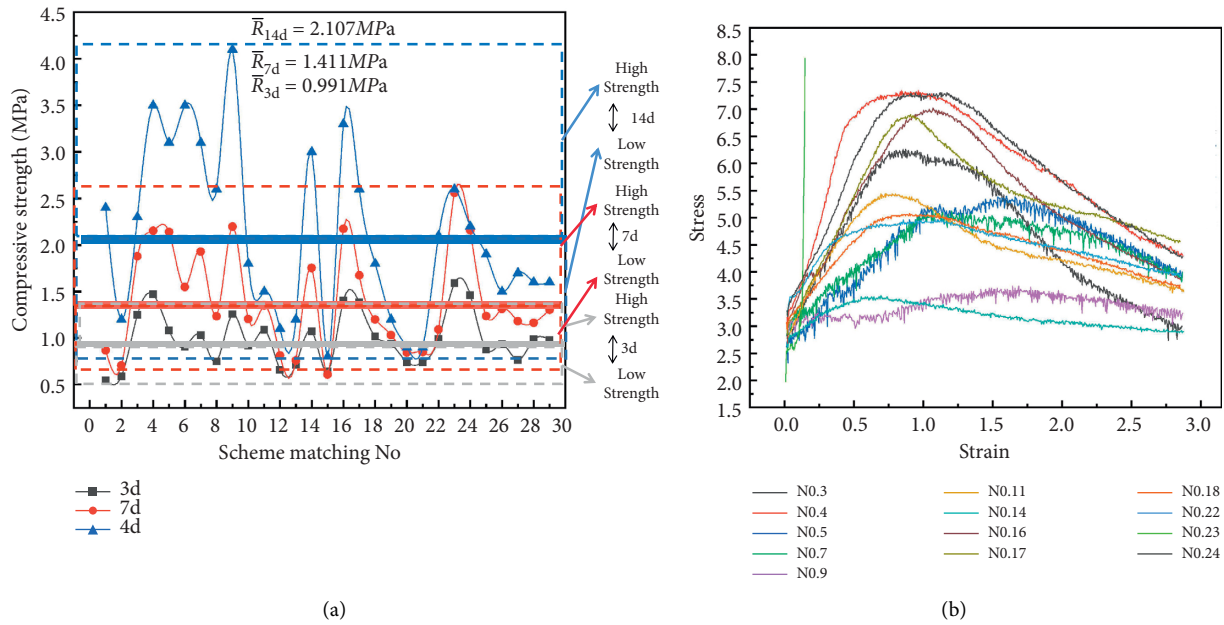


FIGURE 6: Change in compressive strength at different ages. (a) Compressive strength at different ages. (b) Stress-strain curve of the high-strength test block.

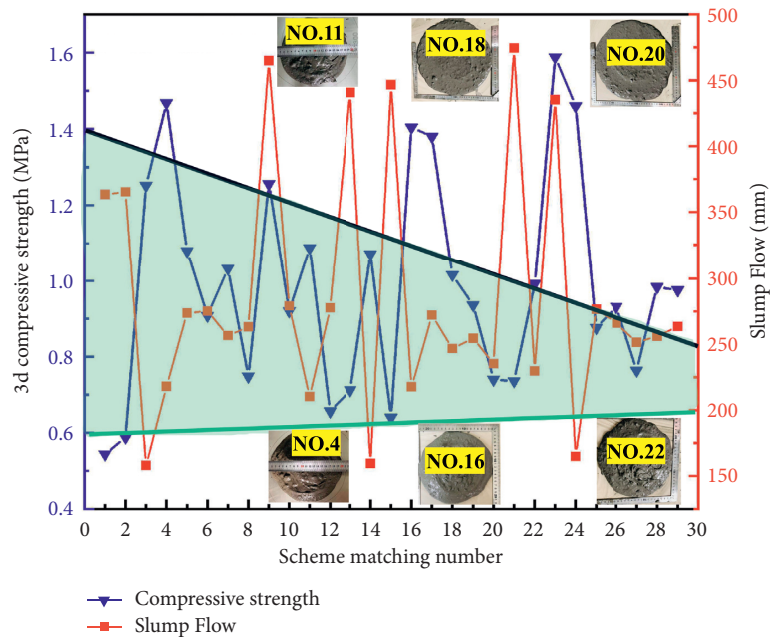


FIGURE 7: Interaction diagram of compressive strength and expansion at different ages under different proportion numbers.

TABLE 3: Optimization of and expansion under different compressive strengths.

Matching number	Ratio number factor parameter	3d uniaxial compressive strength (MPa)	Degree of expansion (mm)
4	X1 = 25%; X2 = 85%; X3 = 1 : 6; X4 = 9%	1.468	218
11	X1 = 15%; X2 = 80%; X3 = 1 : 6; X4 = 12%	1.088	210
16	X1 = 20%; X2 = 85%; X3 = 1 : 7; X4 = 9%	1.404	217.5
18	X1 = 25%; X2 = 80%; X3 = 1 : 5; X4 = 9%	1.016	246.5
20	X1 = 25%; X2 = 80%; X3 = 1 : 7; X4 = 9%	0.740	235
22	X1 = 20%; X2 = 85%; X3 = 1 : 6; X4 = 6%	0.992	229.5

TABLE 4: Analysis of variance of experimental results of the linear model.

Source	Sum of squares	Mean square	F value	P value
Model	0.88	0.22	3.86	0.0147
X_1	0.095	0.095	1.68	0.2077
X_2	0.67	0.67	11.85	0.0021
X_3	0.07	0.07	1.23	0.2778
X_4	0.039	0.039	0.68	0.4178
Residual	1.36	0.057		
Lack of fit	1.33	0.066		
Pure error	0.033			

TABLE 5: Analysis of the fitting degree of each model by the response surface method.

Model source	R^2 correction value	R^2 estimate	Remarks
Linear model	0.3915	0.0618	Recommended
2FI model	0.4352	Negative	
Cubic model	0.9344	Negative	

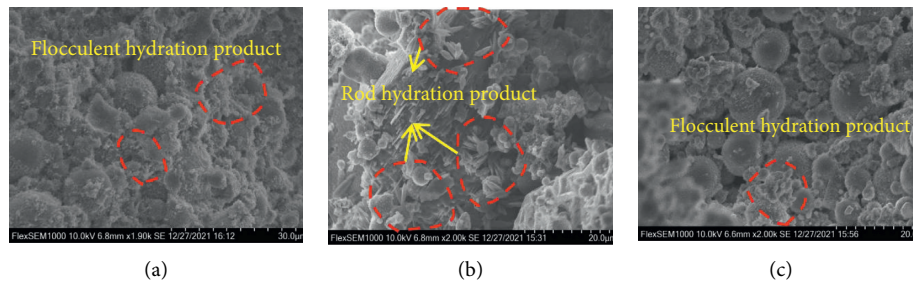


FIGURE 8: SEM of the typical filling material test block. (a) SEM hydration products of No. 18 filling material. (b) SEM hydration products of No. 4 filling material. (c) SEM hydration products of No. 20 filling material.

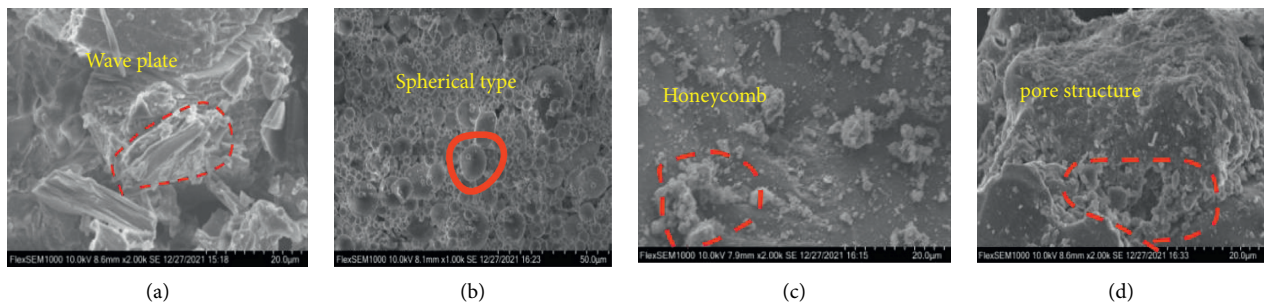


FIGURE 9: SEM structure before multisource coal-based solid waste proportioning experiment. (a) Desulfurized gypsum. (b) Fly ash. (c) Gasification slag. (d) Furnace bottom slag.

evaluation results are shown in Table 5. The closer the correlation coefficient is to 1, the higher the reliability of the model is. The complex correlation coefficient is 0.3915, and the prediction correlation coefficient is 0.0618, which proves that the model has high accuracy. The contour line and 3d response surface of the multiple regression equation of the linear model represent the interaction results of each factor. It can not only predict and optimize the response value but also analyze any single factor to obtain the significance law [20].

4.2. Discussion. From the uniaxial compressive strength and fluidity-related parameters, three typical representative test blocks with ratios 4, 18, and 20 are circled in the inclined ladder area. After cementation, the hydration reaction is severe. The SEM microstructure shows the abundance of rod and flocculent hydration products, which have different promoting effects on the compressive strength of filling materials (Figures 8(a)–8(c)). The microstructure of raw materials used for filling is shown in Figures 9(a)–9(d). Through the comparison of

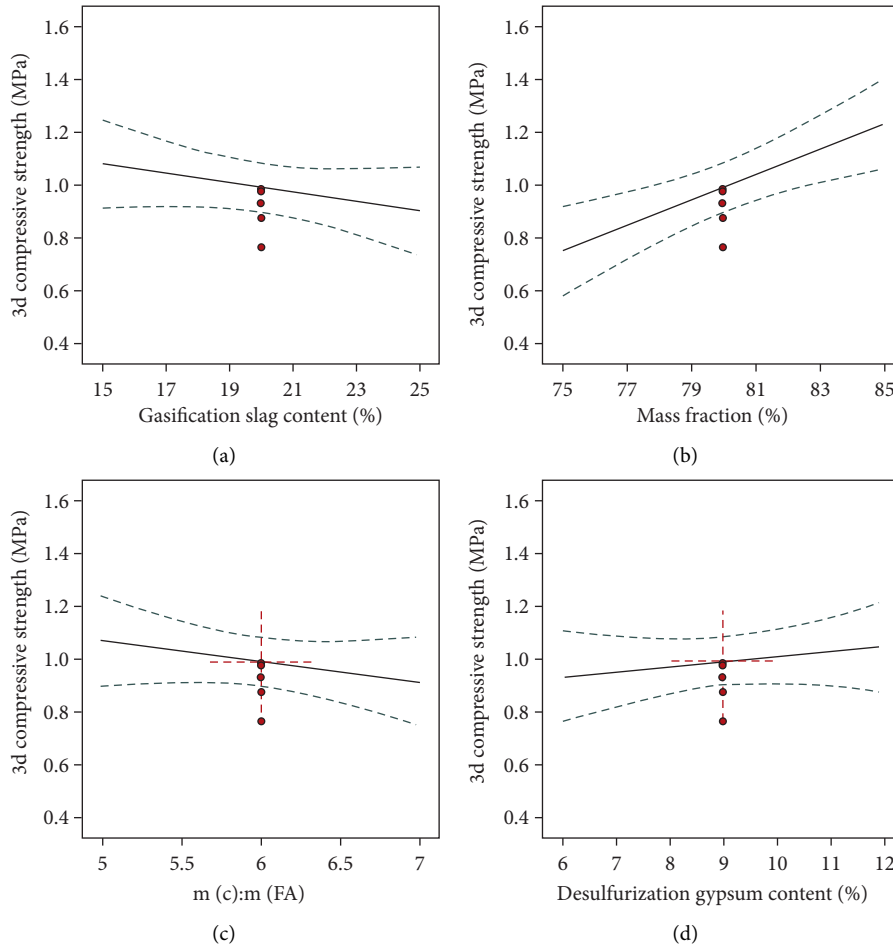


FIGURE 10: Prediction of single-factor effect on 3 d uniaxial compressive strength response surface. (a) X_1 single-factor influence prediction. (b) X_2 single-factor impact prediction. (c) X_3 single-factor impact prediction. (d) X_4 single-factor impact prediction.

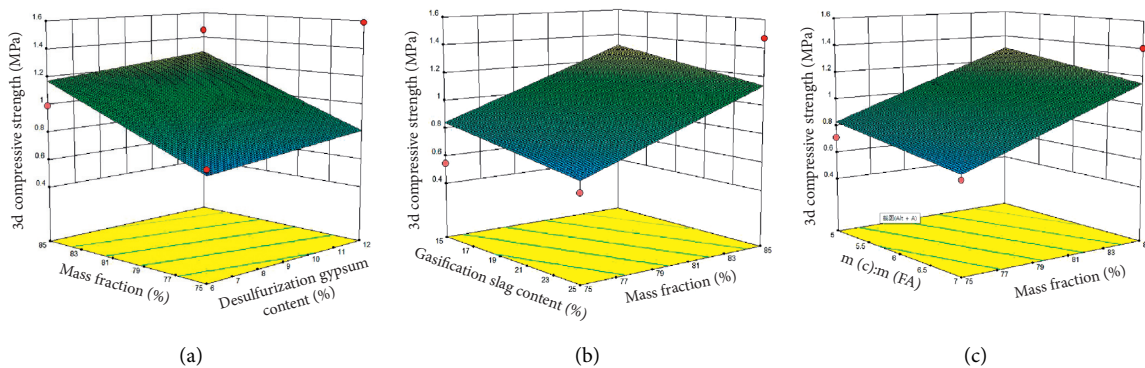


FIGURE 11: Analysis of interaction factors of 3 d uniaxial compressive strength response surface. (a) X_2X_4 interaction cloud. (b) X_1X_2 interaction cloud. (c) X_2X_3 interaction cloud.

the structure between the filling body and the filling body raw materials, we can clearly see that there are different quantities of hydration products in the filling body, which bond the interior of different raw materials together and have a certain compressive strength.

A variety of coal-based solid wastes are mixed and cemented. Compared with the original microstructure of

various solid wastes, the hydration products produced by hydration reaction under the action of cement are different. The early strength of the filling body is mainly due to the hydrolysis reaction and hydration reaction of cement, and the free water becomes bound water. Cement forms cementitious material through a series of chemical reactions to increase its strength. The chemical reaction of the active

components of gasification slag is slow, the hydration products formed in the early stage are less, and the strength is low. Abundant multiform hydration products can promote the compressive strength of filling materials, and the law of compressive strength is demonstrated.

In addition, in order to intuitively study the correlation law of fly ash, coal gasification slag, coal gangue, and cement content on the early compressive strength of the filled consolidated body, the contour map and response surface cloud map of compressive strength varying with factor levels are drawn according to the regression model, as shown in Figures 10 and 11, respectively. According to the results of variance analysis of single-factor and multifactor interaction in Table 5, the 3 d compressive strength of the filling body is very sensitive to the response of a single factor. Among them, the order of significance of single factor: solid mass fraction ($F = 11.85$, $P = 0.0021$) > gasification slag content ($F = 1.68$, $P = 0.2077$) > m(c): m(FA) ($F = 1.23$, $P = 0.2778$) > desulfurization gypsum content ($F = 0.68$, $P = 0.4178$).

5. Conclusion

- (1) SEM and XRD show that the gasification slag has mainly a honeycomb structure. The main component is SiO_2 . Most of the fly ash is of spherical structure, with finer particles. The particle size is mostly distributed below $200 \mu\text{m}$, and its composition is SiO_2 . Desulfurized gypsum is distributed in a thin-walled and columnar structure, and a small amount of desulfurized gypsum can promote the improvement of early compressive strength. The main component of furnace bottom slag is SiO_2 , which is distributed in the combined structure of pores and blocks, and the maximum particle size can reach 25 mm, of which the proportion of furnace bottom slag below 2.5 mm is 56.5%. The main components of coal gangue and cement are SiO_2 and Ca_3SiO_5 , respectively. In addition, the particle size of 2.5~5 mm coal gangue and cement accounting for 80.8% is mostly distributed below $100 \mu\text{m}$, the overall particle size is small, the pore matching effect is better after mixing, and the microstructure of cement is significantly different from that of a variety of solid wastes.
- (2) In view of the combination of bulk coal-based solid waste disposal and green filling mining in the Ningdong mining area, according to experience, 29 groups of proportioning schemes with four factors and three levels of mass fraction (X_1), gasification slag content (X_2), m(c): m(FA) (X_3), and desulfurization gypsum content (X_4) are designed by using the interface response method. The flow characteristics and intensity characteristics of each group are analyzed. The mix proportion of 29 groups of filling materials is divided into high and low uniaxial compressive strength, and 13 groups of high-strength mix proportion are obtained, with the expansion of 200–250 mm. The compressive strength grade is 0.6–1.4 MPa, the flow characteristics and compressive strength characteristics of filling materials are analyzed together, the inclined ladder area obtained by uniaxial compressive strength and expansion is acquired, and six groups of optimal proportion schemes are obtained. At the same time, it is concluded that the compressive strength of filled test blocks at different ages increases with the increase in age, and the higher the mass fraction, the higher the compressive strength. The microscopic test of typical filling test blocks is carried out by SEM. Under the action of cement, the hydration products produced by hydration reaction are different. Meanwhile, a small increase in the content of desulfurized gypsum can significantly improve the cementation performance of the cement. The abundance of rod and flocculent hydration products promotes the compressive strength of filling materials. The law of compressive strength is demonstrated, which shows that it is more reliable and stable when used in coal mine paste filling.
- (3) Comprehensive analysis results show that combined with the response surface method, a single factor has a significant effect on the early compressive strength of the consolidated body at the age of 3 d. The order of significance of each factor is solid mass fraction > gasification slag content > m(c): m(FA) > desulfurization gypsum content. The optimal proportioning scheme is obtained through the design, analysis, and prediction of the central group. The mass fraction is 84%, C: FA is 1 : 5, the content of gasification slag is 15%, the content of desulfurization gypsum is 7%, the content of coal gangue is 10%, and the content of furnace bottom slag is 5%. The supplementary experimental results show that σ_{3d} is 1.35 MPa and the expansion is 200 mm. It provides basic parameters for large-scale utilization of coal-based solid waste, especially gasification slag.

Data Availability

The data that support the findings of this study are available from the corresponding author upon reasonable request.

Conflicts of Interest

The authors declare that they have no conflicts of interest.

Acknowledgments

This work was supported by the National Key Research and Development Program of China (2019YFC1904300), the Institute of Energy, Hefei Comprehensive National Science Center under Grant Nos. GXXT-2020-008 and IE-KYXM-015, the University Synergy Innovation Program of Anhui Province (GXXT-2021-017), and the Basic Research on Underground Utilization of Coal Gangue Based Functional Materials (52130402).

References

- [1] Q. Q. Qian, F. R. Kang, K. Y. Zhang, X. Zhang, S. L. Wang, and X. Y. Liu, "Research Progress on ecological utilization of coal based solid waste," *Journal of Yulin University*, vol. 31, no. 6, pp. 57–62, 2021.
- [2] T. Wei and L. X. Wu, "Restrictive factors and suggestions for the development of modern coal chemical industry in Ningxia," *Research on coal economy*, vol. 41, no. 4, pp. 65–69, 2020.
- [3] X. Y. Han and R. A. Liu, "Study on comprehensive utilization, Storage and Disposal Countermeasures of Industrial Solid Waste in East Base," *Resource conservation and environmental protection*, vol. 5, pp. 66–67, 2015.
- [4] Y. S. Tang, L. F. Zhang, and H. Y. Lv, "Experimental study on Optimization of filling material ratio for preparation of coal based solid waste," *Journal of Mining Science*, vol. 4, no. 4, pp. 327–336, 2019.
- [5] S. J. Wang, "Analysis on present situation and application trend of comprehensive utilization of ash and slag in Ningdong," *Energy Technology*, vol. 18, no. 8, pp. 93–95, 2020.
- [6] X. J. Huo and C. Lu, "Influence of mineral composition and fineness of Portland cement on durability of concrete," *People's Yangtze River*, vol. 51, no. S2, pp. 294–296, 2020.
- [7] B. Bai, Q. Nie, Y. Zhang, X. Wang, and W. Hu, "Cotransport of heavy metals and SiO₂ particles at different temperatures by seepage," *Journal of Hydrology*, vol. 597, Article ID 125771, 2021.
- [8] B. Bai, G.-C. Yang, T. Li, and G.-S. Yang, "A thermodynamic constitutive model with temperature effect based on particle rearrangement for geomaterials," *Mechanics of Materials*, vol. 139, Article ID 103180, 2019.
- [9] MOHURD, *JGJ/T 70-2009, "Standard for test methods for basic properties of building mortar"*, Ministry of Housing and Urban-Rural Development, Beijing, China, 2009.
- [10] Z. D. Cui and H. H. Sun, "Preparation and properties of coal gangue cementitious paste like filling material," *Journal of coal*, vol. 35, no. 6, pp. 896–899, 2010.
- [11] Y. X. Wang and Y. C. Yin, "Solid waste in the "Golden Triangle" of energy and chemical industry has become a treasure, starting the "turnaround" of ecological governance," *Science and Technology Daily*, vol. 6, 2021.
- [12] M. G. Qian, J. L. Xu, and X. X. Miu, "Green mining technology of coal mine," *Journal of China University of Mining and Technology*, vol. 4, pp. 5–10, 2003.
- [13] C. Z. Zhao, H. Q. Zhou, J. B. Bai, and H. Qiang, "Analysis of factors affecting the strength of paste filling materials," *Journal of Liaoning Technical University*, vol. 6, pp. 904–906, 2006.
- [14] Q. W. Sun, H. Zhu, and Z. L. Cui, "Preparation and properties of fly ash coal gangue based cemented filling material," *Chinese Journal of Safety Science*, vol. 22, no. 11, pp. 74–80, 2012.
- [15] A. X. Wu, Y. Wang, and H. J. Wang, "Present situation and trend of paste filling technology," *Metal Mine*, vol. 7, pp. 1–9, 2016.
- [16] K. Cheng, B. G. Yang, B. G. Zhang, D. Li, J. Yang, and R. Zhang, "Present situation and development direction of filling mining technology in coal mines in China," *Coal Technology*, vol. 37, no. 3, pp. 73–76, 2018.
- [17] Y. F. Dou, F. Liu, and W. H. Zhang, "Comparative analysis of response surface modeling methods," *Journal of Engineering Design*, vol. 5, pp. 359–363, 2007.
- [18] L. Li, S. Zhang, Q. He, and X. B. Hu, "Application of response surface method in experimental design and optimization," *Laboratory research and exploration*, vol. 34, no. 8, pp. 41–45, 2015.
- [19] S. L. Liu, G. C. Li, G. L. Liu et al., "Optimization of proportion of slag based solid waste cementitious materials based on response surface methodology," *Silicate Bulletin*, vol. 40, no. 1, pp. 187–193, 2021.
- [20] C. Zhang, X. L. Wang, S. G. Li, C. Liu, J. H. Xue, and H. Liu, "Optimization of modified alkali liquor ratio for hydrogen sulfide treatment in Coal Mine Based on response surface method," *Journal of coal*, vol. 45, no. 8, pp. 2926–2932, 2020.

Research Article

Influence of Multistage Target Temperature and Cyclic Loading/Unloading on the Permeability of Polypropylene Fiber Concrete

Peishan Cen,¹ Erjian Wei ,² and Kunyun Tian ³

¹School of Construction Engineering, Zhengzhou Shengda University, Zhengzhou, Henan, China

²School of Resources and Environmental Engineering, Wuhan University of Science and Technology, Wuhan, Hubei, China

³School of Resource and Security Engineering, Henan University of Engineering, Zhengzhou, Henan, China

Correspondence should be addressed to Erjian Wei; weierjian@wust.edu.cn and Kunyun Tian; tky1153@163.com

Received 15 February 2022; Revised 8 March 2022; Accepted 10 March 2022; Published 25 March 2022

Academic Editor: bing bai

Copyright © 2022 Peishan Cen et al. This is an open access article distributed under the Creative Commons Attribution License, which permits unrestricted use, distribution, and reproduction in any medium, provided the original work is properly cited.

Due to the combined effect of temperature and cyclic loading and unloading, the gas permeability of polypropylene fiber reinforced concrete structures changes during service. However, the current gas permeability test of polypropylene fiber reinforced concrete is based on a single influencing factor or a single test condition (monotonic loading), and the test conditions are quite different from the actual working conditions of the structure. To explore the permeability of polypropylene fiber reinforced concrete under cyclic loading and unloading under the influence of temperature, based on the stress principle that the specimen does not have structural damage and according to the steady-state equation of Darcy's law, the Cembureau method is adopted. The gas permeability of polypropylene fiber reinforced concrete under single loading and unloading and multistage cyclic loading and unloading at eight target temperatures is tested by the triaxial permeability test system. The results showed that (1) when the target temperature was $120^{\circ}\text{C} < T \leq 200^{\circ}\text{C}$ and $200^{\circ}\text{C} < T \leq 280^{\circ}\text{C}$, the fiber experienced two stages of "softening, melting-cooling recovery" and "melting and absorption," which caused damage to the matrix pore structure. The gas permeability at 200°C and 280°C was 246 times and 350 times that at 22°C , respectively. (2) The damage degree of the matrix strength structure increases during cyclic loading and unloading, and the permeability loss rate during cyclic loading and unloading is 1.24~1.57 times that of single loading and unloading. (3) The high target temperature leads to pore structure damage of the matrix, which not only affects the permeability of the matrix but also affects the strength structure of the matrix. When the stress ratio $R \geq 0.37$, the pore structure damage and the strength structure damage of the specimen are superimposed, resulting in the antipermeability effect of the specimen developing in the unfavorable direction. The test simulated the actual working conditions of polypropylene fiber reinforced concrete, providing a reference for building fire protection, seismic design or postdisaster evaluation.

1. Introduction

Concrete and naturally formed rock and soil are macroscopic combinations of discrete particles, which are all porous media. In actual working conditions, they are inevitably affected by the coupling of many factors, such as heat, water and stress. The evolution of influencing factors is closely related to the particle rearrangement [1], which has an important influence on the structural strength and stiffness. In recent years, polypropylene fiber reinforced concrete (PPFRC) has been widely used because of its low permeability at room temperature [2–4] and good fire and explosion resistance [5, 6]. However, the decrease in strength

and increase in permeability after high-temperature damage have adverse effects on durability, which has attracted widespread attention. At present, research on the permeability of PPFRC mainly focuses on the load effect and high-temperature effect.

Relevant studies on the permeability of PPFRC under load show that the antipermeability effect of PPFRC comes from the crack resistance of fibers, which is mainly manifested in the inhibition of the generation and development of cracks in concrete by the bridging effect of fibers and the improvement of permeability resistance [7–9]. In 1963, Romualdi and Batson of the United States proposed the fiber crack arrest theory, also known as the fiber spacing theory. It

is believed that the existence of fibers reduces the propagation force at the crack tip and hinders the development of cracks, and this hindering effect is related to the fiber spacing; the smaller the fiber spacing is, the more obvious the hindering effect is [10–12]. The theory emphasizes the limiting effect of fiber spacing (content) on crack propagation in the matrix but ignores the composite reinforcement effect of the fiber itself, the bond strength between the fiber and matrix and the influence of fiber length on the reinforcement effect of the matrix, so it can only qualitatively explain the reinforcement principle of the fiber. On the basis of fiber crack arrest theory, the introduction of the linear elastic fracture mechanics principle and comprehensive consideration of fiber length, the self-composite effect and bond strength within the matrix are the main theoretical bases for the current study of fiber crack arrest enhancement. In recent years, it has been found that crack propagation is limited and impermeability is improved due to the presence of fiber strength and bonding force after concrete damage [13]. At the same time, in the recovery stage after the load damage of the concrete matrix, the fiber can also improve the crack recovery rate and reduce the permeability coefficient of concrete after cracking [14]. However, the greater the fiber content is, the better the crack resistance and impermeability. There is a threshold for different water cement ratio fiber contents, and the threshold range is generally $0.5 \text{ kg/m}^3 \sim 1.5 \text{ kg/m}^3$ [7, 15–18]. In addition, the impermeability of concrete is greatly related to the load stress. In general, when the stress ratio is less than 0.5, the permeability of the matrix decreases with increasing stress. When the stress ratio exceeds its value, the matrix structure is easily damaged, and the permeability is greatly increased [19–22].

Relevant studies on the permeability of PPFRC after temperature action show that the voids and holes generated in the matrix after the “softening-cooling recovered” and “melting-absorption” of polypropylene fibers at high temperature are important reasons for the increase in permeability [23–30]. However, there are different views on the mechanism of pore formation after polypropylene fiber melting. Kalifa et al. [31] showed that polypropylene fibers were absorbed by the concrete matrix after melting through the “water drop” test, but the test results were greatly affected by the surface treatment degree of the specimen. Khoury [32] pointed out that the viscosity of polypropylene fiber after melting is very high and the molecular diameter (more than 14 nm) is much larger than the pore size of concrete silicate gel or solid-solid distance (1.8 nm) [33], and the possibility of absorption by the concrete matrix is very small. Bosnjak et al. [28] found through a heating test of PPFRC specimens that the PP fiber had no obvious change after the specimen was cooled by continuous heating for 20 min, and the PP fiber was absorbed after continuous heating for 6 h and 2 d. The longer the heating time was, the more obvious the absorption effect was. In addition, the free water and the bound water in the matrix have complex transformation effects at different temperatures [34]. The water loss of concrete materials under the influence of high temperature [35, 36] will lead to changes in pore structure and size as well

as the generation of microcracks [37] and adversely affect the permeability resistance of concrete [38].

The above research explains the action mechanism of polypropylene fiber on concrete permeability under load and temperature. The research results provide an important reference for the engineering application of PPFRC and the fire prevention and seismic design of buildings. However, the above studies are based on a single influencing factor or a single test condition (monotonic loading), and concrete structures are often subjected to complex stress and multiple factors during service. For example, airport runways are subjected to the impact of aircraft landing, coastal buildings are subjected to the impact of waves, and concrete structures in earthquake-prone areas are subjected to cyclic loading and unloading and structural damage after fire. It is more realistic to study the permeability and damage mechanism of PPFRC under cyclic loading and unloading under the influence of temperature.

In view of this, the authors, on the basis of previous research, combined with the actual working conditions, made the PPFRC test block and imposed multilevel target temperatures on the test block. The three-axis permeability test system was used to measure the permeability of PPFRC during single loading and unloading and multistage cyclic loading and unloading. The evolution characteristics of the gas permeability of PPFRC under multistage target temperatures and cyclic loading and unloading conditions are studied.

2. Design of Experiments

The test was carried out by eight target temperatures and two loading and unloading methods. The test process is shown in Figure 1.

2.1. Test Raw Materials and Ratio. The ordinary Portland cement used in the test was produced by Henan Mengdian Group Cement Co., Ltd. and is labeled as P-O 42.5R. The fine aggregate is natural river sand, the fineness modulus is 2.70, and the apparent density is 2562 kg/m^3 . The coarse aggregate is continuous graded gravel with a particle size of 5–20 mm and an apparent density of $2,622 \text{ kg/m}^3$. The test water was ordinary tap water. Polypropylene fiber used for test production was procured from Langfang Shuangyuan Energy Saving Technology Co., Ltd. The length was 15 mm, the diameter was 0.5 mm, the tensile strength was greater than 450 MPa, the melting point was 189°C , and the dosage was 0.9 kg/m^3 . The PPFRC test block volume is $200 \text{ mm} \times 200 \text{ mm} \times 200 \text{ mm}$, and the strength grade is C30. The proportion is shown in Table 1.

2.2. Test System. The triaxial permeability test system for the test was produced by Jiangsu Tuochuang Scientific Research Instrument Co., Ltd., as shown in Figures 2 and 3, which mainly includes three system modules: a three-axis loading servo control system, gas (liquid) flow measurement system, and square block placement cavity.

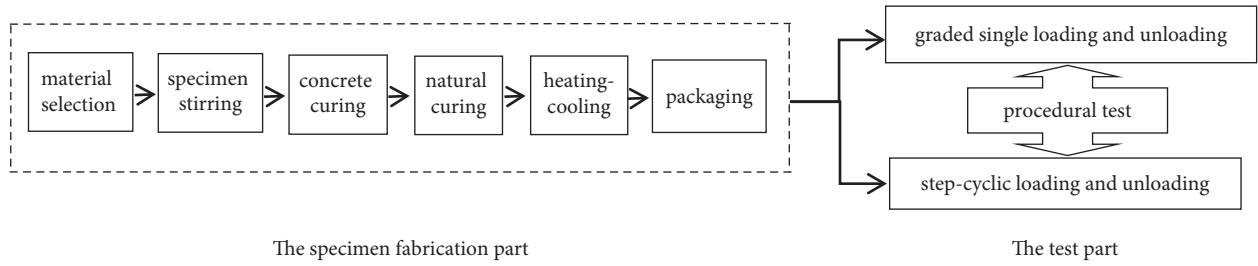


FIGURE 1: Test flow chart.

TABLE 1: PPFRC ratio table.

Strength grade	Cement (kg/m ³)	Water (kg/m ³)	Sand (kg/m ³)	Gravel (kg/m ³)	Fiber (kg/m ³)
C30	360	180	673.4	1146.6	0.9

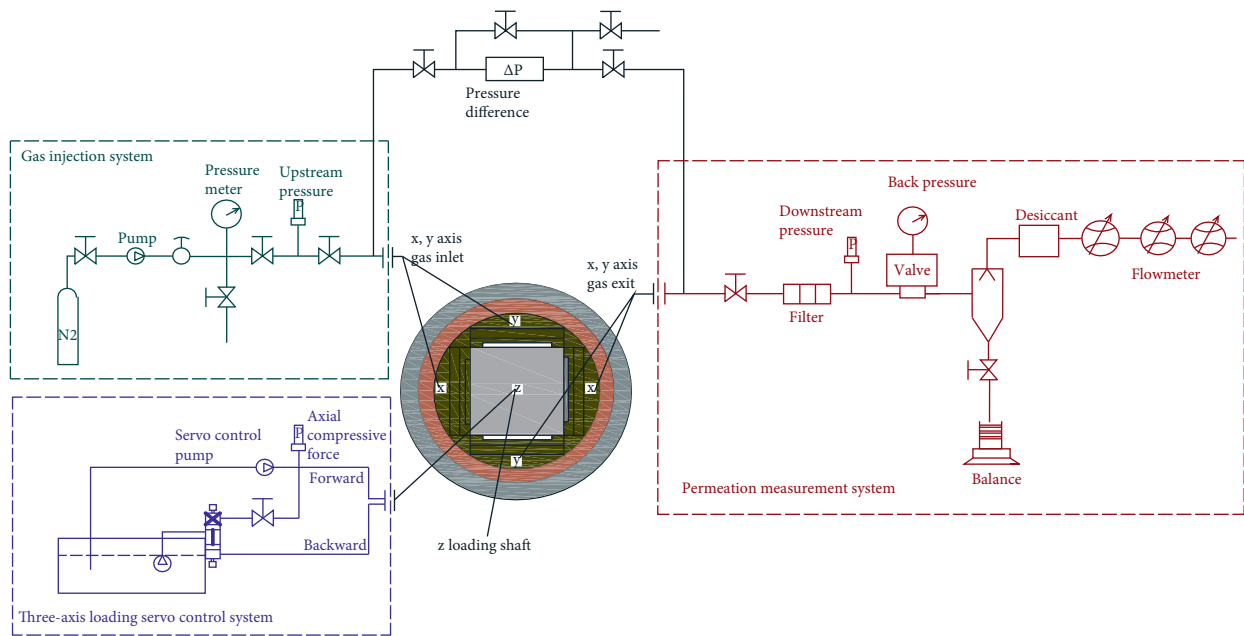


FIGURE 2: Structure principal diagram of the triaxial loading permeability test system.

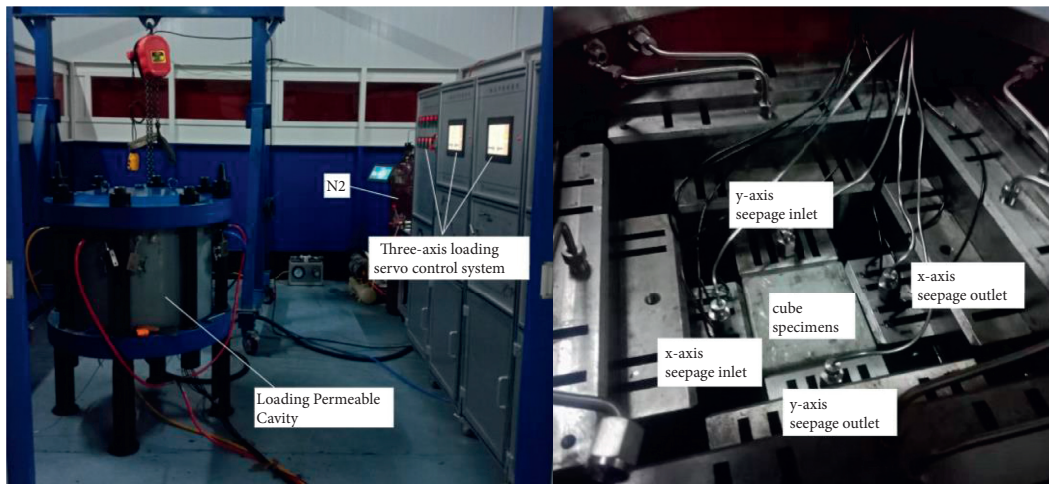


FIGURE 3: Triaxial loading seepage test device.

- (1) Three-axis loading servo control system: piston loading, self-balancing reaction structure; three-axis independent servo system plus central digital system control, control accuracy: $\geq \pm 0.1\%$ f.s. ① Three-axis loading unit: each axis contains two main loading hydraulic cylinders, with a maximum load of 1000 kN, a maximum stroke of 50 mm, and with a measurement control accuracy reaching 0.1% of the maximum force value. It can be steadily loaded for a long period. A Swiss trafag pressure sensor was used. The rated output voltage of the sensor was 2.0 mV/V $\pm 2.5\%$, creep $\pm 0.1\%$, nonlinearity $\pm 0.3\%$, hysteresis $\pm 0.3\%$, and the temperature compensation range was $-10^\circ\text{C} + 40^\circ\text{C}$. ② Servo control system: the Japanese Fuji servo control system is adopted to meet constant pressure and constant rate loading. The loading rate is 0.01~1 kN/s, maximum loading pressure is 40 MPa, control precision is 0.01 MPa, resolution $\leq 0.1\%$, and hysteresis $\leq 0.2\%$.
- (2) Gas flow measurement system: the steady-state method was used to control the flow, with a pressure 0~10 MPa, and permeability coefficient measurement range $10^{-14} \text{ m}^2 \sim 10^{-22} \text{ m}^2$. During the test, it is necessary to cooperate with the triaxial loading cylinder, encapsulate the specimen with the upper and lower pressure heads with seepage channels in the triaxial loading cylinder, and apply a certain amount of hydrostatic pressure (greater than the maximum osmotic pressure of at least 0.5 MPa) before the beginning of the permeability test to ensure that the packaging material was close to the specimen wall.
- (3) Square block placement cavity: three cube specifications are 300 mm, 200 mm, and 100 mm. There are three sets of clamps, and the clamp contains the corresponding rigid cushion block, which is convenient for changing the size of the test sample; an encapsulation pressure of 0~20 MPa is used to ensure that the three axial seals are reliable.

2.3. Heating and Sealing of Specimens. The test block was made according to Table 1; the standard curing time was 28 days. At the end of the curing period, the specimens were subjected to indoor natural air drying for one month. The specimen was heated by a box-type resistance furnace, and the target temperatures were 22°C (room temperature), 40°C , 80°C , 120°C , 160°C , 200°C , 240°C and 280°C . After thermal stability for 6 h, the specimen was removed and cooled naturally to room temperature and then packaged for loading and unloading gas permeability tests. To prevent angular damage to the specimen during the loading process, the gas seepage channel is changed. The Sealing Test Specimen with Angle Copper Strip Fixed Edge Glass Adhesive is shown in Figure 4.

2.4. Test Scheme

- (1) Principle of the seepage test: the steady-state equation based on Darcy's law adopts the Cembureau



FIGURE 4: Edge angle seal of PPFRC.

method. Under a certain pressure difference on both sides of the sample, the gas permeability is related to the viscosity coefficient, flow distance and flow rate, and the permeability is calculated according to formula (1) [39].

$$K_g = \frac{2L\mu Q_0 P_0}{A(P_1^2 - P_2^2)} \quad (1)$$

In the formula, K_g is the gas permeability of the PPFRC test block, m^2 ; μ is the viscosity of the test gas, $\text{S}\cdot\text{N}/\text{m}^2$; Q_0 is the gas flow through the specimen, m^3/s ; P_0 is atmospheric pressure under test conditions, MPa; P_1 is inlet gas pressure, MPa; P_2 is the outlet gas pressure, MPa; A is the square sample area, m^2 ; and L is the length of specimen, m .

- (2) Test scheme: the uniaxial compression test scheme was adopted, with a confining pressure of 0, the compression axial is z -axis, and the loading and unloading rate is 0.1 kN/s. Nitrogen was selected as the permeable gas, the inlet was on one side of the x - and y -axes, the inlet pressure was 1.0 MPa, the outlet was on the other side of the x - and y -axes, and the outlet pressure was 0.5 MPa. The specimens were encapsulated by hydrostatic water with a pressure of 1.5 MPa. To ensure the permeability test effect and prevent damage to the specimen structure [40, 41], the maximum effective stress of the specimen is $0.5f_c$ (f_c is the measured peak stress of the PPFRC specimen). The test was divided into two groups, and eight specimens in each group were subjected to different target temperatures. In the first group, the specimen was subjected to 8-stage single loading, and the permeability of the specimen at each loading level was tested. After loading to $0.5f_c$, the specimen was unloaded to $0.03f_c$, and then the permeability was tested again. The second group of specimens was subjected to 8-stage cyclic loading and unloading (the permeability under load state was tested after loading the n th stage, then the permeability was unloaded to $0.03f_c$, then the permeability was tested again, and the cyclic loading and unloading was carried out successively until the 8-stage loading and unloading was

TABLE 2: Test results of PPFRC loading permeability under different temperatures.

State of stress	Stress ratio (R)	Permeability ($\text{kg}/\times 10^{-17} \text{ m}^2$)							
		22°C	40°C	80°C	120°C	160°C	200°C	240°C	280°C
Graded cyclic loading	0.03	1.85	2.31	8.02	29.65	127.43	397.21	513.52	532.75
	0.10	1.71	2.13	7.46	27.79	119.11	373.92	491.66	512.42
	0.17	1.56	1.96	6.90	25.71	109.45	350.32	462.12	487.28
	0.23	1.41	1.78	6.35	23.68	101.04	330.75	436.64	463.87
	0.30	1.27	1.60	5.78	21.76	93.11	313.45	414.04	441.54
	0.37	1.16	1.44	5.27	19.78	86.32	298.34	403.91	433.56
	0.43	1.07	1.32	4.92	18.31	83.11	290.25	398.36	428.74
	0.50	1.01	1.26	4.77	17.65	81.71	287.27	395.82	425.74
Graded single loading	0.03	1.85	2.31	8.02	29.65	127.43	397.21	513.51	532.70
	0.10	1.69	2.10	7.41	27.38	118.11	367.92	483.66	506.42
	0.17	1.53	1.91	6.77	25.22	107.95	343.32	456.12	479.28
	0.23	1.37	1.72	6.14	23.01	99.04	319.75	428.64	453.07
	0.30	1.22	1.54	5.51	20.89	91.11	301.45	404.04	429.54
	0.37	1.08	1.37	5.00	18.87	84.32	286.34	390.01	414.56
	0.43	0.97	1.23	4.59	17.31	80.11	278.25	380.36	404.74
	0.50	0.90	1.16	4.35	16.43	76.71	271.27	371.82	397.74

TABLE 3: Test results of unloading permeability of PPFRC under different temperatures.

State of stress	Difference of loading-unloading stress ratio	Permeability ($\text{kg}/\times 10^{-17} \text{ m}^2$)							
		22°C	40°C	80°C	120°C	160°C	200°C	240°C	280°C
Graded cyclic unloading	0.07	1.82	2.27	7.86	28.77	117.27	360.32	482.18	499.47
	0.13	1.80	2.23	7.71	28.21	114.82	350.32	470.65	486.40
	0.20	1.76	2.19	7.55	27.62	109.76	337.75	450.97	466.54
	0.27	1.73	2.14	7.35	26.72	105.07	322.20	430.51	445.58
	0.34	1.69	2.08	7.16	25.97	101.81	311.33	419.32	432.05
	0.40	1.65	2.04	6.99	25.13	99.87	302.57	402.02	416.76
	0.47	1.63	2.01	6.90	24.72	98.74	291.30	391.50	401.42
Single unloading	0.47	1.71	2.12	7.25	26.54	111.92	330.70	417.15	426.99

completed). Relevant data were automatically collected, calculated and saved in the experiment, with a data acquisition frequency of 3 seconds. Each loading and unloading stress and measurement residence time was not less than 5 min, and airflow stability was ensured for more than 3 min.

The effective stress of the specimen is calculated according to formula (2) [42], and the stress ratio is calculated according to formula (3).

$$\sigma_e = \sigma_z - \frac{1}{2} (P_1 - P_2), \quad (2)$$

$$R = \frac{\sigma_e}{f_c}. \quad (3)$$

In the formula, σ_e denotes the effective stress, MPa; σ_z is the z axial stress, MPa; R is the specimen stress ratio; and f_c is the peak stress of the specimen under uniaxial compression, MPa.

3. Experiment Results and Analysis

3.1. Test Results

- (1) Test results: the test results are shown in Tables 2 and 3.

The calculation of the data in Tables 2 and 3 shows that the permeability (average) of the specimens at 200°C and 280°C is 246 and 350 times that at 22°C, respectively, indicating that the increase in temperature has a negative impact on the permeability resistance of the specimens. Under the loading conditions, the permeability of the specimen in the cyclic loading and unloading process is 1.00~1.12 times that in the single loading and unloading process, indicating that the cyclic loading and unloading conditions have a negative impact on the permeability resistance of the specimen. When the stress ratio difference is 0.47, the permeability of the specimen in the single unloading process is 1.05~1.14 times that in the cyclic loading and unloading process, indicating that the recovery degree of the specimen under single loading and unloading is higher than that under cyclic loading and unloading.

- (2) R-kg curve: after fitting the stress ratio and permeability data in Table 2, the R-kg relationship curve is obtained, as shown in Figure 5.

Figure 5 shows that ① the R-kg relation curve is similar under the two stress conditions. The R-kg relation curve is steep in the early stage of loading and gentle in the later stage of loading. This indicates

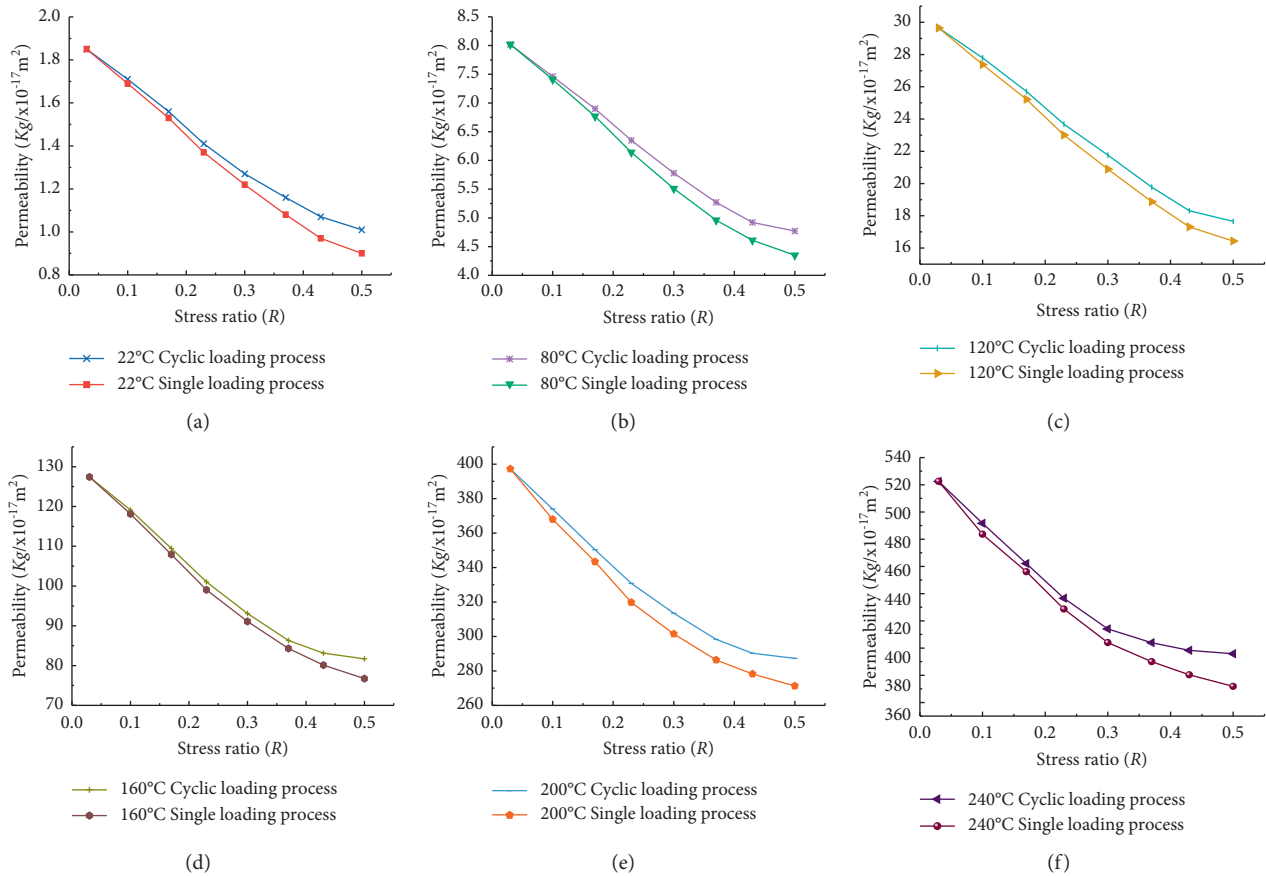


FIGURE 5: Evolution characteristics of the permeability of the specimen during the loading process.

that the permeability decreases significantly with increasing stress at the early stage of loading, and the stress is beneficial to the permeability resistance of the specimen. At the later stage of loading, the decline rate decreases or even remains unchanged with increasing stress. At this time, the stress develops in a disadvantageous direction to the permeability resistance of the specimen. ② With the increase in the target temperature of the specimen, the length of the linear section decreases, and the gentle section increases in the stress period. This indicates that the “window” of the stress beneficial to the impermeability of the specimen becomes narrower after the influence of high temperature, and the specimen develops in the unfavorable direction of impermeability.

(3) T-kg curve: after fitting the temperature (T) and permeability (average) in the loading process of the specimen in Table 2, the T-kg relationship curve is obtained, as shown in Figure 6.

Figure 6 shows that, under the two stress conditions, the change in kg with increasing T experienced three stages. In the first stage, $T < 120^{\circ}\text{C}$, the T-kg linear slope is low, and the increment is small. In the second stage, $120^{\circ}\text{C} \leq T \leq 200^{\circ}\text{C}$, the T-kg myopia exponential function relationship, kg significantly increases. In the third stage, $200^{\circ}\text{C} < T \leq 280^{\circ}\text{C}$,

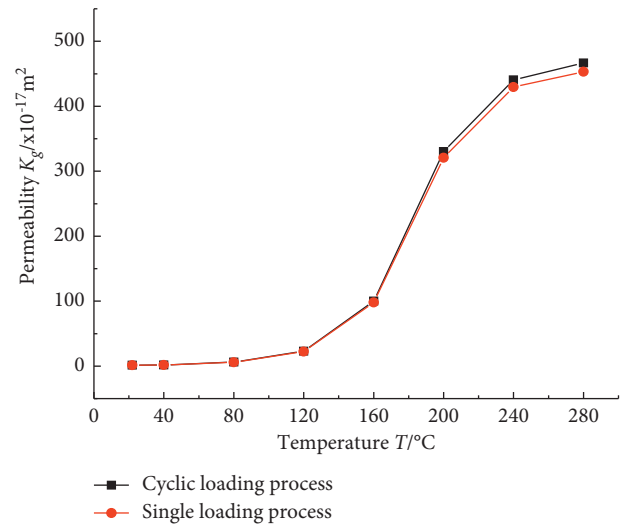


FIGURE 6: Evolution characteristics of permeability under temperature influence.

the increment of kg decreased, and the T-kg curve finally tended to be gentle. This shows that the temperature between $120^{\circ}\text{C} \sim 200^{\circ}\text{C}$ has a significant impact on the seepage rate of the specimen. When the temperature is higher than 240°C , the fiber has completely melted, the total amount of cavity formed by the fiber in the matrix does not increase, and its

permeability tends to be stable, so the third stage of the T-kg curve is flat.

The above results show that the increase in target temperature and cyclic loading and unloading conditions have adverse effects on the impermeability of the specimen.

3.2. Analysis of Permeability Characteristics

3.2.1. Permeability Decline Rate. The permeability change rate is closely related to the stress conditions and temperature factors. The calculation of the permeability change rate of the specimen can intuitively reflect the influence of the two factors. The permeability parameters in Table 2 are calculated according to formula (4) to obtain the permeability decline rate of the specimen. The detailed data are shown in Table 4.

$$k_D = \frac{(k_i - k_{i+1})}{k_i} \times 100\%. \quad (4)$$

In the formula, k_D is the permeability decline rate of the specimen, %; k_i is the permeability of the specimen under stage i loading, m^2 ; and k_{i+1} is the permeability of the specimen under stage “ $i+1$ ” loading, m^2 .

Table 4 shows that under two stress states, k_D undergoes three stages of “Sudden Change” with temperature. The temperature ranges of the three mutations were $40^\circ\text{C} \leq T \leq 120^\circ\text{C}$, $120^\circ\text{C} < T \leq 200^\circ\text{C}$ and $200^\circ\text{C} < T \leq 280^\circ\text{C}$, and the stress ratios were 0.5, 0.43 and 0.37, respectively. It can be seen that the k_D “Sudden Change” stress ratio of the specimen moved forward with increasing temperature.

According to the literature research [7–9, 23–30] conclusions combined with the analysis of experimental results, the permeability of polypropylene fiber concrete under the influence of stress and temperature is mainly related to three factors. First are the physical bonding properties of fiber materials and concrete. Second, the damage degree of the fiber pore structure is affected by temperature. Third, the damage degree of stress affects the strength structure of the specimens.

In the first stage, the target temperature is relatively low, the thermal deformation of the polypropylene fiber is small, and the fiber is closely integrated with the matrix, as shown in Figure 7(a). The low-temperature effect causes little damage to the pore structure of the matrix, and the matrix strength of the specimen is high. At this time, the permeability is mainly dominated by pores and microcracks in the matrix. In reaction to pressure, the two produce a compression effect [22, 43], and the permeability and stress decrease linearly. Due to the good stability of the fiber and the large ductility of the matrix, when the stress continues to increase, the response time of the two to the stress is close to or reaches the limit state (large elastic-plastic deformation), and the straight line segment of the R-kg curve is longer, as shown in Figures 5(a)–5(c). Therefore, the stress value is large when the permeability is “Sudden Change.”

In the second stage, the target temperature is the softening and melting stage of the polypropylene fiber. After cooling, the recovered fiber is separated from the matrix and

generates voids, resulting in different degrees of damage to the pore structure of the matrix, increasing the gas permeability channel and reducing the matrix strength [28, 29], as shown in Figure 7(b). Due to the increase in the permeability channel, the matrix permeability is significantly higher than that in the first stage, as shown in Figure 6. Due to the damage to the pore structure of the matrix, the adhesion between the fiber and the matrix fades, resulting in a decrease in the strength and ductility of the matrix. When the stress response of the three is close to or reaches the limit state, the duration is shortened (the elastic-plastic deformation decreases), and the linear section of the R-kg curve is shortened, as shown in Figures 5(d) and 5(e). Therefore, the stress value decreases when the permeability is “Sudden Change.”

The third stage is the high-temperature influence stage. The microstructure study shows that the polypropylene fiber disappears in the matrix after high temperatures above 200°C , and voids are formed after cooling [31, 44]. The macroscopic results of the specimen after high temperature are consistent with the microscopic results, as shown in Figure 7(c). At this time, the matrix pore structure is greatly damaged, and the strength is significantly reduced. Compared with the first three kinds of fractures, this large cavity is not sensitive to the stress response, resulting in higher permeability than the first two stages, as shown in Figure 6. Due to the large damage degree of the matrix pore structure, the fiber disappears, the matrix becomes brittle material, and the strength decreases to the minimum. In reaction to stress, the elastic-plastic deformation of the matrix is the smallest. At this time, the period of pores and voids in the matrix to reach the limit state is shortened again, and the straight line segment of the R-kg curve is shortened again, as shown in Figure 5(f). Therefore, the stress value decreases again when the permeability is “Sudden Change.”

3.2.2. Permeability Loss. The permeability loss rate can reflect the damage and recovery degree of the specimen after unloading. The smaller the permeability loss rate is, the lower the damage degree of the specimen and the higher the recovery degree. According to the data in Tables 2 and 3, the permeability loss rate of the specimen during unloading is calculated according to formula (5) [45, 46].

$$k_P = \frac{(k_1 - k_{i-U1})}{k_1} \times 100\%. \quad (5)$$

In the formula, k_P is the permeability loss rate; k_1 is the permeability of the specimen under the first stage loading, m^2 ; and k_{i-U1} is the permeability of the specimen under unloading of level i , m^2 .

The data in Table 5 show that k_P increases with increasing temperature and stress. The permeability loss rate of the loading and unloading stress ratio difference $R_D = 0.47$ was calculated. The permeability loss rate of the cyclic loading and unloading process was 1.24~1.57 times that of single loading and unloading. It can be seen that temperature rise and cyclic loading and unloading conditions have adverse effects on the impermeability of PPFRC.

TABLE 4: Permeability decline rate of the specimen during loading.

State of stress	Stress ratio (R)	Permeability decline rate ($k_D/\%$)							
		22°C	40°C	80°C	120°C	160°C	200°C	240°C	280°C
Cyclic loading process	0.10	8	8	7	6	7	6	6	5
	0.17	9	8	8	7	8	6	6	5
	0.23	10	9	8	8	8	6	6	5
	0.30	10	10	9	8	8	5	5	5
	0.37	9	10	9	9	7	5	2	2
	0.43	8	8	7	7	4	3	1	1
	0.50	6	5	3	4	2	1	1	1
Single loading process	0.10	9	9	8	8	7	7	7	6
	0.17	9	9	9	8	9	7	6	5
	0.23	10	10	9	9	8	7	6	5
	0.30	11	10	10	9	8	6	6	5
	0.37	11	11	9	10	7	5	3	3
	0.43	10	10	8	8	5	3	2	2
	0.50	7	6	5	5	4	3	2	2

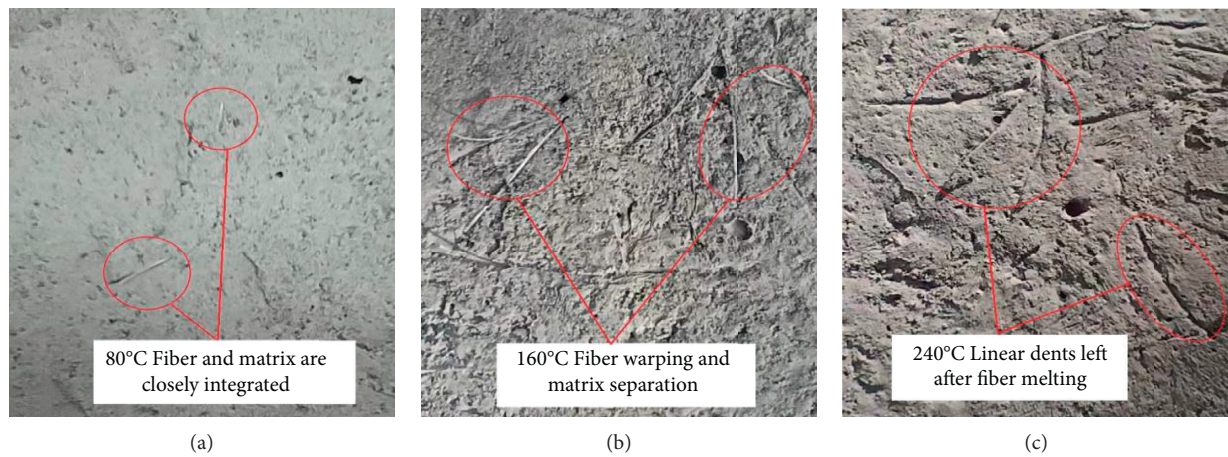


FIGURE 7: Changes in fiber in the matrix under different temperatures.

TABLE 5: Loss rate of unloading permeability of specimens.

State of stress	Difference of loading-unloading stress ratio (R_D)	Permeability loss rate ($k_P/\%$)							
		22°C	40°C	80°C	120°C	160°C	200°C	240°C	280°C
Cyclic nloading process	0.07	1.62	1.73	2.00	2.97	3.43	5.23	6.10	6.25
	0.13	2.70	3.46	3.87	4.86	5.44	7.86	8.35	8.70
	0.20	4.86	5.19	5.86	6.85	9.61	11.17	12.18	12.43
	0.27	6.49	7.36	8.35	9.88	13.47	15.26	16.16	16.36
	0.34	8.65	9.96	10.72	12.41	16.16	18.12	18.34	18.90
	0.40	10.81	11.69	12.84	15.24	17.76	20.42	21.71	21.77
	0.47	11.89	12.99	13.97	16.63	18.69	23.38	23.76	24.65
Single nloading process	0.47	7.57	8.23	9.60	10.49	12.17	16.74	18.77	19.84

Note. The difference between the loading and unloading stress ratio is denoted as R_D , which is equal to the difference between the stress ratio R_i and 0.03 at stage I loading.

The analysis shows that the unloading process of the specimen is not the inverse process of loading. At the early stage of loading, the specimen is in the elastic stage. When the stress is greater than the elastic limit A, the specimen enters the plastic working stage, the closure rate of

microgaps in the matrix is accelerated, and the matrix shape variable is increased. At this time, the matrix structure is partially damaged, the deformation of the specimen will not return to the original state when unloading, and there is deformation loss, as shown in Figure 8. After multistage

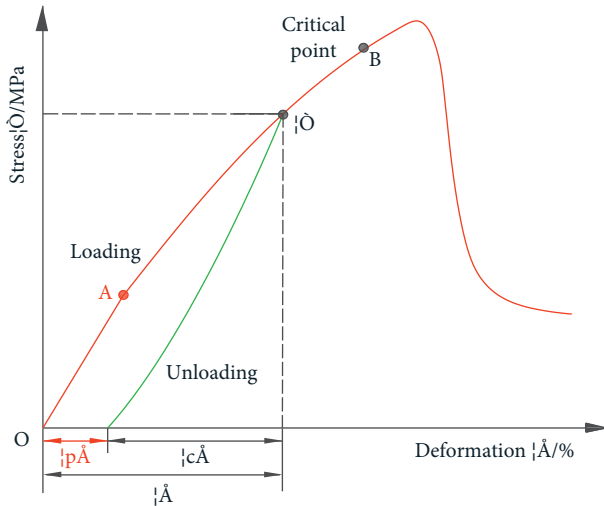


FIGURE 8: Stress-strain of the specimen during loading and unloading.

cyclic loading and unloading, the damage to the matrix strength structure increases [47], and the crack extends or increases, which adversely affects the impermeability of the specimen.

In addition, the average values of k_D and k_p of the specimens under cyclic loading and unloading conditions at $R \leq 0.34$ and $T \leq 120^\circ\text{C}$ were calculated and recorded as k_{D-LL} and k_{p-LL} , respectively. The average values of k_D and k_p of the specimens under cyclic loading and unloading conditions at $R \geq 0.37$ and $T \geq 160^\circ\text{C}$ were calculated and recorded as k_{D-HH} and k_{p-HH} , respectively. After comparison, it is found that the permeability decline rate of the specimen at low temperature and low stress is large ($k_{D-LL} = 8.26$), and the permeability loss rate is small ($k_{p-LL} = 4.88$). Under high temperature and high stress, the permeability decline rate of the specimen was small ($k_{D-HH} = 2.44$), and the permeability loss rate was large ($k_{p-HH} = 20.31$). The analysis shows that the high target temperature leads to damage to the matrix pore structure, which not only affects the permeability of the matrix but also affects the strength structure of the matrix. The pore structure damage and strength structure damage of the specimen are superimposed under the influence of high temperature and high stress conditions. After the superposition of the two, the failure of the pore structure accelerates the failure of the strength structure under high stress, makes the development of the matrix crack faster, and leads to the development of the matrix antipermeability effect in a disadvantageous direction.

4. Conclusions

- (1) When the influence temperature of the specimen is $120^\circ\text{C} \sim 280^\circ\text{C}$, the fiber undergoes two stages, "softening, melting-cooling recovery" and "melting and absorption," which cause damage to the matrix pore structure. The permeability of specimens at 200°C and 280°C is 246 times and 350 times that at 22°C , respectively.

- (2) Compared with single loading and unloading, cyclic loading and unloading have greater damage to the strength structure of the specimen, and the permeability loss rate of the latter is 1.24~1.57 times that of the former.
- (3) After the influence of high temperature, the pore structure damage and strength structure damage of the specimen are superimposed under high stress (stress ratio is between 0.37 and 0.5). The permeability loss rate of the specimen at high temperature and high pressure is 4.16 times that at low temperature and low pressure.
- (4) Although the test process simulates the working conditions of the PPFRC structure, there are still some differences between the test process and the real working conditions due to the limitations of the test equipment. For example, the difference between the heating mode of the resistance furnace and the heating mode of an open fire, as well as the difference between the independence of the heating and load processes of the specimen and the joint action of the two factors when the structure is subjected to fire, will cause changes in the permeability of the component. Therefore, the study of the permeability of components after fire or under the combined action of temperature and pressure is closer to the actual working conditions of the structure.

Data Availability

The data used to support the findings of this study are included within the article.

Conflicts of Interest

The authors declare that there are no conflicts of interest regarding the publication of this study.

Acknowledgments

The authors gratefully acknowledge the financial support from the National Natural Science Foundation of China (51604091), the Science and Technology Innovation Team Program of Henan Universities (22IRTSTHN009), and the Science and Technology Project of Henan Province for tackling key problems (222102320466).

References

- [1] B. Bai, R. Zhou, G. Q. Cai, W. Hu, and G. C. Yang, "Coupled thermo-hydro-mechanical mechanism in view of the soil particle rearrangement of granular thermodynamics," *Computers and Geotechnics*, vol. 137, no. 8, Article ID 104272, 2021.
- [2] C. Du, Y. S. Huang, and W. Sun, "Effect of polypropylene fiber on anti-cracking and anti-permeability properties of concrete," *Low Temperature Architecture Technology*, vol. 5, pp. 55-56, 2005.
- [3] G. S. Islam and S. D. Gupta, "Evaluating plastic shrinkage and permeability of polypropylene fiber reinforced concrete,"

- International Journal of Sustainable Built Environment*, vol. 5, no. 2, pp. 345–354, 2016.
- [4] M. Briffaut, F. Benboudjema, and L. D'Aloia, "Effect of fibres on early age cracking of concrete tunnel lining. Part I: Laboratory ring test," *Tunnelling and Underground Space Technology*, vol. 59, pp. 215–220, 2016.
- [5] R. Serrano, A. Cobo, M. Isabel Prieto, and M. Nieves González, "Analysis of fire resistance of concrete with polypropylene or steel fibers," *Construction and Building Materials*, vol. 122, pp. 302–309, 2016.
- [6] S. M. Liu and H. Y. Hu, "Study of mechanical and resistance to chloride ion penetration properties of hybrid polypropylene fiber reinforced concrete," *Engineering Journal of Wuhan University*, vol. 52, no. 2, pp. 131–138, 2019.
- [7] J. Q. Gong, W. Zheng, and W. J. Zhang, "Influence of shrinkage-reducing agent and polypropylene fiber on shrinkage of ceramic concrete," *Construction and Building Materials*, vol. 159, pp. 155–163, 2018.
- [8] M. R. Latifi, E. Biricik, and A. M. Aghabaglou, "Effect of the addition of polypropylene fiber on concrete properties," *Journal of Adhesion Science and Technology*, vol. 36, no. 4, pp. 345–369, 2022.
- [9] Y. Zhang, *Study on the Mechanical Properties and Damage and Failure Morphology of Polypropylene Fiber Reinforced concrete*, Xi'an University of Technology, Xi'an, China, 2019.
- [10] J. P. Romualdi and G. B. Batson, "Behavior of reinforced concrete beams with closely spaced reinforcement," *ACI Structural Journal*, vol. 60, no. 6, pp. 775–789, 1963.
- [11] J. P. Romualdi and G. B. Batson, "Mechanics of crack arrest in concrete," *Journal of the Engineering Mechanics Division*, vol. 89, no. 3, pp. 147–168, 1963.
- [12] J. P. Romualdi and J. A. Mandel, "Tensile strength of concrete affected by uniformly distributed and closely spaced short lengths of wire reinforcement," *ACI Structural Journal*, vol. 61, no. 6, pp. 27–37, 1964.
- [13] M. H. Duan, Y. Qin, Z. G. Xu, and W. L. Ma, "Effect of polypropylene fiber on the damage and permeability of concrete," *Acta Materialia Composita Sinica*, vol. 38, no. 10, pp. 3474–3483, 2021.
- [14] A. Ding, Q. Wang, and Y. Ibrahim, "Effects of polypropylene fiber content on strength and workability properties of concrete," *Acta Materialia Composita Sinica*, vol. 34, no. 8, pp. 1853–1861, 2017.
- [15] A. N. Ede and A. O. Ige, "Optimal polypropylene fiber content for improved compressive and flexural strength of concrete," *IOSR Journal of Mechanical and Civil Engineering*, vol. 11, no. 3, pp. 129–135, 2014.
- [16] O. Karahan and C. D. Atiş, "The durability properties of polypropylene fiber reinforced fly ash concrete," *Materials & Design*, vol. 32, no. 2, pp. 1044–1049, 2011.
- [17] H. Hasan, N. Maroof, and Y. Ibrahim, "Effects of polypropylene fiber content on strength and workability properties of concrete," *Polytechnic Journal*, vol. 9, no. 1, pp. 7–12, 2019.
- [18] K. R. Akça, Ö. Çakır, and İ. Metin, "Properties of polypropylene fiber reinforced concrete using recycled aggregates," *Construction and Building Materials*, vol. 98, pp. 620–630, 2015.
- [19] K. C. Xu, B. Fu, M. C. Chen, and C. L. Huang, "On the chloride ion permeability of lepidolite slag concrete under pressure," *Journal of Experimental Mechanics*, vol. 31, no. 6, pp. 819–826, 2016.
- [20] W. Wang, W. Jin, and W. Zhe, "Chloride diffusion coefficient of recycled aggregate concrete under compressive loading," *Materials and Structures*, vol. 49, no. 11, pp. 4729–4736, 2016.
- [21] S. Parviz, A. Fadhel, C. Habibur, A. Nossoni, and G. Sarwar, "Cement bonded straw board subjected to accelerated processing," *Cement and Concrete Composites*, vol. 26, no. 7, pp. 797–802, 2003.
- [22] J. X. Yao, B. M. Zhou, F. G. Wang, and X. D. Xu, "Experimental study on thermal insulation performance of straw concrete," *New building materials*, vol. 44, no. 3, pp. 86–89, 2017.
- [23] H. Q. Sun, B. Xu, and C. F. Yuan, "Research on chloride ion permeability of polypropylene fiber reinforced concrete after high temperature," *Concrete*, no. 6, pp. 31–34, 2016.
- [24] A. N. Noumowe, R. Siddique, and G. Debicki, "Permeability of high performance concrete subjected to elevated temperature," *Construction and Building Materials*, vol. 23, no. 5, pp. 1855–1861, 2009.
- [25] G. Mazzucco, C. E. Majorana, and V. A. Salomoni, "Numerical simulation of polypropylene fibers in concrete materials under fire conditions," *Computers and Structures*, vol. 154, pp. 17–28, 2015.
- [26] P. Lura and G. P. Terrasi, "Reduction of fire spalling in high-performance concrete by means of superabsorbent polymers and polypropylene fibers," *Cement and Concrete Composites*, vol. 49, pp. 36–42, 2014.
- [27] M. Zeiml, D. Leithner, R. Lackner, and H. Mang, "How do polypropylene fibers improve the spalling behavior of in-situ concrete," *Cement and Concrete Research*, vol. 36, no. 5, pp. 929–942, 2006.
- [28] J. Bosnjak, J. Ozbolt, and R. Hahn, "Permeability measurement on high strength concrete without and with polypropylene fibers at elevated temperatures using a new test setup," *Cement and Concrete Research*, vol. 53, pp. 104–111, 2013.
- [29] X. P. Yao, Y. Han, and L. Shen, "Experimental study on compressive strength and air permeability of polypropylene fiber reinforced concrete after elevated temperature," *Concrete*, vol. 12, 2020.
- [30] B. Hu, E. J. Wei, J. Li, X. Zhu, K. Y. Tian, and K. Cui, "Nonlinear creep model based on shear creep test of granite," *Geomechanics and Engineering*, vol. 27, no. 5, pp. 527–535, 2021.
- [31] P. Kalifa, G. Chene, and C. Galle, "High-temperature behaviour of HPC with polypropylene fibres: from spalling to microstructure," *Cement and Concrete Research*, vol. 31, no. 10, pp. 1487–1499, 2001.
- [32] G. A. Khoury, "Polypropylene fibres in heated concrete. Part 2: Pressure relief mechanisms and modelling criteria," *Magazine of Concrete Research*, vol. 60, no. 3, pp. 189–204, 2008.
- [33] P. K. Mehta and P. J. M. Monteiro, *Concrete: microstructure, proper-ties, and Materials*, McGraw-Hill, New York, 2006.
- [34] B. Bai, Q. Nie, Y. Zhang, X. L. Wang, and W. Hu, "Co-transport of heavy metals and SiO₂ particles at different temperatures by seepage," *Journal of Hydrology*, vol. 597, Article ID 125771, 2021.
- [35] K. Y. Kim, T. S. Yun, and K. P. Park, "Evaluation of pore structures and cracking in cement paste exposed to elevated temperatures by X-ray computed tomography," *Cement and Concrete Research*, vol. 50, pp. 34–40, 2013.
- [36] G. Wang, C. Zhang, B. Zhang, Q. Li, and Z. Shui, "Study on the high-temperature behavior and rehydration characteristics of hardened cement paste," *Fire And Materials*, vol. 36, 2014.

- [37] V. Vydra, F. Vodák, O. Kapicková, and S. Hošková, "Effect of temperature on porosity of concrete for nuclear-safety structures," *Cement and Concrete Research*, vol. 31, no. 7, pp. 1023–1026, 2001.
- [38] G. Ye, X. Liu, G. D. Schutter, L. Taerwe, and P. Vandeveld, "Phase distribution and microstructural changes of self-compacting cement paste at elevated temperature," *Cement and Concrete Research*, vol. 37, no. 6, pp. 978–987, 2007.
- [39] K. Y. Tian, W. D. Gong, E. J. Wei et al., "Gas pressure relief-permeability increase effect comparative analysis about hydraulic disturbance to soft coal seam and its sandstone roof," *Journal of China Coal Society*, vol. 46, no. 6, pp. 1888–1897, 2021.
- [40] I. N. Yadav and K. B. Thapa, "Fatigue damage model of concrete materials," *Theoretical and Applied Fracture Mechanics*, vol. 108, pp. 195–230, 2020.
- [41] B. W. Liu, G. Peng, X. L. Ma, and J. H. XIE, "Dynamic damage properties of concrete subjected to cyclic loading and unloading with different lateral stresses," *Journal of Yangtze River Scientific Research Institute*, vol. 34, pp. 121–125+131, 2017.
- [42] D. Y. Ma, J. Liu, and J. L. Li, "Research on seepage characteristics of sandstone fracture under JRC, confining pressure and axial pressure," *Journal of Natural Disasters*, vol. 27, no. 6, pp. 109–119, 2018.
- [43] P. Soroushian, F. Aouadi, H. Chowdhury, A. Nossoni, and G. Sarwar, "Cement bonded straw board subjected to accelerated processing," *Cement and Concrete Composites*, vol. 26, no. 7, pp. 797–802, 2003.
- [44] M. Amin, B. A. Tayeh, and I. S. Agwa, "Investigating the mechanical and microstructure properties of fibre-reinforced lightweight concrete under elevated temperatures," *Case Studies in Construction Materials*, vol. 13, Article ID e00459, 2020.
- [45] K. Y. Tian, "Study on technology of hydraulic fracturing relieving pressure and increasing permeability in soft coal seam with hard roof," *Journal of Natural Disasters*, vol. 26, no. 4, pp. 215–220, 2017.
- [46] M. X. Jing and X. L. Yuan, "Experimental research on core stress sensitivity of carbonate rock," *Natural Gas Industry*, vol. 20, pp. 114–117, 2002.
- [47] Z. Liu, L. H. Zhao, X. B. Wu, G. P. Hu, and Q. Y. Zhou, "Damage model of concrete considering hysteretic effect under cyclic loading," *Advanced Engineering Sciences*, vol. 52, no. 4, pp. 117–123, 2020.

Research Article

Swelling Characteristics of Fractal-Textured Bentonite Eroded by Alkaline Solution

Guosheng Xiang ^{1,2,3}, Weimin Ye,¹ Zhijie Hu,² Lei Ge,² and Yinkang Zhou²

¹Department of Geotechnical Engineering, Tongji University, Shanghai 200092, China

²Department of Civil Engineering, Anhui University of Technology, Ma'anshan 243002, China

³Key Laboratory of Soft Soils and Geoenvironmental Engineering (Zhejiang University), Ministry of Education, Hangzhou 310058, China

Correspondence should be addressed to Guosheng Xiang; xiangsh2011@163.com

Received 15 January 2022; Accepted 10 February 2022; Published 24 March 2022

Academic Editor: Xingxin Chen

Copyright © 2022 Guosheng Xiang et al. This is an open access article distributed under the Creative Commons Attribution License, which permits unrestricted use, distribution, and reproduction in any medium, provided the original work is properly cited.

To study the swelling characteristics of bentonite eroded by alkaline solutions, swelling deformation (δ_s) tests on the bentonite subjected to immersion conditions of NaOH and KOH solutions were conducted. It is found that the δ_s of bentonite decreases with the increase in the concentration of alkaline solution. The swelling deformation δ_s of bentonite eroded by NaOH solution exceeds that in the KOH solution for the same level of concentration. Moreover, by performing XRD tests, it is revealed that the reduced swelling performance of bentonite in alkaline solutions is mainly attributed to the dissolution of the swelling mineral, i.e., montmorillonite (Mt.). The higher the concentration of alkali solution, the stronger the dissolution of Mt., thus leading to more significant attenuation of the swelling properties. Besides, the K^+ exhibits low hydration energies, which tends to fit into the silicon-oxygen tetrahedral cavity of smectite, forming a stronger K-linkage which leads to closely spaced crystal layers. The $e-p_e$ fractal relation can be calculated using the δ_s of bentonite eroded by alkaline solution. The $e-p_e$ fitting relation of the experimental data depicts that the dissolution of Mt. minerals in alkaline solution reduces the swelling coefficient κ , however, it increases the surface fractal dimension (D_s).

1. Introduction

Geo-environmental engineering is a major concept related to the human living environment and sustainable development. The related research aspects include pollutant migration, treatment measures, reuse of industrial waste, and comprehensive utilization. In recent years, many researchers have focused on the composition and scale of mineral particles in soil and pore water, ion concentration and chemical composition of pore water, microstructure characteristics, stress history, and thermal expansion performance, especially their coupling process [1–8]. The disposal of high-level radioactive waste (HLRW) is related to sustainable development, energy, and nuclear industry, and is related to the safety of the living environment of future generations, has attracted wide attention around the world. Up to now, deep geological disposal is considered the most feasible method for the disposal of HLRW. The disposal

repository is a complex multibarrier system that includes HLRW in sealed canisters, buffer/backfill materials, and host rocks. Because of its outstanding buffering and backfilling qualities (high swelling capacity, low permeability, and good adsorption properties, etc.), bentonite is considered the artificial barrier material for deep geological repository [9, 10]. During the operational phase of the repository, the concrete surrounding the rock lining deteriorates due to the infiltration of groundwater, thereby initially releasing Na^+ and K^+ to form a strong alkaline pore water solution (pH 13–13.5). In addition, Ca^{2+} and Na^+ are subsequently formed in the later stage, which exhibits a pH of 12–12.5, thus causing irreversible changes in bentonite properties and further threatening the safe use of the repository [11, 12]. Therefore, it is significant to study the swelling performance of bentonite under the action of an alkaline solution to efficaciously design, construct, and maintain the repository.

Montmorillonite (Mt) is the main swelling mineral in bentonite and it largely governs the buffering and backfilling characteristics of bentonite. Savage et al. [13] found that the pore solution formed as a result of cement degradation tends to reduce the swelling properties of bentonite. Chen et al. [14] analyzed the influence of NaOH solution with different concentrations on the Chinese GaoMiaoZi (GMZ) bentonite. The results showed that, due to the dissolution of Mt. in alkaline solution, the wing colloid formed depicted a variety of cracks. With increasing NaOH concentration, the Mt. content decreases whereas the degree of fragmentation increases, which leads to a decrease in the swelling properties. Fernández et al. [15] found that when the highly alkaline solution permeates into the bentonite-based buffer backfill material, the solution will dissolve the minerals present in the bentonite, which will eventually weaken the swelling deformation (δ_s) as well as the self-sealing properties of the backfill material. Furthermore, Xiang et al. [16] studied various changes in bentonite in alkaline solutions, and they revealed that the Mt. content decreased gradually while the specific surface area and adsorption capacity also decreased. The scanning electron microscopy (SEM) micrographs illustrated that the surface fractal dimension (D_s) increased. Sánchez et al. [17] studied the changes in mineral composition of bentonite under different temperature ranges and various concentration levels of alkaline solution with the help of X-ray diffraction (XRD). The results showed that as the concentration and temperature increase, the Mt. content, as opposed to the nonswelling minerals, gradually decreases. In another study, Kamland et al. [18] incorporated alkaline NaCl and saturated CaCl₂ (Ca(OH)₂) as soaking solutions, and they concluded that the swelling property of Wyoming bentonite in saline solution reduced due to the cation exchange reaction, while that in the alkaline solution also reduced mainly because of the Mt. dissolution. Bauer et al. [19] analyzed the effects of temperature and KOH solution concentration on Mt. content, and they found that the dissolution of Mt. was accompanied by a change in crystal shape as the reaction produced zeolite, quartz, and other minerals. Additionally, the reaction turned out to be more vigorous with increasing concentration and temperature. Similarly, Gaucher et al. [20] found that with the increase of the alkaline solution concentration, the dissolution rate of Mt. increased sharply at 60°C especially in highly alkaline solution (pH = 13). Ramirez et al. [21] studied the reaction of bentonite with highly alkaline solutions at different temperatures and observed the precipitation of nonexpansive minerals, i.e., zeolite, whereas the magnesium content in the Mt. increased, which led to the decreased swelling performance. It was noted that a further increase in temperature would intensify the reaction. Herbert et al. [22] analyzed the swelling performance of MX-80 bentonite by incorporating different solutions using transmission electron microscope (TEM), and they found that the change of Mt. and kaolinite content primarily weakens the swelling performance of bentonite. Fernández et al. [23] studied the effects of alkaline solution diffusion and found that brucite was formed on the surface of bentonite that dissolved the Mt. minerals, hence decreasing the swelling properties of the FEBEX bentonite.

The surface morphology of bentonite with regard to encountering moisture is complex in nature, and the δ_s refers to the process of uptake of water by the Mt. content of bentonite. Xu et al. [24] proposed a relationship between swelling force and adsorbed water volume $V_w/V_m = K_p D_s - 3$, where V_w is the final adsorbed water volume of bentonite, V_m is the volume of smectite in bentonite, and as mentioned earlier, D_s is the surface fractal dimension of bentonite. Li et al. [25] explored the calculation method of the osmotic suction coefficient and the osmotic suction of different types of solutions by introducing the Debye–Hückel formula. Moreover, Xu et al. [26] derived the effective stress calculation equation by considering the impact of osmotic suction in the salt solution.

Presently, the research on the mechanistic effect of alkaline solutions on the swelling properties of bentonite is mostly reflected in the properties and mineral content of bentonite. However, the numerical calculation of δ_s of bentonite is scarcely reported and needs research to cover the deficiencies in this particular direction. Therefore, in the current study, NaOH and KOH solutions are used as erosion solutions to study and analyze the attenuation mechanism of δ_s of bentonite, fitting calculations for bentonite δ_s , and explaining the influence of alkali metal cations on the performance of bentonite. Furthermore, this research study is aimed to provide guidance suggestions for the efficacious design and reliable construction of a deep geological repository.

2. Materials and Methods

2.1. Materials. The basic properties of bentonite used in this paper are summarized in Table 1. According to the standard test requirements, the original bentonite is placed inside an oven at 105°C for drying. After that, a 500 g soil sample is weighed each time such that 90 ml of distilled water is sprinkled on the soil sample at a designated water content of approximately 18%. Then the sample is stored by enclosing it in plastic wrapping. In addition, distilled water was used to prepare the NaOH and KOH solutions with prescribed concentrations of 0.3 and 1.0 mol/l (M), respectively.

2.2. Swelling Deformation Test. The moisture content of the saturated soil was remeasured for the sake of accuracy prior to sample preparation. The cutting ring was placed on the base of the prototype machine and was tightened with the help of a hoop. Then, about 58.5 g of wet soil was weighed each time, which was incorporated into the cutting ring in batches while applying a backing plate cover on it afterward. After that, a jack was used to statically press the plate into a cakelike sample with Φ 61.8 mm \times H 10 mm, and a density of 1.7 ± 0.5 g/cm³. This range of density has been widely applied in experimental studies on compacted bentonite [27]. After following the aforementioned requirements, the static pressure was applied and maintained for a period of time [28].

The operation of the δ_s in this study can be explained in seven major steps: (i) preparing three groups of samples (i.e.,

TABLE 1: Basic physical and chemical indices of tested bentonite.

Parameter	Value
Specific gravity	2.75
Liquid limit (%)	210.7
Plastic limit (%)	25.1
Plasticity index I_p	185.6
Total specific surface area (m^2/g)	570
Montmorillonite content (%)	84
Cation exchange capacity (cmol/kg)	60.1

distilled water, NaOH solution, and KOH solution) (ii) setting the loads at six different levels (i.e., 100, 200, 400, 800, 1200, and 1600 kPa), for a total of 30 number of samples, (iii) permeable stone, filter paper, test sample and permeable stone are sequentially placed layer-wise in the bottom of oedometer cell, (iv) installing a dial indicator, adjusting the dial gauge, and recording the initial reading, and then applying the required load at one time, (v) the soaking solution is injected into the oedometer cell and the sample is immersed, (vi) recording the readings of dial gauge (note that the reading interval is shorter in the early stage and longer in the later stage), and (vii) when the pointer of dial gauge remains unchanged for 24 hours, it is considered that the δ_s tests were completed.

2.3. XRD and SEM Test. The XRD tests were used to analyze the mineral composition of bentonite. Prior to testing, the bentonite samples after the δ_s test were washed with distilled water several times to remove the adsorbed salts. The samples were oven-dried at 105°C and pulverized. Thereafter, it was sieved using a 200-mesh sieve, and a small portion was taken for XRD tests. XRD tests were carried out in the Modern Analysis and Test Center of the Anhui University of Technology, China, by using a D-8 ADVANCE X-ray diffractometer by Brook Company, Germany. The target material was copper, while the power was kept at 3 kW. The scanning range of the goniometer was between 3° and 80°.

The SEM tests were used to analyze and determine the overall effect of the micromorphology of bentonite minerals. SEM analysis was also performed using a NANO SEM 430 field emission scanning electron type microscope produced by the FEI company.

3. Test Results

Figure 1 shows the swelling rate of bentonite at a pressure of 100 kPa. It can be seen that the varying trends of bentonite samples soaked in solutions of different concentrations are identical and hence depict three main stages: first gradually increasing, then followed by a relatively sharp increase, and finally reaching a stable state [29, 30]. It can be seen from Figures 1(a) and 1(b) that the swelling rate is the highest in distilled water as it approaches 61%. Hence, it can be inferred that the swelling performance of bentonite is greatly reduced after the action of the alkaline solutions. In addition, it is noteworthy to mention that with the increase in the alkaline concentration, the swelling ratios of bentonite also tend to

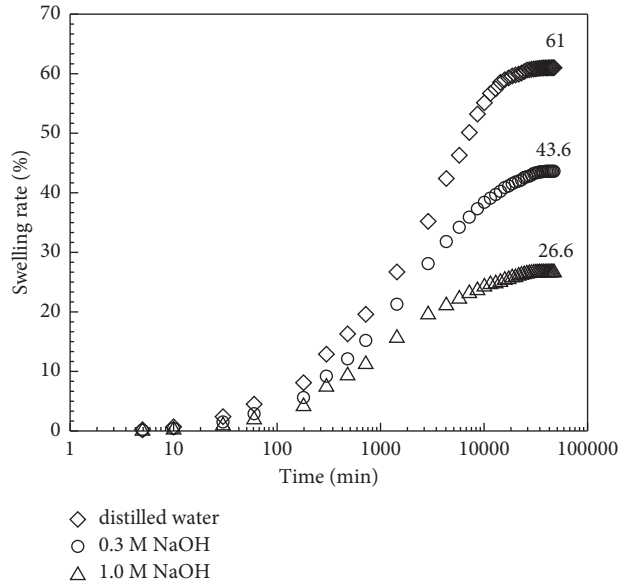
decrease. At 1.0 M, the aforementioned three stages of swelling ratio of bentonite vary with time, but not significantly. It is because the Mt. mineral in bentonite gets dissolved in the alkaline environment. Therefore, with the increase of solution concentration, the reaction is intensified, which reduces the swelling performance.

Figure 2 illustrates the influence of distilled water, 0.3 M NaOH, and KOH solutions on the swelling characteristics of bentonite subjected to an overlying pressure of 100 kPa. It can be seen that the swelling rates of the three solutions increase as distilled water > NaOH > KOH, with the maximum swelling rates recorded to be 61%, 43.6%, and 39.7%, respectively. In an alkaline solution, the δ_s of bentonite experiences a much larger large decrease than in the case of bentonite soaked in distilled water. In the case of KOH solution, the hydration ability of K^+ is low, and it can easily fit inside the cavity of the silicon-oxygen tetrahedral grid, which produces strong K linkage. As a result, the crystal layer contacts become more closely spaced and the expansion deformation is observed to be the minimum [31, 32].

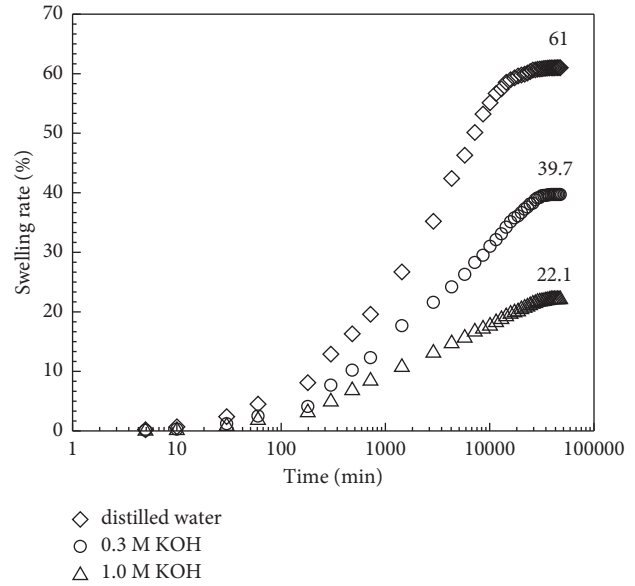
Figure 3 shows the relationship between the maximum δ_s of bentonite and the overlying compressive stress. It can be seen that at the same dry density, the maximum δ_s of bentonite decreases with the load increase. When the overlying pressure equals 100 kPa, the maximum swelling rate is, respectively, distilled water (61%), 0.3 M NaOH solution (43.6%), 1.0 M NaOH solution (26.6%), 0.3 M KOH solution (39.7%), and 1.0 M KOH solution (22.1%). On the contrary, when the overlying pressure is 1600 kPa, the maximum swelling rate is distilled water (10.4%), 0.3 M NaOH solution (8.7%), 1.0 M NaOH solution (4.4%), 0.3 M KOH solution (7.6%), and 1.0 M KOH solution (2.1%), respectively. The two cases were observed to witness reduction by almost 82.95%, 80.05%, 83.46%, 80.86%, and 90.50%, respectively.

Figure 4 shows the XRD diffraction pattern of the bentonite. Figure 4(a) shows the diffraction pattern of bentonite soaked in distilled water such that the diffraction peak intensity of Mt. is 523 CPS. Figures 4(b)–4(e) show the diffraction pattern of bentonite eroded by NaOH and KOH solutions. In addition, the peak values of Mt. correspond to 408, 302, 354, and 215 CPS for samples immersed in 0.3 M NaOH, 1.0 M NaOH, 0.3 M KOH, and 1.0 M KOH, respectively. It can be found that under the erosion of alkaline solutions, the peak diffraction intensity of Mt. gradually decreases, whereas the phenomenon is more significant with increasing concentration. Thus, it is indicated that the dissolution of Mt. minerals is the main reaction process that results in a significant reduction in the δ_s .

Figure 5 is a schematic diagram of the SEM performed on a variety of bentonite samples. The sample (a) soaked in distilled water exhibits compact particle structural integrity, witnessing no fragmentation phenomenon. In addition, the wing-shaped colloids are produced by the hydration of Mt. that are present on the surface of bentonite particles [14]. For samples (b)–(e) in the alkaline solution, the bentonite particles gradually split into small pieces and the wing-shaped



(a)



(b)

FIGURE 1: The relationship curve of bentonite swelling rate and time under 100 kPa.

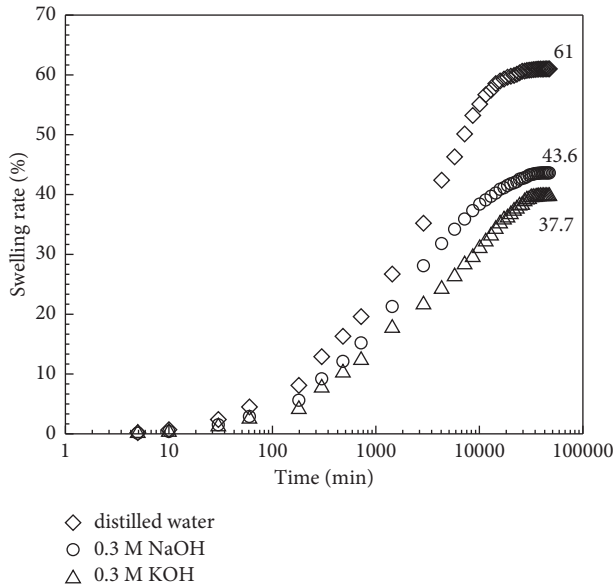


FIGURE 2: The swelling rate of different solutions varies with time at 100 kPa.

colloid gradually gets dissolved with increasing concentration. In the case of 1.0 mol/L NaOH and KOH solutions, the winged colloids were found to disappear completely, while the degree of particle breakage was also high. Comparing the two groups of samples (b) and (d), it can be seen that the bentonite eroded by KOH solution has comparatively larger particles and fewer cracks, which is attributed to the stronger bonding of Mt. crystal layers under the action of K^+ .

4. $e-p_e$ Relationship for Bentonite in Alkaline Solution

The δ_s of bentonite decreases with the increase of effective stress p_e . Based on the fractal theory, Debye-Hückel (D-H) formula can be introduced to obtain the osmotic suction coefficient for the determination of osmotic suction. Then, using the value of osmotic suction, the theoretical calculation method between effective stress and δ_s can be obtained. The $e-p_e$ fitting curve was analyzed to further explore the erosion mechanism of alkaline solutions on bentonite.

According to the fractal theory, Xu et al. [26] deduced the relationship between δ_s of bentonite and modified effective stress p_e in the form of the following equations:

$$e_m = \frac{V_w}{V_m} = K p_e^{D_s-3}, \quad (1)$$

$$e_m = \frac{e}{\alpha}, \quad (2)$$

$$e = \alpha K p_e^{D_s-3} = \kappa p_e^{D_s-3}, \quad (3)$$

where e_m is the void ratio of Mt, V_w is the water absorption volume of the Mt, and V_m is the volume of Mt. In bentonite, K is the swelling coefficient of Mt, p_e is the modified effective stress, e is the total void ratio of the sample, which can be calculated from δ_s , α is the mass fraction of Mt, and κ is swelling coefficient. Based on the fractal theory, p_e can be calculated from the overlying pressure and osmotic stress, and the calculation formula is as given as follows [26]:

$$p_e = \sigma + \pi \left(\frac{\sigma}{\pi} \right)^{D_s-2}, \quad (4)$$

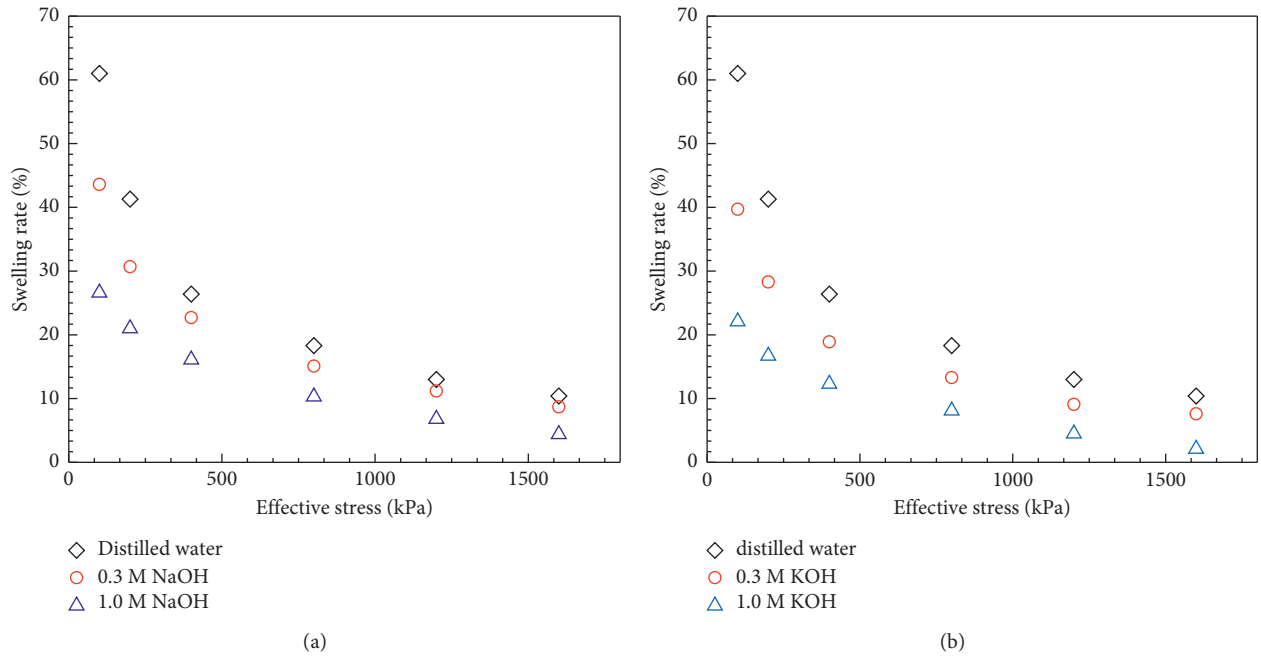


FIGURE 3: The relationship curve of maximum swelling deformation with load.

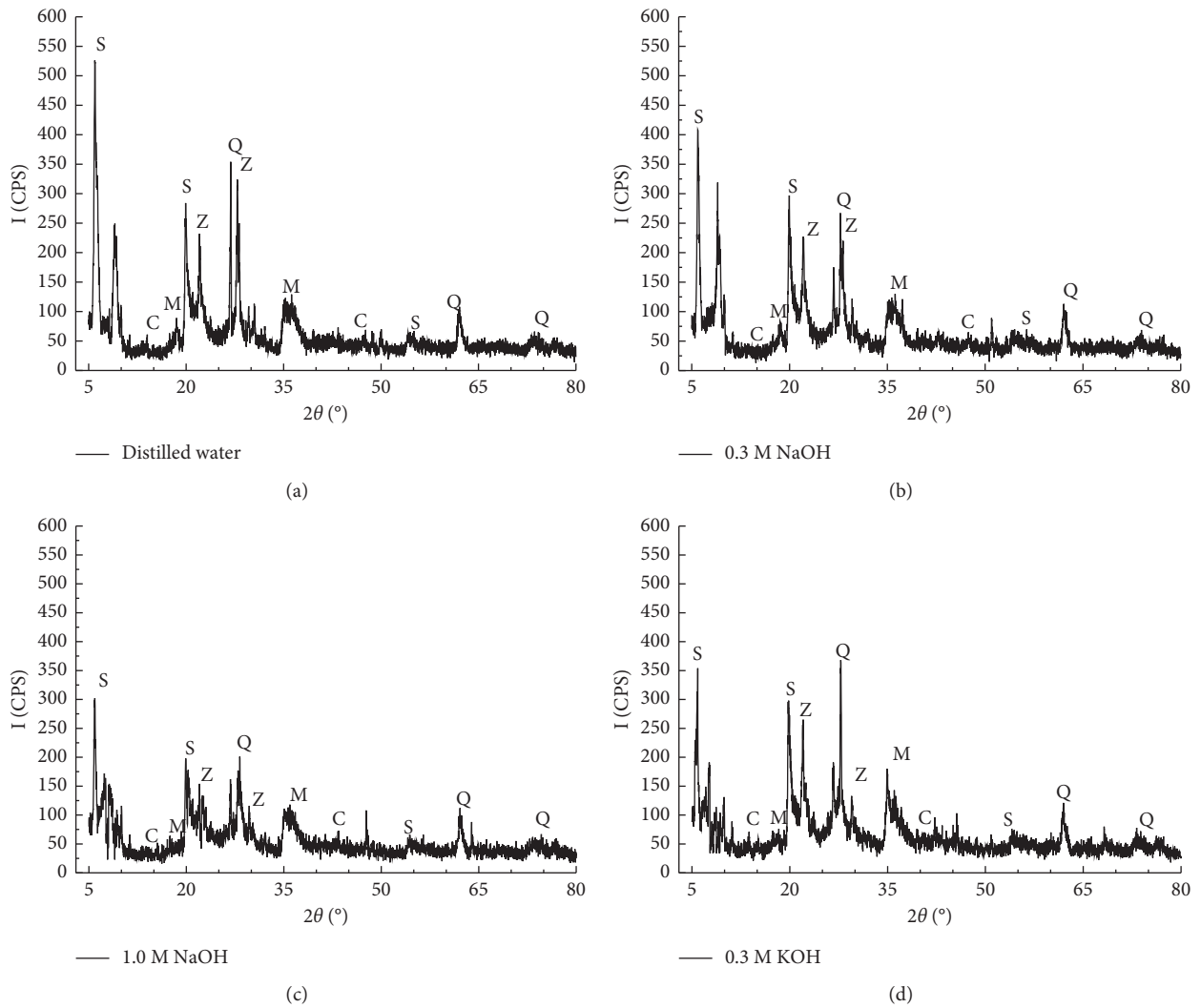


FIGURE 4: Continued.

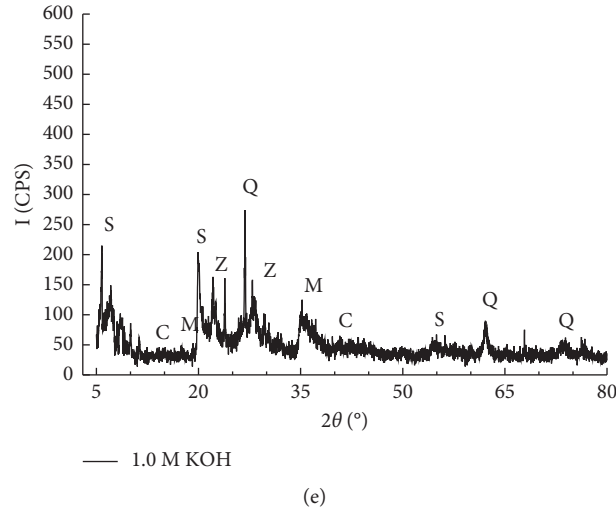


FIGURE 4: XRD diffraction pattern of bentonite sample: (a) distilled water, (b) 0.3 M NaOH, (c) 1.0 M NaOH, (d) 0.3 M KOH, and (e) 1.0 M KOH.

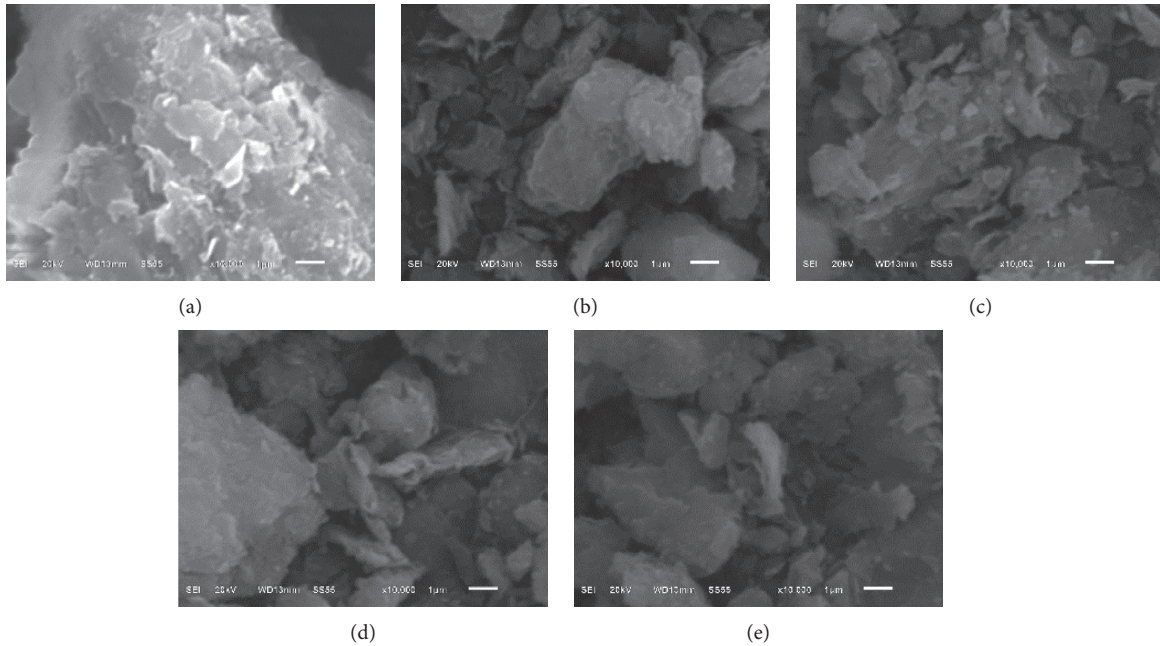


FIGURE 5: Scanning electron microscope (SEM) images of bentonite treated with a variety of alkaline solution concentrations: (a) distilled water, (b) 0.3 M NaOH, (c) 1.0 M NaOH, (d) 0.3 M KOH, and (e) 1.0 M KOH.

where σ is the overlying pressure and π is the osmotic suction of the alkaline solution.

It can be seen from (4) that p_e is related to osmotic suction. Li et al. [25] derived the osmotic suction coefficient and the calculation method of osmotic suction under different solutions based on the D-H formula in the form of

$$\pi = \varepsilon RTc\Phi, \quad (5)$$

where ε is the ion number of solute decomposition (for NaOH or KOH, $\varepsilon = 2$), R is the generalized gas constant (8.314 J/mol/k), T is the absolute temperature, c is the molar concentration of solute, and Φ is the osmotic suction

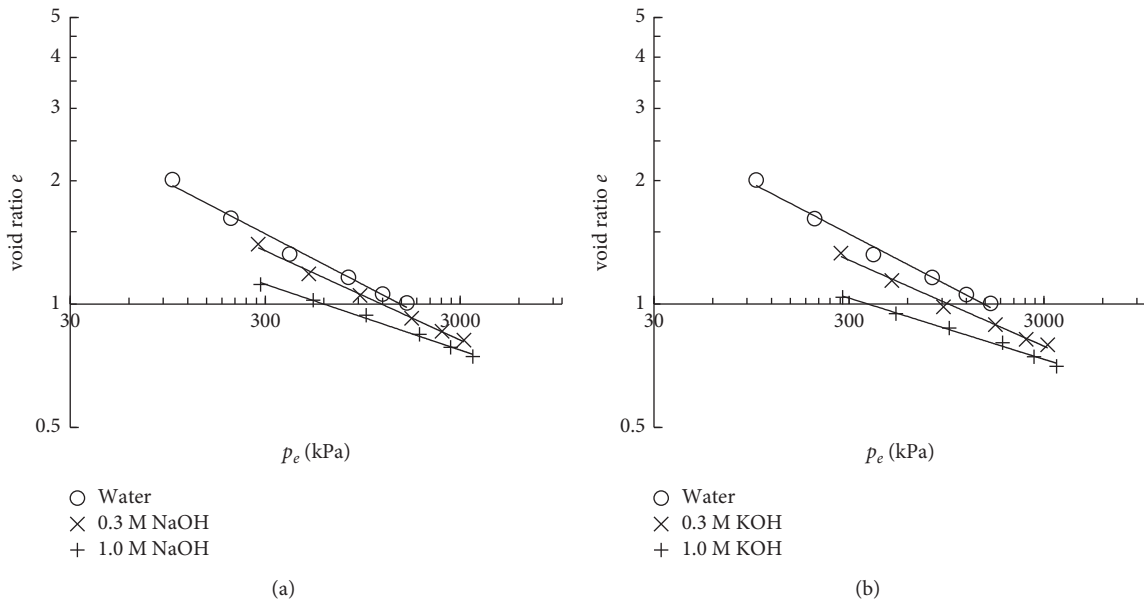
coefficient. The calculation formula of Φ in solution containing monovalent ion electrolyte is given by the equation as follows [33]:

$$\varphi = |z_M z_X| f + m \left(\frac{2v_M v_X}{v} \right) B_{MX} + m^2 \frac{(v_M v_X)^{3/2}}{v} C_{MX} + 1, \quad (6)$$

where z_M, z_X are the chemical valence that correspond to anions and cations, respectively, v_M, v_X correspond to the number of negative cations in the chemical formula, m is the molar number, C_{MX} is the empirical coefficient, and for strong electrolytes the formula of B_{MX} is in the form of following equation:

TABLE 2: Calculation results of osmotic suction in alkali solution.

Concentration	A	NaOH				KOH			
		f	B_{MX}	Φ	π	f	B_{MX}	Φ	π
0.01	0.447	-0.0399	0.294	0.963	46.710	-0.0399	0.392	0.964	46.758
0.05	0.447	-0.0788	0.248	0.934	226.424	-0.0788	0.334	0.938	227.469
0.1	0.447	-0.1024	0.221	0.920	446.083	-0.1024	0.300	0.928	449.913
0.2	0.447	-0.1300	0.190	0.908	880.921	-0.1300	0.261	0.922	894.644
0.3	0.447	-0.1477	0.171	0.904	1315.443	-0.1477	0.237	0.924	1344.129
0.4	0.447	-0.1607	0.158	0.903	1752.266	-0.1607	0.220	0.928	1800.530
0.5	0.447	-0.1709	0.148	0.904	2192.677	-0.1709	0.208	0.934	2264.872
0.6	0.447	-0.1794	0.140	0.906	2637.500	-0.1794	0.198	0.941	2737.817
0.7	0.447	-0.1865	0.134	0.909	3087.348	-0.1865	0.190	0.948	3219.872
0.8	0.447	-0.1928	0.129	0.913	3542.721	-0.1928	0.183	0.957	3711.462
0.9	0.447	-0.1982	0.124	0.917	4004.049	-0.1982	0.178	0.965	4212.970
1.0	0.447	-0.2031	0.121	0.922	4471.718	-0.2031	0.173	0.974	4724.746

FIGURE 6: The e - p_e relationship curve of bentonite in NaOH and KOH solutions.

$$B_{MX} = \beta_{MX}^{(0)} + \beta_{MX}^{(1)} e^{-\alpha I^{1/2}}, \quad (7)$$

where $\beta_{MX}^{(0)}, \beta_{MX}^{(1)}$ can be obtained by looking up the code. f can be calculated by the following formula:

$$f = -A \frac{I^{1/2}}{1 + bI^{1/2}}, \quad (8)$$

where I is the ionic strength, b is an empirical parameter equaling 1.2, and A is the D-H coefficient, which can be calculated by the following equation:

$$A = \frac{1}{3} (2\pi N_A \rho_{sl})^{1/2} (e^2 / (0.4\pi\epsilon_r\epsilon_0 kT))^{3/2}, \quad (9)$$

where N_A is Avogadro constant ($6.023 \times 10^{23}/\text{mol}$), ρ_{sl} is solvent density (0.998 g/cm^3), e is the charge of electrons ($1.60 \times 10^{-19} \text{ C}$), k is Boltzmann constant ($1.381 \times 10^{-23} \text{ J/K}$), and ϵ_r, ϵ_0 are relative dielectric constant (78.36) and vacuum

dielectric constant ($8.8542 \times 10^{-12} \text{ F/m}$), respectively. The calculation results are shown in Table 2.

Figure 6 depicts a fitting relationship curve between the p_e of bentonite and the void ratio e , drawn based on experimental data. It is found that the δ_s of bentonite in an identical solution is in accordance with the unified e - p_e relationship, and as the concentration of solution increases, the curve lowers down. According to the fitted curve equation, the D_s and swelling coefficient κ of bentonite in various solutions can be obtained, as shown in Table 3. It is also important to mention that the D_s of bentonite surface after erosion in alkaline solution is greater than the one observed in the case of distilled water immersion, and it increases with the increase of alkaline solution concentration. Combined with SEM tests, the main reason is that bentonite particles are broken apart under the action of an alkaline solution, thereby producing smaller fragments. Moreover, the surface of flaky Mt. is extremely irregular and corrosion trace extension leads to a rough bentonite surface and increased D_s value [14].

TABLE 3: $e-p_e$ fitting curve of bentonite in different solutions.

Solutions	$e-p_e$	κ	D_s	R^2
Distilled water	$e = 6.084p_e^{-0.247}$	6.08	2.75	0.986
0.3 NaOH	$e = 4.677p_e^{-0.218}$	4.68	2.78	0.994
1.0 NaOH	$e = 2.791p_e^{-0.161}$	2.79	2.84	0.991
0.3 KOH	$e = 4.241p_e^{-0.21}$	4.24	2.79	0.988
1.0 KOH	$e = 2.423p_e^{-0.149}$	2.42	2.85	0.992

In addition, it can be found that the swelling coefficient κ of bentonite in the case of distilled water is the highest, whereas it decreases with the increase in alkali concentration. At the same concentration of alkali solution, the κ of bentonite eroded by NaOH solution is greater than that of KOH solution. On the one hand, the main swelling mineral Mt. in bentonite is dissolved in the alkaline solution and the dissolution rate increases with the increase of alkaline concentration, while on the other hand, K^+ can enter the cavity of the Mt. structure to form K-linkage and the crystal layer is more tightly bonded, which vilifies the swelling performance.

5. Conclusion

The swelling deformation (δ_s) tests of bentonite in alkaline solution, combined with XRD, SEM tests, and analysis, were conducted and the following main conclusions are drawn.

- (1) The δ_s curve of bentonite exhibits the characteristics in the form of three distinct stages. With the increase in the concentration of alkaline solution, the δ_s of bentonite gradually decreases, while the dissolution of swelling mineral Mt. is the main reaction process. K^+ has low hydration ability and easily fits into the silicon-oxygen tetrahedral cavity of Mt, producing stronger K-linkage, which leads to closely spaced crystal layers, thus resulting in lesser δ_s of the bentonite in KOH solution as compared with that in NaOH solution.
- (2) The δ_s of bentonite eroded by alkaline solutions can be calculated by a unified $e-p_e$ fractal relationship. On the double logarithmic coordinate axis, the higher the concentration, the lower the δ_s curve. As the concentration of alkaline solution increases, the dissolution rate of Mt. also increases, hence reducing the swelling coefficient κ . Simultaneously, when Mt. dissolves, the clay particles disintegrate and the surface becomes coarser, which gradually increases the surface fractal dimension (D_s) of bentonite.

Data Availability

The data used to support the findings of this study are available from the corresponding author upon request.

Conflicts of Interest

The authors declare that there are no conflicts of interest regarding the publication of this manuscript.

Authors' Contributions

Guosheng Xiang contributed to the conceptualization and methodology. Weimin Ye contributed to the conceptualization. Contributors to the investigation included Zhijie Hu, Lei Ge, and Yinkang Zhou.

Acknowledgments

This work was supported by the National Natural Science Foundation of China (Grant nos. 41702311 and 42030714), the China Postdoctoral Science Foundation (no. 2019M660096), and the Foundation of Key Laboratory of Soft Soils and Geoenvironmental Engineering (no. 2020P03).

References

- [1] B. Bai, R. Zhou, G. Cai, W. Hu, and G. Yang, "Coupled thermo-hydro-mechanical mechanism in view of the soil particle rearrangement of granular thermodynamics," *Computers and Geotechnics*, vol. 137, no. 8, Article ID 104272, 2021.
- [2] B. Bai, Q. Nie, Y. Zhang, X. Wang, and W. Hu, "Cotransport of heavy metals and SiO₂ particles at different temperatures by seepage," *Journal of Hydrology*, vol. 597, Article ID 125771, 2021.
- [3] B. Yuan, Z. Li, Z. Zhao, H. Ni, Z. Su, and Z. Li, "Experimental study of displacement field of layered soils surrounding laterally loaded pile based on Transparent Soil," *Journal of Soils and Sediments*, vol. 21, no. 9, pp. 3072–3083, 2021.
- [4] L. Wang, A. Zhou, Y. F. Xu, and X. H. Xia, "Consolidation of partially saturated ground improved by impervious column inclusion: Governing equations and semi-analytical solutions," *J. Rock Mech. Geo. Engineering*, 2022.
- [5] R. Taherdangkoo, A. Tatomir, T. Anighoro, and M. Sauter, "Modeling fate and transport of hydraulic fracturing fluid in the presence of abandoned wells," *Journal of Contaminant Hydrology*, vol. 221, pp. 58–68, 2019.
- [6] J. Zhang, G. Niu, X. Li, and D. A. Sun, "Hydro-mechanical behavior of expansive soils with different dry densities over a wide suction range," *Acta Geotechnica*, vol. 15, no. 1, pp. 265–278, 2020.
- [7] X. Cui, Q. Liu, C. Zhang, Y. Huang, Y. Fan, and H. Wang, "Land subsidence due to groundwater pumping and recharge: Considering the particle-deposition effect in ground-source heat-pump engineering," *Hydrogeology Journal*, vol. 26, no. 3, pp. 789–802, 2018.
- [8] X. Chen, Z. Wu, Q. Cai, and W. Cao, "Effect of ultrasonic stimulation on particle transport and fate over different lengths of porous media," *Journal of Hydrology*, vol. 559, pp. 972–983, 2018.

- [9] B. Bai, G.-c. Yang, T. Li, and G.-s. Yang, "A thermodynamic constitutive model with temperature effect based on particle rearrangement for geomaterials," *Mechanics of Materials*, vol. 139, Article ID 103180, 2019.
- [10] G. S. Xiang, W. M. Ye, F. E. Jalal, and Z. J. Hu, "Shear strength of bentonite saturated with saline solutions exhibiting variety of cations," *Engineering Geology*, vol. 298, Article ID 106537, 2022.
- [11] J. Zhang, D. A. Sun, H. Yu, J. Jiang, and Y. Xu, "Swelling of unsaturated GMZ07 bentonite at different temperatures," *Bulletin of Engineering Geology and the Environment*, vol. 79, no. 2, pp. 959–969, 2020.
- [12] G.-s. Xiang, W.-m. Ye, Y. Zhou, and F. E. Jalal, "Combined effects of temperature and salt solution on swelling of GMZ01 bentonite-sand mixtures," *Bulletin of Engineering Geology and the Environment*, vol. 80, no. 9, pp. 6677–6688, 2021.
- [13] D. Savage, D. Noy, and M. Mihara, "Modelling the interaction of bentonite with hyperalkaline fluids," *Applied Geochemistry*, vol. 17, no. 3, pp. 207–223, 2002.
- [14] B. Chen, J. X. Guo, and H. X. Zhang, "Alteration of compacted GMZ bentonite by infiltration of alkaline solution," *Clay Minerals*, vol. 51, pp. 237–247, 2016.
- [15] R. Fernández, J. Cuevas, and U. K. Mäder, "Modeling experimental results of diffusion of alkaline solutions through a compacted bentonite barrier," *Cement and Concrete Research*, vol. 40, no. 8, pp. 1255–1264, 2010.
- [16] G. S. Xiang, W. M. Ye, F. Yu, Y. Wang, and Y. Fang, "Surface fractal dimension of bentonite affected by long-term corrosion in alkaline solution," *Applied Clay Science*, vol. 175, pp. 94–101, 2019.
- [17] L. Sánchez, J. Cuevas, S. Ramírez, D. R. D. León, and S. Leguey, "Reaction kinetics of FEBEX bentonite in hyperalkaline conditions resembling the cement-bentonite interface," *Applied Clay Science*, vol. 33, no. 2, pp. 125–141, 2006.
- [18] O. Karnland, S. Olsson, U. Nilsson, and P. Sellin, "Experimentally determined swelling pressures and geochemical interactions of compacted Wyoming bentonite with highly alkaline solutions," *Physics and Chemistry of the Earth*, vol. 32, no. 1-7, pp. 275–286, 2007.
- [19] A. Bauer and B. Velde, "Smectite transformation in high molar KOH solutions," *Clay Minerals*, vol. 34, no. 2, pp. 259–273, 1999.
- [20] E. C. Gaucher and P. Blanc, "Cement/clay interactions - a review: Experiments, natural analogues, and modeling," *Waste Management*, vol. 26, no. 7, pp. 776–788, 2006.
- [21] D. Savage, C. Walker, R. Arthur, C. Rochelle, C. Oda, and H. Takase, "Alteration of bentonite by hyperalkaline fluids: A review of the role of secondary minerals," *Physics and Chemistry of the Earth*, vol. 32, no. 1/7, pp. 287–297, 2007.
- [22] H.-J. Herbert, J. Kasbohm, H. Sprenger, A. M. Fernández, and C. Reichelt, "Swelling pressures of MX-80 bentonite in solutions of different ionic strength," *Physics and Chemistry of the Earth, Parts A/B/C*, vol. 33, pp. S327–S342, 2008.
- [23] R. Fernandez, U. K. Mader, M. Rodríguez, R. V. Vigil, and J. Cuevas, "Alteration of compacted bentonite by diffusion of highly alkaline solutions," *European Journal of Mineralogy*, vol. 21, no. 4, pp. 725–735, 2009.
- [24] Y. F. Xu, H. Matsuoka, and D. A. Sun, "Swelling characteristics of fractal-textured bentonite and its mixtures," *Applied Clay Science*, vol. 22, no. 4, pp. 197–209, 2003.
- [25] X. Li, C. Li, and Y. Xu, "Representation of volume change for bentonite in saline solution based on modified effective stress," *KSCE Journal of Civil Engineering*, vol. 23, no. 5, pp. 2065–2073, 2019.
- [26] Y. Xu, G. Xiang, H. Jiang, T. Chen, and F. Chu, "Role of osmotic suction in volume change of clays in salt solution," *Applied Clay Science*, vol. 101, pp. 354–361, 2014.
- [27] M. J. L. C. García-Gutiérrez, J. L. Cormenzana, T. Missana, M. Mingarro, and J. Molinero, "Overview of laboratory methods employed for obtaining diffusion coefficients in FEBEX compacted bentonite," *Journal of Iberian Geology*, vol. 32, no. 1, pp. 37–53, 2006.
- [28] Y.-G. Chen, C.-M. Zhu, W.-M. Ye, Y.-J. Cui, and B. Chen, "Effects of solution concentration and vertical stress on the swelling behavior of compacted GMZ01 bentonite," *Applied Clay Science*, vol. 124–125, pp. 11–20, 2016.
- [29] S. M. Rao and T. Thyagaraj, "Role of direction of salt migration on the swelling behaviour of compacted clays," *Applied Clay Science*, vol. 38, no. 1-2, pp. 113–129, 2007.
- [30] G. Xiang, W. Ye, Y. Xu, and F. E. Jalal, "Swelling deformation of Na-bentonite in solutions containing different cations," *Engineering Geology*, vol. 277, Article ID 105757, 2020.
- [31] W.-M. Ye, F. Zhang, Y.-G. Chen, B. Chen, and Y.-J. Cui, "Influences of salt solutions and salinization-desalinization processes on the volume change of compacted GMZ01 bentonite," *Engineering Geology*, vol. 222, pp. 140–145, 2017.
- [32] Y. He, W. M. Ye, Y. G. Chen, and Y. J. Cui, "Effects of K+ solutions on swelling behavior of compacted GMZ bentonite," *Engineering Geology*, vol. 249, pp. 241–248, 2018.
- [33] K. S. Pitzer and G. Mayorga, "Thermodynamics of electrolytes. II. Activity and osmotic coefficients for strong electrolytes with one or both ions univalent," *Journal of Physical Chemistry*, vol. 77, no. 19, pp. 2300–2308, 1973.

Research Article

A Statistic Damage Model of Rocks considering the Effect of Loading Rate

Kai Cui,^{1,2} Bin Hu ,¹ and Jing Li ¹

¹*School of Resources and Environmental Engineering, Wuhan University of Science and Technology, Wuhan, Hubei 430081, China*

²*School of Applied Engineering, Henan University of Science and Technology, Sanmenxia, Henan 472000, China*

Correspondence should be addressed to Bin Hu; hbin74@wust.edu.cn and Jing Li; lijing1994@wust.edu.cn

Received 14 December 2021; Revised 4 January 2022; Accepted 15 January 2022; Published 9 February 2022

Academic Editor: Bing Bai

Copyright © 2022 Kai Cui et al. This is an open access article distributed under the Creative Commons Attribution License, which permits unrestricted use, distribution, and reproduction in any medium, provided the original work is properly cited.

This paper develops a new statistic damage model for rock to mainly study the effect of a loading rate on its mechanical behaviours. The proposed model adopts a new loading rate-dependent damage density function and is capable of describing the macroscopic damage accumulation process for rock samples subjected to external high-speed dynamic loadings. The proposed model can also account for the residual strength of rocks by introducing a modified equivalent strain principle, which considers the contribution of the friction force to the strength of rocks. The friction force is generated by the movements of the nearby microcracks. The predicted stress-strain curves by the proposed model agree with the measured data of salty rock under the conditions of various confining pressures and loading rates. It can be found that both the peak strength and the corresponding axial strain are increased at high-speed loading conditions. At the same time, a transition from ductile failure to brittle failure can be observed in rock samples.

1. Introduction

The mechanical behaviours such as strength and deformation of rock are affected by loading rates [1–4]. The microcracks distributed inside the rock samples will be propagated and result in macroscopic damage [5–9]. Mathematical description of the dynamic loading-induced damage accumulation process plays a crucial role in modelling the rock behaviours.

In terms of strength, [10] proposed dynamic strength criteria for rock-like materials based on theoretical derivation to describe the uniaxial strength characteristics from quasistatic to dynamic uniformly [11] explored the effect of loading rate on the dynamic yield strength of sandstone through experiments. In addition, [12,13] carried out a series of dynamic experiments on the Bukit Timah granite. Based on the experimental results, they modified the Mohr-Coulomb strength criterion of rock to account for the effect of loading rates, which can accurately describe the dynamic response of rocks. Similarly, [14] proposed another strength criterion for the uniaxial dynamic strength of rocks based on

the work of [15] and established a statistical damage model which can reasonably simulate the dynamic deformation process of rock.

At the deformation aspect, [16–19] used the SHPB apparatus to conduct empirical research on the uniaxial dynamic behaviour of salt rock under different confining pressures and loading rates and obtained its steady and dynamic stress-strain curves. The experimental results showed that the salt peak strength of the rock corresponding axial strain would increase significantly with the increase of the loading rate. To simulate the dynamic deformation process of rock, [20] established a dynamic damage model of rock based on the viscoplastic theory by assuming that rock damage was only related to dynamic strain energy. However, [21] suggested that the stress level and the loading rate can also affect the damage law of rock.

The statistic damage models can account for the propagation process of microcracks and characterise the strength and deformation behaviours of rocks, which have been widely applied in geotechnical engineering. [22] developed a damage model to study the effect of freeze-thaw cycles and

confining pressures on the mechanical properties of rocks. [23] applied an equivalent continuum damage model for modelling the impact of weakness planes in rock masses on the stability of tunnels. The temperature may also affect the mechanical properties, which can be described using the statistic damage theory [24–26].

Although the above statistic damage models are widely applied in practice, some of them cannot describe the residual strength of rocks. To overcome such limitation, [27] introduced a rock damage scale factor following the assumption that the damaged components of rocks can still resist external force-induced deformation. At the same time, [28] modified the Lemaitre strain equivalence principle to include the friction force between the nearby microcracks.

This paper aimed to develop a dynamic statistic damage model to study the effect of loading rates on rocks' strength and deformation behaviours. First, the evolution law of the damage factor was assumed to be affected by the loading rates to describe the macroscopic damage accumulation process when the rock samples were subjected to external dynamic loading. Second, the proposed model adopted the modified Lemaitre strain equivalence assumption to consider the residual strength of the rock. The proposed model was used to predict the experimental results of salt rock under different confining pressures and loading rate conditions.

2. Dynamic Stress-Strain Curve of Rock

To study the effect of loading rates on the mechanical behaviours of salty rocks, [16] conducted a series of triaxial tests using the SPHB apparatus under the conditions of various confining pressures and loading rates. The measured stress-strain curves are presented in Figure 1; it can be found that the tangent modulus of rocks samples is gradually decreased during the early loading process, which is mainly induced by the damage of microstructure and the accumulation of plastic deformation. Besides, the stress-strain curves exhibit the feature of strain-softening after the peak strength state as the shear strength decreases considerably against the axial strain. At a given confining pressure, increasing the loading rate will lead to a higher peak shear strength, together with a larger corresponding axial strain, indicating that the strength of salt rock is enhanced at a high-speed loading condition.

Figure 2 shows the dynamic yield strength of the salty rock samples which is not affected by the loading rate ranging from 0.1–1.0/s, and the relationship between the yield strength and the confining pressure under the quasi-static loading conditions can be described using the conventional Mohr-Coulomb strength criteria. However, further increasing the loading rate will significantly increase the dynamic yield strength of rock samples; the most apparent increment happens in the case of $\sigma_3 = 5$ MPa, where the dynamic yield strength is approximately increased from 20 MPa to 62 MPa for the loading rates of 1.0 and 10^3 /s, respectively. To address such a strength enhancement phenomenon, [14] suggested that the strength of rocks consists of two different components: one is the quasi-static

strength that only depends on the confining pressure, whereas the other is the inertia force-induced strength. Increasing the loading rate will increase the inertia force-induced strength, which will play a primary role in forming the strength of rocks.

3. Statistical Damage Rock Model

3.1. Damage Factor. When rock is subjected to external forces, microcracks will gradually initiate and propagate to form random-distributed microcracks. The macroscopic damage accumulation process will decrease the tangent elastic modulus of rock samples and lead to a final failure.

Within the statistic damage theory, rock is assumed to consist of many microscope elements, and some of them will be damaged due to external forces. Assuming N is the number of all microscopic elements within rock and N_d is the number of damaged elements, the damage factor D is usually defined as the ratio between N_d and N as

$$D = \frac{N_d}{N}, \quad 0 \leq D \leq 1. \quad (1)$$

The Weibull distribution is used herein to describe the strength of microscopic elements, namely,

$$P(F) = \frac{m}{F_0} \left(\frac{F}{F_0} \right)^{m-1} \exp \left[- \left(\frac{F}{F_0} \right)^m \right], \quad (2)$$

where F is the element strength parameter corresponding to the failure criterion of rocks, which may be a function of the stress level or axial strain. m and F_0 are the shape and scale parameters, respectively.

We assume that the incremental number of damaged microscopic elements subjected to external forces is calculated as

$$dN_d = NP(F)dF. \quad (3)$$

Substituting equations (1) and (2) into (3), the damage factor D can be integrated as

$$D = \int_0^F P(F)dF \\ = 1 - \exp \left[- \left(\frac{F}{F_0} \right)^m \right]. \quad (4)$$

The damage factor D can quantify the macroscopic damage accumulation process. When D equals 1.0, rock samples will be completely damaged and lose the capability of resisting further deformation.

Figure 3 shows the effect of parameters m and F_0 on the evolution of D concerning F . On the one hand, it can be found that the evolution curve will conduct counterclockwise rotation by increasing the value of m . On the other hand, increasing the values of F_0 will significantly accelerate the macroscopic damage accumulation process.

3.2. Stress-Strain Relation. This study assumes that only a part of the rock sample will be damaged when subjected to

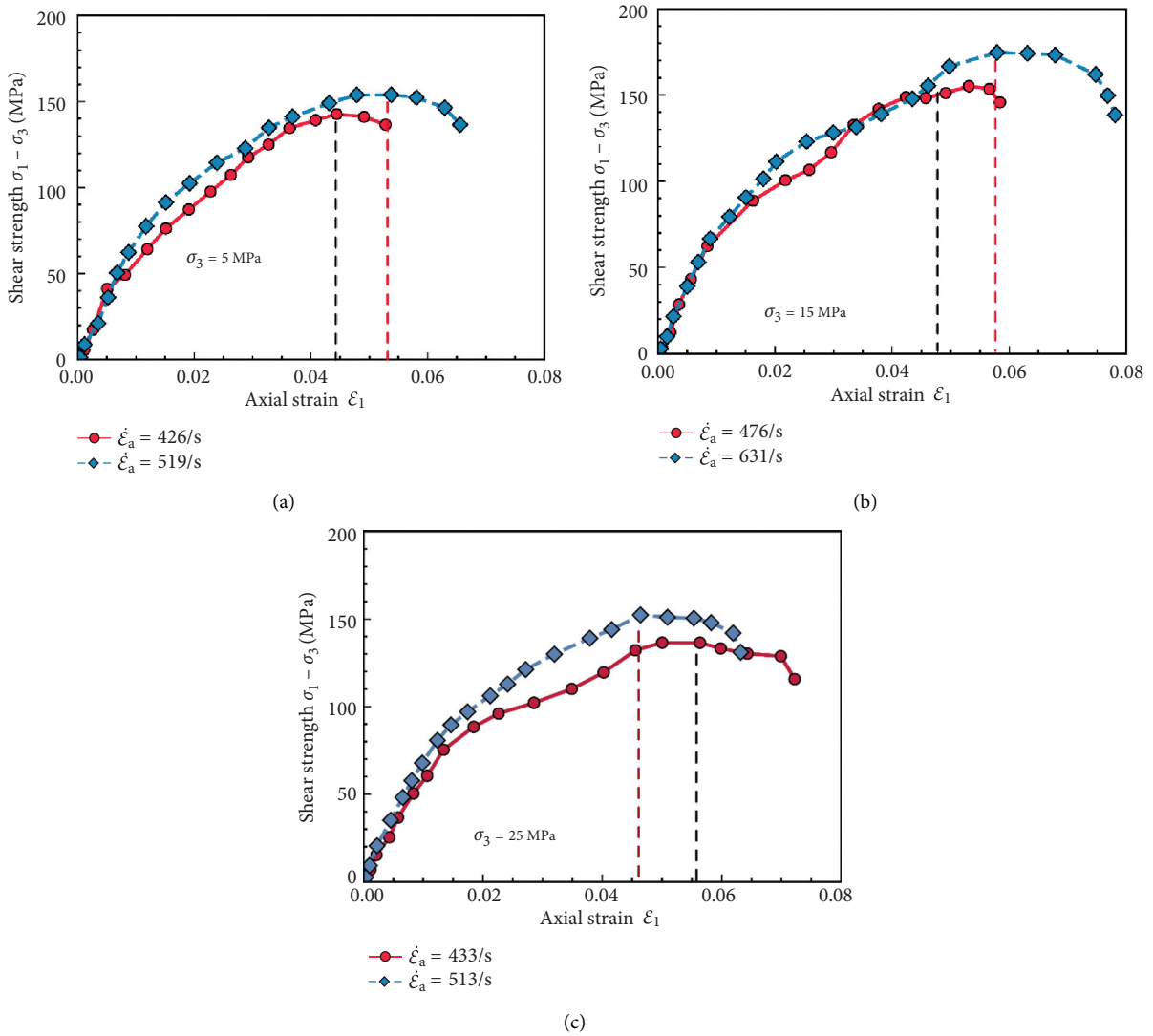


FIGURE 1: Dynamic stress-strain curves of salt rock [16] under different confining pressures and loading rates. (a) Confining pressure $\sigma_3 = 5$ MPa. (b) Confining pressure $\sigma_3 = 15$ MPa. (c) Confining pressure $\sigma_3 = 25$ MPa.

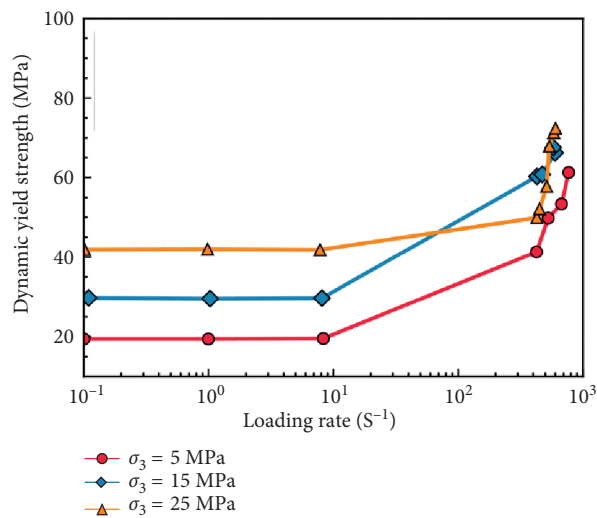


FIGURE 2: Dynamic yield strength of salt rock [16] corresponding to the loading rate at different confining pressures.

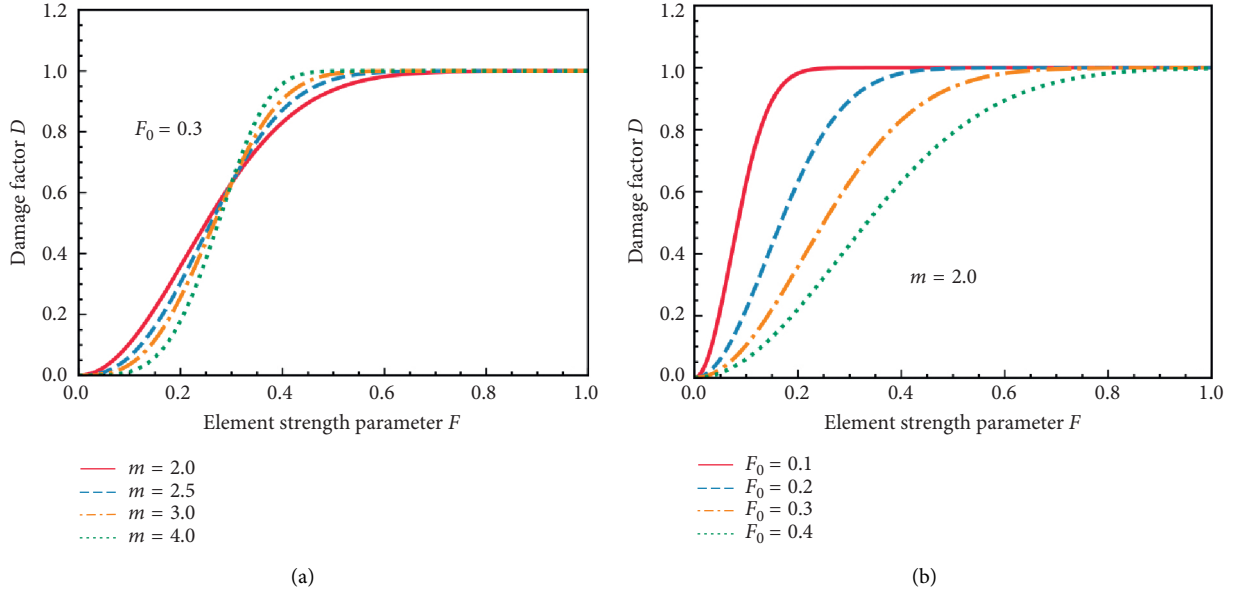


FIGURE 3: Effect of parameters m and F_0 on the evolution of D concerning F . (a) Parameter m . (b) Parameter F_0 .

external forces. The intact component will perform elastic response obeying the generalized Hook's law:

$$\dot{\sigma}'_i = E\dot{\varepsilon}'_i + \mu(\dot{\sigma}'_j + \dot{\sigma}'_k), \quad i, j, k = 1, 2, 3, \dots \quad (5)$$

where σ'_i and ε'_i are the undamaged stress and strain, respectively. E is the elastic modulus, and μ is the Poisson's ratio.

According to the equivalent strain principle, it can be considered that the rock is composed of damaged and undamaged materials under external load, and the damaged part of the material does not have any bearing capacity. The equivalent stress σ is defined as

$$\sigma_i = \sigma'_i(1 - D), \quad i = 1, 2, 3. \quad (6)$$

Substituting equation (6) into (5), the stress-strain relation of rock considering the macroscopic damage accumulation is given by

$$\sigma_i = E\varepsilon_i(1 - D) + \mu(\sigma_j + \sigma_k). \quad (7)$$

We note that equation (7) cannot predict the residual strength of rock samples at different confining pressures because D will turn to be zero after the rock samples are entirely damaged. To overcome this limitation, [28] suggested that the friction force between the nearby microcracks can contribute to the residual strength of rocks. After that, the stress-strain relation is modified to account for the residual strength σ_{residual} as

$$\sigma_i = E\varepsilon_i(1 - D) + D\sigma_{\text{residual}} + \mu(\sigma_j + \sigma_k), \quad (8)$$

where σ_{residual} is the residual strength of the rock. When $\sigma_{\text{residual}} = 0$, (8) will degenerate to the original Lemaitre strain equivalence assumption.

To consider the effect of the loading rate on the mechanical behavior of rocks, the evolution law of the damage ratio D in (9) is modified as

$$D = 1 - \exp\left\{-\left[\frac{\varepsilon_1}{F_0}\left(1 + \alpha \ln\left(\frac{\dot{\varepsilon}_1}{\varepsilon_{\text{ref}}}\right)\right)\right]^m\right\}, \quad (9)$$

where α is a non-negative material constant, and ε_{ref} is the reference loading rate that is chosen as $\varepsilon_{\text{ref}} = 10^{-5}$.

3.3. Model Parameter Calibration. The proposed statistic damage model for rocks includes six material parameters. The values of the elastic modulus E , Poisson's ratio μ , and the residual strength of σ_{residual} can be determined through the measured stress-strain curve of rock samples at a specific confining pressure. Parameter α should be calibrated by conducting another test with a different loading rate.

To calibrate the parameters m and F_0 , the measured peak strength state of the rock samples should be used. For a conventional triaxial test ($\sigma_2 = \sigma_3$), the stress-strain relation represented in (8) is simplified as

$$\sigma_1 = E\varepsilon_1(1 - D) + D\sigma_{\text{residual}} + 2\mu\sigma_3. \quad (10)$$

Once the peak strength state is reached, the derivative of σ_1 with the corresponding ε_1 should be zero, namely,

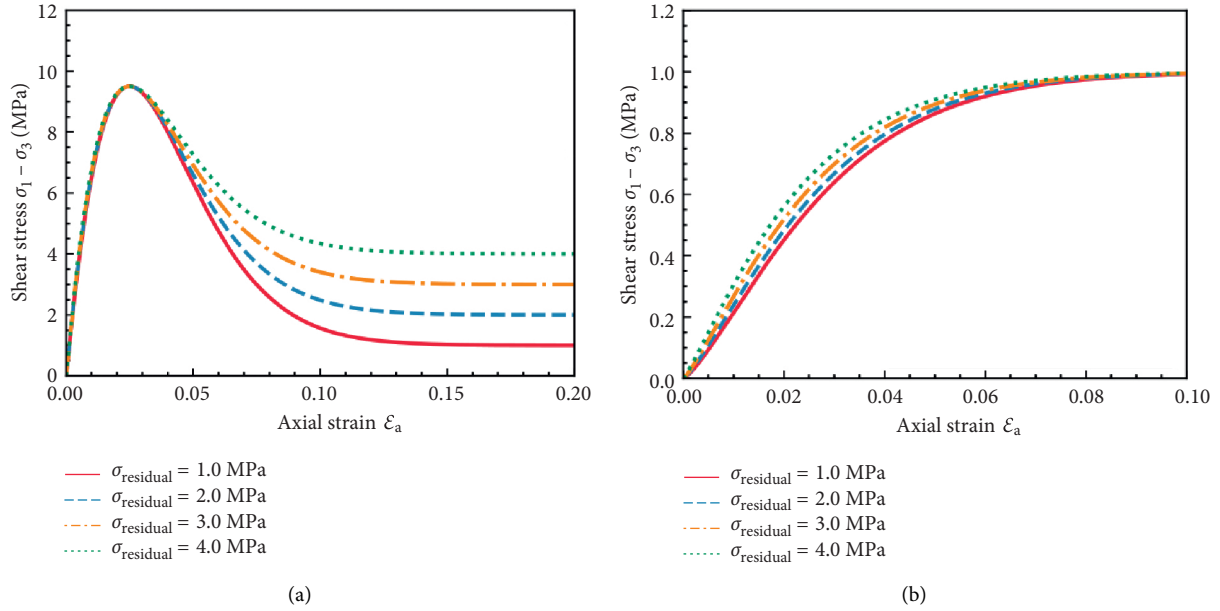
$$\frac{\partial \sigma_1}{\partial \varepsilon_1}\bigg|_{\varepsilon_1 = \varepsilon_{\text{peak}}, \sigma_1 = \sigma_{\text{peak}}} = 0, \quad (11)$$

where σ_{peak} and $\varepsilon_{\text{peak}}$ are the peak strength and the related axial strain.

Substituting (10) into (9) and calculating the derivatives, we obtain

TABLE 1: Model parameters for the proposed model.

Material parameters	Value
Elastic modulus E (MPa)	800.0
Poisson's ratio μ	0.5
Residual strength σ_{residual} (MPa)	1.5
Peak strength σ_{peak} (MPa)	10.0
Axial strain at the peak strength state $\varepsilon_{\text{peak}}$	0.025
Rate-related material constant α	1.0

FIGURE 4: Effect of residual strength σ_{residual} on stress-strain curve and damage curve of rock. (a) Stress-strain curve. (b) Damage curve.

$$\left\{ \frac{\varepsilon_1}{F_0} \left[1 + \alpha \ln \left(\frac{\dot{\varepsilon}_1}{\varepsilon_{\text{ref}}} \right) \right] \right\}^{m-1} = \frac{EF_0}{mE\varepsilon_{\text{peak}} - m\sigma_{\text{residual}}}. \quad (12)$$

The stress-strain relation at the peak strength state can be expressed as

$$\sigma_{\text{peak}} = (1 - D) \cdot E\varepsilon_{\text{peak}} + D \cdot \sigma_{\text{residual}} + 2\nu\sigma_3. \quad (13)$$

Solving equations (12) and (13) will lead to the exact expression of parameters m and F_0 as

$$m = \frac{E\varepsilon_{\text{peak}} [1 + \alpha \ln(\dot{\varepsilon}_1/\varepsilon_{\text{ref}})]}{(E\varepsilon_{\text{peak}} - \sigma_{\text{residual}}) \left[\ln \left(\sigma_{\text{peak}}^{-2\nu\sigma_3 - \sigma_{\text{residual}}} / E\varepsilon_{\text{peak}}^{-\sigma_{\text{residual}}} \right) \right]}, \quad (14)$$

$$F_0 = \left\{ \frac{mE\varepsilon_{\text{peak}} - m\sigma_{\text{residual}}}{E} \left[\varepsilon_{\text{peak}} \left(1 + \alpha \ln \left(\frac{\dot{\varepsilon}_1}{\varepsilon_{\text{ref}}} \right) \right) \right]^{m-1} \right\}^{1/m}.$$

3.4. Parameter Experiment. To investigate the performance of the proposed statistical damage model in modelling the dynamic mechanical behaviours of rocks, a series of case studies were conducted here by letting the confining pressure be 0.5 MPa, and the values of the corresponding model parameters are given in Table 1.

First, we studied the effect of the residual strength on the stress-strain curves of rocks. Unlike the previous statistical damage models, the proposed model introduced a modified equivalent strain principle to account for the contribution of the friction force between the propagated nearby microcracks and the strength of rocks. In the cases of σ_{residual} were chosen to be 1.0, 2.0, 3.0, and 4.0 MPa, the predicted stress-strain curves shown in Figure 4(a) indicated that the strain-softening feature was weakened during the post-failure process, and the rock samples turn to be more ductile, which was confirmed by the evolution of the damage factor against the axial strain, as shown in Figure 4(b).

Second, this paper explored the influence of loading rate on rock dynamic stress-strain curve and damage evolution law, and the calculation results are shown in Figure 5. From Figure 5(a), it can be seen that the loading rate does not affect the residual strength of rock. However, the peak strength of rock σ_{peak} will gradually increase with a gradual increase of $\dot{\varepsilon}_1$. On the contrary, the peak strength of rock σ_{peak} will gradually decrease. The calculation results are consistent with the experimental results of rock under dynamic loading.

According to Figure 5(b), the damage factor D will gradually decrease with the increase of loading rate in a small

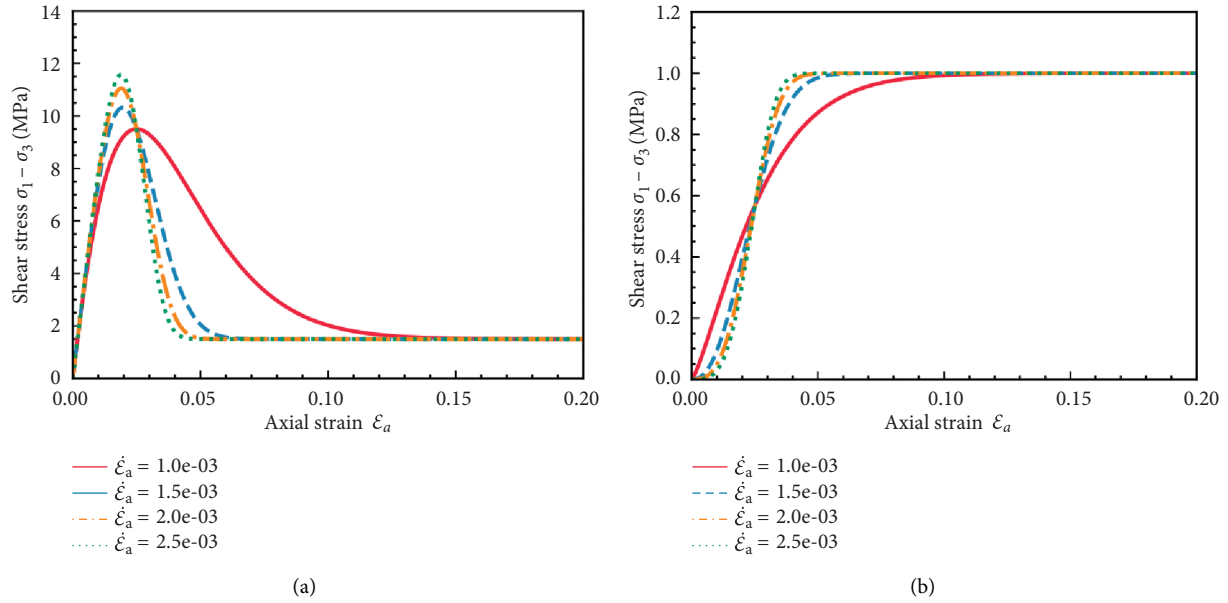


FIGURE 5: Effect of loading rates on stress-strain curve and damage curve of rock $\dot{\epsilon}_1$. (a) Stress-strain curve. (b) Damage curve.

TABLE 2: Model parameters of different kinds of rock.

σ_3/MPa	$\dot{\epsilon}/\text{S}^{-1}$	E/GPa	μ	m	F_0
5	426	7.12	0.25	1.182	0.053
	519	7.21	0.25	1.155	0.057
15	476	7.13	0.25	1.119	0.055
	631	7.24	0.25	1.209	0.063
25	433	6.08	0.25	0.932	0.046
	513	6.95	0.25	1.094	0.052

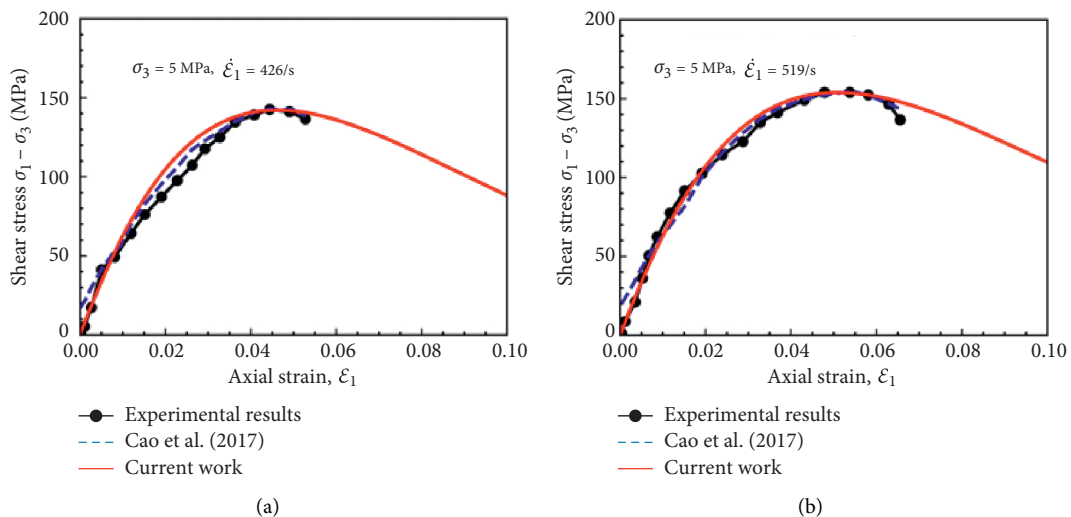


FIGURE 6: Comparison between experimental and model results of dynamic stress-strain curves of salt rock [16] under confining pressure $\sigma_3 = 5 \text{ MPa}$. (a) $\dot{\epsilon}_1 = 426/\text{s}$. (b) $\dot{\epsilon}_1 = 519/\text{s}$.

strain range ($\epsilon_1 \leq 0.025$), and the tangent modulus of rock will also increase. However, with the further increase of axial strain, the growth rate is accelerated with the increase of loading rate, leading to brittle failures of rock more

efficiently, and the stress-strain curve will have a noticeable “stress drop” phenomenon.

The experimental results show that the rock statistical damage model established in this paper can better describe

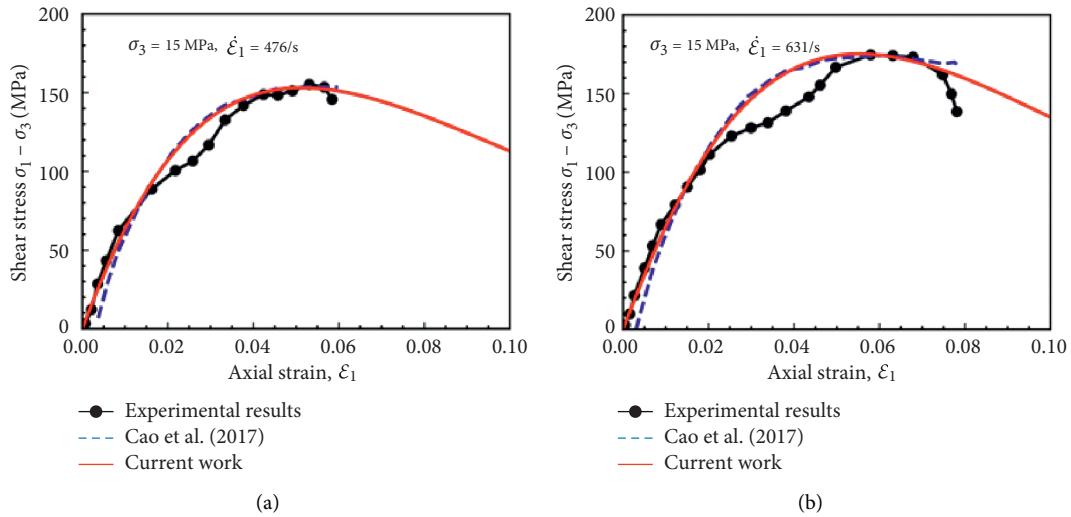


FIGURE 7: Comparison between experimental and model results of dynamic stress-strain curves of salt rock [16] under confining pressure $\sigma_3 = 15 \text{ MPa}$. (a) $\dot{\epsilon}_1 = 476/s$. (b) $\dot{\epsilon}_1 = 631/s$.

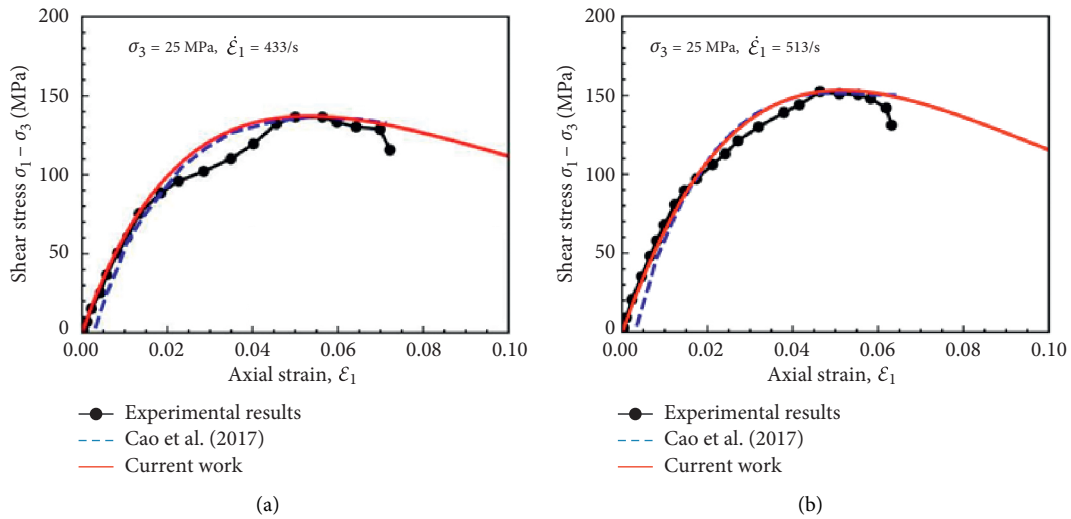


FIGURE 8: Comparison between experimental and model results of dynamic stress-strain curves of salt rock [16] under confining pressure $\sigma_3 = 25 \text{ MPa}$. (a) $\dot{\epsilon}_1 = 433/s$. (b) $\dot{\epsilon}_1 = 513/s$.

the effect of loading rate on the dynamic, progressive failure, and the residual strength of rock.

4. Model Verification

To further verify the performance of the proposed model, especially in describing the effect of loading rate on the dynamic yield strength of rocks, the experimental results of salty rocks are adopted here again. Table 2 gives the values of the model parameters with different confining pressures and loading rates.

The measured and predicted stress-strain curves by the proposed model are shown in Figures 6–8, together with the predictions by [14] as a comparison. Although the two statistic damage models predict similar results and can fit the measured dynamic yield strength quite well, the stress-strain curve predicted by [14] has an unreasonable shear strength

before the external force is applied. Such limitation is overcome by the proposed model, which can better account for the mechanical response of rock samples during the early loading stage. It is noted that the proposed model can be conveniently extended based on further experimental investigation to consider the effect of loading rate on the residual strength of rocks.

5. Conclusion

This paper develops a new statistic damage model for rock to study its dynamic mechanical behaviours. The evolution law of the damage factor is assumed to depend on the loading ratio. Besides, the proposed model adopts a modified equivalent strain principle to improve its performance in modelling the residual strength of rocks. The main conclusions are summarized as follows:

- (1) The microscopic damage accumulation process is affected by the loading rate, resulting in a higher peak strength of rocks. The evolution law of the damage factor is in terms of the axial strain and loading rate.
- (2) The modified equivalent strain principle enables the proposed model to predict a reasonable residual strength of rocks mainly formed by the friction force generated by the movement of the nearby microcracks.
- (3) The proposed model can well describe the stress-strain curves of salty rocks, providing a promising tool to study the dynamic behaviours of rocks.

Data Availability

The data used to support the findings of this study are included within the article.

Conflicts of Interest

The authors declare that they have no conflicts of interest regarding the publication of this paper.

Acknowledgments

This work was supported in part by the National Natural Science Foundation of China under Grant nos. U1802243 and 41672317, in part by the Hubei Province Technical Innovation Special (major projects) Project under Grant no. 2017ACA184, and in part by the Major Science and Technology Projects of WUST Cultivate Innovation Teams under Grant no. 2018TDX01.

References

- [1] S. J. Xie, H. Lin, Y. F. Chen, Y. Wang, R. Cao, and J. Li, "Statistical damage shear constitutive model of rock joints under seepage pressure," *Frontiers of Earth Science*, vol. 8, no. 3, p. 232, Article ID 00232, 2020.
- [2] S. Xie, H. Lin, Y. Wang et al., "A statistical damage constitutive model considering whole joint shear deformation," *International Journal of Damage Mechanics*, vol. 29, no. 6, pp. 988–1008, 2020.
- [3] W. J. Liu, Z. W. Dan, Y. J. Jia, and X. H. Zhu, "On the statistical damage constitutive model and damage evolution of hard rock at high-temperature," *Geotechnical & Geological Engineering*, vol. 38, no. 6, pp. 4307–4318, 2020.
- [4] H. B. Jiang, K. N. Li, and X. B. Hou, "Statistical damage model of rocks reflecting strain softening considering the influences of both damage threshold and residual strength," *Arabian Journal of Geosciences*, vol. 13, no. 7, pp. 1–8, 2020.
- [5] Y. Pan, Z. M. Zhao, L. He, and G. Wu, "A nonlinear statistical damage constitutive model for porous rocks," *Advances in Civil Engineering*, vol. 2020, no. B3, 12 pages, Article ID 8851914, 2020.
- [6] C. T. Zhou, K. Zhang, H. B. Wang, and Y. X. Xu, "A plastic strain based statistical damage model for brittle to ductile behaviour of rocks," *Geomechanics and Engineering*, vol. 21, no. 4, pp. 349–356, 2020.
- [7] K. Chen, "Constitutive model of rock triaxial damage based on the rock strength statistics," *International Journal of Damage Mechanics*, vol. 29, no. 10, pp. 1487–1511, 2020.
- [8] W. Liu, S. Zhang, and B. Sun, "Energy evolution of rock under different stress paths and establishment of A statistical damage model," *KSCCE Journal of Civil Engineering*, vol. 23, no. 10, pp. 4274–4287, 2019.
- [9] J. Lemaitre, *A Course on Damage Mechanics*, Springer, Berlin, Germany, 1992.
- [10] J. Hu, Y. P. Yao, X. D. Zhang, and Y. Wei, "Dynamic strength criterion for rock-like materials," *Chinese Journal of Geotechnical Engineering*, vol. 42, no. 3, pp. 97–104, 2020.
- [11] F. Q. Gong, D. H. Lu, X. B. Li, and Q. H. Rao, "Experimental research of sandstone dynamic strength criterion under different strain rates," *Rock and Soil Mechanics*, vol. 34, no. 9, pp. 2433–2441, 2013.
- [12] H. B. Li, J. Zhao, and J. R. Li, "Experimental study on dynamic mechanical properties of granite under triaxial condition," *Explosion and Shock Waves*, vol. 24, no. 5, pp. 470–474, 2004.
- [13] J. Zhao and H. B. Li, "Estimating the dynamic strength of rock using mohr-coulomb and hoek-brown criteria," *Chinese Journal of Rock Mechanics and Engineering*, vol. 22, no. 2, pp. 171–176, 2003.
- [14] W. G. Cao, X. T. Lin, C. Zhang, and S. Yang, "A statistical damage simulation method of dynamic deformation process for rocks based on nonlinear dynamic strength criterion," *Chinese Journal of Rock Mechanics and Engineering*, vol. 36, no. 4, pp. 794–802, 2017.
- [15] Q. H. Qian and C. Z. Qi, "Dynamic strength and dynamic fracture criteria of rock and rock mass," *Journal of Tong ji University(Natural Science)*, vol. 36, no. 12, pp. 1599–1605, 2008.
- [16] Q. Fang, Z. Ruan, C. C. Zhai, X. Jiang, L. Chen, and W. Fang, "Split Hopkinson pressure bar test and numerical analysis of salt rock under confining pressure and temperature," *Chinese Journal of Rock Mechanics and Engineering*, vol. 31, no. 9, pp. 1756–1765, 2012.
- [17] Q. Z. Wang, W. Li, and X. L. Song, "A method for testing dynamic tensile strength and elastic modulus of rock materials using SHPB," *Pure and Applied Geophysics*, vol. 163, no. 5-6, pp. 1091–1100, 2006.
- [18] Q. Z. Wang, W. Li, and H. P. Xie, "Dynamic split tensile test of Flattened Brazilian Disc of rock with SHPB setup," *Mechanics of Materials*, vol. 41, no. 3, pp. 252–260, 2009.
- [19] X. Li, Y. Zou, and Z. Zhou, "Numerical simulation of the rock SHPB test with a special shape striker based on the discrete element method," *Rock Mechanics and Rock Engineering*, vol. 47, no. 5, pp. 1693–1709, 2014.
- [20] L. X. Xie, G. M. Zhao, and X. R. Meng, "Research on excess stress constitutive model of rock under impact load," *Chinese Journal of Rock Mechanics and Engineering*, vol. 32pp. 2772–2781, z1, 2013.
- [21] W. G. Cao, H. Zhao, L. Zhang, and Y. J. Zhang, "Simulation method of dynamic triaxial deformation process for rock under invariable strain rate," *Chinese Journal of Geotechnical Engineering*, vol. 32, no. 11, pp. 1658–1664, 2010.
- [22] H. M. Zhang, X. Z. Meng, and G. S. Yang, "A study on mechanical properties and damage model of rock subjected to freeze-thaw cycles and confining pressure," *Cold Regions Science and Technology*, vol. 174, Article ID 103056, 2020.
- [23] G. Xu, M. Gutierrez, C. He, and S. Wang, "Modeling of the effects of weakness planes in rock masses on the stability of tunnels using an equivalent continuum and damage model," *Acta Geotechnica*, vol. 16, no. 7, pp. 2143–2164, 2021.

- [24] B. Bai, R. Zhou, G. Q. Cai, W. Hu, and G. C. Yang, "Coupled thermo-hydro-mechanical mechanism in view of the soil particle rearrangement of granular thermodynamics," *Computers and Geotechnics*, vol. 137, no. 8, Article ID 104272, 2021.
- [25] B. Bai, G. C. Yang, T. Li, and G. S. Yang, "A thermodynamic constitutive model with temperature effect based on particle rearrangement for geomaterials," *Mechanics of Materials*, vol. 139, Article ID 103180, 2019.
- [26] W. L. Feng, C. S. Qiao, T. Wang, M.-y Yu, S.-J. Niu, and Z.-Q. Jia, "Strain-softening composite damage model of rock under thermal environment," *Bulletin of Engineering Geology and the Environment*, vol. 79, no. 11, pp. 4321–4333, 2020.
- [27] S. Q. Yang, W. Y. Xu, L. D. Wei, and C. D. Su, "Statistical constitutive model for rock damage under uniaxial compression and its experimental study," *Journal of Hohai University(Natural Sciences)*, vol. 32, no. 2, pp. 200–203, 2004.
- [28] H. C. Li and S. Zhang, "A constitutive damage model of rock based on the assumption of modified Lemaitre strain equivalence hypothesis," *Rock and Soil Mechanics*, vol. 38, no. 5, pp. 1321–1326+1334, 2017.

Research Article

Breakage Characteristics of Quartz Sand Based on Ring Shear Tests: Implications for the Fragmentation Processes of Rock Avalanches

Xinxin Zheng ¹, Ruichen Chen ¹, Jian Chen ¹, Song Chen ², and Lulu Shi ¹

¹School of Engineering and Technology, China University of Geosciences Beijing, Beijing 100083, China

²School of Urban Geology and Engineering, Hebei GEO University, Shijiazhuang 050031, China

Correspondence should be addressed to Jian Chen; jianchen@cugb.edu.cn and Song Chen; chennsongg@163.com

Received 7 December 2021; Accepted 16 December 2021; Published 13 January 2022

Academic Editor: Bing Bai

Copyright © 2022 Xinxin Zheng et al. This is an open access article distributed under the Creative Commons Attribution License, which permits unrestricted use, distribution, and reproduction in any medium, provided the original work is properly cited.

To investigate the effects of internal shear fragmentation on dry granular flow, in this study a series of ring shear tests were performed on quartz sand samples under different normal stresses (100 kPa, 200 kPa, and 300 kPa), shear displacements (3 m, 5 m, 10 m, 15 m, and 20 m), and shear rates (30 deg min⁻¹, 60 deg min⁻¹, and 90 deg min⁻¹). Next, the grain-size distributions, fractal dimensions, and microcharacteristics of the quartz sand before and after the experiments were compared and analyzed. The study results show that grain breakage under shearing preferentially occurs at the edges of the particles and forms a bimodal distribution in frequency grain-size distribution curves, which is consistent with observations of rock avalanches. The fine particles prevent the coarse particles from breaking, in turn leading to the ultimate grain-size distribution and stable fractal dimension (2.61) of quartz sand at relatively small shear displacements compared with the travel distance of rock avalanches. The results of this study suggest that the fragmentation of rock avalanches during the shear spread stage may be far less significant than previously believed. Therefore, the fragmentation effect is not considered to be a major factor of the hypermobility in the late stage of rock avalanches.

1. Introduction

Rock avalanches are distinguished by their massive scale, rapid speed, and extensive travel distances, all of which are extremely dangerous and destructive [1, 2]. Therefore, it is of great significance to clarify the kinematic characteristics and mechanism of rock avalanches for their monitoring and early warning.

Since Heim conducted a series of field investigations and described the hypermobility of the debris flow of the Elm landslide which occurred in Switzerland in 1881 [3], various theoretical models have been proposed to explain the high-speed and long-runout movement mechanism of rock avalanches [4], including the cushion of trapped air [5, 6], frictional melting [7–9], substrate liquefaction [10, 11], dynamic fragmentation [12–14], acoustic fluidization [15, 16], and momentum transfer motion [17]. However, these hypotheses are still widely debated, due to the rarity of the field

evidence [18]. The fragmentation hypothesis proposed by Davies may be the most promising hypothesis at present [19], due to the fact that intense fragmentation is characteristic of rock avalanches. Recently, increasing numbers of studies regarding dynamic fragmentation have been published [20–23].

Based on the fact that granular flow is influenced by multiple factors, dynamic fragmentation is more of a complex process controlled by a nonsingle mechanism [24–28]. Most fragmentation occurs during the early stage of movement, which is dominated by collision [29]. Further fragmentation of the block is caused by factors such as shearing during later transport, and it is unevenly distributed throughout the landslide body [30].

A typical facies model of rock avalanches has been proposed by Dufresne et al. [30]. The significant differences in the grain-size distribution of different facies suggest that the fragmentation process in rock avalanches is complex.

Some studies have explored the fragmentation characteristics and mechanisms based on the sedimentation characteristics of the rock avalanches. For example, some researches have indicated that the rock avalanches exhibit grain size differentiation with the accumulation of distance; that is, the fragmentation gradually increases with the development of the rock avalanches movement process [10, 27, 30–33]. Hewitt [34] pointed out that rugged topography exerts an essential influence on the morphology and structure of rock avalanche accumulations and that topographic obstruction not only limits the fragmentation process in rock avalanches but also creates different facies. Shugar and Clague [27] and Dufresne et al. [30] suggested that lithology is partially responsible for the differences occurring in particle size fractions. In addition, Perinotto et al. [35] compared the morphological characteristics of particles in rock avalanche deposits and identified the fact that the particle refinement after reaching a certain level of particle collisional fragmentation during rock avalanche is mainly dependent on the shear effect. However, similar to the results on the grain size of carapace facies [27, 29], numerous studies have indicated that the grain-size distribution did not vary significantly with the travel distance [36–38].

These inconsistent findings have indicated that the sedimentary characteristics of rock avalanches remain ambiguous, and a clear model for fracture characteristics is lacking. These field investigations are influenced not only by the original lithology and topography but also by the scarcity and limitation of outcrops. Therefore, it is necessary to conduct tests in a more ideal and simplified environment.

More recently, some studies had revealed the frictional weakening with the velocity [39–41], yet their explanations have differed from one another. Wang et al. [40] observed the frictional weakening is caused by thermal pressurization and moisture fluidization, Hu et al. [41] held there is thixotropy in dry particle flow under a high-speed shearing, and Jiang et al. [39] proposed that the dynamic fragmentation and elastic energy release were the causes of the frictional weakening.

There have also been an increasing number of ring shear tests carried out to study the fracture characteristics of dry granular flow. For example, the tests carried out by Dubovskoi et al. [42] revealed that a small static load combined with shear could cause significant particle fragmentation. In addition, Zhang and McSaveney [28] suggested that shear displacement and normal stress are the factors affecting fragmentation, rather than the shear strain rate. The test results for the landslide soils roughly indicated that the grain size limit appears to occur at a displacement of 3 m [43]. Furthermore, Coop et al. [44] noted that stable grading exists in carbonate sand under large displacement shear. Although the abovementioned studies have presented the grain size characteristics, they have not systematically explained the elevation process or the mechanism of fragmentation.

The characteristics of the grain-size distribution and fragmentation limits are very critical issues, as they are significant for understanding the fragmentation and emplacement

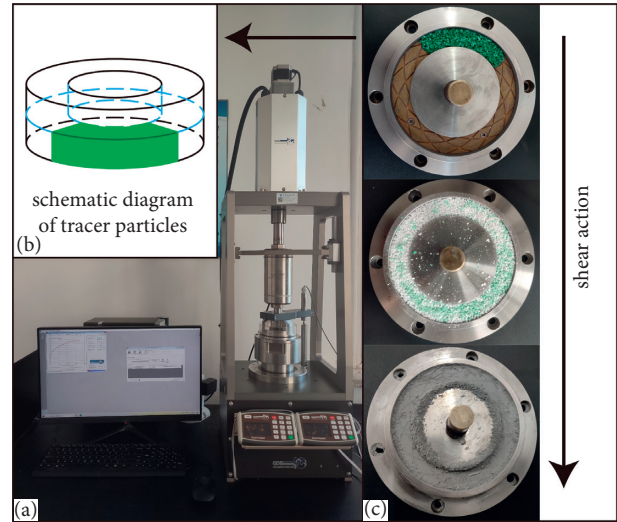


FIGURE 1: Diagrams of the experimental apparatus. (a) GDS ring shear instrument. (b) Schematic diagram of the initial position of the tracer particles. (c) Photograph of tracer results.

TABLE 1: Parameters of the instrument.

	Maximum load	Distinguishability	Accuracy (%)
Axial force	5 kN	1 N	0.2
Torque	200 Nm	0.001 Nm	0.2

processes. Meanwhile, the fragmentation limit also determines to a certain extent whether the dynamic fragmentation could continue throughout the emplacement process of rock avalanches. Previous complex field findings and experimental results have prompted us to conduct a more systematic study regarding the fragmentation characteristics under shear. We have yet to explore the process of disintegration and collision fragmentation in the early stage of rock avalanches, nor have we explored the rheological weakening [41] or frictional weakening under thermalization [40,45,46]. The main purpose of the present study was to explore the characteristics of shear fragmentation and its effect. We systematically analyzed the results of long-displacement ring shear tests in terms of shear stress variation, grain-size distribution and fractal dimension variation, and particle microscopic characteristics, so as to provide insights regarding the shear fragmentation effect of rock avalanches.

2. Methodology

2.1. Materials and Experiment Setups. The experiment aimed to investigate the fragmentation characteristics of dry granular flow during the large-displacement shear process. A GDS(RST) ring shear instrument was used in this study to simulate the continuous strains of granular flow (Figure 1(a)). The inner and outer ring diameters of the shear box are 70 mm and 100 mm, respectively, with a height of 5 mm and an area of 0.004 m^2 . The other detailed instrument parameters are listed in Table 1.

Dry quartz sand with angular shapes was used in this experiment. With the exception of the tests of different grain

TABLE 2: Details of the tests conducted.

No.	Normal stress (kPa)	Shear rate (deg min ⁻¹)	Shear rate (mm s ⁻¹)	Shear displacement (m)
1	100/200/300	60	0.74	15
2	200	30/60/90	0.37/0.74/1.11	15
3	200	60	0.74	3/5/10/15/20

sizes, all tests used 1-1.5 mm coarse quartz sand, which could provide a more distinct difference in the fragmented process than well-graded sand grains. Compared to calcareous sand, quartz sand has a more uniform angular shape and greater density (2,000 kg/m³), making it more closely resemble rock fragments [47]. In addition, quartz sand can provide more microscopic information to reveal the dynamic processes of fragmentation [48,49]. In the experiments, 30 g of quartz sand granules was weighed and placed evenly throughout the shear box, and the initial porosity of the specimens was controlled at 43.47%. The tracer experiments showed that the dyed particles were dispersed in both the horizontal and longitudinal directions after the shearing (Figures 1(b) and 1(c)). Table 2 illustrates the three test groups with different normal stresses, shear rates, and shear displacements. The normal stresses of 100 kPa, 200 kPa, and 300 kPa in group 1, respectively, correspond to the burial depths of approximately 5 m, 10 m, and 15 m. The data recording interval was 1 s.

2.2. Grain-Size Distribution and Fractal Dimension. The grain-size distributions of the samples were determined using a HELOS H2566 laser grain size analyzer (0.01 to 3,500 μm). The average value of 10 measurements of each sample was taken as the final grain-size distribution. The cumulative grain-size distributions and frequency grain-size distributions were both used to qualitatively assess the differences in grain size.

The fragmentation of rock material always produces small-size particles, and these continue to be crushed to produce even smaller particles, which is generally considered to be self-similar behavior [25, 50]. The fractal dimension, FD , was employed to quantitatively determine the degree of shear fragmentation. In order to calculate the FD , the relationship between the mass percentage and FD is reconstructed as follows:

$$\frac{M(r)}{M(r_0)} = \frac{\int_0^r 4/3\pi\rho x^3 d(N/N_0)}{\int_0^{r_{\max}} 4/3\pi\rho x^3 d(N/N_0)}, \quad (1)$$

$$\frac{M(r)}{M(r_0)} = \left(\frac{r}{r_{\max}}\right)^{3-FD},$$

where $M(r)$ is the total mass of particles with a size larger than r , $M(r_0)$ is the total mass of particles, r_0 is related to the average grain size, N_0 is the total number of particles, r_{\max} is the maximum particle size, and FD is the fractal dimension. In a double logarithmic coordinate system of $M(r)/M(r_0)$ — r , the slope of the regression line fitted at each point is equal to $3-FD$ [25].

2.3. Morphometric and Microscopic Method. The elongation ratio and circularity were used to quantitatively assess the morphological changes of the particles before and after shearing. The elongation ratio was defined as I/L (L is specified as the longest dimension of the particle and I is the longest dimension perpendicular to L). The circularity was defined as the ratio of the area of a particle to the area of a circle with the same circumference $C = 4\pi A/d^2$ [51], where A denotes the two-dimensional projected area of the particle and d denotes its equivalent perimeter. As the particles approach a circular form, the values increase from 0 to 1. The above analysis was performed based on optical microscope magnification photographs. Next, the surface textures of quartz sand were observed and photographed using scanning electron microscopy (Zeiss supra 55), after having been sputter-coated with gold by Quorum SC7620. The frequency of the microtextures was then counted for analysis [52–54].

3. Results

3.1. Shear Strength. The influence of the particle size (0.25–0.5 mm, 0.5–1 mm, 1–1.5 mm, and 1.5–2 mm) was tested under normal stress of 200 kPa at a shear rate of 60 deg min⁻¹. Figure 2 illustrates the control of particle size on shear strength. The smaller the average particle size was, the greater the shear strength would be, although the increase was small (0.5–3 kPa).

Figure 3 presents the shear stress-displacement relationship for 1-1.5 mm quartz sand at a shear rate of 60 deg min⁻¹, but under the normal stresses of 100 kPa, 200 kPa, and 300 kPa. Clearly, the shear strength of quartz sand particles increases with the normal stress. In addition, a slight increase in shear strength with displacement is observed in Figure 3, where the shear strength changes from 80 kPa to 85 kPa under 300 kPa. It can be seen that when the maximum size of the particles is reduced, the shear stress increases by 1% to 6%.

The relationship between the strain rate and shear stress was also tested and analyzed (Figure 4). Consistent with the experimental results of Zhang and McSaveney [28], the difference in shear strength of the samples at different shear rates in this study was also very minimal, with $a < 1\%$ change in the mean values. The most noteworthy aspect is that all of the shear stress-displacement curves exhibit significant fluctuations, reaching up to 24% of the respective average values.

3.2. Changes in Grain-Size Distribution and Fractal Dimension after Shearing Action. Previous research has shown that particle fragmentation is independent of the

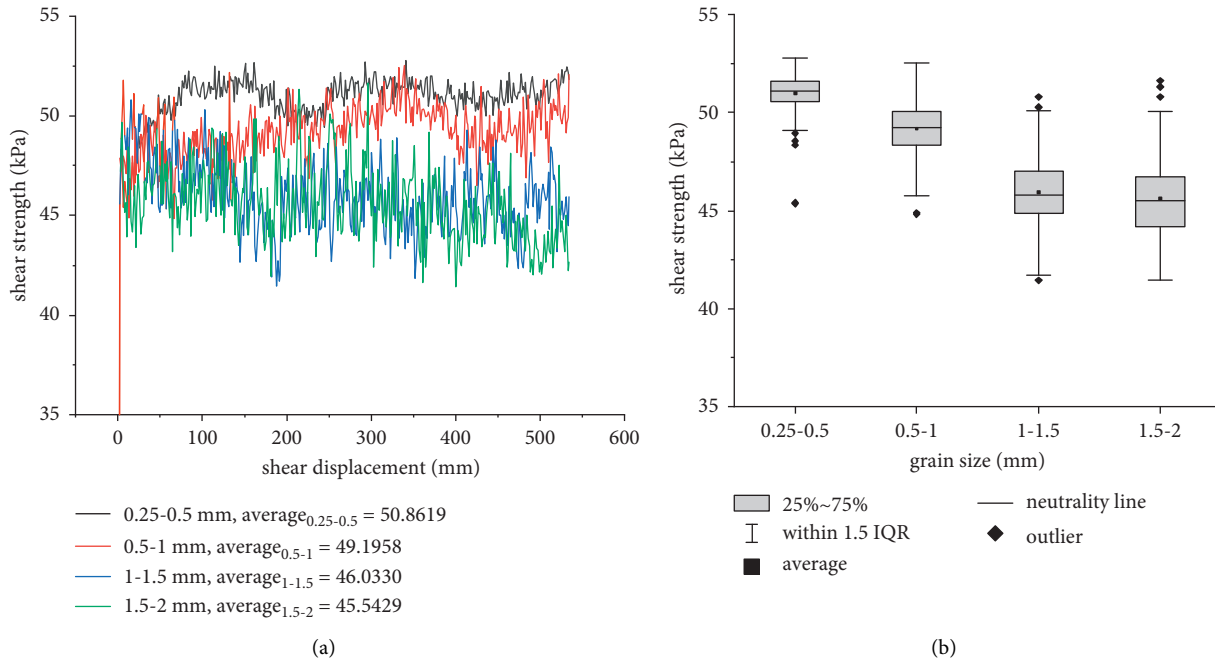


FIGURE 2: Distribution of shear strength in different grain sizes. (a) Shear stress-displacement curves of particles with different grain sizes. (b) Box plot of shear strength for different grain sizes.

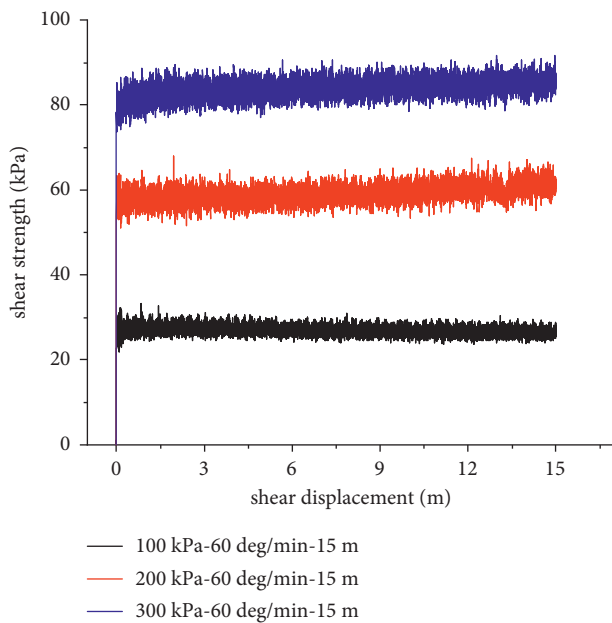


FIGURE 3: Shear stress-displacement curves under different normal stresses.

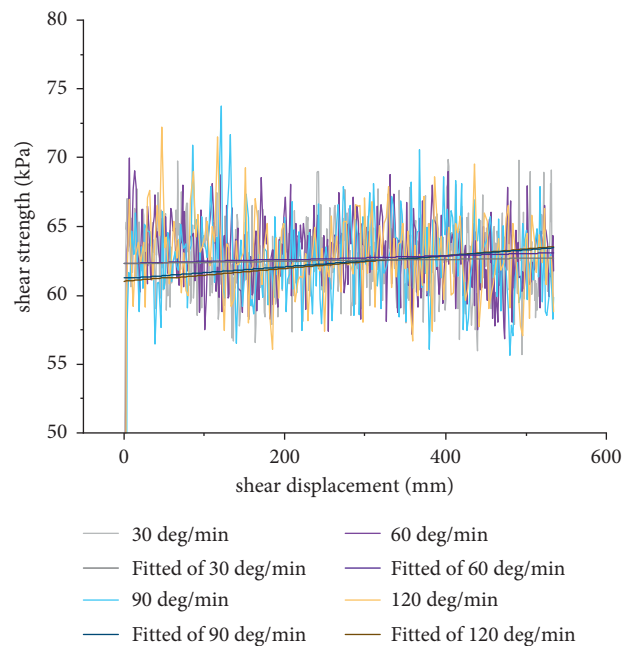


FIGURE 4: Shear stress-displacement curves at different shear rates.

shear rate and is only related to the normal stress and shear displacement [28]. In order to further investigate the characteristics of the shear fragmentation, experiments similar to the previous study were first carried out. Figure 5 presents the cumulative grain-size distribution curves and the frequency grain-size distribution curves at the same shear rate (60 deg/min) and shear displacement (15 m), but under normal stresses of 100 kPa, 200 kPa, and 300 kPa. The results reveal that the shear process, respectively, produced

2.79%, 27.27%, and 47.83% of the fragments below $100 \mu\text{m}$ (Figure 5(a)) and that the coarse peak shown in Figure 5(b) clearly shifted to the left ($1,593.86 \mu\text{m}$, $936.59 \mu\text{m}$, and $657.27 \mu\text{m}$). In addition, the conclusion reached by Zhang and McSaveney [28], namely, that the shear strain rate does not affect the grain-size distribution, is also verified here (Figure 6).

Figure 7 presents the evolution of grain-size distributions with shear displacements (200 kPa, 60 deg/min). At a shear

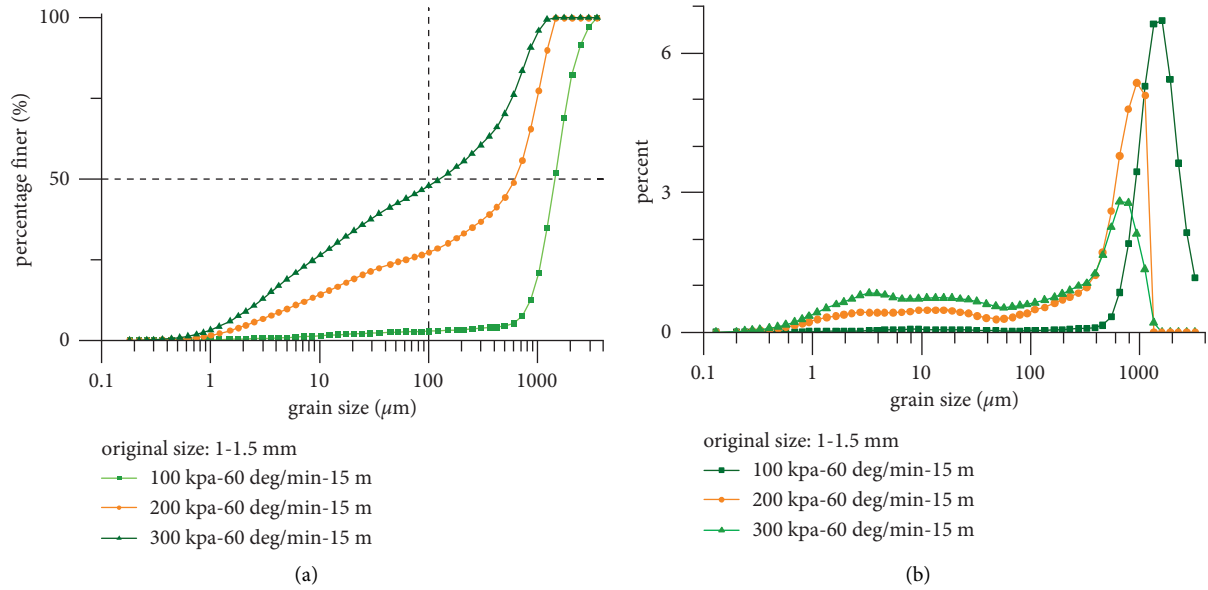


FIGURE 5: Evolution of grain size distribution with normal stresses. (a) Cumulative grain-size distribution curves after shearing at 15 m at a shear rate of 60 deg/min under the normal stresses of 100 kPa, 200 kPa, and 300 kPa. (b) Frequency grain-size distribution curves after shearing at 15 m at a shear rate of 60 deg/min and under the normal stresses of 100 kPa, 200 kPa, and 300 kPa.

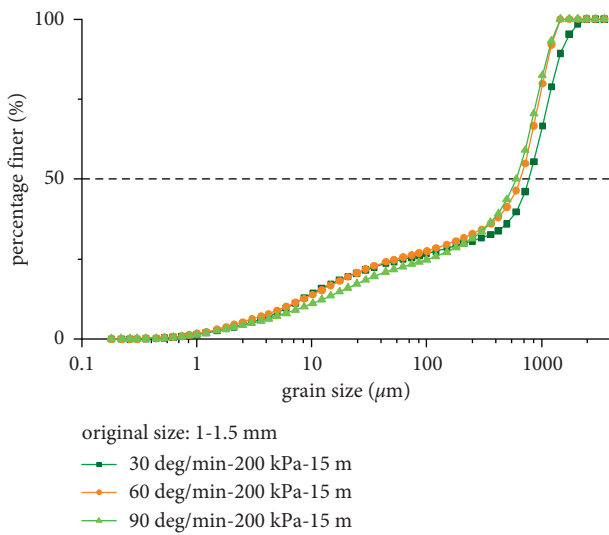


FIGURE 6: Cumulative grain-size distribution curves after shearing at 15 m at the shear rates of 30 deg/min, 60 deg/min, and 90 deg/min under a normal stress of 200 kPa.

displacement of less than 10 m, the cumulative grain-size distribution curve shifts to the left as the displacement increases (Figure 7(a)). At the same time, the coarse peak of the frequency grain-size distribution curve also gradually shifts towards the left side, and the fine peak at 15 μm becomes more and more apparent (Figure 7(b)). After the shear displacement exceeds 10 m, no significant differences are found in the grain-size distributions (as seen in the curves of 15 m and 20 m in Figures 7(a) and 7(b)). In addition, it can be seen that the changes of these curves are mainly attributed to the increase in the powder grade fragments below 80 μm (Figure 7(b)). The most striking result to emerge is that a bimodal distribution

develops following a large shear displacement (at 10 m and above). The fine peaks are about 15 μm, which is about 1/70 of the original size of the quartz sand. Bimodal distribution is often observed in the shear zone of rock avalanches, as seen in Figure 7(c) [30]. It is worth noting that the cumulative grain-size distributions of 200 kPa–60 deg/min–15 m in Figures 5(a), 6, and 7(a) are the results of different tests. Similar results indicate that these ring shear tests are stable and credible.

The fractal dimensions of the grain-size distributions were calculated, and the results are shown in Table 3. The coefficient of determination R^2 is greater than 0.8, which illustrates that the particle fragmentation under shear conforms to the fractal law. The higher the value of fractal dimension (FD) is, the higher the degree of fragmentation will be [25]. The fractal dimension results for Group A and Group B (Table 3) further indicate that particle fragmentation is related to the normal stress, but not the strain rate. In addition, Group C demonstrates that the FD increases with increasing shear displacement between 3 m and 15 m. The degree of particle fragmentation increases while the increasing rate of FD decreases. After 15 m of shear displacement, the fractal dimension reaches 2.5936, which is only 2% different from the fractal dimension of 2.6140 at 20 m. The small difference in FD indicates that the degree of fragmentation is basically stable following a large shear displacement.

3.3. Microscopic Characteristics of Particles under Shearing Action. 100 coarse particles (1–1.5 mm) were randomly selected from the samples following different displacements tests and observed under a low-magnification microscope. It is clear that the morphological characteristics of the particles have changed with the shear displacement (Figure 8). Figure 9 quantitatively illustrates the elongation ratio

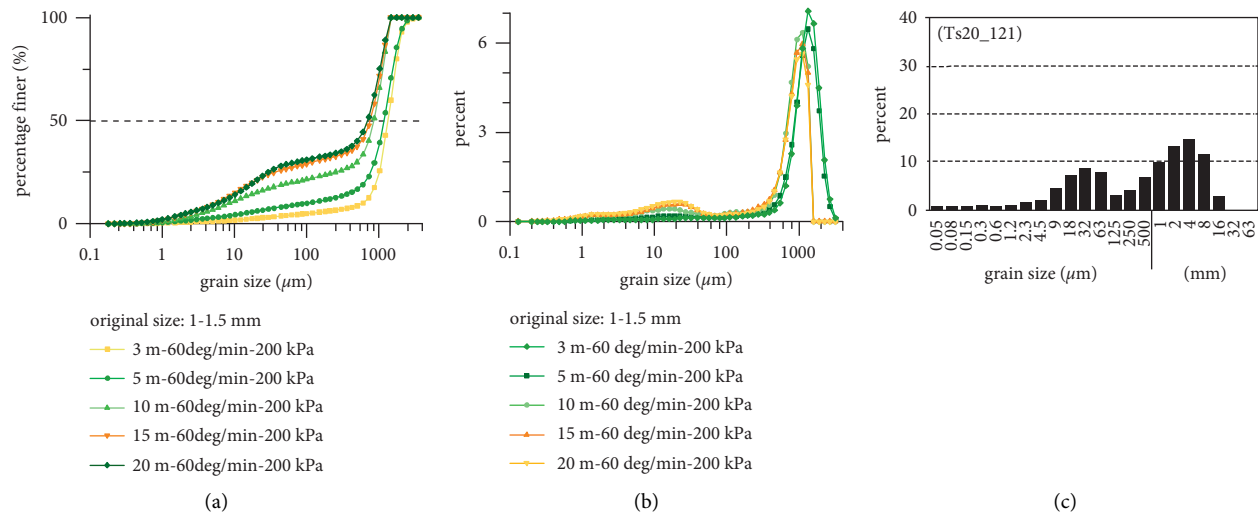


FIGURE 7: Evolution of grain size distributions with shearing displacements. (a) Cumulative grain-size distribution curves at a shear rate of 60 deg/min under a normal stress of 200 kPa after shearing at 3 m, 5 m, 10 m, 15 m, and 20 m. (b) Frequency grain-size distribution curves at a shear rate of 60 deg/min under a normal stress of 200 kPa after shearing at 3 m, 5 m, 10 m, 15 m, and 20 m. (c) Grain-size distribution histograms of the shear zone at Tschirgant showed bimodal distributions [30].

TABLE 3: Fractal dimensions of the different tests.

Group	Normal stress (kPa)	Shear rate (deg min ⁻¹)	Shear displacement (m)	Fractal dimension FD	Coefficient of determination R ²
A	100	60	15	1.8600	0.8167
	200			2.6044	0.9058
	300			2.7884	0.9113
B	200	30	15	2.5778	0.8621
		60		2.5908	0.8771
		90		2.5730	0.9055
C	200	60	3	2.0547	0.8348
			5	2.2813	0.8609
			10	2.4966	0.8364
			15	2.5936	0.8322
			20	2.6140	0.8393

and circularity of samples. The mean value of the circularity of the original particles is 0.77, which is significantly lower than that of the sheared samples (Figure 9(a)). The index of circularity also clearly shows an increasing trend and finally stabilizes at about 0.90. With the exception of the closer mean values, the homogeneity of the particle morphology was also enhanced (i.e., a decrease in variance). Figure 9(b) shows the change of the elongation ratio, which represents a similar meaning to circularity. The elongation ratio eventually stabilizes at about 1.3 with the shear displacements of 10 m. It is important to note that neither index converges to 1 with shear infinitely and instead both stabilize at a given value.

Figure 10 presents the surface microtextures of quartz sand with the different displacements. A total of 200 quartz sand grains without shearing and 400 0.7 mm fragments (15 m) were observed. Figure 10 and Table 4, respectively, exhibit the surface microtextures of the unshered samples (origin particles) and sheared samples (15 m). The sheared samples exhibit a more angular shape than the unshered samples. The large conchoidal fractures and parallel steps are

highly developed in the original particles, yet significantly reduced in the shear samples. Few smooth surfaces are observed in the original samples, and most of the original particles exhibit high relief. Curved ridges are very common in the original particles, while the sheared samples present clearer and straighter edges. The smooth surfaces, breakage blocks, and small conchoidal fractures appear more frequently in the shear samples.

4. Discussions

In response to the previous hypothesis that the crushed fine-grained fraction would act as a lubricant to reduce friction [35], the test results of different grain sizes reveal that the reduction of the initial grain size leads to a slight increase in friction (Figure 2). In addition, the shear stress-displacement curves also exhibit no significant decrease in shear stress during shear fragmentation (Figure 3), despite the fact that the grain sizes had become significantly finer (300 kPa, 15 m). Therefore, it is believed that the decrease in the particle size caused by fragmentation does not produce a

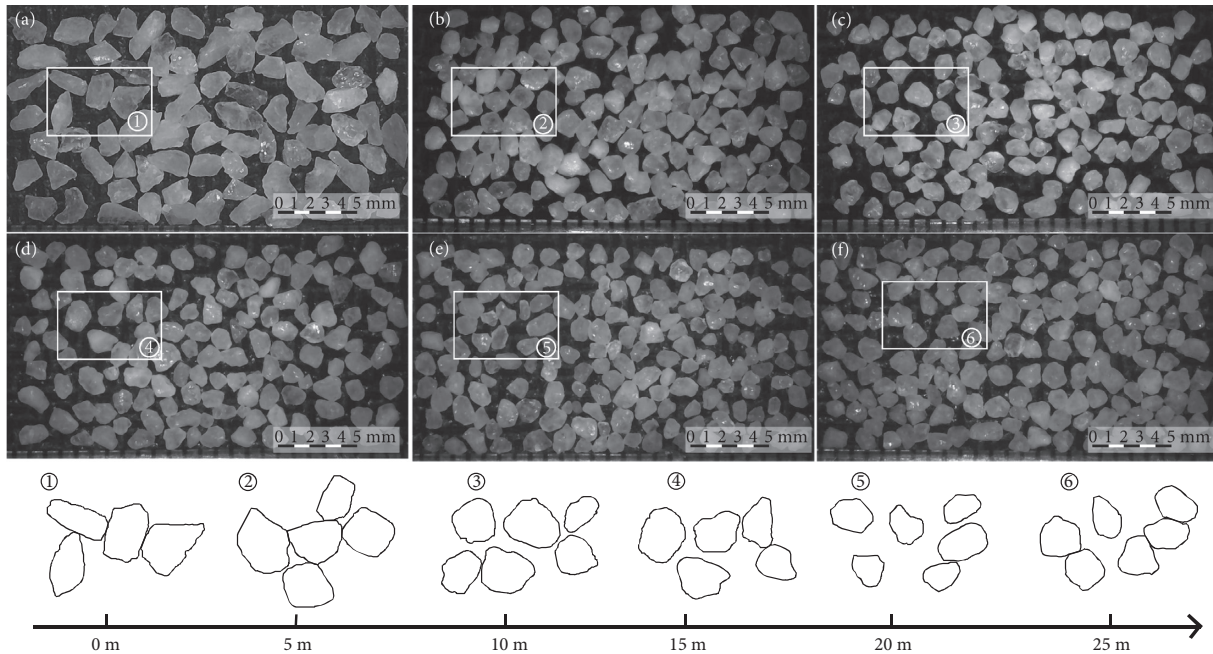


FIGURE 8: Morphometric changes in coarse particles (1-1.5 mm) under shear under optical microscopy.

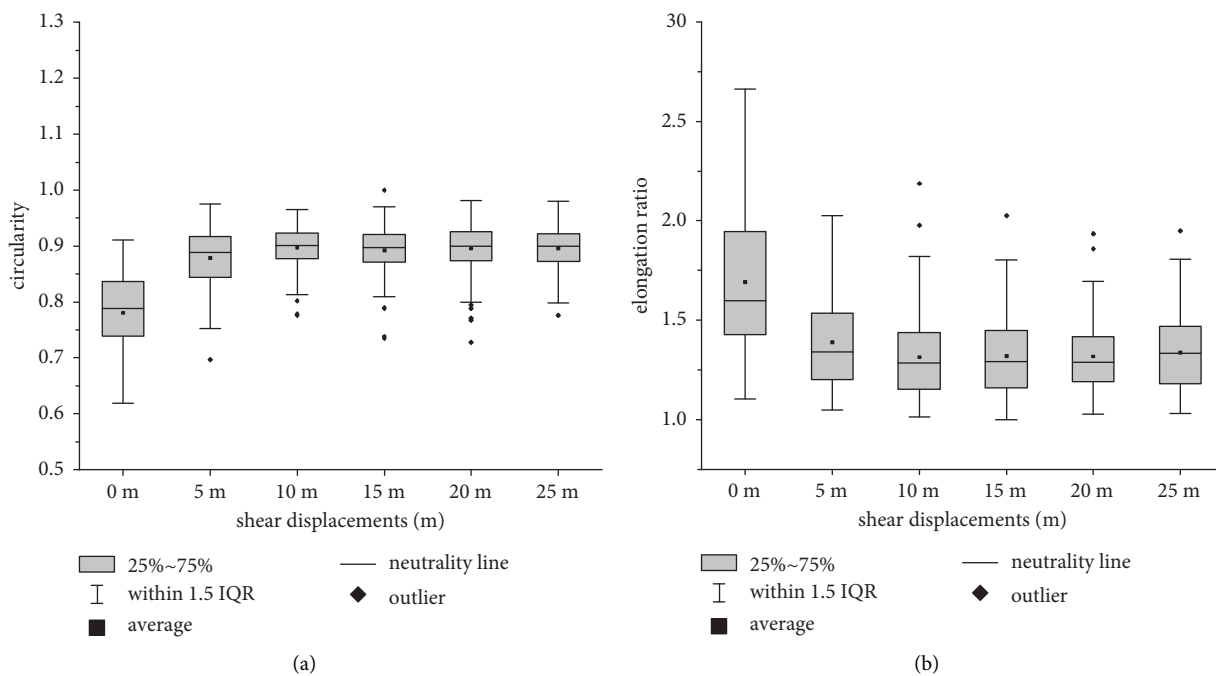


FIGURE 9: Box plot of circularity variation and elongation change of samples under shear. (a) Circularity of quartz sand after shearing at 0 m, 5 m, 10 m, 15 m, 20 m, and 25 m. (b) Elongation of quartz sand after shearing at 0 m, 5 m, 10 m, 15 m, 20 m, and 25 m.

powder lubrication or friction reduction effect during the simple shear process.

All of the shear stress-displacement curves exhibit obvious fluctuation of shear stress (maximum 10 kPa) during the shearing. However, the statistical results also reveal that the standard deviation or coefficient of variation of the shear stress present no significant change (Table 5), which signifies that the fluctuation is high yet stable throughout the shear

process. Therefore, the fluctuation is considered to be caused by the change of the friction in the roll bite rather than fragmentation.

Dynamic fragmentation is an important hypermobility hypothesis [12, 39]. However, it is difficult to achieve in the laboratory. The major aim of this experiment is to investigate whether fragmentation is the dominant mechanism of hypermobility of rock avalanches, by determining whether

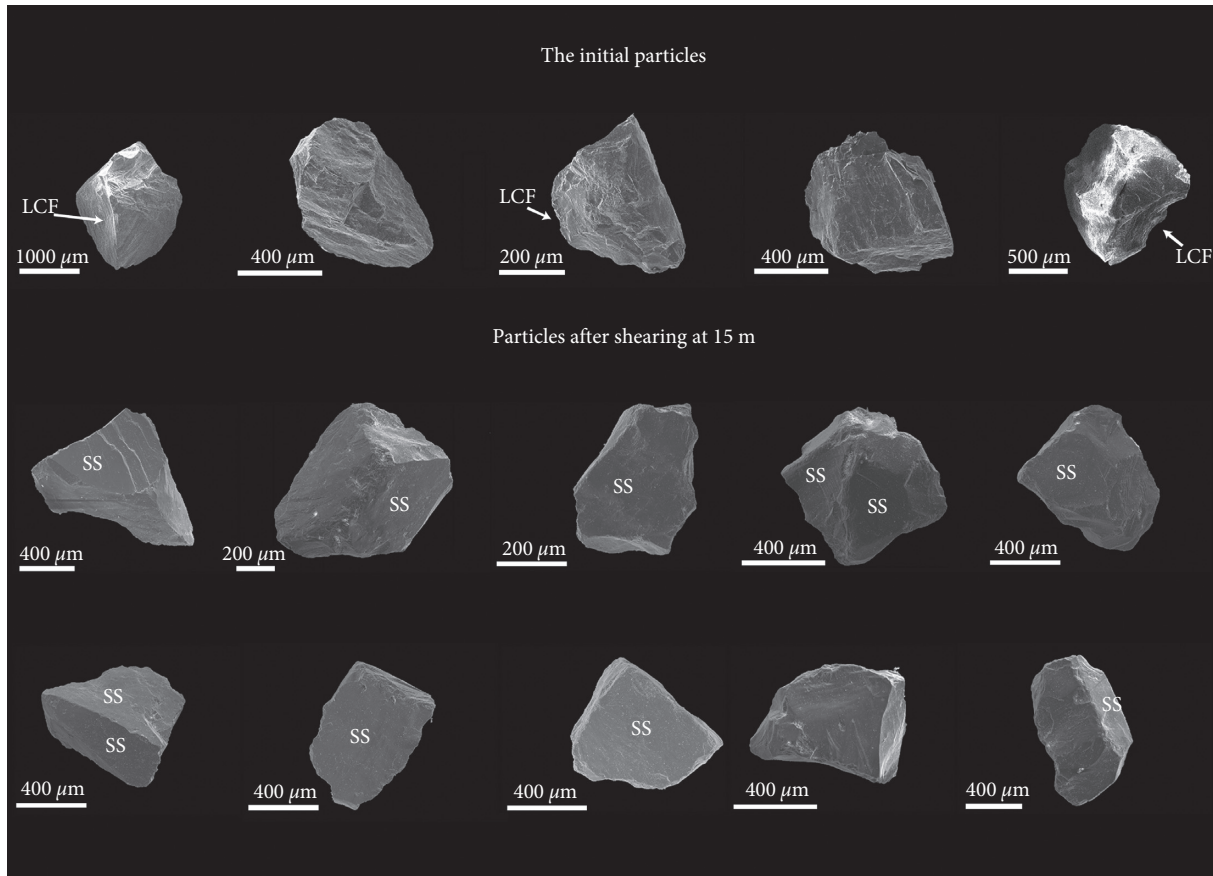


FIGURE 10: Scanning electron microscope images of particles for the original grain sizes and grain sizes larger than $700 \mu\text{m}$ after shearing at 15 m (SS and LCF, respectively, represent the smooth surface and large conical fracture).

TABLE 4: Variation of surface texture frequency of the quartz sand surfaces.

Original quartz sand		Quartz sand after shearing at 15 m	
Microtextures	Frequency (%)	Microtextures	Frequency (%)
(1) Angular outline	37	(1) Angular outline	71
(2) High relief	89	(2) High relief	12
(3) Breakage blocks	24	(3) Breakage blocks	67
(4) Large conchoidal fracture ($>100 \mu\text{m}$)	53	(4) Large conchoidal fracture ($>100 \mu\text{m}$)	19
(5) Parallel steps	69	(5) Parallel steps	37
(6) Smooth surface	18	(6) Smooth surface	86

fragmentation occurs throughout the emplacement process. The results of the grain-size distribution and fractal dimension in this study have provided important insights regarding the characteristics of shear fragmentation. The GSD curves present the breakage of the particles under the shear process, despite the fact that the grain-size distribution curves no longer change significantly following large displacements. The fractal dimension (Figure 11), as a quantitative measure of fragmentation [55], further proves the above finding that the fractal dimension increases with displacement, and the increment decreases gradually (i.e., the slope in Figure 11(c) decreases). This phenomenon indicates that the stable grading caused by shear was indeed present, which signifies that the breakage of particles became

very weak and could be ignored following large shear displacements.

Both the GSD and FD show that the degree of fragmentation is sensitive to the change of the normal stresses, which may have been the reason for the variation in GSD in the different positions. In addition, the stable grading displacement of different normal stresses all occurred at around 15 m, which indicates that the effect of the normal stresses on the displacement of the stable shear may not be significant.

Perinotto et al. [35] demonstrated that the grinding limit of collisional crushing (dynamic disintegration) is $500 \mu\text{m}$, while the breakage of particles below $500 \mu\text{m}$ mainly relies on the shear process. However, our results illustrated that the fragmentation during shearing also has a limit. According to

TABLE 5: Analysis of shear stress-displacement relationship.

Shear rate	Shear displacement	0–180 mm	180–360 mm	360–540 mm
30 deg/min	Average	62.82895	62.67682	62.5622
	Standard deviation	2.328623	2.116855	2.511495
	Coefficient of variation	0.037063	0.033774	0.040144
60 deg/min	Average	63.37705	63.27953	62.52094
	Standard deviation	2.525111	2.196046	2.527427
	Coefficient of variation	0.039843	0.034704	0.040425
90 deg/min	Average	63.16634	62.78268	62.62475
	Standard deviation	3.131989	2.655836	3.077403
	Coefficient of variation	0.049583	0.042302	0.04914
120 deg/min	Average	63.63144	62.77638	62.43142
	Standard deviation	2.994802	2.542645	2.926624
	Coefficient of variation	0.047065	0.040503	0.046877

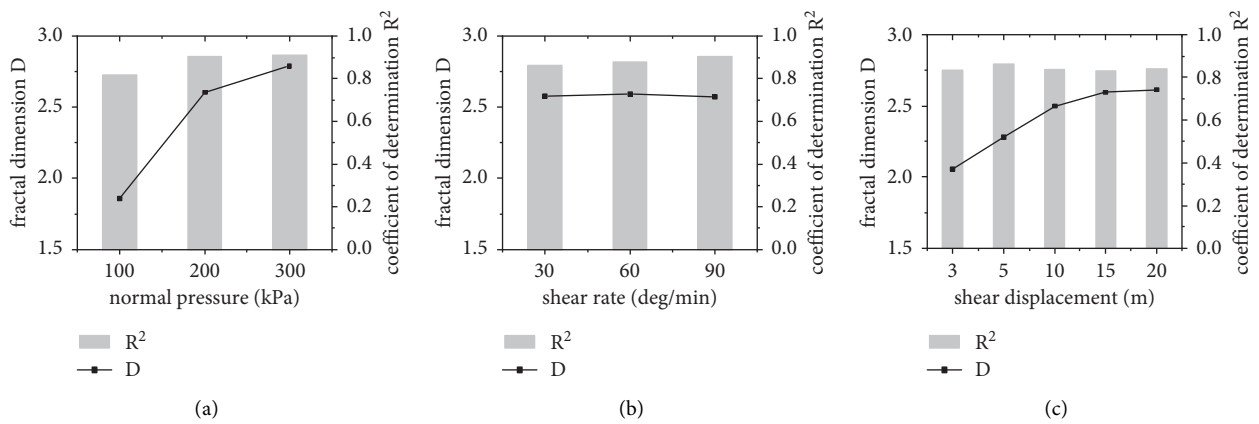


FIGURE 11: Fractal dimension under different shear conditions. (a) Fractal dimension after shearing 15 m at a shear rate of 60 deg/min and normal stresses of 100 kPa, 200 kPa and 300 kPa. (b) Fractal dimension after shearing at 15 m at a shear rate of 30 deg/min, 60 deg/min, and 90 deg/min under a normal stress of 200 kPa. (c) Fractal dimension at a shear rate of 60 deg/min and a normal stress of 200 kPa after shearing at 3 m, 5 m, 10 m, 15 m, and 20 m.

the results, the stable grading of particles breakage during shearing is considered to appear very quickly (15 m) compared with the several km of travel distance in real rock avalanches. This signifies that the material would almost cease breaking soon at the late stage of the emplacement.

It is worth noting that the distinct bimodal distribution of GSD is observed in our tests, which is consistent with that found in the field (Figure 7(c) from Dufresne et al. [30]). Meanwhile, our tests indicated that the bimodal structure did not appear in the early shear stage; then it became more and more obvious as the displacement increased (>10 m). The bimodal distribution may be responsible for the generation of the stable grading during shearing. Both the field data [30] and the results of this experiment indicated that the grain size of the fine peak is much smaller than the coarse peak. A reasonable explanation for stable grading is that a “wrapping structure” was formed by very fine particles wrapping around the coarse particles. Crosta et al. [25] demonstrated that the increase of the coordination number would reduce the probability of breaking of the coarse particles. In other words, the breaking tends to occur in similar-sized particles [30, 35, 56, 57]. For the breakage of the fine particles, the smaller the size is, the more difficult it is

to occur. Compared to the field results, in this study the coarse particles maintained a higher content in this study, which may be a result of the higher strength of the quartz sand and smaller normal stress.

Based on the statistical results of the circularity and elongation, the particles were considered mainly reduced along the long axis during the shear process. The morphology of the particles gradually tends to be spherical, which may enhance the ability to resist the shear fragmentation. Both indicators seem to reach a limit at a shear displacement around 10 m, which is basically consistent with the displacement of stable grading, implying that the interparticle action is no longer sufficient to change their geometry. The results of scanning electron microscope also present the morphological changes of the quartz sand during the shear process. Compared with unsheared samples, significant fracture characteristics in sheared samples including the increase of smooth surfaces, fresh sharp edges, and small conchoidal fractures at particle edges were widely observed. All of these morphology changes of the quartz sand indicate that shear fragmentation tends to occur at the edges due to their sharp geometry, where is prone to stress concentration. It is also believed that for other materials, the stress is always

more concentrated at the edges, and the broken is more likely to occur to produce fine particles, which would produce bimodal distribution to reduce the contact between coarse particles and consequently affect shearing breakage.

This was a series of simplified experiments, and the normal stress used mainly corresponds to a burial depth of 10 m, which is the thickness of the front deposits of some rock avalanches [11, 36, 58, 59]. The reason for which we did not use larger normal stress was that there would have been an excessive loss (spillage) of fine particles through the clearances of the equipment. In addition, a roughly linear relationship between shear stress and normal stress was found in this study (Figure 3). Therefore, it is believed that the pattern behavior of this test is applicable to larger normal stresses.

Another limitation of this study was the slow shear rate. Based on the experiments of Zhang and McSaveney [28] as well as the stable grading results in our experiments, ring shear tests with different rates at the shear displacement of 15m were performed to investigate the effect of shear rate on the ultimate grain-size distribution. Both our experimental results and those of Zhang and McSaveney showed that the change in shear strain rate does not have a distinct effect on the shear stress or the degree of fragmentation [28] (Figures 4 and 6). However, all of these tests were performed at a lower shear rate. In addition, further systematic experiments on shear rates at different displacements should be conducted in the future. Preview studies regarding the effects of loading rate on rock fracture have illustrated that the increase of loading rate leads to the elevation of more internal joints [60,61]. This suggests that high-speed shear compared to low-speed shear may result in more intense breakage, even producing stress waves. In the present study, the ultimate grain-size distribution was considered to have been caused by the wrapping structure, which should also be present in large shear rate tests. Therefore, it is believed that stable grading is also applicable to high-speed shearing.

The grain size range often spans several orders of magnitude, from relatively intact rock prior, to the onset of rock avalanches and to disintegration into debris particles of deposits [62]. Combined with the present experimental features, the fragmentation of rock avalanches is perhaps mainly caused by the premovement collisional effects, including both the impact between the gravity-driven sliding body and the movement path and collisional effects within the individual blocks [25]. In the spreading stage, the materials may have been quickly reached an ultimate grain-size distribution, and the frictional weakening at this stage may have been controlled by mechanisms such as heat vapor effect [40, 63, 64], or rheological weakening [41], rather than dynamic fragmentation. The main regret of this study is that it does not explain the formation of the discontinuous shear zone, which is significantly finer than other facies.

5. Conclusions

The aim of this research was to investigate the shear fragmentation characteristic of dry granular flow, which is important for understanding the fragmentation effect of rock avalanches. Compared with previous studies, regular

quartz sand was employed for ring shear tests, and the grain-size distribution and micromorphology were analyzed. Based on the results, the following conclusions were reached:

- (1) The stable grading of the shearing process on quartz sand was observed, which indicates that the particles almost ceased breaking following a relatively large displacement. Meanwhile, the results show that the shear friction did not decrease with the increased fineness of the particles, which is consistent with various other grain size comparison tests, indicating powder lubrication may not be the major factor for friction reduction.
- (2) The microscopic characteristics and bimodal distribution of sheared samples indicate that the fragmentation of the angular particles develops preferentially on the edges. In addition, the increase of the fine fragments, which are much smaller than the coarse particles (more than 50 times), effectively prevents the breaking of coarse particles, thereby resulting in a stable grading.
- (3) The displacement of the stable grading in this study was much smaller than the travel distance of real rock avalanches. Considering the gradual thinning of rock avalanches in the spreading process, it is believed that the violent fragmentation of the rock avalanche no longer occurred in the later stage of the movement (spreading stage). This acts as a challenge to the dynamic fragmentation hypothesis.
- (4) Further high-speed ring shear experiments regarding the fragmentation characteristics should be conducted. In addition, the characteristics and formation of the shear zone of the rock avalanches should also be further investigated.

Data Availability

Some or all data and models that support the findings of this study are available from the corresponding author upon reasonable request.

Conflicts of Interest

The authors have no conflicts of interest to declare.

Acknowledgments

This work was supported by the National Key Research and Development Program of China (Grant no. 2018YFC1505003) and the National Natural Science Foundation of China (Grant no. 41571012). The authors would like to sincerely thank Dr. Dwen Li and Dr. Linlin Li from National Institute of Natural Hazards of China for their assistance with the experiments.

References

- [1] S. A. Dunning, *Rock avalanche in high mountains*, PhD thesis, University of Luton, Luton, UK, 2004.
- [2] O. Hungr and S. G. Evans, "Entrainment of debris in rock avalanches: an analysis of a long run-out mechanism," *The*

- Geological Society of America Bulletin*, vol. 116, no. 9-10, pp. 1240-1252, 2004.
- [3] A. Heim, "Der bergsturz von elm," *Zeitschrift der Deutschen Geologischen Gesellschaft*, vol. 34, no. 1, pp. 74-115, 1882.
- [4] F. Legros, "The mobility of long-runout landslides," *Engineering Geology*, vol. 63, no. 3, pp. 301-331, 2002.
- [5] R. L. Shreve, "Leakage and fluidization in air-layer lubricated avalanches," *The Geological Society of America Bulletin*, vol. 79, no. 5, pp. 653-658, 1968.
- [6] M. Zhang, Y. Yin, S. Wu, Y. Zhang, and J. Han, "Dynamics of the niuniangou creek rock avalanche triggered by 2008 Ms 8.0 wenchuan earthquake, sichuan, China," *Landslides*, vol. 8, no. 3, pp. 363-371, 2011.
- [7] L. Masch, H. R. Wenk, and E. Preuss, "Electron microscopy study of hyalomylonites-evidence for frictional melting in landslides," *Tectonophysics*, vol. 115, no. 1-2, pp. 131-160, 1985.
- [8] F. V. De Blasio and A. Elverhøi, "A model for frictional melt production beneath large rock avalanches," *Geophysical Research: Earth Surface*, vol. 113, no. F2, 2008.
- [9] W. Hu, R. Huang, M. McSaveney et al., "Superheated steam, hot CO2 and dynamic recrystallization from frictional heat jointly lubricated a giant landslide: field and experimental evidence," *Earth and Planetary Science Letters*, vol. 510, pp. 85-93, 2019.
- [10] Y.-F. Wang, Q.-G. Cheng, A.-W. Shi, Y.-Q. Yuan, Y.-H. Qiu, and B.-M. Yin, "Characteristics and transport mechanism of the Nyixoi Chongco rock avalanche on the Tibetan Plateau, China," *Geomorphology*, vol. 343, pp. 92-105, 2019.
- [11] Q. Zeng, L. Zhang, T. Davies et al., "Morphology and inner structure of Luanshibao rock avalanche in Litang, China and its implications for long-runout mechanisms," *Engineering Geology*, vol. 260, Article ID 105216, 2019.
- [12] T. R. Davies and M. J. McSaveney, "The role of rock fragmentation in the motion of large landslides," *Engineering Geology*, vol. 109, no. 1-2, pp. 67-79, 2009.
- [13] M. J. McSaveney and T. R. Davies, "Surface energy is not one of the energy losses in rock comminution," *Engineering Geology*, vol. 109, no. 1-2, pp. 109-113, 2009.
- [14] E. T. Bowman, W. A. Take, K. L. Rait, and C. Hann, "Physical models of rock avalanche spreading behaviour with dynamic fragmentation," *Canadian Geotechnical Journal*, vol. 49, no. 4, pp. 460-476, 2012.
- [15] H. J. Melosh, "Acoustic fluidization," *American Scientist*, vol. 71, no. 2, pp. 158-165, 1983.
- [16] G. S. Collins and H. J. Melosh, "Acoustic fluidization and the extraordinary mobility of sturzstroms," *Journal of Geophysical Research: Solid Earth*, vol. 108, no. B10, 2003.
- [17] W. V. Gassen and D. M. Cruden, "Momentum transfer and friction in the debris of rock avalanches," *Canadian Geotechnical Journal*, vol. 26, no. 4, pp. 623-628, 1989.
- [18] Q. Zeng, J. Zhu, L. Liao et al., "High mobility of the channelized ancient Linka rock avalanche within the Bangong - nujiang suture zone, SE Tibetan Plateau," *Engineering Geology*, vol. 282, no. 3, Article ID 105999, 2021.
- [19] T. R. Davies, M. J. McSaveney, and K. A. Hodgson, "A fragmentation-spreading model for long-runout rock avalanches," *Canadian Geotechnical Journal*, vol. 36, no. 6, pp. 1096-1110, 1999.
- [20] M. J. McSaveney and T. R. H. Davies, "Rapid rock mass flow with dynamic fragmentation: inferences from the morphology and internal structure of rockslides and rock avalanches," *Landslides*, vol. 49, pp. 285-304, 2006.
- [21] T. R. H. Davies, M. J. McSaveney, and A. M. Deganutti, "Dynamic rock fragmentation causes low rock-on-rock friction: dynamic rock fragmentation causes low rock-on-rock friction," in *Proceedings of the 1st Canada-U.S.*, pp. 27-31, Rock Mechanics Symposium, Vancouver, Canada, 2007.
- [22] F. V. De Blasio, "Friction and dynamics of rock avalanches travelling on glaciers," *Geomorphology*, vol. 213, pp. 88-98, 2014.
- [23] T. R. H. Davies, N. V. Reznichenko, and M. J. McSaveney, "Energy budget for a rock avalanche: fate of fracture-surface energy," *Landslides*, vol. 17, no. 17, pp. 3-13, 2020.
- [24] B. Bai, G. C. Yang, T. Li, and G. S. Yang, "A thermodynamic constitutive model with temperature effect based on particle rearrangement for geomaterials," *Mechanics of Materials*, vol. 139, Article ID 103180, 2019.
- [25] G. B. Crosta, P. Frattini, and N. Fusi, "Fragmentation in the val pola rock avalanche, Italian alps," *Journal of Geophysical Research Earth Surface*, vol. 112, no. F1, 2007.
- [26] F. V. De Blasio, "Rheology of a wet, fragmenting granular flow and the riddle of the anomalous friction of large rock avalanches," *Granular Matter*, vol. 11, no. 3, pp. 179-184, 2009.
- [27] D. H. Shugar and J. J. Clague, "The sedimentology and geomorphology of rock avalanche deposits on glaciers," *Sedimentology*, vol. 58, no. 7, pp. 1762-1783, 2011.
- [28] M. Zhang and M. J. McSaveney, "Rock avalanche deposits store quantitative evidence on internal shear during runout," *Geophysical Research Letters*, vol. 44, no. 17, pp. 8814-8821, 2017.
- [29] M. Charrière, F. Humair, C. Froese, M. Jaboyedoff, A. Pedrazzini, and C. Longchamp, "From the source area to the deposit: collapse, fragmentation, and propagation of the Frank Slide," *The Geological Society of America Bulletin*, vol. 128, pp. 332-351, 2016.
- [30] A. Dufresne, A. Bösmeier, and C. Prager, "Sedimentology of rock avalanche deposits - case study and review," *Earth-Science Reviews*, vol. 163, pp. 234-259, 2016.
- [31] D. M. Cruden and O. Hungr, "The debris of the Frank Slide and theories of rockslide-avalanche mobility," *Canadian Journal of Earth Sciences*, vol. 23, no. 3, pp. 425-432, 1986.
- [32] S. A. Dunning and P. J. Armitage, "The grain-size distribution of rock-avalanche deposits: implications for natural dam stability," *Natural and Artificial Rockslide Dams*, vol. 133, no. 1, pp. 479-498, 2011.
- [33] A. Dufresne and S. A. Dunning, "Process dependence of grain size distributions in rock avalanche deposits," *Landslides*, vol. 14, no. 5, pp. 1555-1563, 2017.
- [34] K. Hewitt, "Catastrophic rockslides and the geomorphology of the hunza and gilgit river valleys, Karakoram Himalaya," *Erdkunde*, vol. 55, no. 1, pp. 72-93, 2001.
- [35] H. Perinotto, J. L. Schneider, P. Bachelery, F. Bourdonnec, and L. Michon, "The extreme mobility of debris avalanches: a new model of transport mechanism," *Journal of Geophysical Research: Solid Earth*, vol. 120, no. 12, pp. 8110-8119, 2006.
- [36] Z. Ren, K. Wang, K. Yang et al., "The grain size distribution and composition of the Touzhai rock avalanche deposit in Yunnan, China," *Engineering Geology*, vol. 234, pp. 97-111, 2018.
- [37] J.-Y. Luo, Z.-M. Xu, Z. Ren et al., "Rock avalanche-debris geometry and implications for rock-avalanche genesis," *Geomorphology*, vol. 334, pp. 60-75, 2019.
- [38] J. Chen, R. C. Chen, D. D. Mi, X. X. Zheng, and Y. C. Gao, "Kinematic processes and fragmentation characteristics of Walai rock avalanche landslide in Tibet," *Advanced Engineering Sciences*, vol. 56, no. 6, pp. 30-39, 2020.

- [39] Y. Jiang, G. Wang, and T. Kamai, "Fast shear behavior of granular materials in ring-shear tests and implications for rapid landslides," *Acta Geotechnica*, vol. 12, no. 3, pp. 645–655, 2017.
- [40] Y. F. Wang, J. J. Dong, and Q. G. Cheng, "Velocity-dependent frictional weakening of large rock avalanche basal facies: implications for rock avalanche hypermobility," *Journal of Geophysical Research: Solid Earth*, vol. 122, no. 3, pp. 1648–1676, 2017.
- [41] W. Hu, C. S. Chang, M. McSaveney et al., "A weakening rheology of dry granular flows with extensive brittle grain damage in high-speed rotary shear Experiments," *Geophysical Research Letters*, vol. 47, no. 11, 2020.
- [42] A. N. Dubovskoi, L. M. Pernik, and A. L. Strom, "Experimental simulation of rockslide fragmentation," *Journal of Mining Science*, vol. 44, no. 2, pp. 123–130, 2008.
- [43] M. Zhang, Y. Yin, and M. McSaveney, "Dynamics of the 2008 earthquake-triggered wenjiagou creek rock avalanche, qingping, sichuan, China," *Engineering Geology*, vol. 200, pp. 75–87, 2016.
- [44] M. R. Coop, K. K. Sorensen, T. Bodas Freitas, and G. Georgoutsos, "Particle breakage during shearing of a carbonate sand," *Géotechnique*, vol. 54, no. 3, pp. 157–163, 2004.
- [45] B. Bai, R. Zhou, G. Q. Cai, W. Hu, and G. C. Yang, "Coupled thermo-hydro-mechanical mechanism in view of the soil particle rearrangement of granular thermodynamics," *Computers and Geotechnics*, vol. 137, no. 8, Article ID 104272, 2021.
- [46] B. Bai, L. Guo, and S. Han, "Pore pressure and consolidation of saturated silty clay induced by progressively heating/cooling," *Mechanics of Materials*, vol. 75, pp. 84–94, 2014.
- [47] C.-X. Tong, G. J. Burton, S. Zhang, and D. Sheng, "Particle breakage of uniformly graded carbonate sands in dry/wet condition subjected to compression/shear tests," *Acta Geotechnica*, vol. 15, no. 9, pp. 2379–2394, 2020.
- [48] K. Vos, N. Vandenberghe, and J. Elsen, "Surface textural analysis of quartz grains by scanning electron microscopy (SEM): from sample preparation to environmental interpretation," *Earth-Science Reviews*, vol. 128, pp. 93–104, 2014.
- [49] R. Chen, J. Chen, J. Ma, and Z. Cui, "Quartz grain surface microtextures of dam-break flood deposits from a landslide-dammed lake: a case study," *Sedimentary Geology*, vol. 383, pp. 238–247, 2019.
- [50] H. Xie and W. G. Pariseau, "Fractal character and mechanism of rock bursts," *International Journal of Rock Mechanics and Mining Sciences & Geomechanics Abstracts*, vol. 30, no. 4, pp. 343–350, 1993.
- [51] E. P. Cox, "A method of assigning numerical and percentage values to the degree of roundness of sand grains," *Journal of Paleontology*, vol. 1, no. 3, pp. 179–183, 1927.
- [52] P. J. M. Costa, C. Andrade, A. G. Dawson et al., "Microtextural characteristics of quartz grains transported and deposited by tsunamis and storms," *Sedimentary Geology*, vol. 275–276, pp. 55–69, 2012.
- [53] W. C. Mahaney, *Atlas of Sand Grain Surface Textures and Applications*, Oxford, New York, NY, USA, 2002.
- [54] M. O. Molén, "A simple method to classify diamicts by scanning electron microscope from surface microtextures," *Sedimentology*, vol. 61, no. 7, pp. 2020–2041, 2014.
- [55] E. Perfect, "A simple method to classify diamicts by scanning electron microscope from surface microtextures," *Engineering Geology*, vol. 48, no. 3, pp. 185–198, 1997.
- [56] R. A. Bagnold, "Experiments on a gravity-free dispersion of large solid spheres in a Newtonian fluid under shear," *Proceedings of the Royal Society of London: Mathematical, Physical and Engineering Sciences*, vol. 225, no. 1160, pp. 49–63, 1954.
- [57] K. J. Hsü, "Catastrophic debris streams (sturzstroms) generated by rockfalls," *The Geological Society of America Bulletin*, vol. 86, no. 1, pp. 1291–1240, 1975.
- [58] Y.-F. Wang, Q.-G. Cheng, Q.-W. Lin, K. Li, and H.-F. Yang, "Insights into the kinematics and dynamics of the Luanshibao rock avalanche (Tibetan Plateau, China) based on its complex surface landforms," *Geomorphology*, vol. 317, pp. 170–183, 2018.
- [59] Y. Zhu, F. Dai, and X. Yao, "Preliminary understanding of the emplacement mechanism for the Tahman rock avalanche based on deposit landforms," *The Quarterly Journal of Engineering Geology and Hydrogeology*, vol. 53, no. 3, pp. 460–465, 2019.
- [60] Z. X. Zhang, S. Q. Kou, J. Yu, Y. Yu, L. G. Jiang, and P.-A. Lindqvist, "Effects of loading rate on rock fracture," *International Journal of Rock Mechanics and Mining Sciences*, vol. 36, no. 5, pp. 597–611, 1999.
- [61] H. Y. Pan, D. Ge, T. J. Zhang, X. G. Dong, L. Zhang, and A. Zhou, "Influence of strain rate on the rock fracture propagation law," *Journal of China Coal Society*, vol. 43, no. 3, pp. 675–683, 2018.
- [62] K. Hewitt, J. J. Clague, and J. F. Orwin, "Legacies of catastrophic rock slope failures in mountain landscapes," *Earth-Science Reviews*, vol. 87, no. 1–2, pp. 1–38, 2008.
- [63] B. Bai, Q. K. Nie, Y. K. Zhang, X. L. Wang, and W. Hu, "Cotransport of heavy metals and SiO₂ particles at different temperatures by seepage," *Journal of Hydrology*, vol. 597, Article ID 125771, 2021.
- [64] S. Boutareaud, A. M. Boullier, M. Andréani et al., "Clay clast aggregates in gouges: new textural evidence for seismic faulting," *Journal of Geophysical Research: Solid Earth*, vol. 115, Article ID B02408, 2010.

Research Article

Nonlinear Viscoelastic-Plastic Creep Model of Rock Based on Fractional Calculus

Erjian Wei,^{1,2} Bin Hu ,^{1,2} Jing Li ,^{1,2} Kai Cui,^{1,2} Zhen Zhang,^{1,2} Aneng Cui,^{1,2} and Liyao Ma^{1,2}

¹School of Resources and Environmental Engineering, Wuhan University of Science and Technology, Wuhan, Hubei, China

²Hubei Key Laboratory for Efficient Utilization and Agglomeration of Metallurgic Mineral Resources, Wuhan, Hubei, China

Correspondence should be addressed to Bin Hu; hbin74@wust.edu.cn and Jing Li; lijing1994@wust.edu.cn

Received 6 December 2021; Accepted 28 December 2021; Published 13 January 2022

Academic Editor: Bing Bai

Copyright © 2022 Erjian Wei et al. This is an open access article distributed under the Creative Commons Attribution License, which permits unrestricted use, distribution, and reproduction in any medium, provided the original work is properly cited.

A rock creep constitutive model is the core content of rock rheological mechanics theory and is of great significance for studying the long-term stability of engineering. Most of the creep models constructed in previous studies have complex types and many parameters. Based on fractional calculus theory, this paper explores the creep curve characteristics of the creep elements with the fractional order change, constructs a nonlinear viscoelastic-plastic creep model of rock based on fractional calculus, and deduces the creep constitutive equation. By using a user-defined function fitting tool of the Origin software and the Levenberg-Marquardt optimization algorithm, the creep test data are fitted and compared. The fitting curve is in good agreement with the experimental data, which shows the rationality and applicability of the proposed nonlinear viscoelastic-plastic creep model. Through sensitivity analysis of the fractional order β_2 and viscoelastic coefficient ξ_2 , the influence of these creep parameters on rock creep is clarified. The research results show that the nonlinear viscoelastic-plastic creep model of rock based on fractional calculus constructed in this paper can well describe the creep characteristics of rock, and this model has certain theoretical significance and engineering application value for long-term engineering stability research.

1. Introduction

Rock rheology is a process in which the rock mineral structure is constantly adjusted with time, resulting in the continuous change of stress and strain state with time [1–7]. The rheological effect of rock is obvious in slope, tunnel, roadway, and other projects, which is a very important feature of rock materials [8–13]. A large number of engineering practices show that the long-term stability of a project is closely related to the rheological properties of rock [14–17]. Rock creep is an important part of rock rheological mechanics theory, and research on rock creep constitutive models is the core content of the theory [18–21]. Therefore, research on rock creep constitutive models will have very important theoretical significance and practical engineering value.

Many scholars have carried out research on rock creep constitutive models and have achieved fruitful research

results. Xu et al. [22] proposed a nonlinear viscoplastic body (NVPB) and connected it with a five-element linear model to establish a famous river-sea model. Xia et al. [23] established a unified rheological mechanical model including 15 rheological mechanical properties. Based on the rheological damage degradation effect of rock masses, Zhang et al. [24] established a creep damage constitutive model with variable parameters. Wang et al. [25] proposed a nonlinear viscoelastic-plastic rheological model of the damage effect of dry-wet cycles on rock. Hu et al. [26] proposed a reversible nonlinear viscoelastic model (RNVE) to describe the recoverable viscoelastic response. The creep models established by the above researchers have achieved good results in describing the rheological characteristics of rock at various stages. However, some models have complex structures and a large number of elements, which increase the number of parameters and are unfavorable for engineering promotion. Therefore, seeking a creep model that can be composed of

fewer elements has become a goal pursued by many rock rheological constitutive model researchers. Yin et al. [27] proposed a soft element based on fractional calculus theory, which provides a way to build a creep model with fewer elements. Based on fractional calculus theory and damage variables, Chen et al. [28] proposed a creep constitutive model to describe the time-varying damage characteristics of marble in the Jinping II hydropower station. Liu et al. [29] established the Burgers creep model based on fractional order. Based on fractional order theory, Liao et al. [30] established a nonlinear creep model of warm frozen silt under three-dimensional stress conditions. Gao et al. [31] established a variable fractional rheological model to describe the whole-stage creep behavior of rock and further discussed the physical significance of fractional order. Huang et al. [32] introduced the relationship between the fractional viscosity coefficient and stress to describe the nonlinear relationship of creep strain increase in each stage. By establishing the relationship between a damage variable and the initial damage, the creep model of the acceleration stage was improved. Xiang et al. [33] introduced the Almeida fractional derivative into the elastic-viscoplastic model of soft soil, established a new fractional creep model, and analyzed and determined the kernel function with the best performance of the model. Peng et al. [34] derived the creep compliance of a fractional constitutive model and established a wellbore creep model including the drilling pressure process. Xu and Jiang [35] used an interior point algorithm to solve the corresponding nonlinear optimization constraint problem and studied the fractional order constitutive relation model represented by a fractional element network.

The above research can well apply fractional calculus theory to the construction of rock creep models, but the fractional creep element is not discussed in depth. In this paper, by discussing the influence of the change in fractional order on the creep characteristic curve of rock, creep elements of different orders are innovatively used to construct a nonlinear viscoelastic-plastic creep model of rock, and a nonlinear creep model of rock with fewer parameters is developed using fewer elements. On this basis, the creep test results are nonlinearly fitted to verify the rationality and applicability of the constructed model.

2. Creep Element Based on Fractional Calculus

Usually, calculus is a positive integer derivative and integral, and fractional calculus is a mathematical method used to study the properties and applications of differential and integral operators of arbitrary order. Fractional calculus has many forms, such as the Grunwald-Letnikov (GL) type, Riemann-Liouville (RL) type, Caputo type, and Weyl type fractional calculus, among which the RL type is widely used. This paper uses the Riemann-Liouville theory [27, 36] and defines a β -order integral of the function $f(t)$ as

$$\frac{d^{-\beta} f(t)}{dt^{-\beta}} = {}_0D_t^{-\beta} f(t) = \int_0^t \frac{(t-\tau)^{\beta-1}}{\Gamma(\beta)} f(\tau) d\tau. \quad (1)$$

The fractional differential is defined as

$$\frac{d^{\beta} f(t)}{dt^{\beta}} = {}_0Dt_{\beta} f(t) = \frac{d^n}{dt^n} [{}_0Dt_{-(n-\beta)} f(t)]. \quad (2)$$

In formulas (1) and (2), $\beta > 0$ and $n-1 < \beta \leq n$ (n is a positive integer); $\Gamma(\beta)$ is a gamma function defined as

$$\Gamma(\beta) = \int_0^{\infty} e^{-t} t^{\beta-1} dt \quad (\text{Re}(\beta) > 0). \quad (3)$$

The Laplace transform of the fractional calculus is

$$\left. \begin{aligned} L[{}_0D_t^{-\beta} f(t), p] &= p^{-\beta} \bar{f}(p) \quad (\beta > 0) \\ L[{}_0D_t^{\beta} f(t), p] &= p^{\beta} \bar{f}(p) \\ (f(t) \text{Integrable near by } t=0, 0 \leq \beta \leq 1) \end{aligned} \right\}, \quad (4)$$

where $\bar{f}(p)$ is the Laplace transform of $f(t)$.

The stress-strain relationship described by the fractional calculus is

$$\sigma(t) = \xi \frac{d^{\beta} \varepsilon(t)}{dt^{\beta}}. \quad (5)$$

Clearly, when $\beta=0$, it is the stress-strain relationship of an ideal solid, and when $\beta=1$, it is the stress-strain relationship of an ideal fluid. Therefore, when $0 < \beta < 1$, the state of matter can be described as between an ideal solid and ideal fluid. Scott-Blair called the mechanical element satisfying formula (5) a Scott-Blair element, as shown in Figure 1. This element is actually a two-parameter element containing ξ and β , which can better reflect the nonlinear gradual process of rheological problems.

When the stress is constant, the element will describe the creep phenomenon, a Laplace transform is performed on both sides of formula (5) at the same time, and the following equation can be obtained:

$$\bar{\varepsilon}(s) = \frac{\sigma_0}{\xi s^{\beta+1}}. \quad (6)$$

For formula (6), the creep equation of the Scott-Blair element is obtained using a Laplace inverse transformation:

$$\varepsilon(t) = \frac{\sigma}{\xi} \frac{t^{\beta}}{\Gamma(1+\beta)}. \quad (7)$$

According to formula (7), the creep curves of different β values under certain stresses can be drawn, as shown in Figure 2.

From the above diagram, when $\beta=0$, the strain is a certain value that reflects the strain characteristics of an ideal solid after a certain stress. When $\beta=1$, the strain increases linearly with time, which reflects the strain characteristics of an ideal fluid under a certain stress. When $0 < \beta < 1$, the strain increases greatly at the beginning and then slightly, while the strain rate decreases gradually to close to 0 and tends to be stable. At this time, the curve presents the characteristics of rock attenuation creep and steady-state creep. When $\beta > 1$, the strain and strain rate increase rapidly,

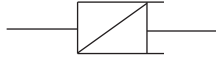


FIGURE 1: Diagram of the Scott-Blair element components.

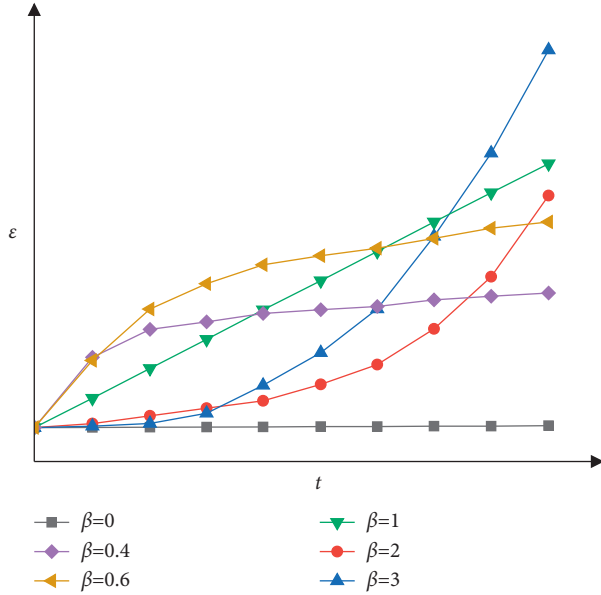


FIGURE 2: Variation characteristics of the strain with time under different β values.

and the curve presents the characteristics of the accelerated creep stage of rock.

3. Nonlinear Viscoelastic-Plastic Creep Model

When the stress in rock is lower than its long-term strength, the rock generally experiences the two stages of decay creep and steady creep. In general, the Burgers model can describe the creep characteristics of rock at this time. As mentioned in the previous section, when $0 < \beta < 1$, the creep element can describe the material state between an ideal solid and ideal fluid, and it can be considered that the element is a composite element containing elastic elements and viscous elements; the Kelvin body in the Burgers model describes the viscoelastic characteristics of the rock, so we can consider that a creep element at $0 < \beta < 1$ can replace the Kelvin body in the Burgers model, which can not only describe the first two stages of rock creep similar to the Burgers model but also reduce the number of elements. When the stress in rock exceeds its long-term strength, the rock will enter the accelerated creep stage after experiencing the first two creep stages. From the analysis in the previous section, it can be seen that when $\beta > 1$, rock creep presents the characteristics of the accelerated creep stage, so we can consider that the creep element when $\beta > 1$ is used to describe the accelerated creep stage of rock. Therefore, we can construct a nonlinear viscoelastic-plastic creep model based on fractional calculus, as shown in Figure 3.

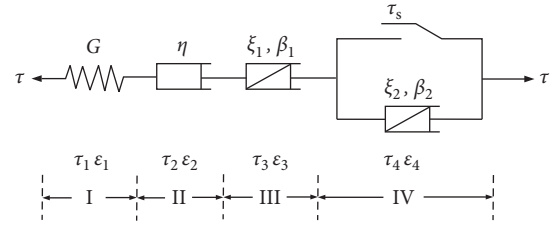


FIGURE 3: Schematic diagram of the rock nonlinear viscoelastic-plastic creep model.

It can be seen from Figure 3 that when $\tau < \tau_s$, I, II, and III are all involved in creep deformation. The state equations of the creep model are

$$\tau = \tau_1 = \tau_2 = \tau_3, \quad (8)$$

$$\varepsilon = \varepsilon_1 + \varepsilon_2 + \varepsilon_3, \quad (9)$$

$$\begin{aligned} \tau_1 &= G\varepsilon_1, \\ \tau_2 &= \eta\dot{\varepsilon}_2, \end{aligned} \quad (10)$$

$$\tau_3 = \xi_1 \frac{d^{\beta_1} \varepsilon_3(t)}{dt^{\beta_1}}.$$

From formula (10),

$$\begin{aligned} \varepsilon_1 &= \frac{\tau_1}{G}, \\ \varepsilon_2 &= \frac{\tau_2}{\eta} t, \end{aligned} \quad (11)$$

$$\varepsilon_3 = \frac{\tau_3}{\xi_1} \frac{t^{\beta_1}}{\Gamma(\beta_1 + 1)}.$$

From formulas (8), (9), and (11), we can get

$$\varepsilon(t) = \frac{\tau}{G} + \frac{\tau}{\eta} t + \frac{\tau}{\xi_1} \frac{t^{\beta_1}}{\Gamma(\beta_1 + 1)}. \quad (12)$$

Formula (12) is the creep equation of the rock nonlinear viscoelastic-plastic creep model when $\tau < \tau_s$.

When $\tau \geq \tau_s$, I, II, III, and IV all participate in creep deformation. The state equations of the creep model are

$$\tau = \tau_1 = \tau_2 = \tau_3 = \tau_s + \tau_4, \quad (13)$$

$$\varepsilon = \varepsilon_1 + \varepsilon_2 + \varepsilon_3 + \varepsilon_4, \quad (14)$$

$$\begin{aligned} \tau_1 &= G\varepsilon_1, \\ \tau_2 &= \eta\dot{\varepsilon}_2, \\ \tau_3 &= \xi_1 \frac{d^{\beta_1} \varepsilon_3(t)}{dt^{\beta_1}}, \\ \tau_4 &= \xi_2 \frac{d^{\beta_2} \varepsilon_4(t)}{dt^{\beta_2}}. \end{aligned} \quad (15)$$

From formula (15),

$$\begin{aligned}\varepsilon_1 &= \frac{\tau_1}{G}, \\ \varepsilon_2 &= \frac{\tau_2}{\eta} t, \\ \varepsilon_3 &= \frac{\tau_3}{\xi_1} \frac{t^{\beta_1}}{\Gamma(\beta_1 + 1)}, \\ \varepsilon_4 &= \frac{\tau_4}{\xi_2} \frac{t^{\beta_2}}{\Gamma(\beta_2 + 1)}.\end{aligned}\quad (16)$$

From formulas (13), (14), and (16), we can get

$$\varepsilon(t) = \frac{\tau}{G} + \frac{\tau}{\eta} t + \frac{\tau}{\xi_1} \frac{t^{\beta_1}}{\Gamma(\beta_1 + 1)} + \frac{\tau - \tau_s}{\xi_2} \frac{t^{\beta_2}}{\Gamma(\beta_2 + 1)}.\quad (17)$$

Formula (17) is the creep equation of the rock nonlinear viscoelastic-plastic creep model when $\tau \geq \tau_s$.

4. Verification of the Creep Model

By fitting the creep equation derived in the above section to rock creep test data, the rationality and applicability of the model constructed in this paper can be verified. In this paper, the relevant data of Wang et al. [37] on the shear creep test of granite are used. In this test, a shear creep test of saturated granite subjected to 2.216 MPa normal stress is carried out by applying shear stress in different grades. The applied shear stresses are 5.084 MPa, 8.132 MPa, 11.180 MPa, 14.228 MPa, and 17.276 MPa. The shear creep test results of granite are shown in Figure 4.

To show the creep deformation more clearly under different shear stresses, the Boltzmann superposition principle is used to process the test data, and the results are shown in Figure 5.

Figure 5 shows that when the shear stress is small, the creep process of the granite only includes the decay creep stage and steady creep stage. When the shear stress is large, the creep process presents the three stages of complete rheology. Based on the test results, a user-defined function fitting tool of the Origin software was used. When $\tau < \tau_s$, the fitting function was as in formula (12). When $\tau \geq \tau_s$, the fitting function was as in formula (17). The Levenberg-Marquardt optimization algorithm was used to fit and analyze the creep test data of the granite under different shear stresses. The fitting curve is shown in Figure 6, and the creep model parameters, shown in Table 1, are obtained by fitting.

It can be seen from Figure 6 that the creep test data of rock under various loads are in good agreement with the fitting curves, and the correlation coefficients in Table 1 are basically close to 1, indicating that the nonlinear viscoelastic-plastic creep model based on fractional calculus constructed in this paper can well describe the instantaneous deformation, decay creep stage, steady creep stage, and accelerated creep stage of rock and further illustrate the rationality and applicability of the model.

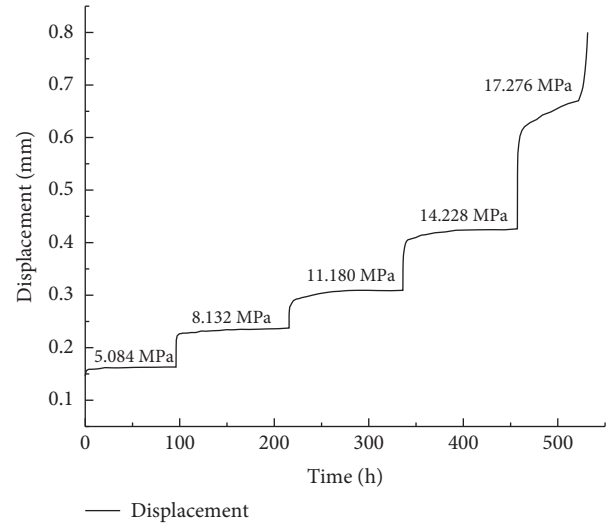


FIGURE 4: Shear creep test curve.

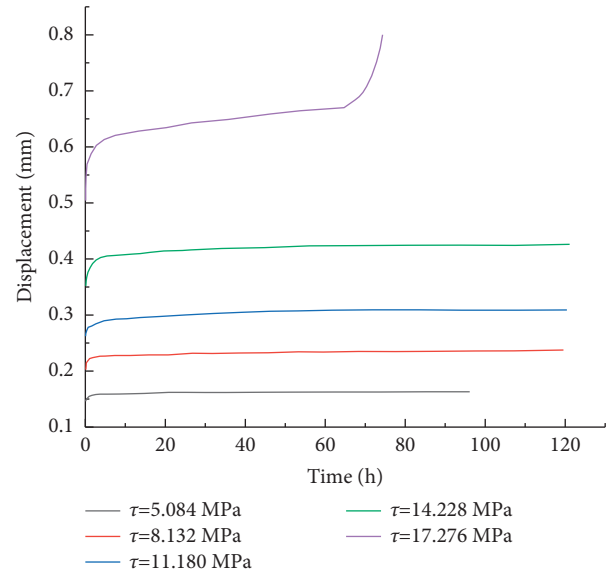


FIGURE 5: Test results after processing.

5. Parameter Sensitivity Analysis

Figures 7 and 8 show the parameter sensitivity analysis on the fractional order β_2 and viscoelastic coefficient ξ_2 , respectively, and discuss their influence on the rock creep process. Specifically, when analyzing the parameter sensitivity of the fractional order β_2 , the other model parameters use the values in Table 1, and the influence law is discussed by changing the value of the fractional order β_2 . Figure 7 shows that with the increase in the fractional order β_2 , the rock quickly enters viscoelastic-plastic deformation, and the rock creep enters the accelerated creep stage earlier. For the analysis of the parameter sensitivity of the viscoelastic coefficient ξ_2 , the same method is used. The other model parameters use the values in Table 1. The influence law is discussed by changing the value of the viscoelastic coefficient

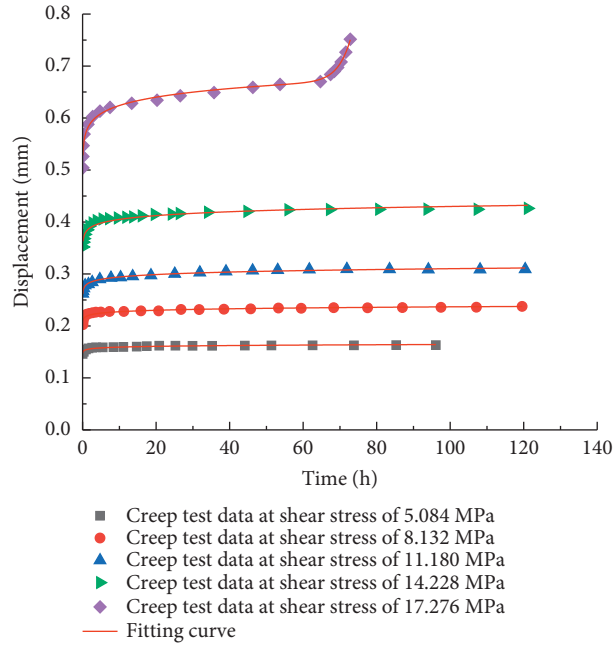


FIGURE 6: Test data and fitting curve.

TABLE 1: Creep parameter identification results.

Shear stress (MPa)	G (MPa)	η (MPa·mm ⁻¹ ·h)	ξ_1 (MPa·mm ⁻¹ ·h ^{β_1})	β_1	ξ_2 (MPa·mm ⁻¹ ·h ^{β_2})	β_2	R^2
5.084	132.366	2.869×10^{20}	44.301	0.018			0.9958
8.132	135.856	2.108×10^{25}	51.949	0.024			0.9954
11.180	138.087	5.454×10^{25}	57.345	0.031			0.9967
14.228	139.375	7.411×10^{27}	51.804	0.034			0.9943
17.276	168.487	4.476×10^{18}	37.525	0.043	2.101×10^{16}	13.605	0.9928

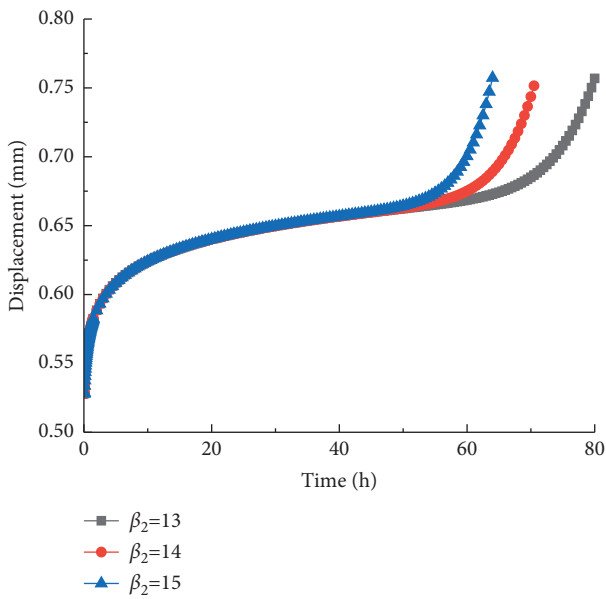


FIGURE 7: Creep curves under different fractional orders.

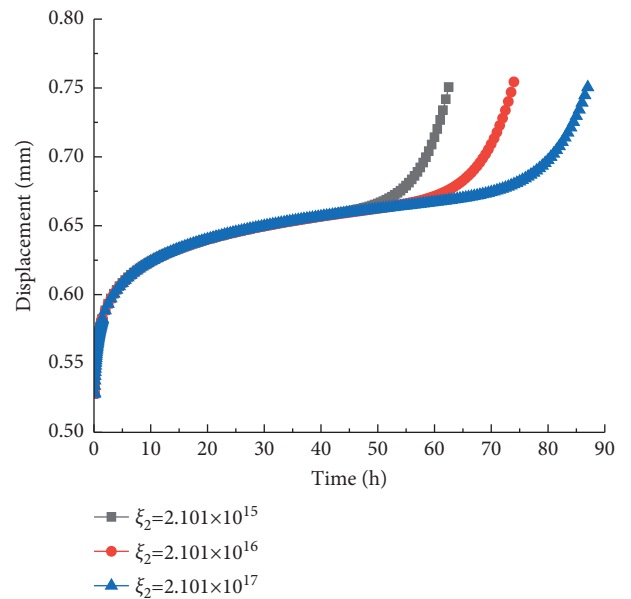


FIGURE 8: Creep curves under different viscoelastic coefficients.

ξ_2 . It can be seen from Figure 8 that with the gradual increase in viscoelastic coefficient ξ_2 , it takes more time for rock to have viscoelastic-plastic deformation, and the time for accelerated creep of rock is delayed.

6. Conclusions

Based on fractional calculus theory, this paper constructs a nonlinear creep model of rock and verifies the model. The main conclusions are as follows:

- (1) Based on fractional calculus theory, a nonlinear viscoelastic-plastic creep model is constructed by combining the fractional creep elements (β_1 and β_2 orders), spring elements ($\beta=0$), and viscous elements ($\beta=1$). The model has fewer components and fewer parameters and can describe the characteristics of each rock creep stage.
- (2) By using the nonlinear curve fitting of the Origin software and the Levenberg–Marquardt optimization algorithm, the creep test data are fitted and compared. It is concluded that the fitting curve is in good agreement with the experimental data, which shows the rationality and applicability of the nonlinear viscoelastic-plastic creep model based on fractional calculus. The model has certain theoretical significance and engineering application value for the long-term stability research of related projects.
- (3) Through the sensitivity analysis of the fractional order β_2 and viscoelastic coefficient ξ_2 , their influence law on the rock creep process is obtained.

Data Availability

The data used to support the findings of this study are included within the article.

Conflicts of Interest

The authors declare that they have no conflicts of interest.

Acknowledgments

This research was financially supported by the National Natural Science Foundation of China under grant nos. U1802243 and 41672317, in part by the Hubei Province Technical Innovation Special (Major Project) Project under grant no. 2017ACA184, and in part by the Major Science and Technology Projects of WUST Cultivate Innovation Teams under grant no. 2018TDX01.

References

- [1] G. Peng, Z. Q. Chen, and J. R. Chen, "Research on rock creep characteristics based on the fractional calculus meshless method," *Advances in Civil Engineering*, vol. 2018, Article ID 1472840, 6 pages, 2018.
- [2] B. Hu, P. Z. Pan, W. W. Ji, S. T. Miao, D. C. Zhao, and T. b. Yao, "Study on probabilistic damage constitutive relation of rocks based on maximum-entropy theory," *International Journal of Geomechanics*, vol. 20, no. 2, pp. 1–10, Article ID 06019018, 2020.
- [3] B. Bai, R. Zhou, G. Q. Cai, W. Hu, and G. C. Yang, "Coupled thermo-hydro-mechanical mechanism in view of the soil particle rearrangement of granular thermodynamics," *Computers and Geotechnics*, vol. 137, no. 8, Article ID 104272, 2021.
- [4] H. Tang, D. P. Wang, and Z. Duan, "New Maxwell creep model based on fractional and elastic-plastic elements," *Advances in Civil Engineering*, vol. 2020, Article ID 9170706, 11 pages, 2020.
- [5] B. Hu, J. Li, J. Sheng, and Z. Ye, "Crack cause in the high slope of Chinese ancient copper mine relics: a three-dimensional non-linear finite difference analysis," *IEEE ACCESS*, vol. 8, pp. 13987–13997, 2020.
- [6] J. Sun, "Rock rheological mechanics and its advance in engineering applications," *Chinese Journal of Rock Mechanics and Engineering*, vol. 26, no. 6, pp. 1081–1106, 2007.
- [7] B. Bai, Q. K. Nie, Y. K. Zhang, X. L. Wang, and W. Hu, "Cotransport of heavy metals and SiO₂ particles at different temperatures by seepage," *Journal of Hydrology*, vol. 597, Article ID 125771, 2021.
- [8] S.-Q. Yang, P. Xu, Y.-B. Li, and Y.-H. Huang, "Experimental investigation on triaxial mechanical and permeability behavior of sandstone after exposure to different high temperature treatments," *Geothermics*, vol. 69, pp. 93–109, 2017.
- [9] Q. Zhang, Z. P. Song, J. B. Wang, Y. W. Zhang, and T. Wang, "Creep properties and constitutive model of salt rock," *Advances in Civil Engineering*, vol. 2021, Article ID 8867673, 29 pages, 2021.
- [10] B. Hu, A. N. Cui, K. Cui, Y. Liu, and J. Li, "A novel nonlinear creep model based on damage characteristics of mudstone strength parameters," *PLOS ONE*, vol. 16, no. 6, pp. 1–17, Article ID e0253711, 2021.
- [11] R. Hou, K. Zhang, J. Tao, X. Xue, and Y. Chen, "A nonlinear creep damage coupled model for rock considering the effect of initial damage," *Rock Mechanics and Rock Engineering*, vol. 52, no. 5, pp. 1275–1285, 2019.
- [12] J. Wang, B. Hu, J. Chang, W. P. Wang, and H. L. Li, "Case studies and evaluation of green mining considering uncertainty factors and multiple indicator weights," *Geofluids*, vol. 2020, Article ID 8893224, 15 pages, 2020.
- [13] H. Lin, X. Zhang, Y. X. Wang et al., "Improved nonlinear nishihara shear creep model with variable parameters for rock-like materials," *Advances in Civil Engineering*, vol. 2020, Article ID 7302141, 15 pages, 2020.
- [14] R.-l. Shan, Y. Bai, Y. Ju, T.-y. Han, H.-y. Dou, and Z.-l. Li, "Study on the triaxial unloading creep mechanical properties and damage constitutive model of red sandstone containing a single ice-filled flaw," *Rock Mechanics and Rock Engineering*, vol. 54, no. 2, pp. 833–855, 2021.
- [15] H. Li, N. T. William, J. Daemen, J. Zhou, C.-k. Ma, and C. K. Ma, "A power function model for simulating creep mechanical properties of salt rock," *Journal of Central South University*, vol. 27, no. 2, pp. 578–591, 2020.
- [16] P. Cao, Y. D. Wen, Y. X. Wang, H. P. Yuan, and B. X. Yuan, "Study on nonlinear damage creep constitutive model for high-stress soft rock," *Environmental Earth Sciences*, vol. 75, pp. 1–8, 2016.
- [17] K. Cui, B. Hu, A. N. Cui, J. Li, E. J. Wei, and Z. Zhang, "An extended super/subloading surface model for soft rock considering structure degradation," *PLOS ONE*, vol. 16, no. 10, pp. 1–16, Article ID e0258813, 2021.

- [18] L. Yang and Z.-d. Li, "Nonlinear variation parameters creep model of rock and parametric inversion," *Geotechnical & Geological Engineering*, vol. 36, no. 5, pp. 2985–2993, 2018.
- [19] Z.-y. Wang, J. Xu, Y.-p. Li, and Y. Wang, "Rheological damage FEA of hydro-mechanical coupling for rock mass," *Journal of Central South University of Technology*, vol. 14, no. S1, pp. 324–328, 2007.
- [20] B. Hu, E. J. Wei, J. Li, X. Zhu, K. Y. Tian, and K. Cui, "Nonlinear creep model based on shear creep test of granite," *Geomechanics and Engineering*, vol. 27, no. 5, pp. 527–535, 2021.
- [21] Y. Zhao, Y. Wang, W. Wang, W. Wan, and J. Tang, "Modeling of non-linear rheological behavior of hard rock using triaxial rheological experiment," *International Journal of Rock Mechanics and Mining Sciences*, vol. 93, pp. 66–75, 2017.
- [22] W. Y. Xu, S. Q. Yang, and W. J. Chu, "Nonlinear viscoelastoplastic rheological model (hohai model) of rock and its engineering application," *Chinese Journal of Rock Mechanics and Engineering*, vol. 25, no. 3, pp. 433–447, 2006.
- [23] C. C. Xia, X. D. Wang, C. B. Xu, and C. S. Zhang, "Method to identify rheological model by unified rheological model theory and case study," *Chinese Journal of Rock Mechanics and Engineering*, vol. 27, no. 8, pp. 1594–1600, 2008.
- [24] Q. Y. Zhang, W. D. Yang, J. G. Zhang, and C. H. Yang, "Variable parameters-based creep damage constitutive model and its engineering application," *Chinese Journal of Rock Mechanics and Engineering*, vol. 28, no. 4, pp. 732–739, 2009.
- [25] X. Wang, B. Hu, H. Tang, X. Hu, J. Wang, and L. Huang, "A constitutive model of granite shear creep under moisture," *Journal of Earth Sciences*, vol. 27, no. 4, pp. 677–685, 2016.
- [26] B. Hu, S.-q. Yang, and P. Xu, "A nonlinear rheological damage model of hard rock," *Journal of Central South University*, vol. 25, no. 7, pp. 1665–1677, 2018.
- [27] D. S. Yin, J. J. Ren, C. L. He, and W. Chen, "A new rheological model element for geomaterials," *Chinese Journal of Rock Mechanics and Engineering*, vol. 26, no. 9, pp. 1899–1903, 2007.
- [28] B.-R. Chen, X.-J. Zhao, X.-T. Feng, H.-B. Zhao, and S.-Y. Wang, "Time-dependent damage constitutive model for the marble in the Jinping II hydropower station in China," *Bulletin of Engineering Geology and the Environment*, vol. 73, no. 2, pp. 499–515, 2014.
- [29] J. S. Liu, H. W. Jing, B. Meng et al., "Fractional-order creep model for soft clay under true triaxial stress conditions," *Arabian Journal of Geosciences*, vol. 834, pp. 1–13, 2020.
- [30] M. Liao, Y. Lai, E. Liu, and X. Wan, "A fractional order creep constitutive model of warm frozen silt," *Acta Geotechnica*, vol. 12, no. 2, pp. 377–389, 2017.
- [31] Y. Gao and D. Yin, "A full-stage creep model for rocks based on the variable-order fractional calculus," *Applied Mathematical Modelling*, vol. 95, pp. 435–446, 2021.
- [32] P. Huang, J. Zhang, N. Jean Damascene, C. Dong, and Z. Wang, "A fractional order viscoelastic-plastic creep model for coal sample considering initial damage accumulation," *Alexandria Engineering Journal*, vol. 60, no. 4, pp. 3921–3930, 2021.
- [33] G. J. Xiang, D. S. Yin, C. X. Cao, and Y. F. Gao, "Creep modelling of soft soil based on the fractional flow rule: simulation and parameter study," *Applied Mathematics and Computation*, vol. 403, pp. 1–10, 2021.
- [34] Y. Peng, J. Zhao, and Y. Li, "A wellbore creep model based on the fractional viscoelastic constitutive equation," *Petroleum Exploration and Development*, vol. 44, no. 6, pp. 1038–1044, 2017.
- [35] H. Xu and X. Jiang, "Creep constitutive models for viscoelastic materials based on fractional derivatives," *Computers & Mathematics with Applications*, vol. 73, no. 6, pp. 1377–1384, 2017.
- [36] Q. Wu and J. H. Huang, *Fractional Calculus*, Tsinghua University Press, Beijing, China, 2016.
- [37] M. F. Wang, B. Hu, H. F. Jiang, G. J. Ou, and L. Gan, "Experiment and model investigation on shear rheological mechanical properties of granite," *Journal of Central South University*, vol. 45, no. 9, pp. 3111–3120, 2014.

Research Article

Study on Strengthening Mechanism of Epoxy Resin/Rubber Concrete Interface by Molecular Dynamics Simulation

Lijuan Li, Dajing Qin , Zhijun Xu , and Yong Feng

Henan University of Technology, Zhengzhou 450001, China

Correspondence should be addressed to Zhijun Xu; xuzhijunhaut@163.com

Received 12 December 2021; Accepted 20 December 2021; Published 11 January 2022

Academic Editor: Bing Bai

Copyright © 2022 Lijuan Li et al. This is an open access article distributed under the Creative Commons Attribution License, which permits unrestricted use, distribution, and reproduction in any medium, provided the original work is properly cited.

Rubber concrete has high environmental and economic benefits. However, the difference in the physical and chemical properties of the interface causes a weak interface between rubber and concrete, which limits the use of rubber concrete to a certain extent. Based on the macroexperiment of epoxy resin (EP) modified rubber concrete, from the nanoscale level, three interface models of Rh (natural rubber)/C-S-H, EP/C-S-H, and Rh/EP/C-S-H were constructed by molecular dynamics simulation to explore the interaction between epoxy resin and rubber cement-based interface and reveal its microreinforcement mechanism. The results of interaction energy, radial distribution function, and mean square displacement show that the addition of EP not only improves the interface interaction energy between Rh and C-S-H but also provides a large number of hydrogen bond donors and receptors, promotes the diffusion of Ca, and increases the adhesion between Rh and cement matrix. The results of the analysis of mechanical properties show that the elastic modulus of the rubber concrete interface model is improved and the interface properties are improved after adding EP.

1. Introduction

With the continuous development of industries in various countries, the contradiction between the shortage of natural resources and the rapid development of society is becoming increasingly fierce. The low carbon green development and the utilization of waste resources will also become the rigid requirements of social sustainable development. With the rapid development of the global automobile industry and transportation industry, the use of automobile tires has increased sharply, and the output of waste tires is also increasing. However, the waste rubber is not easy to degrade naturally, and direct landfill is easy to cause soil pollution. Incineration will produce a large number of toxic and harmful gases and cause air pollution. Therefore, the disposal of solid waste from waste tires has become a serious global social problem (Figure 1).

Rubber concrete is a kind of special concrete based on ordinary concrete and modified by adding a certain amount of waste rubber particles or rubber powder. Compared with ordinary plain concrete, it can not only improve the

mechanical properties of concrete but also solve the problem of difficulty in treatment of waste tires. However, after the waste rubber aggregate is added to the concrete, it will not only affect the cement hydration reaction of the concrete but also form many weak interface transition zones in the new composite material composed of nonpolar rigid bodies and organic elastomers. The weak interface problem usually leads to the early failure of the composite material. This has seriously hindered the development and application of rubber concrete (Figure 2). In addition, epoxy resin (EP) concrete has high strength, short curing time, and good durability [1], but the impact resistance of EP is poor (belonging to brittle material), while rubber has good impact resistance (belonging to elastic material). The modulus of EP adhesive and rubber particles is close, and the adhesion is good, which improves the interfacial adhesion. The modified EP concrete with rubber particles or EP-modified rubber concrete can effectively improve the flexural performance, crack resistance, and impact resistance of concrete. EP rubber elastic concrete combines the advantages of the above two materials and has broad application prospects.

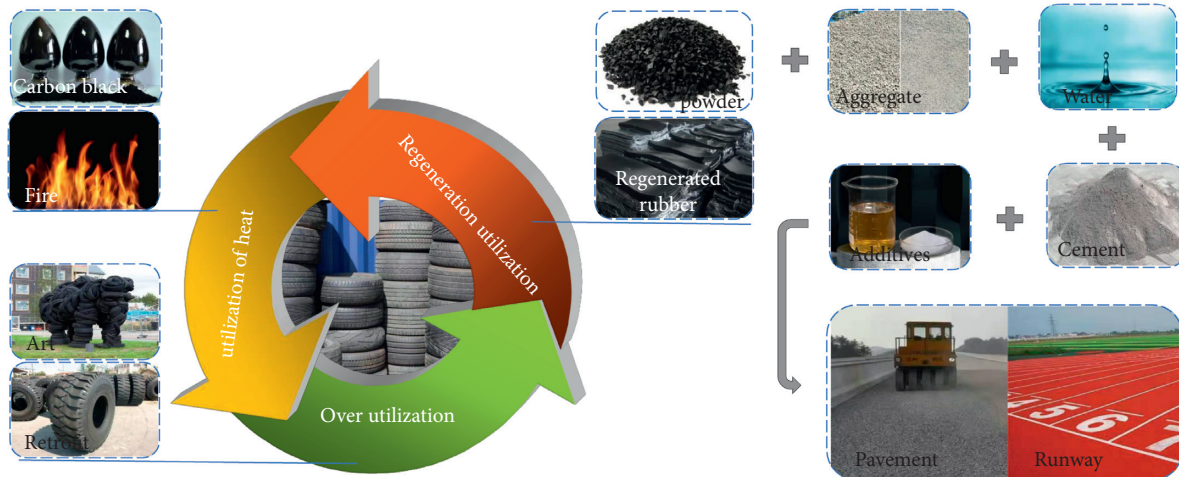


FIGURE 1: Recycling of waste rubber.

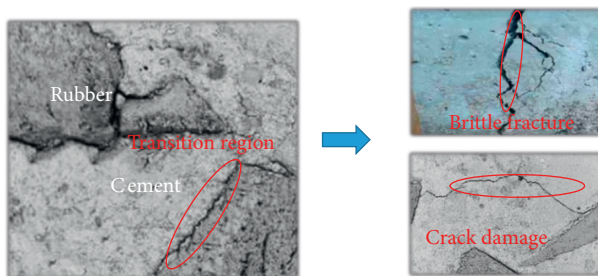


FIGURE 2: Electron microscopic picture of the interface transition zone and macroscopic failure form.

Because the stiffness of rubber is difficult to be significantly improved, improving the bond between rubber and cement matrix is considered to be the key. Therefore, some studies have found that adding modifiers or improving the preparation method of rubber concrete can improve the interfacial adhesion between rubber and cement matrix, so as to improve the mechanical properties of rubber concrete [2–7]. As mentioned above, one of the most successful methods is to add the epoxy resin material into the rubber concrete. The complementarity of the two in physical properties makes the treated rubber particles not only improve the compressive strength and splitting tensile strength of rubber concrete but also enhance the deformation resistance of rubber concrete [8]. Compared with soil, rubber concrete is a mixed structure. Although there are research methods similar to Yuan et al. [9] using a macromodel to explore the mechanical properties of the soil before and after modification, there is no ideal model [10–12] that can directly observe its internal material displacement, which is similar to the transparent soil, and there is no research method similar to the finite element model and physical model that can study its coupling deformation mechanism [13–17]. Although the above research methods can be achieved in the future, however, the traditional research tools cannot explain the influence of epoxy resin on the mechanical properties and micromorphology of rubber concrete on the molecular atomic scale. Therefore, in order

to overcome this shortcoming, researchers at home and abroad found that the molecular dynamics simulation (MD) can be used to study the interface interaction and reinforcement mechanism of composite concrete on a nanoscale level, and this atomic research method is popular. Han et al. [18] proposed a new surface treatment method using polyvinyl alcohol (PVA) to improve the hydrophilicity of waste rubber and studied the interfacial strengthening mechanism between PVA and waste rubber/cement slurry through MD. Du et al. [19] used the framework of experimental analysis and MD to study the nanostructure of resin/cement interface and found that the resin enhanced the adhesion energy and Young's modulus of cement. Although epoxy resin/rubber concrete has been widely used, there is still a lack of theoretical basis and root cause research to support it, which is very important for the follow-up research and development of high-performance epoxy resin/rubber concrete cement.

In this study, strong polar groups were introduced into the rubber surface to produce a strengthening bond between rubber and the cement matrix, so as to improve the interfacial bonding performance between the rubber and cement matrix and improve the mechanical strength of rubber cement concrete. The interaction energy, radial distribution function, mean square displacement, and mechanical properties were calculated by using the above molecular dynamics calculation method. This study verifies the application effect of EP in rubber concrete composites in macro experiments and reveals its interface behavior, micromechanism, and mechanical properties on the molecular scale. This study provides basic theoretical support for the application of epoxy resin/rubber concrete and has guiding significance for the development of higher quality composite concrete in the future.

2. Materials and Methods

2.1. Model Construction. The establishment of a reasonable initial model plays an important role in the success of simulation calculation. As an important part of the research,

concrete is a kind of composite material that can play its mechanical properties only by the bonding effect of cement. Calcium silicate hydrate (C-S-H) is the most important binding phase in cement-based materials, accounting for 60%–70% of hydration products. Its structure and mechanical properties are equivalent to the “DNA” of cement-based building materials at the molecular level [20–22]. In this study, tobermorite 11 was used to establish the initial structural model. The model was widely applied in the study of the structure and dynamics of the C-S-H gel and was successfully applied to the evolution of C-S-H performance. Then, it is expanded twice along the X direction and triple along the y direction and kept unchanged in the Z -direction to form an expanded monomer. In addition, in order to establish the interface phase between tobermorite 11 and EPS, C-S-H was sheared along the $[0\ 0\ 1]$ direction (z -direction) to obtain a parallel C-S-H substrate with a size of $22.5\ \text{\AA} \times 22.1\ \text{\AA}$.

The rubber used for rubber concrete mainly comes from waste truck tires and bridge truck tires. Most automobile tire materials are mainly composed of natural rubber or synthetic rubber, but the comprehensive performance of natural rubber is superior to synthetic rubber. The output of natural rubber is low and the demand is large. Its recycling has high social, economic, and environmental benefits. Therefore, in this study, the rubber is simplified to natural rubber. Natural rubber is an elastic solid obtained from the natural latex of rubber tree after a certain process or treatment. Its main component is cis-1,4-polyisoprene. A rubber chain containing 16 monomers was constructed in the polymer module. Then, the Rh amorphous cells were constructed with an amorphous cell at the specified temperature (289 K) and at fine precision. In this study, E-51 epoxy resin was selected as the main material of this study, and its molecular structure is shown in Figure 3(a). It contains unique active groups and polar groups. In epoxy resin concrete, epoxy resin is generally used together with curing agents and diluents. In this study, the TEPA fatty amine curing agent and diluent BGE are used, and the cured epoxy resin models are constructed according to the curing reaction principle [23], as shown in Figure 3(b), respectively. Considering that the epoxy resin cannot be completely cured, the amorphous epoxy resin cell is constructed with uncured E51 and cured E51 at 1 : 1 (mass ratio). Finally, the Rh/C-S-H (2196 atoms), EP/C-S-H (1829 atoms), and Rh/EP/C-S-H (2873 atoms) interface models (as shown in Figure 3(c)) are constructed with the build layer, and the sizes of each model are $22.5\ \text{\AA} \times 22.1\ \text{\AA} \times 94.5\ \text{\AA}$ (model 1), $22.5\ \text{\AA} \times 22.1\ \text{\AA} \times 109.3\ \text{\AA}$ (model 2), and $22.5\ \text{\AA} \times 22.1\ \text{\AA} \times 111.9\ \text{\AA}$ (model 3), respectively. The Z -direction is larger than X and y because a $50\ \text{\AA}$ vacuum layer is added. Its purpose is to make the polymer interact only with one side of the hydrated calcium silicate surface, so as to ensure that it does not interact with the periodic image of the calculation unit. At the same time, the size of the system box along the vertical direction is large enough to fully observe the configuration change of the C-S-H surface polymer.

2.2. Force Field and Simulation Details. Force field is a basic energy function, which is used to calculate the potential energy of the atomic system and simulate the interaction between atoms in the average mode of molecular dynamics simulation. The compass force field is used in this study. The compass force field is the first molecular force field to unify the force field of organic molecular systems and inorganic molecular systems, which can effectively predict the microstructure and dynamic properties of polymer materials and has been widely used in many aspects [24]. In addition, since it can include most of the energy calculations and the potential energy of the interaction between different atoms and molecules in silicic acid materials, and the experiments show that compass is in good agreement with its experimental data, the compass force field is fully applicable to the simulation of cement hydration products [25, 26].

The smart method is used to optimize the structure of the composite materials for 10000 steps and 3 times. This process can basically eliminate the local unreasonable structure in the process of model construction and ensure the convergence of the model. Then, the composite system was annealed in the NPT ensemble with a simulation time of 200 ps: it was heated from 200 K to 800 K and then cooled to 200 K for 20 cycles. The conformation with the lowest potential energy after annealing was calculated by molecular dynamics. Its parameters were set as NVT ensemble, compass force field, and temperature of 298 K. The atom-based method was used for van der Waals interaction and electrostatic interaction. The cut-off distance is $15.5\ \text{\AA}$. The Andersen method is used for temperature control and the Berendsen method is used for pressure control. The step size is 1 fs and the time is 500 ps. The operation results are output every 50 steps.

3. Results and Discussion

3.1. Interaction Energy. According to the energy calculation of the three interface models under the same conditions, the interaction energy reflects the interaction between the inorganic phase and the organic phase [27]. The binding energy is not only an important standard to evaluate the adhesion and miscibility between C-S-H and polymer but also an important index to measure the adsorption strength in the adsorption process, which is contrary to the interaction energy [28, 29]. The greater the absolute value, the stronger the interaction force. The calculation formula of E_{inter} is shown in the following formula:

$$E_{\text{inter}} = E_{\text{total}} - (E_{\text{surface}} + E_{\text{polymer}}) = -E_{\text{bind}}, \quad (1)$$

where E_{inter} is the interface interaction energy, E_{surface} is the energy of C-S-H crystal surface, E_{polymer} is the total energy of polymer, and E_{bind} is the binding energy of C-S-H surface and amorphous mixed polymer. The calculation results are shown in Figure 4.

It can be seen from Figure 4 that the energy ratios of E_{Total} , E_{Surface} , $E_{\text{Non-bond}}$, and E_{Coulomb} of the three models are similar. The difference is in the van der Waals effect. It

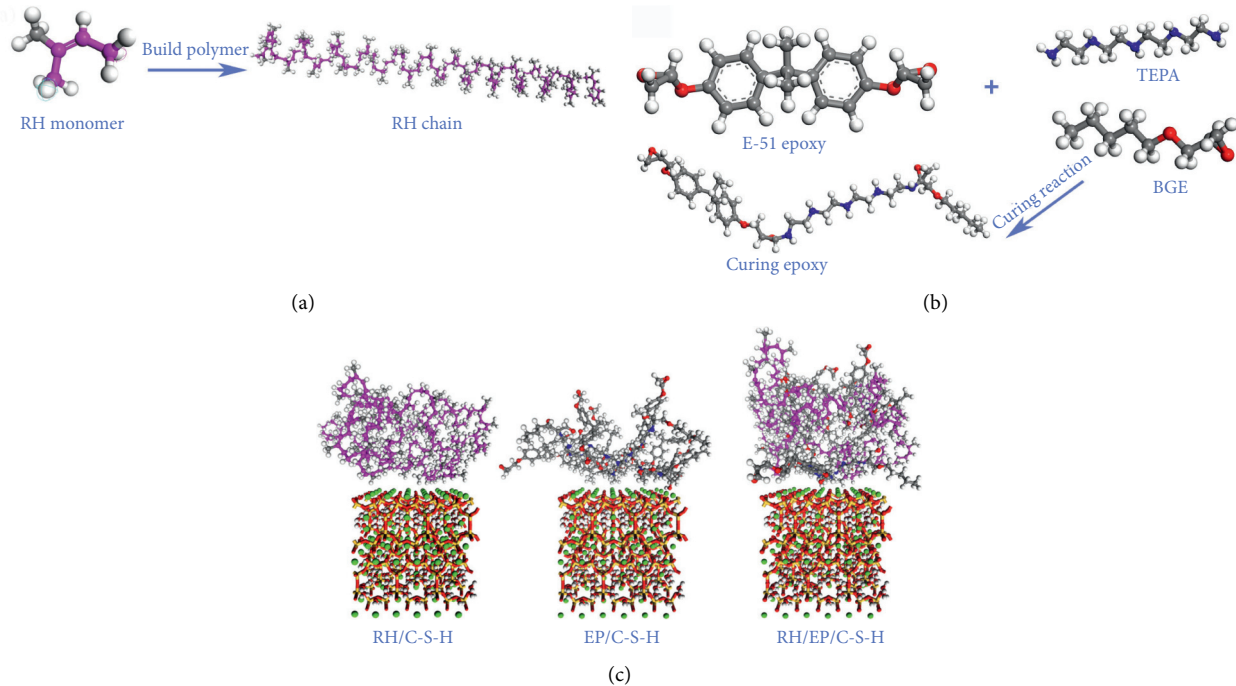


FIGURE 3: (a) Construction of Rh, (b) construction of EP, and (c) construction of three interface models (pink: carbon chain; white: H; red: O; blue: N; green: Ca; yellow: Si).

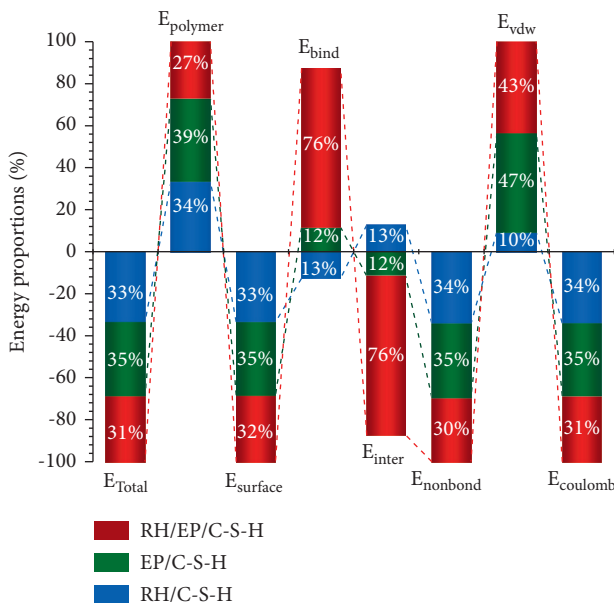


FIGURE 4: Percentage of energy of three models.

can be seen that van der Waals is the main force controlling the intermolecular interaction. The interaction energy of each system is negative, which shows that the molecules at the interface of models 2 and 3 attract each other and release heat during the combination process. The composite system is a thermodynamically stable system. In addition, the two interface interaction energies E_{inter} are increased relative to model 1, indicating that the interaction between components is enhanced and the formed system is stable. It also

shows that EP increases the bonding and stability of the RH concrete interface. The binding energy of Rh/C-S-H is negative, which is not conducive to the combination of the two interfaces. This phenomenon is consistent with reality, indicating that the additional energy of EP has a strong interaction with C-S-H.

3.2. Radial Distribution Function. To further investigate the interaction between C-S-H and polymer molecules, the equilibrium trajectory of the system is analyzed by the radial distribution function. The radial distribution function $g(r)$ represents the ratio of the probability of finding B particles when the distance from a particle is r to the probability of finding B particles when they are completely randomly distributed, that is, the ratio of regional density to the average density of B particles. It can characterize the microstructure information of the system and reflect the interaction between particles [30]. By comparing the r -value and peak height in the $g(r)$ diagram, we can identify whether there is an interaction between atoms and their mode and strength. Each model contains hydrated calcium silicate, and many kinds of literature have proved that the calcium in hydrated calcium silicate plays a major role in the adhesion of cement. Next is the hydroxyl in the hydrated calcium silicate. Oxygen can bridge the Ca ion [31] in the C-S-H channel, form a new calcium silicate gel and fill it into the crack, and enhance the bonding between the inorganic and organic interface. This process has been confirmed in our previous studies [32]. In order to avoid repetition, this study focuses on the interaction between cement-based materials and polymers. In addition, if there is an obvious

peak of RDF between the two atoms, it indicates that there is a strong spatial correlation between them; that is, there is a stable chemical bond. Intermolecular forces include hydrogen bond and the van der Waals (vdW) action. Generally, the hydrogen bond action range is 2.6–3.1 Å, the van der Waals (vdW) action range is 3.1–5.0 Å, and the VDW action greater than 5.0 Å is very weak [33].

From the calculation results in Figure 5, we can find that in addition to the chemical bond between Ca and atoms in the polymer (Ca-H_r, Ca-N, Ca-H_e, Ca-C_e, and Ca-C_r), the H bond is also another important chemical bond between cement-based materials and polymer. In particular, the interaction between N, O, and Ca in epoxy resin and the hydrogen bonding between H and O in water molecules and Rh and H and O in EP (H_h-H_e, H_h-H_r, O_h-H_r, and O_h-H_e) greatly increase the interface binding energy [34]. In addition, the peak height of model 2 is not only higher than that of model 1 but also the position of the peak is higher. The peak value of Ca-N ($x=2.25$, $y=17.1258$) in model 3 is higher than that of model 2 ($x=2.25$, $y=9.842$), which further proves that the combination of epoxy resin and hydrated calcium silicate is better, and the comprehensive application of epoxy resin and rubber increases its interface interaction. It shows that the addition of EP provides hydrogen bond donors and receptors to the interface. The hydrogen bond is a strong intermolecular interaction, which verifies the reason for the enhancement of the above interaction energy.

3.3. Mean Square Displacement. The previous analysis of interaction energy and radial distribution has revealed the change of chemical bond type and stability after the addition of EP, and it can be seen that the binding energy mainly depends on the interaction between Ca in tobermorite 11 and amorphous polymer. In order to characterize the dynamic behavior, only the EP and the difference before and after EP is added to RH concrete. The mean square displacement (MSD) of the Ca atom corresponding to the model is calculated to reflect the diffusion of Ca. The MSD can characterize the diffusion behavior of molecules and is an effective method to study molecular diffusion. The MSD is defined as the square of the difference between atomic displacement and the average of all other atomic displacements [35], which can be obtained from the following equation:

$$\langle r^2(t) \rangle = \frac{1}{N} \sum_{i=1}^N \langle |r_i(t) - r_i(0)|^2 \rangle, \quad (2)$$

where $r_i(t)$ represents the position of i atoms at time t , $r_i(0)$ is the original position of i atoms, and MSD considers three-dimensional coordinates. The larger MSD value at time t indicates that the atom diffuses rapidly and is far away from the original position.

As shown in Figure 6, the greater the slope of the MSD curve, the greater the fluidity of particles. After the addition of RH and EP, the Ca atom interface model diffuses continuously with time, and the diffusion becomes more intense

after they are added together. This result shows that the adsorption capacity of Ca atoms on the substrate surface is weakened, resulting in the reduction of local constraints on Ca atoms. C_r, H_r, N, and O_e of EP and Rh attract Ca atoms, resulting in the decline of the ability of C-S-H to capture the Ca atoms. At the same time, the interface model on C-S-H increases the diffusion coefficient of the Ca atom on its surface more than twice from Rh to EP and then to Rh/EP, indicating that the joint application of RH and EP is conducive to the diffusion of Ca on the aggregate and can effectively accelerate the bonding between hydrated calcium silicate and polymer. In addition, the calculation result is the embodiment of the Ca radial distribution function, and it is also a reason for the strong interaction energy between models 2 and 3.

3.4. Mechanical Properties. Mechanical properties refer to the mechanical characteristics of materials under various external loads in different environments. Young's modulus, shear modulus, and bulk modulus are the main parameters of mechanical properties. Young's modulus (E) is an index to evaluate the rigidity of materials and a measure of the ability of materials to resist elastic deformation. The greater the shear modulus (G), the higher the hardness and yield strength of the material, which are the measures of the ability of the material to resist plastic deformation. The greater the bulk modulus (K), the greater the breaking strength of the material [36, 37]. The static elastic mechanical properties of models 1, 2, and 3 in the equilibrium state after optimized annealing are analyzed by Ms, and the elastic coefficient matrix of the model can be obtained. It is known that the model is not an extreme heteromorphic material and can be simplified to isotropic material. For isotropic materials, there are only two independent elastic constants in the calculation principle, which are obtained by elastic matrix and two lame coefficients λ and μ . Finally, each modulus can be obtained from formulas (3), (4), and (5) [38, 39]:

$$E = \mu \frac{3\lambda + 2\mu}{\lambda + \mu}, \quad (3)$$

$$G = \mu, \quad (4)$$

$$K = \lambda + \frac{2}{3}\mu, \quad (5)$$

where E is Young's modulus, G is the shear modulus, and K is the bulk modulus. The calculated mechanical property parameters are shown in Figure 7.

From the calculation results, it can be found that the mechanical property parameters of models 2 and 3 are slightly larger than model 1, and model 3 is lower than model 2, mainly because models 2 and 3 contain epoxy resin, and model 3 contains rubber. As mentioned earlier, E , K , and G are measures of material rigidity. The greater their value, the stronger the material rigidity [40]. The calculated results are consistent with previous experiments. Although model 3 does not exceed the mechanical properties of model 2, the combination of the two improves the mechanical properties

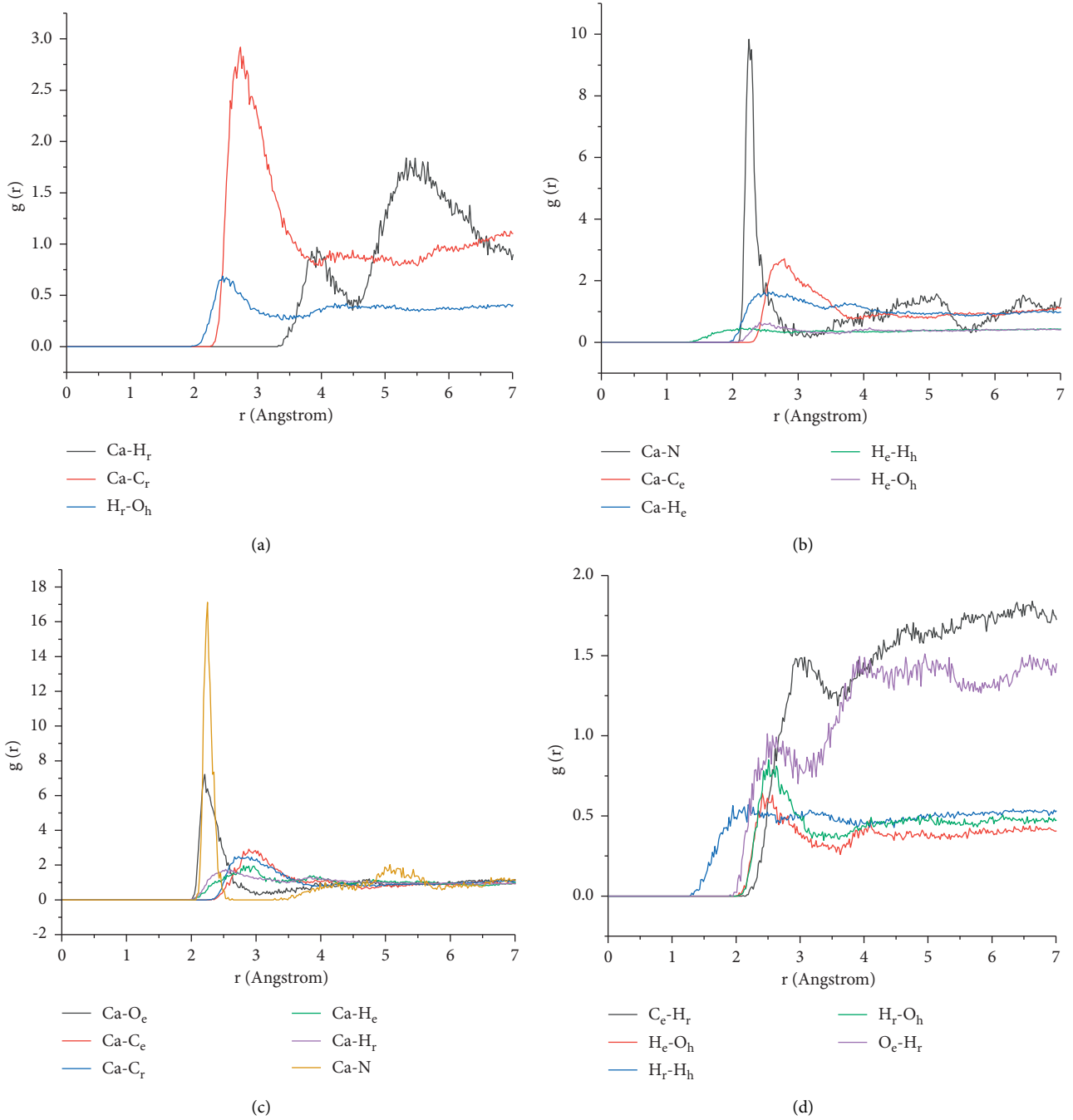


FIGURE 5: RDF of C-S-H and atoms in the polymers (a) RH/C-S-H RDF, (b) EP/C-S-H RDF, and (c) RH/EP/C-S-H RDF.

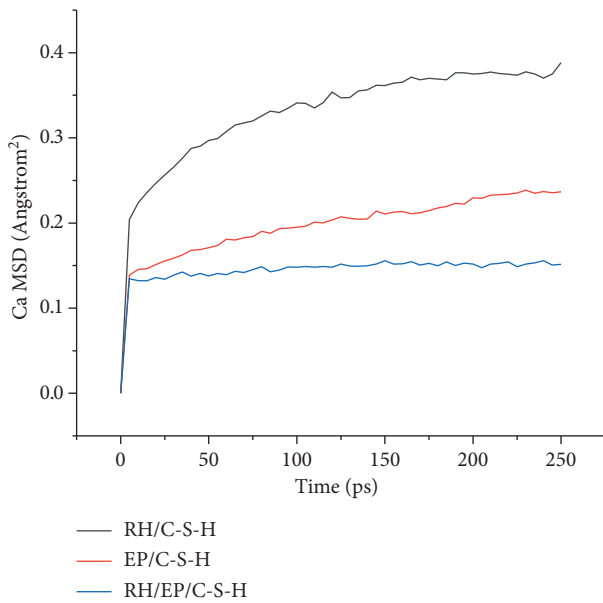


FIGURE 6: Mean square displacement of three models of Ca.

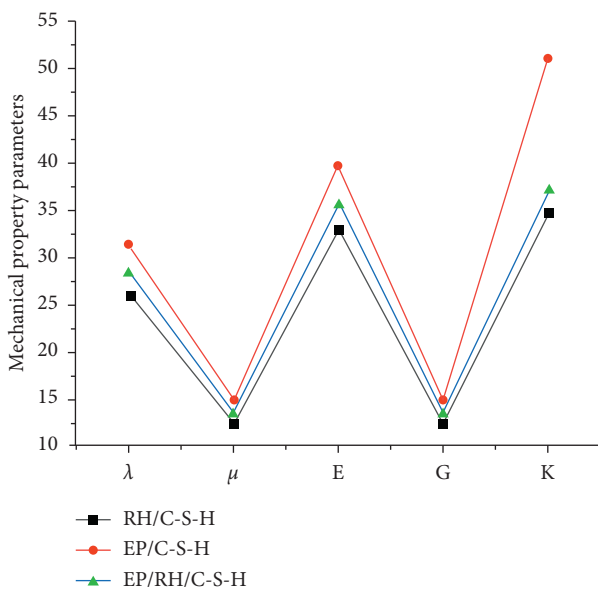


FIGURE 7: Main mechanical property parameters of three models.

of model 1, reduces the consumption of epoxy resin, achieves the purpose of energy conservation and environmental protection, provides basic theoretical support for the application of modified rubber concrete, and has reference significance for the development of better EPS concrete in the future.

4. Conclusion

In this study, three interface models were constructed by the molecular dynamics simulation method, and their interaction energy, radial distribution function, MSD, and mechanical properties were calculated. The following conclusions were obtained:

- (1) The interaction energy shows that EP increases the bonding and stability of the RH concrete interface. In addition, the energy ratio of other energy is basically the same except for the VdW force. It can be explained that van der Waals force is the main reason for the difference of action energy among the three.
- (2) Radial distribution function analysis shows that there is a strong interaction between N atoms in models 2 and 3 and Ca atoms in C-S-H. In addition, the addition of EP provides a large number of hydrogen bond donors and receptors for the Rh/C-S-H interface interaction, which enhances the interface interaction between models 2 and 3.
- (3) The mean square displacement shows that the joint application of EP and RH is conducive to the diffusion of calcium on the aggregate and can effectively accelerate the combination of hydrated calcium silicate and polymer.
- (4) In the calculation results of static mechanical properties, it is found that the addition of EP obviously increases Young's modulus (E), bulk modulus (k), and shear modulus (G) of the interface model, which indicates that its rigidity is enhanced and the interface properties are improved, which not only retains the excellent characteristics of rubber concrete but also enhances its interface mechanical properties.

Data Availability

The data used to support the findings of this study are available from the corresponding author upon request.

Conflicts of Interest

The authors declare that they have no conflicts of interest regarding the publication of this paper.

Acknowledgments

This study was supported by the National Natural Science Foundation of China (51978247), the Innovative Funds Plan of Henan University of Technology (2020ZKCJ21), and Zhengzhou Collaborative Innovation Project (21ZZXTCX09).

References



- [1] R.-M. Diaconescu, M. Barbuta, and M. Harja, "Prediction of properties of polymer concrete composite with tire rubber using neural networks," *Materials Science and Engineering: B*, vol. 178, no. 19, pp. 1259–1267, 2013.
- [2] N. S. Joekes, "Use of tire rubber particles as addition to cement paste," *Cement and Concrete Research*, vol. 30, no. 9, pp. 1421–1425, 2000.
- [3] B. S. Mohammed, A. B. Awang, S. S. Wong, and C. P. Nhavene, "Properties of nano silica modified rubbercrete," *Journal of Cleaner Production*, vol. 119, pp. 66–75, 2016.

- [4] G. Li, Z. Wang, C. K. Y. Leung et al., "Properties of rubberized concrete modified by using silane coupling agent and carboxylated SBR," *Journal of Cleaner Production*, vol. 112, pp. 797–807, 2016.
- [5] F. Xu, C. Peng, J. Zhu, and J. Chen, "Design and evaluation of polyester fiber and SBR latex compound-modified perlite mortar with rubber powder," *Construction and Building Materials*, vol. 127, pp. 751–761, 2016.
- [6] K. B. Najim and M. R. Hall, "Crumb rubber aggregate coatings/pre-treatments and their effects on interfacial bonding, air entrapment and fracture toughness in self-compacting rubberised concrete (SCRC)," *Materials and Structures*, vol. 46, no. 12, pp. 2029–2043, 2013.
- [7] E. Ganjian, M. Khorami, and A. A. Maghsoudi, "Scrap-tyre-rubber replacement for aggregate and filler in concrete," *Construction and Building Materials*, vol. 23, no. 5, pp. 1828–1836, 2009.
- [8] S. Wang, "Influence of epoxy resin adhesive on elastic concrete properties," *Chinese adhesive*, vol. 25, no. 3, pp. 9–12, 2016.
- [9] B. Yuan, Z. Li, Y. Chen et al., "Mechanical and microstructural properties of recycling granite residual soil reinforced with glass fiber and liquid-modified polyvinyl alcohol polymer," *Chemosphere*, vol. 268, Article ID 131652, 2021.
- [10] B. Yuan, Z. Li, Z. Zhao, H. Ni, Z. Su, and Z. Li, "Experimental study of displacement field of layered soils surrounding laterally loaded pile based on transparent Soil," *Journal of Soils and Sediments*, vol. 21, no. 9, pp. 3072–3083, 2021.
- [11] B. Yuan, M. Sun, L. Xiong, Q. Luo, S. Pradhan, and H. Li, "Investigation of 3D deformation of transparent soil around a laterally loaded pile based on a hydraulic gradient model test," *Journal of Building Engineering*, vol. 28, no. 3, Article ID 1010124, 2020.
- [12] B. Yuan, M. Sun, Y. Wang, L. Zhai, Q. Luo, and X. Zhang, "Full 3D displacement measuring system for 3D displacement field of soil around a laterally loaded pile in transparent soil," *International Journal of Geomechanics*, vol. 19, no. 5, Article ID 04019028, 2019.
- [13] B. Yuan, Z. Li, Z. Su, Q. Luo, M. Chen, and Z. Zhao, "Sensitivity of multistage fill slope based on finite element model," *Advances in Civil Engineering*, vol. 2021, Article ID 6622936, 13 pages, 2021.
- [14] B. Bai, Q. Nie, Y. Zhang, and X. Wang, "HuCo transport of heavy metals and SiO₂ particles at different temperatures by seepage," *Journal of Hydrology*, vol. 597, Article ID 125771, 2021.
- [15] B. Bai, G. Yang, T. Li, and G. Yang, "A thermodynamic constitutive model with temperature effect based on particle rearrangement for geomaterials," *Mechanics of Materials*, vol. 139, Article ID 103180, 2019.
- [16] X. Que, Z. Zhu, Z. Niu, and W. Lu, "Estimating the strength and deformation of columnar jointed rock mass based on physical model test," *Bulletin of Engineering Geology and the Environment*, vol. 80, pp. 1557–1570, 2020.
- [17] B. Bai, R. Zhou, G. Cai, W. Hu, and G. Yang, "Coupled thermo-hydro-mechanical mechanism in view of the soil particle rearrangement of granular thermodynamics," *Computers and Geotechnics*, vol. 137, no. 8, Article ID 104272, 2021.
- [18] Q. Han, Y. Yang, J. Zhang et al., "Insights into the interfacial strengthening mechanism of waste rubber/cement paste using polyvinyl alcohol: experimental and molecular dynamics study," *Cement and Concrete Composites*, vol. 114, Article ID 103791, 2020.
- [19] J. Du, Y. Bu, and Z. Shen, "Interfacial properties and nano-structural characteristics of epoxy resin in cement matrix," *Construction and Building Materials*, vol. 164, pp. 103–112, 2018.
- [20] S. Jin, J. Li, W. Xu, and Q. Ding, "Heterogeneous nature of calcium silicate hydrate (C-S-H) gel: a molecular dynamics study," *Journal of Wuhan University of Technology-Materials Science Edition*, vol. 35, no. 2, pp. 435–440, 2020.
- [21] A. Kumar, B. J. Walder, and A. K. Mohamed, "The atomic-level structure of cementitious calcium silicate hydrate," *Journal of Physical Chemistry C*, vol. 121, no. 32, 2017.
- [22] D. Fan and S. Yang, "Mechanical properties of C-S-H globules and interfaces by molecular dynamics simulation," *Construction and Building Materials*, vol. 176, pp. 573–582, 2018.
- [23] S. K. Ooi, W. D. Cook, G. P. Simon, and C. H. Such, "DSC studies of the curing mechanisms and kinetics of DGEBA using imidazole curing agents," *Polymer*, vol. 41, no. 10, pp. 3639–3649, 2000.
- [24] C. Yu, K. Hu, Q. Yang, and J. Chen, "Multi-scale observation of oxidative aging on the enhancement of high-temperature property of SBS-modified asphalt," *Construction and Building Materials*, vol. 313, Article ID 125478, 2021.
- [25] A. Al-Ostaz, W. Wu, H. D. Cheng, and C. R. Song, "A molecular dynamics and microporomechanics study on the mechanical properties of major constituents of hydrated cement," *Composites Part B*, vol. 41, no. 7, pp. 543–549, 2010.
- [26] S. Huang, "Study on mechanical properties of hydrated calcium silicate by molecular dynamics simulation," *Silicate Bulletin*, vol. 37, pp. 1687–1692, 2018.
- [27] R. Toth, A. Coslanich, M. Ferrone et al., "Computer simulation of polypropylene/organoclay nanocomposites: characterization of atomic scale structure and prediction of binding energy," *Polymer*, vol. 45, no. 23, pp. 8075–8083, 2004.
- [28] H. Wang, X. Lu, Y. Leng et al., "Molecular dynamics simulations on the interaction between polymers and hydroxyapatite with and without coupling agents," *Acta Biomaterialia*, vol. 5, no. 4, pp. 1169–1181, 2009.
- [29] J. Xiao, H. Huang, J. Li, H. Zhang, Z. Wei, and H. Xiao, "Computation of interface interactions and mechanical properties of HMX-based PBX with Estane 5703 from atomic simulation," *Journal of Materials Science*, vol. 43, no. 17, pp. 5685–5691, 2008.
- [30] B. G. Levine, J. E. Stone, and A. Kohlmeyer, "Fast analysis of molecular dynamics trajectories with graphics processing units-radial distribution function histogramming," *Journal of Computational Physics*, vol. 230, no. 9, pp. 3556–3569, 2011.
- [31] P. Wang, G. Qiao, Y. Zhang et al., "Molecular dynamics simulation study on interfacial shear strength between calcium-silicate-hydrate and polymer fibers," *Construction and Building Materials*, vol. 257, Article ID 119557, 2020.
- [32] Y. Feng, D. Qin, L. Li, Y. Li, C. Wang, and P. Wang, "EVA enhances the interfacial strength of EPS concrete: a molecular dynamics study," *Journal of Experimental Nanoscience*, vol. 16, no. 1, pp. 383–397, 2021.
- [33] G. D. Merfeld, A. Karim, B. Majumdar, S. K. Satija, and D. R. Paul, "Interfacial thickness in bilayers of poly(phenylene oxide) and styrenic copolymers," *Journal of Polymer Science Part B: Polymer Physics*, vol. 36, no. 17, pp. 3115–3125, 2000.
- [34] D. Hou, J. Zhang, Z. Li, and Y. Zhu, "Uniaxial tension study of calcium silicate hydrate (C-S-H): structure, dynamics and mechanical properties," *Materials and Structures*, vol. 48, no. 11, pp. 3811–3824, 2015.

- [35] C. Yu, K. Hu, G. Chen, R. Chang, and Y. Wang, "Molecular dynamics simulation and microscopic observation of compatibility and interphase of composited polymer modified asphalt with carbon nanotubes," *Journal of Zhejiang University-Science*, vol. 22, no. 7, pp. 528–546, 2021.
- [36] Q. Yuan, L. Wan, X. Shi et al., "Interface interaction and mechanical properties simulation of HA-Cs composite," *Journal of Shenzhen University (Science and Technology edition)*, vol. 35, pp. 83–90, 2018.
- [37] T. Sun, J. Xiao, F. Zhao, and H. Xiao, "Study on the compatibility, interface interaction and mechanical properties of Cl-20 /DNB eutectic PBXs," *Energetic Materials*, vol. 23, no. 4, pp. 309–314, 2015.
- [38] L. Qiu and H. Xiao, "Molecular dynamics study of binding energies, mechanical properties, and detonation performances of bicyclo-HMX-based PBXs-ScienceDirect," *Journal of Hazardous Materials*, vol. 164, no. 1, pp. 329–336, 2009.
- [39] Z. Wei, J. Xiao, W. Zhu, and H. Xiao, "Molecular dynamics simulations of RDX and RDX-based plastic-bonded explosives," *Journal of Hazardous Materials*, vol. 164, no. 2-3, pp. 1082–1088, 2009.
- [40] R. Li, Q. Wei, X. Wang, and S. Long, "Molecular dynamics simulation of mechanical properties of alumina materials," *Tool Technology*, vol. 64 pages, 2014.

Research Article

Research and Analysis on the Influence of Small Clear Distance Drilling and Blasting Method on the Existing Tunnel Structure

Haibin Huang,¹ Peng Li,¹ Chuang Wang,¹ Bingxiang Yuan ,² Minjie Chen ,²
and Weimin Feng²

¹Zhuhai Dahengqin Co., Ltd., Guangzhou 519000, Zhuhai, China

²School of Civil and Transportation Engineering, Guangdong University of Technology, Guangdong 510006, Guangzhou, China

Correspondence should be addressed to Bingxiang Yuan; yuanbx@gdut.edu.cn

Received 5 December 2021; Accepted 15 December 2021; Published 29 December 2021

Academic Editor: Bing Bai

Copyright © 2021 Haibin Huang et al. This is an open access article distributed under the Creative Commons Attribution License, which permits unrestricted use, distribution, and reproduction in any medium, provided the original work is properly cited.

In order to study the vibration influence of tunnel drilling and blasting method on the built tunnel with small clear distance, taking the intersection of Zhuhai Dahengqinshan No. 1 tunnel and Zhuji urban rail tunnel as the engineering background, we used ABAQUS finite element software to conduct numerical simulation analysis on the influence of different blasting loads on existing tunnels with small clear distance in Zhuji tunnel construction. The following conclusions were drawn: the blasting construction of the tunnel under construction had the greatest impact on the vault of the existing tunnel; when the peak load was reduced by half, the stress value, vertical displacement, and resultant velocity of Mises were also reduced by half, which indicates that reducing the peak value of blasting load appropriately can ensure the safety of tunnel construction. When the peak load is 2.7 MPa, the measured and simulated values were less than the resultant velocity limit required by the specification. In addition, the relative error between the measured value and the simulated value was less than 5%, indicating the accuracy of the numerical simulation.

1. Introduction

With the continuous development of urban subway network, the utilization scale of urban underground space is also gradually expanding. In the limited underground space, the construction of small spacing tunnel has obvious advantages and plays a positive role in tunnel construction [1–3]. At present, drilling and blasting method is mostly used in small spacing tunnel construction in China [4, 5]. If the distance between the tunnels is too small, the construction of the tunnel drilling and blasting method will inevitably affect the structural safety of the existing tunnel, disturb the surrounding rock, and then cause a series of environmental diseases of the surrounding buildings [6–8]. Therefore, great attention should be paid to the influence of drilling and blasting construction on the existing tunnel structure.

At present, domestic and foreign scholars have done some research on vibration caused by tunnel drilling and blasting construction. Wang et al. [9] recorded and analyzed the field monitoring data of a tunnel blasting and concluded

that when the main frequency of blasting vibration through the tunnel is less than 50 Hz, the existing highway roads will not produce resonance. Hao et al. [10] used LS-DYNA to discuss the changes of vibration velocity and equivalent stress of the surrounding rock caused by different clearance under blasting. It is found that the larger the clearance, the lesser the disturbance of the surrounding rock and the faster the attenuation of the vibration velocity of the existing tunnel. Luan et al. [11] relied on the Mongolian road tunnel project and used the finite element software to obtain the result that, in the blasting construction of large section tunnel, the radial vibration velocity of the support structure of the early excavated tunnel is greater than the vertical and tangential vibration velocity.

The geological condition of Zhuhai Dahengqinshan Tunnel project is poor, and the vertical clear distance between the two tunnels is small (the minimum clear distance is 3.5 m). The drilling and blasting construction of the Zhuji tunnel will cause disturbance to Dahengqinshan Tunnel. Therefore, it is necessary to improve the design scheme through numerical simulation to ensure the safety of tunnel

structure and surrounding buildings in the construction process of the Zhuji tunnel step method [12–14].

In this study, taking the intersection of Zhuhai dahengqinshan No. 1 tunnel and Zhuji urban rail tunnel as the engineering background, we used the ABAQUS finite element software to compare with the field monitoring data. This study systematically studied the influence of different blasting loads on the existing tunnel structure with a small clear distance.

2. Engineering Overview and Field Monitoring

2.1. Overview of Engineering Example. The Dahengqinshan Tunnel is located in Hengqin new area of Zhuhai City. It is one of the “aorta” of Hengqin Island. This section of tunnel is underneath the planned Zhuji urban rail tunnel on the right line YK1+281 and the left line ZK1+289, with a buried depth of about 100 m. The minimum vertical clearance between two tunnels is 3.5 m, and the position plane relation of the two tunnels is shown in Figure 1. The design standard of Dahengqinshan No. 1 tunnel is 60 km/h, which is a two-way 6-lane municipal tunnel of urban main road. The tunnel is constructed by spray anchor support, composite lining, and CRD method. The design standard of the Zhuji urban rail tunnel is 160 km/h double-track intercity railway, which is constructed by the step method.

2.2. Field Monitoring Projects. Because the blasting excavation of the Zhuji tunnel will cause the segment deformation of Hengqinshan Tunnel, which has a great influence on the stress change of the surrounding rock, reliable monitoring methods are needed to ensure personnel safety and tunnel construction efficiency. According to the engineering geological report and the construction characteristics of CRD method, the monitoring items of vault subsidence, arch foot displacement, and blasting vibration on the left line of Dahengqinshan Tunnel in cross section are set up (Figure 2).

3. Model Establishment

3.1. Model Simplification and Material Parameters. The construction conditions simulated in this study are as follows: after the second lining construction of Dahengqinshan Tunnel, which is a built tunnel, Zhuji urban rail tunnel passes through as a new tunnel. Using ABAQUS finite element software, based on the survey data of Dahengqinshan project and BIM model data, we establish a three-dimensional geological model to generate rock mass element. The model in this study is 240 m long, 100 m wide, and 135 m high (Figure 3). In Figure 3, the lower side is the Dahengqinshan double-track tunnel, and the upper side is the Zhuji tunnel. As some tunnel sections of Dahengqinshan No. 1 tunnel include SD2 and SD3 sections, and according to the project data, part of SD1 section is far away from the overlapping intersection of the two tunnels, and the impact is far less than the overlapping intersection; Dahengqinshan Tunnel is simplified to only SD2 and SD3 sections in this simulation. Considering that the influence of elevation

difference caused by tunnel slope on the calculation is also quite small, the model is simplified with no slope. On the other hand, due to the buried depth of the Hengqinshan Tunnel, considering the influence range of the tunnel construction and the fact that the surface is undulating but basically on the same horizontal plane, the top of the model is simplified to a plane. In ABAQUS modeling and calculation, the tunnel lining adopts plate shell element and C35 concrete material, which is calculated according to the elastic constitutive model, and the soil around the tunnel adopts solid element and the modified Mohr–Coulomb model. According to the results of field tests and investigation reports, the specific material parameters of the model are shown in Table 1.

3.2. Boundary Condition. After analysis, the soil adopts tetrahedral elements with 1380685 grids and 30851 elements in total. The model grid diagram is shown in Figure 4. In the simulation process, the tectonic stress of soil is not considered, and only the self-weight of soil is considered as the initial ground stress. Constraints in three directions are imposed on the bottom surface of the model, and displacement constraints in the normal direction of the corresponding surface are imposed on the model side. The role of constraints is to make the constraints on the model area consistent with the actual rock-soil interaction.

3.3. Explosive Load. In this study, the triangular load model [15–17] is selected to simulate the influence of blasting stress wave on the surrounding rock. The pressure load changing with time is applied along the wall of the Zhuji urban rail tunnel to simulate the impact caused by blasting. The load loading diagram and load curve diagram are shown in Figures 5 and 6 respectively.

The peak value of explosive load is determined by explosive density, explosive velocity, explosive roll diameter, and hole diameter. According to the theoretical calculation method [18], the peak value of blast hole under the condition of noncoupling charge is calculated according to the following equation:

$$P_b = \frac{1}{8} \rho_0 D^2 \left(\frac{R_c}{R_b} \right), \quad (1)$$

where P_b is the peak pressure of blast hole, ρ_0 is the explosive density, D is the detonation velocity of explosive, R_c and R_b are the radius of charge roll and blast hole respectively, η is the increasing multiple of the collision between explosive gas and hole wall, and its value range is $\eta = 8 \sim 11$.

According to reference [18–20], the pressure load formula equivalent to the pressure load on the centerline of blast hole is

$$P_e = \left(\frac{2r_0}{a} \right) P_b, \quad (2)$$

where P_e is the equivalent pressure, r_0 is the hole radius, and a is the hole spacing.

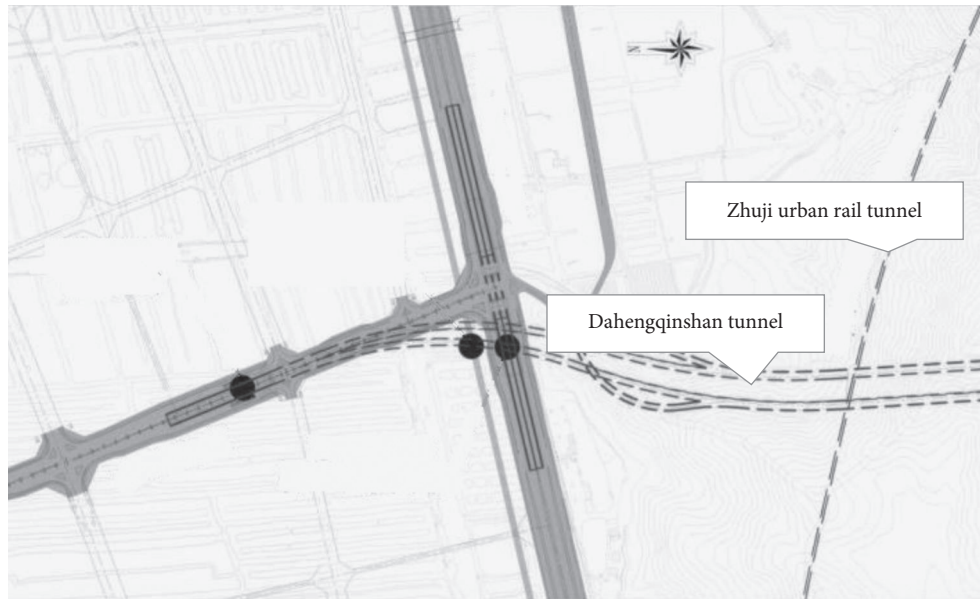


FIGURE 1: Plane relation diagram of tunnel position.

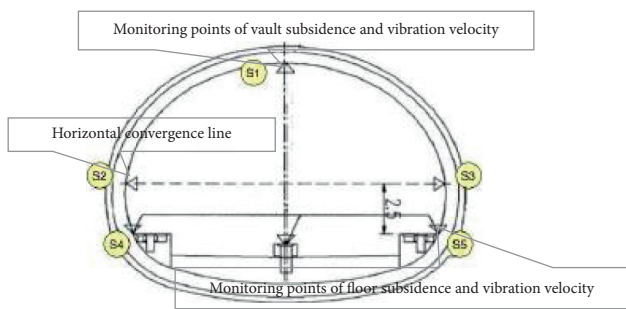


FIGURE 2: Layout of displacement measuring points on the left line of Dahengqinshan Tunnel.

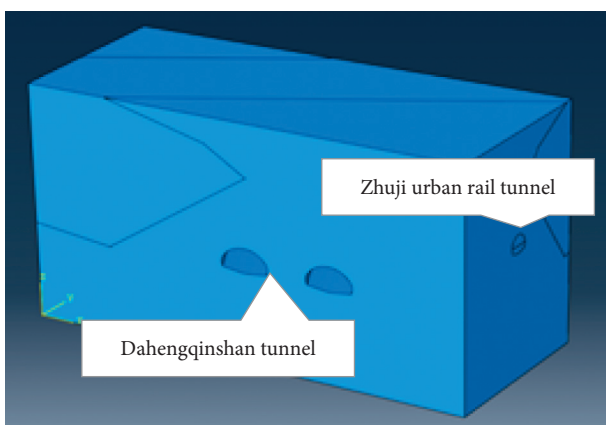


FIGURE 3: Overview of the tunnel model.

4. Influence Analysis of Blasting Peak Load

4.1. Selection of Monitoring Points and Excavation Sections. In order to determine the maximum impact effect on the tunnel, monitoring points are arranged on a section

(ZK1 + 252) of the left line of Dahengqinshan Tunnel directly below the Zhuji urban rail tunnel. Five monitoring points are arranged at the vault, left arch waist, right arch waist, left arch foot, and right arch foot on ZK1 + 252 section, with numbers of 9851, 1108, 970, 191, and 487 respectively. Figure 7 shows the location of monitoring points and the direction of tunnel excavation.

In tunnel construction, it is generally believed that, within the range of 3–5 times of tunnel diameter, the influence of tunnel construction is quite obvious, and it can be considered that the construction has little impact on the surrounding environment beyond the range of 3–5 times the tunnel diameter [21, 22]. Therefore, as shown in Figure 8, the Zhuji urban rail tunnel is divided into 16 sections from left to right in the X direction. The excavation depth of each section is 15 m, and the total length of the Zhuji urban rail tunnel is 240 m. The 16 sections correspond to the excavation depth of the Zhuji tunnel in turn: 15 m, 30 m, 45 m, 60 m, 75 m, 90 m, 105 m, 120 m, 135 m, 150 m, 165 m, 180 m, 195 m, 210 m, 225 m, and 240 m, so as to analyze the impact of drilling and blasting construction of the Zhuji urban rail tunnel on the left line of Dahengqinshan Tunnel. This section analyzes the dynamic influence of the continuous excavation of the Zhuji tunnel under the peak load of 5 MPa and 10 MPa on the left line structure of Dahengqinshan Tunnel.

4.2. Tunnel Construction Process

- (1) The first analysis step: the soil layer was established, the soil layer parameters were given, the boundary conditions, were imposed, and then the initial in situ stress balance was carried out.
- (2) According to 16 sections, the excavation of each section of the Zhuji tunnel corresponds to one analysis step, with a total of 17 steps.

TABLE 1: Material parameters.

Name of soil layer	Volumetric weight (kN/m ³)	Constitutive model	Elastic modulus (GPa)	Poisson ratio	Friction angle (°)	Cohesion (MPa)
Granite fracture zone	25.6	Modified Mohr-Coulomb	2.3	0.25	30	22
Moderately weathered granite	25.6	Modified Moore-Coulomb	4.72	0.19	37	35
C35 concrete	24	Linear elasticity	31.5	0.19	-	-

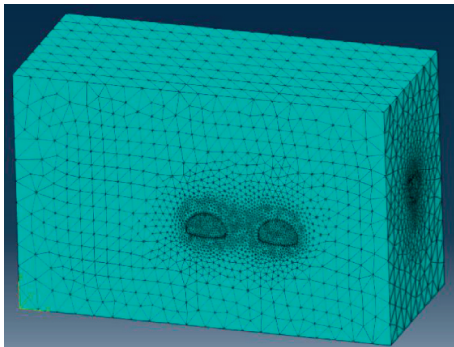


FIGURE 4: Model grid diagram.

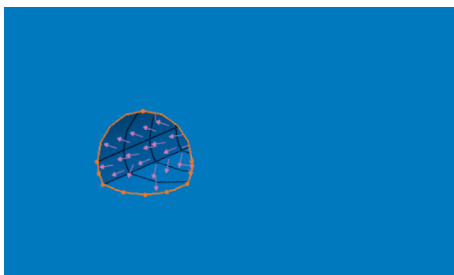


FIGURE 5: Schematic diagram of load loading.

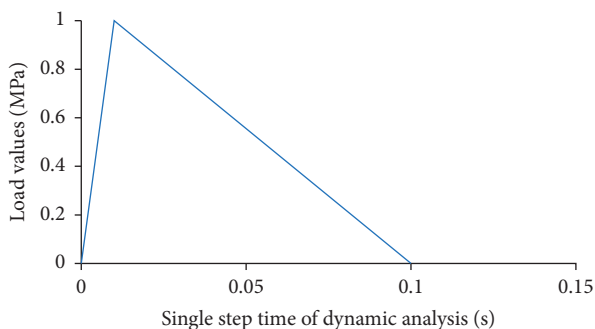


FIGURE 6: Schematic diagram of load curve.

(3) When the function of making the element disappear is to be realized, ABAQUS software will multiply the corresponding part of the overall stiffness matrix by a fairly small coefficient, and the mass, stress, strain, damping, and output element load will also be zero. “Activation” is to realize the reappearance effect of the element by changing the stiffness of the element

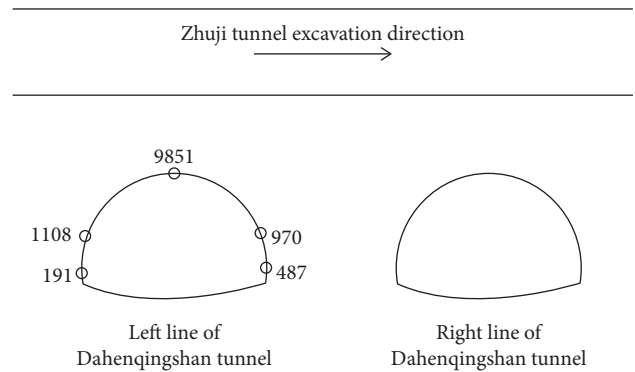


FIGURE 7: Corresponding position of point number.



FIGURE 8: Schematic diagram of tunnel excavation direction and depth.

in the whole. Using this method, the process simulation of tunnel excavation can be realized.

4.3. Numerical Simulation Results

(1) When the peak load is 10 MPa, the relationship between the excavation depth of the Zhuji tunnel and the Mises stress, and vertical displacement and blasting speed of each monitoring point is shown in Figure 9. In Figure 9(a), the peak stress of Mises at the vault is the largest, which is 34 MPa, corresponding to the monitoring point 9851. The peak stress of the arch foot on both sides is the second, corresponding to the monitoring point 191 and the monitoring point 478, and the peak stress is 18 MPa and 12 MPa, respectively. As shown in Figure 9(b), the maximum vertical displacement of the arch vault

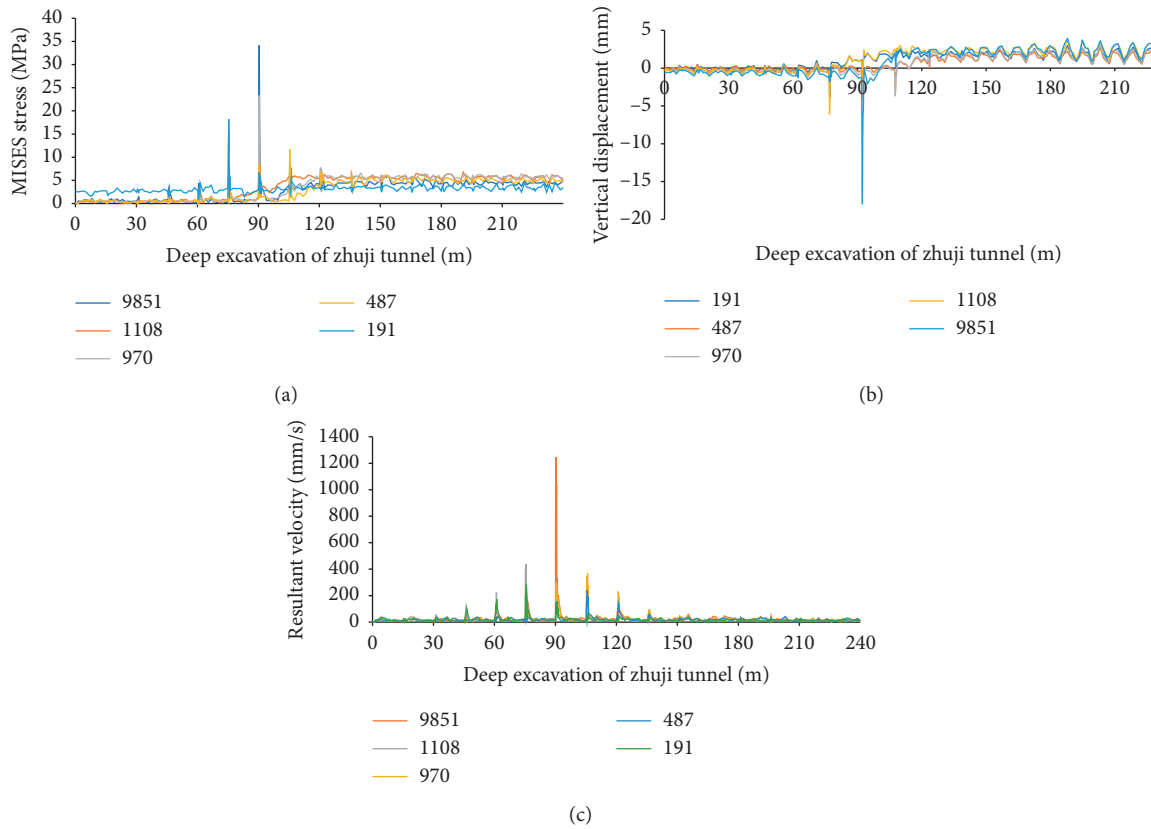


FIGURE 9: Numerical simulation results under 10 MPa peak load. (a) Mises stress excavation-excitation depth curve. (b) Vertical displacement-excitation depth curve. (c) Resultant velocity-excitation depth curve.

is 18 mm. The maximum vertical displacement measured at the left arch waist monitoring point 1108 is 6 mm, and the right arch waist monitoring point 970 is 3.7 mm. The displacement direction is downward.

As for the speed of each section, it can be seen from Figure 9(c) that the speed measured at the monitoring point 9851 on the top of the tunnel at the excavation depth of 90 m is the largest, reaching 1246 mm/s. The peak velocities measured by the monitoring points 970 and 1108 at the left and right arch waists are also quite high, which are 368 mm/s and 439 mm/s respectively.

- (2) When the peak load is 5 MPa, the calculation results are shown in Figure 10. Similar to the calculation results of peak load of 10 MPa, the maximum stress peak value measured at the top monitoring point of tunnel is 16.7 MPa (Figure 10(a)). The results measured at monitoring point 970 are the second, and the peak stress is 12 MPa. The Mises stress value of each monitoring point after excavation is relatively stable, and its value is between 4 and 6 MPa. As shown in Figure 10(b), the maximum displacement peak is monitoring point 9851, which is 9.3 mm, and the larger value point is 1108, which is 3 mm.

For the speed of each section, the maximum velocity peak is monitoring point 9851, the value is 625 mm/s,

followed by two monitoring points 970 and 1108, and the values are 184 mm/s and 220 mm/s.

4.4. Analysis. Compared with Figures 9 and 10, it can be seen that the peak load of 5 MPa graphic trend is basically consistent with 10 MPa. When the blasting peak load is reduced from 10 MPa to 5 MPa, the Mises stress at the vault is reduced by 51%, the vertical displacement is reduced by 48%, and the maximum resultant velocity is reduced by 50%. The vertical displacement and maximum velocity of the left arch waist are reduced by 50%, and the right arch waist is also reduced by 50%. When the peak load is reduced by half, the maximum Mises stress peak, vertical displacement, and resultant velocity are basically reduced by half. It can be seen that the value of the peak load has a great influence on the existing tunnel. By reducing the peak load of blasting appropriately, we can ensure the safety of the existing tunnel and the construction efficiency of the tunnel under construction.

Combined with the analysis of the numerical simulation results, the Mises stress value, vertical displacement, and resultant velocity all reached the peak value at the excavation depth of 90 m in the Zhuji tunnel. This is because when the excavation depth reaches 90 m, Zhuji urban rail tunnel is closest to the left line of Dahengqinshan, which has the greatest disturbance to the existing tunnel. Before the excavation depth of 90 m, the vertical deformation of each

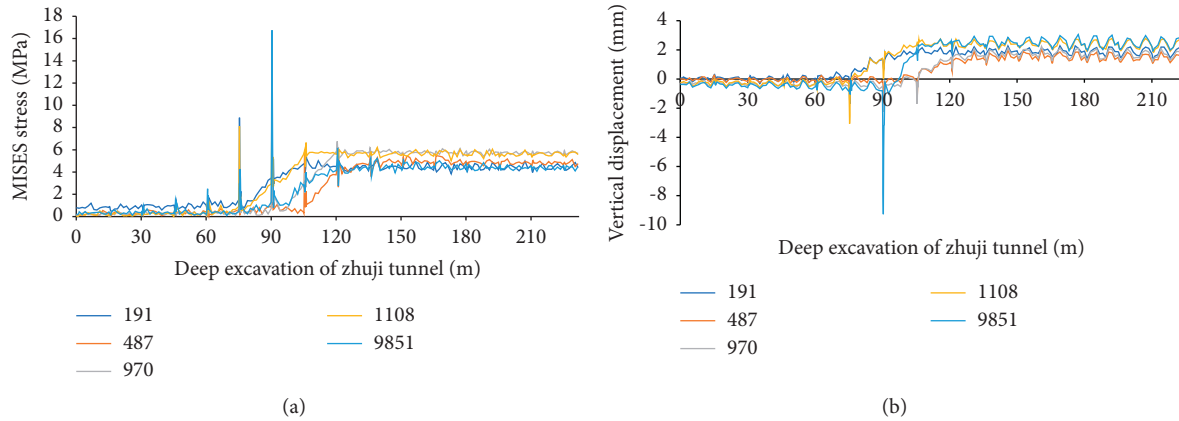


FIGURE 10: Numerical simulation results under 10 MPa peak load. (a) Mises stress excavation-excitation depth curve. (b) Vertical displacement-excitation depth curve.

point is settlement and increases with the increase of excavation depth. After 90 m, with the increase of excavation depth, each measuring point shows uplift and then tends to be stable. This is because the upper tunnel has been far away from the left line of the existing tunnel and constructed above the right line. At this time, the data of each measuring point of the right line tunnel are the same as the vertical deformation of the left line before the excavation depth of 90 m, which is manifested as settlement. Due to stratum loss, the left line tunnel bulges at this time. In addition, when the excavation depth is 60 m to 180 m in the middle section, the dynamic effect is more obvious.

5. Application Research

It can be seen from partial explosive parameters in Table 2 that when the ratio of cartridge to blast hole is 0.5, the peak value of equivalent load can be calculated as 2.7 MPa by equations (1) and (2).

Under the influence of blasting construction of small clear distance tunnel, the existing tunnel will produce vibration, and the vibration velocity is the main parameter to analyze and evaluate the dynamic influence [23–25].

In the numerical simulation analysis of this study, the vibration velocity corresponds to the resultant velocity in the output results. The resultant velocity is a scalar whose value is the vector sum of the velocities in three directions. According to the specification [26–28] and the engineering data of the Hengqinshan Tunnel project, the maximum vibration velocity of the tunnel is required to be 15 cm/s.

Therefore, the main purpose of this study is to calculate the maximum vibration velocity corresponding to each excavation section during the excavation of Dahengqinshan Tunnel passing through the existing tunnel. And we compare it with the maximum vibration velocity vibration value required by the specification, so as to simulate whether the vibration of the existing tunnel during the construction of small spacing drilling and blasting method meets the engineering requirements. As shown in Table 3, we select and analyze the resultant velocity values of each measuring point

corresponding to the five excavation depths that have the greatest impact on the left line of Dahengqinshan Tunnel.

It can be seen from Table 3 that the monitoring points at different positions of the tunnel section have different maximum resultant velocity values during the process of the Zhuji urban rail tunnel crossing above the left line of the Dahengqinshan Tunnel. The maximum resultant velocity calculated by the measuring point 9851 at the vault is 11.28 cm/s, which is greater than the other four measuring points. The resultant velocity of the five measuring points on the cross section reaches the peak under different excavation depths of the Zhuji tunnel. Among them, the measuring point 9851 reached the peak at the depth of 78 m, and then the Zhuji tunnel continued to be excavated. With the increase of excavation depth, the closing speed at the vault decreased [29–31]. The simulated resultant velocity of the left arch waist measuring point 1108 and the left arch foot measuring point 191 reaches the maximum at the depth of 60 m of tunnel excavation, which are 2.54 cm/s and 3.91 cm/s, respectively. The maximum velocity of the right arch waist 970 is 3.49 cm/s, which is obtained at the excavation depth of 84 m. The right arch foot measuring point 487 reaches the maximum speed of 1.97 cm/s at the excavation depth of 90 m.

The resultant velocity of the measuring point 9851 at vault under different excavation depths is greater than that of the other four measuring points [32, 33]. This is because the stress wave caused by the blasting load of the tunnel will continue to decay along the distance in the process of transmission in the rock stratum, and the distance from the vault to the tunnel is shorter than that from the arch waist and arch foot to the tunnel. Similarly, the resultant velocity of measuring points 1108 and 970 located at arch waist is larger than that of measuring points at the arch foot, which is also because the distance from the stress wave to the arch waist is shorter than that to the arch foot. Compared with the speed limit of 15 cm/s given above, the simulation values of each monitoring point on the left line are less than 15 cm/s. So it is more appropriate to use the peak load of 2.7 MPa for construction.

Therefore, the construction of the Zhuji urban rail tunnel has the greatest impact on the vault of the left line section

TABLE 2: Partial explosive parameters.

Name of explosive	Cartridge diameter (mm)	Explosive density (g/cm ³)	Explosive detonation velocity (m/s)
EL-102 emulsion oil	20	1.05	3500
No. 2 rock explosive	22	1.1	2100~3000
No. 3 rock explosive	22	1.0	1600~1800

TABLE 3: Maximum closing speed of each monitoring point.

Excavation depth (m)	Resultant velocity (cm/s)				
	191	1108	9851	970	487
54	2.27	3.87	1.68	0.49	0.35
60	2.54	3.91	3.61	0.83	0.35
78	1.39	2.94	11.28	3.11	1.15
84	0.82	1.78	10.72	3.49	1.67
90	0.68	1.29	5.89	3.31	1.97
Maximum	2.54	3.91	11.28	3.49	1.97

TABLE 4: Maximum vibration velocity component of monitoring points at tunnel vault.

Monitoring location	Vibration (cm/s)		
	X direction	Y direction	Z direction
Vault (ZK1 + 252)	8.17	4.73	6.85

(ZK1 + 252) of Dahengqinshan Tunnel. The maximum value of vibration velocity in the field monitoring data of the monitoring point at the vault of this section is sorted out in Table 4. It can be seen that the relative error between the field monitoring data and the numerical simulation results at the vault is less than 5%, and the monitoring results of the actual project are less than the vibration velocity limit (15 cm/s) required by the specification, which can be in good agreement. It shows that the numerical simulation is more accurate and can reflect the vibration rate distribution law of different locations of the existing tunnel structure in the construction of small spacing tunnel drilling and blasting method. Taking the numerical simulation results of finite element software as the reference value, the safety accident prevention of tunnel overlapping cross section can be greatly improved.

6. Conclusions

Based on the Zhuhai Dahengqinshan No. 1 tunnel and Zhuji urban rail tunnel project, according to the field investigation results, this study used ABAQUS finite element software to simulate the tunnel drilling and blasting construction and systematically studied the influence of the existing tunnel structure caused by the blasting peak load. After a comprehensive analysis, the following main conclusions are as follows:

- (1) The blasting peak load has different effects on the measuring points in different parts of the tunnel structure, and the blasting of the tunnel under construction has the greatest influence on the vault of the existing tunnel section.
- (2) When the blasting peak load is reduced from 10 MPa to 5 MPa, the Mises stress, vertical displacement, and resultant velocity of each measuring point on the left section of Dahengqinshan Tunnel (ZK1 + 252) are basically reduced by half.
- (3) The Mises stress value, vertical displacement, and combined velocity of each measuring point reached the peak at 90 m depth of Zhuji tunnel excavation and then decreased and stabilized with the increase of excavation depth.
- (4) When the peak load is 2.7 MPa, the measured value and the simulated value are less than the speed limit (15 cm/s) required by the specification, and the relative error between the measured value and the simulated value is less than 5%. It is appropriate to use the load peak of 2.7 MPa for construction.

Data Availability

The data used to support the findings of this study are available from the corresponding author upon request.

Conflicts of Interest

The authors declare that they have no conflicts of interest regarding the publication of this study.

Acknowledgments

The authors would gratefully like to acknowledge the support provided by the National Natural Science Foundation of China (no. 51978177) and by the Key R&D projects of Zhuhai Dahengqin Co., Ltd. (no. SG88-2018-444B3).

References

- [1] J. Wang, F. Wu, and D. Qiu, "Construction technology and development prospect of underground space in China," *Architectural Technology*, vol. 49, no. 6, pp. 578–580, 2018.
- [2] Q.C Zhang, Z. Dai, and Y. Shi, "Key technologies of new tunnel close crossing existing metro tunnel," *Journal of railway engineering*, vol. 37, no. 6, pp. 58–63, 2020.
- [3] X. Jia, F. Xin, and J. Zheng, "Study on design and construction technology of small clear distance parallel stacked mine tunnel," *Urban rapid rail transit*, vol. 34, no. 5, pp. 111–118, 2021.
- [4] J. Li, "Key technologies of tunnel excavation and support by drilling and blasting method," *China highway*, vol. 11, pp. 87–89, 2020.
- [5] C. Zhang, X. Zhu, and S. Peng, "Key technologies for construction of small clear distance mining tunnel under existing buildings," *Sichuan architecture*, vol. 41, no. 3, pp. 229–231, 2021.

- [6] X. Wang, W. Wang, and D. Du, "Study on fluid structure coupling of small clear distance interchange tunnel," *Journal of disaster prevention and mitigation engineering*, vol. 38, no. 4, pp. 700–708, 2018.
- [7] Ji. Ling, C. Zhou, S. Lu, N. Jiang, and H. Li, "Modeling study of cumulative damage effects and safety criterion of surrounding rock under multiple full-face blasting of a large cross-section tunnel," *International Journal of Rock Mechanics and Mining Sciences*, vol. 147, 2021.
- [8] H. Wang, Y. Wang, M. Wang, and Q. Zong, "Numerical analysis of the influence of foundation pit blasting on a nearby metro tunnel," *Shock and Vibration*, vol. 2021, Article ID 5585726, 15 pages, 2021.
- [9] R. Wang, D. Yuan, F. Dang et al., "Influence scope of blasting vibration for construction of new tunnel undercrossing existing roads," *Rehabilitation Medicine*, vol. 34, no. 3, pp. 238–244, 2017.
- [10] H. Ruijun, "Dynamic response analysis of small clear distance tunnel under blasting load," *Water resources and hydropower technology*, vol. 51, no. S2, pp. 291–297, 2020.
- [11] L. Guitao, Z. Wang, Z. Song, and H. Yu, "Analysis of the influence of lately excavated tunnel blasting on the vibration of early excavated tunnel in small-space tunnel," *IOP Conference Series: Earth and Environmental Science*, vol. 643, no. 1, Article ID 012025, 2021.
- [12] B. Bai, G. Yang, and G. Yang, "A thermodynamic constitutive model with temperature effect based on particle rearrangement for geomaterials," *Mechanics of Materials*, vol. 139, Article ID 103180, 2019.
- [13] B. Yuan, M. Sun, L. Xiong, Q. Luo, S. P. Pradhan, and H. Li, "Investigation of 3D deformation of transparent soil around a laterally loaded pile based on a hydraulic gradient model test," *Journal of Building Engineering*, vol. 28, no. 3, Article ID 1010124, 2020.
- [14] X. Que, Z. Zhu, and W. Lu, "Anisotropic constitutive model of pentagonal prism columnar jointed rock mass," *Bulletin of Engineering Geology and the Environment*, vol. 79, no. 1, pp. 269–286, 2020.
- [15] M. Sheng, Y. Yao, and J. Sun, "Experimental study on far zone explosion load of blast hole during borehole blasting," *Blasting*, vol. 36, no. 3, pp. 1–8, 2019.
- [16] X. Que, Z. Zhu, Z. Niu, and W. Lu, "Estimating the strength and deformation of columnar jointed rock mass based on physical model test," *Bulletin of Engineering Geology and the Environment*, vol. 80, no. 2, pp. 1557–1570, 2021.
- [17] S. Luo, Y. Peng, and W. Lu, "Numerical simulation of blasting damage and damage mechanism in deep tunnel excavation," *Journal of rock mechanics and engineering*, vol. 40, no. S1, pp. 2760–2772, 2021.
- [18] L. Tao, *Urban Underground Engineering*, Science Press, Beijing, China, 2011.
- [19] B. Bai, D. Rao, T. Chang, and Z. Guo, "A nonlinear attachment-detachment model with adsorption hysteresis for suspension-colloidal transport in porous media," *Journal of Hydrology*, vol. 578, Article ID 124080, 2019.
- [20] C. Cui, K. Meng, C. Xu, Z. Liang, H. Li, and H. Pei, "Analytical solution for longitudinal vibration of a floating pile in saturated porous media based on a fictitious saturated soil pile model," *Computers and Geotechnics*, vol. 131, Article ID 103942, 2021.
- [21] L. Wang, Li Xiang, F. Guo, S. Tang, X. Lu, and A. Hanif, "Influence of reactivity and dosage of MgO expansive agent on shrinkage and crack resistance of face slab concrete," *Cement and Concrete Composites*, vol. 2022, Article ID 104333, 2021.
- [22] J. Xiao, W. Qu, H. Jiang, L. Li, J. Huang, and L. Chen, "Fractal characterization and mechanical behavior of pile-soil interface subjected to sulfuric acid," *Fractals - Complex Geometry, Patterns, and Scaling in Nature and Society*, vol. 29, no. 2, Article ID 2140010, 2021.
- [23] I. D. Isaac and C. T. T. Bubb, "Engineering aspects of underground cavern excavation at Dinorwic - Part 3. A study of blast vibrations, Part 1," *International Journal of Rock Mechanics and Mining Sciences & Geomechanics Abstracts*, vol. 18, no. 6, 1981.
- [24] B. Yuan, Z. Li, Z. Su, Q. Luo, M. Chen, and Z. Zhao, "Sensitivity of multistage fill slope based on finite element model," *Advances in Civil Engineering*, vol. 2021, Article ID 6622936, 13 pages, 2021.
- [25] B. Bai, R. Zhou, G. Cai, W. Hu, and G. Yang, "Coupled thermo-hydro-mechanical mechanism in view of the soil particle rearrangement of granular thermodynamics," *Computers and Geotechnics*, vol. 137, no. 8, Article ID 104272, 2021.
- [26] Y. Wu, J. Cui, J. Huang, W. Zhang, N. Yoshimoto, and L. Wen, "Correlation of critical state strength properties with particle shape and surface fractal dimension of clinker ash," *International Journal of Geomechanics*, vol. 21, no. 6, Article ID 04021071, 2021.
- [27] GB 6722-2014, *Safety Regulations for Blasting*, State Standardization Publishing House, Beijing, China, 2014.
- [28] B. Yuan, Z. Li, Z. Zhao, H. Ni, Z. Su, and Z. Li, "Experimental study of displacement field of layered soils surrounding laterally loaded pile based on Transparent Soil," *Journal of Soils and Sediments*, vol. 21, no. 9, pp. 3072–3083, 2021.
- [29] K. Meng, C. Cui, Z. Liang, H. Li, and H. Pei, "A new approach for longitudinal vibration of a large-diameter floating pipe pile in visco-elastic soil considering the three-dimensional wave effects," *Computers and Geotechnics*, vol. 128, Article ID 103840, 2020.
- [30] B. Yuan, Z. Li, Y. Chen et al., "Mechanical and microstructural properties of recycling granite residual soil reinforced with glass fiber and liquid-modified polyvinyl alcohol polymer," *Chemosphere*, vol. 268, Article ID 131652, 2021.
- [31] B. Bai, Q. Nie, X. Wang, and W. Hu, "Cotransport of heavy metals and SiO₂ particles at different temperatures by seepage," *Journal of Hydrology*, vol. 597, Article ID 125771, 2021.
- [32] B. Yuan, C. Rui, G. Deng, T. Peng, Q. Luo, and X. Yang, "Accuracy of interpretation methods for deriving p-y curves from model pile tests in layered soils," *ASTM Journal of Testing and Evaluation*, vol. 45, no. 4, pp. 1238–1246, 2017.
- [33] B. Yuan, M. Sun, Y. Wang, L. Zhai, Q. Luo, and X. Zhang, "Full 3D displacement measuring system for 3D displacement field of soil around a laterally loaded pile in transparent soil," *International Journal of Geomechanics*, vol. 19, no. 5, Article ID 04019028, 2019.